Lecture Notes in Civil Engineering

Scott Walbridge · Mazdak Nik-Bakht · Kelvin Tsun Wai Ng · Manas Shome · M. Shahria Alam · Ashraf el Damatty · Gordon Lovegrove *Editors*

Proceedings of the Canadian Society of Civil Engineering Annual Conference 2021

CSCE21 General Track Volume 2

Springer

Lecture Notes in Civil Engineering

Volume 240

Lecture Notes in Civil Engineering (LNCE) publishes the latest developments in Civil Engineering - quickly, informally and in top quality. Though original research reported in proceedings and post-proceedings represents the core of LNCE, edited volumes of exceptionally high quality and interest may also be considered for publication. Volumes published in LNCE embrace all aspects and subfields of, as well as new challenges in, Civil Engineering. Topics in the series include:

- Construction and Structural Mechanics
- Building Materials
- Concrete, Steel and Timber Structures
- Geotechnical Engineering
- Earthquake Engineering
- Coastal Engineering
- Ocean and Offshore Engineering; Ships and Floating Structures
- Hydraulics, Hydrology and Water Resources Engineering
- Environmental Engineering and Sustainability
- Structural Health and Monitoring
- Surveying and Geographical Information Systems
- Indoor Environments
- Transportation and Traffic
- Risk Analysis
- Safety and Security

To submit a proposal or request further information, please contact the appropriate Springer Editor:

– Pierpaolo Riva at pierpaolo.riva@springer.com (Europe and Americas);
– Swati Meherishi at swati.meherishi@springer.com (Asia - except China, and Australia, New Zealand);
– Wayne Hu at wayne.hu@springer.com (China).

All books in the series now indexed by Scopus and EI Compendex database!

More information about this series at https://link.springer.com/bookseries/15087

Scott Walbridge · Mazdak Nik-Bakht ·
Kelvin Tsun Wai Ng · Manas Shome ·
M. Shahria Alam · Ashraf el Damatty ·
Gordon Lovegrove
Editors

Proceedings of the Canadian Society of Civil Engineering Annual Conference 2021

CSCE21 General Track Volume 2

Springer

Editors
Scott Walbridge
University of Waterloo
Waterloo, ON, Canada

Kelvin Tsun Wai Ng
University of Regina
Regina, SK, Canada

M. Shahria Alam
University of British Columbia - Okanagan Campus
Kelowna, BC, Canada

Gordon Lovegrove
University of British Columbia - Okanagan Campus
Kelowna, BC, Canada

Mazdak Nik-Bakht
Concordia University
Montreal, QC, Canada

Manas Shome
Matrix Solutions Inc.
Edmonton, AB, Canada

Ashraf el Damatty
University of Western Ontario
London, ON, Canada

ISSN 2366-2557 ISSN 2366-2565 (electronic)
Lecture Notes in Civil Engineering
ISBN 978-981-19-0506-3 ISBN 978-981-19-0507-0 (eBook)
https://doi.org/10.1007/978-981-19-0507-0

This Springer imprint is published by the registered company Springer Nature Singapore Pte Ltd.
The registered company address is: 152 Beach Road, #21-01/04 Gateway East, Singapore 189721, Singapore

Contents

About the Editors

Dr. Scott Walbridge Ph.D., P.Eng. (Alberta) is a Professor at the University of Waterloo, where he has worked since completing his Ph.D. at the EPFL in Lausanne, Switzerland in 2005/6. Dr. Walbridge currently serves as Technical Committee (TC) Vice-Chair for the CSA S157 Design Code (Strength Design of Aluminum Structures) and TSC Chair for CSA S6 (Canadian Highway Bridge Design Code) Section 17 (Aluminum Structures). He is also a member of CSA W59 and W59.2 (Canadian structural steel and aluminum welding codes). In addition to his work on various structural design codes, he also currently serves as the Program Director for the University of Waterloo's new undergraduate program in Architectural Engineering. His research has investigated topics in various areas including: fatigue of steel and aluminum welded connections, performance of steel and aluminum mechanical connections, vibration of aluminum pedestrian bridges, and stability of aluminum structures. He was awarded an Alexander von Humboldt Fellowship related to his research on metal fatigue in 2016–2017.

Dr. Mazdak Nik-Bakht is an Associate Professor of Construction Engineering & Management in the Department of Building, Civil and Environmental Engineering at Concordia University, Montreal. He is the director of Compleccity Lab and a co-director of Centre for Innovation in Construction and Infrastructure Engineering & Management (CICIEM) at Gina Cody School of Engineering & Computer Science. He has a Ph.D. in Construction Engineering & Management from the University of Toronto (2015), as well as a Ph.D. in Structural Engineering from Iran University of Science and Technology (2011). Dr. Nik-Bakht is a licensed Professional Engineer with Professional Engineers Ontario and has years of professional experience as a structural designer, structural engineering division head, and project manager in structural & infrastructure rehabilitation projects. A new course called 'Big Data Analytics for Smart City Infrastructure' to train the next generation of construction and infrastructure engineering professionals was developed by him in 2019 and has been delivered annually ever since.

Dr. Kelvin Tsun Wai Ng is Professor of Environmental Systems Engineering at University of Regina, Canada. His major fields of interest are in waste management and environmental sustainability, particularly in development of (i) sustainable waste management system, (ii) evidence-based waste policy, and (iii) data-driven waste collection and disposal methods. His projects have been funded by a number of provincial and federal agencies, including NSERC, Mitacs, Communities of Tomorrow, Innovation Saskatchewan, Ministry of Environment, and City of Regina, etc. Dr. Ng is a Professional Engineer with Permission to Consult in Saskatchewan, Canada. He is also the instructor for a number of popular courses at the Faculty of Engineering, and has received the 2017 President's Award for Teaching Excellence.

Manas Shome Ph.D., P.Eng. is a Principal Engineer at Matrix Solutions, a Calgary based environmental engineering consulting firm. Based in Edmonton, he provides technical leadership on water resources engineering projects. He obtained a B.Sc. and M.Sc. in Civil Engineering at the Bangladesh University of Engineering and Technology and earned his Ph.D. in Civil Engineering from the University of Alberta in 1995. His professional experience includes more than 30 years in sustainable water resources management, river engineering, computational modelling of rivers and drainage systems, design of hydraulic structures and environmental impact assessment studies. An expert in the field of hydrology and hydraulic engineering, he frequently serves as an expert witness at regulatory hearings. Outside his consulting practice, Manas enjoys research, teaching, and watching sports. His research outcomes have been published in prestigious peer-reviewed journals, and in conference proceedings. He is a co-recipient of the 2010 Keefer Medal award and recipient of the 2015 Excellence in Teaching award from the University of Alberta's Faculty of Extension. He has been elected to the grade of Fellow by the CSCE in 2019. Manas has been involved with CSCE since 2000 serving on the Edmonton section in various roles including Chair, and on the organizing committee of the 2012 Annual Conference in Edmonton, Alberta.

Dr. M. Shahria Alam is a Professor of Civil Engineering at the University of British Columbia (UBC)'s Okanagan Campus and the Director of Green Construction Research & Training Center (GCRTC) at UBC. He is currently serving as the Chair of the Engineering Mechanics & Materials (EMM) division of the Canadian Society for Civil Engineering (CSCE). His research interests include applications of smart materials like shape memory alloys and sustainable construction materials, performance-based design, repair/retrofit of structures, and self-centering structures. Dr. Alam is the Director of the Applied Laboratory for Advanced Materials & Structures (ALAMS) at UBC. He has authored over 250 peer-reviewed articles and holds several patents. He is the recipient of several national and international awards including CSCE's Pratley Award. He is also an active member of several ACI and ASCE code committees.

Dr. Ashraf el Damatty Professor and Chair of the Department of Civil and Environmental Engineering at the University of Western Ontario, London, Ontario, Canada. He is a Fellow of the Canadian Society of Civil Engineering and Fellow of the Engineering Institute of Canada. He is a Research Director at the WindEEE Research Institute. He holds the title of High-End Expert at Tongji University and Sichuan Universities, China. He obtained a BSc. and M.Sc. from Cairo University in 1986 and 1991, Ph.D. in Structural Engineering from McMaster University, Canada, in 1995, and an MBA in 2016 in Higher Education Management from University College, London, UK. He is the founder of the Canadian Society of Civil Engineering (CSCE) Steel Structures Committee and serves currently as the Chair of the CSCE Structures Division. Dr. El Damatty has consulted on many projects in North America and the Middle East. He has written about 250 publications, supervised more than 30 Ph.D. and 20 M.Sc. students and has been invited as keynote speaker in many countries around the globe. He received several awards including the Alan Yorkdale Award by ASTM, Honourable Mention in 2014 Casimir Gzowski Medal Competition, 2015 CSCE Whitman Wright Award, 2016 CSCE Horst Leipholz Medal and Western University Faculty Scholar Award, and the 2018 professional Engineers of Ontario Engineering Medal of Research of Development. His research work has influenced the international codes and engineering practice worldwide.

Dr. Gordon Lovegrove is an MBA/Civil Engineer with over 30 years of experience in smarter growth, housing, sustainable transportation, safety, economics, and project management. Dr. Lovegrove was the point man that got the award-winning Universal Transportation Pass (U-Pass) for UBC that tripled transit use at both campuses. His current research focus is on zero-emission, hydrogen-powered rail (hydrail), including several industry partnerships to develop Canada's first hydrail switcher locomotive. Dr. Lovegrove is founding partner of the SMARTer Growth Partnership (smartergrowthpartnership.ca), an Associate Professor / founding member of UBCO's School of Engineering (ok.ubc.ca), VP Technical Programs for the Canadian Society of Civil Engineering (csce.ca); and, co-author of several best practice guides on sustainable development, health, and safety. He brings 20 years of practical industry development experience plus 14 years of engineering research and design expertise. His research team includes electrical, mechanical, and civil engineering graduate students, plus computer science coders and research assistants.

Taloyoak, Nunavut—Sewage Treatment Feasibility Study

K. Johnson and D. Browne

1 Introduction

The Hamlet of Taloyoak is located on the Boothia Peninsula approximately 1,300 km west of Iqaluit and 1,200 km northeast of Yellowknife. Taloyoak had a population of approximately 1,029 in 2016, and this population is expected to grow over the next 20 years to reach a population of approximately 1,413 in 2040.

Wastewater from the community is currently trucked and discharged to a natural (non-engineered) series of ponds. The ponds ultimately discharge to a natural wetland system to the south, which flows into Spence Bay, which is within the St Roch Basin. The pond system has no flow control structures, so it operates as a continuous discharge facility in the summer months. During the winter months, freezing of the ponds causes the discharge to stop. From a wastewater process perspective, the ponds would be expected to operate as a continuous discharge facultative lagoon system during the summer months, and a sedimentation lagoon system during the winter months.

Concerns have been raised with the current wastewater management strategy. More specifically since the ponds do not have any flow control structures, there is a concern that the current natural series of ponds does not have capacity to store the current and future annual wastewater generation from the community.

K. Johnson (✉)
EXP, St. Albert, Canada
e-mail: ken.johnson@exp.com

D. Browne
Government of Nunavut, Pangnirtung, Canada

S. Walbridge et al. (eds.), *Proceedings of the Canadian Society of Civil Engineering Annual Conference 2021*, Lecture Notes in Civil Engineering 240,
https://doi.org/10.1007/978-981-19-0507-0_1

2 System Requirements

The proposed sewage treatment facility must meet the long-term needs of the Hamlet, as well as the regulatory requirements of the Hamlet's water license. The design horizon for the Taloyoak sewage lagoon was set 20 years ending in 2040 based upon design guidelines for Arctic lagoons. The 2016 population of the community was 1030 and the estimated population in 2040 is 1410.

The sewage generation for the purposes of design is based upon the recorded water use in the community. The recorded water use in Taloyoak over a three-year period from 2017 to 2019 was on average 47,327,000 L per year. Based upon a population of 1029 people (2016), the per capital water use is 126 L/capita/day (L/c/d). Based upon the 2040 population of 1410, the annual sewage generation is estimated to be 65,000 m^3.

The configuration selected for the passive facultative lagoon is a single cell, which retains the sewage for 10 to 12 months before discharge into a supplementary wetland treatment system. The Government of Nunavut is currently engaged in amending the community water license and effluent requirements to increase the allowable effluent concentrations discharged from the wastewater system. It should be noted that, based on research facilitated by the Government of Nunavut, effluent criteria of 120 mg/L BOD_5, 120 mg/L Total Suspended Solids, and 1.25 mg/L un-ionized ammonia are environmentally-appropriate effluent discharge limits for marine water bodies within the Territory of Nunavut. A conservative, more stringent requirement on effluent concentrations was applied to this design—specifically, 45 mg/L BOD_5, 45 mg/L Total Suspended Solids, 1.25 mg/L un-ionized ammonia, and 1×10^4 CFU/100 mL Fecal Coliforms at the downstream end of the wetland.

3 Review of Potential Sites

A total of six wastewater treatment facility sites (5 new sites and the existing lagoon) were identified and investigated. Sites 1, 2 and 5 were screened from further consideration due to a variety of issues including drainage related, access related, availability of a wetland area and community proximity.

The new two sites recommended for further assessment and that were subsequently approved by Hamlet Council were the focus of the feasibility study. The two sites, Site 3 and Site 4, were retained for further consideration due to their potential for developing a suitable facility and their opportunity to incorporate the existing wetland and ocean discharge point (Fig. 1).

Fig. 1 Wastewater sites considered in Taloyoak

4 Sites 3 and 4

Development of Site 3 would require the construction of an engineered single lagoon cell, and construction of a new access road. Discharge from the lagoon could be directed into the existing treatment ponds followed by supplemental treatment in the existing wetland. The site contains a seasonal stream that bisects the site, which would require consideration of runoff diversion around the site. Development of a lagoon on Site 3 may also require the removal of ice-rich soil and replacement with thaw stable material, as a measure to avoid thaw settlement due to permafrost degradation. It is further anticipated that there will be a requirement for the redirection of the drainage course and stabilization of the flow channel by removal, and replacement of the underlying saturated soil.

Development of Site 4 would require the construction of an engineered lagoon cell and construction of a new access road. Discharge from the lagoon could be directed into the existing treatment ponds followed by supplemental treatment in the existing wetland. The site is overlain by tundra, with surficial boulders and it is reported that most of the site is well drained with no evidence of contained moisture. Soils are reported as sand to silty sand with gravel and occasional cobbles and boulders, and soil depth is reported as approximately 1 m to bedrock. The presence of granular materials on the site and the proximity of bedrock suggests that significant thaw settlement of any earth structures on the site is not anticipated.

Based upon the anticipated stability of the site, Site 4 was selected over Site 3 as the best location for the development of the new sewage lagoon.

5 Wetland Treatment

The anticipated performance of a stand-alone retention lagoon will not provide a discharge that is compliant with the ocean discharge criteria without additional supplemental treatment. A significant number of Nunavut communities make use of wetland systems are an effective means of achieving this supplemental treatment.

The ecological assessment of the existing wetland was conducted in July 2015 and noted that the wetland is achieving some improvement of the quality of the existing lagoon effluent. As part of the detailed design of the lagoon and wetland systems, the development of a wetland model specific to the wetland area will provide explicit estimates of the removal performance of biodegradable material, fecal coliforms, suspended solids, and nutrients.

6 Anticipated Lagoon Performance

The removal mechanisms within a facultative lagoon include both physical and biological processes. The physical process of sedimentation will remove BOD_5 and suspended solids through settling. Nunavut-specific cold climate studies have reported BOD_5 in the range of 25 to 180 mg/L and Total Suspended Solids ranging from 25 to 115 mg/L from sedimentation treatment in a single cell lagoon.

Over winter the lagoon will be covered by a significant layer of ice, and therefore, the only treatment process that may occur is sedimentation. In early summer no significant improvement in quality is anticipated during the period when the ice on the lagoon thaws. It is further anticipated that decanting of lagoon contents may start in August and should not start any later that early September to take advantage of the treatment process that can occur through an active wetland.

The period, over which biological improvements will occur, is estimated to be 45 days, which is consistent with the observed performance of other lagoons in Nunavut for effluent BOD_5 reduction in the period between of July, and September. It is further assumed that the lagoon contents will warm to 5 °C over this period. The BOD_5 in the decanted effluent is conservatively estimated at approximately 100 mg/L at the end of this 45-day period.

7 Anticipated Wetland Performance

The wetland downstream of the existing lagoon has an area of approximately 7.5 ha. The wetland is transected by a meandering, and slow-moving stream flowing in the north to south direction. Not all the wetland area may be incorporated into the wetland treatment activity, but the area may be maximized with the use of berm structures to disperse the flow and reduce the channelization. The anticipated performance of the

wetland is Total Suspended Solids 13 mg/L; Carbonaceous BOD 37 mg/L; Ammonia Nitrogen 0.21 mg/; Total Phosphorous 0.47 mg/L; and E.coli 181 cfu/100mls. The performance estimates for the wetland were based upon local studies that were benchmarked against an extensive data base of wetland performance information.

8 Lagoon Schematic Design

The recommended schematic design of a sewage retention lagoon is presented in Fig. 2. The lagoon is 260 m long and 160 m wide and operates with a 1 m freeboard. The berm structures have recommended slopes of 3.5:1 on the exterior, and 3:1 on the interior, and the lagoon will include a synthetic liner system. The working depth of the lagoon is 2 m, with an additional sludge zone of 1 m. The discharge system for the lagoon is a fuel driven pump system that pumps over the berm into the existing pond and wetland treatment system.

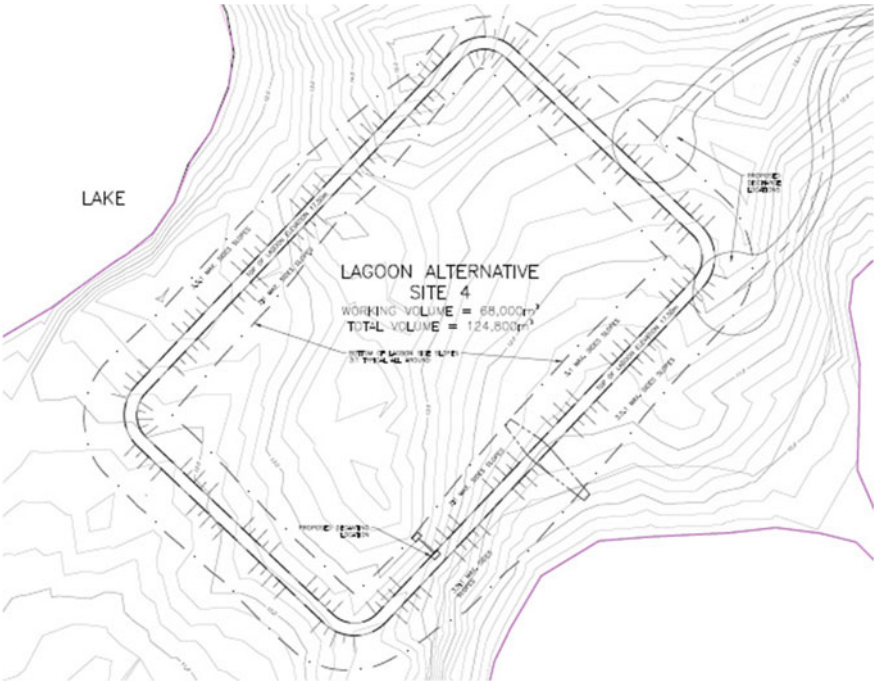

Fig. 2 Site 4 Schematic lagoon design

9 Conclusions and Recommendation

1. An initial list of 6 candidate sites for a wastewater facility was identified. Following an initial site review this list was screened to include only Site 3 and Site 4.
2. It is anticipated that a lagoon and wetland treatment system will provide an effluent that meets the effluent quality requirements.
3. The application of a 10–12 month retention lagoon system with impermeable berms and active (pumped) decanting is the most appropriate treatment system.
4. A minimum lagoon volume of 65,000 m^3 is required. This is in addition to allowances for freeboard and sludge storage.
5. Site 4 is recommended for advancing to detailed design.

Numerical Modelling of Reinforced Concrete Walls in Nuclear and Industrial Structures Under Seismic Loading

Mohamed Abouyoussef and Mohamed Ezzeldin

1 Introduction

The consequences of seismic events on reinforced concrete (RC) nuclear and industrial structures could be catastrophic. For example, Tōhoku Earthquake and Tsunami in Japan 2011 are the costliest natural disasters of all time, even without accounting for indirect losses, primarily because of the failure of the Fukushima Daiichi nuclear station. During the Maule, Chile 2010 and Christchurch, New Zealand 2011 seismic events, concrete crushing at RC wall boundary elements, global buckling of wall segments, and buckling and fracture of reinforcing bars were observed [1, 2]. This situation has created a critical need to quantify the seismic response of such critical structures under different levels of seismic hazard. However, most seismic-related research studies have been performed on conventional RC shear wall buildings [3]. Therefore, several studies [4, 5] have demonstrated that the seismic performance of RC walls in nuclear and industrial structures, including hysteretic behavior, peak strength, and effective elastic stiffness, has not been yet adequately quantified to enable robust seismic performance assessment. This is mainly because of the complex nonlinear behavior of such walls (mainly dominated by shear mechanisms) and the several wall design characteristics that typically result in significant discrepancies in their seismic performance. In addition, walls in nuclear and industrial structures are uniquely designed to have [6, 7]: (1) a limited number of openings to prevent radiation leaks, thus resulting in walls with very low aspect ratios (i.e., height-to-length ratios less than 1), and/or (2) relatively large thicknesses for radiation shielding as well as blast and fire protection, thus a portion of the wall section between the two reinforcement curtains can be unreinforced. As the aspect ratio of the wall decreases, the wall is much more likely to fail in shear. Shear failures are brittle and are not

M. Abouyoussef (✉) · M. Ezzeldin
McMaster University, Hamilton, Canada
e-mail: abouyoum@mcmaster.ca

S. Walbridge et al. (eds.), *Proceedings of the Canadian Society of Civil Engineering Annual Conference 2021*, Lecture Notes in Civil Engineering 240,
https://doi.org/10.1007/978-981-19-0507-0_2

preceded by significant yielding, either in flexure or in tension induced by shear. Three major failure modes of low aspect ratio walls are diagonal tension, diagonal compression, and sliding shear.

As an object-oriented open-source finite-element program for numerical simulation, the Open System for Earthquake Engineering Simulation (OpenSees), has increasingly become one of the most influential open platforms for earthquake engineering research due to its powerful nonlinear numerical simulation capabilities, various effective algorithms, open framework, and sustainable integration of the latest research outcomes [8, 9]. For example, the fiber beam element model has been widely adopted in OpenSees to simulate specimens that are predominately controlled by flexural behavior [10]. However, this element is incapable of simulating the coupled in-plane/out-of-plane bending as well as the in-plane shear and coupled bending-shear behavior of RC shear walls.

In this respect, the current study develops a 3D numerical model in OpenSees [8], using the multi-layer shell element [11, 12], to simulate the cyclic response of RC shear walls with low aspect ratios similar to those used in nuclear and industrial structures. Following a background of the modelling technique adopted in the current study, a summary of the experimental program used to validate the developed 3D model and a description of the model are presented. Finally, a comparison between the experimental and numerical 3D model results is presented.

2 Background

The multi-layer shell formulation [12] is implemented in OpenSees using the "ShellMITC4" element. This is a four-node shell element based on the theory of mixed interpolated tensorial components (MITC) proposed by [13]. Specifically, the multi-layer shell element is based on the principles of composite material mechanics [11, 12]. The element contains several layers with different thicknesses and different material properties such as concrete layers and rebar layers, as shown in Fig. 1. The strains/curvatures of the middle layer of the shell element are obtained and the strains/ curvatures of the other layers can be determined based on the plane-section assumption [11, 12]. The stress in each layer is calculated based on the corresponding

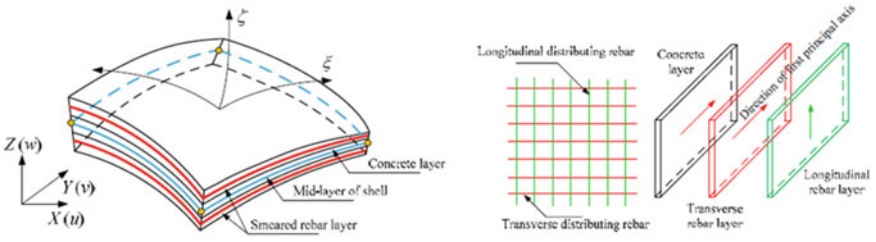

Fig. 1 Location of the rebar layers in multi-Layer shell element [11]

material constitutive law, and the internal forces of the element are determined by the numerical integration of the stress in all layers.

The multi-layer shell element is capable of simulating coupled in-plane/out-of-plane bending as well as in-plane direct shear and coupled bending-shear behavior of RC shear walls [11, 12, 14]. The rebars within this element are smeared into one or more layers and such layers can be either isotropic or orthotropic based on the longitudinal and transverse reinforcement ratios, as shown in Fig. 1 [11, 12]. The stresses over a layer thickness are assumed to be consistent with those at the mid-surface of that layer. Therefore, if the underlying wall is subdivided into any number of layers, the multi-layer shell element can simulate the actual stress distribution over the wall thickness.

3 Experimental Program

The test results of two RC shear walls (i.e., specimens SW1 and SW2) reported by Luna et al. [4] were used in the current study to validate the developed numerical model. Such walls were selected in the current study because they had different reinforcement (i.e., 0.67% and 1.00%) and aspect (i.e., 0.94 and 0.54) ratios. A brief overview of the experimental program is presented in the current section.

3.1 Test Matrix

Table 1 summarizes the wall dimensions and aspect ratios, compressive strength of concrete, yielding strength of reinforcement, and reinforcement details. Where ρ_v and ρ_h are the vertical and horizontal reinforcement ratios, respectively. The vertical and horizontal rebars in SW1 are #4 Grade 60 ASTM A615 [4]. While the vertical and horizontal rebars in SW2 are #4 Grade 60 ASTM A706 [4]. As shown in Fig. 2, for SW1, the spacings of the vertical and horizontal bars are 197 mm and 203.2 mm, respectively. Also, for SW2, the vertical bar spacing is 143 mm, while the horizontal bar spacing is 127 mm.

Table 1 Summary of wall dimensions and reinforcement details

Wall ID	Length (mm)	Height (mm)	Web reinforcement ρ_h(%)	Web reinforcement ρ_v(%)	f_c' (MPa)	f_y(MPa)	Aspect ratio
W1	3000	4321	0.67	1.00	24.82	462	0.94
W2	3000	8765	0.67	1.00	48.26	434	0.54

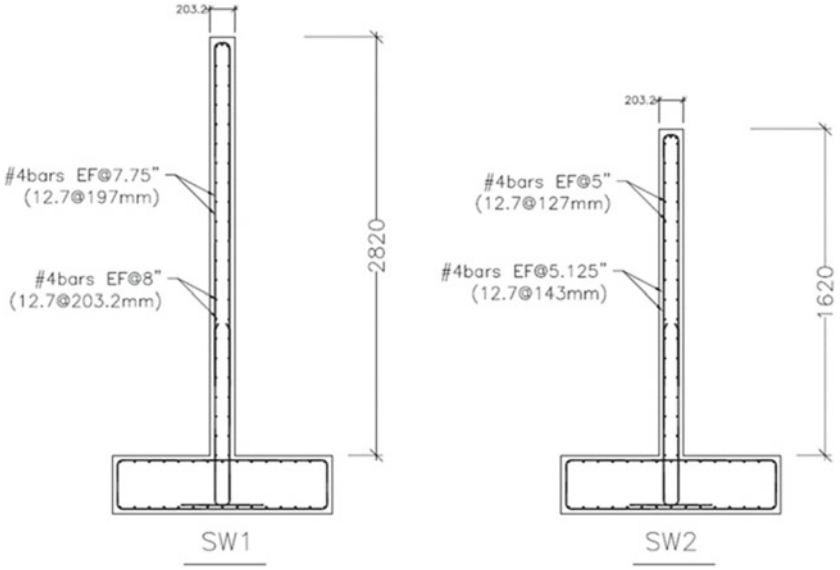

Fig. 2 SW1 and SW2 dimensions and reinforcement details (based on data from Luna et al. [4])

3.2 Test Setup and Loading Scheme

The setup for cyclic testing included a reusable base that was fixed to a concrete structural floor of the laboratory by post-tensioned steel rods [4]. The wall foundation was fixed to the reusable base using similar post-tensioned rods [4]. The cyclic loading scheme consisted of a series of displacement-controlled loading cycles at the top of the walls to simulate the effect of seismic demands. The walls were cycled twice at each displacement level until failure.

4 Numerical Model

4.1 Element Model

The overall steps for defining the multi-layer shell element in OpenSees [15] are shown in Fig. 3. The element size has a direct influence on the accuracy of the analysis solutions due to the strain localization phenomena [16]. Specifically, the model depends on the crack band theory [16] and the slope of the softening branch of cracked concrete is proportionally related to the element size. In the current study, a sensitivity analysis is performed, and 150 elements (15 and 10 elements in the wall vertical and horizontal direction, respectively) are used for SW1 and SW2. All

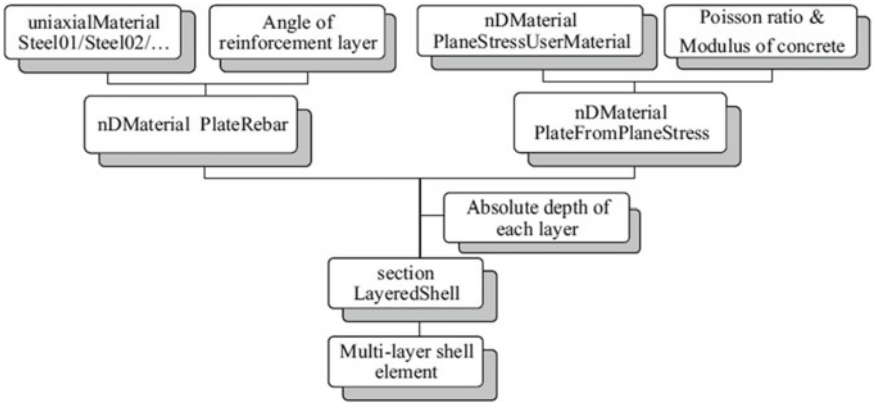

Fig. 3 Framework of multi-layer shell element [12]

degrees of freedom of the nodes located at the wall base are fully fixed and the lateral cyclic displacement was applied in the model at the wall top.

4.2 Material Model

The multi-layer shell element incorporates two-dimensional material constitutive models. Figure 4 shows the cyclic behavior of the concrete model developed by [17, 18] and used in the current study [11]. As shown in Fig. 4, the concrete model depends

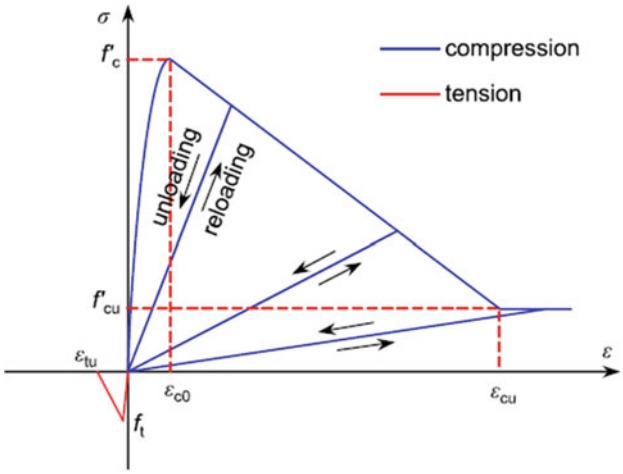

Fig. 4 Stress-strain relationship for concrete under cyclic loading [11]

Table 2 Concrete properties used in the OpenSees model

Wall ID aspect ratio	f_c' (MPa)	f_t (MPa)	f_{cu} (MPa)	e_{co} (MPa)	e_{cu} (MPa)	e_{tu} (MPa)	S_{tc} (MPa)
SW1 (AR = 0.94)	21.50	2.20	4.30	0.0025	0.008	0.001	0.08
SW2 (AR = 0.54)	35.5	3.55	8.00	0.004	0.009	0.0002	0.08

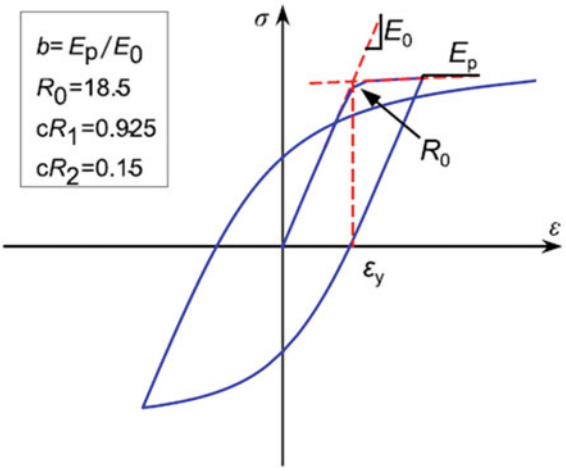

Fig. 5 Stress-strain relationship for steel under cyclic loading [11]

on the concete compressive strength, f_c', tensile strength, f_t, crushing strength, f_{cu}, strain at maximum strength, e_{co}, strain at crushing strength, e_{cu}, ultimate tensile strain, e_{tu}, and shear retention factor, S_{tc}. Table 2 summarizes the different concrete properties used for SW1 and SW2.

For the steel shown in Fig. 5, the Giuffre-Menegotto-Pinto model (steel02 in OpenSees based on Filippou et al. [19]) was adopted for the uniaxial stress-strain relationship of the wall reinforcement. The reinforcement yield strength, f_y, and Young's modulus, E_o, was determined based on experimental tensile tests. The strain hardening ratio, which represents the post yielding stiffness to the initial stiffness was taken as 0.36% and 0.1% for SW1 and SW2, respectively, as reported by Luna et al. [4]. The parameters Ro, cR1, and cR2, which control the curve shape of the transfer from elastic to plastic, were taken as 10, 0.925, and 0.15 for SW1 and 20, 0.925, and 0.15 for SW2, respectively.

5 Validation of the Numerical Models with the Experimental Results

Figures 6 and 7 compare the numerical model predictions and the experimental results for specimens SW1 and SW2, respectively. As can be seen in the figures, the model can simulate the most relevant characteristics of the cyclic response, including the initial stiffness, peak load, stiffness degradation, strength deterioration, hysteretic shape, and pinching behavior at different drift levels.

5.1 Wall Capacity

As presented in Table 3, the maximum lateral load errors in the push direction are 16% and 12% for SW1 and SW2, respectively, while maximum lateral load errors in the pull direction are 13% and 16% for the same walls.

5.2 Energy Dissipation

Energy dissipation through hysteretic damping, E_d, is an important aspect in seismic design because it reduces the amplitude of the seismic response. E_d is presented as the area enclosed by the load-displacement curve passing through the envelope

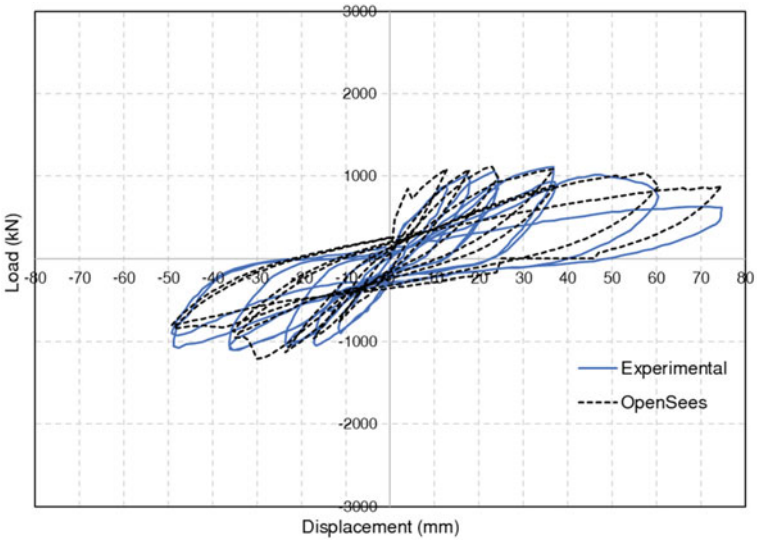

Fig. 6 Experimental and numerical hysteresis loops of Wall W1 (aspect ratio = 0.94)

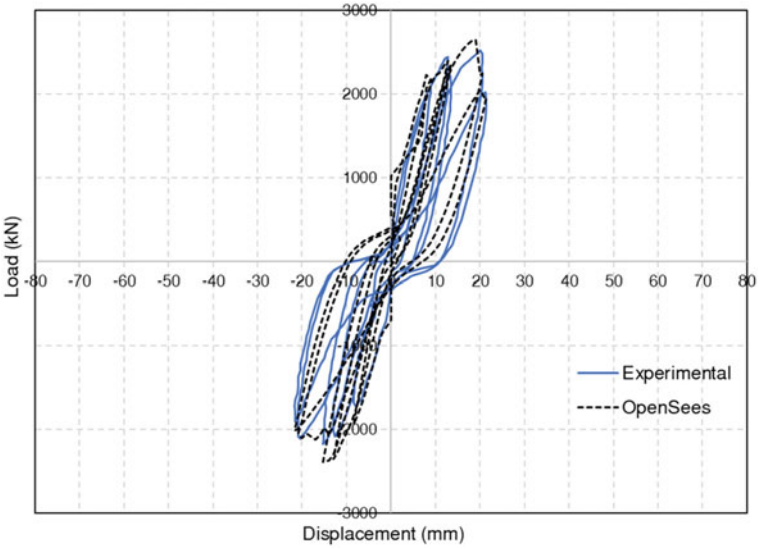

Fig. 7 Experimental and numerical hysteresis loops of Wall W2 (aspect ratio = 0.54)

Table 3 Comparison between the experimental and the model results

Wall ID aspect ratio	Error in the push direction (%)	Error in the pull direction (%)
SW1 (AR = 0.94)	16	13
SW2 (AR = 0.54)	12	16

values. Figure 8 shows the energy dissipation for W1 and the maximum difference between the experimental and numerical results is 14%. Also, for W2, the maximum error is 13%, as shown in Fig. 9.

6 Conclusion

The current study developed a 3D numerical OpenSees model through a multi-layer shell to simulate the cyclic response of RC shear walls with low aspect ratios similar to those used in nuclear and industrial structures. Based on the validation results, it can be concluded that the developed model is capable of simulating the complex behavior of various types of RC shear walls. The study outcome assists in providing an effective tool and a useful reference for further research studies on the seismic behavior of RC shear walls with low aspect ratios using OpenSees.

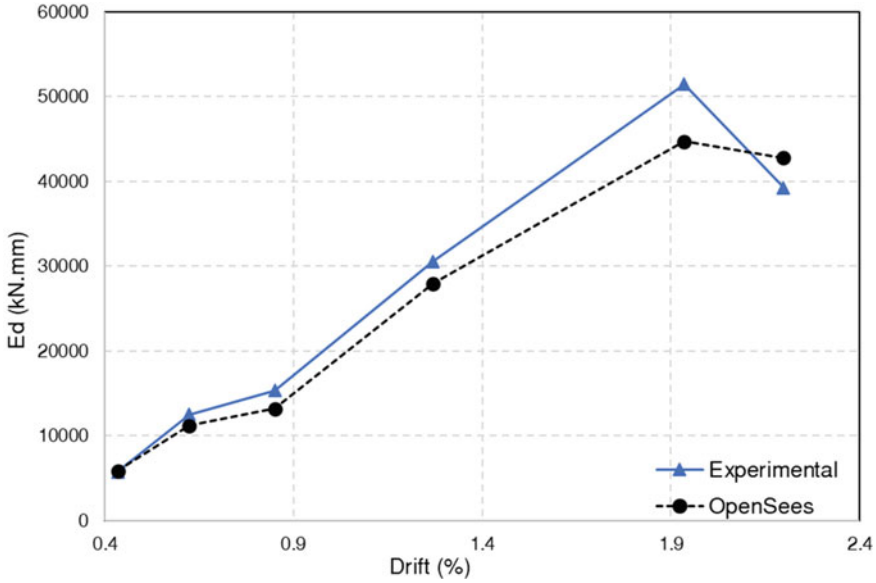

Fig. 8 Energy dissipation of Wall W1 (aspect ratio = 0.94)

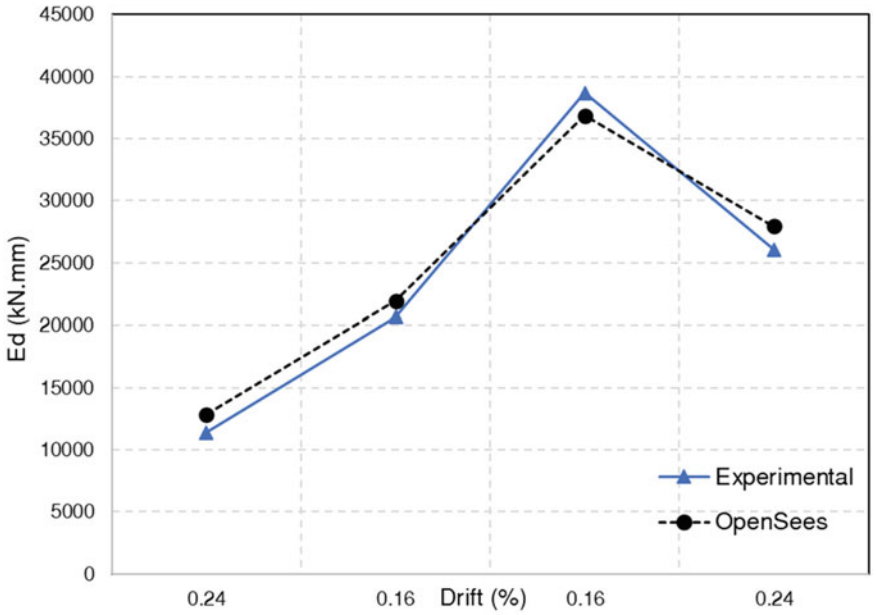

Fig. 9 Energy dissipation of Wall W2 (aspect ratio = 0.54)

References

1. Elwood KJ (2013) Performance of concrete buildings in the 22 February 2011 Christchurch earthquake and implications for Canadian codes. Can J Civ Eng 40(3):759–776
2. Worldwide AIR (2010) Chile earthquake
3. Gulec CK, Whittaker AS (2009) Performance-based assessment and design of squat reinforced concrete shear walls. MCEER, Buffalo, NY
4. Luna B, Whittaker A, Rivera J (2013) Seismic behavior of low aspect ratio reinforced concrete shear walls
5. Parulekar YM, Reddy GR, Vaze KK, Pegon P, Wenzel H (2014) Simulation of reinforced concrete short shear wall subjected to cyclic loading. Nucl Eng Des 270:344–350
6. Huang Y-N, Whittaker AS, Luco N (2008) Performance assessment of conventional and base-isolated nuclear power plants for earthquake and blast loadings. No 19. MCEER
7. Whyte CA (2012) Hybrid simulation of the seismic response of squat reinforced concrete shear walls. PhD dissertation, UC Berkeley
8. McKenna F, Fenves G, Scott M (2000) Open system for earthquake engineering simulation. University of California. Berkeley, CA. http://www.opensees
9. Mazzoni S, McKenna F, Scott MH, Fenves GL (2006) OpenSees command language manual. Pac Earthq Eng Res (PEER) Center 264
10. Massone LM, Orakcal K, Wallace JW (2006) Shear-flexure interaction for structural walls. Spec Publ 236:127–150
11. Ji X, Ya, Sun, Qian J, Lu X (2015) Seismic behavior and modeling of steel reinforced concrete (SRC) walls. Earthq Eng Struct Dyn 44(6):955–972
12. Lu X, Xie L, Guan H, Huang Y, Lu X (2015) A shear wall element for nonlinear seismic analysis of super-tall buildings using OpenSees. Finite Elem Anal Des 98:14–25
13. Dvorkin EN, Pantuso D, Repetto EA (1995) A formulation of the MITC4 shell element for finite strain elasto-plastic analysis. Comput Meth Appl Mech Eng 125(1–4):17–40
14. Xie L, Lu X, Lu, Xinzheng, Huang Y, Ye L (2014) Multi-layer shell element for shear walls in OpenSees. Comput Civ Build Eng 2014:1190–1197
15. Dvorkin EN, Bathe K-J (1984) A continuum mechanics based four-node shell element for general non-linear analysis. Eng Comput
16. Jirásek M, Bauer M (2012) Numerical aspects of the crack band approach. Comput Struct 110:60–78
17. Ile N, Reynouard JM (2000) Nonlinear analysis of reinforced concrete shear wall under earthquake loading. J Earthq Eng 4(02):183–213
18. Saatcioglu M, Razvi SR (1992) Strength and ductility of confined concrete. J Struct Eng 118(6):1590–1607
19. Filippou FC, Popov EP, Bertero VV (1983) Effects of bond deterioration on hysteretic behavior of reinforced concrete joints. 137–147

Fresh and Mechanical Properties of One-Part Alkali-Activated Self-Consolidating Concrete

Dima M. Kanaan and Ahmed M. Soliman

1 Introduction

Self-consolidating concrete (SCC) is in many ways very distinct from conventional concrete. A low yield stress value is required to ensure a minimum force to start the flow. Also, adequate stability is required to withstand aggregates' segregation and excessive bleeding [1]. The emphasis on developing highly natural concrete flow that spreads without mechanical consolidation makes this knowledge even more valuable. SCC systems' design is considered to be sophisticated as it is directly correlated with the binder nature, liquid to powder ratio, and new generations of efficient admixtures [2, 3]. Furthermore, the use of one or more mineral materials in addition to cement is a must to increase the powder content. Therefore, highly flowable concrete requires a comprehensive understanding of its various components and their impact on the fresh, mechanical and durability characteristics [4].

Recently, a rapidly growing effort was opened by the production of innovative cement-free flowable concrete towards decreasing the emissions of GHG to the atmosphere. For example, alkali-activated materials (AAMs) would replace cement-based concrete completely and would meet sustainability and eco-friendly criteria directly. AAMs are highly versatile, as they can be prepared with a wide range of precursors and activators. The resulted polycondensation network binds the aggregates and any inert material. AAM systems, which are fairly commonly used, have strong but not outstanding properties in the concrete industry.

In contrast to OPC-based concrete mixtures, AAMs demonstrated higher mechanical properties at an early age and better resistance to aggressive environments [5–7].

D. M. Kanaan (✉) · A. M. Soliman
Concordia University, Montreal, Canada
e-mail: dima.kanaan@mail.concordia.ca

A. M. Soliman
e-mail: ahmed.soliman@concordia.ca

S. Walbridge et al. (eds.), *Proceedings of the Canadian Society of Civil Engineering Annual Conference 2021*, Lecture Notes in Civil Engineering 240,
https://doi.org/10.1007/978-981-19-0507-0_3

AAMs' main properties are strongly influenced by design parameters such as binder content, alkali concentration, and liquid/binder ratio [8–10]. The hardened properties also depend on the particle size distribution, the chemical composition, and the crystalline phases of the precursors used [11–14]. It is essential to realize that the production of AASCC is not widely investigated as ordinary SCC. This can be due to the limited data on its rheological and mechanical performance under high alkaline environments. However, the wide variety of precursors and activators significantly affect the rheology of the AAM systems in addition to the size or shape of aggregates. Extremely alkaline mediums also have a significant adverse effect on the performance of chemical admixtures and, as a result, impact the workability of SCC mixtures [7, 15]. These are probably some of the most significant challenges of today's industrial-scale Alkali-Activated SCC production (AASCC).

In many recent studies, questions have been raised about the main factors that influence the fresh, mechanical, and durability properties of AASCC. Factors found to have a more predominant effect on the performance of AASCC were the total binder content and type, activator type, dosage, and molar ratio, in addition to admixture type and dosage [16, 17]. For example, Manjunath and Narasimhan [11] have studied the effect of increasing the powder content on the workability of AASCC. It was found that an increase of 100% acidic slag content up to 900 kg/m^3 resulted in a satisfactory mechanical and workability performance satisfying the EFNARC guidelines. It was also reported that the viscosity of sodium silicate, as part of the alkaline solution, prevented bleeding and segregation. Recent studies [8, 9, 18, 19] have shown that the fluidity level of FA-based mixtures decreases as the percentage of GGBFS substitutes increases due to angular morphology and faster reactivity in a highly alkaline environment. Ushaa et al. [8], for example, observed that workability and later age strength improved when replacing FA with GGBFS by up to 30% and 15% silica fume, but resulted in more cohesive and sticky mixtures, especially with silica fume. Huseien and Shah [19] observed that AASCC mixtures' workability improved when FA replaced GGBFS at 40%, 50%, and 60%. Shafiq et al. [18] reported a reduction in AASCC slag/ceramic waste mixtures' flowability as slag content and NaOH molarity increased. On the other hand, Huseien et al. [20] noted that the use of ceramic waste powder significantly affected workability and plastic viscosity when GGBFS was substituted by >50% while the strength decreased.

The superplasticizer employed in [16] was not effective at adjusting the self-compacting characteristics, while the use of 9.02 M and 9.23 M molarities in the activator solution resulted in higher mechanical strengths. [21] observed that the compressive strength and microstructure characteristics prepared with FA-based AASCC were affected by different superplasticizers (SP) with up to 7% dosages, cured at 70 C for 48 h. A loose and porous interfacial transition zone (ITZ) was detected using a low SP dosage that reduced the compressive strength, but a dense ITZ (high SP dosage) was observed that improved strength. On the other hand, Nematollahi and Sanjayan [22] have indicated that the different SPs' effect on the workability and strength of the FA-based mixtures mainly depends on the type of activator and SP. For example, Naphthalene-based SP was an effective type when

using 8 M NaOH solution, whereas modified Polycarboxylate-based SP was the most effective type when using the multi-compound activator.

The development of AASCC from an increasingly diverse range of waste-based precursors and activators has restricted its popularity, standardization, and production. In light of earlier studies' results, the present study aimed to design and conduct an experimental program to examine the potential production of one-part AASCCs mixtures against the backdrop of the identical OPC mortar characteristics. Also, it aims to explore the effect of the nature, concentration, and combination of various source materials and dry-powder activators on AASCC fresh and hardened properties cured under ambient curing conditions.

2 Experimental Program

2.1 Materials

The main precursor material used to produce single and binary AASCC precursor blends was ground granulated blast furnace slag (GGBFS). Its basicity coefficient Kb was 1.07, and Blain fineness was 585 m^2/kg. Fly ash (Class-F FA) and silica fumes (SF) with different weight percentages were also used in this study to replace GGBFS. Table 1 shows the chemical and physical properties of all used binders. For all AASCC mixtures, a combination of two dry-powder activators was used to activate the source materials, namely, anhydrous sodium metasilicate (Na_2SiO_3) and Sodium carbonate (Na_2CO_3). The used Na_2SiO_3 had a molar ratio of 1.0 and a density of 1.09 g/cm^3. The Na_2CO_3 powder was ≥99.5% purity and had a density of 2.53 g/cm^3. Natural siliceous sand with a fineness modulus of 2.5, a specific gravity value of 2.68, and water absorption of 1.5% was used as an inert material. Furthermore, coarse aggregates with a maximum nominal size of 19 mm, a specific gravity value of 2.71, and water absorption of 0.4% was also used. Their volumetric contents were set to 60% and 40%, respectively.

The X-Ray Diffraction (XRD) patterns for the unreacted three precursor materials are shown in Fig. 1. It can be seen that slag is mainly amorphous, without significant crystalline phases, and shows a peak hump between 2θ of 25° and 35° due to the amorphous components. The ultra-fine SF shows an amorphous state pattern as well. The unreacted FA includes crystalline phases such as quartz (SiO_2), mullite

Table 1 Chemical compositions of source materials

Oxide (%)	SiO_2	CaO	Al_2O_3	Fe_2O_3	MgO	K_2O	SO_3
GGBFS	36.5	37.6	10.2	0.5	11.8	0.4	1.0
FA	48.9	3.8	23.3	14.9	0.7	1.7	0.2
SF	94.0	0.4	0.1	0.1	0.4	0.9	1.3

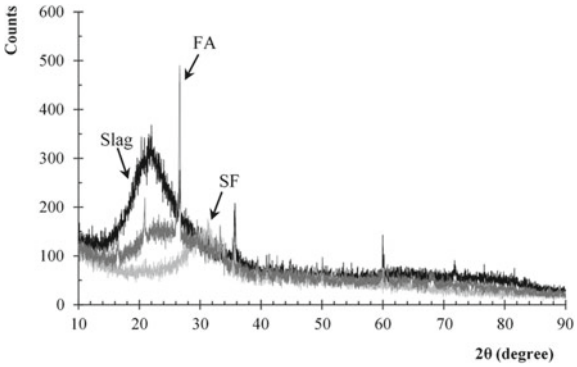

Fig. 1 XRD patterns of source materials **a** slag, **b** SF and **c** FA

($Al_6Si_2O_{13}$), and anorthic ($CaSi_2O_5$) with a broad, amorphous hump between 2θ of 15° and 35°.

2.2 Mixtures' Proportions and Designations

In this study, various combination levels of precursor materials, i.e., single and binary, were used to produce different AASCC systems. The total binder content was kept constant at 525 kg/m^3, providing a relatively high-volume of fine content (paste volume of 381–448 l/m^3), complying with the SCC design guidelines [23]. The dry-powder activator was added at three levels (i.e., 16, 20, and 25% by mass of the precursor material) for all AASCC mixtures. The levels were chosen based on several trial-and-error tests until reaching those levels that provide sufficient alkalinity without efflorescence. The water-to-binder (w/b) ratio was fixed at 0.40 by mass of the binder. Detailed information on the proportions for all mixtures are presented in Table 2.

The mixtures were divided into two groups: single-precursor and binary-precursor. The main varying parameter between concrete mixtures in the same group is the activator's content (i.e., 16, 20, and 25%) MetaNa_2SiO_3 + Na_2CO_3 activators ratio. Single AASCC mixtures are composed of 100% slag designated code S-16%, S-20%, and S-25%. On the other hand. two binary-precursor groups were tested: (i) Binary-1 mixtures with 90% slag and 10% SF, with a designated code B1-16%, B1-20% and B1-25%; and (ii) Binary-2 with 70% slag and 30% FA coded as B2-16%, B2-20% and B2-25%

Table 2 AASCC mixtures' compositions

Class	Mix I.D	Slag (kg/m^3)	FA (kg/m^3)	SF (kg/m^3)	Sand (kg/m^3)	CA (kg/m^3)	Paste vol (L/m^3)
Single	S-16	525	0	0	661	830	438
	S-20	525	0	0	654	830	441
	S-25	525	0	0	646	830	444
Binary-1	B1-16	472.5	0	52.5	652	835	440
	B1-20	472.5	0	52.5	652	830	442
	B1-25	472.5	0	52.5	652	825	443
Binary-2	B2-16	367.5	157.5	0	641	845	440
	B2-20	367.5	157.5	0	637	845	442
	B2-25	367.5	157.5	0	637	840	443

2.3 Mixtures' Preparation

AASCC mixtures were prepared by blending all solid materials (i.e., aggregates, binders, and activators) for about 2 min before adding water to the mixtures. Then, water was added to the mixture, and all the ingredients were mixed for around 5 min until having a homogenous mixture.

All mixtures were evaluated based on their fresh behavior relative to the EFNARC specification by maintaining the filling ability, passing ability, and segregation resistance at the recommended range. For hardened AASCC mixtures, compressive strength development at the ages of 7, and 28 days were measured using 100 mm × 200 mm cylindrical samples according to ASTM-C 39 [24]. All samples were sealed and cured using plastic bags to prevent moisture loss from mixtures and eliminate efflorescence evolution.

3 Results and Discussions

3.1 Slump Flow

The results of the slump flow test are reported in Table 3 for single-precursor mixtures. As the dosage of the dry-powder activators increased in the mixture, i.e., 16%, 20%, and 25%, the obtained slump flow diameter increased substantially. Except for S-16% and S-20% mixtures where the EFNARC-2005 requirements were not met. The slump flow test can also be used to determine the AASCC mixtures' viscosity by reporting the time in seconds required to reach 500 mm flow diameter (T_{500}). S-25% AASCC is the only single-precursor mixture that showed satisfactory results based on the EFNARC-2005 guideline. For mixtures of similar precursor combination (single), the increase in activator dosage from 16% up to 20% had limited effect

Table 3 Slump flow test results for AASCC mixtures

Mixture I.D	S-16%	S-20%	S-25%	B1-16%	B1-20%	B1-25%	B2-16%	B2-20%	B2-25%
Slump flow (mm)	30	510	690	443	448	583	698	795	833
T_{500} (s)	–	4.60	2.02	13.6	8.82	3.05	2.44	1.41	1.13

on the shift of mixtures to the SCC class, yet resulted in a considerable increase of 30 mm and 510 mm, respectively.

The slump flow test was also conducted for the two sets of binary mixtures replacing slag with either 10% SF or 30% FA and activated with up to 25% activator dosage. It is clear that as 10% SF replaced the slag, the slump flow diameter decreased, keeping B1-16% and B1-20% beyond the EFNARC-2005 specification range. However, the highest slump flow diameter was reported 583 mm in 3.05 s for B1-25% mixture, as the dosage of $MetaNa_2SiO_3 + Na_2CO_3$ increased up to 25%. A drop in the slump flow diameter of 15.5% was measured as the amount of SF increased from 0 to 53 kg/m^3 in the mixtures relative to the single slag mixture (S-25%). For B2 binary-precursor mixtures, it can be concluded that the replacement of the slag revealed an increase in the slump flow diameter values. For example, high activator dosage from 16 to 25% resulted in about 19% and 5% increase in the achieved flowability in <3 s.

Figure 2 shows the effect of incorporating a combination of two dry-powder activators on the workability of AASCC mixtures. It can be noticed that as the dosage of the activators increased in AASCC mixtures, the slump flow increased within each mixture group. The single-precursor slump flow for S-25% was limited to 690 mm, which was obtained after increasing the activator dosage by approximately 1.5 times compared to the S-16% mixture dosage. A similar trend was observed in binary-precursor mixtures while replacing slag with 10% SF. For example, in the B1 group,

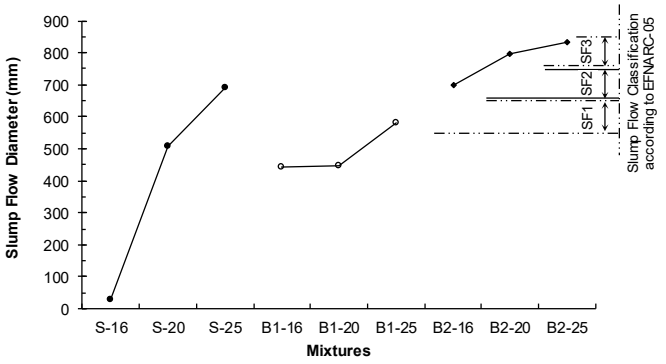

Fig. 2 Slump flow test results for AASCC mixtures

the addition of 16, 20, and 25% activator dosage increased the slump flow values from 443 to 448 mm and 583 mm, respectively. However, as the activator dosage increased, all other B2 mixtures' filling capacity using 30% FA were >700 mm in <1.0 s. It can be concluded that replacing slag with 10% SF at the highest activator dosage in B1 mixtures decreased the slump flow values and shifted the mixture to the slump flow class 1. (SF1, as per Fig. 2). In the case of extremely congested reinforced structures, using a B1 mixture is critical. Conversely, as FA ratio increased by up to 30% using a higher activator dosage of about 20%, the mixtures tended to move from the slump flow class of SF2 to SF3. This means that better surface finishing characteristics would be obtained from a set of mixtures containing less slag, but it would harder to overcome the segregation.

3.2 Passing Ability

The passing ability test results for single-precursor mixtures are shown in Table 4. Extreme blocking was exhibited in mixtures containing 100% slag with the lowest activator dosage of about 16%. The passing ability values showed a significant improvement as the activator dosage increased by up to 25%. On the other hand, an improvement in the passing ability was observed as the activator dosage increased in binary-precursor mixtures. AASCC mixtures replacing slag with 10% SF and activated with up to 20% activator dosage, i.e., B1-16% and B1-20%, revealed a noticeable blocking at 0.55. However, B1-25% reported better performance, with a 36% increase in the measured blocking ratio. A better passing ability value of AASCC mixtures flowing through reinforcement bars was seen in the second set of binary mixtures using 30% FA. The blocking ratio of B2 AASCC mixtures is shown in Table 4, with results ranging from 0.88 to 1 as the activator dosage increased. The blocking ratio must be between 0.8 and 1 as per the EFNARC guidelines, and thus all B2 mixtures have met the fresh behavior requirements for the test performed.

The L-box test was used to evaluate the dynamic stability of AASCC mixtures. Generally speaking, all AASCC mixtures prepared with a high dry-powder activator dosage, i.e., 25%, exhibited better passing ability than those made with lower content. It is clear from Fig. 3 that single-precursor mixtures with the minimum difference between activator dosages 16% and 20% (4%) exhibited the minimum ratio in the L-box test (≤0.65). Single-precursor mixtures' passing ability increased by up to 85%

Table 4 Passing ability test results for AASCC mixtures

Mixture I.D	S-16%	S-20%	S-25%	B1-16%	B1-20%	B1-25%	B2-16%	B2-20%	B2-25%
L-box ratio, h_2/h_1	0.55	0.65	0.85	0.55	0.55	0.75	0.88	0.94	1.00

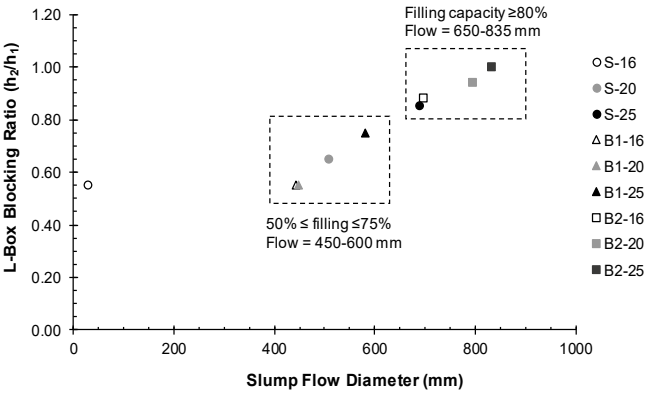

Fig. 3 Relation between slump and L-box blocking ratio

while using up to 25% activator dosage. Similarly, the binary-1 mixtures, i.e., B1-16, B1-20, and B1-25, the maximum with the lowest slump flow values (<590 mm), had the minimum ratio in the L-box test ($\leq$0.75). In contrast, as the activator dosage increased from 16 to 25%, the passing ability varied between 0.88 and 1.0 in binary-2 mixtures.

3.3 Segregation Resistance

Table 5 presents the segregation resistance test results for 100% slag single-precursor mixtures activated with up to 25% activators dosages. It was evident that the segregation potential increased marginally by about 5% as the activators' dosages increased in the single-precursor mixtures. However, for binary-precursor mixtures, all B1 mixtures were found viscous, as slag was replaced with 10% SF, and the SI was about 7% even when the activator dosage increased from 20 to 25%. In B2 mixtures where slag was replaced with 30% FA, relatively high percentages of segregation were determined. B2-16%, for instance, resulted in 15% segregation, which is less than 12% provided by B2-20%. However, B2-25% reported higher segregation potential, with about an 80% increase in the measured stability ratio compared to B2-16%.

The segregation resistance ratio must be below 15% as per the EFNARC guidelines. Generally speaking, all mixtures exhibited good passing ability with a segregation potential as the activator dosage increases. However, an exception was observed

Table 5 SI% test results for AASCC mixtures

Mixture I.D	S-16%	S-20%	S-25%	B1-16%	B1-20%	B1-25%	B2-16%	B2-20%	B2-25%
SI (%)	0	2	5	2	7	7	15	17	27

in single-slag mixtures with 16% and 20% activator dosages and binary B1 (slag-SF) mixtures. On the contrary, B2 mixtures containing 367.5 kg/m^3 of FA tended to be segregated (SI ~ 15 to 30%), particularly mixtures containing 25% of dry-powder activators.

3.4 Effect of Activator Dosage

When determining the fresh characteristics of AASCC mixtures, the type and dosage of alkaline activators and their combination play a fundamental role. The most commonly used activators for the alkali activation process are sodium hydroxide and sodium silicate (water glass) due to their high alkalinity potential [25]. Compared with other activators, sodium carbonate (Na_2CO_3) yields a lower early age strength due to its lower pH potential. Therefore, the activation with Na_2CO_3 would delay the formation of early age strength-giving products [26]. This can be due to the fast reactions between the dissolved calcium ions (Ca^{2+}) from slag with sodium and carbonate ions from the activator before the formation of C-A(N)-S-H gels [27]. On the other hand, the use of synthetic silica chemicals such as anhydrous sodium metasilicate (Na_2SiO_3) resulted in better workability and high strength values of slag and FA one-part mixtures [22]. This could be attributed to the fact that the anhydrous metasilicate particles were not fully dissolved at an early age, which resulted in an improved level of workability. Overall, the enhancement in AASCC workability could be attributed to the combination of sodium metasilicate and Na_2CO_3 and their contents.

3.5 Effect of Precursor Combination

The lack of effective chemical admixtures to enhance the flowability of one-part AASCC mixtures necessitates the use of proper precursor materials. In binary systems, slag replacement with different silica fume (SF) ratios or fly ash (FA) class F can adjust the distribution of the particle size of the binder materials. The initial porosity of the systems would also be adjusted and reduced, which can improve the fresh concrete's workability. The use of binary-precursor blends in AASCCs showed significantly better workability than slag-precursor mixtures with an activator dosage of at least 16%. However, binary-precursor blends with 30% FA tended to segregate due to their particle size, morphology, and bulk density variations compared with slag-based mixtures.

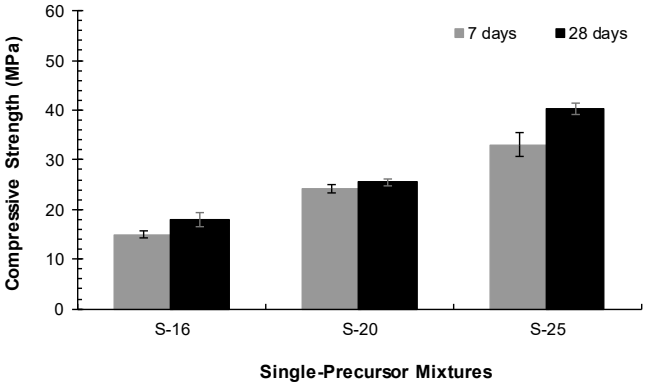

Fig. 4 Compressive strength results for the AASCC single-precursor mixtures

3.6 Compressive Strength

The compressive strength results of single-precursor AASCC mixtures using 100% slag and activated with up to 25% activator dosage are shown in Fig. 4. At 7 days of age, the highest measured compressive strength value was 35 MPa in S-25% relative to S-16% and S-20%, respectively. It is apparent that, as the activator dosage increased to 25%, the strength value increased by about 121% compared with 16%. This can be attributed to the fact that alkali-activated slag mixtures' strength progression is very fast due to the spontaneous reaction at the very early stage of hydration. In single-precursor mixtures, as the activator dosage increases, the pore solution retains higher Si and Na concentrations, accelerating the C-S-H precipitation process [28, 29]. A similar trend was obtained at 28 days of age. For example, the highest compressive strength value was achieved by S-25% with about 40 MPa higher than S-20% and S-16% with 58% and 123% increase, respectively. This can be due to the continued microstructural growth of 100% slag AASCC mixtures that contributed to strength development until later ages. A mixture achieved the highest 90-day strength with a 25% activator dose of approximately 46.3 MPa compared to S-20% (26 MPa) and a 16% activator dose (22 MPa), respectively. Generally speaking, the higher the activator dosage is responsible for the higher pH, silicate, and carbonate ions in the system resulting in continuous reactions with Ca^{2+} ions from the slag leading to precipitation of C-(A)-S-H. The results obtained are in good agreement with [30], where the main factor affecting the alkali-activated slag mixture's mechanical characteristics is the type of anion accompanying the activators after the high pH value. This would lead to the formation of stable hydration products.

Figure 5 shows the compressive strength values for the binary-precursor mixtures activated with a combination of two dry-powder activators. In both sets of binary AASCC mixtures, slag was replaced by either 10% SF (B1 mixtures) or 30% FA as B2 mixtures. The highest strength was achieved for both binary sets using the highest activator dosage of 25% compared to the remaining two mixtures with about 16 and

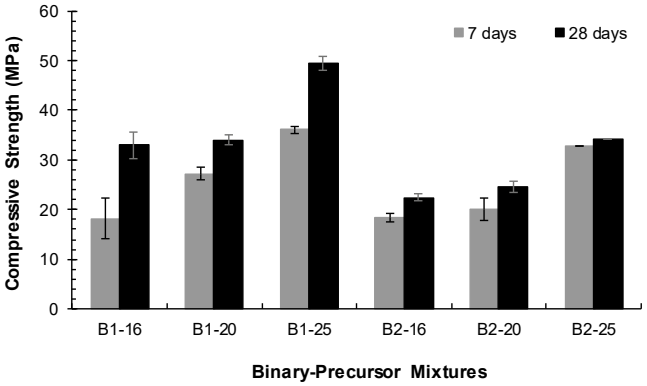

Fig. 5 Compressive strength results for the AASCC binary-precursor mixtures

20% activator dosages. For instance, at 7 days of age, B1-25% achieved the highest strength at 36 MPa, which is 98% higher than that of the binary mixture with the lowest activator dosage of 16% at the same age.

At 28 days, both the B1-16% and B1-20% revealed almost similar strength values at 33 and 34 MPa, respectively, compared to 49.5 MPa at B1-25%. It is noteworthy that the mechanical performance of AASCC binary mixtures was improved by replacing slag with SF. This is in line with the previous studies [31, 32], which reported an improvement in the compressive strength of alkali-activated concrete using SF. This can be due to the slag activation reaction and the SF micro-filling and nucleation effect that led to a dense matrix.

As for the binary set of mixtures using 30% FA, the increase in strength was gradual as the activator dosage increased at different ages. At later ages, the highest activator dosage mixtures (with about 25%) continued to achieve higher strength values than that of the lower to moderate dosages. At 28 days of age, mixtures B2-16% and B2-20% appeared to achieve relative strength values of 22.4 and 24.5 MPa than 34.3 MPa in B2-25%. This implies that the optimum activator dosage for obtaining the highest compressive strength was 25%. It should be noted that the difference in chemical composition between slag and FA significantly affected the alkali-activation mechanisms. The single-precursor blend of AASCC, i.e., S-25%, achieved the highest strength than B2-25%. This can be attributed to the high reaction rate of slag-based mixtures due to their nature than to the crystalline pozzolanic nature of FA-based mixtures. During the second cycle of the reaction process, FA was partially dissolved and participated [33]. A compact and denser matrix was obtained for the binary-precursor 70% slag and 30% FA mixture as the slag content was higher than FA in the AASCC matrix.

4 Conclusions

This study aimed to investigate the potential production of dry-powder Alkali-activated SCC using GGBFS as the main source material and multi-dry powder activators i.e., Na_2SO_3 and Na_2CO_3 as an alternative to cement in concrete mixtures. The study focused on identifying the main parameters affecting the performance of different AASCC mixtures, including the type and fineness of source materials, nature and concentration of activators. The following conclusions can be drawn from the results of this study:

- The combination of multi dry-powder activators and precursors not only increased the workability of AASCC mixtures but also enhanced the microstructure and compressive strength.
- As the activator dosage was increased, all mixtures showed substantial filing and passing abilities with potential for segregation.
- The substitution of the slag by 30% FA in the binary-precursor set resulted in a decrease in friction between aggregates and paste and better flowability relative to the 10% SF replacement of the slag, which had an adverse effect. This can be due to the distinct nature and morphology of the used precursor materials.
- The compressive strength findings in the binary-precursor set were significantly improved when slag was replaced with 10% SF due to the slag activation reaction as well as the SF micro-filling and nucleation effect, which resulted in a dense matrix.

References

1. Ling G, Shui Z, Sun T, Gao X, Wang Y, Sun Y, Li Z (2018) Rheological behavior and microstructure characteristics of SCC incorporating metakaolin and silica fume. Materials 11(12):2576
2. Heikal M, Zohdy KM, Abdelkreem M (2013) Mechanical, microstructure and rheological characteristics of high performance self-compacting cement pastes and concrete containing ground clay bricks. Constr Build Mater 38:101–109
3. Shunsuke H, Kazuo Y (1999) Interaction between cement and chemical admixture from the point of cement hydration, absorption behaviour of admixture, and paste rheology. Cem Concr Res 29(8):1159–1165
4. Khayat KH, Ghezal A, Hadriche MS (2000) Utility of statistical models in proportioning self-consolidating concrete. Mater Struct 33(5):338–344
5. Bernal SA, Provis JL, Fernández-Jiménez A, Krivenko PV, Kavalerova E, Palacios M, Shi C (2014) Binder chemistry–high-calcium alkali-activated materials. In: Alkali activated materials. Springer, Dordrecht, pp 59–91
6. Walkley B, San Nicolas R, Sani MA, Rees GJ, Hanna JV, van Deventer JS, Provis JL (2016) Phase evolution of C-(N)-ASH/NASH gel blends investigated via alkali-activation of synthetic calcium aluminosilicate precursors. Cem Concr Res 89:120–135
7. Palacios M, Puertas F (2004) Stability of superplasticizer and shrinkage-reducing admixtures Stability of superplasticizer and shrinkage-reducing admixtures in high basic media. Mater Constr 54(276):65–86

8. Ushaa T, Anuradha R, Venkatasubramani G (2015) Performance of self-compacting geopolymer concrete containing different mineral admixtures
9. Sashidhar C, Jawahar JG, Neelima C, Kumar DP (2015) Fresh and strength properties of self compacting geopolymer concrete using manufactured sand. Int J ChemTech Res (IJCRGG) 8:183–190
10. Patel YJ, Shah N (2018). Study on workability and hardened properties of self compacted geopolymer POLYMER concrete cured at ambient temperature. Indian J Sci Technol 11(1)
11. Manjunath R, Narasimhan MC (2018) An experimental investigation on self-compacting alkali activated slag concrete mixes. J Build Eng 17:1–12
12. Van Deventer JS, Provis JL, Duxson P (2012) Technical and commercial progress in the adoption of geopolymer cement. Miner Eng 29:89–104
13. Palomo Á, Fernández-Jiménez A, López-Hombrados C, Lleyda JL (2011) Railway sleepers made of alkali activated fly ash concrete. Revista Ingeniería de Construcción 22(2):75–80
14. Neupane K, Kidd P, Chalmers D, Baweja D, Shrestha R (2016) Investigation on compressive strength development and drying shrinkage of ambient cured powder-activated geopolymer concretes. Aust J Civ Eng 14(1):72–83
15. Bakharev T, Sanjayan JG, Cheng YB (2000) Effect of admixtures on properties of alkali-activated slag concrete. Cem Concr Res 30(9):1367–1374
16. Santana HA, Neto JSA, Júnior NSA, Ribeiro DV, Cilla MS, Dias CM (2020) Self-compacting geopolymer mixture: dosing based on statistical mixture design and simultaneous optimization. Constr Build Mater 249:118677
17. He J, Bu X, Bai W, Zheng W, Gao Q, Wang Y (2020) Preparation and properties of self-compacting alkali-activated slag repair mortar. Constr Build Mater 252:119034
18. Shafiq I, Azreen M, Hussin M (2017) Sulphuric acid resistant of self compacted geopolymer concrete containing slag and ceramic waste. In: MATEC Web of Conferences
19. Huseien GF, Shah KW (2020) Durability and life cycle evaluation of self-compacting concrete containing fly ash as GBFS replacement with alkali activation. Constr Build Mater 235:117458
20. Huseien GF, Sam ARM, Shah KW, Mirza J (2020) Effects of ceramic tile powder waste on properties of self-compacted alkali-activated concrete. Constr Build Mater 236:117574
21. Demie S, Nuruddin MF, Shafiq N (2013) Effects of micro-structure characteristics of interfacial transition zone on the compressive strength of self-compacting geopolymer concrete. Constr Build Mater 41:91–98
22. Nematollahi B, Sanjayan J, Shaikh FUA (2015) Synthesis of heat and ambient cured one-part geopolymer mixes with different grades of sodium silicate. Ceram Int 41(4):5696–5704
23. EFNARC (2005). Specification and guidelines for self-compacting concrete. European Federation of Producers and Applicators of specialist products for structures, 32 pp
24. ASTM C 39 (2001) The American Society for Testing Materials, Standard test method for compressive strength of cylindrical concrete specimens, West Conshohocken (PA), VSA
25. Yan Z, Sun Z, Yang J, Yang H, Ji Y, Hu K (2021). Mechanical performance and reaction mechanism of copper slag activated with sodium silicate or sodium hydroxide. Constr Build Mater 266:120900
26. Atiş CD, Bilim C, Çelik Ö, Karahan O (2009) Influence of activator on the strength and drying shrinkage of alkali-activated slag mortar. Constr Build Mater 23(1):548–555
27. Bernal SA, Provis JL, Myers RJ, San Nicolas R, van Deventer JS (2015) Role of carbonates in the chemical evolution of sodium carbonate-activated slag binders. Mater Struct 48(3):517–529
28. Gebregziabiher BS, Thomas R, Peethamparan S (2015) Very early-age reaction kinetics and microstructural development in alkali-activated slag. Cement Concr Compos 55:91–102
29. Gruskovnjak A, Lothenbach B, Holzer L, Figi R, Winnefeld F (2006) Hydration of alkali-activated slag: comparison with ordinary Portland cement. Adv Cem Res 18(3):119–128
30. Fernández-Jiménez A, Puertas F (2003) Effect of activator mix on the hydration and strength behaviour of alkali-activated slag cements. Adv Cem Res 15(3):129–136
31. Kim T, Kang C (2020) The mechanical properties of alkali-activated slag-silica fume cement pastes by mixing method. Int J Concr Struct Mater 14(1):1–15

32. Alanazi H, Hu J, Kim YR (2019) Effect of slag, silica fume, and metakaolin on properties and performance of alkali-activated fly ash cured at ambient temperature. Constr Build Mater 197:747–756
33. Puertas F, Martínez-Ramírez S, Alonso S, Vázquez T (2000) Alkali-activated fly ash/slag cement strength behavior and hydration products. Cem Concr Res 30:1625–1632

A Review on Bond Performance and Splice Behavior of FRP Bars to Concrete

Bahareh Nader Tehrani, Ahmed S. Farghaly, Alireza Asadian, and Brahim Benmokrane

1 Introduction

Corrosion is a severe problem associated with steel-reinforced concrete (RC) structures, especially those exposed to a harsh environment. Replacing steel rebars with fiber-reinforced polymer (FRP) reinforcing bars is a viable solution to this problem. Different properties of FRP bars and steel bars should be considered in the design FRP-RC structures. FRP reinforcing bars show linear elastic behavior up to failure; in contrast, steel bars exhibit plastic behavior [1]. Moreover, there are differences in their bond behavior that should be taken into consideration. One of the primary concerns associated with FRP-RC structures is the lap splicing of reinforcements. In order to avoid bond failure and excessive slippage, the splice length should be designed carefully [2]. Extensive research endeavors focused on tensile splicing of FRP bars under static loading [3–9]. There are limited studies investigating lap splicing of FRP reinforcements in RC columns [10–13]. Also, the seismic response of RC members with lap spliced FRP bars is not well investigated in the literature. Consequently, there is no recommendation for lap splicing of FRP bars subjected to seismic loading in available codes and standards. Therefore, it is vital to investigate the bond performance of FRP bars under cyclic loading. In the current study, the knowledge of existing research studies on lap splicing of GFRP bars is summarized, including the primary factors affecting the bond performance of FRP bars. Moreover, a comparison between available provisions on development length and bond strength in three north American standards is presented. Previous research studies were also used to compare the available provisions in design standards and guidelines.

B. Nader Tehrani (✉) · A. S. Farghaly · A. Asadian · B. Benmokrane
Department of Civil Engineering, University of Sherbrooke, Sherbrooke, QC, Canada
e-mail: Bahareh.nader.tehrani@usherbrooke.ca

S. Walbridge et al. (eds.), *Proceedings of the Canadian Society of Civil Engineering Annual Conference 2021*, Lecture Notes in Civil Engineering 240,
https://doi.org/10.1007/978-981-19-0507-0_4

2 A Review of Existing Code Provisions on Bond Strength and Development Length

Development length refers to the length needed to be embedded into the concrete to develop the required tensile stress in the bar. A review of three north American design standards and guidelines on bond strength and development/splice length of FRP bars is presented in this section. The equations proposed by these codes to calculate the FRP bar development length and bond strength are presented.

2.1 CSA S806-12

CSA S806-12 [14] suggests the following equation for the development length of bars in tension:

$$l_d = 1.15 \frac{k_1 k_2 k_3 k_4 k_5}{d_{cs}} \frac{f_F}{\sqrt{f'_c}} A_b \tag{1}$$

In which the terms $d_{cs} \leq 2.5 d_b$, and $\sqrt{f'_c} \leq 5\text{MPa}$.

In Eq. (1), l_d is development length of the deformed bar in tension; f_F and f'_c are design stress in FRP tension reinforcement at the ultimate limit state and concrete compressive strength, respectively; d_{cs} is the smaller of the distance from the center of the bar being developed to the closest concrete surface or two-thirds of the center-to-center spacing of bars being developed;d_b is the nominal diameter of a bar;A_b is the area of a bar; k_1 is bar location factor; k_2 is concrete density factor; k_3 is bar size factor;k_4 is bar fiber factor; k_5 is bar surface profile factor.

Based on CSA S806-12 [14], $1.3l_d$ is recommended to calculate the splice length in tension. CSA S806-12 has no equation to calculate the bond strength of FRP bars; however, in the literature, the equilibrium of forces was used to calculate the average bond strength over the splice length (u) as follows [4, 10]:

$$u \pi d_b 1_b = f_f A_b \tag{2}$$

$$u = \frac{d_{cs} \sqrt{f'_c}}{1.15(k_1 k_2 k_3 k_4 k_5) \pi d_b} \tag{3}$$

As can be seen, bond strength based on this equation is independent of the embedded length of FRP bars in concrete. As this equation obtained by l_d equal to the development length, it can only be used when the embedded length is equal to the development length. In other words, this equation yields the maximum bond strength. However, in the literature, it is used to calculate the bond strength for any

embedded length, so the obtained bond strength is constant even by changing the embedded length.

2.2 CSA S6-19

CSA S6-19 [15] proposes the following equation for the development length of bars in tension which is derived by modifying its expression for the steel bars:

$$l_d = 0.45 \frac{k_1 k_4}{d_{cs} + K_{tr} \frac{E_{FRP}}{E_s}} \left(\frac{f_{FRPu}}{f_{cr}} \right) A_b \tag{4}$$

In which the terms $d_{cs} + K_{tr} \frac{E_{FRP}}{E_S} \leq 2.5 d_b$, and

$$K_{tr} = \frac{A_{tr} f_y}{10.5 s n} \tag{5}$$

where l_d refers to tension development length of deformed bar; f_{FRPu}, f_{cr}, and f_y are specified tensile strength of an FRP bar, concrete cracking strength, and specified yield strength of steel reinforcement, respectively; E_{FRP} and E_S denote modulus of elasticity of FRP bar and steel bar, respectively; d_{cs} is the smaller of the distance from the center of the bar being developed to the closest concrete surface or two-thirds of the center-to-center spacing of bars being developed; K_{tr} is transverse reinforcement index representing the contribution of confining reinforcement; A_{tr} refers to reinforcement area within l_d crossing the potential bond-splitting crack; d_b and A_b are diameter and area of a bar, respectively; s is maximum center to center spacing of transverse reinforcement within a distance l_d; *n* is the number of bars being developed along the potential plane of splitting; k_1 and k_4 are is bar location and bar surface factor, respectively. CSA S6-19 recommends $1.3 l_d$ is for the splice length in tension.

Like CSA S806-12 [14], there is no equation in CSA S6-19 [15] to calculate the bond strength. The following equation is derived based on the equilibrium of forces which can be used to calculate the maximum bond strength (u):

$$u = \frac{f_{cr}(d_{cs} + K_{tr} \frac{E_{FRP}}{E_s})}{0.45 k_1 k_4 \pi d_b} \tag{6}$$

2.3 ACI 440.1R-15

ACI 440.1R-15 recommends the following equation for FRP bar development length in tension:

$$l_d = \frac{\alpha \frac{f_{fr}}{0.083\sqrt{f_c'}} - 340}{13.6 + \frac{C}{d_b}} d_b \tag{7}$$

In which the terms $\frac{C}{d_b} \leq 3.5$, and

$$f_{fr} = min(f_{fu}, [\sqrt{\frac{(E_f \varepsilon_{cu})^2}{4} + \frac{085\beta_1 f_c'}{\rho_f} E_f \varepsilon_{cu}} - 0.5 E_f \varepsilon_{cu}]) \tag{8}$$

In Eq. (7), l_d is deformed bar development length in tension;f_{fr}, f_c', and f_{fu} are required bar stress in FRP, concrete compressive strength, and FRP bar design tensile strength, respectively; *C* is the lesser of the cover to center of the bar being developed or one-half of the center-to-center spacing of bars being developed; d_b is the diameter of a bar; α is bar location factor; E_f is design modulus of elasticity of FRP bar; ε_{cu} denotes concrete ultimate strain; β_1 is a factor that depends on concrete compressive strength, which varies between 0.65 to 0.85; ρ_f refers to FRP reinforcement ratio.

ACI 440.1R-15 considers no classification for splice length because the FRP bar full tensile strength is not required to be developed. Accordingly, $1.3l_d$ is proposed for all lap splices in tension. According to ACI 440.1R-15 the bond strength of FRP reinforcing bars (u) is calculated based on the following equation:

$$\frac{u}{0.083\sqrt{f_c'}} = 4.0 + 0.3\frac{C}{d_b} + 100\frac{d_b}{l_d} \tag{9}$$

where l_d is an FRP bar embedded length in concrete.

2.4 Comparison of Existing Code Provisions

The design provisions of three North American codes on FRP bond strength and development length were discussed in previous sections. The factors affecting the development length considered in the code provisions are summarized in Table 1 to illustrate their differences.

As shown in Table 1, some factors such as concrete strength, concrete cover, space between bars, bar location, bar diameter, and bar stress are considered for all these standards. Concrete density and fiber type are taken into account only in CSA S806-12 [14]. Transverse reinforcement and the number of bars being developed are considered only in CSA S6-19 [15]. Unlike Canadian design standards, the effect of bar surface on development length is ignored in ACI 440.1R-15. It is important to note that in the ACI 440.1R-15 equation, the nonlinearity of bond over development length is considered while CSA S806-12 and CSA S6-19 consider linear relation between bond and development length.

Table 1 Factors for determining development length in code provisions

Design standards	$f_c^{'}$	Concrete density	Transverse reinforcement	Concrete cover	Space between bars	Number of bars being developed	Bar location	Bar surface	Bar fiber	d_b	f_{fr}
CSA S806-12	✓	✓	×	✓	✓	✓	✓	✓	✓	✓	✓
CSA S6-19	✓	×	✓	✓	✓	✓	✓	✓	×	✓	✓
ACI 440.1R-15	✓	×	×	✓	✓	×	✓	×	×	✓	✓

Table 2 Selected database for comparing the provisions of different codes

Design standards	Specimens	Test parameters
Naqvi [10]	9 columns	Reinforcement type, splice length, confinement, the spacing of lateral reinforcement, axial load level, concrete type
Aly et al. [2]	2 beams	Splice length
Asadian et al. [3]	1 beam	Splice length
Choi et al. [16]	24 beams, 9 slabs	Splice length, concrete cover, bar spacing, surface condition
Esfahani et al. [4]	13 beams	Transverse reinforcement, surface condition, bar diameter, concrete compressive strength
Tighiouart et al. [7]	16 beams	Bar diameter, splice length

In the current study, to examine the capability of different code provisions to predict splice length under static and seismic loading, test results of 9 concrete columns, 56 beams, and 9 slabs reinforced with lap spliced bars were collected from the existing literature (Table 2). Due to the space limitation, these specimens' full details, including their geometric and material properties, could not be presented in this paper. However, they were fully presented in the literature. The selected members include two different materials: carbon FRP (CFRP) and glass FRP (GFRP) with different surface conditions. The concrete compressive strength varies from 23 to 70 MPa. Also, the database represents a wide range of reinforcement ratios.

The required splice length of selected specimens was calculated according to three North American standards to compare the experimental results with analytical ones. Figure 1 displays the provided splice to the required splice length ratio based on codes versus the observed experimental failure mode. As can be seen, for 20 out of 74 cases, the splitting failure mode was observed despite providing more splice length than the required one based on CSA S806-12 [14]. It means that predicted splice length of 27% of specimens was unconservative based on CSA S806-12 [14]. This ratio was 28% and 8% based on CSA S6-19 and ACI 440.1R-15, respectively. It seems that ACI 440.1R-15 provides more conservative splice length than two Canadian standards.

3 Critical Factors for Bond Strength of FRP Bars to Concrete

3.1 Embedment Length

As observed in the literature, the bond strength decreases by increasing the embedment length [7, 9, 16, 17]. The bond strength equation provided by ACI 440.1R-15 confirms this conclusion. Naqvi [10] evaluated the behavior of spliced GFRP-RC

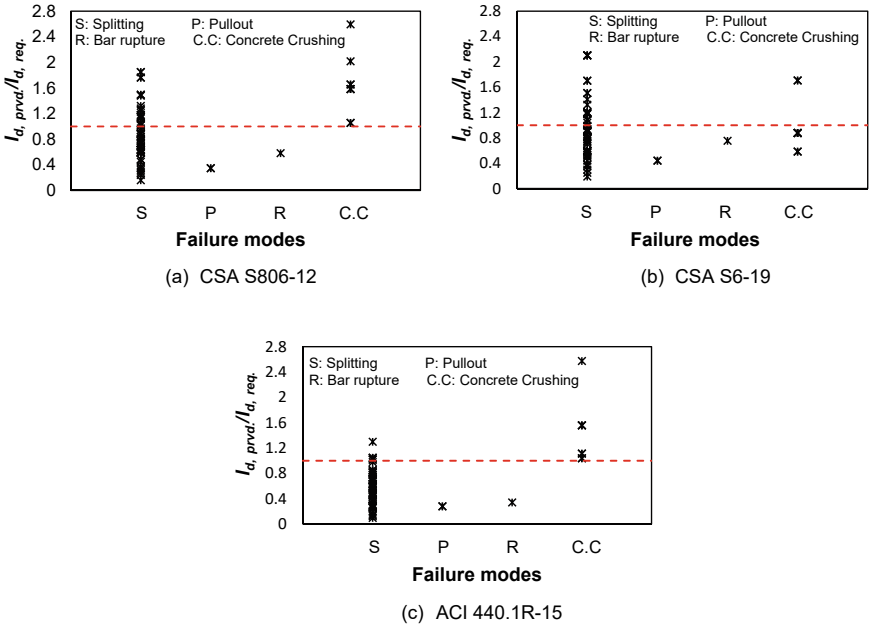

Fig. 1 Comparison of design standards based on the results of existing experimental studies

columns under cyclic loading. Findings of [10] research study showed that while the full bond force was not transferred by splice length of 40 and $50d_b$ due to splitting cracks and bond slippage, a splice length of $60d_b$ was capable of transferring the full bond stress along the splice length.

3.2 Transverse Reinforcement

There are two components for the bond forces acting on the interface between reinforcing bars and concrete: radial and longitudinal components. The former component acting perpendicular to bar length can eventually result in splitting of the surrounding concrete. The later component acting along the bar length prevents the bar from pulling out of the concrete. When adequate confinement is provided, the longitudinal component of the bond forces may go above the shear capacity of concrete, increasing the possibility of pullout failure. However, when the radial component exceeds the tensile resistance providing by the concrete, splitting failure may occur. It is worth noting that the rib area is an essential factor for confinement to be effective. While in steel bars with high rib area, transverse reinforcement can effectively improve bearing force and the bond strength, low rib area in FRP bars may decrease the effect of transverse reinforcement.

As the effect of transverse reinforcement is highly dependent on the bar surface configuration, different results were observed in the literature. Harajli and Abouniaj [18] concluded that transverse reinforcement significantly increases the bond strength of GFRP bars. Esfahani et al. [4] observed that confinement increases the bond strength of ribbed bars, while it has no considerable effect on the bond strength of sand-coated bars. Basaran and Kalkan [17] reported no effect or even, in some cases, negative effect for confinement on the bond strength of FRP bars.

3.3 Concrete Cover and Space Between Bars

More concrete cover results in more confinement for GFRP bars. Therefore, a direct effect is expected for the concrete cover and the transverse reinforcement. If the concrete cover is insufficient to apply adequate confinement to FRP bars, splitting failure occurs before pullout failure. Increasing concrete cover can switch the failure mode from splitting failure to pullout failure.

It was showed in [5] and [18] research studies that the bond strength of steel bars is more affected by increasing the concrete cover and space between bars than GFRP bars. It may be due to the larger rib area of steel bars. The results of [18] study also indicated that increasing the concrete cover affects the bond strength of ribbed bars while it does not affect thread-wrapped bars. The findings of [16] and [17] showed that increasing the concrete cover or bar spacing increases the FRP bar bond strength. Also, the concrete cover of greater than $2.5d_b$ has no considerable effect on bond behavior. In fact, for bars with a smaller bar diameter, a smaller concrete cover is sufficient, while a larger bar diameter needs more concrete cover to prevent splitting failure.

3.4 Surface Condition

There are different methods to manufacture FRP bars: sand coated, spiral pattern, ribbed, indented surface, and braided surface. Based on surface conditions, different mechanical interlocking and, as a result, different bond strength may be obtained. References [4, 17, 18] reported that mechanical load-bearing bars exhibited better bond performance in comparison to friction load-bearing bars. They observed that the sand grain size of FRP bars could change the bond mechanism from friction to mechanical interlocking so that coarse sand-coated CFRP bars experienced about 25% greater bond strength than that of fine sand-coated CFRP bars. Baena et al. [19] concluded that surface condition has a significant effect on the bond strength. Based on [20] findings, rib height and spacing have a considerable effect on bond behavior. However, there are still some contradictions about the effects of surface conditions on the bond strength based on different research studies. References [16] and [6] reported that the bond strength of the FRP reinforcing bars is not considerably affected by

the surface condition. This was in agreement with [21] and [5], who confirmed no bar surface effect on the bond strength. CSA S806-12 is the only North American standard that considers the effect of bar surface condition on the bond strength.

3.5 Concrete Compressive Strength and Concrete Type

Concrete compressive strength is a factor that is considered in all design standards for calculating the development length. Davalos et al. [22] study indicated that the bond strength obtained based on ACI 440.1R is unconservative for the low concrete compressive strength, while CSA S806 yields conservative results. However, for high-strength concrete, ACI 440.1R is more conservative than other design standards. The findings of Esfahani et al. [4] and [17] showed that the effect of concrete compressive strength on the bond strength is negligible. However, in some cases increasing the concrete compressive strength improved the bond strength.

The effect of concrete type is also investigated in the literature. Harajli et al. [23] reported that using fiber-reinforced concrete (FRC) improves the bond strength of FRP bars to concrete. It was also agreed with the results of [10] research study. It was showed that using steel FRC (SFRC) improves the performance of RC columns reinforced with spliced GFRP bars. It prevents spalling of concrete and increases the confinement level. Zemour et al. [9] investigated the effect of self-consolidating concrete (SCC) on the bond strength of FRP bars. They concluded that the bond strength of bars in the SCC specimens was slightly lower than that of their NC counterparts, whereas a concrete-type factor of 1.2 was recommended to apply to the SCC beams.

3.6 Diameter and Modulus of Elasticity of Bars

As reported in the literature, the bond strength decreases by increasing the bar diameter. When the bar diameter increases, the void trapped at the interface of concrete and bar increases. This weak interface can result in a decrease in bond strength. Also, increasing the contact area of the bar with concrete may cause this decrement. According to Esfahani et al. [4] and [17] findings, reducing the bond strength is more in mechanical load-bearing bars. It is due to fixed rib depths of bars, leading to changing the load transferring mechanism from mechanical to frictional.

The effect of modulus of elasticity was also well investigated in the literature. Mosley et al. [5] concluded that the bar modulus of elasticity substantially influences the bond strength. References [6] and [17] also reported that increasing the bar modulus of elasticity results in increased bond strength.

3.7 Bar Casting Position

The top casting position of horizontal FRP bars may result in a decrease in bond strength. This reduction in bond strength is considered as a modification factor in different design standards. An average reduction in the bond strength due to the top-casting position of FRP reinforcing bars was reported about 7% by [6]. A top bar factor of 1.3 was recommended by [6], while [24] recommended 1.08 to 1.38 modification factor for NC concrete and 1.11 to 1.22 for high-strength concrete. Zemour et al. [25] reported less than 9% reduction due to the casting position effect in 10 beam specimens. They concluded that the effect of casting position on the bond performance depends on the splice length, concrete type, and the depth of concrete cast beneath the bar. The SCC beams showed lower bond strength reduction than the NC beams due to the casting position effect. Specimens with 400 mm beam height experience no reduction in bond strength due to the casting position of bars, while the 600 mm high specimens reported lower bond strength due to the casting position of bars. Comparing the results of two beam-end test specimens, [26] observed that the bond strength of top-cast bars is 66% of bottom-cast bars.

4 Conclusion

In this paper, a review of the bond behavior of FRP bar to concrete is presented. The following conclusions can be drawn:

1. Development length and bond strength of FRP bar to concrete based on three North American codes is summarized. To better understand their differences, the factors which are considered in each design code were compared. The equation proposed by CSA S6-19 is derived by modifying its expression for the steel bars. Generally, the two Canadian standards consider more factors affecting the bond strength. In contrast, limited parameters (embedment length, concrete strength, concrete cover, bar spacing, bar location, bar diameter, and bar stress) are taken into account in ACI 440.1R-15.
2. Investigation of 74 specimens from the literature showed that the splice length prediction was unconservative in 27, 28, and 8% of specimens based on CSA S806-12, CSA S6-19, and ACI 440.1R-15, respectively. The splitting failure mode was observed in these specimens despite providing the splice length more than the code recommendations. It is important to note that the database selected for code evaluation does not include all available data on GFRP and CFRP rebars which may influence the ratios mentioned above. Moreover, the database includes the test results on the old generations of GFRP and CFRP rebars. The FRP industry has evolved over the past decades, resulting in the new generation of GFRP and CFRP rebars with the superior bond strength and mechanical properties. This emphasizes that future research should investigate the bond

strength of the new generation of GFRP and CFRP rebars and revisit available design equations.

3. According to previous research studies, factors affecting FRP bar's bond strength to the concrete are comprehensively discussed. Embedment length, transverse reinforcement, concrete cover, bar spacing, surface condition, concrete strength and type, and bar diameter and modulus of elasticity were the factors investigated in this paper. While the effect of some factors was identical in different research studies, there are still contradictory opinions about the effects of some factors, including transverse reinforcement, surface condition, and concrete compressive strength, which should be more investigated in future studies.

Acknowledgements This research study was conducted with funding from the Tier-1 Canada Research Chair in Advanced Composite Materials for Civil Structures and Natural Sciences and Engineering Research Council of Canada (NSERC).

References

1. ACI Committee 440 (2015) Guide for the design and construction of structural concrete reinforced with fiber-reinforced polymer bars (ACI 440.1R-15). American Concrete Institute, Farmington Hills, MI
2. Aly R, Benmokrane B, Ebead U (2006) Tensile lap splicing of bundled CFRP reinforcing bars in concrete. J Compos Constr 10(4):287–294
3. Asadian A, Eslami A, Farghaly AS, Benmokrane B (2019) Splice strength of staggered and non-staggered bundled glass fiber-reinforced polymer reinforcing bars in concrete. ACI Struct J 116(4)
4. Esfahani MR, Rakhshanimehr M, Mousavi SR (2013) Bond strength of lap-spliced GFRP bars in concrete beams. J Compos Constr 17(3):314–323
5. Mosley CP, Tureyen AK, Frosch RJ (2008) Bond strength of nonmetallic reinforcing bars. ACI Struct J 105(5):634
6. Pay AC, Canbay E, Frosch RJ (2014) Bond strength of spliced fiber-reinforced polymer reinforcement. ACI Struct J 111(2)
7. Tighiouart B, Benmokrane B, Mukhopadhyaya P (1999) Bond strength of glass FRP rebar splices in beams under static loading. Constr Build Mater 13(7):383–392
8. Yan F, Lin Z, Yang M (2016) Bond mechanism and bond strength of GFRP bars to concrete: a review. Compos B Eng 98:56–69
9. Zemour N, Asadian A, Ahmed EA, Khayat KH, Benmokrane B (2018) Experimental study on the bond behavior of GFRP bars in normal and self-consolidating concrete. Constr Build Mater 189:869–881
10. Naqvi S (2016) Lap splice in glass fiber reinforced polymer-reinforced concrete rectangular columns subjected to cyclic-reversed loads
11. Tabatabaei A, Eslami A, Mohamed HM, Benmokrane B (2018) Strength of compression lap-spliced gfrp bars in concrete columns with different splice lengths. Constr Build Mater 182:657–669
12. Tabatabaei A, Eslami A, Mohamed HM, Benmokrane B (2019) Compression splices of GFRP bars in unconfined and confined concrete columns. J Compos Constr 23(6):04019046

13. Tabatabaei A, Mohamed HM, Eslami A, Benmokrane B (2020) Proposed design equations for lap splice of glass fiber-reinforced polymer bars under compression in concrete. ACI Struct J 117(2)
14. Canadian Standards Association (CSA) (2012) Design and construction of building components with fiber reinforced polymers (CAN/CSA S806-12). CSA Group, Mississauga, ON, Canada
15. Canadian Standards Association (CSA) (2019) Canadian highway bridge design code (CAN/CSA S6-19). CSA Group, Mississauga, ON, Canada
16. Choi D-U, Chun S-C, Ha S-S (2012) Bond strength of glass fibre-reinforced polymer bars in unconfined concrete. Eng Struct 34:303–313
17. Basaran B, Kalkan I (2020) Investigation on variables affecting bond strength between frp reinforcing bar and concrete by modified hinged beam tests. Compos Struct 112185
18. Harajli M, Abouniaj M (2010) Bond performance of GFRP bars in tension: experimental evaluation and assessment of ACI 440 guidelines. J Compos Constr 14(6):659–668
19. Baena M, Torres L, Turon A, Barris C (2009) Experimental study of bond behaviour between concrete and frp bars using a pull-out test. Compos B Eng 40(8):784–797
20. Hao Q, Wang Y, He Z, Ou J (2009) Bond strength of glass fiber reinforced polymer ribbed rebars in normal strength concrete. Constr Build Mater 23(2):865–871
21. Wambeke BW, Shield CK (2006) Development length of glass fiber-reinforced polymer bars in concrete. ACI Mater J 103(1):11
22. Davalos JF, Chen Y, Ray I (2012) Long-term durability prediction models for GFRP bars in concrete environment. J Compos Mater 46(16):1899–1914
23. Harajli M, Hamad B, Karam K (2002) Bond-slip response of reinforcing bars embedded in plain and fiber concrete. J Mater Civ Eng 14(6):503–511
24. Chaallal O, Benmokrane B (1993) Pullout and bond of glass-fibre rods embedded in concrete and cement grout. Mater Struct 26(3):167–175
25. Zemour N, Asadian A, Ahmed EA, Benmokrane B, Khayat KH (2019) Experimental study on splice strength of glass fiber-reinforced polymer reinforcing bars in normal and self-consolidating concrete. ACI Mater J 116(3)
26. Ehsani M, Saadatmanesh H, Tao S (1993) Bond of GFRP rebars to ordinary-strength concrete. Spec Publ 138:333–346

A Novel Productivity Measure for Steel Fabrication Fitting Process

L. Marshall, A. Suliman, and Z. Lei

1 Introduction

The steel industry has been an important long-time contributor to Canadian economy. Pairing this with the growing interest in off-site construction and off-site construction research over the past decade [1], and the difficulty of measuring and controlling productivity in the construction industry [2] makes for an ideal opportunity for improvement within the steel fabrication process. As the construction and manufacturing industries continue to change with new technology, and the use of off-site construction becomes more common it will be necessary for manufacturers to keep up with these new trends. To do this, understanding productivity and productivity metrics are critical elements of the improvement process [3].

Productivity concerns are always at the forefront in a construction or manufacturing setting, as this is an area where constant improvement can be desired. In areas of fabrication where a manual process is required, the concerns of productivity increase. You can no longer rely on the consistent output of a programmed machine and must rely on the fluctuating capacity of individual workers. The fitting process in industrial steel fabrication is not exempt from this lag in productivity. It is apparent that within the entire process of steel fabrication, the stations that involve a manual process instead of a machine process are areas where productivity is harder to control. Often these stations will experience backups and bottlenecks if they cannot keep up with production coming upstream of the station. Pairing these manual processes with the inherent nature of steel fabrication, which is an area with low repetitiveness in production and a diverse range of products [4], adds an extra degree of difficulty in tracking and controlling the productivity.

L. Marshall (✉) · A. Suliman · Z. Lei
Off-Site Construction Research Centre, University of New Brunswick, Fredericton, Canada
e-mail: lmarsha1@unb.ca

S. Walbridge et al. (eds.), *Proceedings of the Canadian Society of Civil Engineering Annual Conference 2021*, Lecture Notes in Civil Engineering 240,
https://doi.org/10.1007/978-981-19-0507-0_5

Understanding the process at the fitting station was necessary moving forward in the study. Unlike other stations where the same process is followed every time, the fitting station could be subject to different actions and processes with each different assembly. A general description of what is expected at the fitting station is as follows: (1) Beam and column assemblies are moved to the fitting station via conveyor belt from the Computerized Numerical Control (CNC) coping machines, (2) The beams and columns are then separated onto four distinct fitting benches, generally separated by complexity (3) When the beams and columns are at the fitting bench, a 'fitter helper' will go retrieve the other pieces making up the assembly (stiffeners, end plates, etc.), (4) When all pieces of the assembly are available to the fitter, they then complete the process of attaching the pieces through either bolting, or tack welding (tacking) onto the larger structural member, (5) The fitted assembly is moved to the welding station (if welding is required).

Like any station, a reliable productivity metric is imperative in understanding and quantifying the productivity of the fitting station. Process and productivity improvements are imperative to ensure products continue to meet industry standards for quality and productivity and as noted by [3]. For areas such as the manual process of the steel fitting station in this case, a reliable productivity metric system is a critical element in productivity performance evaluation and improving the process. Due to the nature of the manual process at the fitting station, where each assembly that enters the station could be subject to a different procedure than the one before, developing this productivity metric becomes more complex. The variation in the work being done with each entering assembly means that the current metric being trialed of "parts fit per man hour" fails to capture much of what is being done at the fitting station.

The objective of this current study is to determine an appropriate measure for the productivity at the fitting station. The measure being trialed for the productivity is the number of parts fit on an assembly per man hour; this metric does not provide an understanding of the different processes that happen at the fitting station and does not help management to understand the actual productivity of the station, and individual workers. This study will provide the industry partner with a new metric for the productivity that encompasses all the processes that happen at the fitting station, giving an accurate and fair way of measuring the productivity.

With the findings of this study, management at the fabrication shop will be able to understand the process and productivity at a higher level than previously. The new metric will help provide an accurate representation of the station performance, and will provide additional benefits including plant scheduling, predictive modelling, and a starting point for automatic data collection. These changes will look to help the industry partner keep up with the productivity growth many off-site construction sectors are seeing [5].

This paper is outlined as follows: (1) a background and brief literature review (2) a description of the study and the steps taken to ensure accurate and efficient time study, (3) the results of the study in the form of normalized values of the data collected and the calculated results, (4) a discussion of the results and what they mean in terms of the productivity metric and the next steps for the plant, and (5) a

summary of the challenges and limitations of the study and importance of this study to the facility.

2 Background and Literature Review

This literature review focuses on past research relating to the topic of productivity measurement and tracking, as well as productivity modelling and prediction in the steel manufacturing industry. The topic of productivity measurement in the construction industry is a popular and well studied topic. As previously mentioned with the current trends in construction and the need to understand performance, the study of productivity metrics is becoming increasingly popular.

Traditional measures of labour productivity in the steel industry focus on non-distinctive measures such as hours per metric tonne produced, or even value-added per tonne even more recently [6, 7]. While comparing the performance of steel manufacturers in Japan and the US in their studies, the two metrics mentioned above were used to assess performance. Their work recognized the limitations of using a metric like hours per metric tonne produced, stating "tonnage-based measures make no adjustment for differences in steel 'quality' and the extent of finishing operations" recognizing that there are differences in steel pieces being fabricated [7]. While it was argued that value-added per tonne was a more accurate measure, it can be difficult to apply and track as a labour productivity metric and was used primarily as a comparison between two separate companies.

The research and methodology completed for this project follows a similar framework to that proposed by [8]. Their research identified a 3-phase approach consisting of (1) Productivity measurement, (2) Data Acquisition, and (3) Productivity Model Development [8]. The research performed for this study focuses on mainly the first phase which lays the groundwork to build off for the remaining two phases. In terms of productivity measurement, [8] defined three essential criteria for the metric as follows "(1) The output measurement should have high correlation with the labor hours and must be quantifiable. (2) The output measurement should be independent from productivity-influencing factors, such as site conditions and labor skills, and (3) The output measurement should be easy to track and cost effective to implement". For steel fabrication in particular, Song and AbourRizk [8] noted a potential obstacle in defining a productivity metric; "Fabricated pieces are unique… a simple count of steel piece without considering its uniqueness and complexity does not truly reflect the amount of work". Their research illustrates similar thoughts and experiences as our current study did in terms of a productivity metric.

In a thesis study on regression-based analytics for steel fabrication productivity modeling [9] noted that when measuring productivity in steel fabrication "an approach needs to account for sufficient project details such as product uniqueness in design, complexity, and uncertainty involved in steel fabrication processes". The methodology in their research confirms that for the modelling of steel fabrication, appropriate dependent and independent variables must be selected for an accurate

model. Correlation coefficients are calculated between several variables to determine which shall be used for the multiple linear regression model. This process ensures that the metrics being used to model the productivity of the fabrication adequately capture the uniqueness and complexity with each different steel piece.

The novelty of the proposed research lies within its data driven productivity measure, with a simple methodology that can be applied to any station in the process. Traditional metrics such as hours per metric tonne, or parts fit per man hour fail to capture the differences in steel pieces being fabricated. Previous research on this topic relies on more complex models generated from historically available data to generate productivity measurements. This left a gap where an accurate and representative metric was desired without the need for advanced modelling and need of historical data. Our methodology presents an alternative that can easily be implemented to any station within the steel fabrication process, building off previous research on a productivity measurement framework such as that proposed by Song and AbourRizk [8].

3 Proposed Method

The study design consisted of six steps performed over the course of four months at a combination of the research centre and the industry partner location. The planning and analysis of the data was performed at the University of New Brunswick, with the time study being performed at the fitting station at the industry partner location in Saint John, New Brunswick. The different components of the study include initial data review to confirm a need for the study, initial observations to draft a data collection sheet, testing of the data collection sheet, and a time study / data collection. Figure 1 provides a visualization of the study design.

The first step of the process was an initial review of data from the fitting station in the form of timecards that the manufacturer historically collected. The timecard data was entered in by the fitters themselves and included information on the just the number of pieces fit per unit of time. A basic analysis of the data was completed but the results did not provide the expected value from management. The results were valuable for baselining, but the data being collected was not detailed enough to determine areas of improvement for specific actions at the station. The lack of

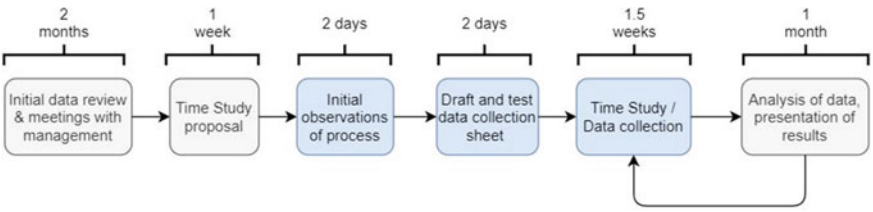

Fig. 1 Flowchart of the complete study process

useful data provided by the timecards presented an opportunity for a time study. The proposed time study involved the observation of the process and development of a data collection sheet, collection of the data, as well as analysis of the results to determine productivity levels and establish a new productivity metric.

The first step at the industry partner location was an initial observation of the station to determine how it worked. During this phase there was no observations recorded, but the process was observed to determine all the activities being performed. As previously mentioned, the fitting process as a wide range of processes and not every assembly is the same. It was therefore necessary that an adequate number of assemblies at several different benches were observed to capture every process at the station.

After observing the process, a data collection sheet was drafted to be used for the time study. Due to the multiple different processes, the data sheet was separated into five sections (due to the five distinct processes), which included the loading of the assembly, preparing the assembly, fitting pieces, inspection, and unloading. Each of these processes was then broken into sub-actions to provide the most accurate representation of the process. The initial draft of the data collection sheet was then taken back to the plant where it was tested and modified to ensure its validity to be used for the time study. An example of the designed data sheet for the time entry section is presented in Fig. 2.

The first-time study was performed over the course of seven business days. Each day one fitting bench was chosen to observe, and the different processes and actions were documented to the minute. This provided consistent daily data and over the course of the study all different benches and operators had the chance to be observed. Due to the nature of the very specific observation and only one station observed per

Process	Action	Start Time	End Time	Elapsed Time	Comments
Loading Assembly	Loading Sub Task 1				
	Loading Sub Task 2				
Preparing Assembly	Preparing Sub Task 1				
	Preparing Sub Task 2				
	Preparing Sub Task 3				
Fitting	Fitting Sub Task 1				# Coping cuts = ...
	Fitting Sub Task 2				# Tacks = ...
	Fitting Sub Task 3				# Bolts = ...
	Fitting Sub Task 4				
	Fitting Sub Task 5				
Inspection	Inspection Sub Task 1				
Unloading	Unloading Sub Task 1				

Fig. 2 Sample fitting station time collection sheet

day, the study was only able to provide a limited amount of data points, however data that was gathered was very accurate.

After collection of the data, a statistical analysis was performed. The analysis included calculations with the data to determine value added, non-value added, and cycle times. These times along with work measures that were collected were used in a correlation analysis, and subsequent linear regression modelling. The results of the analysis were able to provide a good understanding of station productivity, however due to the lack of data points a second time study was proposed to collect more data.

The second time study was performed over a similar 1.5 weeks. The difference between the second study and the first was that several of the facility's staff were used for the study. This was done to speed up the data collection process, and as well to limit travel between different health districts due to COVID-19 restrictions. The staff members were given a presentation about how the data collection process should be completed and how data should be entered into the sheet.

With both the studies completed, result validation tests were performed to ensure a statistically sufficient sample size had been collected. After each of the studies, a sample size calculation (elaboration in the following section) was performed to ensure the proper sample size had been calculated. After both studies the sample size was considered accurate to a 90% confidence level. The next step in the validation included looking through the data to ensure all outliers were removed before the analysis, this consisted of manually removing clear outliers, as well as meetings with industry partners to review data. The studies performed were able to provide sufficient data to ensure an accurate analysis could be performed.

4 Study Results and Discussion

Each assembly that entered the fitting bench was observed start to finish. The observations recorded included the loading times, the time spent reviewing the shop drawings and the time spent marking outlines on the structural member (these are all considered loading and preparation times). When the fitting of the pieces started, the times for tack welding, bolting, cutting, and grinding were recorded, and along with these times, the number of actions was also recorded (number of tacks, number of bolts, number of cuts, etc.). Table 1 shows an example of 10 data points that include some of the important information recorded in the time study.

The data in Table 1 provides an example of how different the work done at the fitting bench can be with each different assembly that enters the station. All data in Table 1 has a normalization factor applied to it to ensure confidentiality with the industry partner. A statistical description of the *entire* dataset can be found in Table 2.

Table 2 describes the collected dataset in whole based on statistical measures. It also presents the major differences that can be expected for each assembly entering the station. The difference in the work being done to each different assembly highlights the need for a more in-depth way to measure the productivity.

Table 1 Example of collected data

Assembly number	# Pieces fit	# Tack welds	# Bolts used	# Coping cuts	VA time (min)	Non-VA time (min)	Cycle time (min)
1	7	21	0	0	19	33	64
2	2	4	0	0	8	7	21
3	11	14	4	4	24	13	34
4	5	4	5	0	12	11	36
5	8	30	0	4	70	70	212
6	4	0	12	0	10	3	15
7	2	4	0	0	5	8	13
8	14	13	41	0	59	48	257
9	5	4	6	0	12	30	59
10	2	0	6	2	30	21	82

Table 2 Statistical results of the collected data

Value	# Pieces fit	# Tack welds	# Bolts used	# Coping cuts	VA time (min)	Non-VA time (min)	Cycle time (min)
Maximum	14	30	41	8	76	70	257
Minimum	0	0	0	0	4	3	11
Mean	4	7.6	2.8	0.64	18.43	18.03	57.98
Median	3	6	0	0	14.5	14.5	45
Standard deviation	2.90	6.60	5.91	1.42	12.75	11.95	47.43

With the results of the preliminary study, a standard lean manufacturing formula was used to calculate how many additional cycles would be required. Equation (1) shows the empirical formula used from [10].

$$n = \left[40\frac{\sqrt{n'\sum x^2 - \left(\sum x\right)^2}}{\sum x}\right]^2 \tag{1}$$

where n' is the preliminary study size, x is the amount of value-added time measured, and n is the number of cycles need to observe. The first round of tests resulted in the following: $n' = 20$, $\sum x = 239$, and $\sum x^2 = 3033$.

The results of this indicated that 99.2 data points (approximately 80 more) would need to be performed in the second round of the study.

With the second study complete, a second statistical test was performed to ensure a sufficient sample size. Based on the standard deviation of the value-added time, a

sample size calculation was performed based on formula 2 below [11].

$$SampleSize = \frac{z^2\sigma^2}{E^2} \tag{2}$$

where z is the z-score based on a 90% confidence interval (1.645), σ is the standard deviation of the Value-Added time (12.747 min), and E was the error rate (2). The results of this test determined a sample size of 109.92 data points was necessary for 90% accuracy.

With both the time studies completed, a total of 90 complete and usable data points were obtained with all outliers removed, meaning we can be just less than 90% confident (86.34%) in our sample size. With these data points, a Microsoft Excel correlation analysis was performed between different measures of the work (i.e., number of tacks, bolts, cuts, number of pieces, weight of pieces, etc.), and different measure of the time (tacking, bolting & cutting times, cycle time, value added time, etc.). The values in the time measurement column include the following:

- **Tacking Process time**, which is the complete process to tack weld a piece onto the assembly including reviewing the drawing, measuring and marking the location, grinding the piece, and tacking it on.
- **Tacking and Grinding time**, which is similar to the previous but without the reviewing and marking (this was done to distinguish between Value added and non-Value added).
- **Bolting Time**, which is the complete time it takes to bolt a piece onto the assembly.
- **Coping Time**, which is the time it takes to cut out a piece of the assembly.

The results in Table 3 indicate which work measure is correlated to the time for each different process. In the initial study, the tacking process time, and tacking and grinding times were most closely correlated with the number of pieces tacked on to the

Table 3 Correlation analysis results

Time measurement	Initial study (~30 data points)		Second study (~100 data points)	
	Highest correlation	Correlation value	Highest correlation	Correlation value
Tacking process time	Number of parts tacked on	0.960	Number of parts tacked on	0.708
Tacking and grinding time	Number of parts tacked on	0.960	Number of parts tacked on	0.640
Bolting time	*(Number of bolts) x (number of parts bolted)	0.977	*Number of bolts used	0.907
Coping time	Number of coping cuts	0.932	Number of coping cuts	0.514

*Means a change in the highest correlated variable

assembly, the bolting was most closely correlated with the product of the number of bolts used and the number of parts being bolted, and the coping time with the number of coping cuts made. In the second round of observations, all the highest correlations remained the same apart from the bolting time which can be better represented by just the number of bolts being used. An important note about the metrics chosen is that they are all measures that are possible to be known before the fitting process begins. This is important when considering future models to predict the time at the fitting station, for example because all the inputs used in the proposed cycle time equation are known before the work starts, a spreadsheet with this equation implemented can be easily used to track performance.

The lower correlation values in the second round of observations are expected to be as a result of having multiple people performing observations, unlike the one person performing observations in the first round of the study, as well as a greater number of fitters being observed (increasing the differences presented by a fitter's individual style of work). While the values are lower it is important to highlight that the correlations presented in the table remain the highest of all the different measures tested and provide the best description of the time expected for each process at the station. The following are a detailed description of the correlations.

- *Tacking Process Time*: This was most closely correlated with the number of parts tacked. This is because each part that is tacked on requires a similar amount of work to be done before it can be put on the assembly. This process starts with the review of the shop drawings to determine where the piece fits on to the assembly. The next step is the measuring and marking, which is done by marking the beam or column with chalk where the part will be tacked on. The part is then grinded to smooth out rough or sharp edges caused by the CNC saw or plate processor. Finally, the parts are tack welded on to the assembly. This entire process is repeated for each piece that must be tacked on to the assembly.
- *Tacking and Grinding Time*: This time is again most closely correlated with the number of parts tacked on to the assembly. This time is like the previous however it leaves out the reviewing and marking times. This was done to present a way to determine the non-value-added time of the process (i.e., Tacking Process Time subtract Tacking and Grinding Time).
- *Bolting Time*: This time is most closely correlated with the number of bolts being used. The number of pieces being bolted on can be left out of the correlation, because the time required to complete the process lies within the actual bolting time. For example, one piece being bolted on with 10 bolts will take longer than three pieces being bolted on with two bolts each (6 bolts total). The bolting time is the time the worker spends positioning the pieces on the assembly, manually the bolts, and then fully fastening them with the impact gun. This time does not include reviewing or marking because the holes are already drilled, and it is clear where the pieces must go (unlike the tacked pieces as there is no indication where the pieces must go apart from the shop drawings).
- *Coping Time*: This time is most closely correlated with the number of coping cuts to be made on the assembly. Some of the cuts required on the sections are too

small or are positioned in a way that the CNC coping machine can not fully cut them out. If this is the case the fitters must cut out the pieces with a cutting torch, and then grind the rough edges left. The total number of these cuts is the measure correlating to the time.

Using the results of the correlation analysis, Microsoft Excel data analysis was used to make a linear regression model for each of these process times. Equations (3)–(6) show the equations developed that can model the times for the fitting station work. Each equation produces a normalized value (in minutes) for confidentiality.

$$TackingProcessTime = 4.32(\#PartsTacked) + 7.62 \tag{3}$$

$$Tacking\&GrindingTime = 2.35(\#PartsTacked) + 3.68 \tag{4}$$

$$Boltingtime = 0.82(\#Bolts) + 0.46 \tag{5}$$

$$CopingTime = 1.18(\#CopingCuts) + 0.77 \tag{6}$$

The four equations above make it possible to calculate the cycle time for each assembly based on the expected work to be done. Because all the measure being used are values available before work is done on the assembly, it makes it possible to predict and compare the actual cycle time (which is something the fitters record in the timecards) between the expected cycle time for a given assembly. This makes it possible to gauge productivity based on historical values and provides an accurate way to track employee and station performance.

The results of this study prove that measuring the productivity of the industrial steel fitting station by just counting the number of parts fits is an inaccurate description of the work being done at the station. By only considering the number of pieces fit, all the actual work done on the piece is not considered, and the number of just the pieces will not give an indication on the complexity of work nor the different aspects of the process.

To determine the accuracy of the new metric compared to the old metric, the root mean square error (RMSE) of the two metrics was calculated. RMSE formula applied in this study is simply the square root of the mean of the squared difference between the actual and estimated data points of the fitting work time. For each data point, the cycle time was estimated using the new metric (containing the separate components), and the old metric (using just the total number of pieces fit). These estimations were then compared with the actual cycle time of each point to determine the RMSE. Table 4 shows the input values for the RMSE test.

The result of this test showed the new metric, which considered the separate components, to be 42.4% more accurate than the currently used metric. With this we can confidently say that considering each part of the process separately and combining them to set a benchmark cycle time based on the expected work to be

Table 4 RMSE test

	Old metric (total parts fit)	New metric (separate components)
Measurement	Value	Value
# Data points	90	90
Sum R^2	93,368.15	39,477.62
RMSE	32.21	20.94
Difference	42.4%	

done allows for a more accurate way to measure the productivity as it considers all aspects of a wide range of work seen at the fitting station.

While the study was capable of producing accurate and meaningful results, there were some limitations to the design of the study. These limitations started with the station itself. Because the fitting station is four separate benches and four separate workers, there is a factor of the fitter skillset that was not captured. While it can be assumed for the most part that the workers produce at a similar level, there is a gap in the skill and the speed at which a senior experienced fitter can perform work than a new and less experienced employee. The next limitation was in the second round of the time study. Because only one station could be observed at a time by one person, it would take a significant amount of time to produce an adequate number of data points for the analysis. To account for this, five staff members from the industry partner performed the time study and recorded results. This was an efficient way of recording data however the potential for mistakes in data recording or having different people measure in a different way was a potential. Given this limitation the data produced by the second round of observations presented the same trends as seen in the first round of the study. The final limitation was in the analysis phase of the study. When looking at correlations and regressions only a linear regression model was considered. It is possible that considering additional data points and performing a more in-depth analysis with a multivariable regression model may refine the conclusion presented even more. Regardless of these limitations the results of this study still prove the necessity of considering additional factors when tracking the productivity at the fitting station.

5 Conclusion

Productivity will always be important metric to track in a setting such as that of the industrial steel fabrication process. For many machines that are programed for a certain job it is easy to track and predict their productivity and output. For a station such as the fitting station, which is a completely done by the fitters, it becomes more difficult to track and predict productivity. This problem becomes increasingly harder when there are different workers at the station, and different work being done on each assembly. Tracking the productivity by just the number of parts fit per man hour can

be unfair for workers fitting more complex assemblies and can be misleading when estimating station productivity. To account for this, a productivity metric accounting for these different processes is proposed in this study.

The productivity measure proposed was found based on a time study to observe the process and determine how to quantify the productivity. The results of the time study were used to perform a correlation analysis to determine which work measures affected the process time the greatest. With these measures, a linear regression model was produced capable of predicting/estimating the cycle time (output) based on given work measure for each assembly (input). With this estimation it is possible to set a benchmark cycle time based on the expected work, and productivity can be tracked in a more accurate way considering the different process being performed, rather than just counting the number of parts.

The results obtained in this study and correlation analysis showed that the cycle time can be estimated by a combination of the number of parts being tacked, the number of bolts being used, and the number of coping cuts. This was determined because the tacking process time was closely correlated with the number of parts tacked, the bolting time was closely correlated with the number of bolts used, and the coping time was closely correlated with the number of coping cuts made. These results prove that the productivity cannot be measured by just the number of parts alone, and that the entire process time must be broken up into individual processes to more accurately represent the station.

The time study was able to produce accurate results, however the study design still had some limitations. The fitter skill and the different people performing the study causes concerns for some of the accuracy of the data. In the analysis phase of the study, performing just a linear regression of the data points suggests there is a possibility for a more accurate model using multiple variables. With all the limitations considered, the results are considered accurate and prove the need for the study and why additional measure need to be considered in the metric.

Overall, this study proves that the fitting station cannot be modelled by just the number of parts that are being fit on each assembly. The 42% increase in accuracy between the new metric and the old metric show there is a need to consider the individual components not just the number of pieces fit, and this new proposed productivity metric meets that goal. With the results of this study, the industry partner will be able to implement a more accurate way of basing the performance of the fitting station based off historical values. The drawbacks from this metric from the industry partner standpoint is that is not as intuitive as the metric being trialed. Although the new metric results in a more accurate estimation, it is harder to visualize than parts per hour. This is something that has the potential to be mitigated through automatic data collection and productivity visualization tools (such as Power BI for example), or spreadsheet tracking of the data. The benefits of having an equation capable of estimating cycle times will be to help with production scheduling, job estimates, and employee performance tracking. This study also opens the door for future work at the fitting station and the fabrication plant. Some of this included setting up an automated data collection procedure and linking this to a spreadsheet and automatically tracking productivity.

Acknowledgements The Authors would like to thank all funding sources that made this work possible. This research was supported financially by MITACS accelerate program (Appl.# IT18462), as well as Ocean Steel Ltd. (OSCO Construction Group) who facilitated this project both financially and with technical guidance.

References

1. Hosseini MR, Martek I, Zavadskas EK, Ajbinu AA, Arashpour M, Chileshe N (2018) Critical evaluation of off-site construction research: a Scientometric analysis. Autom Constr 87:235–247
2. Motwani J, Kumar A, Novakoski M (1995) Measuring construction productivity: a practical approach. Work study
3. Park H, Thomas SR, Tucker RL (2005) Benchmarking of construction productivity. J Constr Eng Manage 131(7):772–778
4. Hofacker A, Gandhi D (2009) Analysis of the productivity in structural steel fabrication processes
5. Eastman CM, Sacks R (2008) Relative productivity in the AEC industries in the United States for on-site and off-site activities. J Constr Eng Manage 134(7):517–526
6. Lieberman MB, Kang J (2008) How to measure company productivity using value-added: a focus on Pohang Steel (POSCO). Asia Pac J Manage 25(2):209–224
7. Lieberman MB, Johnson DR (1999) Comparative productivity of Japanese and US steel producers, 1958–1993. Jpn World Econ 11(1):1–27
8. Song L, AbouRizk SM (2008) Measuring and modeling labor productivity using historical data. J Constr Eng Manage 134(10):786–794
9. Mohsenijam A (2019) Advancing regression based analytics for steel fabrication. Prod Model 4–72
10. Santos J, Wysk RA, Torres JMTA-TT (2014) Improving production with lean thinking. In: NV-1 o. Wiley, Hoboken
11. Evans MJ, Rosenthal JS (2009) Probability and statistics: the science of uncertainty. Freeman, W.H, p 2

Iqaluit, Nunavut—Sewer Main Replacement in Permafrost

I. Crawford, K. Johnson, S. Plourde, S. Turner, J. Harasimo, R. Sithole, M. Lafleur, and C. Keung

1 Background

The construction of the accommodation and sealift area of the Crystal II Air Base, now known as the City of Iqaluit, was completed in 1941 as part of the original series of airfields used for ferrying aircraft from North America to Europe along what was called the Crimson Route. The original level of service of this area, referred to as Lower Base, was trucked water and sewage until 1985, when piped services were constructed, which included the piped services from Access Vault (AV) 205 to Access Vault (AV) 211.

Shallow buried sewers are a common practice for the construction of piped sewers in Iqaluit and Nunavut. At the time of the installation of the original buried sewer and water system, placing buried services within the active layer was thought to be an appropriate construction approach. However, with time, it was discovered that shallow buried services could significantly deteriorate from freeze-thaw forces experienced within the dynamic active layer, and in several cases destroying the pipe by crushing it and ultimately constricting the flow (Fig. 1).

A replacement project was advanced in 1996, and the replacement of segments AV207 to AV208 was completed. The observations made during the 1996 replacement suggested that the ground conditions in the active layer were poor, and special design provisions were needed for future construction in the neighbourhood. These

I. Crawford · K. Johnson (✉) · S. Plourde · M. Lafleur · C. Keung
EXP, St. Alberta, Canada
e-mail: ken.johnson@exp.com

S. Turner · J. Harasimo
City of Iqaluit, Iqaluit, Canada

R. Sithole
Colliers, Iqaluit, Canada

S. Walbridge et al. (eds.), *Proceedings of the Canadian Society of Civil Engineering Annual Conference 2021*, Lecture Notes in Civil Engineering 240,
https://doi.org/10.1007/978-981-19-0507-0_6

Fig. 1 Project limits of sewer replacement access vault 205 to access vault 211 in lower base

provisions included attention to the dewatering of the construction trench, and supplementary insulation in the trench to make sure that the installed pipe stayed independent from the active layer and was not prone to freeze thaw dynamics of the active layer.

2 Geotechnical Considerations

Although there does not appear to be any large areas where bedrock or large boulders are present, the terrain of Iqaluit is highly variable and encountering bedrock or large boulders during construction is not uncommon. This is particularly significant in areas of new construction where excavation and blasting of rock may be required to achieve the appropriate depth of installation of the pipe and the AVs. However, no rock was encountered during the installation of the 1985 sewer or the replacement work in 1996.

It is also very possible that the soil in the construction area is contaminated with hydrocarbons. This is a characteristic of the entire Lower Base area, as a legacy of the military fuel storage activity in this area associated with the airfield operations almost 80 years ago. Provisions should be made for construction in fuel-contaminated soils to control risks associated with potential removal and remediation work.

3 Sewage Flow Estimates

The design sewage flow is one of the most important calculations incorporated into the design criteria. The appropriate sewer pipe sizing is based upon current estimated sewage flows from the upstream neighborhoods of Iqaluit and includes recent developments, as well as the anticipated development within the service area. A conservative approach was applied by estimating a maximum potential loading from anticipated future developments, as well as the addition of existing buildings to the piped service.

Future flows were estimated using growth projections, which applied a conservative estimate of future flows based on background information and current knowledge of the City's development plans. Based on the City of Iqaluit General Plan, three population projections were used in the design criteria (low = 2.04%, medium = 2.87%, high = 3.38%).

4 Sewer Depth, Alignment and Pipe Strength

Iqaluit's municipal guideline recommends a minimum cover of at least 3.0 m from the finished grade to the top of pipe. This is intended to reduce the influence of active layer thawing dynamics acting on the pipe, which can cause pipe deformation and complete collapse due to external pressures developing during freeze back of the active layer. Climate change and the associated impacts within the active layer may further influence the stability of buried services in Iqaluit in the future.

The existing sewer profile provides only between 2.0 and 2.5 m of cover from the finished grade to the top of the pipe. One major constraint to the possibility of deepening the sewer profile is the downstream connection near AV211, which requires crossing over a 2300 mm diameter culvert. Going under the existing culvert is also not an option for gravity conveyance because there is insufficient grade to connect to AV 211. Therefore, to maintain minimum grades and hydraulic flow, the invert elevation at AV 211 will dictate the upstream profile of the new sewer.

The existing water and sewer mains occupy the south edge of Mivvik Street. Replacement of the sewer along this existing alignment conveys a multitude of constructability issues since this would require working within a very wet area with existing water supply, water recirculation, and sewer mains, as well as multiple water and sewer service connections to the adjacent buildings. An opportunity exists to reduce these construction issues, achieve a significant savings in construction costs and reduce the risk of cross contamination by constructing the new sewer main in its own separate trench on the north edge of the street.

The municipal guidelines require the use of DR11 (ratio of pipe outer diameter divided by the wall thickness) polyethylene pipe with a minimum pressure rating of 1100 kPa (160 psi). However, since the depth of burial may be under the recommended 3.0 m, to provide adequate pipe strength, and freeze protection, additional

design considerations are necessary which include: installation of DR9 polyethylene pipe with a minimum pressure rating of 1380 kPa (200 psi) complete with 50 mm applied polyurethane insulation and FRP jacket, and; the installation of additional board insulation over the pipe to maintain the permafrost within the pipe zone.

5 Pipe Zone and General Backfill

In situations where ice-rich or silty soils are encountered within 0.5 m below the specified pipe base, over excavation of at least 450 mm may be necessary to remove ice-rich soil that could thaw and contribute to pipe movement. The pipe zone material for dry trench conditions should consist of well-graded, natural sand and/or fine gravel. For wet trench conditions, a coarser material such as a well-graded, rounded to sub-rounded, natural gravel is preferred to stabilize the trench.

As the new sewer lines require a pipe diameter of at least 450 mm, there may not be sufficient space in the existing trench to maintain the spacing requirements between the proposed sewer and the existing watermains. In addition, in the situations where there are 3 pipes in a trench, namely water supply main, water recirculation main, and sewer main, it is desirable to align the sewer on the outside portion of the trench to further reduce the risk of cross contamination.

6 Access Vault Considerations

Access Vaults (AVs) are prefabricated, double walled, insulated metal units, installed at least 0.5 m below the base of the pipes. The typical temperature within the of the AVs will be between 5 and 10 °C, which is the result of the heat radiated from the sewer main going through the AV. Although the base of the AVs are insulated to provide a thermal break, the above freezing ambient temperature with the AV may cause some long term thaw below the AV. If thawing occurs, the stability of the AV may be compromised because of differential movement and can cause additional stresses on the pipe connections at the outside of the vaults. Breaks in the piping connected to the AVs have been observed in the past. To counter this effect, the thaw stability of the soils underlying the AVs must be considered.

Two additional considerations relating to potential differential movement of the AVs structures, are the insulation beneath the steel base of the AV, which protects the permafrost below the AV from thawing, and the use of flexible couplings in the piping connect to the AVs to accommodate the differential movement.

Access Vaults are essential structures that may cost more than $125,000 each. Therefore, opportunities to maintain the existing AVs could provide potential substantial savings. However, considering hydraulic performance, existing conditions of the AVs, construction factors and realignment of existing flows, the installation of new AVs in conjunction with the work may be necessary.

7 Construction Considerations

As the site is in the downtown core of Iqaluit, this project becomes significantly more challenging from a construction execution standpoint. The contractor will be required to safely contend with maintaining access and service to existing businesses, overhead electrical wires, excavation adjacent to and across existing roadways, managing heavy vehicular and pedestrian traffic, and limited workspace within the Right of Way.

If the desired alignment of the new sewer is along the existing sewer alignment, this will require removal and replacement of the existing sewer and likely the watermain piping. Thus, the project challenges, anticipated construction duration, and project/construction costs will be significantly increased due to the necessity of designing and maintaining a continuous sewer bypass and temporary water supply.

Alternatively, constructing a separate trench for the sewer main on the north site of the Mivvik Street would significantly reduce the project complexity, construction duration, service disturbances, and costs. As an order of magnitude estimate, installing the sewer main in the north side of Mivvik Street may generate a savings of up to 50 percent of the project costs.

8 Recommendations

The following design criteria are recommended for the capacity upgrades to the sewer main between AV 205 to AV211. The specific criteria include.

1. To estimate the future sewage flows in 2050, the current flows should apply a high growth rate scenario of 3.38%.
2. To address anticipated future sewer flows, sewer pipe diameters are recommended to be at least 450–500 mm.
3. To reduce the complexity, risk, schedule and cost of the sewer replacement, the new sewer main alignment should be constructed along the north side of Mivvik Street.
4. To provide adequate pipe strength, and freeze protection, it is recommended that DR9 insulated polyethylene pipe be installed, with a minimum pressure rating of 1380 kPa (200 psi) complete with 50 mm applied polyurethane insulation and FRP jacket.
5. To address the anticipated shallow installation depth of the pipe and the anticipated dynamics of the active layer along the pipe alignment, it is recommended that dewatering and over excavation in the pipe zone be undertaken, along with the installation of additional board insulation over the pipe-zone to maintain the permafrost.

6. To improve hydraulic performance and to address the deterioration of the existing Access Vaults, it is recommended that new AVs be installed in conjunction with the replacement of the sewer main from AV205 to AV211.
7. To manage the anticipated legacy soil and subsurface water contamination within the project, it is recommended that a contaminant management plan be developed which will include a provision for no terrestrial discharges.

Numerical Simulations of 15-Degree Inclined Dense Jets in Stagnate Water Over a Sloped Bottom

Xinyun Wang and Abdolmajid Mohammadian

1 Introduction

Inclined dense jets, or negatively buoyant jets are often discharged from desalination plants or wastewater treatment industrial outfall systems. This is required to obtain proper discharge specifications to make sure the brine has adequate mixing to minimize the risk to the marine creatures.

A sketch of inclined dense jet in stagnant water is shown in Fig. 1. The jet is discharged from the a round diffuser with initial velocity. It will reach the highest height and then falls back to the bottom and is then developed as a density current.

The experimental study on inclined dense jets has started and improved in the past 50 years. Zeitoun and Mcllhennry [1] firstly carried out a laboratory experimental study with various inclinations. Roberts et al. [2] presented an experimental study of 60° jet inclination with PIV and LIF technology and defined parameters related to the jet mixing and developments. Lane-Serff et al. [3] conducted an experimental study on the dense jets with a wide range from 15° to 75°, the instability on the inner side of the jet was observed in their study. Shao and Law carried out an experimental study with inclination of 30 and 45 with LIF and PIV technology [4], they found the elevation of the discharge nozzle height, where the Coanda effect will influence the jet mixing, hence the boundary influence can not be ignored. Besides these, more and more experimental studies were carried out [5–9]. These experimental studies provided useful information of the inclined dense jet both in terms of geometrical and dilution information.

With the development of CFD (computational fluid dynamics), the numerical modeling has started to play an important role on prediction of the outfall systems. Vafeiadou et al. [10] were the first researchers to perform the numerical study of the

X. Wang (✉) · A. Mohammadian
University of Ottawa, Ottawa, Canada
e-mail: xwang457@uottawa.ca

S. Walbridge et al. (eds.), *Proceedings of the Canadian Society of Civil Engineering Annual Conference 2021*, Lecture Notes in Civil Engineering 240,
https://doi.org/10.1007/978-981-19-0507-0_7

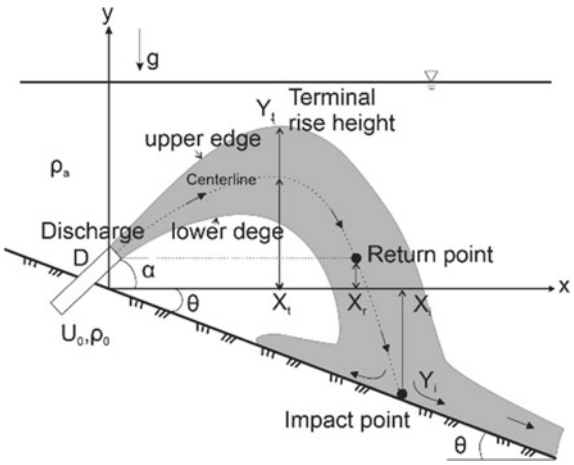

Fig. 1 Side view of inclined dense jet on a sloped bottom (slope angle θ) in stagnant water with inclination angle(α) (modified after [14]

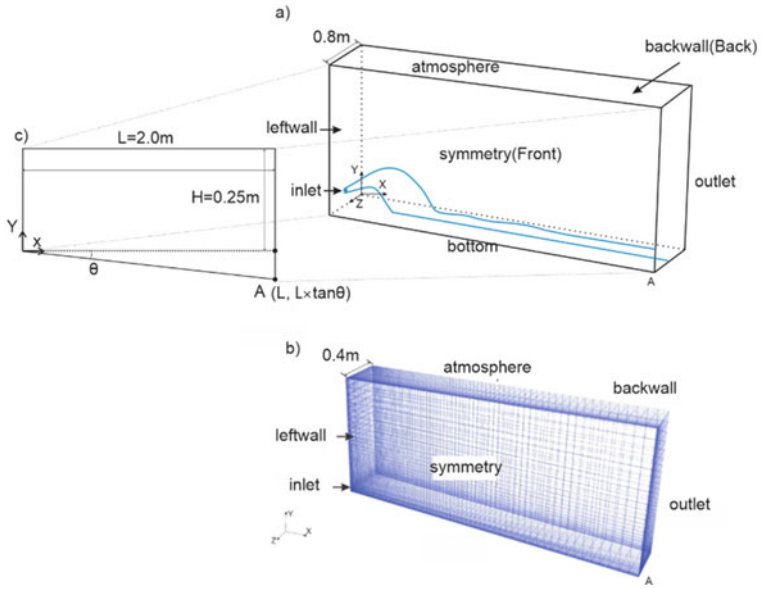

Fig. 2 **a** The experimental tank with sloped bottom; **b** Computational domain with mesh system; **c** x-y plane view

inclined dense jets. Their results had a good agreement with experimental studies. Oliver et al. [11] used the k-ε model for the simulation of the inclined dense jet. They initially calibrated the model with an experimental study on the vertical buoyant jets then applied it to the negatively buoyant jets. Kheirkhah Gildeh et al. [12] applied four different turbulence models to discover the performance of the models in prediction of the inclined dense jet with 45° and 60° in stagnant water. The Realizable k-ε and LRR turbulence model showed a better agreement with previous studies. Ardalan and Vafaei [13] also carried out a CFD study with the k-ε model with thermal-saline buoyant jets with a discharge angle of 45° in stationary water.

In many cases, the 60° discharge angle is considered as the design standard, however, with a shallow water depth, the jet will have a surface interaction which may cause a large area of brine pollution, so for a larger discharge angle, a larger water depth is needed. Considering that there is very limited research on the small discharge angle and with a sloped bottom, how the sloped bottom affects the development of the inclined dense jet with small inclination, is the main research topic in this study.

2 Methodology

2.1 Dimensional Analysis of Inclined Dense Jet

The side view of a typical inclined dense jet in stagnant water on a slopped bottom is shows in Fig. 1. The jet is discharged through a round nozzle of diameter (D) with velocity (U_0) and an initial angle α to the horizontal bottom (dash line), the slopped bottom with an inclination angle of θ, the ρ_0 and ρ_a are the density of the jet and receiving water respectively.

Return point and impact point can usually be treated as the same point in the horizontal situation. They should be addressed separately when there is a slopped bottom, or with a larger elevation.

All the flow properties can be represented related to three fluxes:

Flux of mass (Q_0), flux of momentum M and flux of buoyancy B_0,which can be defined as $Q = \frac{\pi d^2 U_0}{4}$; $M = \frac{\pi d^2 H_0^2}{4}$; $B = g'Q$. From these fluxes, there are two important length scales that are commonly used in jet analysis: $\mathrm{L_m} = \frac{M^{3/4}}{B^{1/2}} and \mathrm{L_q} = \frac{Q}{M^{1/2}}$

An important parameter related to jet study is densemetric Froude number, which can be presented as $Fr = \frac{U_0}{\sqrt{g_0' D}}$; $g_0^{'} = \frac{g(\rho_0 - \rho_a)}{\rho_a} or \mathrm{L_m} = \frac{M^{3/4}}{B^{1/2}} = (\frac{\pi}{4})^{1/4} DFr$

All the geometrical properties such as jet highest location (X_t, Y_t), return point (X_r) and impact point X_i can be a function of Fr number and discharge angle. Similarly, this can be applied to the dilution properties [2], the dilution at y_t and return point or impact point S_m, S_r S_i can be presented as $\frac{S_m}{Fr} = C1$, $\frac{S_r}{Fr} = C2$, $\frac{S_i}{Fr} = C3$. $C1$, $C2$ and $C3$ are the parameters which can be obtained from experimental studies.

2.2 Computational Setup

This study adopted the multi-fluid solver "twoLiquidMixingFoam" within the open source framework of OpenFoam to solve the Navier–stokes governing equations. A domain of 0.8 m width, 2 m length and 0.25 m height was considered for the numerical modeling setup. This flow problem is symmetric and a grid of 404,800 structured cells was found to be adequate in resolving the flow features for the given domain.

The nozzle diameter (D) for the inlet was 0.0108 m with 15° inclination. For the inlet, the boundary conditions were $U = 0.72\frac{\mathrm{m}}{\mathrm{s}}, u = U \times \cos(\theta), v = U \times \sin(\theta), w = 0, k = 0.006u^2, \varepsilon = \frac{0.06u^3}{D}, T = 20°\mathrm{C}$. The surrounding water density was set to 998.2063 kg/m^3. The initial conditions are listed in Table 1.

The flow was assumed to be incompressible in this study, the density for both jet and ambient water was calculated by Eq. (1) propose by Millero and Poisson [15]:

$$\rho = \rho_t + \mathrm{AS} + \mathrm{BS}^{2/3} + \mathrm{CS} \tag{1}$$

where

$$\begin{aligned} A =& 8.24493 \times 10^{-1} - 4.0899 \times 10^{-3} T + 7.6438 \times 10^{-5} T^2 \\ & - 8.2467 \times 10^{-7} T^3 + 5.3875 \times 10^{-9} T^4 \end{aligned}$$

$$B = -5.72466 \times 10^{-3} + 1.0227 \times 10^{-4} T - 1.6546 \times 10^{-6} T^2$$

$$C = 4.8314 \times 10^{-4}$$

ρ_t is the density of water, which varies with the temperature as follows:

$$\begin{aligned} \rho_t =& 999.842594 + 6.793952 \times 10^{-2} T - 9.095290 \times 10^{-3} T^2 + 1.001685 \times 10^{-4} T^3 \\ & - 1.120083 \times 10^{-6} T^4 + 6.536336 \times 10^{-9} T^5 \end{aligned} \tag{2}$$

Table 1 Initial conditions of the simulation

Diameter (m)	Velocity (m/s)	Froude number	Density deference (kg/m^3)	Jet density(kg/m^3)	L_m
0.0108	0.72	10	21.77179	1019.9781	0.101
0.0108	0.72	15	12.27659	1010.483	0152
0.0108	0.72	20	7.864012	1006.070	0.202
0.0108	0.72	25	5.45867	1003.665	0.253

3 Results and Discussion

3.1 Jet Trajectory and Flow Characteristics

The trajectory is the main geometrical characteristic of the jet. It can be derived from the maximum concentration or velocity contour map. Many studies stated that the concentration and velocity trajectory almost coincide with each other, [4, 16] while some studies argued that the concentration trajectory often descended faster than the velocity one [4, 12], this phenomenon can be found in this study (Fig. 3).For brevity, we only present the concentration trajectory. Figure 4 shows the trajectory of the jet on the horizontal bottom where the results have a good agreement with previous studies.

The trajectory of other sloped angle with different Froude number are also presented in Fig. 5. The dotted line presents the nominal horizontal bottom. The trajectory gets longer with a larger slope.

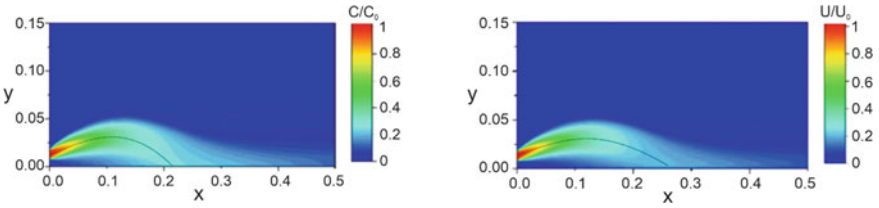

Fig. 3 **a** The concentration contour along the jet. **b** The velocity contour along the jet

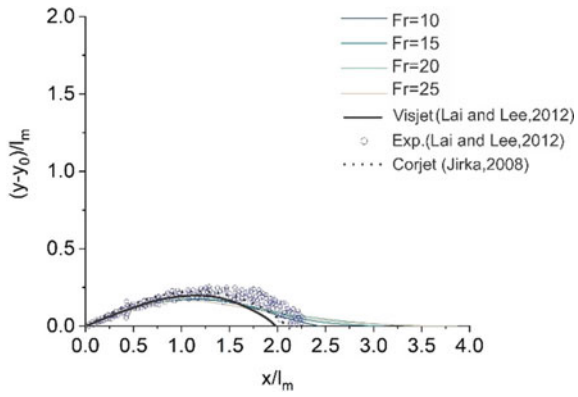

Fig. 4 Normalized centerline trajectories ($\theta = 0°$)

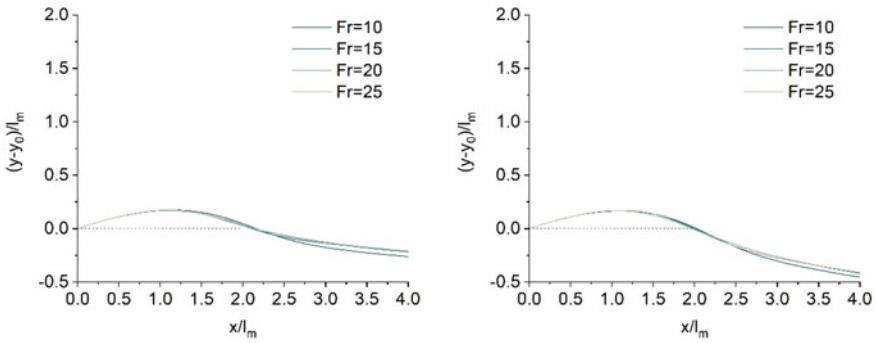

Fig. 5 Normalized centerline trajectories (θ =3°and θ =6°)

3.2 Location of Terminal Rise Height

There are two method to derive the terminal rise height, the first one obtains the 3% cut-off level of concentration from the jet centerplate [4] (Fig. 6a). Another method applies the 25% concentration contour of C_{max} (C_{max} = cross-section maximum concentration) [17] (Fig. 6b). In this study the first method based on C = 3%C_0 is applied. The horizontal location of terminal rise height (Xt) can be easily obtained.

Kikkert et al. pointed out that the upper half of the jet is sharper than the lower part and it is closer to the jet centerline, which means the upper half of the jet is less affected by detrainment [18, 4]. Although this conclusion is carried out under the inclination of 30°, 45°or 60°, a similar trend can be found in this study (Fig. 7); the black contour line presents each 10% concentration difference. It is obvious that the lower half of the jet has more detrainment compared with the upper half.

The location where the jet touches the boundary is called return point or impact point or impingement point. Typically, the return point and impact point are not the same, because the return point is where the jet falls back to the same height as the discharge height, while, the impact point is where the jet touches the bed. When the discharge height is relatively small, these two points are treated as the same point.

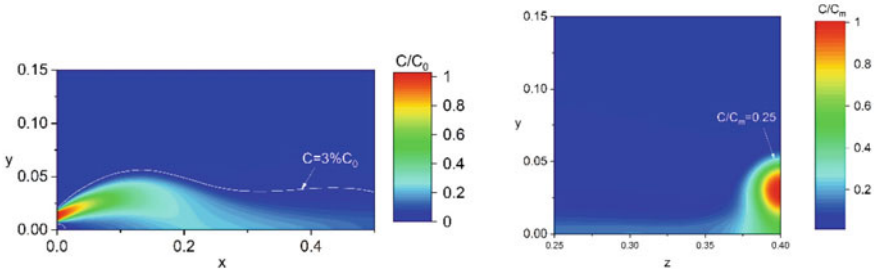

Fig. 6 Two methods for deriving the terminal rise height

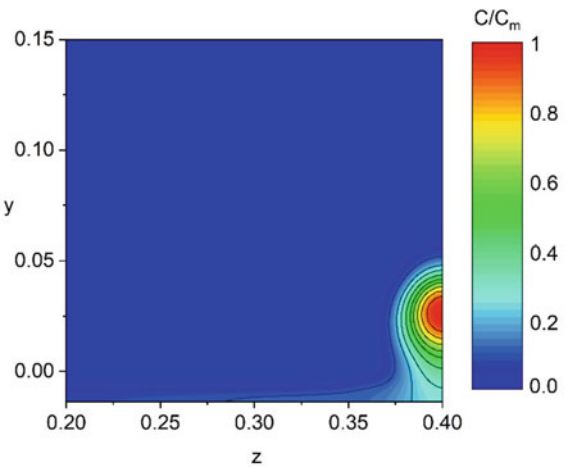

Fig. 7 Concentration contour of vertical profile at the terminal rise height

Mixing is significantly reduced after the impingement takes place since the jet will move along the bottom with less detrainments. However, when the jet discharge height is higher or there is a slope at the bottom, these two points will show quite different properties.

3.3 The Location of the Return Point

The return point can be derived from the trajectory [4]. In this study, a slice (red line) at the same height as the discharge port are obtained (Fig. 8), the concentration is plotted against the horizontal location. The highest point represents the location of the return point and concentration. The horizontal location normalized by D and F is plotted in the Fig. 9. It shows that the jet will move further with a higher Froud number.

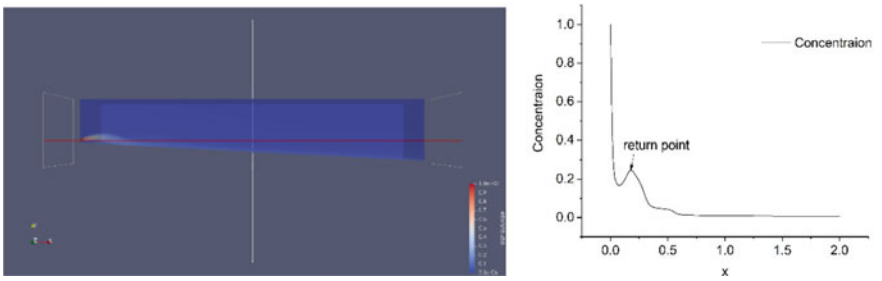

Fig. 8 Illustration of the method for return point

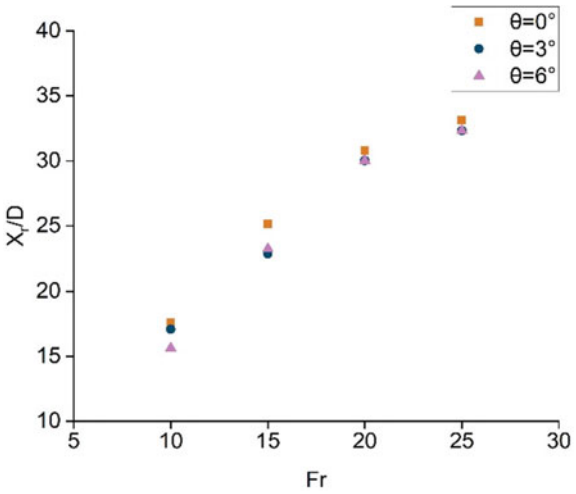

Fig. 9 Horizontal location of the return point (X_r) normalized by diameter (D) versus Froude number (Fr)

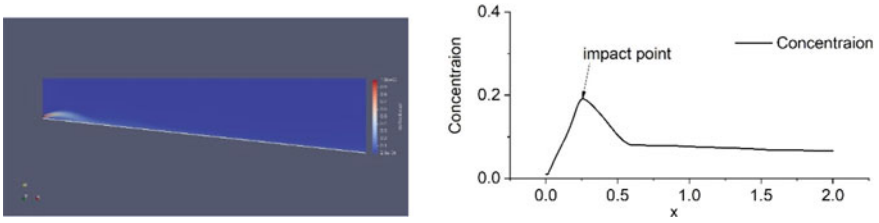

Fig. 10 Illustration of the method for finding the impact point

3.4 The Location of the Impact Point

The similar method of deriving the return point location is also applied here to find out the location of the impact point (Fig. 10).

The horizontal and vertical locations of the impact point are normalized with the L_m, as shown in Fig. 11. The jet moves further compared with the horizontal bottom.

3.5 Dilution at the Minimum Dilution Point, Return Point and Impact Point

The dilution at the terminal rise height, return point (impact point on a horizontal bottom) are also highly important in design applications. The impact point location and dilution are slope-related, so with different slope angles, the dilution is different.

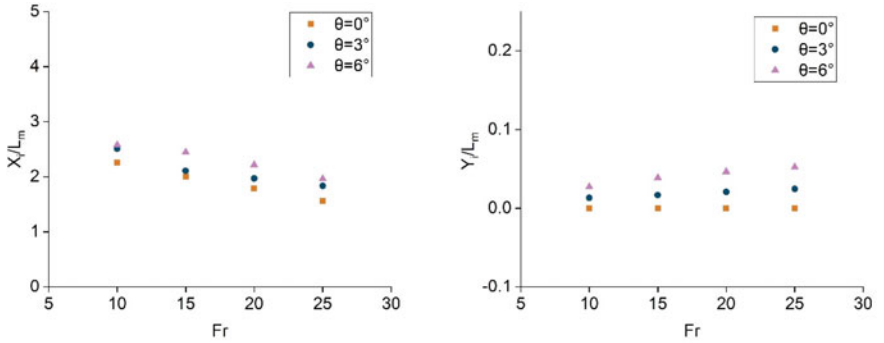

Fig. 11 Location of impact point for different Froude numbers and different slopes (Y_i is absolute value)

With a larger slope, the dilution at the impact point gets higher. All the geometric and dilution parameters are listed in Table 2.

3.6 The Dilution Variation on the Slope After the Impact Point

The jet eventually falls back to the bottom and as it moves along the bottom boundary, it will continue affecting the creatures growing on the sea bed.

Due to the limitation of the paper length, only Fr = 10 is presented here. Linear relations between the dilution (S/Fr) and horizontal location (X/DFr) are shown in Fig. 12. Compared with the horizontal bottom, the mixing can be increased by 10% with a slopped bottom.

4 Conclusion

The results from a numerical investigation on the behaviour of the inclined dense jet over a sloped bottom by CFD have been presented. A discharge angle of 15° with 4 different initial conditions on three different slope angles (0° 3° and 6°) are applied in OpenFOAM with a RANS turbulence model. This study aims to find out the jet development with a small discharge angle on a sloped bottom.

Geometrical and dilution properties were compared with the limited previous experimental data. The numerical and experimental results showed a good agreement and the slope affected the jet trajectory and dilution especially after the return point. The dilution on the slope showed a linear relation with the location on the slope. The jet not only moved downward, but it also spread out to both sides. The effect

Table 2 Geometric and dilution parameters from this study compared with previous studies

	Parameter	This study	Lai and Lee [19]	Visjet [19]	Kikkert [18]	Crowe [20]	Corjet [21]	Oliver [22]
Vertical location of terminal right height	Y_t/L_m	0.50	0.44	0.44	0.52	0.57	0.55	0.63
Horizontal location of terminal right height	X_t/L_m	1.30	1.22	1.19	1.47/1.22	1.45		1.4
Horizontal location of return point	X_r/L_m	1.64	2.41	2.15	2.53/2.13	2.51	1.9	2.39
Centerline Minimum dilution	S_m/Fr	0.29	0.27	0.24		0.2(corjet) 0.23(visual plumes)		0.25
Return point dilution	S_r/Fr	0.36	0.43	0.41			0.39	0.48
Impact point	S_i/Fr	0.364($\theta=0°$) 0.421($\theta=3°$) 0.483($\theta=6°$)						

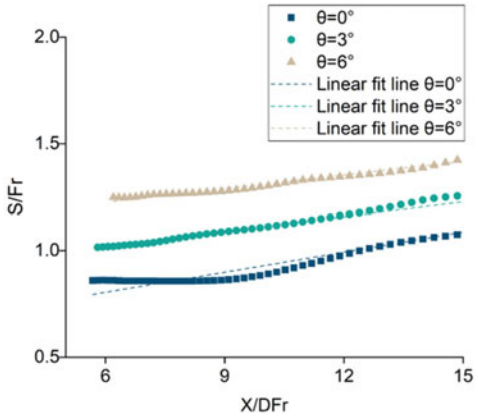

Equation	y = a + bx		
slope	0°	3°	6°
a	0.617	0.883	1.097
b	0.0313	0.0230	0.0214
R^2	0.9124	0.98	0.98

Fig. 12 Variation of jet dilution along the slope after the impact point (Fr = 10)

of boundary conditions on the inclined dense jet development will be addressed in a future study.

Acknowledgements The research was supported by Natural Sciences and Engineering Research Council of Canada (NSERC).

References

1. Zeitoun MA, McIlhenny WF (1971) Conceptual designs of outfall systems for desalination plants. In: Offshore technology conference
2. Roberts PJ, Ferrier A, Daviero G (1997) Mixing in inclined dense jets. J Hydraul Eng 123(8):693–699
3. Lane-Serff GF, Linden PF, Hillel M (1993) Forced, angled plumes. J Hazard Mater 33(1):75–99
4. Shao D, Law AWK (2010) Mixing and boundary interactions of 30° and 45° inclined dense jets. Environ Fluid Mech 10(5):521–553
5. Bashitialshaaer R, Larson M, Persson KM (2012) An experimental investigation on inclined negatively buoyant jets. Water 4(3):720–738
6. Bloomfield LJ, Kerr RC (2002) Inclined turbulent fountains. J Fluid Mech 451:283
7. Cipollina A, Brucato A, Grisafi F, Nicosia S (2005) Bench-scale investigation of inclined dense jets. J Hydraul Eng 131(11):1017–1022
8. Papakonstantis IG, Christodoulou GC, Papanicolaou PN (2011) Inclined negatively buoyant jets 1: geometrical characteristics. J Hydraul Res 49(1):3–12
9. Papakonstantis IG, Christodoulou GC, Papanicolaou PN (2011) Inclined negatively buoyant jets 2: concentration measurements. J Hydraul Res 49(1):13–22
10. Vafeiadou P, Papakonstantis I, Christodoulou G (2005) Numerical simulation of inclined negatively buoyant jets. In: The 9th international conference on environmental science and technology
11. Oliver CJ, Davidson MJ, Nokes RI (2008) k-ε Predictions of the initial mixing of desalination discharges. Environ Fluid Mech 8(5):617–625
12. Kheirkhah Gildeh H, Mohammadian A, Nistor I, Qiblawey H, Yan X (2016) CFD modeling and analysis of the behavior of 30° and 45° inclined dense jets–new numerical insights. J Appl Water Eng Res 4(2):112–127
13. Ardalan H, Vafaei F (2019) CFD and experimental study of 45° inclined thermal-saline reversible buoyant jets in stationary ambient. Environ Process 6:219–239
14. Jirka GH (2008) Improved discharge configurations for brine effluents from desalination plants. J Hydraul Eng 134(1):116–120. With permission from ASCE
15. Millero FJ, Poisson A (1981) International one-atmosphere equation of state of seawater. Deep Sea Res Part A. Oceanogr Res Papers 28(6):625–629
16. Zhang S, Jiang B, Law AWK, Zhao B (2016) Large eddy simulations of 45 inclined dense jets. Environ Fluid Mech 16(1):101–121
17. Jirka GH (2004) Integral model for turbulent buoyant jets in unbounded stratified flows. part i: single round jet. Environ Fluid Mech 4(1):1–56
18. Kikkert GA, Davidson MJ, Nokes RI (2007) Inclined negatively buoyant discharges. J Hydraul Eng 133(5):545–554
19. Lai CC, Lee JH (2012) Mixing of inclined dense jets in stationary ambient. J Hydro-Environ Res 6(1):9–28
20. Crowe A (2013) Inclined negatively buoyant jets and boundary interaction. Doctoral dissertation, University of Canterbury, Civil and Natural Resources Engineering

21. Bleninger T, Jirka GH (2008) Modelling and environmentally sound management of brine discharges from desalination plants. Desalination 221(1–3):585–597
22. Oliver CJ, Davidson MJ, Nokes RI (2013) Removing the boundary influence on negatively buoyant jets. Environ Fluid Mech 13(6):625–648

Optimal Design of Truss Structures with Natural Frequency Constraints Utilizing IWSA Algorithm

Mohammad Farhadmanesh, Arash Asadi Abadi, and Amirhossein Cheraghi

1 Introduction

Optimum design of structures is a significant issue among engineers and researchers since the material consumption amount directly impacts the total cost of construction projects and the sustainability of the structure. When it comes to structural optimization problems, gradient-based solution becomes inviable to a large extent since acquiring the gradient information of the problems is difficult or even impossible. Besides, having a well-chosen starting point for these techniques is crucial; otherwise, it could lead to divergence. An alternative method for structural optimization problems is using stochastic optimization techniques or metaheuristics that has received much attention especially in the last decade. In structural optimization, the ultimate purpose is to build a structure with the least possible cost while meeting some code-specified constraints.

Among these constraints, avoiding detrimental dynamic responses of structures by keeping the natural frequencies in a desirable range is an essential one. Natural frequencies of structures contain useful information as they can determine the dynamic responses of structures. In other words, the response of most low-frequency vibration problems is a function of their natural frequencies and modal shapes, and hence if subject to frequency constraints, unwanted dynamic responses due to the resonance phenomenon could be avoided. Resonance phenomenon occurs when the external excitation frequency is equivalent or near to the natural frequency of the

M. Farhadmanesh (✉) · A. Cheraghi
Department of Civil and Environmental Engineering, University of Utah, Salt Lake City, USA
e-mail: mohammad.farhadmanesh@utah.edu

A. Cheraghi
e-mail: a.cheraghi@utah.edu

A. Asadi Abadi
School of Civil Engineering, Iran University of Science and Technology, Tehran, Iran

S. Walbridge et al. (eds.), *Proceedings of the Canadian Society of Civil Engineering Annual Conference 2021*, Lecture Notes in Civil Engineering 240,
https://doi.org/10.1007/978-981-19-0507-0_8

structure. This phenomenon can increase the amplitude of the structures during excitation and could escalate the damage level of the structure or may even be the underlying reason for its collapse, such as the Angers Bridge collapse in 1850. Although various control measures have been introduced to effectively mitigate the unwanted effects of resonance effect, for some structures, a more convenient approach could be to design under frequency constraints. This way, an optimal design could be achieved that obviates the need for costly damage measures while ensuring that the structure avoids the undesired frequencies.

Structural optimization with frequency constraints is highly non-linear and non-convex with many local optimums, which calls for a powerful optimization algorithm to handle the problem. Weight reduction has a conflict with natural frequencies, especially if they are lower bounded. In recent years, researchers have employed many metaheuristics to address these optimization problems [1–4].

Water strider algorithm (WSA) is a newly developed metaheuristic introduced by [5] in which the life cycle of water strider bugs are the inspiration for devising an efficient metaheuristic algorithm, which has been shown to be superior to classical optimization methods and competitive with many state-of-the-art ones. The interesting aspect of this algorithm is its efficiency despite using simple mathematical equations, unlike many modern metaheuristics. Improved water strider algorithm (IWSA) was later developed by [6] in which an opposition-based learning (OBL) technique and a mutation method for the best-so-far solution have been added to the standard WSA, making it a more robust algorithm. This paper is concerned with conducting research for assessing the computational performance of the newly developed metaheuristic algorithms WSA and IWSA for size or size-layout optimization of trusses subject to natural frequency constraints and comparing their performance with each other and other methods available in the literature.

2 Statement of the Optimization Problem

Structural optimization with multiple frequency constraints aims at minimizing structural weight by choosing the best possible design variables. The design variables in this framework consist of nodal coordinates (layout variables) and cross-sectional areas of the elements (sizing variables). The mathematical formulation of the problem can be stated as follows:

$$\text{Find } X = [x_1, x_2, \ldots, x_2]; \quad To \text{ minimize } W(X) = \sum_{i=1}^{nm} \rho_i A_i L_i$$

$$\text{Subject to : } \begin{cases} \omega_j \leq \omega_j^* \\ \omega_k \geq \omega_k^* \\ x_{i\,\min} \leq x_i \leq x_{i\,\max} \end{cases} . \tag{1}$$

where X is a vector containing the design variables, W(X) is the weight of the structure, ρ_i, A_i, L_i and nm represent the density, cross-sectional area, length of the member, and the number of members, respectively. ω_j is the j th natural frequency, and ω_j^* is its upper bound; likewise, ω_k is the k th natural frequency of the structure, and ω_k^* is its lower bound. x_i is the i th component of the design vector, x_{imin} and x_{imax} are its minimum and maximum allowable values, respectively. In order to handle the constraints, the well-known penalty function is used. Hence, the cost function (target function) is defined as:

$$P(X) = W(X) \times (1 + \varepsilon_1 \upsilon)^{\varepsilon_2}; \upsilon = \sum_{i=1}^{q} \upsilon_i; \upsilon_i = \begin{cases} 0 & \text{if the ith constraint satisfied} \\ \left| 1 - \frac{\omega_i}{\omega_i^*} \right| & \text{else} \end{cases} \tag{2}$$

where P(X) signifies the cost function. υ is the sum of the violation from the design constraints, and q is the number of constraints. ε_1 is set as 2 for the 1st and 2nd problem, and it is set equal to unit for the 2nd problem. In order to balance the intensification and diversification capabilities of the algorithms, ε_2 is set as linearly increasing. For the 1st and 3rd problem, it is started from 1.5 and reaches 6 at the end of the optimization process. For the 2nd problem, however, it starts with 1.5 and ends up with 3 at the end of the optimization. This strategy penalizes the unfeasible candidate solutions more severely as the optimization algorithms proceeds, but lets the algorithm explore more regions in the initial steps.

3 Metaheuristic Algorithms

In this study, WSA and IWSA algorithms are applied for the optimal design of truss structures with frequency constraints. In the following subsections, these two algorithms are briefly explained:

3.1 Water Strider Algorithm

Nature, as the oldest and most knowledgeable teacher, has been the inspiration for developing many successful optimization algorithms; from the genetic algorithm (GA) [7], as a classical optimization method, to krill herd (KH) [8] as a state-of-the-art one. If one looks carefully into the nature, they can find a behavior or mechanism that has been optimized for a very long time. Researchers, knowing this fact, have tried to formulate these phenomena mathematically so as to develop optimization algorithms.

Insects utilize complicated and smart behaviors like intelligent communication, navigation, foraging, and avoiding predators. Water strider algorithm (WSA) mimics territorial behavior, intelligent ripple communication, mating methods, feeding mechanism, and succession of water strider bugs to devise a metaheuristic optimization algorithm. The steps of the algorithm are as follows:

3.1.1 Birth

The search space in the WSA algorithm is considered to be the lake in which all the water striders (WSs) or candidate solutions live in. The WSs are randomly generated in the search space in the first step:

$$\mathrm{WS}_{\mathrm{i}}^{0} = \mathrm{Lb} + \mathrm{rand}.(\mathrm{Ub} - \mathrm{Lb});\ \mathrm{i} = 1, 2, \ldots, \mathrm{nws} \tag{3}$$

where $\mathrm{WS}_{\mathrm{i}}^{0}$ is the initial position of the i^{th} water strider in the lake. Lb and Ub represent the lower and upper bound of variables, respectively. rand is a random number between [0, 1], and nws is the number of WSs. The initial positions of WSs are evaluated by the target function to obtain their fitness.

3.1.2 Territory Establishment

Water striders set up territories to defend their properties, i.e., foods and mating resources. In order to form nt number of territories, the WSs are sorted according to their fitness, and $\frac{\mathrm{nws}}{\mathrm{nt}}$ number of groups are orderly created. The *j*th member of each group is assigned to the *j*th territory, such that $\mathrm{j} = 1, 2, \ldots, \mathrm{nt}$. Thus, the number of WSs living in each territory is equal to $\frac{\mathrm{nws}}{\mathrm{nt}}$. The WS in each territory with the best and worst fitness is considered to be female and male, respectively.

3.1.3 Mating

In every territory, mating is demanded by the male WS (keystone), while the food resources are required by the female WS. Utilizing the ripple communication system, the keystone sends ripples to the female WS to mate. The probability of either attraction or repulsion from the female WS is assumed to be $\mathrm{p} = 50\%$. The next position of the keystone is updated based on the reaction of the female as:

$$\begin{cases} \mathrm{WS}_{\mathrm{i}}^{\mathrm{t}+1} = \mathrm{WS}_{\mathrm{i}}^{\mathrm{t}} + R.rand; & \text{if mating happens (with probability of } p) \\ \mathrm{WS}_{\mathrm{i}}^{\mathrm{t}+1} = \mathrm{WS}_{\mathrm{i}}^{\mathrm{t}} + R.(1 + \mathrm{rand}); & \text{otherwise} \end{cases} \tag{4}$$

The length of R is equal to the distance between the male and female WS:

$$R = WS_F^{t-1} - WS_i^{t-1} \tag{5}$$

where WS_i^{t-1} and WS_F^{t-1} denote the male and female WS in the $(t-1)$th cycle, respectively.

3.1.4 Feeding

Since the keystone consumes a great deal of energy during the mating process, it has to forage for food resources in the new position. The fitness of the keystone is evaluated in the new position. In case the fitness reduces, the male WS moves towards the best WS of the lake (WS_{BL}) to find food according to the following formula:

3.1.5 Death and Succession

$$WS_i^{t+1} = WS_i^t + 2\text{rand}.(WS_{BL}^t - WS_i^t) \tag{6}$$

The keystone's fitness is calculated in the new position. If it is worse than the previous fitness, it will die, and a new WS will replace it:

$$WS_i^{t+1} = Lb_j^t + \text{rand}.\left(Ub_j^t - Lb_j^t\right) \tag{7}$$

where Ub_j^t and Lb_j^t represent the maximum and minimum values of the WS's position in the *j*th territory.

3.1.6 WSA Termination

If the termination condition is not met, the algorithm will return to the mating step for a new loop. Since the structural analysis is costly, the maximum number of function evaluations (MaxNFE) is considered as the termination condition herein, same as the literature for a fair comparison.

3.2 Improved Water Strider Algorithm (IWSA)

Many metaheuristic algorithms have been enhanced to make them more efficient, especially for engineering objectives. Two ideas based on OBL, initially proposed by [9] for machine learning, and a kind of mutation operator adopted from the genetic algorithm were incorporated in WSA to make it a more suitable global optimization algorithm.

3.2.1 Opposition-Based Learning (OBL)

For optimization purposes, OBL was utilized to calculate the candidate solution and the opposite candidate simultaneously and to keep the fitter one and omit the other. The opposite of a number $x \in [l, u]$ is defined as:

$$\tilde{x} = l + u - x \tag{8}$$

In which l and u are the lower bound and the upper bound of the arbitrary number x.

Zhang and Jin [10] introduced a more generalized form of OBL, and it was named generalized space transformation search (GSTS). GSTS was defined as follows:

Let $P = (x_1, x_2, \ldots, x_D)$ and $Q = (\hat{x}_1, \hat{x}_2, \ldots, \hat{x}_D)$ represent two different points distributed in a D-dimensional space, where $x_1, x_2, \ldots, x_D \in \mathbb{R}$ and $\hat{x}_1, \hat{x}_2, \ldots, \hat{x}_D \in \mathbb{R}$. Assume $l = (l_1, l_2, \ldots, l_D)$ and $u = (u_1, u_2, \ldots, u_D)$ are the lower and the upper bounds of the D-dimensional space, respectively. The opposite point $\breve{P} = \left(\breve{x}_1, \breve{x}_2, \ldots, \breve{x}_D\right)$ of the point P is determined as:

$$\breve{x}_i = \lambda(l_i + u_i) - \left(x_i - \hat{x}_i\right); \quad i = 1, 2, \ldots, D \tag{9}$$

where λ named elastic factor is a random number drawn from interval [0,1]. It should be mentioned that the transformation made by GSTS may fall outside the allowable range of variables, in which case a random solution in the search space is produced to replace the violated solution:

$$x_0^* = Lb + \kappa.(Ub - Lb); \text{ if } x_0^* < x_{min} \text{ or } x_0^* > x_{max} \tag{10}$$

where κ is a random number in [0,1], and x_{min}, x_{max} indicate the minimum and maximum allowable values of variables, respectively.

Utilizing OBL increases the capability of the optimization algorithms in terms of diversification and intensification of the search space. In the IWSA algorithm, the GSTS is applied to the initial random population (Sect. 3.1.1). The initial population in the metaheuristic algorithms plays a significant role in capability of the algorithms. In fact, random initialization might increase the probability of searching fruitless regions of the search space. In order to enhance the convergence speed, employing random numbers and their opposites is more beneficial than using pure randomness to generate initial estimates in the absence of prior knowledge about the solutions. After a random population is generated, the opposite population is calculated accordingly. In case the opposite population fitness is improved, it will replace the initial random population; otherwise, the initial population remains unchanged.

3.2.2 Mutation

To improve the exploration ability of the standard WSA algorithm, a mutation operator inspired by the genetic algorithm, is employed to enrich the algorithm to search more promising regions of the search space and help it escape local optimums. This operator is applied on the best-so-far solution achieved (WS_{BL}). One of the components of WS_{BL} is selected randomly, and it is regenerated with the variables' range in the best territory:

$$x_j = x_{j,min} + \text{rand}.(x_{j,max} - x_{j,min}) \tag{11}$$

where x_j is the chosen component, and $x_{j,min}$ and $x_{j,max}$ are the minimum and the maximum values of all the components in the best water strider's territory, respectively. A probability named "pro" is herein defined for mutation application. After a number of experimental studies and by a wise decision, the pro was set equal to 30%. The regenerated WS is evaluated by the target function, and if the mutated WS is fitter than the WS_{BL}, it will replace the best WS of the lake, and otherwise, the WS_{BL} will be unaltered.

4 Test Problems

In this section, the performance of the WSA and IWSA algorithms is compared by optimizing three different trusses. For a more comprehensive comparison, some other results reported in the literature are also provided here. The population size of the algorithms (nws) has been set to be 50, and the number of territories was set equal to 25. The termination condition is 4000, 9000, and 20,000 structural analyses for the first, second, and third examples, respectively. The three benchmark trusses characteristics are provided in Table 1. The two algorithms were run 30 times independently for the first two problems, and 20 independent runs were carried out for the last one to provide reasonable statistical results.

4.1 The 52-Bar Dome Truss Structure

The first example is a spatial dome-shaped truss structure which is considered for simultaneous sizing and layout optimization subject to two frequency constraints. For the sake of symmetry, the dome's members are grouped into 8 variables as seen in Fig. 1a, and 5 independent nodal coordinates are taken into account as layout variables during the optimization process.

Figure 1b and c illustrate the initial layout of the structure and the final layout of the dome after optimization, respectively. The obtained design is provided in Table 2,

Table 1 Characteristics of the three problems

Benchmark problem	52-bar dome truss	Spatial 72-bar truss	600-bar dome truss
Young's modulus (GPa)	210	69.8	200
Density (kg/m^3)	7800	2770	7850
Lumped masses (kg)	M = 50	M = 2270	M = 100
Size variables (cm^2)	$1 \leq A_i \leq 10$	$0.645 \leq A_i \leq 50$	$1 \leq A_i \leq 100$
Layout variables (m)	$-2 \leq dz_A, dz_B, dz_F, dx_B, dx_F \leq 2$	-	-
Frequency constraints (Hz)	$f_1 \leq 15.916, f_2 \geq 28.648$	$f_1 = 4, f_3 \geq 6$	$f_1 \geq 5, f_3 \geq 7$

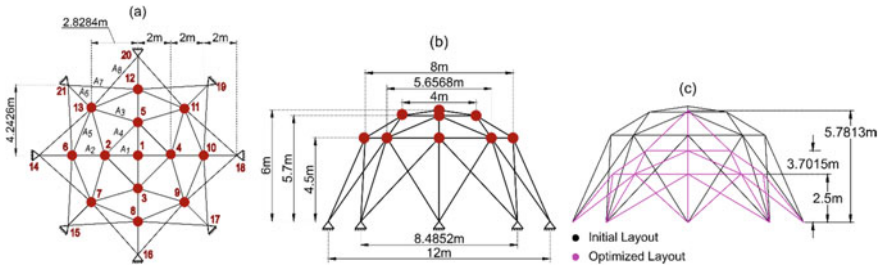

Fig. 1 Schematic of the 52-bar truss structure

Table 2 The best design of IWSA for the 52-bar truss (coord. (m), A (cm^2), f (Hz), weight (kg))

z_1	x_4	z_4	x_{10}	z_{10}	A_1	A_2	A_3
5.7813	2.1796	3.7015	3.8970	2.5000	1.0000	1.2056	1.2476
A_4	A_5	A_6	A_7	A_8	f_1	f_2	weight
1.4579	1.3441	1.0000	1.7311	1.3481	11.3224	28.6482	195.39

which shows that it has satisfied the frequency constraints. Considering the statistical results of the different algorithms given in Table 3, it can be stated that the IWSA algorithm was the most successful metaheuristic among all the methods. The acceptable mean value and standard deviation also prove the robustness of the proposed method. Besides, the performance of Enhanced Charged System Search (ECSS) and the standard Water Strider Algorithm (WSA) demonstrate their competence in the

Table 3 Comparison of the statistical results for the 52-bar

Algorithm	IWSA	WSA	NHGA [11]	PSO [12]	CSS [13]	ECSS [13]	HS [14]	FA [14]
Best	**195.39**	196.79	236.05	228.38	205.24	197.34	214.94	197.53
Mean	213.00	215.31	274.16	234.3	213.10	205.62	229.88	212.80
Std	12.08	21.08	37.46	5.22	7.39	6.92	12.44	17.98
NFE	4000	4000	-	11,270	4000	4000	20,000	10,000

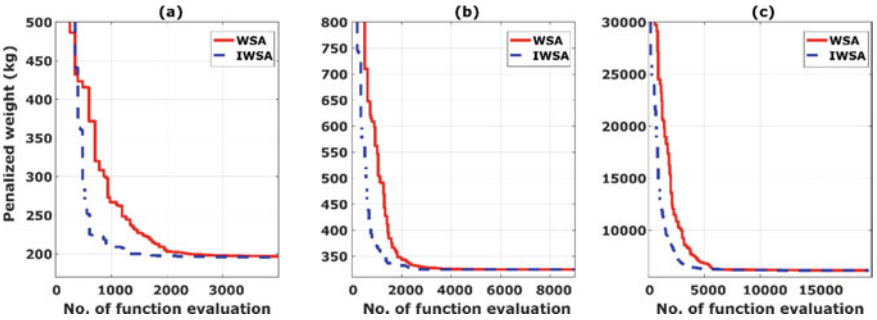

Fig. 2 Convergence curves for the best run of the three problems

best result of Table 3. Figure 2a illustrates the higher convergence rate of the IWSA algorithm than that of its standard version.

4.2 The Spatial 72-Bar Truss Structure

The second test problem is a 72-bar spatial truss structure, as shown in Fig. 2. The truss elements are grouped into 16 cross-sectional areas as shown in Table 4 for the first floor (similar for other floors). Therefore, this is a size optimization with 16 design variables (Table 5).

By carefully observing the results given in Table 6, it can be said that the IWSA algorithm produces the best performance among all the methods considered here. The standard WSA also performs well in terms of the best result obtained; however, the mean result and the standard deviation clearly show that the IWSA algorithm is more robust than its standard version. This is mainly due to the OBL method which

Table 4 First floor elements groupings for the 72-bar truss

A_1	A_2	A_3	A_4
(1, 5) (2, 6) (4, 8) (3, 7)	(8, 3) (7, 4) (7, 2) (6, 3) (8, 1) (5, 4) (5, 2) (6, 1)	(5, 6) (8, 7) (8–5) (7, 6)	(5, 7) (6, 8)

Table 5 The best design of IWSA for the 72-bar truss (A (cm^2), f (Hz), weight (kg))

A_1	A_2	A_3	A_4	A_5	A_6	A_7	A_8	A_9	A_{10}
16.8156	7.8804	0.6450	0.6450	13.1912	8.1183	0.6450	0.6450	7.9022	7.9241
A_{11}	A_{12}	A_{13}	A_{14}	A_{15}	A_{16}	f_1	f_3	weight	
0.6450	0.6450	3.3238	7.8450	0.6450	0.6450	4.0000	6.0000	324.40	

Table 6 Comparison of the statistical results for the 72-bar truss

Algorithms	IWSA	WSA	CSS [13]	ECSS [13]	TLBO [15]	MCTLBO [15]	FA [4]
Best	**324.34**	324.41	328.81	328.39	327.568	327.575	324.36
Mean	327.59	336.74	337.70	335.77	328.684	327.693	325.1738
Std	10.71	38.44	5.42	7.20	0.73	0.125	0.6785
NFE	9000	9000	4000	4000	15,000	15,000	11,920

Table 7 The best design of IWSA for the 600-bar truss (A (cm^2), f (Hz), weight (kg))

A_1(1,2)	A_2(1,3)	A_3(1,10)	A_4(1,11)	A_5(2,3)	A_6(2,11)	A_7(3,4)
1.2153	1.3493	4.7198	1.5369	17.8329	38.8172	12.7846
A_8(3,11)	A_9(3,12)	A_{10}(4,5)	A_{11}(4,12)	A_{12}(4,13)	A_{13}(5,6)	A_{14}(5,13)
15.8123	11.0541	9.1679	8.9563	9.1549	7.2735	4.6992
A_{15}(5,14)	A_{16}(6,7)	A_{17}(6,14)	A_{18}(6,15)	A_{19}(7,8)	A_{20}(7,15)	A_{21}(7,16)
7.2002	5.2763	3.6494	7.8112	3.9146	2.1961	4.6208
A_{22}(8,9)	A_{23}(8,16)	A_{24}(8,17)	A_{25}(9,17)	f_1	f_3	weight
3.8837	1.7489	4.6599	1.8228	5.00089	7.00005	6130.55

provides a more promising search space for IWSA and makes it less sensitive to the initial random population. The Firefly Algorithm (FA) shows good results, too; nonetheless, the number of function evaluations that are needed to reach this result is much more than that for the IWSA and WSA algorithms. The best design achieved by IWSA and the natural frequency associated with this design is provided in Table 6. The higher convergence speed of IWSA in comparison to WSA for this problem is seen in Fig. 2b (Table 7).

4.3 The 600-Bar Dome Truss Structure

The last problem is the 600-bar spatial dome-shaped truss structure consisting of 216 nodes shown in Fig. 3. The lumped masses are attached to all free nodes. The structure is radially symmetric and could be generated by 15° rotations of a substructure having 9 nodes and 25 elements, as depicted in Fig. 4. The nodes coordinate of the

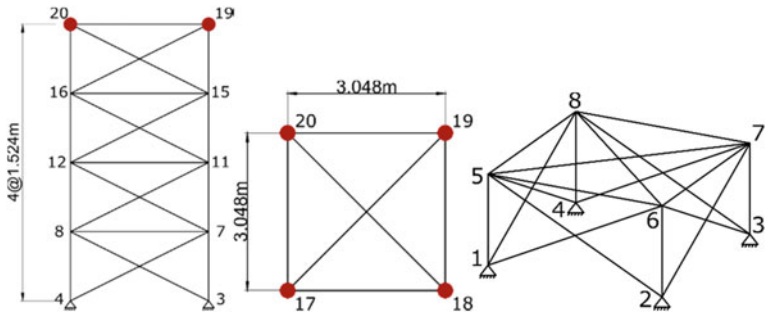

Fig. 3 Schematic of the 72-bar space truss

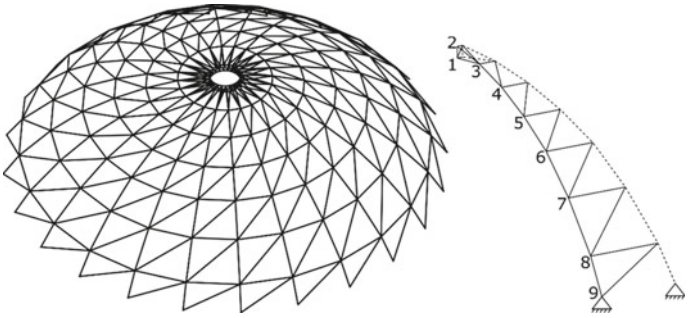

Fig. 4 Schematic of the 600-bar dome truss structure

substructure is provided in Table 8. The substructure's elements are considered as the design variables, while the topology of the structure is assumed to be constant during the optimization. Thus, this is a size-optimization with 25 decision variables.

The statistical results of the 600-bar truss provided in Table 9 show that the IWSA, WSA, ECBO, and cascade algorithms clearly outperform the other methods. Enhanced Colliding Bodies Optimization (ECBO) has shown a great performance in many engineering problems such as [16]; in addition, the cascade optimization procedure is a powerful state-of-the-art optimization method. These two algorithms are chosen to assess the viability of the proposed metaheuristics. As for the best and mean results in the 20 independent runs, the IWSA algorithm outperforms its

Table 8 Coordinates of the nodes for the 600-bar dome truss

Nodes	1	2	3	4	5	6	7	8	9
Coord.	1 0 7	1 0 7.5	3 0 7.25	5 0 6.75	7 0 6	9 0 5	11 0 3.5	13 0 1.5	14 0 0

Table 9 Comparison of the statistical results for the 600-bar truss

Algorithms	IWSA	WSA	DPSO [17]	ECBO [2]	Cascade [2]	CPA [3]	HS [3]	BB-BC [3]
Best	**6130.55**	6138.62	6344.55	6171.51	6140.51	6336.85	6357.59	6394.64
Mean	6341.78	6723.38	6674.71	6191.50	6175.33	6376.01	6631.48	6704.11
Std	456.07	941.39	473.21	39.08	34.08	90.39	304.09	551.65
NFE	20,000	20,000	-	20,000	20,000	40,000	40,000	40,000

standard version. This problem is rather a complex real-world problem which not only calls for a more promising search space, but also requires a mechanism to help it avoid local optimums in its way towards the global optimum. IWSA, thanks to the OBL method, features a promising search mechanism and also exploits a mutation technique to avoid the local minimums. These are the features that the standard version of the algorithm lacks. The convergence history of the algorithms in Fig. 2c also shows the higher speed of the improved version. Nonetheless, considering the mean results and the standard deviation, it can be seen that the ECBO and cascade optimization algorithms have slightly better results than the IWSA algorithms, which shows their competence to solve a real-world optimization problem as well.

5 Conclusion

In order to construct a more resilient structure in the face of future excitations, the resonance phenomenon cannot be ignored. While many studies consider weight minimization of the structure subject to stress and displacement constraints, in this study, two recently developed metaheuristic algorithms called water strider algorithm (WSA) and improved water strider algorithm (IWSA) were selected to conduct research in weight minimization of three benchmark truss structures subject to multiple frequency constraints. The results of the IWSA algorithm were compared with its standard version and some of the well-known, state-of-the-art optimization methods. The results clearly demonstrated the superiority of the improved version over its standard version and showed its competence compared to the other methods reported in the literature. This also demonstrates that the mechanisms used in the IWSA algorithm worked successfully and could be utilized in other methods to enhance their performance as well.

References

1. Carvalho JPG, Lemonge ACC, Carvalho ÉCR, Hallak PH, Bernardino HS (2018) Truss optimization with multiple frequency constraints and automatic member grouping. Struct Multidiscip Optim 57(2):547–577. https://doi.org/10.1007/s00158-017-1761-x
2. Kaveh A, Ilchi Ghazaan M (2016) Optimal design of dome truss structures with dynamic frequency constraints. Struct Multidiscip Optim 53(3):605–621. https://doi.org/10.1007/s00158-015-1357-2
3. Kaveh A, Zolghadr A (2018) Optimal design of cyclically symmetric trusses with frequency constraints using cyclical parthenogenesis algorithm. Adv Struct Eng 21(5):739–755. https://doi.org/10.1177/1369433217732492
4. Lieu QX, Do DTT, Lee J (2018) An adaptive hybrid evolutionary firefly algorithm for shape and size optimization of truss structures with frequency constraints. Comput Struct 195(January):99–112. https://doi.org/10.1016/j.compstruc.2017.06.016
5. Kaveh A, Dadras Eslamlou A (2020) Water strider algorithm: a new metaheuristic and applications. Structures 25(June):520–541. https://doi.org/10.1016/j.istruc.2020.03.033
6. Kaveh A, Ghazaan MI, Asadi A (2020) An improved water strider algorithm for optimal design of skeletal structures. Period Polytech Civ Eng. https://doi.org/10.3311/PPci.16872
7. Holland JH (1992) Adaptation in natural and artificial systems: an introductory analysis with applications to biology, control, and artificial intelligence. 1st MIT Press ed. Complex Adaptive Systems. MIT Press, Cambridge, Mass
8. Gandomi AH, Alavi AH (2012) Krill herd: a new bio-inspired optimization algorithm. Commun Nonlinear Sci Numer Simul 17(12):4831–4845. https://doi.org/10.1016/j.cnsns.2012.05.010
9. Tizhoosh HR (2005) Opposition-based learning: a new scheme for machine intelligence. In: International conference on computational intelligence for modelling, control and automation and international conference on intelligent agents, web technologies and internet commerce (CIMCA-IAWTIC'06), vol 1, pp 695–701. IEEE, Vienna, Austriahttps://doi.org/10.1109/CIMCA.2005.1631345
10. Zhang Y, Jin Z (2020) Quantum-behaved particle swarm optimization with generalized space transformation search. Soft Comput 24(19):14981–14997. https://doi.org/10.1007/s00500-020-04850-7
11. Lingyun W, Mei Z, Guangming W, Guang M (2005) Truss optimization on shape and sizing with frequency constraints based on genetic algorithm. Comput Mech 35(5):361–368. https://doi.org/10.1007/s00466-004-0623-8
12. Gomes HM (2011) Truss optimization with dynamic constraints using a particle swarm algorithm. Expert Syst Appl 38(1):957–968. https://doi.org/10.1016/j.eswa.2010.07.086
13. Kaveh A, Zolghadr A (2011) Shape and size optimization of truss structures with frequency constraints using enhanced charged system search algorithm. Asian J Civ Eng 12(4):487–509
14. Miguel LF, Fadel, and Leandro Fleck Fadel Miguel. (2012) Shape and size optimization of truss structures considering dynamic constraints through modern metaheuristic algorithms. Expert Syst Appl 39(10):9458–9467. https://doi.org/10.1016/j.eswa.2012.02.113
15. Farshchin M, Camp CV, Maniat M (2016) Multi-class teaching–learning-based optimization for truss design with frequency constraints. Eng Struct 106(January):355–369. https://doi.org/10.1016/j.engstruct.2015.10.039
16. Kaveh A, Farhadmanesh M (2018) Optimal seismic design of steel plate shear walls using metaheuristic algorithms. Period Polytech Civ Eng. https://doi.org/10.3311/PPci.12119
17. Kaveh A, Zolghadr A (2016) Optimal analysis and design of large-scale domes with frequency constraints. Smart Struct Syst 18(4):733–54. https://doi.org/10.12989/SSS.2016.18.4.733

Evaluation of Shear Transfer Strength in FRP Concrete Composite Using Nonlinear Finite Element Analysis

Moataz Mahmoud, Mohamed Eladawy, and Brahim Benmokrane

1 Introduction

Over the past two decades, Glass Fiber Reinforced Polymer (GFRP) has been proved to be an effective alternative to conventional steel as a flexural and shear reinforcement in several reinforced concrete (RC) structure elements under different load conditions. Moreover, reinforcing the concrete elements with FRP bars has been recommended to improve the durability and extend the RC structures' serviceability. Consequently, the design and construction requirements of FRP-RC structure elements were provided in distinct and specially prepared design codes and guidelines such as; ACI440-15, CAN/CSA S806-12, and AASHTO-LRFD-19. There are several ongoing challenges related to internal FRP reinforcement performance, such as the bond, dowel-action, and excessive deflection. It worth mentioning that there are many different types of FRP reinforcing bars and various types of surface treatment, resulting in changes in the bond and cohesion strength. Limited research has been conducted to investigate the shear transfer strength of concrete-to-concrete interfaces reinforced by FRP reinforcement [4, 5, 11].

The push-off tests are usually adopted for studying shear transfer mechanisms. Push-off specimens have been employed to overcome the direct shear transfer mechanism. It was developed by (Anderson 1960) to study the shear-slip behavior of concrete joints connecting precast concrete girders and cast-in-place slabs. These

M. Mahmoud (✉) · M. Eladawy · B. Benmokrane
Department of Civil and Building Engineering, University of Sherbrooke, Sherbrooke, QC, Canada
e-mail: Moataz.mahmoud@Ushearbrooke.ca

M. Eladawy
e-mail: Mohamed.Eladawy@Ushearbrooke.ca

B. Benmokrane
e-mail: Brahim.Benmokrae@USherbrooke.ca

S. Walbridge et al. (eds.), *Proceedings of the Canadian Society of Civil Engineering Annual Conference 2021*, Lecture Notes in Civil Engineering 240,
https://doi.org/10.1007/978-981-19-0507-0_9

specimens allow a better understanding of the behavior on the interface through an experimental test. These small specimens provide an accurate understanding of the load transfer mechanism and allow a more effective experimental campaign than full-scale specimens. Although the push-off test is nonstandard, it is a widely recognized experimental test used to study shear transfer mechanisms accurately.

Alkatan [4], and ALRuwaili [5] investigated the use of GFRP reinforcement as a shear transfer reinforcement at the cold-joint concrete joints with as-cast rough interfaces. Large-scale double L-shaped push-off specimens with cold-joint conditions at their interfaces were constructed and tested. The studied parameters were the reinforcement stiffness, concrete compressive strength, and the shape of the reinforcement (stirrups and headed bars). The test results revealed that specimens with GFRP reinforcement showed a remarkable shear transfer capacity at higher slipped values compared to steel reinforced interfaces. In addition, the reinforcement stiffness was found to be the main parameter in the shear transfer mechanism. Moreover, Interfaces with GFRP headed bars and stirrups with similar stiffness exhibited similar behavior and strength. In addition, GFRP reinforced interfaces with headed bars and stirrups showed remarkable ductility and post-ultimate load-carrying capacity when GFRP headed bars were used.

Several ongoing challenges are related to internal FRP reinforcement performance, such as the bond, dowel-action, excessive deflection, and shear (CSA Committee S6.1-19). The dowel action of FRP is considered negligible compared to steel reinforcement due to the lower transverse strength of FRP. More specifically, the strength of GFRP is approximately two to three times that of steel, allowing for bridge deck strength requirements to be met, but has a much lower elastic modulus, reducing overall stiffness. Reduced stiffness leads to increased deflection and severe cracking (that is, larger crack widths). However, more research data, especially about means of connecting the panels to the supporting beams, is needed to formulate definitive design provisions for these deck slabs. Therefore, this study a step forward to investigate the shear-friction behavior of GFRP-reinforced concrete elements.

2 Finite Element Model of Push-Off Test

2.1 Methodology

The finite element (FE) method has become a powerful gadget for the numerical analysis of a wide range of engineering problems. An accurate finite element model permits a considerable reduction in the number of experiments needed for the prediction of structural behavior. This study aims to investigate the feasibility of using the GFRP as a shear transfer reinforcement across interfaces between concretes employing a refined three-dimensional (3D) finite element (FE) model implemented in the program ABAQUS. The proposed model was validated using the experimental

results by Alkatan [6], and ALRuwaili [5]. The test specimen consists of two L-shaped concrete blocks. The shear plane, part of the L-shape web, is 250 mm wide and 500 mm long [6]. While the web dimensions for [5] specimens were 250 mm in wide and 469 and 419 mm in long. The flange of the L-shape is 250 mm wide, 500 mm long, and 250 mm thick. A small gap was provided between the connected parts in the direction of the applied load to allow free slip between these parts.

The concrete body was modeled with two identical "L" -shaped parts, combined as one part through surface-to-surface contact. The concrete was considered solid homogenous. A 3D stress element was used to simulate the concrete behavior and FRP reinforcement. A truss element was used to simulate the steel reinforcement behavior in the concrete blocks. A constant-mesh element of 25 mm size was applied in the model. The whole geometric model of the push-off specimen presents in Fig. 1. Appropriate constraints were used to describe the interaction between components. Surface to surface contact between the two concrete blocks was employed. The penalty contact method of ABAQUS was used for tangential behavior. The coefficient of friction was also set. The left concrete block was assumed to be the master surface. The traction–separation model was used to simulate the cohesion between concrete interfaces.

The primary law of traction–separation behaviors -linearly and elastically increase until up to the maximum traction or separation and decrease after initiation of damage- was considered. Embedded regions were used for the simulation of rebar inside the concrete block. Rigid steel plates were used at the top and bottom of the push-off specimens to prevent local concrete crushing. The bottom boundary was fixed. The displacement control method was used for loading. The load was applied to the top of steel plate as shown in Fig. 2. At the beginning of the analysis, the applied displacement was set to zero and then the displacement was increased linearly according to amplitude function.

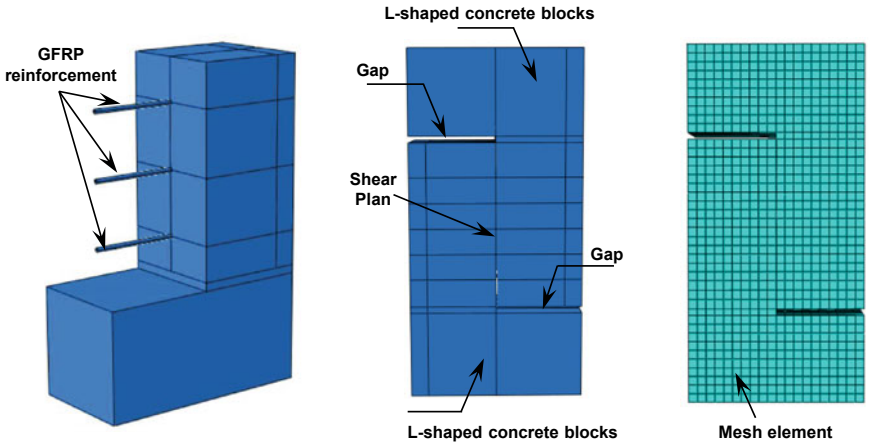

Fig. 1 Model of push-off specimen and finite element mesh

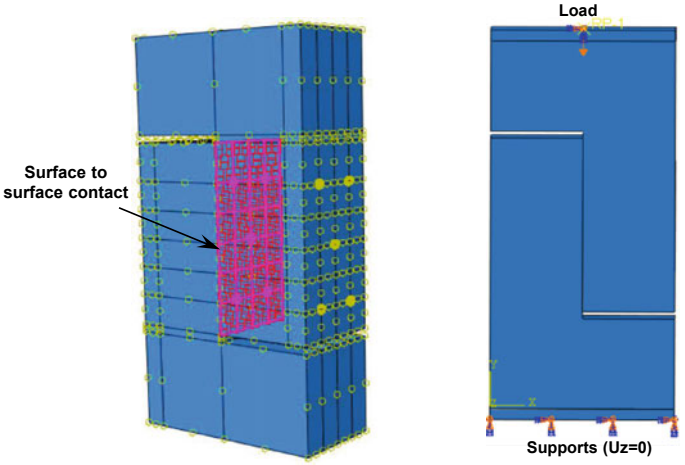

Fig. 2 Interaction and boundary conditions

2.2 Material Modeling

Concrete: The damaged plasticity model (CDP) available in ABAQUS was employed to model the concrete damage. This material model is based upon two main failure mechanisms of concrete, which are tensile cracking and compressive crushing. In this investigation, the dilation angle for concrete plasticity and is assumed 31 degrees, as recommended by (Esfahani 2017). Other plasticity parameters such as; K, eccentricity, the ratio of biaxial compressive strength to uniaxial compressive strength were assumed as 0.67, 0.1, and 1.16, respectively.

GFRP Bars: FRP bars were modeled assuming an orthotropic material with a linear and elastic constitutive behavior. Defining orthotropic material like GFRP was accomplished by specifying the engineering constants for bars from previous research ([2, 10], and Slimani 2013). Linear elasticity in an orthotropic material is most easily defined by giving the "engineering constants" the three moduli E_1, E_2, E_3, Poisson's ratios v_{12}, v_{13}, v_{23}, and the shear Modulus G_{12}, G_{13}, G_{23}, associated with the material's principal directions.

3 Calibration of the Model and Investigation on Material Parameters

In this section, the previously presented push-off specimens [5, 6] were examined considering the GFRP stiffness and geometry. Five push-off specimens were modeled and analyzed. Two specimens C-30 and C-35, are modeled without any reinforcement

across the interface, and the shear plane areas are different. The third specimen, FH3-30, is reinforced with three GFRP headed bars across the shear plane area. While the specimens, FH5-30 and FH5-A2, the shear plane areas are different, and the reinforcement is increased to five GFRP headed bars. Figure 3 shows reinforcement details of simulated push-off specimens. Table 1 provides the summary of details of the simulated specimen and Test and FEA results.

Comparing the FEA results and experimental results in terms of ultimate shear load V_u and slip displays a good agreement. The maximum discrepancy between the test results and FEA simulations is about 2% in terms of ultimate shear load, while about 25% for the slip. Consequently, the model was able to predict, with reasonable accuracy, the shear load–slip behavior.

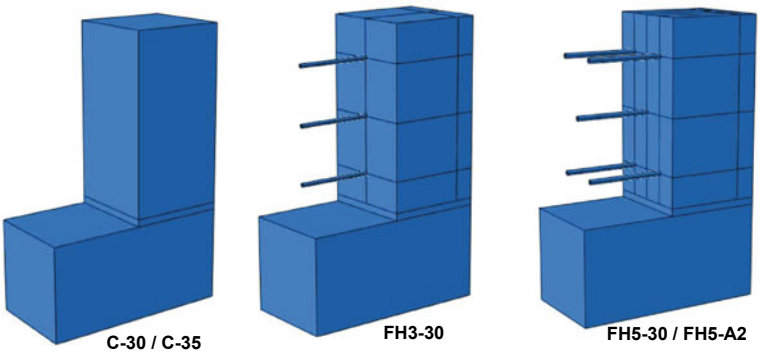

Fig. 3 Reinforcement details of simulated push-off specimens

Table 1 Details of the simulated specimen and test and FEA results

Specimen ID	A_{cv} (mm^2)	f_c' (MPa)	$E_{\rho v}$ (N/mm^2)	Experimental results		FEA Results		FEA./Exp	
				V_u (KN)	Slip (mm)	V_u (KN)	Slip (mm)	Load (%)	Slip (%)
C-30	125,000 (250 × 500)		0	332	0.34	330	0.41	0.99	1.20
FH3-30		30	182	362	0.44	362	0.51	1.00	1.16
FH5-30			304	433	0.94	423	0.84	0.98	0.89
C-35	75,000 (250 × 300)	35	304	216	0.28	215	0.35	0.99	1.25
FH5-A2			507	264	1.00	258	0.91	0.98	0.91

4 Parametric Study

Effects of parameters on ultimate shear load Vu and slip are investigated based on the above-calibrated FEA model. The parameters include the shear plane area and GFRP reinforcement stiffness. The shear plane areas for specimens C0-A and C0-B are 300 $\times$ 500 mm^2 and 300 $\times$ 600 mm^2 without any reinforcement across the interface. Model FH3-4A, FH3-4B are reinforced with three GFRP headed bars #4 across the different shear plane areas. While the specimens, FH3-5A and FH5-B, are reinforced with three GFRP bars #5. Similarly, FH5-4A, FH5-4B, FH5-5A, FH5-5B, FH8-4A, FH8-4B are reinforced with various numbers and diameters of GFRP headed bars across the different shear plane areas. Figure 4 displays reinforcement details of simulated specimens. Table 2 provides the summary of details of the simulated specimen and FEA results.

The FEA results indicate that using GFRP reinforcement across concrete joint increases its shear transfer resistance by 6% to 19%. This observation coincides with [4, 5] findings, GFRP shear reinforcement provides additional shear frictional resistance to the interface's cracking. Moreover, the FEA results revealed that increasing the shear plane area from 150,000 mm^2 to ^{180,000} mm^2 enhanced the shear transfer capacity for all models with an average of 18%. Further, raising the GFRP reinforcement stiffness (diameter or numbers) has marginal increases of shear transfer capacity for all models with an average of 3%. The ultimate shear capacity of all the GFRP bars reinforcement models was attained at a slip value in the range of 0.53 to 0.72 mm. Figure 5 illustrates typical maximum tensile principal stresses of all models. The tensile principal stresses can be used in FEA in order to show the cracking patterns.

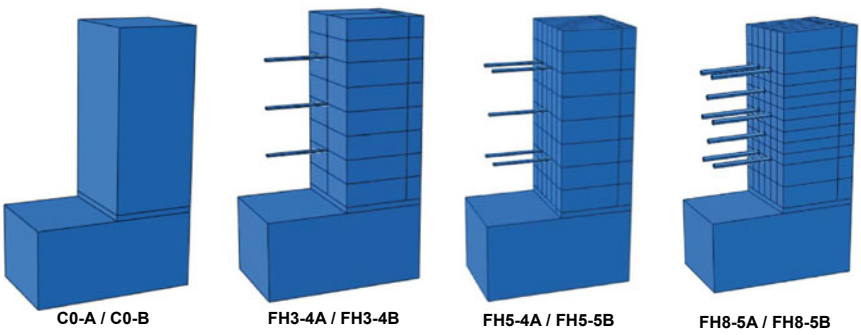

Fig. 4 Reinforcement details of simulated specimens in the parametric study

Table 2 Results of the finite-element parametric study

Specimen ID	A_{cv} (mm^2)	f_c' (MPa)	$E_{\rho v}$ (N/mm^2)	FEA results		Strength increase (%)
				V_u (KN)	Slip (mm)	
C0-A	150,000 (300 × 500)	30	0	396	0.47	0
FH3-4A			152	423	0.53	7.1
FH5-4A			253	436	0.58	10.4
FH3-5A			238	432	0.57	9.4
FH5-5A			396	450	0.61	14
FH8-5A			632	472	0.66	19.5
C0-B	180,000 (300 × 600)	30	0	479	0.57	0
FH3-4B			127	509	0.59	6.0
FH5-4B			212	520	0.63	8.5
FH3-5B			198	516	0.61	7.7
FH5-5B			330	529	0.67	10.5
FH8-5B			528	547	0.72	14.2

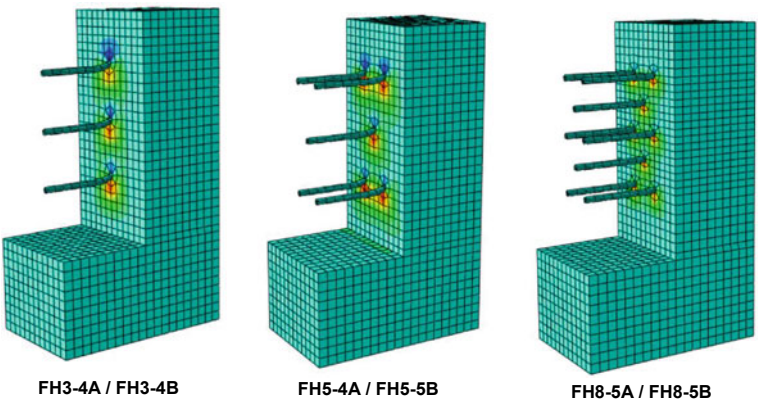

Fig. 5 Typical maximum tensile principal stresses in concrete at the failure

5 Summary and Conclusion

In this paper, the finite element analysis was used for predicting the shear transfer response of push-off test specimens reinforced with GFRP bars across their shear plane. Five different push-off specimens were simulated and analyzed in terms of ultimate shear load and slip. The results of the analyses compared to the test results showed good agreement. A parametric investigation was performed to study the shear plane area's influence and GFRP reinforcement stiffness on the ultimate shear load

and slip. Based on the work presented in this paper, the following conclusions can be drawn:

1. The FEA adequately predicted the experimental response of the tested GFRP push-off specimens. The FE model can be an effective tool for providing insight into the behavior and the various aspects affecting shear transfer mechanism in FRP-RC precast girders supporting cast-in-place slabs.
2. The push-off models reinforced with GFRP shear reinforcement demonstrated a remarkable shear transfer mechanism strength at the cold-joint concrete joints with as-cast rough interfaces.
3. Increasing the GFRP reinforcement stiffens had an insignificant influence on the shear transfer strength. Raising the shear plane area improved the shear transfer strength by 18%.

Additional research targeting connecting the cast-in-place slabs to the supporting FRP-RC beams still needed to formulate definitive design provisions for these deck slabs.

Acknowledgements The authors wish to express their gratitude and sincere appreciation to the Natural Science and Engineering Research Council of Canada (NSERC), the NSERC Research Chair in Innovative FRP Reinforcement for Concrete Structures, the Tier-1 Canada Research Chair in Advanced Composite Materials for Civil structures, the Fonds Québécois de la Recherché sur la Nature et les Technologies (FQRNT), the Canadian Foundation for Innovation (FCI), and the exceptional efforts of the technical staff of the CFI structural laboratory in the Department of Civil Engineering at the University of Sherbrooke. The financial support from SFTec, Inc., Montreal, Quebec, Canada.

References

1. AASHTO LFRD Bridge Design Specifications (2 Ed.) (2019) American association of state highway and transportation officials. 978- l-56051-71 7-7
2. Alachek I, Reboul N, Jurkiewiez B (2020) Experimental and finite element analysis of push-out shear test for adhesive joints between pultruded GFRP and concrete. Int J Adhes Adhes 98:1–13. https://doi.org/10.1016/j.ijadhadh.2020.102552
3. Raza A, Khan QZ, Ahmad A (2019) Numerical investigation of load-carrying capacity of GFRP-reinforced rectangular concrete members using CDP model in ABAQUS. Adv Civil Eng J. ID 1745341. https://doi.org/10.1155/2019/1745341
4. Alkatan J (2016) FRP shear transfer reinforcement for composite concrete construction M.A.Sc thesis, Department of Civil and Environmental Engineering, University of Windsor, Windsor, Canada
5. Alruwaili MS (2018) Shear transfer mechanism in FRP reinforced composite concrete structures. M.A.Sc thesis, Department of Civil and Environmental Engineering, University of Windsor, Windsor, Canada
6. American Concrete Institute (ACI Committee 440) (2015) Guide for the design and construction of structural concrete reinforced with fiber-reinforced polymer (FRP) Bars (ACI 440.1R-2015), Farmington Hills, MI
7. Canadian Standards Association (CSA) (2012) Design and construction of building structures with fiber reinforced polymers (CAN/CSA S806–12), Rexdale, Ontario, Canada, 198 p

8. Canadian Standards Association (CSA) (2019) Commentary on CSA S6.1–19, Canadian highway bridge design code (CAN/CSA S6.1–19), Rexdale, Ontario, Canada, 798 p
9. Canadian Standards Association (CSA) (2015) Specification for fiber-reinforced polymers (CAN/CSA S807–15), Rexdale, Ontario, Canada, 27 p
10. Castellano A (2018) Evaluation of damage anisotropy induced in GFRP composite materials by an innovative ultrasonic experimental approach. Eng Struct Mat J 4(1):35–47
11. Connor AB, Kim YH (2016) Shear-transfer mechanisms for glass fiber-reinforced polymer reinforcing bars. ACI Struct J 113(6):1369–1380
12. Hafezolghorani M, Hejazi E, Vaghei R, Jaafar MSB, Karimzade K (2017) Simplified damage plasticity model for concrete. Struct Eng Int 27:68–78
13. Kamanehazari H, Tadbiri F (2012) Behavior of High Strength Concrete (HSC) reinforced beam with GFRP bars using plastic damaged concrete model. CTTS J 2(3): 272–276. ISSN: 2279–0535
14. Santos PMD, Júlio NBS (2014) Interface shear transfer on composite concrete members. ACI Struct J 111(1):113–122
15. Sun C, Xiao J, Lange DA (2017) Simulation study on the shear transfer behavior of recycled aggregate concrete. Struct Concr J 2018(19):255–268. https://doi.org/10.1002/suco.201600236
16. Williams CS, Massey JB, Bayrak O, Jirsa JO (2017) Investigation of interface shear transfer using push- through tests. ACI Struct J 114(1):173–185
17. ABAQUS Analysis user's manual 6.14. Providence (RI, USA): Dassault Systems Simulia Corp.; (2014)

Numerical Modeling of Microplastics Fate and Transport in a Stretch of the Fraser River

G. Babajamaaty, A. Mohammadian, and A. Pilechi

1 Introduction

Plastics with less than 5 mm in size are called microplastics [6]. In addition to economic importance of rivers for humans, they are primary elements of ecosystem [1]. Microplastic pollution of aquatic environments such, as oceans and rivers, is an increasing global concern. Production of 280 million tons a year of plastics and their after use waste intensify this anxiety [5]. Durability, widespread occurrence and harmful health effects have made microplastics a serious threat to aquatic ecosystems. Human activities and surrounding industries have close relation with the amount of microplastics in water resources. Fraser River is one of the most important water resources in British Columbia, Canada that its basin covers nearly one-quarter (more than 220,000 km^2) of British Columbia province [4]. It rises at Fraser Pass and flows more than 1375 kms to its mouth at Strait of Georgia at the city of Vancouver. Although because of low crowd and industrial sites near Fraser River and no dams on its main pathway, it's one of the most virgin rivers [7], but around there industrial activities have been increased recently that contribute to release of Microplastics in this area. The objective of this study is to numerically investigate transport of microplastics in a highly urbanized and industrialized stretch of the Fraser River located between Douglas Island and the Strait of Georgia.

G. Babajamaaty · A. Mohammadian (✉)
Department of Civil Engineering, University of Ottawa, Ottawa, ON, Canada
e-mail: amohamma@uottawa.ca

A. Pilechi
National Research Council, Ottawa, ON, Canada
e-mail: abolghasem.pilechi@uottawa.ca

S. Walbridge et al. (eds.), *Proceedings of the Canadian Society of Civil Engineering Annual Conference 2021*, Lecture Notes in Civil Engineering 240,
https://doi.org/10.1007/978-981-19-0507-0_10

2 Methodology

The numerical model used in this study consists of a three-dimensional hydrodynamic model and a three-dimensional Particle Tracking Model (PTM). The hydrodynamic model is based on the TELEMAC modeling system. The PTM simulate movement of the microplastic particles within the system using the hydrodynamic information (i.e. velocities and water level) calculated by the hydrodynamic model at each time step of the simulation.

3 Domain of Study

The selected area in this study is a 35-km stretch of the Fraser River extended from Douglas Island to the mouth of Fraser River in the Strait of Georgia. The upstream extent of the model was selected based on the observation provided in [9] which showed salinity values near zero at light green point (see Fig. 1) located in the upper region of the region of interest. The model domain starts from right at downstream end of the Douglas Island assuming negligible salt water intrusion effect from the ocean at the upstream boundary of the domain.

Fig. 1 Study Area (base map from Google Earth) and the salinity station

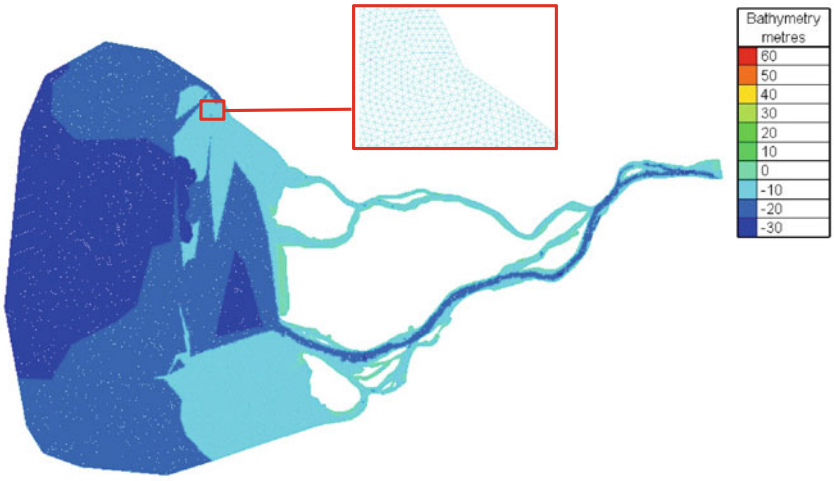

Fig. 2 Computational Mesh and a zoomed region (Vertical Datum reference to MSL)

4 Computatinal Mesh

The base mesh of the model was created using BlueKenue 3.3.4. The mesh consists of 116,408 triangular prism elements with uniform edge length of 100 m (Fig. 2). The mesh has four sigma layers [8] in the vertical direction.

High resolution bathymetry data with the resolution varying of 10 m to 50 m obtained from the Public Works and Government Services Canada - Pacific Region (Geomatic Services Division), and was used to setup the model. All of the elevation data in this study (bathymetry and water level) are referenced to the mean sea level (MSL) vertical datum.

5 Simulation

The friction coefficient of the bottom is constant which is set to 0.04 everywhere. Horizontal turbulence model is a constant model and vertical turbulence model is a mixing length model. The duration of simulation in this study was 41 days from 01 June 2020 to 11 July 2020 consisting of two full spring-neap tidal cycles (i.e. 30 days) and 11 days for the model spin-up. Based on previous studies upstream flow canbe considered as fresh water so the salinity is approximately zero and the salinity of downstream is 30 ppt. Time step of this model is 4 s.

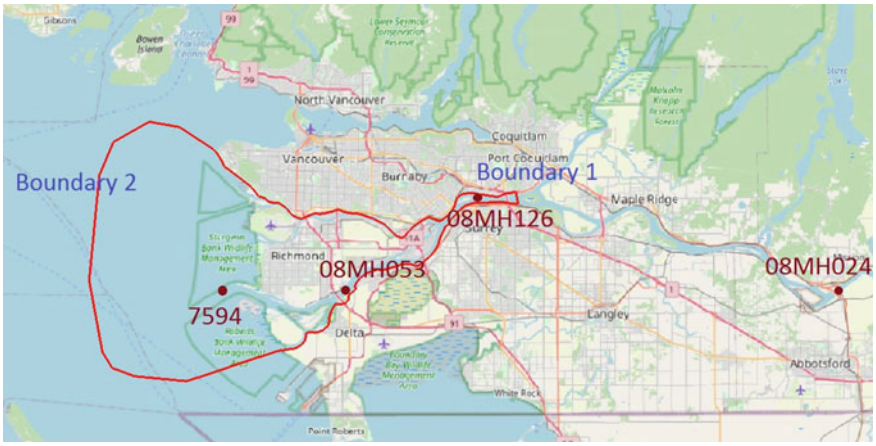

Fig. 3 Model boundaries and water level and discharge stations

6 Boundary Conditions

Two boundaries have been assigned for this model (Fig. 3). Freshwater discharge was prescribed at the upstream boundary just near Douglas Island. The downstream open boundary of the model in the straight of Georgia was forced by tidal elevation.

The discharge data were downloaded from the website of Government of Canada. The historical discharge data of PORT MANN PUMPING (08MH126) and MISSION(08MH024) stations were used. The PORT MANN PUMPING station is located closer to the upstream boundary of the model. However, its available data is only until 1992. In order to derive time series of discharge information for the simulation period in 2020, the data from the MISSION station (available up to 2020), and MANN PUMPING station were processed together using a multilayer perceptron artificial neural network (MLP) algorithm.

The water level records at Sand Heads, B.C. station 7594 were downloaded from the website of Government of Canada, fisheries and oceans Canada part, and used at Boundary2 (Fig. 3).

7 Particle Tracking Model

The movement of microplastics in the river was simulated using a three-dimensional Particle Tracking Model (PTM) developed at the National Research Council Canada in collaboration with University of Ottawa. The model uses hydrodynamic information calculated by the hydrodynamic model at each time step of the simulation, and solve a three-dimensional advection–diffusion equation (Eq. 1) in a Lagrangian system to determine particle position at the each time step of the simulation [2].

$$X(t + \Delta t) = X(t) + Adv + Diff \tag{1}$$

In order to determine position of the particles in the model solve Eq. 1 in the horizontal (*x,y*) and vertical (*z*). The model uses first-order Euler method for calculating advective transport (*Adv*) of the particle,

$$Adv = U_p \Delta t \tag{2}$$

where U_p is the water velocity applied on the particle, and Δt is the time step. Contribution of turbulence to particles motion was represented by the diffusion term (*Diff*) in Eq. 1, and was calculation using Random Walk Particle Tracking (RWPT) model [3],

$$Diff = \mathrm{R}\sqrt{2K\Delta t} \tag{3}$$

where K is a diffusion coefficient, and R is a random number between -1 and 1 with a normal distribution. The PTM simulation as conducted at time step of $\Delta =$ 15 min and using a constant diffusion coefficient $K = 1\mathrm{e}{-3}$ (m2/s).The particles were uniformly realised on every 10 m along Boundary1 at each time step of the simulation. Reflecting boundary condition was applied along the shoreline to avoid particles escape from tom the domain.

8 Result and Discussion

30-day water level, velocity and salinity time series of the model were extracted. Time series of salinity and velocity are shown below (Figs. 4 and 5) to demonstrate that the results of the model are reasonable. Water level datasets of the Deas Island Tunnel station (08MH053) (Fig. 3) (show on the figure where this station is located) from the website of the Government of Canada were downloaded. Data of the model at the location of station number 08MH053 and downloaded data were compared and the result was shown on a graph (Fig. 6) which shows a reasonable agreement between the measured and modeled results.

The PTM model provides spatial distribution of the particles realised at the upstream boundary of the model (Boundary 1 in Fig. 3). The three-dimensional nature of the PTM model also enables determining vertical position of the particles within the water columns at each time step. Figure 7 illustrated distribution of the particles at last time step of the 30-day simulation which shows relative abundance of particles in difference regions of the model stretch. This information can be used in post-processing clustering algorithms to identify the zone with higher potentials for microplastics accumulation based on hydrodynamic and topographic characteristics. In the modeled case in this study, the fresh water from the upstream flows over and mixes with denser seawater driven by tides in lower depths. This in addition to the

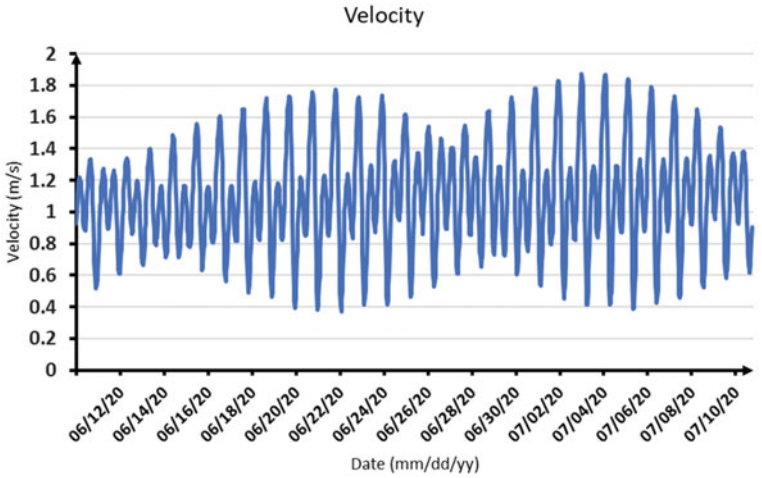

Fig. 4 Modeled free surface velocity magnitude at station 08MH053

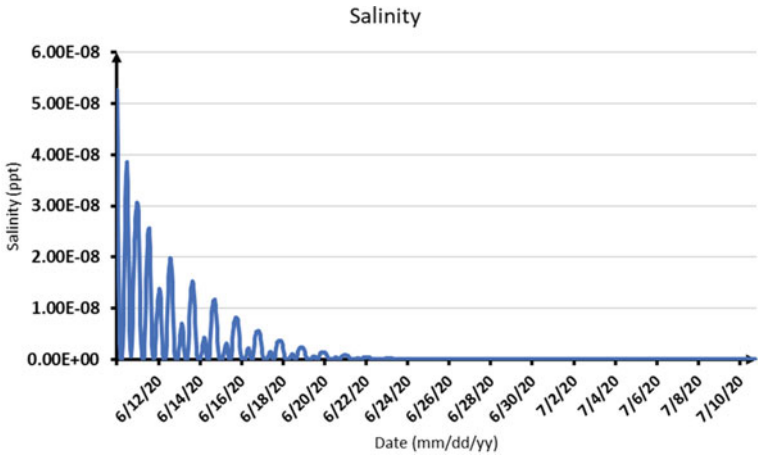

Fig. 5 Model free surface salinity at station 08MH053

fact that particles were uniformly released close to the water surface at the upstream boundary, have caused insignificant transport of particles in the water column in most regions in this example. However, the vertical circulations/eddies generated in some regions of the model have caused abrupt changes in particle positions within the water columns, as showed in Fig. 7, which also confirms capability of the PTM in simulating vertical transport of the particles.

The result of the PTM can also inform residence time of the microplastic pollution in different regions of the system. From the total number of 60,000 particles realised into the domain during the simulation, less than 13,500 particles reached to the ocean.

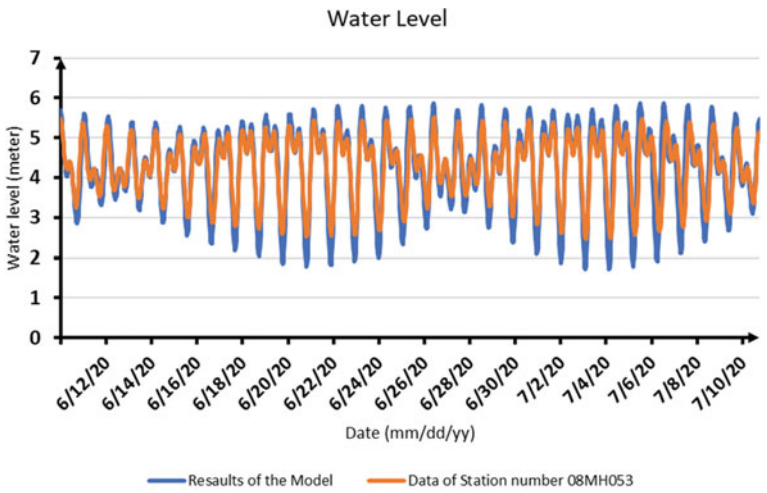

Fig. 6 Comparison of water level data of the station and results of model

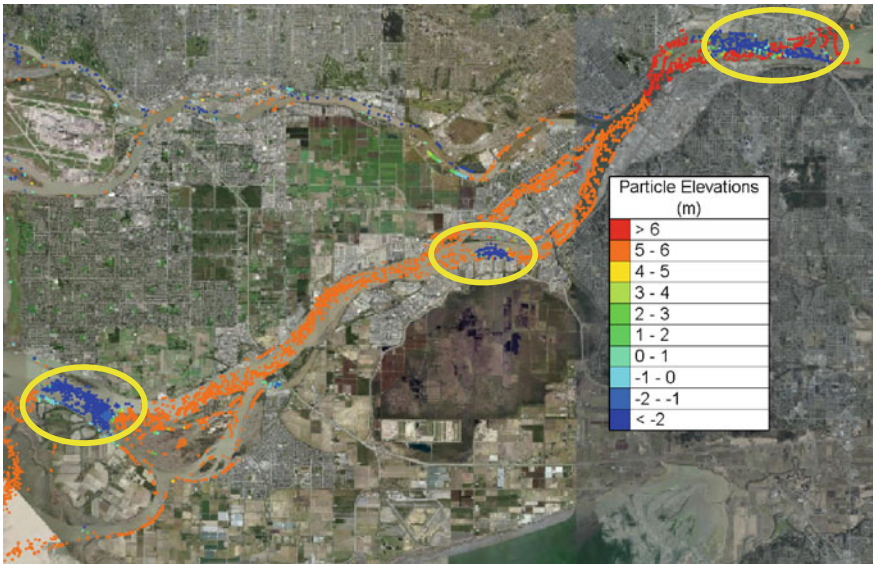

Fig. 7 Snap shot of modeled particles distribution by the PTM at time step 150. Note: Particle elevations are referenced to the mean sea level (MSL)

This mean that more than 77% of the released particles accumulated in the system. It is acknowledged that this value is influenced by boundary treatment method and the time step used in the PTM. However, it also signifies the importance of more

detail investigation of microplastics, and other contaminants transport supported by high-resolution numerical simulations and field measurement in this area.

9 Summary and Conclusion

A numerical analysis was conducted in a highly urbanised and industrialised stretch of the Fraser River extended between Douglas Island and the Strait of Georgia to better understand fate and transport of microplastics within the system. A three-dimensional numerical model was developed coupling an Eulerian hydrodynamic model and a Lagrangian Particle Tracking Model (PTM) for the stretch of interest. Hydrodynamic condition and transport of neutral particles carried by water particle within the system was simulated for 30 days. Reasonable agreement was observed between the hydrodynamic model results the measured data. The PTM simulation provided information of the spatio-temporal distribution of the particles and indicated likelihood of particles accumulation in some regions of the stretch, and value of using this tool for improving understanding of microplastics fate and transport in coastal and riverine environment.

From the simulation conducted in this study, it was found that the hydrodynamic mesh solution in both horizontal and vertical direction, the discharge rate at the upstream, time step size of the simulation, boundary treatment method used in the PTM, and quality of the bathymetry data are the main factors which can influence behaviour of the particles. Future studies will be focused on improving performance of this tool through adjusting different influencing parameter, and using more complex boundary treatment methods for modeling particles interaction with bed and the shoreline.

References

1. Costanza R, d'Arge R, Groot R, Farber S, Grasso M, Hannon G, Limburg K, Naeem S, O'Neill RV, Paruelo J, Raskin RG, Sutton P, Belt M, Belt H (1996) The value of the world's ecosystem services and natural capital. Nature. Report of Workshop organised by NCEAS, Santa Barbara, Calif 387: 253–260
2. Jalón-Rojas I, Wang XH, Fredj E (2019) Technical note: On the importance of a three-dimensional approach for modelling the transport of neustic microplastics. Ocean Sci Discuss 1–11. https://doi.org/10.5194/os-2018-136
3. Hunter JR, Craig PD, Phillips HE (1993) On the use of random walk models with spatially variable diffusivity. J Comput Phys 106(2):366–376
4. Clague JJ, Roberts NJ, Miller B, Menounos B, Goehring B (2021) A huge flood in the Fraser River valley, British Columbia, near the Pleistocene Termination. Geomorphology 374:107473. https://doi.org/10.1016/j.geomorph.2020.107473
5. Koelmans AA, Gouin T, Thompson R, Wallace N, Arthur C (2014) Plastics in the marine environment: ET&C perspectives. Environ Toxicol Chem 33:5–10
6. Lin V (2016) Research highlights: Impacts of microplastics on plankton. Environ Sci Process Impacts 18: 160–163

7. Peucker-Ehrenbrink B, Bourdages M, Beaurepaire M, Paine J, Klein F, Galy V, Mincer TJ, Gillies SL, Marsh SJ (2018) Microplastics in the Fraser River, B.C., Canada. American Geophysical Union, Fall Meeting 2018. 2018: H33Q-2297
8. Phillips NA (1957) Sigma A co-ordinate system having some special advantages for numerical forecasting. J Meteorol 14: 184–185
9. Tsz Yeung Leung A, Stronach J, Matthieu J (2018) Modelling behaviour of the salt wedge in the fraser river and its relationship with climate and man-made changes. J Mar Sci Eng 6: 130–159.

Preliminary Analysis of Permafrost Degradation in Ingraham Trail, Northwest Territories

Danrong Wang, Susan L. Tighe, and Shunde Yin

1 Introduction

Permafrost represents the ground including bedrock, sediments, and soil that is below or at 0 °C in two consecutive years or longer. Permafrost usually underlies the active layer of the ground which thaws in summer and freezes in cold weather [14]. Due to global warming, the ground temperature increases, which induces thawing permafrost that is sensitive to the temperature change [2]. The permafrost terrain has experienced different levels of degradation and the permafrost layer is subjected to freeze–thaw cycles and turns into an active layer. As a result, impacts and potential risks caused by permafrost degradation are brought upon vegetation, biochemical processes, hydrology system, and engineering infrastructures [15]. Thus, as a result of climate change, not only the temperature changes, the hydrologic impacts are also induced, where the water table is deemed to decline with boosting baseflow with thawing permafrost [11, 19].

Design of infrastructures such as pavements built in the permafrost should consider the impact of climate change such as the frost heave and thaw settlement associated pavement damages [16, 17]. It has been noted that thaw settlement and frost heave can be the major cause of damage to infrastructures located in the permafrost area. For instance, it was investigated in 1990 that about 83.5% of the damage of Qinghai-Tibet Highway was caused by thaw settlement, while 16.5% of the damage was caused by frost heave [18].

On the other hand, the number of frozen days decreases most significantly in the areas where the permafrost is distributed discontinuously, islandly, or in the

D. Wang (✉) · S. L. Tighe · S. Yin
Department of Civil and Environmental Engineering, University of Waterloo, Waterloo, Canada
e-mail: peggie.wang@uwaterloo.ca

S. L. Tighe
Department of Civil Engineering, McMaster University, Hamilton, Canada

S. Walbridge et al. (eds.), *Proceedings of the Canadian Society of Civil Engineering Annual Conference 2021*, Lecture Notes in Civil Engineering 240,
https://doi.org/10.1007/978-981-19-0507-0_11

Fig. 1 Differential Settlements of the road structure along Ingraham Trail [13]

transitional areas. The significant changes in beginning dates of freeze and thaw have also been observed in these areas [12]. These areas are considered to be more sensitive to temperature change as the ground has a higher temperature and the soil has higher ice content [3].

Ingraham Trail, also known as Highway 4 (Hwy 4) in NWT, extends 69.2 km east from Yellowknife to Tibbitt Lake. Ingraham Trail connects three great territorial parks and provides access to Yellowknife. The extensive discontinuous permafrost within the entire Ingraham Trail is not treated, so the existing Highway 4 is experiencing a high level of uncertainty due to climate change [7]. The deformation of the road structure can be observed along Ingraham Trail as shown in Fig. 1.

2 Numerical Modeling of Frost Heave and Thaw Settlement in Pavements

In pavement engineering particularly, [9] uses the finite element method to discretize the pavement into one-dimension elements and nodes vertically, where the ground is treated as a continuous medium and is evaluated linearly throughout the space domain. A finite element model predicting thaw settlement with the incorporation of surface roughness was developed [9]. In this paper, a one-dimensional Galerkin finite element model has been developed in MATLAB, following the approach described in [9] and [8], for simplicity and relevance to pavement engineering practice. The following sections provide the mathematical basis of the THM coupling processes

involved in the determination of frost heave and thaw settlement in pavements on Ingraham Trail. This includes the theory regarding the hydraulic and thermal fields, as well as the implementation of the phase change effect between freezing and thawing processes. The overburden effect and ice segregation are also introduced in the model.

2.1 Fluid Flow in Porous Media

The model is assumed on a one-dimensional basis with the fluid flowing vertically. The soil deformation in the unfrozen soil is assumed to be negligible, where the consolidation is not considered. The fluid is assumed to flows in the unfrozen zone only. Also, the fluid movement is considered to happen only by the means of liquid water migration, and the ice cannot move. The vapor movement is not considered in this case either. Based on these assumptions, the unsaturated fluid flow can be described by Darcy's Law as shown in Eq. 1.

$$v = -\frac{k}{\mu}\nabla p \tag{1}$$

where v is the fluid flux; k is the permeability; μ is the viscosity; ∇p is the pressure gradient.

The fluid flow follows the law of mass conservation, which can be achieved by using the Richards equation as shown in Eq. 2.

$$\frac{\partial \theta}{\partial t} = \frac{\partial}{\partial z}\left[K(\theta)\left(\frac{\partial \mathbf{h}}{\partial z} + 1\right)\right] \tag{2}$$

where θ is the volumetric content; t is the time; z is the vertical coordinate; K is the hydraulic conductivity and $K = (k\rho_w g)/\mu$; ρ_w is the density of water; g is the gravitational acceleration; h is the total pressure head and in this case $p = \rho_w gh$.

By implementing the phase change effect to the above two equations, the governing one-dimensional equations for the unsaturated fluid flow can be obtained as the Eq. 3.

$$\frac{\partial \theta_w}{\partial t} = K\frac{\partial^2 h}{\partial z^2} - \frac{\rho_i}{\rho_w}\frac{\partial \theta_i}{\partial t} \tag{3}$$

where θ_w and θ_i are the volumetric content for unfrozen water and ice respectively; ρ_i is the density of ice.

To solve Eqs. 3, 4 is adopted by extending the relationship between the pressure head h and the volumetric water content θ_w, in which the relationship can be determined by Eq. 5, using laboratory data [5, 8].

$$\frac{\partial \theta_w}{\partial t} = \frac{\partial \theta_w}{\partial h_p} \frac{\partial h}{\partial t} \tag{4}$$

$$\theta_w = \frac{\phi}{A_w \left| h_p \right|^a + 1} \tag{5}$$

where h_p represents the pore water pressure head; ϕ is the porosity of the soil; A_w and a are both the best fit soil parameters.

Correspondingly, the relationship between the hydraulic conductivity K and the pressure head h can be described by Eq. 6 [5, 8].

$$K = \frac{K_s}{A_k \left| h_p \right|^b + 1} \tag{6}$$

where K_s is the saturated hydraulic conductivity; A_k and b are both the best fit soil parameters.

Besides, the fluid may not be able to move through all the pores when ice exists. The resultant reduction of the hydraulic conductivity can be described using an empirical relationship in Eq. 7 as follows [8].

$$K_f = Kh_p \times 10^{-E\theta_i}, E\theta_i \geq 0 \tag{7}$$

where K_f is the reduced hydraulic conductivity by considering the ice effect; E is a factor related to the saturated hydraulic conductivity K_s as shown in Eq. 8 [8]. The E factor can also be specified with a value when utilizing the model.

$$E = \frac{5}{4}(K_s - 3)^2 + 6 \tag{8}$$

2.2 *Heat Transfer*

Similar to the fluid flow, the heat conduction is considered to be one-dimensional by utilizing Fourier's law as shown in Eq. 9 and obtaining Eq. 10.

$$q_T = -\lambda_T \nabla T \tag{9}$$

$$\lambda_T \frac{\partial^2 T}{\partial z^2} = C \frac{\partial T}{\partial z} \tag{10}$$

where q_T is the heat flux; λ_T is thermal conductivity; ∇T is temperature gradient; C is the volumetric heat capacity.

When the fluid flow exists, the heat convection as well as the phase change effect is also taken into consideration by assuming thermal equilibrium between the soil and fluid, as per the law of energy conservation as shown in Eq. 11.

$$\begin{aligned}&[\lambda_w\theta_w + \lambda_i\theta_i + \lambda_s(1-\phi)]\frac{\partial^2 T}{\partial z^2} + C_w v\frac{\partial T}{\partial z}\\&= [C_w\theta_w + C_i\theta_i + C_s(1-\phi)]\frac{\partial T}{\partial t} - L\frac{\rho_i}{\rho_w}\frac{\partial \theta}{\partial t}\end{aligned} \tag{11}$$

where λ_w, λ_i and λ_s are the thermal conductivity for water, ice, and soil; C_w, C_i and C_s are the volumetric heat capacity for water, ice, and soil; L is the latent heat coefficient, where latent heat is the "hidden" heat energy change when the phase changes, without the temperature changes, which is supposed to be a constant value equal to that of the bulk water [8].

2.3 Phase Change Effect

Both Eqs. 3 and 11 introduce a term representing the phase change effect, which is approached through the isothermal process. Equations 12 and 13 are compared with each other during a computation time step.

$$\Delta Q_1 = C_m(T^{t+\Delta t} - T_f) \tag{12}$$

$$\Delta Q_2 = L(\theta_u - \theta_n) \tag{13}$$

where ΔQ_1 is the amount of heat extracted during Δt in a unit volume of soil; T_f is the freezing-point depression; ΔQ_2 is the required amount of heat to be extracted from the unit volume of the soil so that the soil can be frozen; θ_n is the minimum volumetric water content for ice.

When ΔQ_1 is greater than ΔQ_2, the temperature is set to T_f for the freezing process, while the computed temperature is set to T_f when ΔQ_1 is less than ΔQ_2 for the thawing process. The phase change term in Eqs. 3 and 11 can be computed by Eq. 14 as follows [8].

$$\frac{\rho_i}{\rho_w}\frac{\partial \theta_i}{\partial t} = \frac{1}{L}\frac{\Delta Q}{\Delta t} \tag{14}$$

2.4 Ice Segregation Process with the Overburden Effect

The overburden includes the sum of the weight of the materials (i.e., soil, water, ice) as well as the surcharge stresses. When the segregated ice does not exist (i.e., $\theta_i < \phi - \theta_n$), the available pores can accommodate the ice volume. The overburden is assumed to be upheld by the soil. When the ice segregation exists, the overburden weight is held by the ice lenses, and the minimum volumetric water content for ice θ_n can be computed in Eq. 15 as follows [8].

$$\theta_n = \frac{\phi}{A_w \left| h_p(\theta_n) + h_o \right|^a + 1} \tag{15}$$

where h_o is the hydraulic head representing the total overburden weight.

In these regards, Eq. 16 can represent the one-dimensional displacement (i.e., thaw settlement and frost heave).

$$\theta_s = \theta_i - (\phi - \theta_n) \tag{16}$$

where θ_s is the amount of the segregated ice, which represents frost heave when it is greater than zero and represents thaw settlement when it is negative.

3 Numerical Investigation of Frost Heave and Thaw Settlement in Yellowknife Pavements

Based on the frost heave and thaw settlement model, the resultant displacements caused by permafrost degradation on Ingraham Trail, Yellowknife, is investigated, without engineering intervention.

3.1 Basic Frost Heave and Thaw Settlement Analysis

For simplicity, a uniform soil column profile is assumed for the pavement structure at Ingraham Trail, Yellowknife as per AASHTO Recommended Minimum Thickness of Highway Layers. Based on the low volume nature of the roads in NWT, the thickness of 30 mm of the surface treatment layer is adopted with the lowest Equivalent Single Axle Loading (ESAL) traffic assumed from the guide [1]. The location of the water table is assumed to be 50 cm below the road surface as it is close to the lake. The subgrade material is assumed to be the same as the aggregate base in this case. The soil column can be divided into two layers with the water table exists below the subgrade. The constant element length is set to be 1 cm each. The discretization of

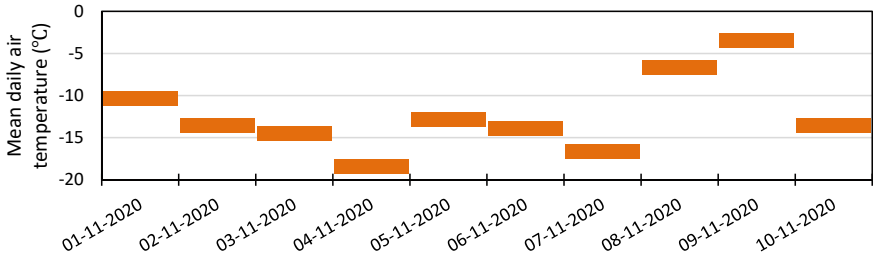

Fig. 2 Upper-temperature boundary conditions from November 1st to November 10th, 2020

the finite element model includes 51 nodes and two elements, where the second layer is located at 3 cm deep from the surface (i.e., node 4).

In the finite element model, the fully implicit method is used for moisture transport while the Crank-Nicolson method is used for heat transport for time integration. The time step increment is set to be 1 h, with the update of every time step. The whole simulation duration is 29 days, with 1st as Day 1 and 30th as Day 30. The simulation period is every November from 2013 to 2020.

The upper pore pressure and the lower temperature boundary condition is assumed to be natural. The lower pore pressure is set to be zero constantly. The surface temperature can be specified to be the mean daily air temperature [6]. Figure 2 illustrates the temperature boundary conditions from November 1st to November 10th, 2019 as an example. The initial condition of the surface pore pressure head is assumed to be −50 cm of the water. The initial volumetric ice content is also set to be constant as 0 for all the nodes.

The overburden is assumed to be 10 psi as the road is covered by packed snow for at least one-third of a year, due to the local climate condition. Table 1 lists the soil parameters for each layer of the material based on the empirical assumption.

3.2 Impact of Climate Change in Terms of Global Warming

Based on the climate change in terms of global warming, the temperature at the surface is adjusted from the year 2020 to the year 2050, with an assumed 2% temperature increase each year. The results of projected frost heave and thaw settlement are shown in Fig. 3. The figure demonstrates the impact of the warming temperature on the permafrost degradation, causing the decreased frost heaves, which implies increased thaw settlements. The resultant cumulative settlements were computed as shown in Fig. 4, with the base year as 2020, where the negative value indicated thaw settlements. The results are only based on the simulation of one month (November) each year. More representative cumulative settlements can be obtained by simulating the entire year.

Table 1 Soil parameters for each layer of the pavement structure

Soil layer parameter	Layer 1—Asphalt surface	Layer 2—Granular base & subgrade
Physical properties		
Soil density ρ_s	2.2 g/cm^3	1.5 g/cm^3
Soil porosity ϕ	0.2	0.45
Thermal Properties		
Freezing point depression T_f	0 °C	0 °C
Volumetric heat capacity of soil C_s	0.5 cal/cm^3 °C (2.09×10^6 J/m^3·K)	0.2 cal/cm^3 °C (8.37×10^5 J/m^3·K)
Thermal conductivity of the soil λ_s	10 cal/cm^3 hr °C (1.51×10^{11} J/m^3·s·K)	3 cal/cm^3 hr °C (4.52×10^{10} J/m^3·s·K)
Unfrozen water content factor θ_n	0.3	0.1
Moisture characteristics for drying curve		
A_w	0.0001	0.005
a	2	0.9
Unsaturated hydraulic conductivity function		
Saturated hydraulic conductivity k_s	36 cm/hr (1.00×10^{-4} m/s)	0.36 (1.00×10^{-6} m/s)
A_k	0.00005	0.004
b	4	2

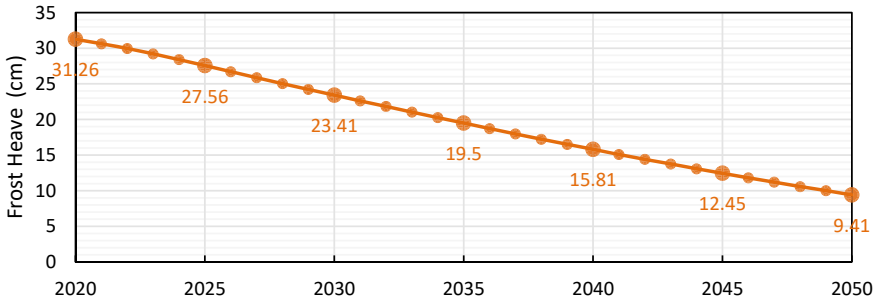

Fig. 3 Projected frost heaves for November (2020–2050) with the impact of global warming

3.3 Impact of Climate Change in Terms of the Water Table Change

The water table is adjusted from 2020 to 2050 to reflect another impact of climate change, with an assumed 1 cm increase in the water table for each decade. This

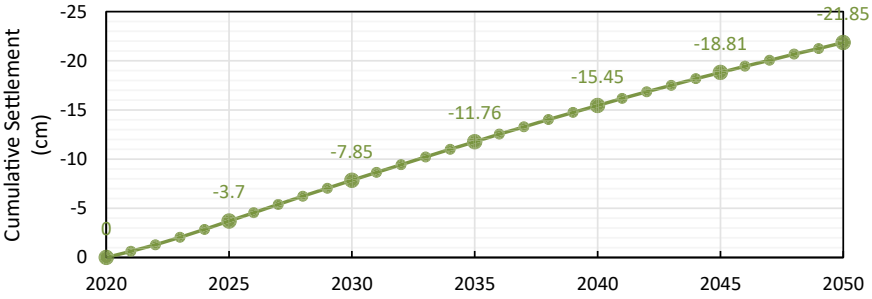

Fig. 4 Cumulative thaw settlements for November (2020–2050) with the impact of global warming

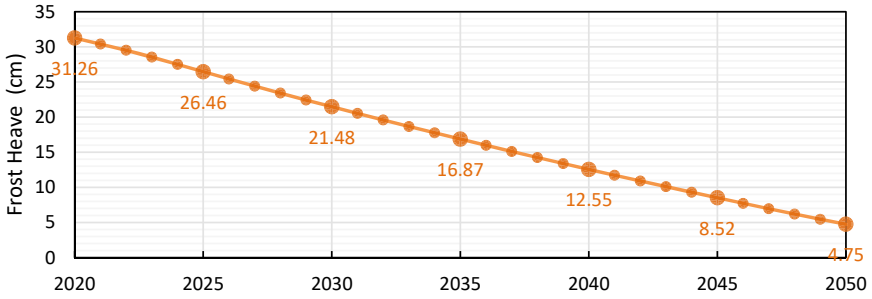

Fig. 5 Projected frost heaves for November (2020–2050) with the impact of water table change

represents the decline of the water table elevation, where the lowered water table is expected as a result of permafrost degradation [10]. The water table adjustment was performed by increasing the node number of the model. The results of frost heave are shown in Fig. 5, which shows the significant decrease of the frost heave for November in each year individually. This indicates increasing thaw settlements, and the cumulative settlements are shown in Fig. 6, with the base year as 2020. This implies the thawing permafrost with the declining water table has a great impact on the worsening settlement.

3.4 Impact of Intervention by Thermal Insulation

The simulation is also performed with the potential permafrost protection technique such as thermal insulation, with insulation materials (such as polystyrene and polyurethane) installed within the embankment to prevent the heat flow [4]. The main characteristic of these materials is the low thermal conductivity, which provides high heat resistance to prevent heat transfer to the permafrost. In this simulation case, the thermal conductivity is adjusted to be the same for the two layers of materials as 3

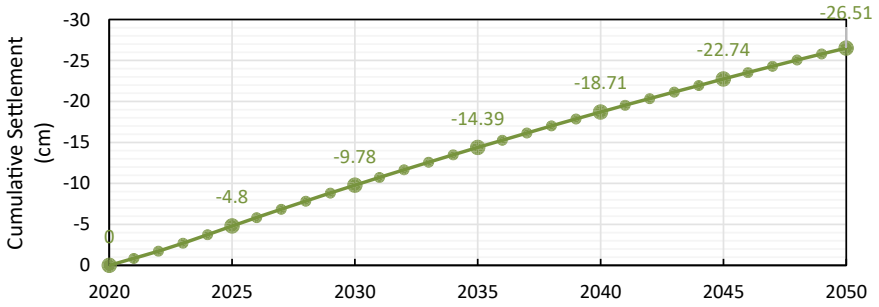

Fig. 6 Cumulative thaw settlements for November (2020–2050) with the impact of water table change

Cal/cm^{3}hr °C (4.52 × 10^{10} J/m^3·s·K). The other parameters and conditions are kept the same.

The frost heave for each November from 2013 to 2020 simulated by the model is illustrated in Fig. 7. The frost heaves vary from each year with great uncertainty, where the greatest difference can be up to 22.15 cm between 2016 and 2017. This demonstrates that the varied thaw settlement is caused due to permafrost degradation with the changing climate in recent years. With different frost heaves caused in the same season each year, it is difficult to maintain the pavement structure's resilience unless some protections are applied to mitigate the permafrost degradation impact.

It can be seen from the figure that the frost heaves in November are changed with a significant decrease after the protections are applied. This verifies insulation

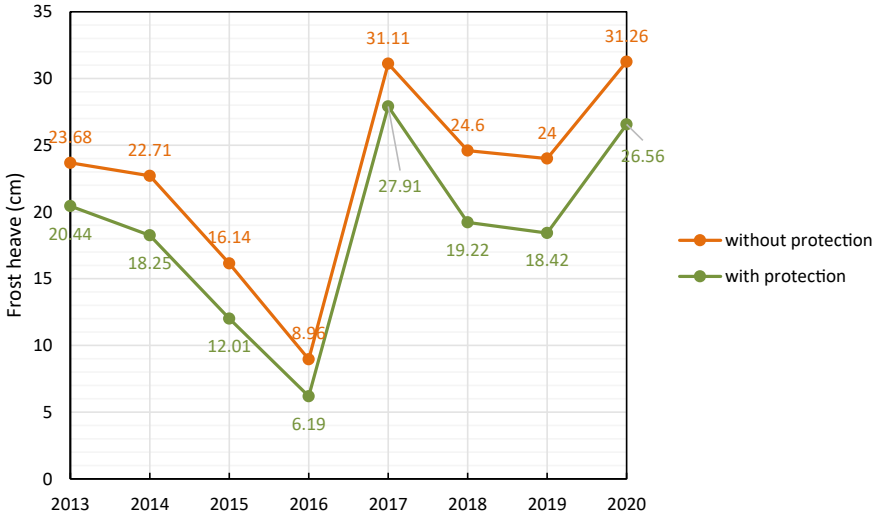

Fig. 7 Simulated frost heave for each November from 2013 to 2020

materials play a critical role in reducing thaw settlement. Though the parameters are assumed, a more accurate quantitative simulation can be performed with the exact properties of the materials by conducting laboratory and field tests.

4 Conclusions

Climate change has caused various kinds of issues. Permafrost is affected by the evolving active layer associated degradation. The differential settlement of the road is one of the consequences affecting the safety and resilience of the infrastructure. Ingraham Trail in Yellowknife, NWT, is investigated in this paper with its frost heave and thaw settlement by a one-dimensional finite element model.

This model is based on the theory of fluid flow in porous media and heat transfer with the application of mass conservation law and energy conservation law. Although the consolidation effect is neglected in this model, it can be incorporated in the mass balance equation when necessary. The phase change effect is considered during the isothermal process, while the overburden effect is also taken into the consideration for the ice segregation process. The model is implemented in MATLAB using the Galerkin finite element method and the finite difference method. Although the numerical oscillation is not obvious in the current study, it's noted that a stabilized finite element scheme [20] will be incorporated in solving the energy balance equation, to avoid the numerical oscillation for potential heat convection dominated scenarios.

Numerical investigation on the frost heave and thaw settlement of pavement on Ingraham Trail, Yellowknife, NWT has been carried out, in response to climate change trends and hypothetical engineering interventions. Each November from 2013 to 2020 was simulated with assumed soil parameters and conditions, while the upper-temperature boundary conditions are specified with the mean daily air temperature data. The settlements were also projected for November from 2020 to 2050 with the anticipated impacts of climate change. Another simulation was performed for pavements on Ingraham Trail with potential insulation materials to provide heat resistance, an emerging technique to mitigate thaw settlement for pavements built in permafrost areas. The following are conclusions and recommendations based on the numerical investigations:

1. With multiple freeze–thaw cycles for the same season in eight years from 2013 to 2020 that are simulated, the settlement of the pavement structure is affected by climate change in recent years. The main reason is the freeze–thaw and permafrost degradation caused by global warming. The temperature in the same season does not remain stable from year to year which causes the varied frost heaves.
2. With the adjustment of increased temperature and lowered water table as the consequences of climate change, frost heave and thaw settlement in November from 2020 to 2050 were projected. The cumulative settlements were also computed with the base year 2020, which demonstrates the impact of climate

change in terms of global warming and water table increase on the increased thaw settlements of the pavement.

3. The effect of the potential remedy solution using insulation materials is investigated for each November from 2013 to 2020, and the simulated frost heaves were compared with those without intervention. A significant decrease in frost heave3.s can be seen in the scenario with insulation materials. This implies the necessity of implementing some protections to mitigate permafrost degradation impacts.
4. As the pavement structure is unknown due to the lack of borehole logs, a geotechnical investigation is recommended in order to develop a more representative finite element model.
5. The soil parameters of the local soils under freeze–thaw cycles should be investigated by conducting laboratory tests for better understanding the impact of climate change on frost heave and thaw settlement via finite element simulations.

Acknowledgements Support of Natural Science and Engineering Research Council (NSERC) and Titan Environmental Containment Ltd. is greatly appreciated.

References

1. AASHTO (1993) AASHTO guide for design of pavement structure. Washinton, DC
2. Anisimov OA, Fitzharris B, Hagan JO, Jeffries R, Marchant H, Nelson FE, Prowse T, Vaughan DG (2001) Polar regions (arctic and antarctic). Climate change 2001: impacts, adaptation, and vulnerability: contribution of working group ii of the intergovernmental panel on climate change, 801–841
3. Cheng G, Wu T (2007). Responses of permafrost to climate change and their environmental significance, Qinghai-Tibet Plateau. J Geophys Res Earth Surf 112(2). Blackwell Publishing Ltd. https://doi.org/10.1029/2006JF000631
4. Doré G, Zubeck H (2009) Cold regions pavement engineering. American Society of Civil Engineers
5. Gardner W (1958) Some steady-state solutions of the unsaturated moisture flow equation with application to evaporation from a water table. Soil Sci 85(4):228–232
6. Government of Canada (2020) Daily Data. https://climate.weather.gc.ca/climate_data/daily_data_e.html?StationID=51058
7. Government of Northwest Territories (2014) 13. Permafrost | Environment and Natural Resources. https://www.enr.gov.nt.ca/en/state-environment/13-permafrost. Accessed 28 October 2020
8. Guymon GL, Berg RL, Hromadka TV (1993) Mathematical model of frost heave and thaw settlement in pavements. Hanover, NH
9. Hildebrand EE (1985) Prediction of thaw settlement and surface roughness for highways in permafrost areas. University of Waterloo
10. Jin H, He R, Cheng G, Wu Q, Wang S, Lü L, Chang X (2009) Changes in frozen ground in the source area of the yellow river on the qinghai-tibet plateau, China, and their eco-environmental impacts. Environ ResLett 4(4). Institute of Physics Publishing. https://doi.org/10.1088/1748-9326/4/4/045206
11. Jin XY, Jin HJ, Iwahana G, Marchenko SS, Luo DL, Li XY, Liang SH (2020) Impacts of climate-induced permafrost degradation on vegetation: a review. National Climate Center

12. Li X, Jin R, Pan X, Zhang T, Guo J (2012) Changes in the near-surface soil freeze-thaw cycle on the Qinghai-Tibetan Plateau. Int J Appl Earth Observ Geoinf 17(1): 33–42. Elsevier B.V. https://doi.org/10.1016/j.jag.2011.12.002
13. Liu MC (2020). Evaluating thermal regime of cold region roads for climate change adaptation. UWSpace
14. Muller SW (1948) Permafrost; or, permanently frozen ground and related engineering problems. Ann Arbor, J.W. Edwards
15. Nelson FE, Anisimov OA, Shiklomanov NI (2001) Subsidence risk from thawing permafrost. Nature 410(6831): 889–890. Nature Publishing Group. https://doi.org/10.1038/35073746
16. Tighe SL, Cowe Falls L, Haas R, MacLeod D (2006) Climate impacts and adaptations on roads in Northern Canada. Transportation research board 85th annual meeting. Transportation Research Board, Washington, DC
17. Tighe SL, Smith J, Mills B, Andrey J (2008) Evaluating climate change impact on low-volume roads in southern Canada. Transport Res Record: J Transport Res Board 2053(1): 9–16. SAGE Publications Sage CA: Los Angeles, CA. https://doi.org/10.3141/2053-02
18. Tong C, Wu Q (1996) The effect of climate warming on the Qinghai-Tibet Highway, China. Cold Regions Sci Technol 24(1): 101–106. Elsevier. https://doi.org/10.1016/0165-232X(95)00012-Z
19. Walvoord MA, Kurylyk BL (2016) Hydrologic impacts of thawing permafrost-a review. Vadose Zone J 15(6): vzj2016.01.0010. Wiley. https://doi.org/10.2136/vzj2016.01.0010
20. Yin S, Dusseault MB, Rothenburg L (2009) Thermal reservoir modeling in petroleum geomechanics. Int J Numer Anal Methods Geomech 33(4): 449–485. John Wiley & Sons, Ltd. https://doi.org/10.1002/nag.723

What Modular and Offsite Construction Contract Administration Can Learn from Court Dispute Cases

E. Chan, S. Han, and M. Nik-Bakht

1 Introduction

The construction projects are increasingly complex, and the disputes it generates are also increased [15]. Arcadis [2] reported that the number of disputes in North America, the UK, Europe, and the Middle East had shown no sign of reduction over the past five consecutive years. However, the time required to resolve the disputes, and subsequently, the project delays, have had an increasing trend. Along with advancements in technology and complexity in design and construction processes, construction contracts become more complicated. Construction disputes can occur for various uncertainties and risks. Besides, the adaptation of modular and offsite construction (MOC) has risen worldwide [11]. However, there are yet no standard contracts for MOC (at least in Canada), so MOC projects usually adopt the standard contracts structured for conventional and on-site construction (COC) and modify them to suit project requirements. As such, higher potentials exist for contractual disputes in MOC projects. Previous efforts in the area of contractual disputes have mainly focused on the COC, which has different features from MOC even though construction activities are the same as standard code and material [18].

To provide effective preventive mechanisms to eliminate the contractual disputes in MOC projects, first and foremost, a proper understanding of the risks and underlying causes in construction contracts is needed. This study has set three objectives: *(i)* to develop a literature-based analysis framework with contract sources of ambiguity; *(ii)* to evaluate the causes of disputes by analyzing the selected Canadian Superior court cases; and *(iii)* to analyze the relevant terms from Canadian standard contracts that can address the significant causes of dispute resulted from the case analysis.

E. Chan (✉) · S. Han · M. Nik-Bakht
Concordia University, Montreal, QC 3G 1M8, Canada
e-mail: ei_chan@live.concordia.ca

S. Walbridge et al. (eds.), *Proceedings of the Canadian Society of Civil Engineering Annual Conference 2021*, Lecture Notes in Civil Engineering 240,
https://doi.org/10.1007/978-981-19-0507-0_12

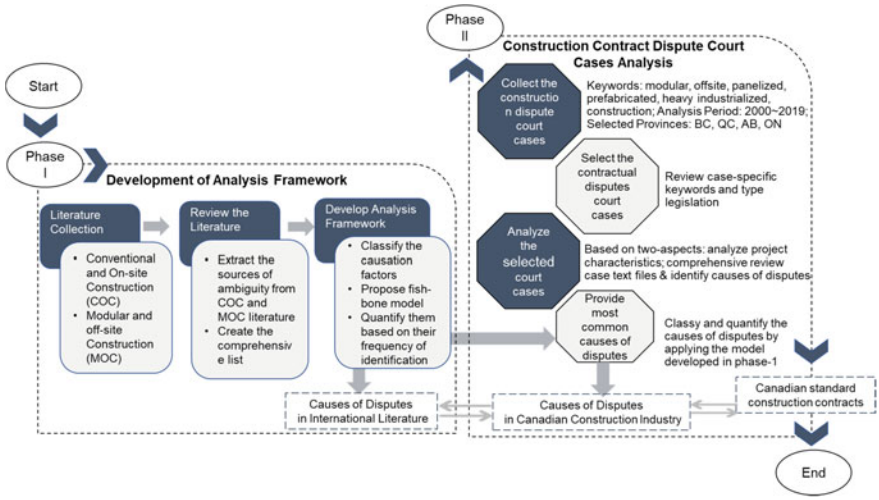

Fig. 1 The flow of research methodology

2 Literature Review

Increased competitiveness and complexity in the construction industry tend to create more claims and disputes among contracting parties. In order to reduce the construction claims and disputes, it is essential to enhance the understanding of contracting parties on the core reasons or problematic areas in the contract documents. Several researchers have attempted to identify the common causes of disputes from different perspectives. Many researchers, such as [5, 14, 16, 19], and Odeh and Battaineh [17] conducted questionnaire surveys with construction professionals to identify the common causes of disputes in the industry. Cakmak and Cakmak [8] defined the causes of conflicts and disputes from the responsible parties' perspective through literature analysis. Moreover, some researchers [1, 12] among others) identified the causes of construction litigation through the literature analysis. However, previous studies have either taken a niche perspective in evaluating specific disputes or have discussed the sources of contractual confusions qualitatively and subjectively. There is not enough information that identifies the causes of disputes and litigation claims, particularly for MOC projects. This study proposed a framework to evaluate the causes of disputes systematically for both construction methods to address these gaps.

3 Research Methodology

The high-level methodology of this study and the steps are presented in Fig. 1, which mainly comprises two phases. In phase 1, the qualitative approach is applied to extract the sources of contractual disputes documented in the literature for both conventional and on-site Construction (COC) and modular and offsite Construction (MOC) methods. These extracted sources are used to develop an analysis framework that can be classified and quantified. A previously developed conceptual framework was structured as a four-level hierarchy: categories, subcategories, classes, and subclasses [3]. We started with the same structure. The sources of ambiguities from literature are clustered according to the similarity and relevance. This proposed model allows us to quantify the weighted percent based on the overall frequency of indication that provides the level of importance for clustered sources.

In phase 2, construction court cases during the past twenty years at the level of Superior Courts of four selected Canadian provinces, i.e., Quebec, Alberta, Ontario, and British Columbia, are gathered from the Canadian legal information institute [7] through searching keywords. The collected cases are scanned manually (i.e., by reviewing the case-specific set of keywords and legislation types) to filter contractual dispute cases. Then, selected cases are analyzed in two aspects: project characteristics for a better understanding of the case and comprehensive analysis to extract causes of dispute. The proposed analysis framework from phase 1 was applied to the collected data, to classify and quantify the causes of dispute. The results are discussed and compared to identify commonalities and differences between the literature-based and court case analysis. Also, relationships were extracted between the causes and clauses from general conditions of Canadian standard contracts that can address those causes.

3.1 Literature Survey and Development of Analysis Framework

The relevant articles are primarily collected using the keywords search from the sources: google scholar, Concordia library, and research gate. The search-words used are conventional construction, on-site construction, stick-built, modular construction, prefabricated construction, panelized construction, industrialized building system (IBS), and heavy industrialized construction. This study aims to identify contract sources of ambiguity and disputes; thus, construction contracts, construction disputes, contract claims, contract ambiguity, contract administration, and management are added as search-words. A total of 105 articles are selected, which comprise 57 COC articles and 48 MOC articles. The selected articles are published in different journals, proceedings, periodic articles, web pages, and dissertations during the past 34 years. A rising number of articles, particularly MOC literature, can be seen during

the past ten years. The selected articles are published in various sources such as journals, conference proceedings, review reports, thesis papers, books, periodic articles, and websites.

The selected articles are then reviewed to extract contract sources of ambiguity. A total of 396 sources of ambiguities are extracted by reviewing the selected literature (i.e., 57 COC articles and 48 MOC articles). These extracted sources are taken as the subclasses, which is the lowest level of the proposed analysis framework. The clustering procedure begins by classifying the subclasses into relevant classes based on the similarity. These classified classes are then assigned to the subcategories underneath five major categories. A new subcategory is added if the existing subcategories are not enough to represent for classes. Quantitative analysis is performed and re-assigned those that did not have enough support into another relevant subcategory. The clustering process was done within several rounds, and Fig. 2 presents the finalized model.

As a result, the proposed fishbone model consists of fifteen subcategories with two to seven classes underneath. In Fig. 6, the categories that are the top-five level of the model (single-digit), subcategories that are subsidiaries of each category (double-digit), and classes that are clustered under each subcategory (triple-digit) are introduced. The issues related to the linguistic form of a construction contract are clustered in the 'Language' category, the 'Contract' category includes the contract form and content related issues, and design-related confusions, project stakeholders as a source of confusion, and effects of external factors are clustered under the 'Design', 'Stakeholders',' External Factors' categories respectively. A detailed explanation of each category, subcategory, class, and subclass is introduced elsewhere. Once the proposed classified fishbone model is finalized, quantify them to provide the level

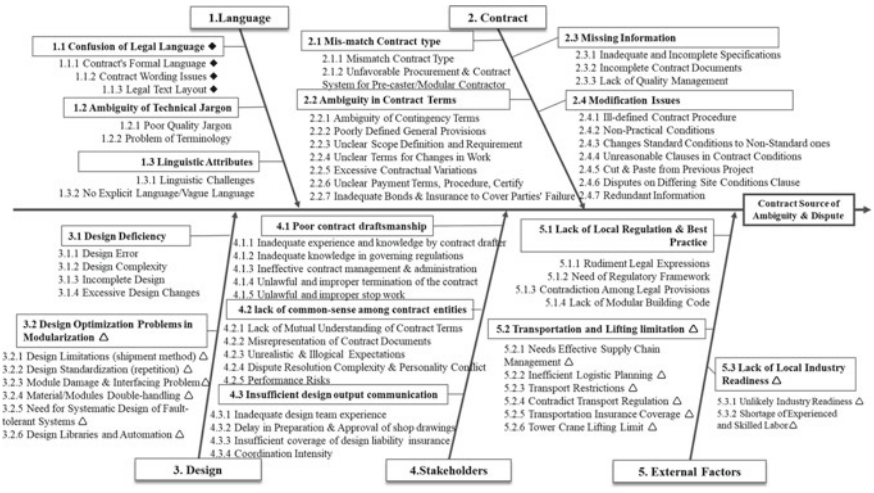

Fig. 2 Proposed literature-based analysis framework (Fishbone Model) (subcategories and classes identified in ◆ COC literature only and △ MOC literature only)

of importance of each subcategory. The weighted percentage of each subcategory is computed with Eq. 1 based on the overall total frequency of sources of ambiguities (i.e., 243 sources of ambiguities from COC literature and 153 sources of ambiguities MOC literature). Each subcategory's support level (weight) is the ratio between each subcategory frequency, and the overall total frequency of sources of ambiguity is expressed as a percentage.

$$\text{support level(weight)}\% = \frac{\text{the sum of frequency at each subcategory}}{\text{Overall total frequency}} \times 100 \quad (1)$$

The quantified model with support level (weight) % at subcategories and categories can be seen in Fig. 3.

The literature-based model (Fig. 3) shows that 'ambiguity in contract terms' subcategory is the most critical issue for COC projects with 31%. In contrast, the lack of local industry readiness subcategory is a major issue for MOC projects with 25%. Poor contract draftsmanship of the 'Stakeholders' category is relatively critical for both COC and MOC, with 16% and 9%, respectively. Not all subcategories and classes are identified as sources of ambiguity in both COC and MOC literature. Some subcategories: transportation and lifting limitation, lack of local industry readiness, and design optimization problems are found as issues only in MOC literature. Similarly, 'confusion of legal language' subcategory is only found in COC literature.

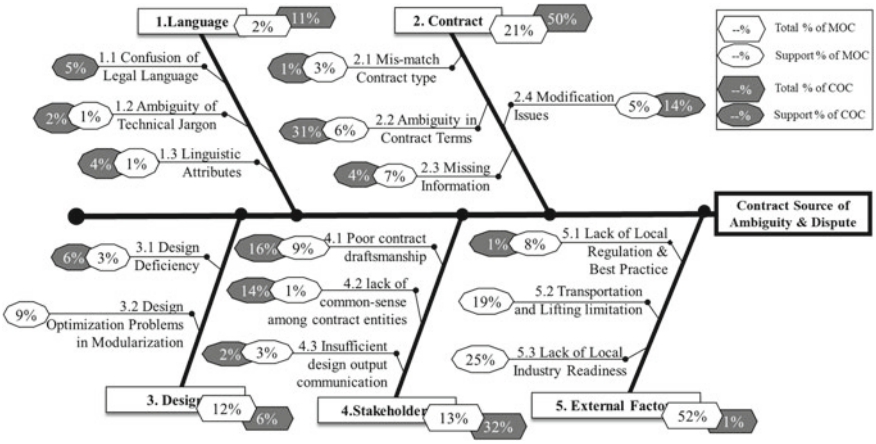

Fig. 3 Literature-based proposed fishbone model with support %

3.2 Construction Contract Dispute Court Cases Analysis

In phase two, we analyze the construction dispute court cases to evaluate the impact of each of the sources of ambiguity and disputes in action. The proposed analysis framework from phase 1 (i.e., fishbone model) will be applied to evaluate each source's contribution level in court case analysis. In this respect, it is worth noting the structure of the Canadian judicial system. The Canadian judicial system is structured with a four-level hierarchy according to legal authority. Provincial and Territorial (lower) courts are the starting point for most cases that come into the system. Then, Provincial and Territorial Superior Courts are the backbone of the Canadian judicial system. More severe cases and appeals from lower court decisions will be heard—the Provincial and Territorial Court of Appeal that will hear the appeal from Superior Court decisions. Finally, the Supreme Court of Canada (SCC), the highest level and final court of appeal in the Canadian Judicial system, will hear the appeal from the court of appeal decisions. In this study, we focus the cases at the Provincial and Territorial Superior Courts for a broader number of COC and MOC cases.

3.3 Collection and Selection of Relevant Court Cases

The electronic version of court cases from all Canadian courts is accessible from the Canadian Legal Information Institute [7]. We first used the keywords to retrieve the construction-related court cases and then set the analysis period for twenty years (from 2000 to 2019). The search words used to retrieve the construction-related cases are construction, modular, offsite, panelized, prefabricated, and heavy industrial. The resource page allows us to retrieve the documents/cases that include the search words—a total of 6,152 cases from thirteen provinces. We narrow down to cases at four provinces: British Columbia (BC), Ontario (ON), Alberta (AB), and Quebec (QC). Build ForceCanada [6] forecasted that the construction industry in these four provinces continues to have significant growth in the near future. Besides, BC, ON, and AB provinces have the most significant number of cases. A total of 4708 court cases, 2266 cases in BC, 1335 cases in ON, 925 cases in AB, and 182 cases in QC based on MOC and COC's consideration. The next step is to eliminate the non-contractual dispute cases by scanning case-specific keywords and legislation references. Some example sets of keywords used to eliminate the cases are: 'software, data, copyright, hospitals, evidence', 'children, spousal support, income, friends, horse,'. Examples of legislation references used to eliminate the cases are 'Divorce Act,' 'Criminal Code,' 'Bankruptcy and Insolvency Act,' 'Family Relations Act'. As a result, one hundred and seventy-eight contractual dispute court cases from four provinces (i.e., BC: 40 cases, ON 108 cases, AB:15 cases, and QC: 15 cases) are selected for further analysis.

3.4 Analysis of Selected Superior Court Cases

The selected court cases are analyzed, and this section describes the results. These selected cases include various projects from new construction such as commercial buildings, residential buildings, healthcare services, heavy construction projects such as bridges, highway construction projects, and renovation and rectification projects. By reviewing the case text files, we found that twenty cases are the MOC projects, and the remaining one hundred and fifty-eight (158) cases are COC projects and their sub-trades. The plaintiff and defendant's typology was analyzed to find out which party is more likely to initiate the litigation filing, and the results are shown in Table 1.

The study found that the General Contractor (GC) is the major initiator, filing for litigation against the client, regardless of the construction type (i.e., COC or MOC). Subcontractor as plaintiff has the second-highest number of cases against general contractor (GC) as defendant among COC cases. For MOC cases, the subcontractor as plaintiff and the client as the defendant has the second-highest number of cases. The third-highest number of cases found the client as plaintiff and general contractor as the defendant for both MOC and COC cases. As a continuous effort to analyze the project information: types of contracts and forms of agreement are used to formalize the contractual relationships. Figures 4a, b illustrate the distribution of types of contracts and forms of agreement used by the selected cases. The stipulated price contract has the highest rank among the selected court cases, followed by unit price contracts and cost-plus fees contracts. There is no MOC project with a standard contract, while 25 COC cases with standard contracts seek judgment at the court. Both MOC and COC Projects with non-standard written contracts have the highest numbers of litigious disputes during the past twenty years.

In the next step, we analyzed the selected cases to extract the causes of disputes and identify commonalities and differences between international literature-based causes and those in the Canadian construction industry. The proposed analysis framework developed in phase 1 was used to evaluate, classify, and quantify these causes. Forty-three (43) causes of disputes are identified from the twenty (20) MOC cases, and four-hundred-sixty-three causes (463) of disputes are found from one-hundred fifty-eight (158) COC cases (refer to Table 2). The causes from these cases are classified into the relevant classes of the proposed analysis framework. The weighted percentage of each subcategory will be calculated with Eq. 1 from phase 1. The sum-frequency of each subcategory from MOC cases is divided by the total identified frequency in MOC cases (i.e., 43 refer to Table 2). The same scenario is complied for the weighted percentage calculation of COC cases.

Figure 5 presents the support level of subcategories and categories based on their frequency. Based on the case analysis, 'ambiguity in contract terms' is a major concern for the Canadian construction industry, with more than 70% of the total frequency. This, interestingly, applies to both MOC and COC projects. 'Poor contract draftsmanship' is another relatively critical issue found among the court cases, accounting for 18% of total MOC frequency and 12% of total COC frequency.

Table 1 Typology of involved trial parties in selected court cases

X	No. of MOC cases				X	No. of COC cases				
	Defendant									
Plaintiff	GC	Client	Subcon	Consultant	Insurance	GC + Consultant	Client + Consultant	Sub-Subcon	GC + Insurance	GC + Client
GC		72	5	1	3		1			
		6	1							
Subcon	27	8			1			2		5
	2	5							1	
Client	15			8		2			2	
	4		1							
Consultant		5								
Sub-Subcon			1							

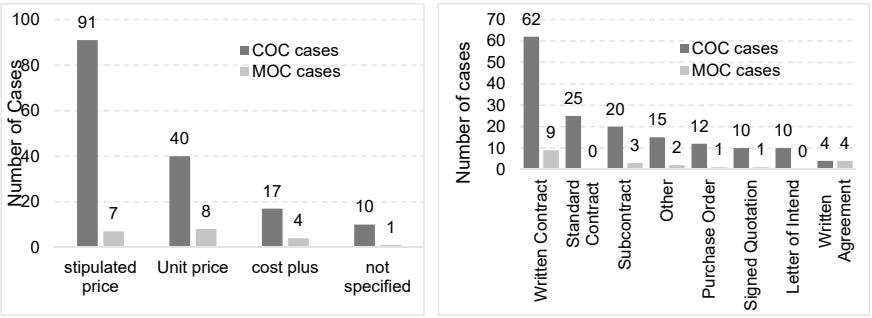

(a) Type of Contract types used by selected cases (b) Forms of Agreements used by selected cases

Fig. 4 Contractual typology between parties involved in selected court cases

The third-ranked subcategory is the 'lack of common-sense among contract entities accounting' with 7% of total MOC frequency and 6.8% of total COC frequency. Other subcategories which only found among COC project cases are 'missing information' (2%) and 'modification issues' (3%) of contract formation and contents, 'design deficiency', 'insufficient design output communication', and 'confusion of legal language' with 0.4% each. 'Transportation and lifting limitations' are cited only in MOC projects with 2% of the total.

A comparison between the case-based (bottom-up) and literature-based (top-down) analyses helps to find out their commonality and differences based on the method of construction (i.e., COC and MOC). Not all literature-identified sources are found in causes of litigation. Focusing on the top-most three ranks of COC (see Fig. 6) shows a similar trend (i.e., rank) in the level of importance of subcategories between literature and case-based ranking. However, discrepancies are found in the comparison between MOCs (see Fig. 7). Unlike the MOC literature, ambiguities related to external factors such as 'lack of local industry readiness', 'transportation and lifting limitation' could not be spotted in MOC court cases in Canada. The MOC's case analysis results showed that, just like the COC cases, 'ambiguity in contract terms' is the most critical issue in the Canadian construction industry. At the classes level (see Table 2), 'unclear payment terms' is a major issue for MOC cases, while the 'unclear terms for changes in contract' is a major concern for COC cases. After all, this comparison shows that MOC projects in the Canadian construction industry call for improvement of clarity in contract terms, knowledge enforcement for better contract management and administration practice.

3.5 Discussion

Based on the analysis outputs (Fig. 4a, b), stipulated price contracts and modified non-standard written contracts are the most common modes of agreement in both MOC

Table 2 Causes of litigation claim from selected court cases

Classes from proposed analysis framework	Causes of litigation claims	Frequency	
		MOC	COC
2.2.6 Unclear payment terms, procedure, certify	Unpaid payments (final payments, progress payments, holdback/withhold)	14	129
2.2.4 Unclear terms for changes in work	Unpaid extras/changes, defective costs, delay claims, back charge, reimburse installment, claim for overpaid	12	168
2.2.2 Poorly defined general provisions	Dispute in contract terms, ambiguous terms, vague and uncertain contract terms	4	32
2.2.7 Inadequate bonds & insurance to cover parties' failure	Insurance coverage	1	17
4.1.4 Unlawful and improper termination of the contract	Termination performance	4	25
4.2.5 Performance risks	Negligent performance	3	24
4.1.3 Ineffective contract management & administration	Poor contract management & administration, communication issues	4	16
5.2.1 Need to develop effective supply chain management	Delay in delivery	1	0
4.1.5 Unlawful and improper stop work	Stop Work/Suspension	0	11
2.3.2 Incomplete contract documents	Missing information in contract document	0	10
4.1.2 Inadequate knowledge in governing regulations	Knowledge in applicable law, improper inspection	0	6
2.4.4 Unreasonable clauses in contract conditions	Contract modification issues	0	4
2.4.7 Redundant information	Conflict/Contradict Terms	0	4
4.2.2 Misrepresentation of contract documents	Misinterpretation of contract terms	0	4
2.4.3 Changes to standard contract conditions & add non-standard conditions	Amended the standard conditions	0	3
1.1.2 Contract wording issues	Wording issue	0	2
4.2.1 Lack of mutual understanding of contract terms	Lack of mutual understanding, lack of common-sense	0	3
4.3.1 Inadequate design team experience	Breach of rules of the art	0	2
3.1.1 Design error	Design defect	0	1
3.1.3 Incomplete design	Vague and incomplete design drawings	0	1
4.2.3 Unrealistic & illogical expectations	Unrealistic expectations	0	1
	Total Frequency	43	463

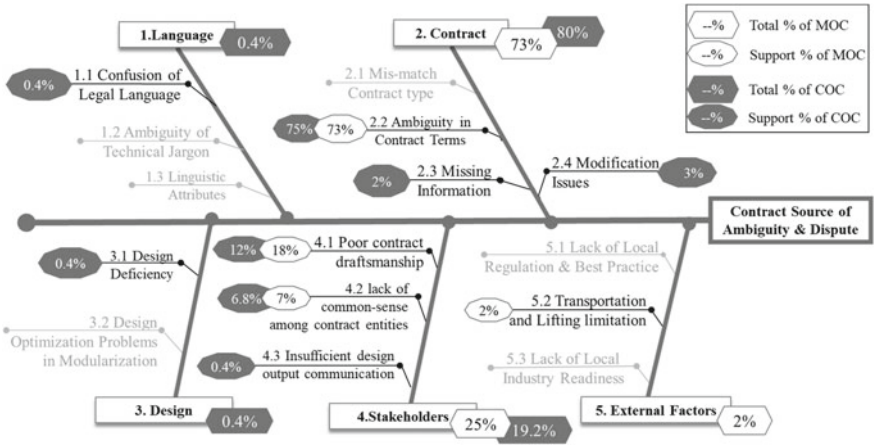

Fig. 5 Case-based proposed fishbone diagram with support %

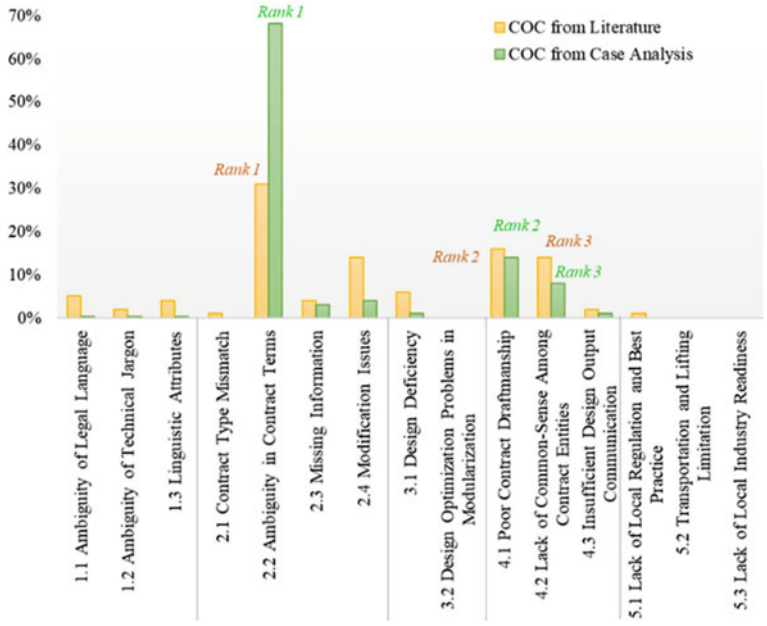

Fig. 6 Comparison of COC's literature and court cases analyses

and COC project cases. Therefore, we then focused on evaluating the general conditions of standard lump-sum contracts. CCDC 2 stipulated price contract is the most popular and commonly used standard contract in the Canadian construction industry [10]. CCDC 14 design-built stipulated price contract, on the other hand, is the most suitable one for MOC [4, 18]. These contracts have twelve general conditions that

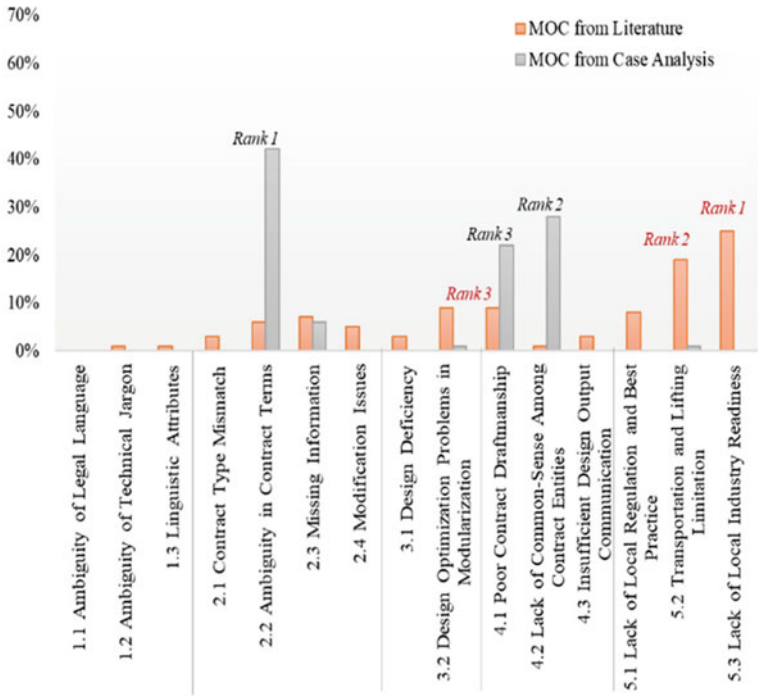

Fig. 7 Comparison of MOC's literature and court cases analyses

support developing construction contract documents depending on project requirements. Therefore, trial parties (i.e., clients and general contractors) often review contract documents carefully to enhance their justification when claims and disputes arise.

In accordance with the number of Canadian court cases in MOC projects, 'payment issues' (i.e., progress payment, final payment, withhold) are the primary concerns. Causes of progress payment disputes include disputes in the certified progress payment amount, late payments, withhold payments resulting from conflicts and disputes in quantity take-off methods. Causes of final payment disputes are rejection or withhold/unpaid of the final contract amount. Addressable general condition articles from CCDC 2 and CCDC 14 are the '5.2 Applications for Progress Payment' and '5.3 Progress Payment' that describe the progress payment timeline for project participants following the dates of submission for the payment claims. Similarly, the remaining conditions from 5.4 to 5.9 in CCDC 2 and CCDC 14 can be used to resolve the final payment disputes. Although the standard contracts can eliminate payment timeline issues, some payment-related terms from standard contracts require modifying to suit the MOC method. For example, the general condition 5.2.3 in CCDC 14, described below, only allows the design-builder (i.e., general contractor/modular

company) to claim the project costs when the contracted works are performed, and products are delivered at the *place of the works* (final destination/construction site).

> 5.2.3 The amount claimed shall be for the value, proportionate to the amount of the Contract, of the Design Services and of the Work performed and Products delivered to the Place of the Work as of the last day of the payment period. [9]

This payment definition is only suitable for the COC method. The completed works are measured and certified based on the on-site completion inspection but not applicable for the MOC method. In MOC, most of the construction works (up to 85–90%) are completed in the manufacturing factory, and the remaining works (e.g., transportation and installation) are done on-site [13]. One more feasible study is required to investigate 'Products' to establish a progress payment timeline for MOC projects. According to the general condition 5.2.8, the design-builder can claim proportionately to the products delivered on-site.

> 5.2.8 Applications for payment for Products delivered to the Place of the Work but not yet incorporated into the Work shall be supported by such evidence as the Payment Certifier may reasonably require to establish the value and delivery of the Products. [9]

In other words, the modular construction company can claim the project costs once the modules are fabricated and before transporting them to the site (i.e., prior to incorporating them into the place of work). However, the definition of 'Products' might not be interpreted as modules among the contractual parties since the standard contracts express it as material, machinery, equipment, and fixtures incorporated into the work. The unfavorable terms that do not allow to claim uninstalled create a financial burden for modular contractors/ Design-Builder. Therefore, a contract for the MOC project may need to add contract terms that allow claiming for modules or components yet to deliver to the place of the work and delivered but not yet incorporated into the work. Simultaneously, extend the insurance coverage for the modules or components during transportation or stored elsewhere (i.e., not at the site and not at the factory). In that way, the modular manufacturer can reduce the financial burden, and the client can reduce the potential risks. Moreover, modular builders and clients often dispute the completed project quality and defect issues that caused final payment rejection or withheld the contract balance amount. This study has some limitations, such as insufficient number of MOC court cases and the scale of the project to be analyzed in the selected provinces. Therefore, wider coverage of MOC court cases for more rounded analysis framework for MOC projects is recommended.

4 Conclusion

Modular construction has gained attention recently around the globe. Hard and hassle for broader adaptation of MOC in the construction industry have been spotlight; however, fewer studies in identifying the causes of disputes in MOC projects and court case analysis have been found. Accordingly, this study intends to provide

the analysis framework that comprises a comprehensive list of causes of disputes in both MOC and COC projects through literature and court case analysis. The proposed analysis framework was applied to evaluate the causes of litigious claims from Canadian court cases. The comparison result showed that ambiguous contract terms and stakeholders-related confusions are the common causation of litigious claims in the Canadian construction industry during the past twenty years. Payment issues are the greatest concern for MOC contractors. Therefore, revised payment terms were suggested as a primary step for forming the standard contract required for MOC and resolving that issues. This study contributes to construction insiders recognizing common causes of contractual disputes in MOC projects from literature and real court cases. This will assist in taking preventative actions proactively to the potential contractual losses and court cases.

References

1. Almutairi S (2015) Causes of litigation in the Saudi Arabian construction industry. Arizona State University, Master of Science
2. Arcadis (2019) Global construction disputes report 2018: laying the foundation for success, 1–31
3. Azghandi-Roshnavand A (2019) Evaluation of construction contract documents to be applied in modular construction focusing ambiguities; A text processing approach. Master of Applied Science, Building, Civil and Environmental Engineering, Concordia University
4. Azghandi-Roshnavand A, Nik-Bakht M, Han SH (2019) Towards automated analysis of ambiguity in modular construction contract documents (A Qualitative & Quantitative Study). Advances in informatics and computing in civil and construction engineering. Springer, Cham, pp 343–350
5. Baloyi M, Agumba JN (2014) Causes of disputes in construction projects in South Africa: a case of Gauteng Province. In: Proceedings 8th Construction Industry Development Board (CIDB) Postgraduate Conference, Johannesburg, South Africa, 179–187
6. Build Force Canada (2020) Construction & maintenance looking forward- national summary. Build Force Canada. Accessed 26 June
7. CanLII (2020) Canadian legal information institute. https://www.canlii.org/en/
8. Cakmak E, Cakmak PI (2014) An analysis of causes of disputes in the construction industry using analytical network process. Procedia Soc Behav Sci 109:183–187
9. CCDC14. 2013. Design-Build Stipulated Price Contract. In General Conditions of the Design-Build Stipulated Price Contract. Canadian Construction Documents Committee. 1–32
10. Chehayeb A, Al-Hussein M, Flynn P (2007) An integrated methodology for collecting, classifying, and analyzing Canadian construction court cases. Can J Civ Eng 34(2):177–188
11. Harvey C (2016) Factors that influence the adoption of modular construction in Western Canada. Royal Roads University, Victoria
12. Jagannathan M, Delhi VSK (2020) Litigation in construction contracts: literature review. J Legal Affairs Dispute Resol Eng Constr 12(1):03119001
13. Kamali M, Hewage K (2017) Development of performance criteria for sustainability evaluation of modular versus conventional construction methods. J Clean Prod 142:3592–3606
14. Mahamid I (2016) Micro and macro level of dispute causes in residential building projects: studies of Saudi Arabia. J King Saud Univ Eng Sci 28(1):12–20
15. McLachlin B (2011) Judging the 'Vanishing Trial' in the construction industry. Constr Law Int J 5(2):9–14

16. Mohamed HH, Ibrahim AH, Soliman AA (2014) Reducing construction disputes through effective claims management. Am J Civil Eng Archit 2(6):186–196
17. Odeh AM, Battaineth HT (2002) Causes of construction delay: traditional contracts. Int J Project Manag 20(1):67–73
18. Smith RE (2014) Offsite and modular construction explained. Offsite Construction Implementation Resource, 1–6
19. Zhao X, Hwang B, Phng W (2014) Construction project risk management in Singapore: resources, effectiveness, impact, and understanding. KSCE J Civ Eng 18(1):27–36

Conceptual Drainage Design of an Urban Rail Transit Project

H. Minchau and A. Van Boven

1 Introduction

1.1 Background

The proposed Metro Line Light Rail Transit is an extension of the existing Metro Line, continuing from the Northern Alberta Institute of Technology (NAIT) in Edmonton, Alberta, connecting the northwest end of the city to downtown. This paper focuses on the conceptual stormwater management plan for Phase 2 of the extension, which begins at the north end of the Blatchford neighbourhood with a bridge crossing the Yellowhead Highway and CN Rail Yard, then continues north and then west where the Metro Line will terminate at the Campbell Road Park and Ride. This Phase 2 extension, shown in Fig. 1, is 9.4 km long and will include 7 stations, 1 bridge, 2 transit centres, 1 Operations and Maintenance Facility (OMF), and 2 underpasses.

1.2 Problem Statement

The urban rail transit alignment passes through developed neighbourhoods as well as open fields that have planned neighbourhood developments. The addition of a trackway can change the drainage patterns which could result in increased flow rates, elevated water levels, and changes to water quality [1]. These potential impacts will have to be evaluated to ensure that the sewers have adequate capacity and potential flooding is mitigated. As such, a hydrological specialist is necessary in urban rail

H. Minchau (✉) · A. Van Boven
Stantec Consulting Ltd., Edmonton, AB T5J 0K4, Canada
e-mail: hannah.minchau@stantec.com

S. Walbridge et al. (eds.), *Proceedings of the Canadian Society of Civil Engineering Annual Conference 2021*, Lecture Notes in Civil Engineering 240,
https://doi.org/10.1007/978-981-19-0507-0_13

Fig. 1 Proposed metro line LRT extension phasing plan and station locations [3]

designs to both protect rail systems from flooding and ensure that new railways will not adversely affect the stormwater management system [8].

2 Approach to Urban Rail Stormwater Management

Stormwater management is required along the trackway to meet the local municipal standards and provincial standards. For the Metro Line LRT, the approach to stormwater management was developed to meet the City of Edmonton LRT Design Guidelines, the City of Edmonton Design and Construction Standards, the latest storm IDF curves from EPCOR, and Alberta Environment's Stormwater Management Guidelines. The objectives of stormwater management as outlined in the guidelines/standards are:

- to provide runoff quantity and quality improvement to meet environmental objectives,
- to maintain the existing level-of-service for major and minor storm systems,
- to mitigate the impacts of runoff on LRT operations,
- to relocate conflicting infrastructure out of the LRT right-of-way (ROW).

The stormwater management system for the trackway has been designed such that existing issues are not worsened and, in some cases, are improved. The design approach to meet these stormwater management objectives is outlined as follows:

- Water Quality Improvement Measures—Grit management and contaminant removal are addressed by promoting sedimentation and filtration using LID features and catch basins.
- Peak Flow Attenuation—Increased runoff will be mitigated by storing excess runoff and controlling release rates.
- Flooding Control—Flooding will be mitigated through LRT trackway/road grading, storage, and conveyance.
- Relocation and Abandonment of Existing Sewers—Sewers within the trackway and/or station footprints will be abandoned and relocated with the existing level of service to mitigate any adverse impacts to the stability of the trackway.

Stormwater from the trackway needs to be managed to ensure the existing sewer systems can handle the changes. Edmonton's overall drainage system uses the major/minor system concept for managing stormwater. The minor system refers to the sewer catch basins and underground pipes, where the capacity is designed for the more frequent 1:5-year rainfall events. The major system refers to stormwater in excess of the minor system that ponds on the surface and flows overland, generally for rainfall events up to the 1:100-year. The track right of way (ROW) has its own level of service design requirements depending on the type of track that is proposed. In some instances, the track ROW level of service exceeds the existing drainage system and stormwater management will be required. The level of service design criteria summarized below is taken from the [7] LRT Design Guidelines, City of Edmonton Design and Construction Standards Volume 3 Drainage [6], and recommendations from the drainage team based on previous experience:

- Minor System
  - Design to a 1:5-year rainfall event (outside of the track ROW)
  - Design to a 1:5-year rainfall event within the ROW for direct fixation and embedded track
  - Design to a 1:25-year rainfall event within the ROW for ballasted track
- Major System
  - Evaluate the drainage facility requirements up to the 1:100-year rainfall event
- Trackway Drainage

- Trackway underpasses are to be designed for a peak run-off from a 1:100-year rainfall event
- Trackway bridges/elevated guideways are to be designed for a peak run-off from a 1:100-year rainfall event

There are additional best management practices that can reduce the impact of hydrological hazards on urban rail system infrastructure and mitigate the effects of rail urbanization on stormwater quantity and quality. For example, the Urban Rail Development Handbook recognizes that it is difficult to adapt stormwater infrastructure during a project's design life and precautionary designs should model the design exceedance flood to evaluate inundation in tunnel passes [8]. Ultimately, each urban rail system has its own unique hydraulic requirements, climate conditions and construction limitations, which require effective and intelligent urban rail drainage system solutions.

3 Existing Drainage Infrastructure

The section of the city that the proposed rail alignment runs through is serviced by a mix of separated sewers (where water flows in separated storm and sanitary pipes) as well as older developments serviced by a combined sewer area (where storm and sanitary flows are carried within the same pipe). Drainage basins along the proposed rail alignment were delineated and analyzed for the connecting sewer system so that the existing capacity of the sewers could be determined and maintained.

Storm, sanitary and combined sewers within the proposed track right-of-way alignment are required to be relocated and properly abandoned, unless they are crossing the alignment or are deep enough that they will not pose problems with construction and operation of the LRT (governed by the local standards). Sewer infrastructure that needs to be abandoned will be replaced to maintain the existing level of service, that is, relocated sewer infrastructure will be replaced with the same size and carrying capacity.

For this project, many sewers were identified for relocation. However, a few sewers were evaluated based on depth, sewer diameter, relocation complexity, and approved for guideline exemptions provided the sewer would not adversely affect the trackway and LRT operation.

4 Proposed Drainage System

Mitigation is required where the proposed level of service for the trackway is greater than what the existing sewer system can handle, or where runoff generation has increased due to changes on the ground surface.

4.1 Increase in Runoff and Storage Requirements

Drainage catchment areas were delineated for the pre- and post-development conditions. These catchment areas were compared and the change in impervious area was calculated. If a catchment area increased in impervious area, usually from paved road widening and adding a concrete trackway, then the runoff generation would be greater. Essentially, if the trackway was constructed within the existing roadway, then there would be no increase in runoff and no storage required. If the trackway was constructed in grass/field area, there would be an increase in runoff and would require mitigation. Storage is required for this increase in stormwater runoff.

Stormwater management modelling software was used to perform a hydrologic assessment for each catchment area and the runoff hydrograph was computed for the pre- and post-development conditions for the 1:5-year and 1:100-year design storm events. All flows greater than the 1:5-year pre-development peak runoff require storage for the 1:5-year post-development conditions. For the 1:100-year post-development condition, the minor system can accept all flows up to the 1:5-year pre-development peak rate. All flows above this rate will either go to storage or flow overland to the major system. The storage required for the 1:100-year event was based on equating overland peak flow volumes for the post-development conditions to those of the pre-development conditions. Figures 2 and 3 are general hydrographs that illustrate how the required storage volume was determined for the 1:5-year and 1:100-year events.

Most of the catchments for the Metro Line LRT extension obtained an increase in impervious area. The storage requirement for the 1:100-year event was greater than for the 1:5-year event. Therefore, the 1:100-year event was used resulting in a total

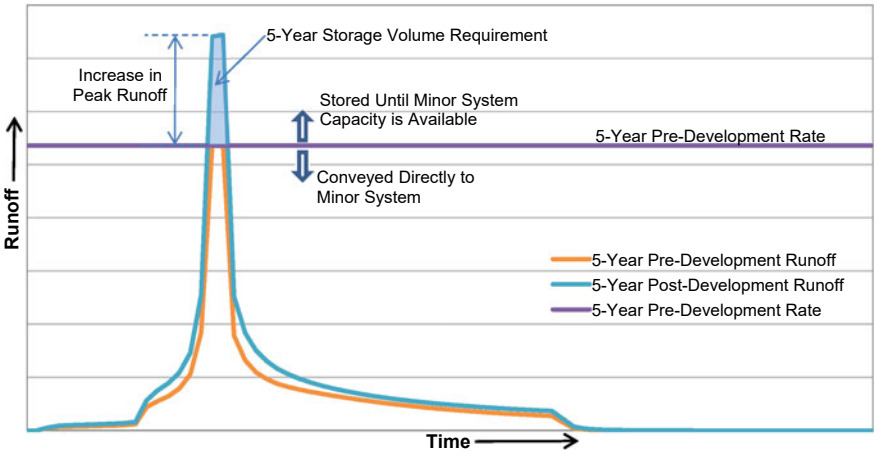

Fig. 2 5-year 4-h peak mitigation storage requirements [3]

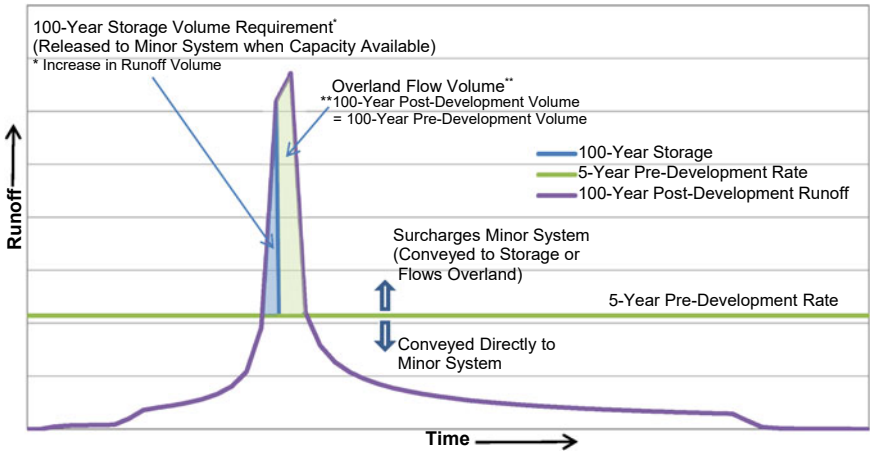

Fig. 3 100-year 4-h peak mitigation storage requirements [3]

of 3,991 m^3 of storage required to mitigate the increased runoff generation due to increased impervious area.

4.2 Surface Ponding and Overland Flow Storage Requirement

The track alignment was analyzed in terms of the larger picture of overland stormwater flow (i.e., the major storm system concept). Flooding or large volume ponding could occur if major storm flow were cut off from existing overland drainage paths due to the addition of the trackway. Additionally, stormwater that terminates at a sag location along the trackway could cause issues with operation and safety of the rail vehicles. If strategic trackway and roadway grading does not work to reduce ponding at the trackway, then storage would be required to bring down ponding/mitigate overland flow paths to acceptable levels set by the local municipality and urban rail standards.

Along the Metro Line LRT extension, no overland flow paths were cut off, however, multiple flow routes terminate in sag locations along the trackway. Based on preliminary investigations into the sag contours, allowable ponding limits were exceeded at some locations. These locations, however, were flagged as existing ponding nodes to be mitigated by a city-wide flood mitigation program that was underway. Therefore, stormwater mitigation, due to surface ponding and overland flow, was not required at this time and was noted to be evaluated again at the next stage of design once many of the city-wide flood mitigation measures would be implemented.

4.3 Ballast Track Buffer Storage Requirement

The underdrain for ballasted track is recommended to be designed for a 1:25-year rainfall event to keep the ballast dry. It is also crucial that the ballast structure maintains the structural integrity to support anticipated rail loads [5]. The City's minor drainage system is generally sized to convey the 1:5-year rainfall event, while stormwater management facilities (SWMFs) are sized to a variety of different rainfall events. Therefore, mitigation is required for all ballast track sections to buffer the peak flows prior to discharging to the minor drainage system or SWMFs.

Of the 9.4 km Metro Line LRT extension, approximately 3.7 km are proposed to be ballast track and would require 1,097 m^3 of buffer storage via storage tanks/pipes, or 3,470 m^3 of buffer storage via SWMFs (different volumes were calculated based on the pre-development level of service for the receiving infrastructure).

4.4 Underpass Storage Requirement

Grade separation options, where the track alignment is proposed to enter an underpass to cross an intersection or other rail lines, were analyzed at four locations, with underpasses approved at 137 Avenue and 127 Street. These locations require additional sewer abandonments and replacements compared to the at-grade scenario due to the depth and configurations of the underpasses.

The local LRT guidelines require stormwater storage to protect the below grade section from flooding for events up to and including the 1:100 year 24-h event. This level of service for underpasses is greater than what the existing drainage system has capacity for, therefore, stormwater storage is required. The elevations of the trench bottom relative to the nearest storm sewers will determine if a lift station is required to release the stored stormwater into the minor system or if a gravity system is achievable.

A total of 4,197 m^3 of stormwater storage was required between the four analyzed underpass locations for the Metro Line LRT extension. Due to the depth of the underpasses and the inability to relocate some of the large diameter sewers, exemptions to the standards were applied here to maintain the sewers in place with reduced clearances. One underpass, however, was not recommended from a drainage perspective due to the required relocation of a very large diameter sanitary trunk (approximately 425 m of 2,920 mm diameter) plus the relocation of the sanitary trunk extension that was currently under construction. Other sewer relocations in this area became quite complex, with interconnections between multiple sewers, and would require a separate study with modelling on the interconnections and determination of the impact on the overall drainage system. The underpass at the CN Rail crossing was not approved at this time. With the elimination of the two underpasses, the required stormwater storage for the two remaining underpasses was 2,723 m^3.

4.5 LRT Bridge/Elevated Guideway Storage Requirement

The bridge was designed for rainfall events up to and including the 1:100-year rainfall to prevent stormwater overtopping the bridge to private property below and to prevent transporting additional stormwater to the connecting neighbourhoods on each end of the bridge.

The proposed bridge for the Metro Line LRT extension contained a high point near north third of the bridge, so stormwater was to be collected at each end of the bridge. The north end of the bridge required approximately 650 m^3 of stormwater storage and the south end of the bridge required 1,200 m^3 of stormwater storage.

4.6 Proposed Mitigation

Once the required stormwater storage volume is determined, mitigation measures can be evaluated. Several mitigation opportunities were identified for the Metro Line LRT extension, including:

- Low impact development (LID) measures
  - o Rain gardens
- Integration with existing and proposed regional flood mitigation measures, including real-time control stormwater detention facilities and dry ponds
- Underground storage:
  - o Inline and offline oversized storage pipes
  - o Stormwater storage tanks

The proposed mitigation measure should be evaluated based on size, configuration, operation and maintenance, location constraints, and cost. There is not a one size fits all solution. Due to the Metro Line LRT extension alignment traversing already developed neighbourhoods, space was quite limited for above ground LID features or new stormwater management facilities. However, a rain garden was proposed to manage the stormwater from the bridge since the north end of the bridge was adjacent to an existing park with ample space. The south end of the bridge connected to a proposed neighbourhood and stormwater storage was integrated into the planned SWMF for that neighbourhood. The rest of the alignment was managed via underground storage and conveyance to existing stormwater management facilities. The total stormwater storage required for the Phase 2 track alignment was 9,661 m^3 and the total storage proposed along the track alignment based on preliminary construction feasibility was 10,428 m^3.

5 Track Drainage

Track drainage infrastructure is imperative because the negative impacts of stormwater runoff directly degrade rail safety [9]. Trackway drainage selection depends on the type of track, the track slope, and the allowable ponding limits set by the local standards. Drainage inlet placement and spacing is designed based on the track configuration and local trackway design criteria. The track drain pickups would then need to be configured to connect directly into the existing minor drainage system (from a track drain catch basin manhole) or tied into a storage/buffering unit prior to entering the existing minor drainage system.

The Metro Line LRT extension track drainage system varied between ballast track, direct fixation track, embedded track, special trackwork, bridge track drainage, and underpass track drainage. Depending on the track type, a grit management system is configured to maintain the existing water quality. Edmonton, being a cold climate city, uses a sand grit on the tracks to increase friction in winter. Therefore, track drainage is collected in catch basins or is filtered through a geotextile to collect grit prior to/prevent grit from entering the minor storm system or buffer storage units.

6 Conclusion

With the growth of cities and expansion of urban rail lines, many times we are faced with adding a trackway to already developed neighbourhoods and areas where the existing storm system is not adequate as is. Many times, there is existing infrastructure in place that will need to be relocated. If left unchecked, existing drainage patterns can be altered through the addition of an urban trackway that can impact the operation of the rail vehicles and/or the adjacent neighbourhoods. Increases in runoff due to increases in impervious area, surface ponding, overland flow routes, level of service requirements, and water quality need to be evaluated in the design of urban track drainage. Additionally, the drainage of the track surface itself (slopes, inlet placements, etc.) can impact the longevity of the trackway and impact maintenance.

Acknowledgements The lessons learned from this urban rail drainage design project were made possible from the contributions of the City of Edmonton LRT E&R team and the Metro North Partners design team. The authors would like to thank these team members for their thought-provoking questions, review comments and data sharing throughout this project.

References

1. AECOM (2011) Region of waterloo rapid transit project report stormwater management impact assessment. AECOM, Kitchener, ON, Canada
2. Alberta Government (2013) Standards and guidelines for municipal waterworks, wastewater and storm drainage systems: Part 5 stormwater management guidelines. Alberta Queen's Printer, Edmonton, AB, Canada
3. Andrews H (2019) Metro line NW LRT extension phase 2: stormwater management and deep utility relocations preliminary design report. Metro North Partners, Edmonton, AB, Canada
4. Associated Engineering (2016) City-Wide Flood Mitigation Assessment (Phase II, Area 'B'). Associated Engineering, Edmonton, AB, Canada
5. Canadian National Railway, CN (2019) CN engineering specifications for industrial tracks. Office of Chief Engineer Structures, Design, and Construction, Canada
6. City of Edmonton (2015) City of Edmonton – Design and construction standards: Volume 3 drainage. City of Edmonton, Edmonton, AB, Canada
7. City of Edmonton (2017) City of Edmonton – LRT design guidelines. City of Edmonton, Edmonton, AB, Canada
8. Pulido D, Darido G, Munoz-Raskin R, Moody J (2018) The urban rail development handbook. World Bank, Washington, DC, USA
9. Vo PT, Ngo HH, Guo W, Zhou JL, Listowski A, Du B, Wei Q, Bui XT (2015) Stormwater quality management in rail transportation—Past, present and future. Sci Total Environ 512–513(072):353–363

Indigenous Housing Practices as Inspirations for Modern Green Buildings

Z. Kelly and A. Iqbal

1 Introduction

Firstly, the land on which we live must be acknowledged as the unceded territory of the First Nations, Métis, and Inuit peoples. These Indigenous communities include the Haida people of Haida Gwaii and the Inuit people of Arctic Canada including Nunavut, Northwest Territories, Nunavik (Northern Quebec), and Nunatsiavut (Northern Labrador).

The modern western way of life is largely unsustainable. Innovations in clean energy and sustainable building practices are developing continuously. While current inventions that are helping Canada develop into a modern sustainable country are promising, it is important to focus on historically successful methods. Indigenous architecture involves knowledge passed down through generations and is rooted in the connection between human and nature. This involves deep rooted knowledge of elements such as the surrounding climate, topography, and vegetation. Sustainable building must work with the natural environment rather than fight against it. This method of green building is not new; it is thousands of years old and is proven successful among the Indigenous people prior to European contact. Looking at case studies of Indigenous architecture used thousands of years ago, the simplicity and the synergy between these buildings and their surroundings are made clear. While it is understood that modern society will not go back to a time of living without the conveniences to which we have become accustomed, many aspects of these traditional structures can be meaningfully applied to modern green building to improve both efficiency and sustainability.

Z. Kelly · A. Iqbal (✉)
University of Northern British Columbia, Prince George, BC V2N 4Z9, Canada
e-mail: asif.iqbal@unbc.ca

Z. Kelly
e-mail: zkelly@unbc.ca

S. Walbridge et al. (eds.), *Proceedings of the Canadian Society of Civil Engineering Annual Conference 2021*, Lecture Notes in Civil Engineering 240,
https://doi.org/10.1007/978-981-19-0507-0_14

This paper will first review the importance of Indigenous environmental justice, and the traditional methods of the igloo and cedar plank house outlining advantageous technologies used in the history of Indigenous architecture. These methods are then connected to the concepts of bioclimatic design and use of biomaterials, outlining modern applications in green building technology.

2 Traditional Practices

2.1 Indigenous Environmental Justice and Philosophy

Traditional ecological knowledge (TEK) is learned by communities through their interactions with the local environment. This knowledge is often dismissed as unreliable or unscientific, often resulting in the overwhelming favor of Western science. While Western science plays a valuable role, traditional ecological knowledge has in addition a moral compass which results in a more intimate relationship with the environment and the people living within it. Upon European arrival at land so generously supplied with vegetation, meat, water, and other resources, they abandoned the knowledge of the people who belonged to this land and supplies were exploited rather than respected and sustained. This dismissal of resource management based off TEK is what led to a steady decline in resources.

Indigenous communities experience the affects of climate change at a disproportionate level to the rest of the population. As Indigenous people rely more heavily on local natural resources for food, medicine, shelter, and other purposes, they are therefore more affected by the loss of these resources as a result of climate change [3]. The sustainable lifestyle that Indigenous people were once able to adopt is exactly what has left them so vulnerable to climate change. Downing and Cuerrier [3] state that climate change in particular impacts those living in the arctic and subarctic, largely populated by Indigenous people, as the changes in weather cause delayed snow cover, early snow melt, and record lows of ice cover. As well, Downing and Cuerrier [3] point to the increases in storm frequency and severity in warmer climates which lead to flooding, drought, and loss of food security.

Indigenous knowledge and values are often considered inferior to Western scientific knowledge; “Despite the recent adoption of the UN Declaration on the Rights of Indigenous Peoples (UNDRIP) in 2007, Indigenous people continue to be denied their rights and are subjected to climate injustice, remaining largely excluded from the official UN climate negotiations.” [4]. While global approaches to climate change are dominated by Western science and philosophy, Indigenous people have proposed their own solutions through Indigenous environmental or climate change declarations [1]. Nevertheless, Indigenous knowledge continues to be consistently discounted in global research and policy [7].

2.2 Case Studies: Haida Log House and Inuit Igloo

2.2.1 Haida Log House

The Indigenous group known as the Haida people live in Haida Gwaii in Northwestern British Columbia, previously known as the Queen Charlotte Islands. Haida houses were primarily made of cedar sourced from the forest surrounding them [10]. The Haida produced two variations of their cedar plank houses: the two-beam house and the six-beam house.

The two-beam house as shown in Fig. 1 was made of two parallel round beams placed upon two pairs of upright poles. Beneath the beams was a structure consisting of rafters, sills, corner posts, and gables [10].

Macdonald and Huyda [10] describe how the six-beam house as shown in Fig. 2 was more intricately designed with additional tenon joints and other features. These features helped distribute the stress more efficiently resulting in a simple frame able to bear the weight of the six beams which established the roof.

Both structures consisted of a smoke hole in the center of the roof overlooking the hearth in the center of the building. The smoke hole would be covered with planks which could be constantly shifted using a rope or logging poles according to the direction and strength of the wind [10].

Cedar was a primary source for the Haida, and it was imperative for them to be able to source it sustainably. While the cutting down of trees was required, the Haida did so without risking the survival of the species, remaining consistent with their environmental values. Almost every part of the tree including the roots, bark and branches would be used for a variety of purposes [6]. Huang describes how trees would be cut down using red-hot rocks to heat the wood and a chiseling process was used to break it down. Bark was harvested skillfully by collecting small portions of the bark from different sections of the trees [6]. Cedar had countless uses and was

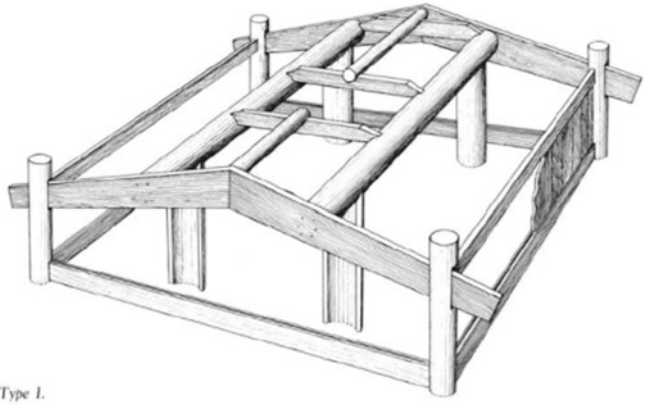

Fig. 1 The two-beam house built by the Haida [10]

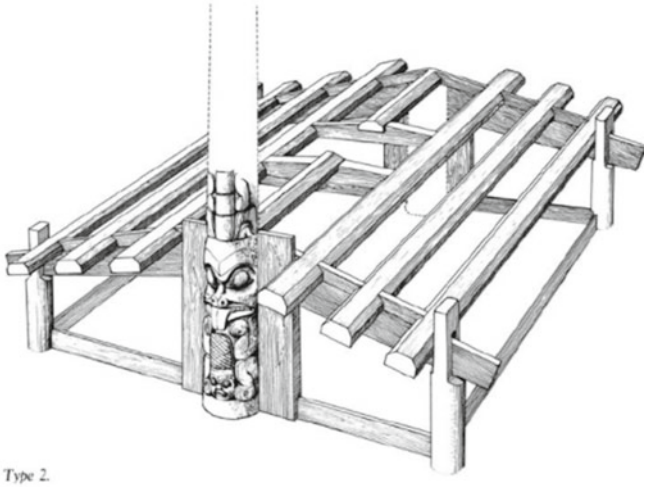

Fig. 2 The six-beam house built by the Haida [10]

used not only for housing but as well clothing, baskets, totem poles, canoes, and art [13].

British Columbia has two native species of Cedar: the Red Cedar and the Yellow Cedar. Huang [6] explains how yellow cedar grows 20–40 m tall and is rarely found in inland regions. He describes that because of the soft and flexible bark of the Yellow Cedar, it is used mostly for clothing and other fibrous materials. Huang [6] also explains that red cedar can grow up to 70 m tall and to 1000 years old. He describes how red Cedar bark is much less pliable than that of the Yellow Cedar. The Red Cedar is therefore used for large structures such as houses and canoes [6].

Cedar bark can be split easily in long planks and is porous, making it a good material for insulation. The air spaces inside the bark make the wood less strong yet much lighter [13]. While all cedar trees are valuable, trees that can produce logs large enough for structures such as houses usually exceed 100 cm in diameter at breast height [13]. Cedar can be sourced locally, is natural, and has beneficial applications without being overprocessed.

In the period following the industrial revolution, logging in Canada done without environmental consideration and conservation has resulted in a depletion of the resources that the people Indigenous to Canada once relied upon and treated with care and respect.

2.2.2 Inuit Igloo

The Inuit live in subarctic Canada where the climate is dominated by the winter season and where days are short with cold winds and temperatures reaching below

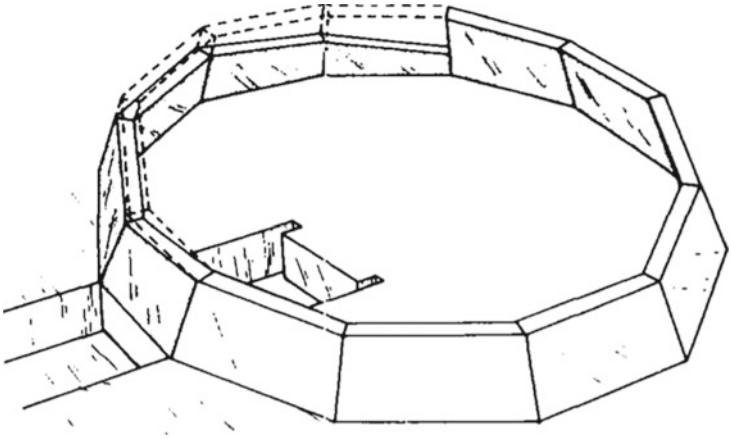

Fig. 3 Construction of an Igloo—Sloping spiral [2]

negative 40 °C. While the Inuit no longer live in Igloos long term, the structure is still used as temporary shelter during hunting trips [8].

Handy [5] describes how the formation of an igloo involves a specific type of packed snow, compressed through storm winds and precipitation. He says that snow blocks are cut vertically out of the surface to create a trench as shown in Fig. 3, which forms the entrance to the igloo. He describes how a block of packed snow is suspended across one end of the trench to support the structure. Snow blocks are placed in a circle starting at the trench and the first few are trimmed at a continuous angle of approximately 30° [5] as shown in Fig. 3.

Blocks are placed in a spiral fashion creating a dome. The dome is not a definite hemisphere—it resembles more of an inverted paraboloid, ensuring structural integrity [5]. Gaps between blocks are packed with loose snow and the outer perimeter of the structure is surrounded by snow piles in order to prevent the loss of warm air [2]. A vent is carved into the top of the igloo off center, with its position depending on the strength and direction of the wind as shown in Fig. 4 [5].

The igloo would occasionally be lined with skin from caribou, whales, or seals in order to further insulate the structure. The skin was hung from cords passing through the walls. Historically, heat and light would be provided by animal fat inside soapstone lamps or heaters called *kudliks* [8]. Because of their porosity, snow blocks are excellent insulators. Kershaw, Scott and Welch [8] explain if a snow block is too thick, it may provide too much insulation to the point where the structure may start melting. The insulation properties of snow blocks can vary with snowpack, temperature, and time of year. Snow blocks are also wind resistant and soundproof as well as abundant, making them an ideal material in the Subarctic [2]. The insulation properties of snow blocks decrease with density as snow porosity decreases with increasing density [8].

Another prominent sustainable feature of the igloo is its aerodynamics. When studied by Cook [2], it was shown that the formation of streamlines over the igloo

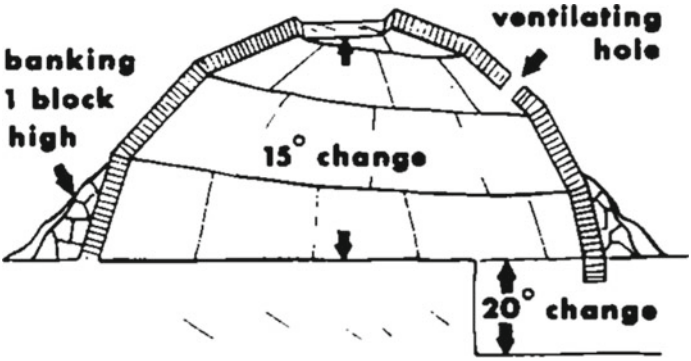

Fig. 4 Cross section of an Igloo [2]

reduces erosion and the migration of loose snow surrounding the structure, preventing it from insulation loss. Streamlines over and around an igloo can be seen in Fig. 5.

Kershaw et al. [8] studies on the shelter characteristics of igloos show that igloos can maintain an increase in temperature of up to 45 °C when supplied with heat. This heat can come from the metabolic heat of the people inside the igloo and the kudliks. Without people or kudliks, temperatures inside igloos were not much higher than outdoor temperatures in these studies. These studies also showed that temperature increase is greatest in smaller structures with more people and kudliks. Heat flux becomes more consistent with time once heat is supplied and temperature slowly decreases when heat is no longer supplied. The warmest section of the igloo is towards the ceiling and the upper elevated portion of the igloo, with the entrance being the coldest [8].

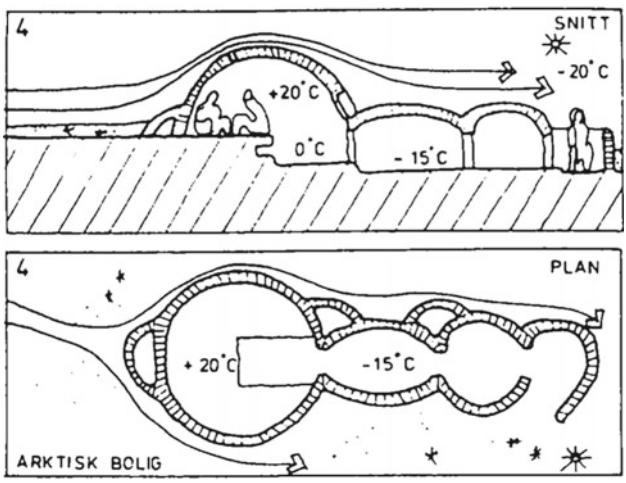

Fig. 5 Aerodynamics of an Igloo [2]

While the igloo no longer has common practical use in the modern Western world, it inspires the use of local and recyclable materials at a low cost as well as the building of structures made specifically for the local climate. This can aid in efficiently producing heat with little to no electricity, saving on both energy and money. A full understanding of the local climate and its complexities is necessary in architecture and engineering to build structures that are practical and sustainable.

3 Modern Sustainable Building Approach

3.1 Modern Green Building Technology

Zhonghua and Xiaohuan [18] describe the United States Green Building Council's (USBC) definition of green building as "a building and using process aiming to reduce the overall impact of the built environment on human health and the natural environment by efficiently using energy, water, and other resources and by reducing waste, pollution and environmental degradation." Increases in economic and social incentives have resulted in a recent rise in popularity towards green building. As a result, countries have begun to develop tools to aid in the design of green buildings such as LEED (Leadership in Energy and Environmental Design) created by the USGBC, and to quantify the concept of green building through rating systems [18]. Examples of qualities to which a green building is rated are shown in Fig. 6.

Yudelson [17] addresses the benefits of green building from a business perspective, and divides them into the following sections: economic, productivity, risk-management, health, public relations and marketing, recruitments, and retention.

3.2 Modern Applications

Vernacular architecture is similar to TEK in that it is based on knowledge of the local climate, culture, and the use of local materials. Indigenous architects are already leading the way in modern vernacular architecture. In his travel to over 250 Indigenous communities, Millette [11] witnessed a "clear and accelerating shift toward what might be called the "taking back" of community planning and architectural design, whereby community members are increasingly taking on active roles in the design of their communities and facilities." [11]. In her article in *The Canadian* Architect, Lewington [9] addresses various aboriginal architects and interviews them relating their architectural styles to their specific histories and cultures.

While it is important to acknowledge that the logging of old growth cedar is no longer ethically or sustainably sourced, the use of biomaterials from other sources has many benefits as well. Biomaterials are easily recyclable, can be produced locally with minimal transportation, and can be processed using simple tools leading to

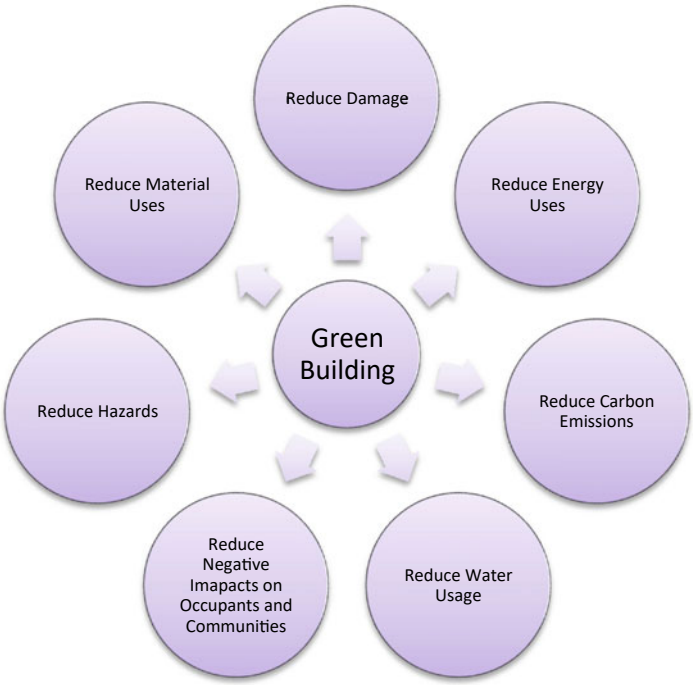

Fig. 6 The critetion of green building based on reducing negative impacts in building design [18]

quicker installation [12]. One challenge in the use of biomaterials is hygrothermal inefficiency. Sandak et al. [12] explain that biomaterials absorb large amounts of moisture causing changes in material dimensions and stability and problems with fungal growth. Materials such as timber are also highly combustible resulting in fire safety challenges. There are methods used to reduce these impacts, but these disadvantages still must be considered.

Bioclimatic design involves basing building designs on local climate [16]. This can be done by taking advantage of sun shading, solar heat, natural ventilation, and construction materials. Watson [16] goes into detail about which methods of bioclimatic design can be used in different climates. The Igloo is an excellent example of bioclimatic design and can be used to inspire more modern adaptations.

4 Impacts of Climate Change

While Indigenous People's philosophy promotes the protection of earth and prevention of climate change, the onset of global warming is inevitable and can assure the changing of Canada's climate. Global warming results in rising sea levels, increasing air and ocean temperature, and the melting of snow and ice over large areas of land.

The warming of the arctic specifically has resulted in decreasing glacial masses and snow cover and increasing plant growth, permanently altering the arctic climate [14].

Within Canada, the effects of climate change have been predicted to be most prominent in northern communities [15]. Although Indigenous communities were forced to change some traditional practices due to European colonization, they still managed to preserve many aspects of their cultures. A large aspect of Indigenous culture is the food and its resources. With the changing climate Indigenous people now must adapt to unpredictable changes in critical resource availability. Indigenous people have experience adjusting to large changes in climate such as changes in sea level through methods such as relocating or adopting new resources [15].

Indigenous architecture is a large inspiration for modern green building, but so are the Indigenous people's abilities to adapt to changes in climate. For example, the smoke hole in the center of the cedar plank house roof would often have planks that could be shifted according to the strength and direction of the wind [10]. Changes in temperatures in the Arctic can be accounted for by using or removing kudliks and animal skins. Many aspects of Indigenous architecture are easily adaptable to changes in climatic conditions, making the architectural knowledge of Indigenous people even more valuable. Regarding large changes in climatic conditions in Canada and more being predicted to come, the knowledge of Indigenous people from all around the world is valuable to account for the type of climate that Canada may experience in the future.

5 Conclusion

Moving forward, the life cycle of modern building needs to be adapted to benefit the environment. With the rise in popularity of green building, methods to incorporate sustainability into building construction have become widely available. Indigenous communities have been using many of these methods for thousands of years. Throughout this time, they were able to maintain a sustainable lifestyle up until first contact. Vernacular architecture and traditional ecological knowledge are concepts used by Indigenous communities which can be applied to modern green building through bioclimatic design and the use of biomaterials.

The Igloo built by the Inuit is a clear example of bioclimatic design in which the structure was optimised to work with extreme weather conditions and materials used were sourced locally while still being effective. The use of cedar planks for the Cedar Plank Houses built by the Haida is a clear example of the successful use of biomaterials in building construction. Local materials result in less interventions, less processing, and with further action can be produced and sourced sustainably. Bioclimatic approaches to green building can be simple and effective in increasing thermal comfort with a decrease in energy usage.

The incorporation of Indigenous knowledge and the advisement of Indigenous organizations are integral to a future of building design that is both socially and environmentally responsible. Traditional Indigenous building methods are necessary

if we are to have a future of building that is based on a philosophy sensitive to our resources, our environment, and the people who live in it. The future of buildings depends on it.

References

1. Chisholm Hatfield S, Marino E, Whyte KP (2018) Indian time: time, seasonality, and culture in Traditional Ecological Knowledge of climate change. Ecol Process 7(25)
2. Cook J (1996) Architecture indigenous to extreme climates. Energy Build 23(3):227–291
3. Downing A, Cuerrier A (2011) A synthesis of the impacts of climate change on the First Nations and Inuit of Canada. Indian J Trad Knowl 10(1):57–70
4. Green D, Raygorodetsky G (2010) Indigenous knowledge of a changing climate. Springer Science + Media 100: 239–242
5. Handy RL (1973) The igloo and the natural bridge as ultimate structures. Arctic 26(4):269–348
6. Huang A (2009) https://indigenousfoundations.arts.ubc.ca/cedar/)
7. Jones R (2019) Climate change and indigenous health promotion. Glob Health Promot 26(3):73–81
8. Kershaw GP, Scott PA, Welch HE (1996) Shelter characteristics of traditional-style inuit snow houses. Arctic 49(4):328–338
9. Lewington J (2017) Profiles: Canada's first nations designers. Can Archit 62(5):26–30
10. Macdonald G, Huyda J (1994) Haida monumental art: villages of the Queen Charlotte Islands. UBC Press, Vancouver, British Columbia, Canada
11. Millette DM (2017) The state of indigenous architecture in Canada. Can Archit 62(5):24
12. Sandak A, Sandak J, Brzezicki J, Kutnar A (2019) Bio-based building skin. Springer, Switzerland
13. Stewart H (2009) Cedar: to the northwest coast indians. D&M Publishers, Vancouver, BC, Canada
14. Serreze MC, Walsh JE, Chapin FS et al (2000) Observational evidence of recent change in the northern high-latitude environment. Clim Change 46:159–207
15. Turner NJ, Clifton H (2009) "It's so different today": climate change and indigenous lifeways in British Columbia Canada. Global Environ Change 19(2):180–190
16. Watson D (2020) Bioclimatic design. Springer, New York, United States
17. Yudelson J (2010) The green building revolution. Island Press, Washington, DC, United States
18. Zhonghua G, Xiaohuan X (2017) Evolving green building: triple bottom line or regenerative design. J Clearn Prod 153:600–607

Numerical Modeling of Jets Near a Hydraulic Jump

X. Chen, X. Yan, and A. Mohammadian

1 Introduction

Municipal wastewater discharges and liquid wastes discharged from desalination plants are often discharged into water bodies through outfall diffusers in the form of wastewater jets. It is necessary to adequately dispose these effluents to avoid serious environmental issues. Therefore, it is better to get a clear understanding of the mixing characteristics of turbulent jets and it has been a topic of significant research [1–10].

Hydraulic jumps are frequently seen in the field of water resources engineering, especially in open channel flows. For example, hydraulic jumps often occurred in rivers and spillways. A sudden rise occurs when flow at higher velocity discharges into a region of relatively lower velocity. As the water height rises, the flow velocity slows down. In this process, a part of the initial kinetic energy is transformed into some potential energy, and there is some energy loses in this process.

Because of the special hydraulic processes, such as energy dissipation and turbulence, it is reasonable to expect that hydraulic jumps can affect the mixing and dispersion processes of wastewater jets. However, to the best of the authors' knowledge, the mixing properties of jets near a hydraulic jump have not yet been studied, and thus the topic requires further investigation.

The mixing properties of wastewater jets can be studied using various methods. The jet discharges in different types and configurations have been widely investigated with physical and numerical methods previously. Physical modeling as the basic method to study the characteristic of flow has been intensively utilized for many years. Especially when complicated surrounding situations are investigated,

X. Chen (✉) · A. Mohammadian
Department of Civil Engineering, University of Ottawa, Ottawa, ON K1N 6N5, Canada
e-mail: xchen139@uottawa.ca

X. Yan
Department of Water Resources Engineering, Dalian University of Technology, Dalian, China

S. Walbridge et al. (eds.), *Proceedings of the Canadian Society of Civil Engineering Annual Conference 2021*, Lecture Notes in Civil Engineering 240,
https://doi.org/10.1007/978-981-19-0507-0_15

experimental method has shown its advantages in the realistic and natural results it can provided. Physical modeling and laboratory experiments play an important role in hydrodynamic researches. Detailed and reliable data obtained from experiments also provide essential reference for the studies with mathematical and numerical approaches. In the 1990s, the application of Particle Image Velocimetry (PIV) and Laser-Induced Fluorescence (LIF) techniques allowed the acquisition of more reliable measurements.

For the aim to obtain a more numerical understanding of effluent discharges mechanisms, various numerical techniques were developed since 1950s, including length-scale, integral and advanced CFD models. In the 1950s, the length-scale models were developed on a basis of non-dimensional numbers to categorize discharge regimes, building up the relationships between experimental data and predictions. The two popular length-scale models are NRFIELD [11–13] and CORMIX [14], that are fast in solution production but are very sensitive to any input changes. When working on the region where is close to the boundary between two regimes, Monte-Carlo testing and an experienced user are required to interpret the input data, to avoid consequently large differences in flow predictions. The inaccuracy of model may also occur when it is applied outside the calibrated parameter-space [15].

Jet integral models were proposed to solve mass and momentum conservation equations along the jet centerline. It is based on the assumptions that the jet profile is axisymmetric and well follows a Gaussian shape without radio variation. In the 1950s and 1960s, the first-order jet integral models were developed on the jet diffusion approach and the jet entrainment closure approach. From the 2000s, the second-order jet integral models were incorporated by commercial packages such as Visual Plumes [16] and CORMIX [16] that are developed by [17–19].

Nevertheless, the limitations of standard integral models are nonnegligible when any of the following issues occur [20–22]: (i) there are significant lateral and horizontal boundary effects; (ii) the jet is discharged in an unstable near-field region; (iii) there is a large volume of re-entrainment in near-field region due to tidal cycles; (iv) the edge is instable because the initial momentum and buoyancy are in contrary directions.

Nowadays, with the increasing ease of computer technology, the CFD tools have been utilized in investigation of jet discharges and showing various strengths compared with the parameter-based approaches. A well developed CFD model is more open and applicable with less restriction and assumptions.

The concerns of CFD models are mainly on its accuracy, stability, computational cost, complication in code and calibrating and validating requirements. Even with modern computational sources, the simulation with CFD modeling takes several days or weeks, which is more expensive than parameter-based approaches. The pursuing in high accuracy in solutions is conflict to the need in reducing computational effort. Therefore, it is critical to balance between stability, numerical diffusion, conservation, boundedness and cost.

The choice of turbulence model is another hot topic in published CFD modeling studies of jet discharges. The Reynolds-averaged Navier–Stokes (RANS) and the Large Eddy Simulations (LES) models have been used widely as the most popular

models for the outfall system designs. RANs models is concentrated on resulting the time-averaged mean velocity field but do not resolve the details of turbulence, while LES models resolve turbulence but require higher computational cost. The RANS approach was used in this study because of its good balance of accuracy and efficiency.

In this study, a total of three cases are studied: a hydraulic jump without a jet, a hydraulic jump with a weaker jet, and a hydraulic jump with a stronger jet.

2 Methodology

2.1 Governing Equations

The governing equations can be expressed as:

$$\nabla \cdot \mathrm{U} = 0 \tag{1}$$

$$\frac{\partial \rho \mathrm{U}}{\partial t} + \nabla \cdot (\rho \mathrm{UU}) = -\nabla \cdot \left(p_{rgh}\right) - gh\nabla\rho + \nabla \cdot (\rho \mathrm{T}) \tag{2}$$

with:

$$\rho = \alpha_1\rho_1 + \alpha_2\rho_2 = \alpha_1\rho_1 + (1-\alpha_1)\rho_2 \tag{3}$$

$$\mathrm{T} = -\frac{2}{3}\overline{\mu}_{eff}\nabla \cdot \mathrm{UI} + \overline{\mu}_{eff}\nabla \mathrm{U} + \overline{\mu}_{eff}(\nabla \mathrm{U})^T \tag{4}$$

$$\overline{\mu}_{eff} = \alpha_1\left(\mu_{eff}\right)_1 + \alpha_2\left(\mu_{eff}\right)_2 \tag{5}$$

$$\left(\mu_{eff}\right)_i = (\mu - \mu_t)_i \tag{6}$$

where t, $\mathbf{U}$, ρ, and p are time, velocity, density, and pressure, respectively. h, g, and α are the height of fluid column, gravitational acceleration, and volume fraction, respectively. μ and μ_t are dynamic viscosity and turbulent viscosity, respectively. The subscript i indicates ambient water ($i = 1$) and water with contaminants ($i = 2$). This study focuses non-buoyant jets, so the properties of the two fluids are identical.

2.2 Turbulence Modeling

The present study uses the standard k-ε model, which can be written as:

$$\frac{\partial k}{\partial t} + \frac{\partial k u_i}{\partial x_i} - \frac{\partial}{\partial x_i}\left(D_{keff}\frac{\partial k}{\partial x_i}\right) = G - \varepsilon \tag{7}$$

$$\frac{\partial \varepsilon}{\partial t} + \frac{\partial \varepsilon u_i}{\partial x_i} - \frac{\partial}{\partial x_i}\left(D_{\varepsilon eff}\frac{\partial \varepsilon}{\partial x_i}\right) = c_{1\varepsilon}\frac{\varepsilon}{k}G - c_{2\varepsilon}\frac{\varepsilon^2}{k} \tag{8}$$

with

$$D_{keff} = \nu_t + \nu \tag{9}$$

$$D_{\varepsilon eff} = \frac{\nu_t}{\sigma_\varepsilon} + \nu \tag{10}$$

$$\nu_t = c_\mu \frac{k^2}{\varepsilon} \tag{11}$$

$$G = 2\nu_t S_{ij} S_{ij} \tag{12}$$

$$S_{ij} = \frac{1}{2}\left(\frac{\partial u_j}{\partial x_i} + \frac{\partial u_i}{\partial x_j}\right) \tag{13}$$

where k and ε are the turbulent kinetic energy and turbulent energy dissipation rate, respectively. G denotes the production of turbulence due to shear. $\sigma_\varepsilon = 1.3$, $c_{1\varepsilon} = 1.44$, $c_{2\varepsilon} = 1.92$, $c_\mu = 0.09$ are model constants.

2.3 Model Setup

The present study solved the governing equations using OpenFOAM. The simulations used a sluice gate and an outlet weir to generate the hydraulic jump. These two hydraulic structures and the bed were set to be walls. The model also had a water-inlet, jet-inlet, atmosphere, and outlet. The velocity at the water-inlet was set to be 0.055 m/s. Three different cases were simulated, and the velocity at the jet-inlet was set as 0 m/s, 0.1 m/s, and 0.5 m/s, respectively. The height of the outlet overflow weir was 0.125 m, and initial water depth was set as 0.125 m, too. The simulations were run up to 180 s. The default time step was set as 0.001 s, but the solver automatically adjusts the actual value according to the numerical stability criteria.

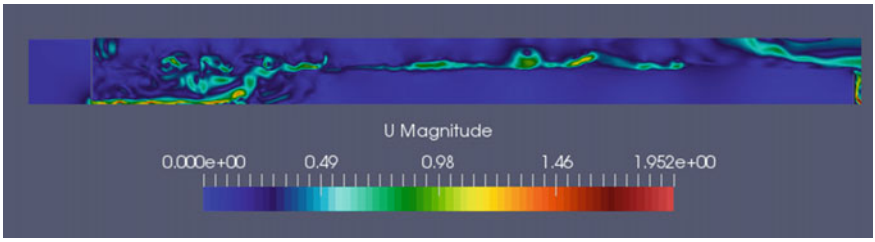

Fig. 1 The flow field for the case without a jet

3 Results and Discussion

3.1 The Case Without a Jet

A total of three simulations were conducted: a hydraulic jump without a jet, a hydraulic jump with a weaker jet, and a hydraulic jump with a stronger jet. Figure 1 presents the flow field for the case with a hydraulic jump, without a jet. As can be seen, a supercritical flow was issued from a gap between the channel bed and the sluice gate, and the magnitude of the jet velocity decreased along the stream-wise direction, and became subcritical flow through a hydraulic jump.

3.2 The Case Without a Weak Jet

Figure 2 shows a momentum jet discharged vertically into the channel. As can be

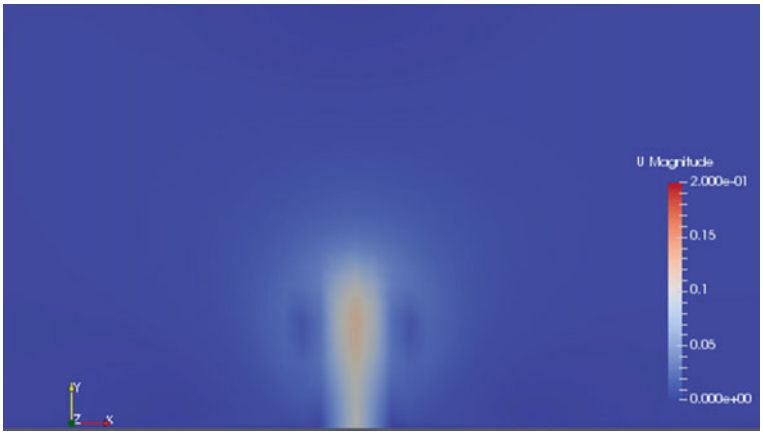

Fig. 2 The flow field for the case with a weaker jet (t = 1 s)

seen, at the very early stage, such as this case, the first second, the jet moved upwards.

Figure 3 shows the flow field around the jet at the third second. The jet was bent over towards the streamwise direction by the cross flow.

The inclination of the jet became more obvious as the flow developed to the fifth second (Fig. 4).

However, the jet trajectory is not stable because the ambient turbulence was quite strong. For example, at the twelve second (Fig. 5), the jet was bent over towards the stream-wise direction.

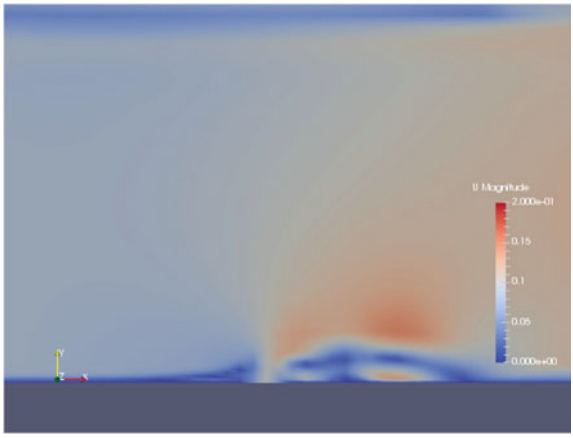

Fig. 3 The flow field for the case with a weaker jet (t = 3 s)

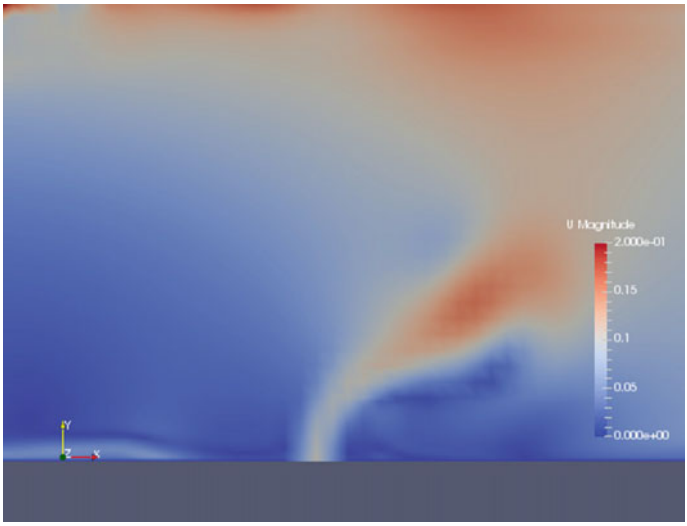

Fig. 4 The flow field for the case with a weaker jet (t = 5 s)

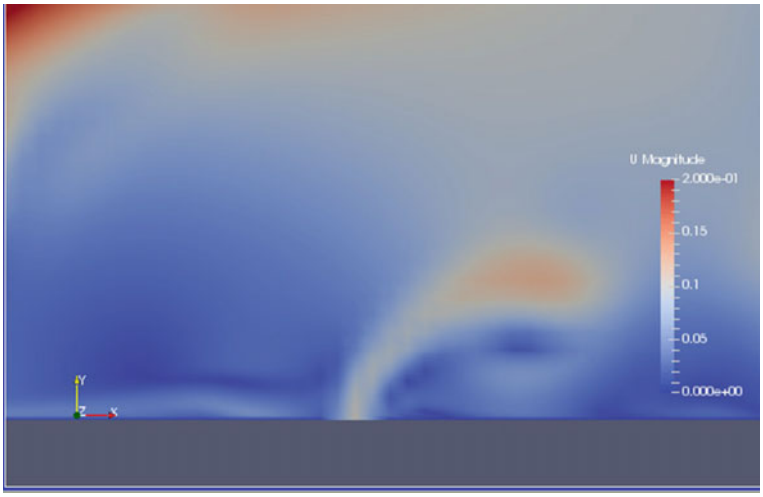

Fig. 5 The flow field for the case with a weaker jet (t = 12 s)

However, at some time instants, such as the 180 s (Fig. 6), the inclination of the jet trajectory became less obvious.

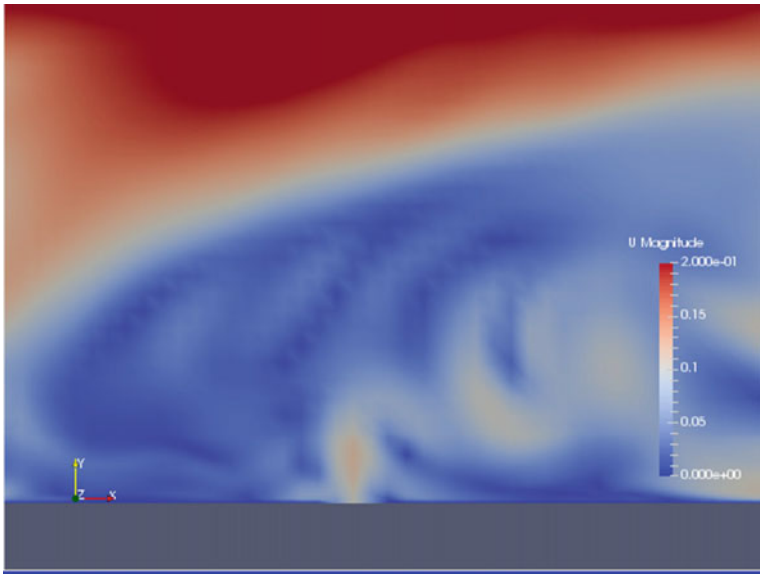

Fig. 6 The flow field for the case with a weaker jet (t = 180 s)

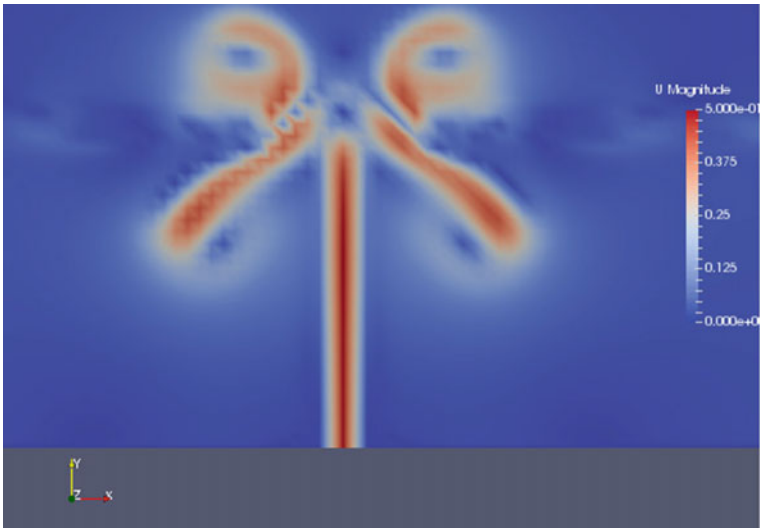

Fig. 7 The flow field for the case with a stronger jet (t = 1 s)

3.3 The Case with a Strong Jet

Figure 7 shows the flow field around a jet at the first second. The jet was quite strong, so it immediately reached the water surface.

The jet is then bent over by the cross flow, such as the situation at the third second (Fig. 8).

Similarly to the weaker jet case, the jet trajectory is also not stable. For example, at the 18 s, a spiral trajectory can be obverted (Fig. 9).

4 Summary and Conclusions

The present study simulated a jet near a hydraulic jump. The hydraulic jump was generated by a sluice gate at the upstream end and an overflow weir at the downstream end. A total of three simulations were conducted: a hydraulic jump without a jet, a hydraulic jump with a weaker jet, and a hydraulic jump with a stronger jet. The results are reasonable from a qualitative judgement. A key novel observation from this study is that the jet trajectory is not stable probably because of the strong turbulence near the hydraulic jump. This study has established a basic numerical model for a jet near a hydraulic jump, and thus it is necessary to conduct an experiment to validate the model. In addition, the present study investigated different cases with different jet velocities, and it will be interesting to investigate the influences of the locations and

Fig. 8 The flow field for the case with a stronger jet (t = 3 s)

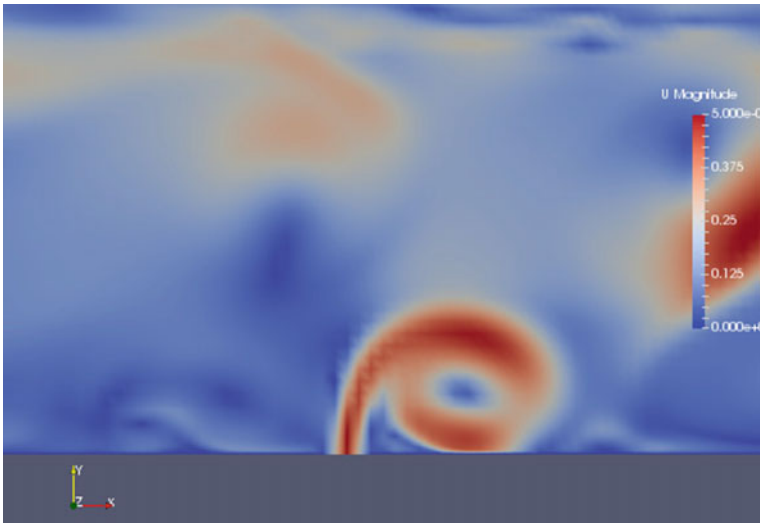

Fig. 9 The flow field for the case with a stronger jet (t = 18 s)

inclinations of the jets. In future studies, buoyant or negatively buoyant jets near a hydraulic jump can also be conducted.

References

1. Mohammadian A, Gildeh HK, Nistor I (2020) CFD modeling of effluent discharges: a review of past numerical studies. Water 12(3):856
2. Yan X, Mohammadian A (2017) Numerical modeling of vertical buoyant jets subjected to lateral confinement. J Hydraul Eng 43:04017016
3. Yan X, Mohammadian A (2019) Multigene genetic-programming-based models for initial dilution of laterally confined vertical buoyant jets. J Marin Sci Eng 7(8):246
4. Yan X, Ghodoosipour B, Mohammadian M (2020) Three-dimensional numerical study of multiple vertical buoyant jets in stationary ambient water. J Hydraul Eng. https://doi.org/10.1061/(ASCE)HY.1943-7900.0001768
5. Yan X, Mohammadian A, Chen X (2019) Three-dimensional numerical simulations of buoyant jets discharged from a rosette-type multiport diffuser. J Marin Sci Eng 7(11):409, 1–15
6. Yan X, Mohammadian A (2020) Evolutionary prediction of the trajectory of a rosette momentum jet group in flowing currents. J Coast Res (in press). https://doi.org/10.2112/JCOASTRES-D-19-00142.1
7. Yan X, Mohammadian A (2019) Numerical modeling of multiple inclined dense jets discharged from moderately spaced ports. Water 11:1–15
8. Yan X, Mohammadian A, Chen X (2020) Numerical modeling of inclined plane jets in a linearly stratified environment. Alexandria Eng J 1–11. https://doi.org/10.1016/j.aej.2020.05.023
9. Kheirkhah Gildeh H, Mohammadian A, Nistor I, Qiblawey H (2015) Numerical modeling of 30° and 45° inclined dense turbulent jets in stationary ambient. Environ Fluid Mech 15:537–562
10. Yan X, Mohammadian A (2019) Evolutionary modeling of inclined dense jets discharged from multiport diffusers. J Coast Res 36(2):362–371
11. Roberts PJW, Snyder WH, Baumgartner DJ (1989) Ocean outfalls. I: submerged wastefield formation. J Hydraul Eng 115:1–25.
12. Roberts PJW, Snyder WH, Baumgartner DJ, Ocean outfalls. II: spatial evolution of submerged wastefield
13. Roberts PJW, Snyder WH, Baumgartner DJ (1989) Ocean outfalls. III: effect of diffuser design on submerged wastefield. J Hydraul Eng 115:49–70
14. Doneker RL, Jirka GH (2007) CORMIX user manual: a hydrodynamic mixing zone model and decision support system for pollutant discharges into surface waters. EPA-823-K-07–001
15. Robinson D, Wood M, Piggott M, Gorman G (2015) CFD modelling of marine discharge mixing and dispersion. J Appl Water Eng Res 4:152–162
16. Frick WE (1984) Non-empirical closure of the plume equations. Atmos Environ 18:653–662
17. Jirka GH (2004) Integral model for turbulent buoyant jets in unbounded stratified flows. Part I: single round jet. Environ Fluid Mech 4:1–56
18. Wang H, Law AW-K (2002) Second-order integral model for a round turbulent buoyant jet. J Fluid Mech 459:397–428
19. Yannopoulos PC (2006) An improved integral model for plane and round turbulent buoyant jets. J Fluid Mech 547:267–296
20. Kikkert GA, Davidson M, Nokes RI (2007) Inclined negatively buoyant discharges. J Hydraul Eng 133:545–554
21. Shao D, Law AWK (2014) Integral modelling of horizontal buoyant jets with asymmetrical cross sections. In: Proceedings of the 7th international symposium on environmental hydraulics, Singapore, 7–9 January 2014
22. Nash JD, Jirka GH (1996) Buoyant surface discharges into unsteady ambient flows. Dyn Atmos Oceans 24:75–84

Shear Behaviour of Reinforced-Concrete Circular-Beams Without Web-Reinforcement

A. Gouda, A. Ali, and H. M. Mohamed

1 Introduction

Finite element (FE) method is one of the most accurate and effective techniques for analyzing complicated structural engineering problems, which provides a convenient and adaptable tool for covering the problems associated with the analysis of RC-beams. These problems include cracking of concrete, nonlinear stress strain response of concrete, shrinkage and creep of concrete, rupture of reinforcing bars, interaction between concrete and reinforcing bars. In recent years, due to progressing capabilities and knowledge of computer hardware and software, the FE method has increased to simulate and analysis the concrete structural elements. Using computer software to construct these elements is, definitely, much faster, and extremely cost-effective. Also, to fully, understand the abilities of a finite element computer package, the researcher must look back at the experimental data and the mathematical background of the software. The results from the finite element analysis are not useful unless the necessary steps are taken to understand what is happening within the model that is created using the software. By understanding the use of finite element programs, more efficient and superior analyses can be done to fully understand the behaviour of every structural components and their contribution to a structure as a whole [5].

One of the major problems facing the civil construction industry is the corrosion of steel reinforcement, which limits the service life of reinforced concrete (RC) structures especially those in harsh environments such as parking garages, bridges, marine structures, and tunnel excavation applications [6]. Using FRP bars as internal reinforcement in these structures would overcome the corrosion problem associated

A. Gouda (✉) · A. Ali
Department of Civil Engineering, Helwan University, Cairo, Egypt

H. M. Mohamed
Department of Civil and Architectural Engineering, College of Engineering, Applied Science University, Manama, Bahrain

S. Walbridge et al. (eds.), *Proceedings of the Canadian Society of Civil Engineering Annual Conference 2021*, Lecture Notes in Civil Engineering 240,
https://doi.org/10.1007/978-981-19-0507-0_16

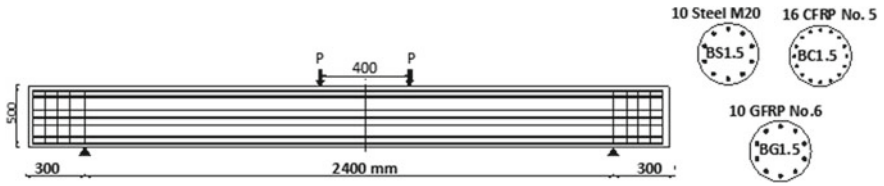

Fig. 1 Reinforcement configuration

with the steel bars [1]. On the other hand, the lack of sufficient experimental and analytical studies on the behaviour of the beams reinforced with FRP bars limits the knowledge and the full understanding of the behaviour of such beams, especially the ones with circular cross section.

The main idea of the current article is to partially fill that gap, in the research work, by presenting the results of numerical and experimental programs that were conducted on three full scale circular beams.

2 Experimental Program

2.1 Test Specimens

A total of three circular beams were constructed and tested to failure (BS1.5, BC1.5 and BG1.5). The main test variable was the type of reinforcing bars. Each beam consisted of 500-mm diameter and 3000-mm length. One beam (BG1.5) was reinforced with sand-coated GFRP bars, one (BC1.5) with sand-coated CFRP bars, and one (BS1.5) with steel bars as control. Two Canadian codes were used to design the specimens, the one for FRP materials, CSA-S806-12 [3], was used to design BC1.5 and BG1.5, and, the one for steel materials, A23.3-14 [2] was used to design BS1.5. The typical dimensions and reinforcement configurations of the beams can be seen in Fig. 1.

2.2 Material Properties

The properties of the beams' reinforcement can be seen in Table 1. The beams were constructed using ready mix, normal weight concrete from a local supplier. The target compressive strengths for the concrete were 35 MPa. The actual compressive (Table 2) and tensile concrete strengths for each beam were determined at the day of testing, by testing at least three concrete cylinders measuring 100 × 200 mm and 150 × 300 mm, respectively.

Table 1 Properties of the reinforcement

Bar diameter (mm)	Nominal cross-sectional area, A_f (mm^2)	Guaranteed tensile strength, f_{fu}* (MPa)	Modulus of elasticity, E_f (GPa)	Tensile strain, ε_{fu} ($\mu\varepsilon$)
GFRP bars				
20 (#6)	285	1105	63.7 ± 2.5	1730
CFRP bars				
15 (#5)	198	1679	141 ± 2.5	1200
Steel bars				
Bar diameter, (mm)	Yield strength, (MPa)		Modulus of elasticity, (GPa)	
20.0	460		200	

*Guaranteed tensile strength: Average value—3 × standard deviation (ACI 440.1R-15)

2.3 Instrumentation and Test Setup

Three linear voltage differential transformers (LVDTs) were used to measure the defection of the beams at the mid-span and at two other locations to obtain the deflection profile of the tested beams. Several 6-mm electrical strain gauges were installed on the reinforcing bars to capture the tensile-strain at the mid-span and different other locations. For the concrete, three 60-mm strain gauges were glued on the top surface to obtain the compressive-strain in the concrete, at the mid-span at three different levels (D, D/8, and D/4). The outputs from the instrumentation were recorded through a data acquisition system (DAQ) connected to a computer.

Figure 2 shows actual photo for the test setup and 3D schematic drawings, as well. As seen in the figure, the shear load was applied to the beams, through two-points, from 1000 kN MTS hydraulic actuator attached to spreader beam. A displacement-controlled mode with 0.6 mm/min rate was utilized to enforce the shear-load.

2.4 Test Results

All the beams failed in diagonal tension failure, beam BS1.5 experienced yielding in the steel bars at the time of failure as well. As seen in Table 2, the maximum measured deflection for BG1.5 was higher than that of BC1.5, which in turn was higher than the one reinforced with steel bars (BS1.5). Increasing the modulus of elasticity, for the reinforcing bars, from 63.7 to 141 and 200 GPa, enhanced and reduced the maximum captured deflection, at the mid-span, by 20.5% and 30.5%, respectively. That hold true for the load carrying capacity, as well, Increasing the modulus of elasticity, also, maximized the strength of the beams by 9.6% and 37.2%, respectively. The low modulus of elasticity would result, generally, in higher strain values in the bars, which

Table 2 Test results

Beam ID	Reinforcing material	f_c' (MPa)	Reinforcement ratio %	Failure load (kN)	Ultimate shear load V_{exp} (kN)	Strain (με)		Deflection (mm)	FE model shear load (kN)
						bars	concrete	Δ_{mid}	
						ε_u	ε_{cu}		
BS1.5	Steel	37.6	1.5	627	313	7098	2611	10.5	295
BC1.5	Carbon	36.3	1.5	501	251	3901	1784	12.0	247
BG1.5	Glass	38.1	1.5	457	229	4340	2000	15.1	222
Average				**528**	**264**	–	–	–	**254**
$\boldsymbol{V_{exp}/V_{Model}}$				–	–	–	–	–	**1.04**
S.D (%)				–	–	–	–	–	**1.7**
COV (%)				–	–	–	–	–	**2**

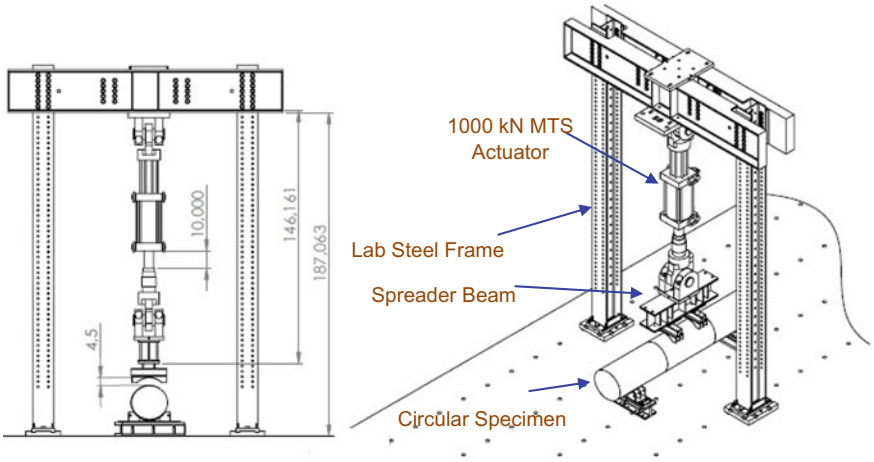

(a) 3-D sketch

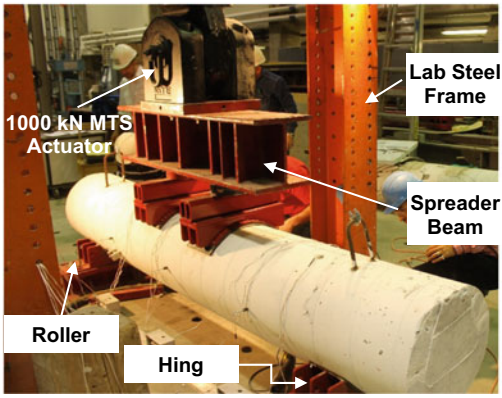

(b) Experimental photo

Fig. 2 Test setup

would cause wider and deeper cracks in the beams and reduced the shear capacity of those beams in terms of un-cracked concrete and aggregate interlock. Also, unlike steel bars, FRP bars are uni-directional materials with low strength and stiffness in the transverse direction. This result in smaller dowel force and, consequently, less contribution shear resistance.

3 Numerical Program

A 3D FE prototypes were built using a sophisticated FE software package, ATENA [4]. The members used to copy the behaviour of the concrete, FRP bars, and the steel reinforcement in addition to the boundary conditions, for the three circular-beams, are concisely explained in the subsequent sections.

3.1 Concrete Properties

In the current essay, to represent the concrete behaviour, a fracture-plastic constitutive relationship called *CC3DNonLinCementitious2* was used. That relationship utilizes Menétrey-Willam failure surface for the plastic behaviour and uses Rankine failure criterion [4]. This fracture-plastic relationship was evolved to combine both fracture and plastic behaviours into a single one that can use plasticity to simulate concrete crushing and fracture mechanics to simulate cracking. This relationship accounts for material nonlinearity, crushing, plastic deformation and cracking in the three orthogonal directions. The concrete compressive strength documented in Table 2 was used as a base to define the concrete properties.

3.2 Reinforcing Bars

To copy the behaviour of the reinforcing bars, link elements called *CCIsoTruss*, with three transition degrees of freedom at each element's node in the three orthogonal directions, were utilized. Three material types were used for the link elements, one for the sand-coated GFRP bars, one for sand-coated CFRP bars, and the last one for the steel reinforcement. The properties used for these materials are documented in Table 1.

3.3 Concrete-Reinforcement Interface

Two bond-slip relationships were used in the current essay, one for the FRP bars and the other for the steel ones. However, both relationships followed the same trend, where each one consisted of upward parabolic branch then a downward part in a linear relationship then finally a constant plateau where the slip keeps increasing, indefinitely, at the same stress value.

3.4 Model Geometry, Loading, and Boundary Conditions

Figure 3 depicts photos for a typical model and the reinforcement details. Four steel plates were utilized to distribute the stresses to the beams. Steel material, with 200-GPa modulus of elasticity and 0.3 Poisson's ratio, was used for those plates. Two plates were used to transfer the shear loads and two plates were used to support the beams. The shear load was applied across the centre-line of the loading-plates. For the supporting plates, the movement in the in-plane directions (X and Y) were restricted, the movement in the out-of-plane direction (Z) was allowed in the upward direction and was prevented in the downward direction to simulate the supporting conditions in the experimental program. According to the mesh sensitivity conducted in the current study, it was found that, mesh size of 0.1-m, in all the directions, is sufficient to achieve the, observed, experimental behaviour of the beams. Any decrease, beyond that, in the mesh size did not result in any noticeable enhancement.

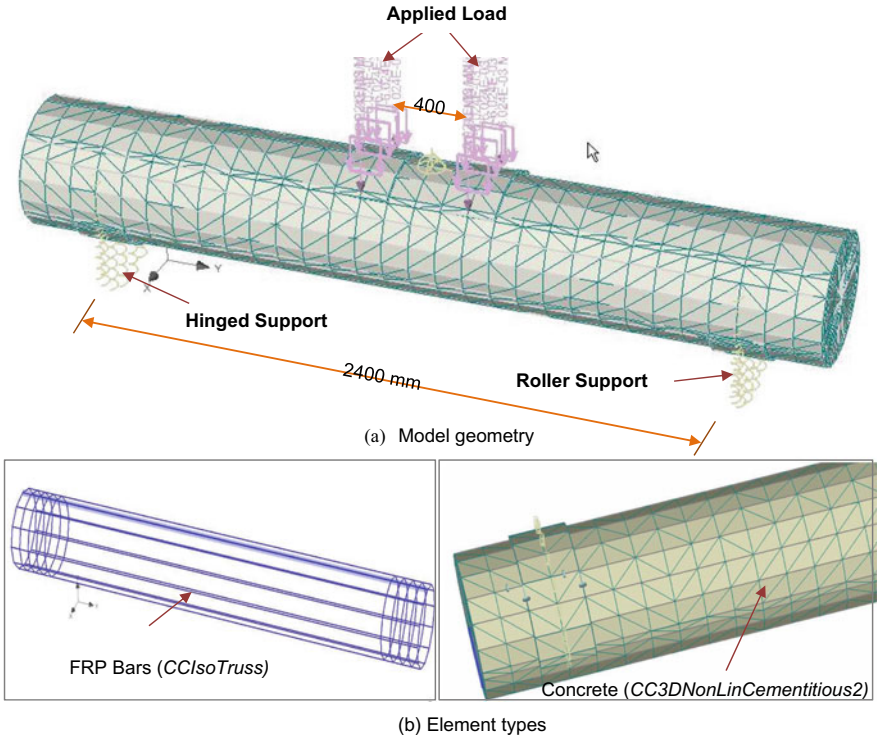

Fig. 3 Model geometry of the circular reinforced concrete beams

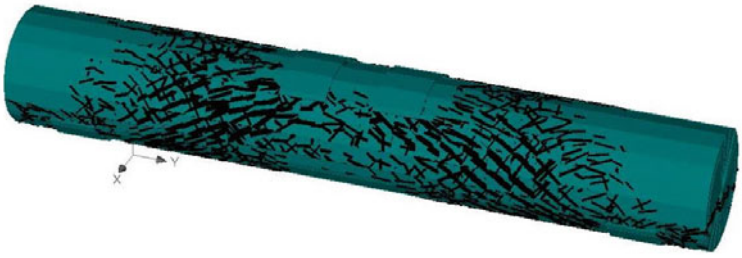

(a) FE model

(b) Experimental

Fig. 4 Cracking patterns

3.5 Numerical Results

The accuracy of the numerical outcomes was confirmed with outcomes of the experimental study, in terms of crack-patterns, load–deflection relationship, load-strain relationship in the reinforcing bars, and the carrying load capacity. The verification process included all the beams tested experimentally (BS1.5, BC1.5, BG1.5).

The crack pattern for one the beams tested in the lab (BS1.5) and the crack pattern for its FE model, counterpart, is shown in Fig. 4. The FE model was able to copy the schematic of the, experimental, cracking pattern to a good accuracy. The model generated vertical and inclined cracks similar to the ones observed experimentally.

The load–deflection relationship, at the mid-span, for all the circular beams is shown in Fig. 5. The FEM copied the behaviour of the beams with good accuracy, in terms of pre- and post-cracking phases. Figure 6 depicts the load-strain relationship, in the reinforcing bars at the mid-length, of the beams. Again, the figure shows that the model was able to copy the strain characteristics of the beams to a good degree. Before cracking the strain's value was not that significant, once the cracks spread in the beams the strains increased, approximately, in a linear way. Also, the model was able to capture the yielding behaviour for the steel-RC beam (BS1.5).

Table 1 shows the shear-loads obtained by the FEM and the ones from the experimental program as well. The mean value for the experimental shear-capacity to the FEM counterparts (V_{exp}/V_{Model}), for all the beams, is 1.04 ± 0.02 with 2% COV.

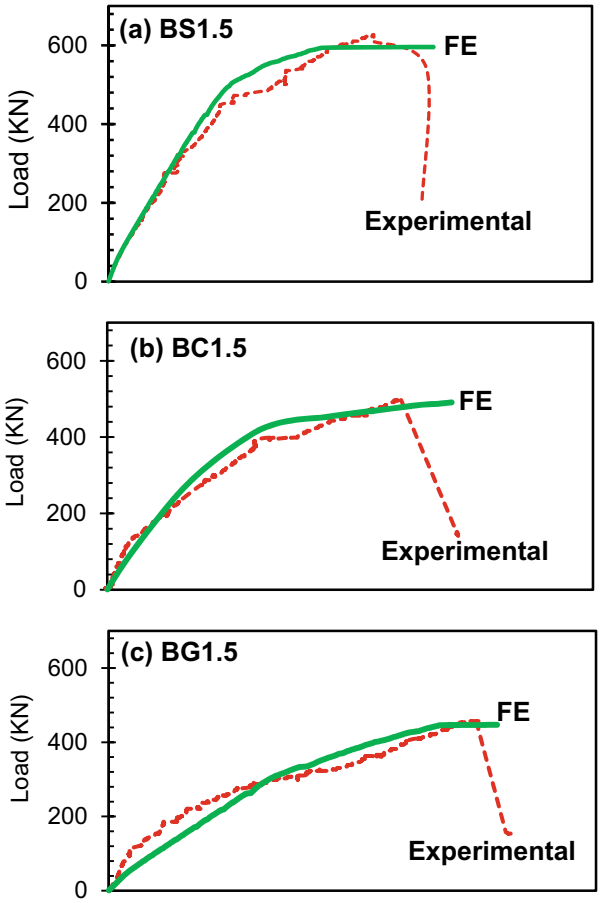

Fig. 5 Load–deflection relationship

4 Conclusion

The behaviour of three full-scale circular-beams, reinforced with steel and FRP bars, were evaluated. Based on the discussions presented, previously, the followings were concluded:

a. All the beams failed in diagonal tension failure.
b. Increasing the modulus of elasticity, for the reinforcing bars, from 63.7 to 141 and 200 GPa enhanced the load-carrying capacity of the circular-beams by 9.6% and 37.2%, respectively

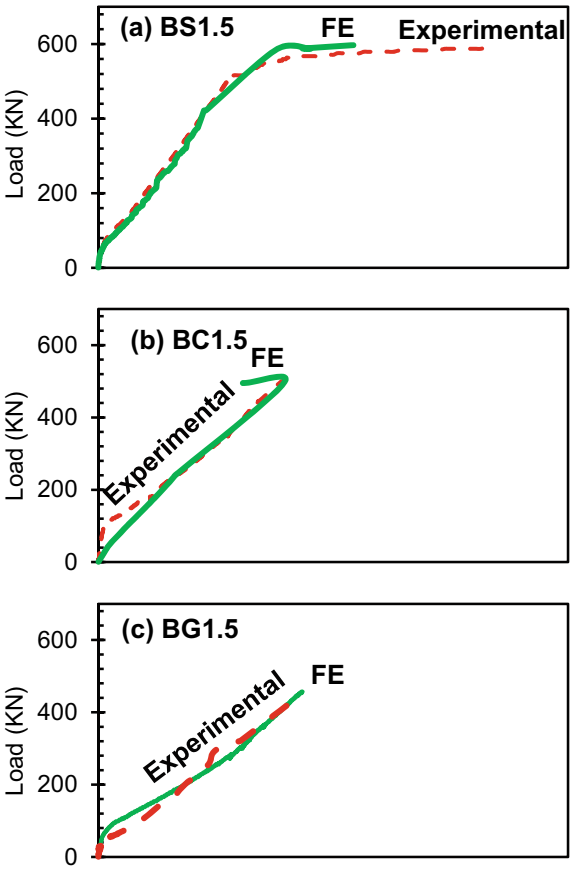

Fig. 6 Load-strain relationship for the reinforcements

c. The FE prototypes were able to copy the characteristics of the beams, tested experimentally, with good accuracy in terms of cracking patterns, load–deflection relationship, load-strain relationship for the reinforcing bars, and the carrying load-capacity.
d. The average value of the shear capacity obtained experimentally to the shear strength obtained by the FE model, (V_{exp}/V_{Model}) for the prototypes, is 1.04 ± 0.02 with 2% COV.

References

1. Ali A (2016) Shear strength and behavior of circular concrete members reinforced with FRP bars and spirals. PhD thesis. University of Sherbrook, Sherbrook, QC, Canada
2. CAN/CSA A23.2-14 (2014) Method of test for concrete. Canadian Standards Association, Rexdale, Ontario, Canada, 203p

3. CAN/CSA S806-12 (2012) Design and construction of building components with fibre-reinforced polymers. Canadian Standards Association, Rexdale, Ontario, Canada, 187p
4. Cervenka V, Jendele L, Cervenka J (2013) ATENA program documentation part 1: theory. Cervenka Consulting Ltd., Prague, Czech Republic
5. Halahla A (2018) Study the behavior of reinforced concrete beam using finite element analysis. In: Proceedings of the 3rd world congress on civil, structural, and environmental engineering (CSEE'18) Budapest, Hungary, 8–10 April 2018, Paper No. ICSENM 103. https://doi.org/10.11159/icsenm18.103
6. NACE International (2014) Corrosion costs and preventive strategies in the United States. FHWA-RD-01-156, Houston

Cross-Sectional Water Velocity in Unsteady Flow Conditions by Pressure Sensors

G. Metri and T.-F. Mahdi

1 Introduction

Mean cross sectional water velocity (U) is essential for the understanding of rivers' behavior. For steady flows, one way to estimate the water velocity is with Chezy's or Manning's uniform equation [2] but these equations don't consider the hysteresis effect of unsteady flows. Therefore, estimating U in unsteady flow conditions is expensive, labor intensive and time consuming through multiple measurements with water flow probes.

For laboratory studies, the particle image velocimetry (PIV) is used to measure the water velocity field [3]. However, it is not applicable over rivers due to its complex calibration and specific operating conditions. Another way to measure the mean cross sectional velocity is by measuring the flow through flowmeters [1], the water depth with water level sensors and computing water velocity with the mass conservation equation (Eq. 1).

$$Q = UA \tag{1}$$

Where Q = discharge (m^3/s), U = mean cross-sectional velocity (m/s) and A = cross-sectional wetted area (m^2).

Therefore, this study objective is to investigate a new approach using pressure sensors to measure cross-sectional water velocity in an unsteady flow with a temporal

G. Metri · T.-F. Mahdi (✉)
Department of Civil, Geological and Mining Engineering, Polytechnique Montreal, 2900 Boul. Édouard-Montpetit, University of Montréal Campus, 2500 Chemin de Polytechnique, Montreal (Quebec) H3T 1J4, Canada
e-mail: tewfik.mahdi@polymtl.ca

G. Metri
e-mail: gabriel.metri@polymtl.ca

S. Walbridge et al. (eds.), *Proceedings of the Canadian Society of Civil Engineering Annual Conference 2021*, Lecture Notes in Civil Engineering 240,
https://doi.org/10.1007/978-981-19-0507-0_17

discretization $\Delta(t)$ of one second. For this purpose, 10 experimentations of unsteady flows composed of 4 measurements each are completed with 3 pressure sensors and one water level sensor over a rectangular experimental flume.

2 Experiments Set-Up

The glass walled rectangular flume is 0.6 m deep, 0.76 m wide, 6.00 m long and has a slope of 0.004 m/m. A 0.76 m × 0.6 m steel gate separates the flume from a 2.35 m^3 tank. All 10 unsteady flow experiments are generated from an instant opening of the steel gate with different initial water levels in the tank. Thus, the experimental hydrograph shapes are similar to an instant dam-break flood which implies a fast variation of water depth and velocity over time. A total of three pressure sensors placed one on top of the others and one water level sensor are located downstream and at the middle of the flume's width to measure respectively the total pressure energy and the water level with the same temporal discretization $\Delta(t = 1s)$.

3 Computation Methods

The unsteady flow Bernoulli's equation [6] computes the cross-sectional water flow velocity in the flume (Eq. 2).

$$\int_1^2 \frac{\partial U_s}{\partial t} ds + \left(gh + \frac{U_s^2}{2} + gz\right)_2 - \left(gh + \frac{U_s^2}{2} + gz\right)_1 = 0 \tag{2}$$

Where h the water level (m), E is the specific energy (m), U_i the flow velocity of the pressure sensor i (m/s), $z_{sensor\,i}$ the distance between the center of the pressure sensor i and the bed of the flume (m), t is the time, s is the longitudinal distance in the flume, g the gravitational acceleration (m/s^2) and z the elevation of the flume's bed. The water level sensor measures the water level over time and is placed 0.2 m upstream of the pressure sensors. therefore, the unsteady parameter $\int_1^2 \frac{\partial U_s}{\partial t} ds$ is neglected because of the short distance between the water level measurement (1) and the pressure sensor (2). The term $\left(gh + \frac{U_s^2}{2}\right)_2$ represent the energy measured by the pressure sensor. Both elevation z_1 and z_2 are similar due to the short distance between point 1 and 2 and the flume's mild slope. Therefore, the specific energy of the pression measurement is defined by Eq. 3.

$$E = (h - z_{sensor_i}) + \frac{U^2}{2g} \tag{3}$$

Therefore, the cross-sectional water velocity is computed from the specific energy equation (Eq. 4).

$$U_i = \sqrt{(E - (h - z_i))2g} \tag{4}$$

The cross-sectional water average velocity is computed with the mean of all U_i. Supposing a 1-D flow, Eq. 5 and 1 computes the wetted area and the discharge over time.

$$A = bh \tag{5}$$

Where b the width of the flume (m). The total flooded volume (TFV) is computed with the trapezoidal rule over time ($\Delta t = 1s$) applied on the measured hydrograph (Eq. 6) [8].

$$\text{TFV} = \frac{\sum_{t=0}^{n-1}(Q_{st} + Q_{s_{t+1}})\Delta t}{2} \tag{6}$$

4 Data Analysis

Every experiment has uncontrollable uncertainties affecting the results [9]. These uncertainties can be considered while evaluating the accuracy and precision of the measurements through the standard deviation σ parameter [10]. However, the small number of experiments per measurements induct a variability in the parameter σ. Therefore, a Markov Chain Monte-Carlo (MCMC) Metropolis-Hasting sampling algorithm calculates the corrected standard deviation of the computed TFV for each initial water level. Figure 2 presents a hypothetical example of the influence of the lack of measurements on the accuracy of the computed mean. Due to the uncertainties on the computed standard deviation present by the lack of measurement, σ would increase compared to the initial value.

The MCMC method is to sample the unnormalized posterior from the bayes equation [4] (Eq. 7) where the density samples of the unnormalized posterior is proportional to the posterior probability density function (PDF).

$$f([\mu, \sigma]|D) = \frac{f(D|[\mu, \sigma])([\mu, \sigma])}{f(D)} \tag{7}$$

where μ is the mean, σ the corrected standard deviation, D the dataset, $f([\mu, \sigma]|D)$ the posterior PDF, $f(D|[\mu, \sigma])$ the Likelihood, $f([\mu, \sigma])$ the prior, $f(D)$ the normalization constant and $f(D|[\mu, \sigma])f([\mu, \sigma])$ the unnormalized posterior PDF. The Normal distribution (Eq. 8) is the proposal PDF used to sample the unnormalized

posterior PDF due to its non-zero probability over its domain which are needed for the Metropolis-Hasting sampling algorithm application [5].

$$f\left([\mu_{s+1}, \sigma_{s+1}]|[\mu_s, \sigma_s]\right) = N([\mu_{s+1}, \sigma_{s+1}]; [\mu_s, \sigma_s], \sigma_q^2) \tag{8}$$

Where σ_q is the standard variation of the proposal, s is the sample's ID and N is the normal distribution. The Metropolis-Hasting sampling algorithm computes a target function (Eq. 9) to evaluates if the next sample will stay at the current location or move to a new one (Eqs. 10 and 11).

$$\tilde{f}\ \left([\mu_{s+1}, \sigma_{s+1}]\right) = \prod_{i=1}^{n} N\left(y_i; \left[\mu_{s+1}, \sigma_{s+1}\right], \sigma_q^2\right) f([\mu, \sigma]) \tag{9}$$

$$\text{if } \frac{\tilde{f}\left([\mu_{s+1}, \sigma_{s+1}]\right)}{\tilde{f}\ \left([\mu_s, \sigma_s]\right)} > 1 \rightarrow [\mu_{s+1}, \sigma_{s+1}] = [\mu_{s+1}, \sigma_{s+1}] \tag{10}$$

$$\text{if } \frac{\tilde{f}(\theta_{s+1})}{\tilde{f}(\theta_s)} < 1 \rightarrow \text{ifrandom} > \frac{\tilde{f}\left([\mu_{s+1}, \sigma_{s+1}]\right)}{\tilde{f}\left([\mu_s, \sigma_s]\right)} \rightarrow$$
$$[\mu_{s+1}, \sigma_{s+1}] = [\mu_s, \sigma_s] else [\mu_{s+1}, \sigma_{s+1}] = [\mu_{s+1}, \sigma_{s+1}] \tag{11}$$

where $\tilde{f}\ ([\mu_{s+1}, \sigma_{s+1}])$ is the target function, i the ID of a measurement, n the total number of measurements, y_i is the measurement of the ID i and random is a randomly generated number between 0 and 1. The Eqs. 12 and 13 present the starting points of μ_0 and σ_0^2 to initiate the Metropolis-Hasting sampling algorithm.

$$\mu_0 = \frac{\sum_{i=1}^{n} y_i}{n} \tag{12}$$

$$\sigma_0^2 = \frac{\sum_{i=1}^{n} (y_i - \mu_1)^2}{n} \tag{13}$$

The starting points of μ and σ impact directly the density sample which is used to represent the posterior PDF. Therefore, the first half of the samples are discarded from the density population in a burn-in phase to ensure that the Monte-Carlo sampling reach the stationary distribution [7]. The MCMC method increases the standard deviation by including the uncertainties from the lack of measurements (Fig. 1). The set formed of 100 000 samples converged with a variability of 0.5% on the corrected standard deviation. This method increases the standard deviation σ by including its uncertainties from the lack of measurements [11] (Fig. 3).

Fig. 1 Experimental set-up: **a** an overall view of the flume, gate and water tank. **b** The water level sensor

5 Validation

The measurements validation is completed by comparing the computed and measured total flooded volume (TFV). The measured TFV (ΔV) is computed from the surface area (A_{tank}) and the water level variation (Δh) in the tank (Eq. 13). After the MCMC metropolis-Hasting sampling algorithm, the coefficient of variation (CV) varies between $CV_{min} = 2.04\%$ and $CV_{max} = 10.3\%$ (Fig. 4). Concerning the accuracy of the experimentations, the relative errors from $e_{r\,min} = 0.09\%$ to $e_{r\,max} = 5.07\%$ and all the measured TFVs are within the range of the computed TFVs uncertainties except for the experiment with the initial water level of 22 cm which has the lowest CV (2.04%). This validation confirms that neglecting the unsteady term in Bernouilli's equation is suitable for the present experimental set-up. Therefore, the precision and the accuracy of the experiments are considered acceptable.

$$\Delta V = Atank \Delta h \tag{14}$$

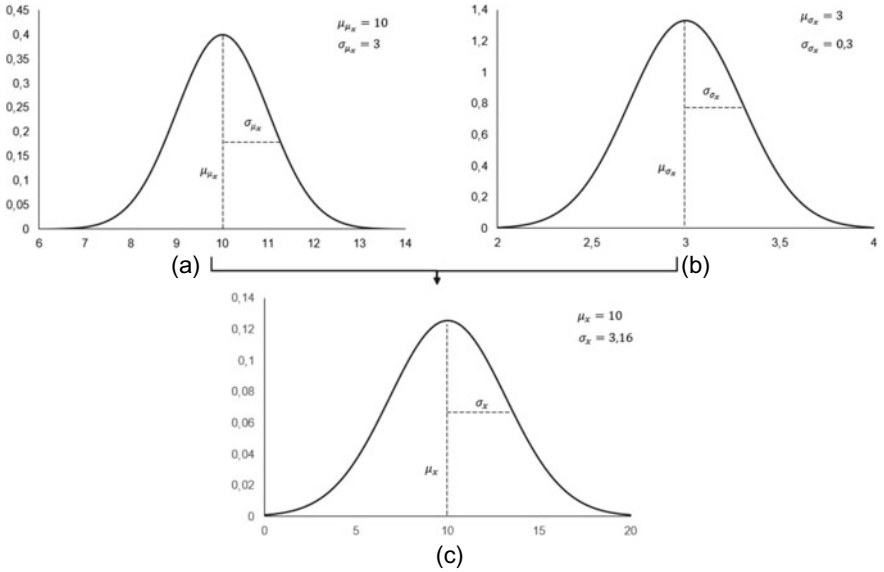

Fig. 2 Example of the Normal distribution for **a** The computed mean with $\mu_{\mu_x} = 10$ and $\sigma_{\mu_x} = 3$. **b** The computed standard deviation with $\mu_{sigma_x} = 3$ and $\sigma_{\sigma_x} = 0.3$. **c** The combination of the mean and standard deviation PDF with $\mu_{\mu_x} = 10$ and $\sigma_{\mu_x} = 3.16$

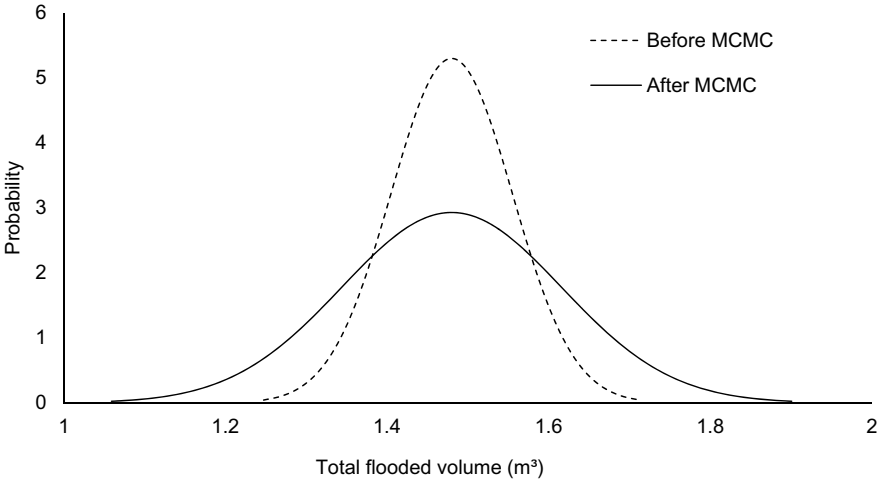

Fig. 3 The influence of the MCMC metropolis-Hasting sampling algorithm on the standard deviation of the computed total flooded volume for an initial water level of 23 cm in the tank

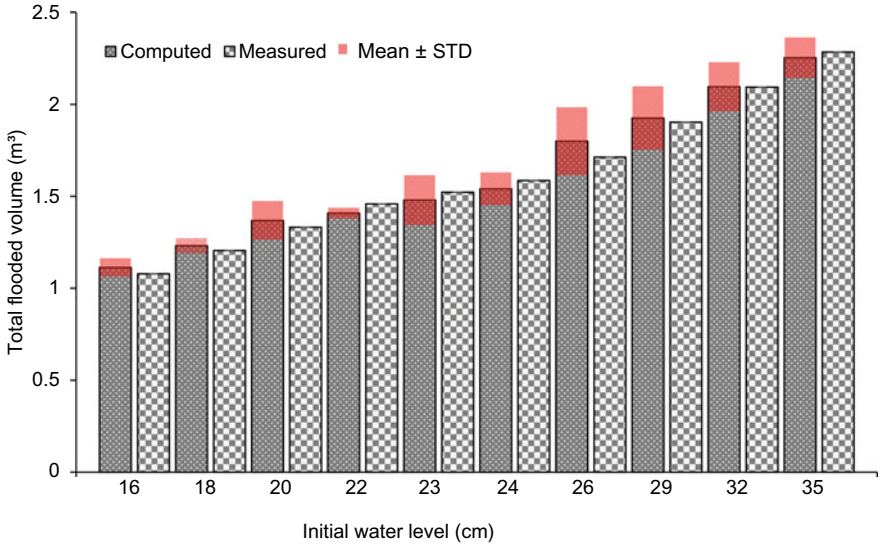

Fig. 4 Comparisons between the computed and measured total flooded volume for all initial water levels

6 Results

The maximum water velocity in the experiments varies between 1.29 m/s and 1.87 m/s. The velocity over time data used to present the results is from an initial water level of 29 cm in the tank (Fig. 5). The mean standard deviation of U over time is 0.17 m/s and the highest uncertainties are located in the first 5 s and the last 20 s of the flood. The beginning of dam-break floods is where the water depth and velocity variation is at its highest. Therefore, the flood wave can be slightly different for each experiment. The uncertainties located at the end of the flood is due to the low water level which can only be measured by 1 pressure sensor ($h < 0.0375$ m) and causes discontinuities in the measurements. This measurement method works for experimental flumes in unsteady flow conditions as long as the water level is above the functioning height of the pressure sensors. The measurement of the mean average cross-sectional velocity supposes that the flow is one-dimensional. However, the use of multiple pressure sensors gives knowledge of the water velocity over the water depth.

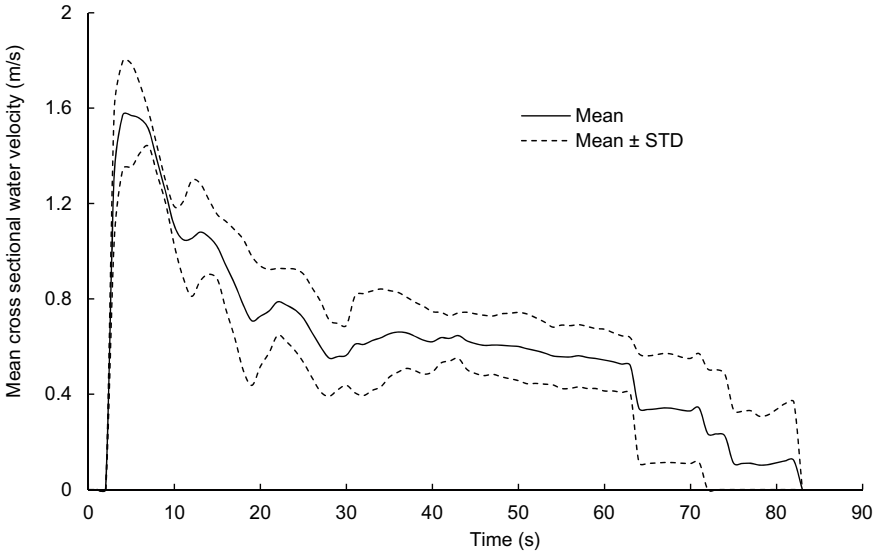

Fig. 5 The mean cross-sectional water velocity profile over time including the uncertainties for an initial water level of 29 cm in the tank

7 Conclusion

Experiments with unsteady flow conditions in a rectangular flume has been conducted to investigate the applicability of pressure sensors to measure the mean cross-sectional water flow velocity over time. A Markov Chain Monte-Carlo Metropolis-Hasting sampling algorithm computed the standard deviation by including the uncertainties from the small number of experiments. Afterward, a validation process comparing the computed and measured total flooded volume (TFVs) evaluates that the experiments precision and accuracy are acceptable. Further studies can estimate the induced error from neglecting the unsteady term in the Bernoulli's equation with a PIV measurement approach. The measured velocity profile over time has a mean standard deviation of 0.17 m/s. Therefore, this study shows a new time effective and simple method to measure average cross-sectional water flow velocity and discharge of unsteady flow conditions with a temporal discretization of 1 s.

Acknowledgements This research was supported in part by a National Science and Engineering Research Council (NSERC) Discovery Grant for the corresponding author, application No: RGPIN-2016-06413, and a Hydro-Quebec and NSERC Collaborative Research and Development Grant, application No: CRSNG RDC 491880-15.

References

1. Beaulieu A, Foucault E, Braud P, Micheau P, Szeger P (2011) A flowmeter for unsteady liquid flow measurements. Flow Meas Instrum 22:131–137. https://doi.org/10.1016/j.flowmeasinst.2011.01.001
2. Choo TH, Hong SH, Yoon HC, Yun GS, Chae SK (2014) The estimation of discharge in unsteady flow conditions, showing a characteristic loop form. Environ Earth Sci 73(8):4451–4460. https://doi.org/10.1007/s12665-014-3731-6
3. Elsinga GE, Scarano F, Wieneke B, van Oudheusden BW (2006) Tomographic particle image velocimetry. Exp Fluids 41(6):933–947. https://doi.org/10.1007/s00348-006-0212-z
4. Goulet J (2020) Probabilistic machine learning for civil engineers. The MIT Press
5. Hill SD, Spall JC (2019) Stationarity and convergence of the metropolis-hastings algorithm: insights into theoretical aspects. IEEE Control Syst Mag 39(1):56–67. https://doi.org/10.1109/MCS.2018.2876959
6. Kwong AHM, Dowling AP (1994) Unsteady flow in diffusers. J Fluids Eng 116(4):842–847. https://doi.org/10.1115/1.2911859
7. Meyn SP, Tweedie RL (1993) Markov chains and stochastic stability, vol 1. Springer, London
8. Rahman QI, Schmeisser G (1990) Characterization of the speed of convergence of the trapezoidal rule. Numer Math 57(1):123–138. https://doi.org/10.1007/BF01386402
9. Taylor J (1997) Introduction to error analysis, the study of uncertainties in physical measurements, 2nd edn
10. van Ravenzwaaij D, Cassey P, Brown SD (2018) A simple introduction to Markov Chain Monte-Carlo sampling. Psychon Bull Rev 25(1):143–154. https://doi.org/10.3758/s13423-016-1015-8
11. Zheng Y, Han F (2016) Markov Chain Monte Carlo (MCMC) uncertainty analysis for watershed water quality modeling and management. Stoch Env Res Risk Assess 30(1):293–308. https://doi.org/10.1007/s00477-015-1091-8

The Effects of Foundation Stiffness on Surface Fault Rupture in Reverse Faults

M Moradi Shaghaghi, M. Tehranizadeh, and B Moradi Shaghaghi

1 Introduction

In terms of distance from the faults, ground motions are divided into far-field and near-field earthquakes. The characteristics of motions in the proximity of a fault zone can be significantly different from those of the far-field. One of these significant and destructive characteristics of near-field motions is surface fault rupture which may cause vital loss of lives and drastic destruction of different structures [10, 11]. The surface fault rupture is the displacement or rupture of the ground surface in the direction of the fault. The importance of this surface rupture has been significantly evident in recent earthquakes such as the 1992 Landers-California earthquake, the 1995 Kobe-Japan earthquake, the 1999 Chi-Chi-Taiwan earthquake, the 1999 Kocaeli-Turkey earthquake and the 1999 Düzce-Turkey earthquake [2, 6, 8].

In 2001 Bray studied the effects of different soil properties on reducing the destructive effects of fault rupture. He made field investigations on 1992 Landers, 1999 Chi-Chi and 1999 Duzce and Kocaeli earthquakes. It was indicated that the type and amount of fault displacement, the depth and properties of soil layers above bedrock play a significant role in the characteristics of surface fault rupture [5, 6]. Moreover, Anastasopoulos and Gazetas investigated the effects of soil-structure interaction on fault rupture path in the 1999 Kocaeli earthquake. They illustrated that the type of the structure's foundation has a significant effect on the response to imposed fault displacements [1, 2].

M. M. Shaghaghi (✉) · M. Tehranizadeh
Faculty of Civil and Environmental Engineering, Amirkabir University of Technology, Tehran, Iran

M. Tehranizadeh
e-mail: tehranizadeh@aut.ac.ir

B. M. Shaghaghi
Faculty of Civil and Environmental Engineering, Tarbiat Modares University, Tehran, Iran

S. Walbridge et al. (eds.), *Proceedings of the Canadian Society of Civil Engineering Annual Conference 2021*, Lecture Notes in Civil Engineering 240,
https://doi.org/10.1007/978-981-19-0507-0_18

Anastasopoulos et al. studied the effects of surcharge load applied to the foundation and the distance of the foundation from fault rupture on the fault rupture-foundation interaction. They concluded that increasing the surcharge load of the foundation would increase the fault rupture-foundation interaction and this may lead to a change in the fault rupture path [4].

In another investigation, Oettle et al. studied the effects of various geotechnical properties and foundation types on the rupture path in dip-slip faults. They stated that in these faults, depth and properties of soil layers above the bedrock have a crucial effect on the rupture path. Besides, they stated that fault displacements could be absorbed by soil layers depending on the height and properties of the layers [9].

Based on the presented literature review, it is apparent that to reduce this destructive effect of near-field earthquakes, all various geotechnical, structural and seismological properties should be studied in detail. One of these important characteristics which can play a crucial role in rupture path is foundation stiffness. Therefore, in this paper, the effects of foundation stiffness on the rupture path of dip-slip faults are studied through numerical analyses.

In some of the seismic design regulations, fault-avoidance-zones have been defined to avoid surface fault rupture. Due to several reasons, implementing these avoidance zones is very difficult, impractical and sometimes senseless. Some of these reasons are listed as follows:

- Distinguishing active faults from inactive ones is a difficult and sometimes costly task. Also, in long structures such as pipelines, bridges, tunnels, embankments, etc., fault interruption in at least one section is inevitable [10], Moradi [12].
- The location of the fault rupture is variable and sometimes does not follow the location of previous cracks and failure occurs in other weaker plates. Therefore, even if the exact location of the fault rupture path is known on the map, sometimes the surface rupture moves several kilometers away [5, 6].
- The propagation of the fault rupture from the bedrock to the ground surface depends on the properties of the soil layers. The geometry and properties of the soil layers dictate the surface rupture path and its type. Sometimes the dispersion and bifurcation phenomena make it difficult to predict the location of the fault by changing the main direction of rupture [6, 7].
- The presence of the structure affects the rupture path and due to the soil-structure-rupture interaction, the pattern of the rupture path could be different from what happens at the free field [4, 8].

2 Finite Element Analysis and Modeling

In this paper, to study the effects of foundation stiffness on the rupture path, static analysis is implemented using finite element software ABAQUS [13]. Since the intensity of destructions in the fault zone are much greater for reverse dip-slip faults, rupture paths in two reverse dip-slip faults with the angles of 45° and 60° and in two different soil types are studied. The soil layer is modeled using the Mohr–Coulomb

Table 1 Properties of soil mediums

Soil type	Density (Kg/m^3)	Modulus of elasticity (MPa)	Poisson ratio	Cohesion (KPa)	Angle of friction (°)
Sand	1800	10	0.30	30	0
Clay	2180	25	0.35	18	32

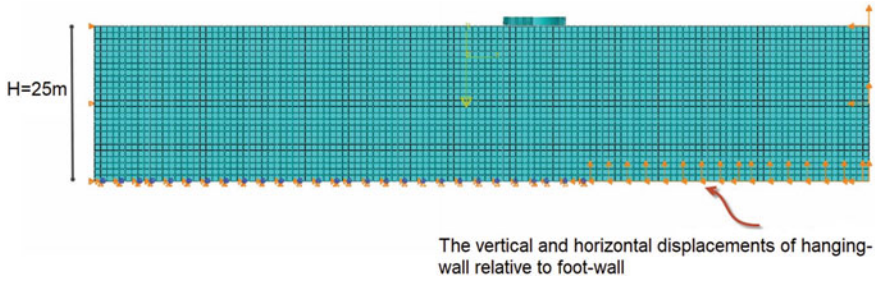

Fig. 1 Schematic soil model with mat concrete foundation and applied fault displacements

failure criterion, which is a linearly elastic-perfectly plastic model. The depth of the soil medium is considered as 25 m. The properties of two soil mediums used in this research are illustrated in Table 1. A schematic model of the 2D soil domain modeled in ABAQUS is illustrated in Fig. 1.

The elements used for modeling the soil layer are plain strain 8-node bilinear, reduced integration with hourglass control elements (CPE8R) with dimensions of 1 m × 1 m [3, 10], Moradi [12].

Furthermore, to study the effects of foundation stiffness on the rupture path, the thickness and length of the foundation are considered as two main variables of this research. The mat foundation is modeled with linear concrete elements with dimensions 0.25 m × 0.25 m and with density of 25 KN/m^3, modulus of elasticity of 26.5 GPa and Poisson ratio of 0.2. The soil-foundation interaction is applied by interface elements between soil and foundation. These elements have high stiffness in compression and zero stiffness in tension, and in shear, they are subjected to Coulomb's friction law [4, 13].

3 Model Verification

The accuracy of modeling soil medium, foundation, soil-foundation interaction and fault displacement is verified by remodeling test No. 29 of paper "Numerical analyses of fault–foundation interaction" by Anastasopoulos et al. This test included a soil layer with a depth of 15 m subjected to a reverse fault with angle 60° and a vertical displacement of 2.5 m at the bottom of the layer [4]. The foundation had a length of

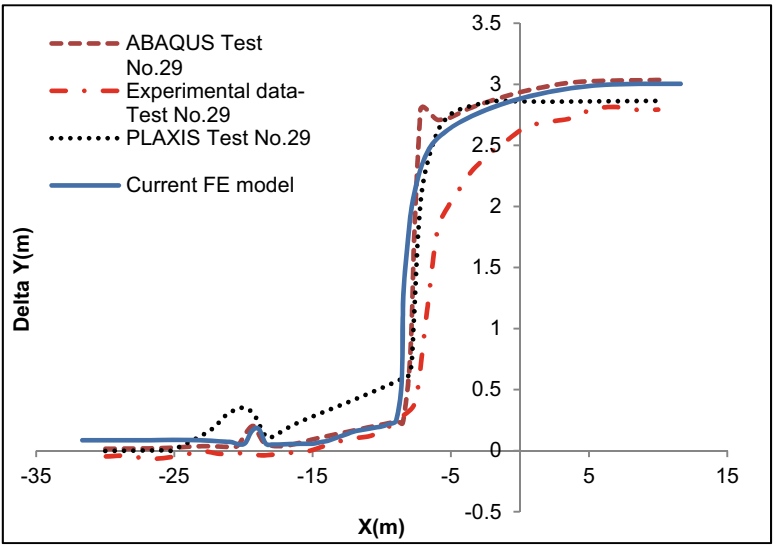

Fig. 2 Comparison of surface vertical displacement of FE model with the results of test No.29 [4]

10 m which was subjected to a surcharge load 90 kPa. The comparison of resulted surface vertical displacement of the FE model of this research with experimental and FE results of the above-mentioned paper obtained using ABAQUS, PLAXIS, are illustrated in Fig. 2.

In Fig. 2, X and Delta Y are surface coordinates of the soil layer and the surface vertical displacement of the soil layer, respectively. In this Figure, the curve with the solid line represents the results of current FE modeling and the dashed and dotted curves represent FE modeling results of test No.29 obtained from ABAQUS and PLAXIS, respectively. Moreover, the dash-dotted curve is related to the experimental results of test No.29.

As it can be seen from Fig. 2, the results obtained from current FE modeling and the results of test No.29 correlate very well.

4 Results and Discussion

4.1 Effects of Foundation Thickness on the Rupture Path

In this part, the effects of foundation thickness as an important parameter of its stiffness on the rupture path is studied. The displacements of the different points of the ground surface of the free field case as a base are compared with the corresponding displacements of cases with different foundation thicknesses. The thickness of the foundation is assumed to be 0.5 m, 1 m, 1.5 m, 2 m and 3 m.

4.1.1 Rupture Path for Reverse Fault with Angle of 45°

The rupture paths for two different soil mediums are shown in Fig. 3. In this Figure, the first row of each column illustrates the free-field case for each soil domain. The rows "b" to "f" illustrate the rupture path when foundations with the thicknesses (d_f) of 0.5 m, 1 m, 1.5 m, 2 m and 3 m are present, respectively. Figure 3 corresponds to the strain contour obtained from ABAQUS.

It can be seen that the rupture path for the cases with foundations is completely different from that one of the free-field case. In addition, as the thickness of the foundation increases, the fault rupture changes its path gradually. For clay medium, which is depicted in Fig. 3a, in the cases with d_f greater than 1 m, the rupture path is directed out of the foundation. Whereas, for redirecting rupture path in the sandy domain, the thickness of the foundation should be greater than 1.5 m (See Fig. 3b).

Figure 4 illustrates the vertical displacements of the various points of ground surface for the free-field case and the cases with different foundation thicknesses. In this figure, vertical lines indicate the location of the foundation. As it is shown in Fig. 4 to examine the effects of thickness on rupture path the mid-point of foundation is located in the middle of surface rupture of free field case. It is observed that with increasing the thickness, rupture path moves out of the foundation, gradually.

According to Figs. 3 and 4, it is obvious that the changes in the rupture path for the clay domain are more noticeable than the sandy domain. Also, in clay medium, the rupture path moves out of the foundation in cases with low foundation thickness.

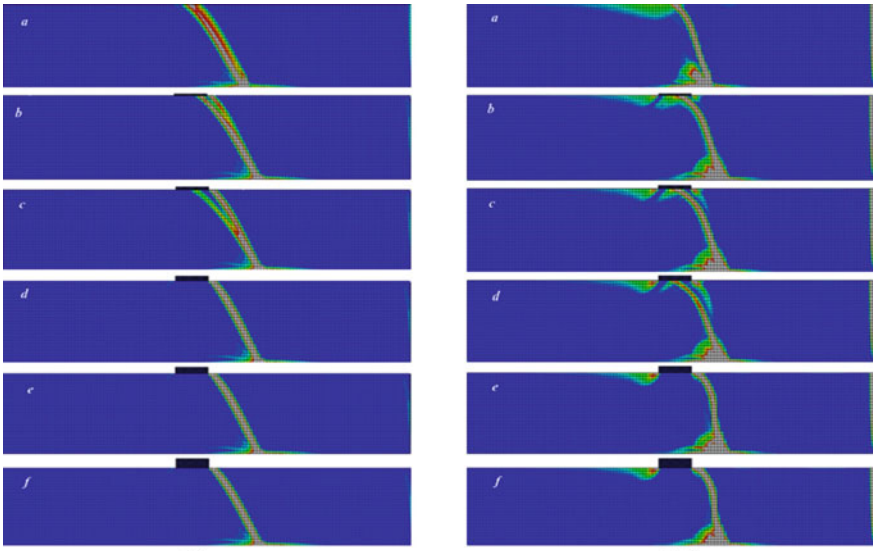

Fig. 3 Rupture path for foundation with different thicknesses in fault 45°. **a** free-field **b** $d_f = 0.5$ m **c** $d_f = 1.0$ m **d** $d_f = 1.5$ m **e** $d_f = 2.0$ m **f** $d_f = 3.0$ m and **A** Clay medium **B** Sand medium

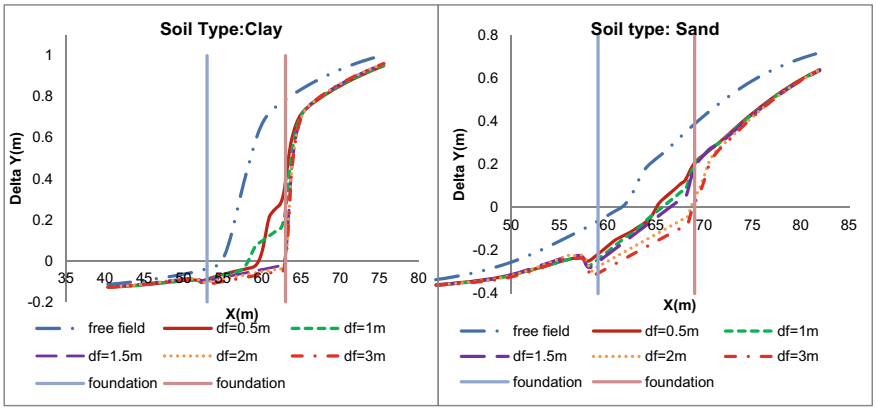

Fig. 4 Vertical displacement of ground surface in fault 45° (Foundation thickness effect)

By taking these results into consideration, it can be concluded that by reducing the angle of friction of soil medium and consequently its shear strength, the effects of soil-structure interaction on the variation of rupture path are more significant.

4.1.2 Rupture Path for Reverse Fault with Angle of 60°

Strain contours and rupture paths obtained from different models with the displacements of fault with angle of 60° are illustrated in Fig. 5. Moreover, diagrams of the vertical displacement of the surface are depicted in Fig. 6 for clay and sand mediums.

According to the rupture paths shown in Fig. 5, it can be seen that the results obtained for models with fault 60° are similar to the ones of fault 45°. Thus, for the clay medium (see Fig. 5a), the rupture path changes gradually by increasing the foundation thickness and moves out of the foundation in thicknesses greater than 1 m, while this value is equal to 1.5 m for sand soil (see Fig. 5b). In addition, Figs. 5 and 6 demonstrate the fact that like the fault 45°, increasing foundation thickness and consequently foundation stiffness has clear positive effects on changing the rupture path in fault with angle of 60°.

4.2 Effects of Foundation Length on the Rupture Path

In this part of the paper, the effects of the foundation length as another important variable in its stiffness are studied on the rupture path. For this purpose, the length of foundations is assumed to be 5 m, 10 m, 15 m and 20 m in the models. It should be noted that in all of these models the thickness of the foundation is assumed to be constant and equal to 1.5 m.

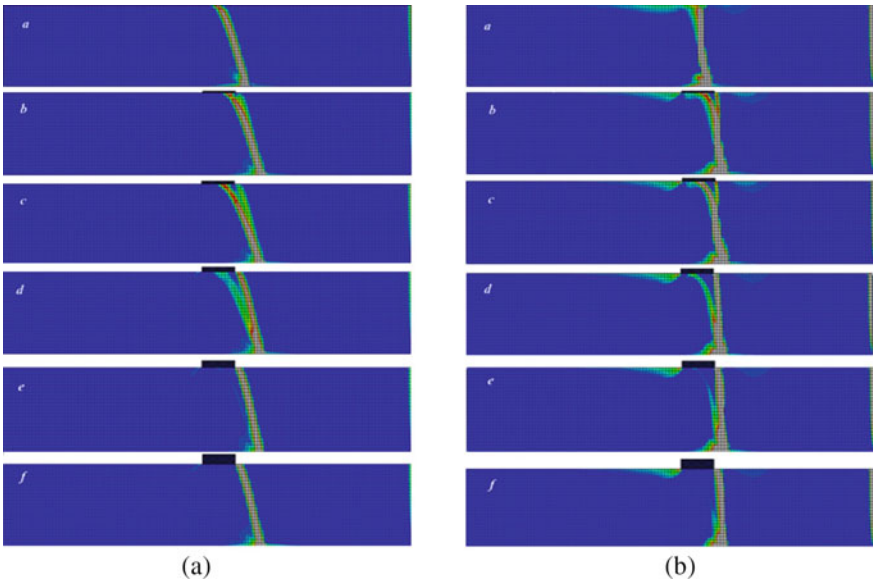

Fig. 5 Rupture path for foundation with different thicknesses in fault 60°. **a** free-field **b** $d_f = 0.5$ m **c** $d_f = 1.0$ m **d** $d_f = 1.5$ m **e** $d_f = 2.0$ m **f** $d_f = 3.0$ m and **A** Clay medium **B** Sand medium

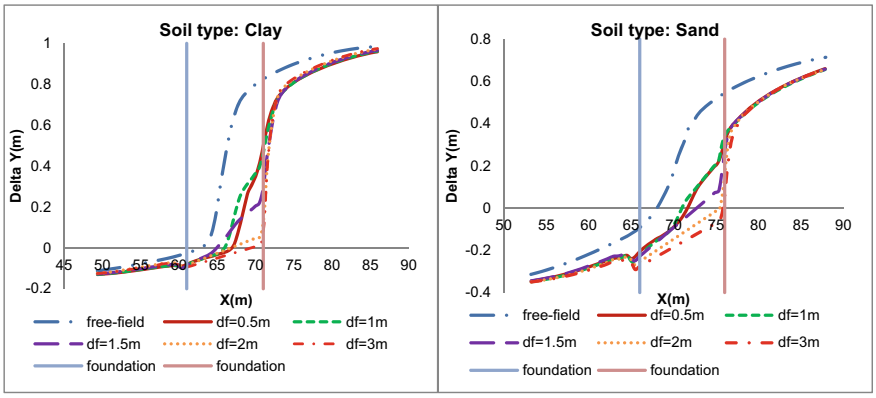

Fig. 6 Vertical displacement of ground surface in fault 60° (Foundation thickness effect)

4.2.1 Rupture Path for Reverse Fault with Angle of 45°

The resulted rupture paths obtained from models with different foundation lengths for the fault with the angle of 45° are demonstrated in Fig. 7 for clay and sand soil types. In Fig. 7, rows "a" illustrate the rupture paths for free-field cases and rows "b" to "f" demonstrate models with L_f equal to 5 m to 20 m for each soil medium.

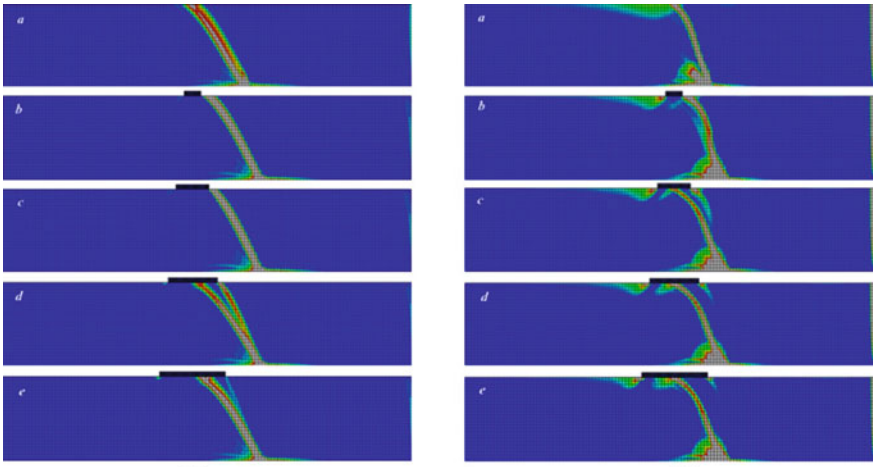

Fig. 7 Rupture path for foundation with different length in fault 45°. **a** free-field **b** $L_f = 5$ m **c** $L_f = 10$ m **d** $L_f = 15$ m **e** $L_f = 20$ m and **A** Clay medium **B** Sand medium

In addition, the vertical displacements of different points of the ground surface are available in Fig. 8.

According to Figs. 7 and 8, it is obvious that increasing the length of the foundation has a negative effect on the rupture path and by increasing the foundation length and consequently reducing foundation stiffness, rupture path approaches to the center of the foundation for two soil types and this may lead to intensive destruction. In other words, the rupture is trapped under the foundation because of two main reasons: first, the reduction of foundation stiffness reduces the effect of soil-structure interaction

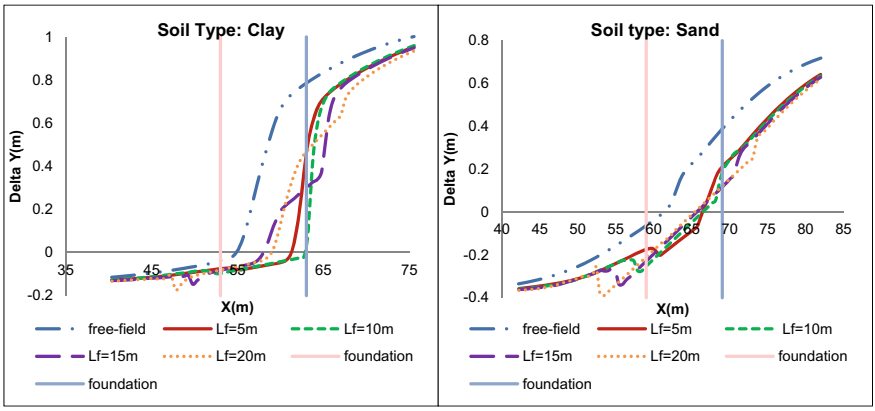

Fig. 8 Vertical displacement of ground surface in fault 45° (Foundation length effect)

on the rupture path and second, as the length of the foundation increases, it is very hard for rupture to move out of foundation due to its large length.

4.2.2 Rupture Path for Reverse Fault with Angle of 60°

The strain contours and consequently the rupture path and the vertical displacement of the ground surface of models with various L_f in two different soil domains with fault 60° are depicted in Figs. 9 and 10, respectively. It can be seen that results obtained

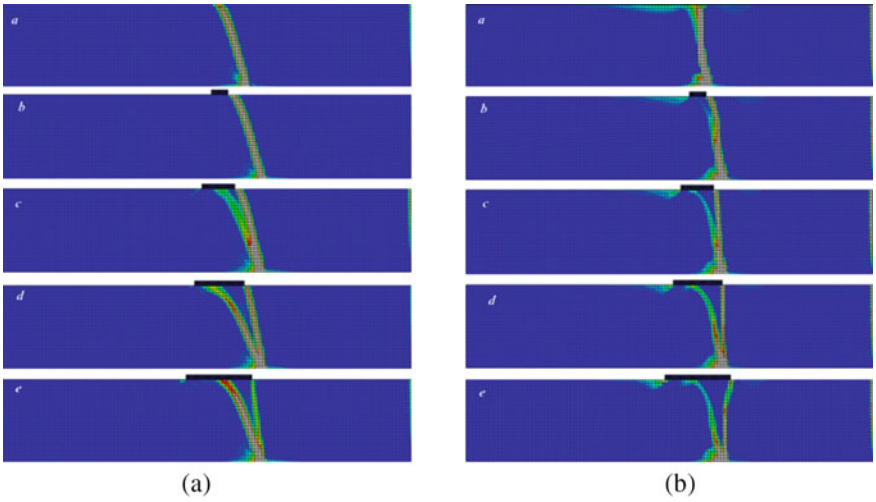

Fig. 9 Rupture path for foundation with different length in fault 60°. **a** free-field **b** $L_f = 5$ m **c** $L_f = 10$ m **d** $L_f = 15$ m **e** $L_f = 20$ m and **A** Clay medium **B** Sand medium

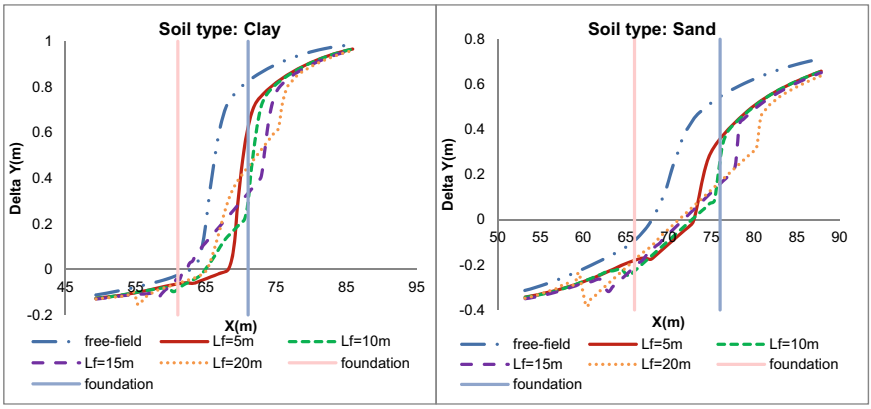

Fig. 10 Vertical displacement of ground surface in fault 60° (Foundation length effect)

for the models with fault 60° are similar to the results of fault 45°. In other words, the increase in the length of the foundation leads the rupture path to the center of the foundation especially in the models with clay medium. As it was discussed earlier, in the clay medium the effects of soil-structure interaction are more significant.

Taking the results shown in Figs. 9 and 10 into consideration, it is obvious that the increase in the length of the foundation has a significant unfavorable effect on the rupture path. Furthermore, when the length of the foundation is larger than 15 m, the rupture is trapped under the foundation and causes an excessive rotation which might probably lead to destruction.

5 Conclusion

In this paper, the effects of foundation stiffness on the rupture path of the reverse faults with angles of 45° and 60° are studied for two different clay and sand soil mediums. Two parameters of foundation thickness and foundation length are the variables of studies. The most significant results obtained from analyses are as follows:

- The foundation stiffness has a significant effect on the rupture path. By increasing the foundation stiffness (increasing the thickness or reducing the length of the foundation) rupture path moves out of the foundation.
- The rupture path moves out of the foundation when the thickness of the foundation is greater than 1.0 m and 1.5 m for the clay and sand medium, respectively.
- When the length of the foundation is greater than 15 m, rupture moves toward the center of the foundation gradually in both soil types especially in the clay medium.
- The effects of soil-structure interaction on the rupture path get more intense by reducing the angle of friction of soil and consequently reducing shear strength. In other words, the effects of soil-structure interaction on changing the rupture path are more significant in clay medium than sand medium.

References

1. Anastasopoulos I, Gazetas G (2007) Foundation-structure systems over a rupturing normal fault: part i. Observation after the Kocaeli 1999 earthquake. Bull Earthq Eng 5:253–275
2. Anastasopoulos I, Gazetas G (2007) Foundation-structure systems over a rupturing normal fault: part ii. Analysis of the Kocaeli case histories. Bull Earthq Eng 5:277–301
3. Anastasopoulos I, Gazetas G, Bransby MF, Davies MCR, El Nahas A (2007) Fault rupture propagation through sand: Finite-element analysis and validation through centrifuge experiments. J Geotech Geoenvironmental Eng 133(8):943–958
4. Anastasopoulos I, Callerio A, Bransby MF, Davies MCR, El Nahas A, Faccioli E, Gazetas G, Masella A, Paulocci R, Pecker A, Rossignol E (2008) Numerical analyses of fault-foundation interaction. Bull Earthq Eng 6:645–675

5. Bray JD, Seed RB, Seed HB (1994) Analysis of earthquake fault rupture propagation through cohesive soil. J Geotech Eng ASCE 120(3):562–580
6. Bray JD (2001) Developing mitigation measures for the hazard associated with earthquake fault rupture. In: Seismic fault-induced failures- possible remedies for damage to urban facilities. University of Tokyo Press, pp 55–80
7. Cole DA Jr, Lade PV (1984) Influence zones in alluvium over dip-slip faults. J Geotech Eng Div ASCE 110(5):599–615
8. Faccioli E, Anastasopoulos I, Gazetas.G, Callerio, A. and Paulocci, R. (2008) Fault rupture-foundation interaction: selected case histories. Bull Earthq Eng 6:557–583
9. Oettle NK, Bray JD (2013) Geotechnical mitigation strategies for earthquake surface fault rupture. J Geotech Geoenvironmental Eng 139(11):1864–1874
10. Mortazavi M (2014) Two- dimensional numerical modeling of reverse fault rupture propagation through soil and its application for earth dams, PhD thesis, Amirkabir University of Technology, Tehran, Iran
11. Mortazavi Zanjani M, Soroush A (2014) Numerical modeling of fault rupture propagation through two-layered sands. Sci Iran A 21(1):19–29
12. Moradi Shaghaghi M (2014) Design criteria for buildings in near fault, MSc thesis, Amirkabir University of Technology, Tehran, Iran
13. Simulia A (2013) 6.13 documentation 2013. Dassault Systems SIMULIA Corporation

Simplified Approach for Fragility Analysis of Highway Bridges

A. Diot, A. Farzam, M.-J. Nollet, and A. Abo El Ezz

1 Introduction

The Southeastern part of the Province of Québec is considered as a moderate seismic hazard zone [7]. However, the high density of population in urban areas such as Montreal and Québec city increases the level of seismic risk [1]. Safeguarding the capacity of a highway bridge network to carry traffic flow after an earthquake is essential for emergency response and recovery activities after strong earthquake events [9]. Fragility analysis that quantifies the probability of damage as function of shaking intensity is an effective approach to evaluate the expected degree of bridge damage and its corresponding post-earthquake functionality [8, 17].

In the province of Québec, 70% of bridges and overpasses were built between 1960 and 1980 [11, 12], when seismic design provisions were not as stringent as current seismic design requirements [5]. In this context, the evaluation of seismic impacts on bridges is crucial to mitigation, emergency and recovery planning for a transportation network [15]. Span failure, damage to bearings, piers and abutments are commonly reported after strong earthquake shaking [18].

The present study of fragility analysis applies a methodology originally proposed for single and multi-span bridge classes in the United States [4] and implemented in the well-known earthquake loss estimation software Hazus [6]. It applies a nonlinear

A. Diot · A. Farzam (✉) · M.-J. Nollet
Department of Construction Engineering, École de Technologie Supérieure, Quebec, QC, Canada
e-mail: azarm.farzam.1@ens.etsmtl.ca

A. Diot
e-mail: antoine.diot.1@ens.etsmtl.ca

M.-J. Nollet
e-mail: Marie-Jose.Nollet@etsmtl.ca

A. A. E. Ezz
Natural Resources Canada, Quebec, QC, Canada

S. Walbridge et al. (eds.), *Proceedings of the Canadian Society of Civil Engineering Annual Conference 2021*, Lecture Notes in Civil Engineering 240,
https://doi.org/10.1007/978-981-19-0507-0_19

static method for fragility curve development. The simplified fragility model is adapted here for seismic hazard in Québec. This approach is proposed as a simplified alternative to rapidly estimate fragility of typical bridges compared to dynamic time history analysis and detailed finite element modelling [14, 19], which requires high computational demand and processing time of input and output data. The aim of this study is to assess the capability of this simplified model to predict the probable damage to bridges in Québec region. A comparative analysis is conducted on Québec multi-span bridge classes between the results of a modified version of the simplified model [4] and those obtained from dynamic analysis [19]. More specifically, the effect of the earthquake magnitude and distance on the fragility curves and their median peak ground acceleration (PGA) for ground motion compatible to Quebec seismicity is investigated.

2 Methodology

The simplified methodology defines fragility curves for a given damage state in terms of (PGA) as seismic intensity measure. The median PGA at the performance point is reached when seismic demand (C_d) is equal to bridge capacity (C_c). The seismic demand is defined as a function of the effective period (T_{eff}) of the bridge and the capacity is dependent on the geometrical and material parameters of the bridge. Figure 1 summarizes the main steps of the methodology with corresponding parameters explained in the following sections.

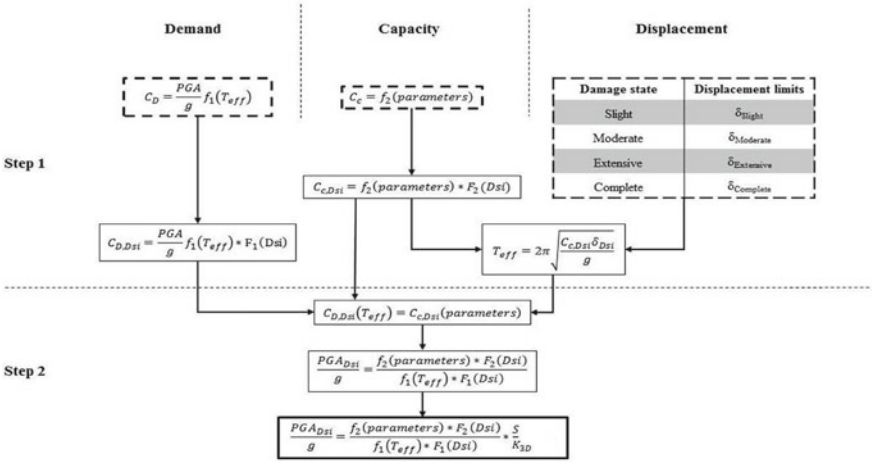

Fig. 1 Summary of the simplified fragility methodology

Table 1 Damage states and corresponding failure mechanisms and drift threshold [4]

Damage state	Displacement thresholds bearings [m]	Pier drift threshold (%)
Slight damage	0.05	0.5
Moderate damage	0.1	1.0
Extensive damage	0.175	2.0
Complete	0.3	5.0

2.1 Damage States

Fragility curves are calculated for four damage states (slight, moderate, extensive and complete) determined for piers and bearings and the corresponding displacement threshold described in Table 1.

2.2 Bridge Capacity

Bridge capacity for each damage state is determined for two different cases: (a) bridges seated on strong bearings with weak piers and (b) bridges seated on weak bearings with strong piers. Bridge capacity for case (a) is expressed by Eq. 1:

$$C_{c,\mathrm{Dsi}} = \lambda_{Q,Dsi} k_p \frac{D}{H} \tag{1}$$

where k_p is a coefficient relative to the geometrical parameters, the material properties and the loading, D is the column diameter (or depth transverse to the axis of bending) and H is the column height. The capacity is then modified for each damage state taking into account the degradation of structural elements by a coefficient $\lambda_{Q,Dsi}$ (Table 2).

Where ξ is a fixity factor and j is an internal lever arm coefficient.

For case (b) bridges seated on weak bearings with strong piers, the bridge capacity is expressed by:

$$C_{c,\mathrm{Dsi}} = \mu_{t,\mathrm{Dsi}} \tag{2}$$

Table 2 Modification factors for capacity [4]

Damage State	λ_Q
Slight	1
Moderate	0,6
Extensive	$\frac{\xi}{k_p}$
Complete	$\frac{j\xi}{k_p}$

where μ_t is a coefficient of sliding friction of the bearings in the transverse direction. It is equal to 0.36 for neoprene bearings [14].

2.3 Seismic Demand

The seismic demand is defined by an idealized input response spectrum as shown in Fig. 2. The first part represents the constant acceleration for short periods and in the second part, the acceleration demand is decreasing by the ratio ($1/T$) for long period response. The demand spectrum is defined in function of the effective period T_{eff} as by Eq. 3:

$$C_{d,Dsi}(T_{eff}) = \frac{PGA_{Dsi}}{g} * min \begin{cases} \frac{S_a(0.3s)}{PGA} * \frac{1}{B_{S,Dsi}} \\ \frac{S_a(1s)}{PGA} * \frac{1}{T_{eff}} * \frac{1}{B_{L,Dsi}} \end{cases} \quad (3)$$

The seismic demand is then modified for each damage state by coefficients $B_{S,Dsi}$ and $B_{L,Dsi}$ for short and long period, to take into account hysteretic energy dissipation at the response level corresponding to each damage state (Fig. 2).

T_{av} is defined as the transition period between the constant acceleration and the decrease of acceleration and is given by Eq. 4:

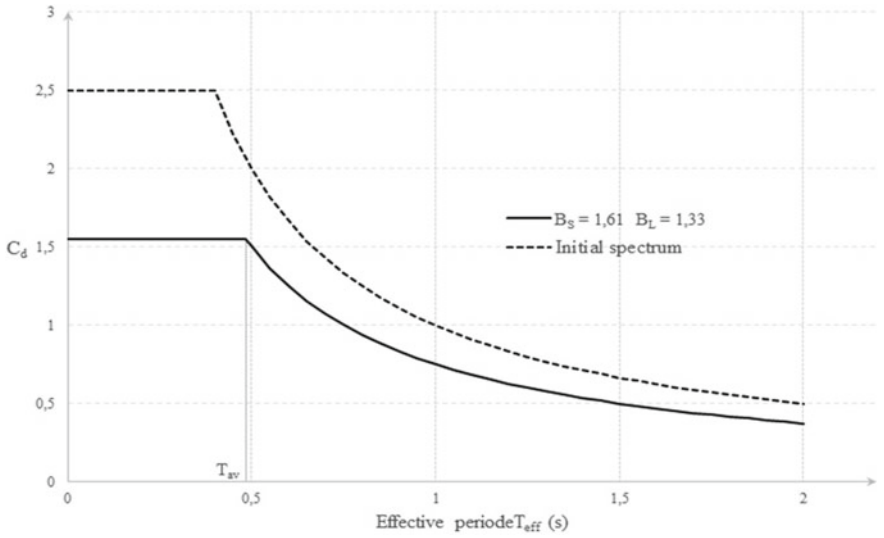

Fig. 2 Input seismic demand spectrum and modified spectrum with coefficient Bs and Bl for energy dissipation at slight damage state

Table 3 Modification coefficients for demand spectrum [4]

Damage State	Piers		Bearings	
	BS	BL	BS	BL
Slight	1,61	1,33	2	1,5
Moderate	1,84	1,44	2	1,5
Extensive	1,93	1,49	2	1,5
Complete	2	1,54	2	1,5

$$T_{av} = \frac{S_a(1)}{S_a(0.3)} * \frac{B_{S,Dsi}}{B_{L,Dsi}} \tag{4}$$

$B_{S,Dsi}$ and $B_{L,Dsi}$ coefficients were developed for weak piers capacity (a) and weak bearings capacity (b) (Table 3).

2.4 Determining Median PGA

The median peak ground acceleration for a damage state PGA_{DSI} is determined based on whether the effective period T_{eff} of the considered damage state D_{si} is greater or smaller than the T_{av}. (Eq. 5). If T_{eff} is less than T_{av}, the short period response governs and if T_{eff} is greater than the T_{av}, the long period response governs. For most of multi-span bridges, the T_{eff} is typically larger than the T_{av}.

$$\frac{PGA_{Dsi}}{g} = \max \begin{cases} C_{c,Dsi} * \frac{PGA}{S_a(0.3)} B_{S,Dsi} \\ C_{c,Dsi} * \frac{T_{eff}}{1} * \frac{PGA}{S_a(1)} B_{L,Dsi} \end{cases} \tag{5}$$

where T_{eff} is determined by Eq. 6:

$$T_{eff} = 2\pi \sqrt{\frac{\delta_{Dsi}}{C_{c,Dsi} * g}} \tag{6}$$

and δ_{Dsi} is the displacement at the top of the pier as a function of the height of the pier and the drift threshold of piers for each damage state (see Table 1).

It should be noted that for the case of T_{eff} larger than the T_{av}, the factor, K_{3D} is added to consider additional contributions to the resistance in the long period response due to the three-dimensional arch action in the bridge deck. The values of K_{3D} depend on the span type, the number of spans and the bearing type and vary from 0.09 for high steel rocker bearings to 0.33 for continuous bridges [4].

2.5 *Bridge Inventory*

The database from the Ministry of Transportation of Québec counts about 9400 bridges [13] where there are 2672 multi-span bridges [19]. Fragility functions are developed for bridge classes defined based on material (concrete, steel), the number of span (single span or multiple span), the span continuity (continuous, discontinuous, in-span hinges or simply supported), the pier type (single column bent, multiple column bents, or pier wall), the bearing type and the abutment type. Table 4 describes the correspondence between the classification of bridges used in the study of [4] and Tavares [19] who studied the nonlinear response of typical Québec bridges under dynamic time history analysis. For example, the multi-span continuous concrete bridge class from Tavares [19] corresponds to the continuous concrete from [4]. The number of bridges in each class in the MTQ database is also listed [13]. MTQ document on inventory of structures [10] classifies bridges mainly by the presence of girders, slab, arc, cable or overpasses. For example, reinforced concrete slab bridge from the MTQ inventory [10] corresponds to both classes of multi-span continuous concrete and multi-span continuous slab as defined by Tavares.

3 Comparative Analysis

The simplified method is first adapted to Québec seismicity by providing demand spectra for different magnitude and distance combinations. The objective is to assess the capability of the adapted simplified model to predict the probable damage to bridges in Québec.

The comparison includes median *PGA* and fragility curves for five bridge classes (Multi-span continuous Concrete, Multi-span continuous Slab, Multi-span continuous Steel, Multi-span simply supported Concrete, Multi-span simply supported Steel), for both capacity models, cases of weak piers (a) and weak bearings (b), and for 8 different magnitude-distance combinations (M6 with distance 10, 15, 20 and

Table 4 Classification of bridges

Basöz and Manders	Tavares	Number of bridges in MTQ database
Continuous Concrete	Multi-span continuous (MSC) Concrete MSC Slab	563 289
Continuous Steel	MSC Steel	177
Multi-Column Bent simply supported	Multi-span simply supported Concrete Multi-span simply supported Steel	664 201

Table 5 Distance and magnitude combinations for seismic demand analysis

Magnitude	Distance (km)			
M6	10	15	20	30
M7	15	25	50	100

30 km and M7 with distance 15, 25, 50 and 100 km), a total of 16 sets of data per bridge class.

PGA values calculated from the adapted simplified model are then compared with the median *PGA* obtained from dynamic time history analysis (THA) data [19]. Results used from Tavares [19] are median calculated for different hazard scenario compatible with Québec region [2] based on four series of ground motion time histories (GMTH) analysis developed for M6 with distance range: 10–15 km and 20–30 km. and M7 with distance: 15–25 km and 50–100 km. It should be noted that in Tavares study some damage states were not reached, such as complete damage state for MSC-Concrete and MSC-Steel, and their study reports only slight damage state median for MSSS-Steel.

Hazard

To adapt the simplified fragility model to Québec region, the hazard is computed for two magnitudes and four distances (Table 5) based on ground motion prediction equation (GMPE) by [3]. The AA13 GMPE for Eastern Canada is currently recommended by the National Building Code of Canada NBCC [16] and is available as discrete values in lookup tables. To facilitate implementation, GMPE is approximated through regression analysis to a closed-form equation. The considered magnitudes and distances are integrated in the closed-form equation to calculate the *PGA*.

3.1 Median-PGA Statistics

Mean values of median *PGA* given by the adapted simplified model are presented in Fig. 3 in dashed lines along with the THA data from Tavares [19] in solid lines. Results are given for both capacity models (weak piers capacity model and weak bearings capacity model), the 8 different combinations of magnitude and distance and for the 5 bridge classes. In general, the mean values of median-*PGA* predicted by the simplified model are higher than values obtained from dynamic analysis by Tavares. The larger average difference for all damage states is observed for MSC Concrete with 40% and the closest results are for MSC Steel with 27%. It should be noted that the THA model used by Tavares does not provide separate fragility results for piers and bearings since the failure mechanisms are activated temporally during the dynamic analysis when the corresponding displacement threshold for a specific damage state are reached for all modelled bridge components (piers, bearings, abutments). Therefore, in the simplified analysis, the median PGA values from both cases of (weak piers capacity

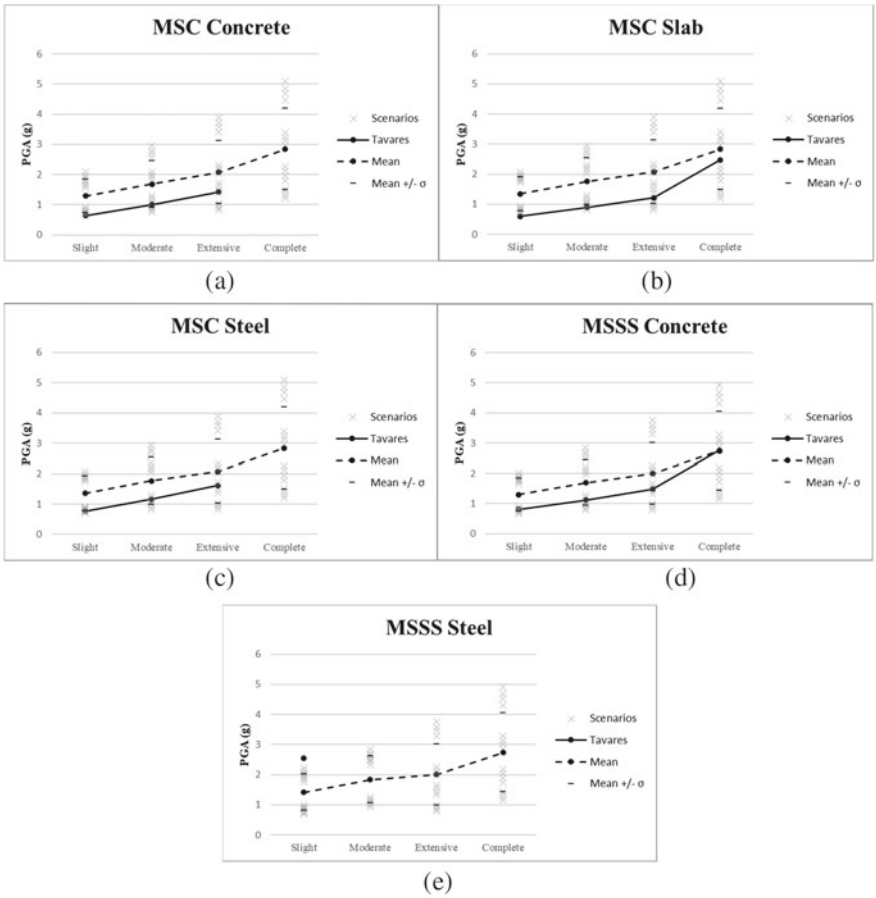

Fig. 3 Median PGA for different damage states (mean values in dashed line and Tavares data in solid line) **a** Multi-span continuous Concrete, **b** Multi-span continuous Slab, **c** Multi-span continuous Steel, **d** Multi-span simply supported Concrete **e** Multi-span simply supported Steel

model and weak bearings capacity model) are considered in the statistical analysis since a specific dominant failure mechanism was not identified a priori for the case study bridge classes.

The 16 realizations of the median *PGA* calculations from the simplified model are then statistically analyzed to generate for each damage state, a mean and standard deviation of the *PGA* thresholds (Table 6). It can be observed on Fig. 3 that the median *PGA* from THA [19] are within one standard deviation of the median *PGA* values from the simplified model for all bridge classes, except for MSSS-Steel slight damage state.

The overall difference in the median *PGA* is attributed to: (1) the structural analysis method (dynamic vs non-linear static) and, (2) the difference between the two

Table 6 Mean and standard deviation statistics for the median PGA estimated from the simplified model for each bridge class

Damage state	Median PGA	MSC-Slab	MSC-Steel	MSC-Concrete	MSSS-Concrete	MSSS-Steel
Slight	Mean (g)	1.25	1.26	1.19	1.22	1.34
	σ (g)	0.53	0.53	0.50	0.52	0.59
Moderate	Mean (g)	1.62	1.63	1.54	1.59	1.73
	σ (g)	0.68	0.69	0.67	0.68	0.73
Extensive	Mean (g)	1.89	1.89	1.89	1.86	1.86
	σ (g)	0.88	0.88	0.88	0.88	0.88
Complete	Mean (g)	2.59	2.59	2.59	2.56	2.56
	σ (g)	1.15	1.15	1.15	1.15	1.15

methods in the values assigned to the damage state thresholds for the piers and the bearing.

For the MSSS steel: in dynamic analysis, the predominant failure mechanism is the bearing sliding without any damage in the piers [19] in addition to that only one damage state has been reached from their analysis. However, in the simplified model, it is assumed that the two failure modes (weak-piers) or (weak-bearings) are both considered in the statistical model for a total of 16 scenarios. Given that the failure in the piers typically predict lower *PGA*, the median results of the statistical analysis showed overall lower *PGA* values.

3.2 Fragility Curves

The mean values of the median *PGA* obtained from the simplified model for each damage state are used to generate fragility curves using a lognormal standard deviation parameter (β) of 0.6 [4]. Figure 4 presents the mean fragility curves from the simplified model combining all magnitude distance scenarios and both weak piers and weak bearings conditions for the MSSS concrete bridge class, which is the most commonly found in Québec inventory. Fragility curves are shown with the upper and lower-bound limits. The THA (Tavares) results are found to be within the upper and lower-bound limits of the simplified model for all damage states. However, in terms of average fragility curves, the simplified model tends to underestimate the fragility (i.e. predict higher median *PGA* values compared to THA) and therefore would predict lower damage potential. On the other hand, the complete damage state average fragility curve shows better matching with the THA.

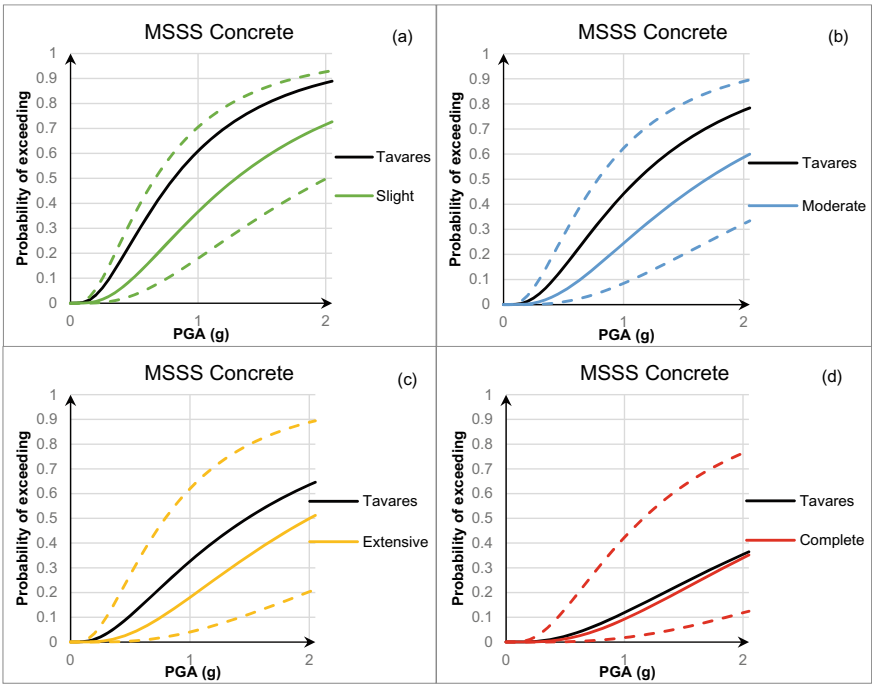

Fig. 4 Fragility curves of mean (in solid lines), upper and lower bounds (dashed lines) for each damage state, and in black results from Tavares

4 Conclusion

A simplified fragility model for bridge classes originally proposed by [4] has been adapted in this study to generate fragility curves for different bridge classes in Québec with consideration of its regional seismicity. The model is applied with consideration of 8 different magnitude-distance scenarios, and two capacity models (weak piers and weak bearings). Considering 16 combinations for each bridge class allows to obtain statistical models for the median *PGA* for each damage state and to develop fragility curves with upper and lower bounds. In the simplified fragility model, it has been observed that the median *PGA* values are higher for weak bearings capacity model than for weak piers capacity model. Both piers and bearings can sustain damage from earthquake shaking, however, it is difficult to predict which one will occur first or would dominate the failure mechanism of the bridge. Therefore, the two capacity models are considered in the estimation of the fragility parameters. The simplified model results were compared with the results of time history analysis (THA) [19]. The THA (Tavares) results are found to be within the upper- and lower-bound limits of the simplified model for all damage states. However, in terms of average fragility curves, the simplified model tends to underestimate the fragility (i.e. predict higher

median *PGA* values compared to THA) and therefore would predict lower damage potential.

Further studies can improve the method related to the capacity estimation for other types of bridge piers and bearings. Moreover, drift threshold used to characterize the damage state can be further refined to better reflect piers conditions for Québec bridges based on structural testing. Based on the inventory study, single-span bridges were reported to be the most frequent bridges in the Province of Québec. However, fragility analyses are scarce for this type of bridge in the literature. Future studies should be conducted to filing this gap to help validate the simplified model for single-span bridges for different types of bearings.

The simplified model provides a rapid approach for estimation of bridge fragilities. The developed fragility curves can be integrated with regional scale seismic risk tools for rapid evaluation of potential damage from strong earthquake events for emergency planning and mitigation studies.

Acknowledgements Funding for this study was provided in part through Natural Resources Canada in partnership with Defense Research and Development Canada.

References

1. Adams J, Rogers G, Halchuk S, McCormack D, Cassidy J (2002) The case for an advanced national earthquake monitoring system for Canada's cities at risk. In: Proceedings of the 7th US national conference on earthquake engineering, Boston, United States
2. Atkinson GM (2009) Earthquake time histories compatible with the 2005 National building code of Canada uniform hazard spectrum. Can J Civ Eng 36(6):991–1000. http://www.nrcresearchpress.com/doi/abs/https://doi.org/10.1139/l09-044
3. Atkinson GM, Adams J (2013) Ground motion prediction equations for application to the 2015 Canadian national seismic hazard maps. Can J Civ Eng 40(10):988–998
4. Basöz N, Mander J (1999) Enhancement of the highway transportation lifeline module in HAZUS. National Institute of Building Sciences (Washington D.C.).
5. CAN/CSA-S6-06 (2006) Code canadien sur le calcul des ponts routiers. Mississauga, Ont.: Association canadienne de normalisation
6. FEMA (2012) Hazus–MH: multi-hazard loss estimation methodology earthquake model. Technical manual, federal emergency management agency, National Institute of Building Science Washington, DC, USA
7. Government of Canada, N.R.C. (2015) "GSC2015PGA." Natural Ressources Canada. http://www.seismescanada.rncan.gc.ca/hazard-alea/zoning-zonage/images/GSC2015PGApdf.pdf
8. Hwang H, Liu JB, Chiu Y-H (2001) Seismic fragility analysis of highway bridges. Mid-America earthquake center CD Release 01–06
9. Lin K-w, Turner LL, Wald D (2014) ShakeCast V3-an enhanced tool for post-earthquake response
10. MTQ (2017) Manuel d'inventaire des structures (Quebec Ministry of transportation.)
11. MTQ (2017) Rapport annuel de gestion 2016–2017. Ministère des transports (Bibliothèque et Archives nationales du Québec: Gouvernement du Québec). https://www.transports.gouv.qc.ca/fr/ministere/organisation/rapport-annuel/Documents/rag-2016-2017.pdf
12. MTQ (2019). Rapport annuel de gestion 2018–2019. Ministère des transports du Québec (Bibliothèque et Archives nationales du Québec: Gouvernement du Québec: Ministère des

transports du Québec). https://www.transports.gouv.qc.ca/fr/ministere/organisation/rapport-annuel/Documents/rag-2018-2019.pdf
13. MTQ (2019) Structure. Québec: Government of Québec
14. Nielson BG (2005) Analytical fragility curves for highway bridges in moderate seismic zones. Ph.D. thesis, Georgia Institute of Technology
15. Nollet M, Abo El Ezz A, Khaled A, LeBoeuf D, Nastev M (2016) Seismic microzonation and vulnerability assessment of buildings and critical infrastructure: a case study of Québec City, Canada. In: 1st international conference on natural hazards & infrastructure, Chania, Greece, 28–30 June, 2016
16. NRCC (2015) National building code of Canada. Ottawa: National Research Council of Canada, Canadian Commission on Building and Fire Code
17. Padgett JE, DesRoches R, Nilsson E (2010) Regional seismic risk assessment of bridge network in Charleston, South Carolina. J Earthquake Eng 14(6):918–933
18. Priestley MJN (1996) Seismic design and retrofit of bridges. Wiley, New York
19. Tavares DH (2012) Évaluation de la vulnérabilité sismique des ponts routiers au Québec à l'aide des courbes de fragilité. Ph.D. thesis, University of Sherbrooke

Proximity Detection on Construction Sites, Using Bluetooth Low Energy Beacons

Khazen Mohammadali, Nik-Bakht Mazdak, and Moselhi Osama

1 Introduction

With the rise of IoT (Internet of Things), indoor location sensing systems have become very popular in recent years. These systems provide a new layer of automation, called automatic object location detection, for monitoring and management of indoor environments [8]. In the construction industry, tracking workers on the job site can enhance the safety and productivity of workers [16]. Although the successful completion of a construction project requires comprehensive and accurate location information for workers and resources,in practice, superintendents tend to manage a number of workers/resources based on manual observations on sites [19]. The drawback with the observation-based method is that it cannot be employed in real-time due to the requirement of having at least one observer for each worker or crew of workers [21]. Besides, the manual method of data collection can be time-consuming and inaccurate. Indoor localization technologies can enable decision-makers to make informed decisions to support the management of construction activities on site. Safety management and productivity monitoring are considered as the two major areas that automated workers/assets localization technologies can contribute to.[18]. Although in most outdoor construction sites GPS (Global Positioning System) can perform effectively, the condition is not the same for indoor construction sites, due to the weakness or absence of GPS signals [20]. Nonetheless, deployment of localization systems in indoor environment is still necessary in a variety of cases from residential to industrial building construction [9]. The present paper describes a newly developed proximity detection system for use on construction jobsites. The main requirements of the developed system include (i) not to interrupt construction

K. Mohammadali (✉) · N.-B. Mazdak · M. Osama
Centre for Innovation in Construction and Infrastructure Engineering & Management (CICIEM), Gina Cody School of Engineering and Computer Science, Concordia University, Montreal, Canada
e-mail: mohammadali.khazen@mail.concordia.ca

S. Walbridge et al. (eds.), *Proceedings of the Canadian Society of Civil Engineering Annual Conference 2021*, Lecture Notes in Civil Engineering 240,
https://doi.org/10.1007/978-981-19-0507-0_20

work-flow (in terms of the device size, the need for electric power or cords, etc.) and (ii) to have an acceptable level of accuracy. The system works through BLE sender and receiver beacons, and this paper explains the lab experiments as well as analytical models developed for estimation of the distance between beacons, through the analysis of transmitted signal strength.

2 Literature Review

There is a wide range of indoor localization technologies that have been tested and used in construction research and development, including active and passive RFID (Radio-frequency identification), Ultra-Wideband (UWD), camera-based and Bluetooth Low Energy (BLE) Each of these technologies has its advantages, based on the domain of application [11]. However, these systems have limitations and drawbacks such as the hardware costs associated with RFID equipment [12], pre-computed environmental data requirements associated with camera-based systems [4], or the sensitivity of the UWB devices to orientation shift. These limitations have, in practice, hindered the deployment of indoor localization technologies on construction sites [18]. However, the advent of Bluetooth Low Energy (BLE) technology has created a large market for proximity sensors. BLE beacon technology is a recently developed wireless technology that improves Bluetooth technology by consuming less energy and having a long lifetime. This technology offers indoor and outdoor tracking options at affordable costs, and they are portable and transferable from one site to another at the end of a project [10].

2.1 Localization Techniques

Localization techniques for wireless localization systems can be classified under three major categories: proximity, triangulation and fingerprinting. Each of these techniques has unique advantages and limitations, according to the domain of application. The proximity technique can provide symbolic relative location information. In other words, it checks the presence of a target node to be positioned in radio coverage of the reference beacon, and also it estimates the distance between the target node and the beacon. It usually relies on a dense grid of receivers that have a fixed position, known and listed in the tracking system. Once a target node is detected by one of the receivers, it is considered to be collocated with that receiver and if multiple receivers detect the target node, then it is matched with the one receiving the strongest signal [17]. Fingerprinting is a localization technique comprising two phases. Firstly, the RSSI (Received Signal Strength Indicator) values measured by a measuring device in the known locations are recorded. These reference values are saved together with the location coordinates into the fingerprint database. Secondly, the device to be localized measures the RSSI values and compares them with the data

in the fingerprint database to predict its location [13]. Last but not least, the trilateration technique uses the RSSI signal from three beacons, the signal is then used as a proxy of distance and acts as the radius of a circle with its center at the access points or beacons. The intersection of three or more circles identifies the position of the target node [5].

2.2 Proximity Detection on Construction Sites

A proximity detection system can estimate the distance between the target and receiving nodes and can detect the matching pairs in which their distance is smaller than a specified threshold. The system is capable of alerting construction operators and workers in real-time during a hazardous proximity situation. Several studies in the literature deployed the proximity detection system on construction sites to improve site safety. In 2017, Park et al. introduced an automated safety monitoring method that integrates BLE-based location tracking and BIM (Building Information Model). By reviewing four-dimensional (4D) BIM, potential safety hazards were defined as unsafe zones for safety monitoring. Real-time workers' locational information was continuously monitored, and this enabled data visualization of the contextual information to monitor behaviors of the workers with respect to the identified dangerous construction zones [15]. In 2020, Mohanty et al. proposed an active warning system to improve construction site safety by using BLE technology. After collecting data on the direction and speed of walking of the workers, a circle of approach to nearby hazardous or prohibited areas was created. The radius of the circle was calculated using workers' walking speed measured near prohibited areas. Having such a moving circle of proximity can be a real-time indicator for all workers' positions [10]. Park et al. [14] introduced a parameter adjustment function to reduce the inconsistency of the alert distances resulting from different types of equipment. They concluded that the developed proximity safety alerts system provides a better understanding of dynamic spatial relationships among equipment, operators, workers, and a surrounding work environment to improve construction safety management [15].

3 Experiment and Data Collection

The main components of the developed system are shown in Fig. 1. The BLE localization systems store the data received from beacons (transmitters and receivers), in databases in the cloud. The communication architecture comprises four parts. (i) Transmitting beacon—The primary function of these beacons is to advertise information including RSSI value, which can be processed to estimated distance. (ii) Receiving beacon—This beacon measures the RSSI value from the transmitting beacon and adds that information in the packet along with its UUID and the timestamp of reception. (iii) Gateway—The information (packet) collected by receiving

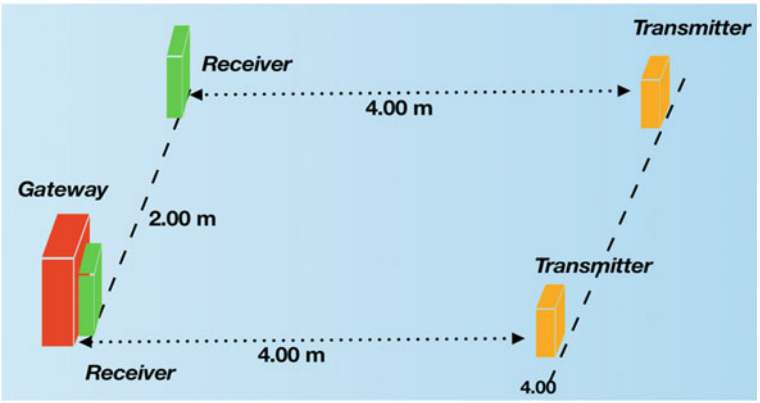

Fig. 1 Placement of the devices for the experiments

beacons is then transmitted to a central cloud computing system through gateways. And last but not least, (iv) Cloud database—The data packets are stored in a database which will be processed by the proximity technique to determine the proximity of the receiving beacon to the fixed transmitting beacons. In order for the entire system to properly identify the location and proximity of different objects, the RSSI records must be translated into physical distances. In the following parts, we explain the lab experiment completed to collect data and create RSSI-distance models for the developed system.

In-lab experiments for the development of RSSI-distance relationship and evaluation of the localization system were conducted in a space of 9.00 m $\times$ 9.00 m $\times$ 3.20 m as shown in Fig. 1. This space provided an open space for testing, as well as movable objects for creating different layouts and examining the effect of obstacles. The effects of signal reflections and noises on BLE signals, caused by the furniture, equipment, and their magnetic fields in the vicinity of the testbed were inevitable.

The receiver beacon was placed on seventeen reference points (stations) which were marked at 25 cm intervals on a straight line with a total length of four meters, to ensure the exact position of the beacon while conducting the experiment. The experiments were performed for four orthogonal orientations of the transmitting beacon, with respect to the receiving beacon. Moreover, the experiments were repeated three times at each station, to obtain a consistent dataset of RSSI values per each reference point. The receiving beacon was moved from the first station (distance from transmitting beacon $= 0$) to the seventeenth reference point (distance from transmitting beacon $= 4.0$ m). The staying time of the transmitting beacon at each reference point was one minute. In the interest of time, the same settings were implemented on two parallel straight lines, two meters away from one another.

Two datasets were collected for the two parallel lines of the RSSI-distance experiment (which we refer to, as tests ‘a’ and ‘b’). Each dataset has three subsets, and each of them contains RSSI records for the four orientations of the transmitting beacon with respect to the receiving beacon at the seventeen reference points. The number

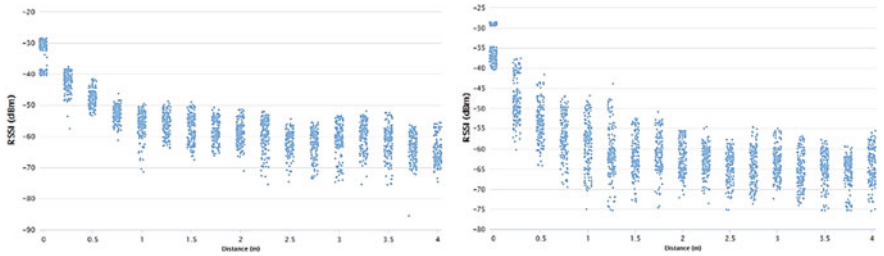

(a) Dataset 'a' (b) Dataset 'b'

Fig. 2 RSSI data collected in the experiment

of RSSI records per staying time period at each station (i.e. one minute) and the total number of records at each station considering all the orientations were 15 and 180 respectively. The total number of RSSI records for tests 'a' and 'b' were 2,955 and 2,959 data points respectively. The scatter plots of the RSSI records versus distance (between the transmitter and receiver) are provided for the two sets in Fig. 2.

4 Model Development

The empirical attenuation relationship is depicted for tests 'a' and 'b', in Fig. 3. As the distance between the transmitting and receiving beacons increases, the RSSI values decrease in all experiments up to a point then it reaches a low plateau. That point in tests 'a' and 'b' was at the 2.75 m and 3.25 m stations, respectively.

The effect of transmitting beacon's orientation with respect to the receiving beacon and its impact on the RSSI was investigated in the experimental work. In Fig. 4, the average value of RSSI records per distance, over the four orientations are illustrated in different patterns of lines. As seen, at each distance, the receiving beacon seems to capture stronger RSSI values for the front and back orientations. Since the BLE chip inside the beacons (regardless of the beacon's shape) has two major axes to

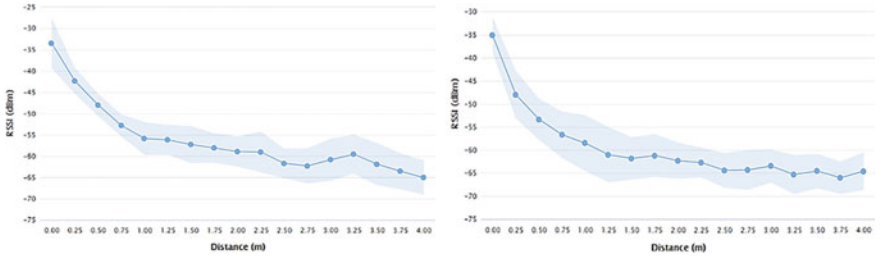

(a) Dataset 'a' (b) Dataset 'b'

Fig. 3 Mean and Standard deviation band plot for the experiment

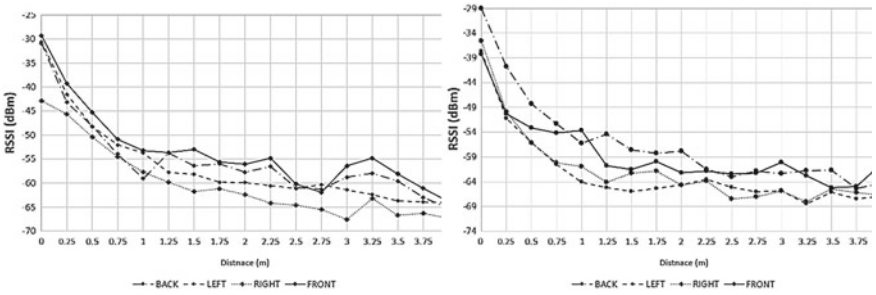

Fig. 4 The average value of RSSI records per distance, separated based on the four orientations

transmit signals, the front and back orientations can be associated with one axis and the right and left ones to the other axis. This seems to cause the similarity of RSSI records between the pair of orientations per each axis, and the difference between the orientation pairs of the opposite axes.

The receiving beacon was not able to receive the acceleration of the transmitting beacon, so the orientation shift of the transmitting beacon couldn't be determined. Besides, the beacons which are worn by workers can frequently change their orientation with respect to receivers on construction sites. Therefore, it is necessary to get enough RSSI records at different orientations of the transmitting beacon with respect to the receiving beacon, to reach a more reliable RSSI-distance relationship on site.

In the model development, we examined the Path-loss propagation and machine learning models, looking for the most accurate one for the distance estimation model due to its direct impact on reliability of the localization system.

4.1 Path-Loss Propagation Model

The measured RSSI values in the same station are fluctuant with time due to the environmental noises. In order to remove the outlier RSSI values, a Gaussian filter which had been proposed by (Zhu et al., 2015) was used in our study. The filter was set in the range of $[\mu - \sigma, \mu + \sigma]$ of the RSSI records for each distance, and the measured values outside this range were ignored. Since studies have shown that the channel fading characteristics follow a lognormal distribution [7], RSSI-distance measurement generally uses the logarithmic distance path-loss model which is formulated as:

$$\mathrm{RSSI} = -10n * \lg\left(\frac{d}{d_0}\right) + A + X_\sigma \tag{1}$$

where $RSSI$ is the Received Signal Strength Indication when the distance between receiving and transmitting nodes is d. Also, A is the RSSI value of the reference point with the known distance of d_0 from the transmitting node, which is captured by the receiving node. n is a path-loss coefficient related to the specific wireless transmission environment; the more obstacles in the test area, the larger the value of n will be. X_σ is a Gaussian-distribution random variable with mean of 0 and variance σ^2. For the convenience of calculations, let $d_0 = 1$ m and X_σ have a mean of zero, so the distance-loss model can be obtained as:

$$\overline{\text{RSSI}} = -10n * log(\text{d}) + \overline{A} \tag{2}$$

where $\overline{A}$ is the average measured RSSI when the reference node is 1 m away from the transmitting node. To calculate the environmental parameter n, the following equation is used [2, 6]:

$$\text{n} = \frac{\text{A} - \overline{\text{RSSI}}}{10*\log(\text{d})}. \tag{3}$$

Thus, the RSSI-distance relationship model can be obtained to predict the distance of the blind beacon through its RSSI value. In our study, to estimate the value of A, 312 RSSI records were collected when the distance was 1 m. As a result, A was estimated as -56.229 dBm. Regarding the n value, the average RSSI value of 16 different distances ranging from 0.25 m to 4.00 m with interval steps of 0.25 m were used. The value of n for the distances are shown in Table 1. Hence, the average value of n is calculated as follows:

$$\text{n} = \sum_{\text{i}=1}^{16} \text{n}_{\text{i}*0.25} = 1.586. \tag{4}$$

Finally, the proposed RSSI-distance relationship is represented by Eq. (5).

$$\text{RSSI} = -15.86 \log(\text{d}) - 56.229. \tag{5}$$

In addition to the conventional method of estimating the values of A and n, the method of fitting a curve to the average RSSI value at different distances $(Avg.RSSI_i, d_i)$, proposed by Zhu et al. [22]. Among different curve fitting methods,

Table 1 The value of n at different distances

Distance	0.25	0.50	0.75	1.00	1.25	1.50	1.75	2.00
n	1.985	1.904	1.430	–	2.528	2.223	1.369	1.309
Distance	**2.25**	**2.50**	**2.75**	**3.00**	**3.25**	**3.50**	**3.75**	**4.00**
n	1.444	1.618	1.408	1.195	1.243	1.224	1.407	1.501

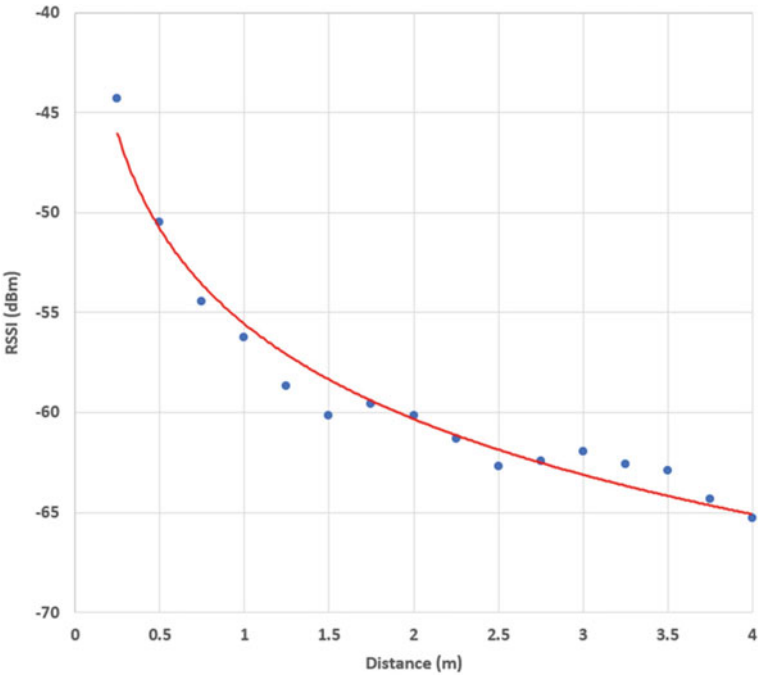

Fig. 5 The average value of RSSI records per distance and RSSI-distance estimation model: red line represents the estimated RSSI-distance model and the blue dots are the average RSSI values at each distance

Logarithmic which had been used by [1] was deployed in our study [22]. This model was developed based on the 5614 RSSI samples at the 16 test stations. The logarithmic regression was carried out by using the average of the RSSI values for each distance. Figure 5 demonstrates the average value of records per distance and the RSSI-distance estimation model. Using logarithmic curve fitting, the path loss model can be expressed by Eq. (6).

$$\mathrm{RSSI} = -18.644 \log(\mathrm{d}) - 55.573 \tag{6}$$

4.2 Machine Learning Models

We trained machine learning models, as alternatives to the path loss method, for predicting the distance through the RSSI values. In this study, several machine learning techniques including Random Forest, Gradient Boosted Trees, Generalized Linear Regression Model and KNN were tested for distance prediction. After splitting the data into training set (75%) and test set (25%), the hyperparameters for

each model were finetuned, and finally the best models from each technique were selected and compared.

Before training the model, two preprocessing steps were taken. Firstly, the outliers caused by environmental noise were identified based on their distance to their nearest RSSI records and were eliminated. In fact, RSSI records of each distance are ranked based on its distance to its 70 nearest neighbors. Based on trial and error, on the reference of the Random Forest (RF) model performance, the number of strongest outliers which were removed per each distance and from the training set is 12 and 204 respectively. Figure 6 shows the removed outliers as green dots. Secondly, the RSSI records were normalized by z-transformation method. The average and standard deviation of the values were calculated, and the scaled value was calculated by $Z =$ (x-Avg.)/SD so that the average value and the standard deviation are 0 and 1. This normalization is necessary for some of our machine learning methods [3].

Four machine learning models were trained in this study and their performance was compared through their accuracy and error. They include Random Forest (RF), Gradient Boosting Decision Tree, Generalized Linear Regression (GLR) and k-Nearest Neighbours (kNN). RF is an ensemble learning method, used for classification and regression. A random forest is an ensemble of multiple decision tree sets with the following modification: each node of a tree represents a best split for one specific attribute. Only a subset of attributes which are specified is considered for the splitting rule selection. After that, the erection of new nodes is repeated until

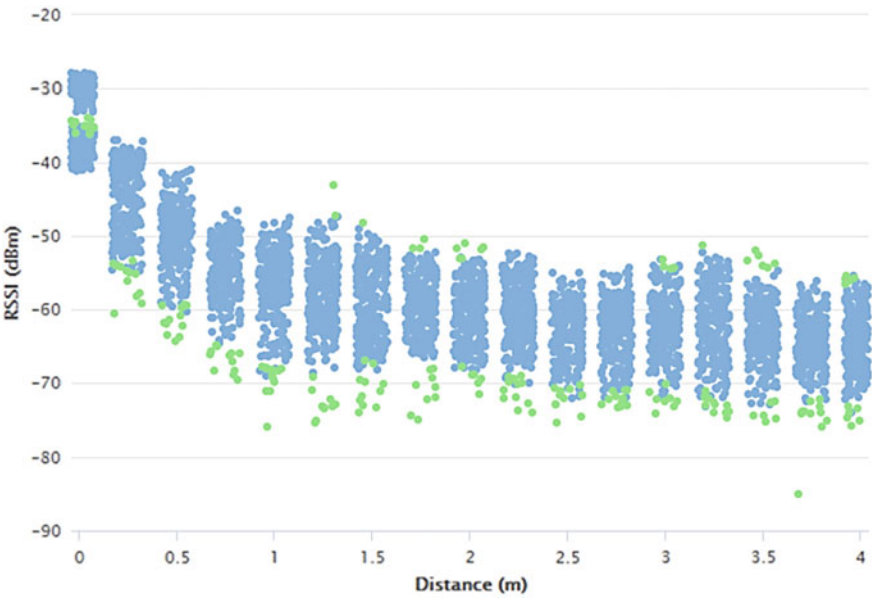

Fig. 6 Scatter plot showing the removed outliers: the green dots are the removed outliers

the stopping criteria are met. The second used algorithm, gradient boosting decision tree, produces a prediction model in the form of an ensemble of decision trees models (Tirumalareddy 2020), built incrementally where each successive estimator gradually reduces the previous model's error. Building the model takes longer time compared to the random forests since each tree has to be built based on the results of a prebuilt tree (Morita et al. 2018).

The third algorithm which was tested is GLM, which is an extension of the traditional linear regression models. The GLM is fitted by solving the maximum likelihood optimization problem (Lanford et al. 2015). This model can accommodate a number of various types of target variables and covariate relationships. Lastly, the kNN is one of the most effective classification algorithms, trained on a set of labeled instances and making predictions based on the classes of the k labeled datapoints which are most similar to the each unlabeled datapoint by using metrics such as Euclidean distance. For each model, we fine-tuned the model parameters through trial and error and optimization, to minimize the prediction model's errors.

5 Results and Discussion

The experiment was designed to make comparison between varied techniques for the distance prediction model which is a fundamental element in the proximity detection system. The prediction results are discussed here for both Path-loss and machine learning models. Mean Absolute Error (MAE), Root Mean Square Error (RMSE) and Mean Percentage Error (MPE) were considered as criteria to make a comparison between the performance of the models. It is noted that the records for 0 m distance between transmitter and receiver were removed from the calculation of MPE. Since the proposed model aims to predict the distance, MAE can provide a good understanding of the true error value. Error was defined as the distance between estimate and actual coordinates in the experiment.

The logarithmic curve fitting model was associated with less error in distance prediction, compared to the conventional path-loss model. Table 3 shows the evaluation metrics for the two models. As seen, for the conventional path-loss model, the MAE, RMSE and MPE was 1.176 m, 2.171 m and −12.0 percent respectively. Applying the logarithmic curve fitting model obviously improved the accuracy of

Table 3 Statistics of the evaluation metrics (MAE, RMSE and MPE) of the models

Model	Conventional path-loss	Logarithmic curve fitting	Random forest	Gradient boosted trees	Generalized linear model	KNN
MAE (m)	1.176	0.961	**0.641**	0.699	0.704	0.648
RMSE (m)	2.171	1.555	**0.822**	0.844	0.858	0.832
MPE (%)	−12.0	−9.9	**−25.1**	−34.7	−37.2	−18.7

distance prediction. The MAE was reduced to 0.961 m, the RMSE was only 1.555 m and MPE was improved to −9.9 percent. The results show that the error in the distance prediction model can be reduced by about 18 percent in terms of MAE by using a logarithmic curve fitting model.

As to machine learning models' performance, a fivefold cross-validation was adapted. As seen in the Table 3, the Random Forest model outperformed all the models in terms of MAE and RMSE which were as low as 0.641 and 0.822 m respectively. By contrast, the Generalized Linear Model had the highest MAE, RMSE and MPE of 0.704 m, 0.858 m and −37.2 respectively among the machine learning models. It can be seen that the Path-loss models had the lowest MPE in comparison with the machine learning models.

6 Concluding Remarks

The results of the study highlight the feasibility of deploying BLE beacon technology as a proximity detection system. In this study, various models were compared to estimate the distance between the transmitting and receiving beacons by using RSSI values. It is found that the tested machine learning models achieved smaller errors compared to the conventional and logarithmic curve fitting path-loss models. An average error of 64 cm in the distance prediction model was achieved, when the beacons are within the range of 4.00 m from one another, by the Random Forest model. Regarding training the models, capturing RSSI records at various orientations of the transmitting beacon with respect to the receiver was found to be necessary due to different behaviour of the transmitter in sending signals in certain orientations. Replacing conventional receivers by the BLE beacon can make a huge difference in applicability of the localization system on site. The level of accuracy achieved in this study makes the system capable of estimating how close the transmitter is from the receiver beacon, rather than only identifying their presence. It can be particularly advantageous in detecting how close construction workers are to specific areas (e.g. danger zones), or even to one another (when enforcing physical distancing on the jobsite). The accuracy of the proposed distance identification system is excellent in close proximity ranges, which can effectively lead to safety improvement on construction sites. Since the laboratory experiments minimize the effect of distractions and noise which normally exist in a construction environment, the influence of other parameters such as weather conditions, construction equipment, and availability of metals requires further investigation to evaluate the effectiveness of deploying the proposed proximity detection systems on site.

Acknowledgements This study was funded by NSERC, under ALLRP5539-85. The authors would also like to acknowledge the support of ReelyActive company with respect to the equipment set up and validation of the results.

References

1. Hing CH, Fong PWK, Syed Zakaria SMM, Kamarudin LM, Zakaria A, Kanagaraj E, Kamarudin K, Rahim YA, Ahmad N (2019) Map-based localization indoor environment for object tracking using RF trackers. In IOP conference series: materials science and engineering, vol 705, no. 1, pp.0–7
2. Huang K, He K, Du X (2019) A hybrid method to improve the BLE-Based indoor positioning in a dense bluetooth environment
3. Iqbal Z, Luo D, Henry P, Kazemifar S, Rozario T, Yan Y, Westover K et al (2018) Accurate real time localization tracking in a clinical environment using bluetooth low energy and deep learning. PLoS ONE 13(10):1–13
4. Jeelani I, Asadi K, Ramshankar H, Han K, Albert A (2021) Real-time vision-based worker localization & hazard detection for construction. Autom Constr 121:103448
5. Karabtcev SN, Khorosheva TA, Kapkov NR (2019) BLE beacon interaction module and mobile application in the indoor-navigation system, 2019 international science and technology conference "EastConf." EastConf 2019:1–6
6. Lee S, Kim J, Moon N (2019) Random forest and WiFi fingerprint-based indoor location recognition system using smart watch. Human-centric computing and information sciences, vol **9**, no. 1
7. Li G, Geng E, Ye Z, Xu Y, Lin J, Pang Y (2018) Indoor positioning algorithm based on the improved rssi distance model. Sensors (Switzerland) 18(9):1–15
8. Liu H, Darabi H, Banerjee P, Liu J (2007) Survey of wireless indoor positioning techniques and systems. IEEE Trans Syst Man Cybern Part C Appl Rev 37(6):1067–1080
9. Mackey A, Spachos P, Song L, Plataniotis KN (2020) Improving BLE beacon proximity estimation accuracy through bayesian filtering. IEEE Internet Things J 7(4):3160–3169
10. Mohanty L, Chae S, Yang Y (2020) Identifying productive working patterns at construction sites using BLE sensor networks. Dev Built Environ 4:100025
11. Moselhi O, Bardareh H, Zhu Z (2020) Automated data acquisition in construction with remote sensing technologies. Appl Sci (Switzerland) 10(8):1–31
12. Motamedi A, Soltani MM, Hammad A (2013) Localization of RFID-equipped assets during the operation phase of facilities. Adv Eng Inform 27(4):566–579
13. Park H, Noh J, Cho S (2016) Three-dimensional positioning system using bluetooth low-energy beacons. Int J Distrib Sens Netw 12(10)
14. Park J, Kim K, Cho YK (2017) Framework of automated construction-safety monitoring using cloud-enabled BIM and BLE mobile tracking sensors. J Constr Eng Manag 143(2):1–12
15. Park J, Yang X, Cho YK, Seo J (2017) Automation in construction improving dynamic proximity sensing and processing for smart work-zone safety. Autom Constr 84:111–120
16. Teizer J, Cheng T, Fang Y (2013) Location tracking and data visualization technology to advance construction ironworkers' education and training in safety and productivity. Autom Constr 35:53–68
17. Topak F, Pekeriçli MK, Tanyer AM (2018) Technological viability assessment of bluetooth low energy technology for indoor localization. J Comput Civ Eng 32(5):1–13
18. Umer W, Siddiqui MK (2020) Use of ultra wide band real-time location system on construction jobsites: feasibility study and deployment alternatives. Int J Environ Res Public Health 17(7)
19. Won D, Chi S, Park MW (2020) UAV-RFID integration for construction resource localization. KSCE J Civ Eng 24(6):1683–1695
20. Xia L, Retscher G, Tian H, Tian H (2010) A case study on the feasibility and performance of an UWB-AoA real time location system for resources management of civil construction projects. J Appl Geod 4(1):23–32
21. Zhao J, Seppänen O, Peltokorpi A, Badihi B, Olivieri H (2019) Real-time resource tracking for analyzing value-adding time in construction. Autom Constr 104:52–65
22. Zhu H, Alsharari T (2015) An improved RSSI-based positioning method using sector transmission model and distance optimization technique. Int J Distrib Sens Netw 2015

Community Resilience Classification Under Climate Change Challenges

M. N. Abdel-Mooty, W. El-Dakhakhni, and P. Coulibaly

1 Introduction

The Earth's ecosystem is an integral part of the life and is interacting with the atmospheric system that maintains the habitability of the planet through keeping the temperature within a certain range[8]. Since the industrial revolution started in the eighteenth century, the earth's atmosphere has been changing continuously, albeit at a slow rate[8]. For example, the quantities of greenhouse gases have significantly increased [8, 14], leading to a global climate change. This increase in greenhouse gases, particularly, resulted in a global rise of temperature, a warmer ocean surface, a higher rate of snow melt, and a continuous sea level rise [10, 14, 15]. Precipitation patterns have also been affected by climate change, resulting in higher frequencies of floods and flash floods [21]. The frequencies of heat waves and droughts have also increased at an alarming rate, resulting in a higher deforestation rate and significant disruption to urban areas and wildlife [9, 17]. The National Climate Assessment Agency has recently highlighted that the changing climate is projected to continue beyond this century, with impacts vary based on the amount of greenhouse gases transferred from the earth surface to the atmosphere [18]. With the global climate

M. N. Abdel-Mooty (✉)
Department of Civil Engineering, McMaster University, 1280 Main Street West, Hamilton, ON L8S 4L7, Canada
e-mail: abdelmom@mcmaster.ca

M. N. Abdel-Mooty · W. El-Dakhakhni
Department of Civil Engineering, McMaster Institute for Multi-Hazard Systemic Risk Studies (INTERFACE), McMaster University, 1280 Main Street West, Hamilton, ON L8S 4L7, Canada
e-mail: eldak@mcmaster.ca

P. Coulibaly
Department of Civil Engineering, NSERC FloodNet, McMaster University, 1280 Main Street West, Hamilton, ON L8S 4L7, Canada
e-mail: couliba@mcmaster.ca

S. Walbridge et al. (eds.), *Proceedings of the Canadian Society of Civil Engineering Annual Conference 2021*, Lecture Notes in Civil Engineering 240,
https://doi.org/10.1007/978-981-19-0507-0_21

changing and urbanization growing rapidly, flood risk across the globe continues to rise in comparison to other natural hazards. Flood events are considered the most occurring climate-induced hazards worldwide [11, 20]. While cities are the social centers of life in any country, cities rely on a series of Critical Infrastructure Networks (CIN) to perform adequately, like transportation networks, power grid, water and wastewater system, to name but a few. Flood events can be the reason for serious disruptions in these CINs, and thus crippling the life within the affected cities. Historical disaster data indicate the continuous increase in urban flood events, with the rising possibility for extreme rainfall in North America [3].

As such, it is critical enhance the resilience of cities in face of such climate-induced hazards. To understand the proposed framework, cities' resilience needs to defined first. Resilience has multiple definitions in literature [4], it can be defined as the capacity of an urban system to recover and reach an acceptable level of functionality after being exposed to a hazard. It can also be defined as the ability of a system to accept a certain level of disturbance, and be able to recover to its original state before the external event that caused the disturbance [5]. Finally, it can be defined as the degree to which a system withstands disturbances while continuing to function [14]. Resilience within the context of this study can be defined using the Four R attributes of Resilience—Robustness, Rapidity, Redundancy, and Resourcefulness [4]. Notably, Robustness stands for the ability of a system to maintain its level of functionality when facing a certain demand level, while Rapidity stands for the ability of the system to bounce back to its original state in a timely manner [1, 4].

The work presented in the current study is a step towards developing a 4-phased analytical platform to assess cities' resilience in the face of flood hazards. The first phase is aimed at finding the different categories at which cities respond to disturbances, namely flood events. This first step of the analysis was carried out by adopting an Unsupervised Machine Learning (ML) clustering technique in an effort to naturally categorize the data given its inherent features. Further details will be provided in the Methodology section.

2 Data Description

The dataset used in this analysis was gathered by integrating the data available in the Canadian Disaster Database [16]. Meteorological events since 1950 were recorded from across the country, however, the focus in this study was on flood events that occurred in the Provinces near the Great Lakes region, and across the border with the United States of America. The data originally contained 214 flood events from across the country, but after data preprocessing and cleaning 152 entries were used in the creation of the machine learning model.

For each flood event, there were different attributes (variables) associated with each flood event (observation). Each observation had 6 variables: Location, Comments, Start date, Fatalities, Injured people, Evacuated people, and Estimated total cost. The Place variable indicates the place where the incident occurred, the

Table 1 Indices for flood cause

Cause	Index
Rain	1
Line heading	2
Snow and rain	3
Spring flood	4

Table 2 Indices for seasonality

Cause	Index
Spring	I
Summer	II
Fall	III
Winter	Iv

Comments give additional observations and context, including how it started, and the Estimated total cost was the total losses due to said event from all sources including property damage, insurance, and compensations.

For the scope of this study, the variables were preprocessed to fit within the desired criteria for the model, as described in the following section. The following variables were developed: Affected people-including Fatalities, Injuries, and Evacuations-, Monetary Losses, Seasonality of flood event, Cause of flooding event, and the Province of the event. After conducting preliminary descriptive data analysis, the Cause Variable included the following causes: Rain, Snowfall, Combined Rain and Snow melting, Spring flood or increase in water level. Each of the mentioned causes and seasons were assigned an index as seen in Tables 1 and 2.

3 Methodology

Clustering is an unsupervised ML technique that categorizes observations in a dataset [13]. Different clustering algorithms were employed in this study, where the first clustering technique used was Neural Net Clustering (NNC) toolbox in MATLAB, where the model uses a shallow neural network to cluster the data according to how they're grouped in the input space [12]. The Self Organizing Maps (SOM) used in NNC possess the ability to learn how to organize the neighboring clusters in the input space. The neurons are arranged in accordance with a topology function that takes different forms; grid, hexagonal, or random topology. The distance between the neurons is calculated using a distance function, whereas the link distance is the most commonly used method in analysis [12]. The second clustering technique used in this study is K-means partitioning algorithm, where it minimizes the square Euclidean distance between points within the clusters and the cluster center for each category of data; this analysis was made using the R programming platform [13]. The final

clustering technique was Principal Component Analysis (PCA). PCA is a dimension-reduction tool that can be used to explain as much of the behavior (variance) of the original data with a much lower set of variables. This dimensionally reduced dataset can be inspected for clusters as it naturally forms within the reduced dimensional space [6].

4 Results and Discussion

The first model used in the analysis was the SOM-ANN Clustering using the NNC toolbox, where the data was imported to MATLAB in the form of a Matrix of 5 columns, each representing one of the variables. The chosen number of clusters was 4, as the intended model was created to choose 4 different categories for flood impact categorization. The weight vector associated with each neuron becomes the center of each cluster, and the neighboring clusters move close to one another in the input space, making it easier for the users to visualize a higher dimension in a two-dimensional space. As shown in Fig. 1a and b, the model has 4 clusters, and each cluster has the number of observations associated with it in the middle. For example, in Fig. 1b, the number 56 which is the largest number indicates 56 inputs in this cluster. Using the neighboring weight distance, the distance between different clusters can also be shown where different color schemes indicate different distances between neurons. The darker the color of the line between neurons the larger the distance, while the lighter the color the closer the clusters are to one another. As can be seen in Fig. 1a, there are 2 neurons that are far from one another, with the lower 2 neurons very close to one another. This means that 4 initially chosen for the model can explain the relationship between the common characteristics of each

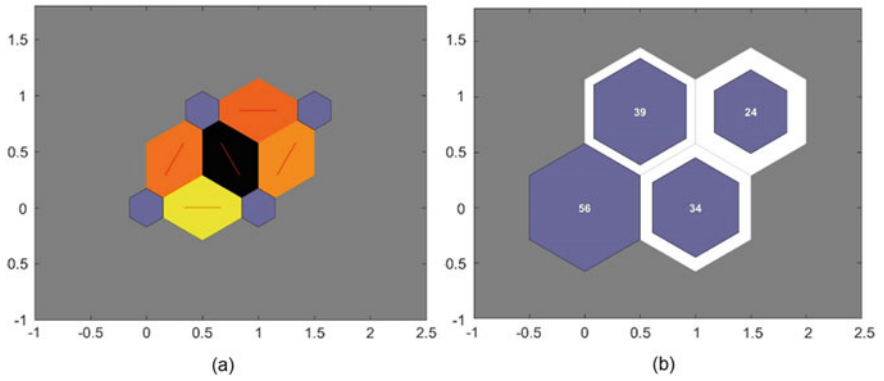

Fig. 1 **a** The Self Organizing Map (SOM) neighboring distance for the clusters, and **b** is the SOM's Sample hit for each cluster

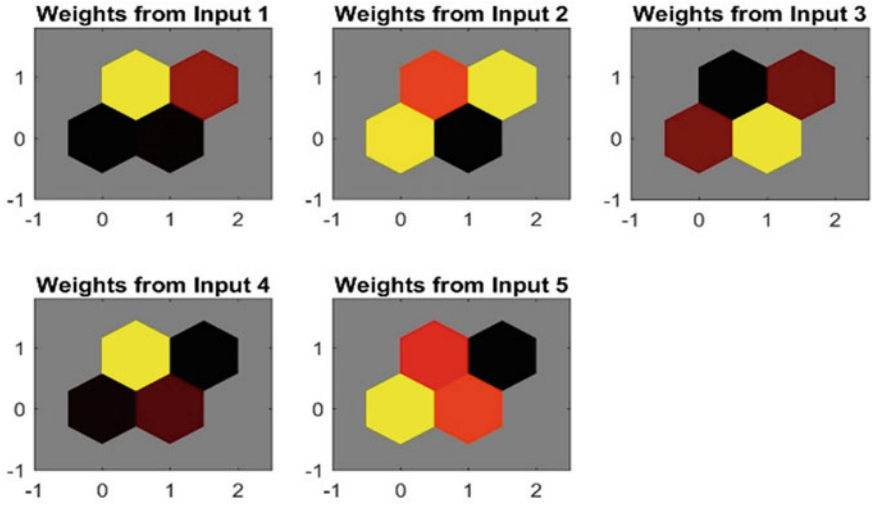

Fig. 2 The weight planes on each Cluster in the SOM algorithm

cluster; however, some of clusters were very similar to one another, indicating that additional analysis is necessary for clear distinction between different clusters.

Figure 2 show the weights associated with each neuron— representing each variable's influence, where the darker colors represent higher weights on each neuron; where inputs 1, 2, 3,4, and 5 are the Affected People, the Monetary Losses, the Season, the Cause, and the Location of each event, respectively. Figure 3 represents the correlation matrix for the 5 variables used in this analysis, and it shows very low correlation between these variables which indicates a high degree of interdependence between the variables, supporting the decision to use Machine Learning algorithms to inspect the inherent features of the dataset.

To develop a more comprehensive model for the clustering objective of this study, the k-means clustering algorithm was utilized. K-means algorithm requires the number of clusters to be predetermined in advance. As such, the elbow method was used. In this method, a loop is created at which with each cycle the value of k changes gradually, from 1 to 15, and the total Within Cluster Sum of Squares (WSS) was computed each time as shown in Fig. 5. In the context of this study, the WSS is estimated as the accumulated sum of the square of the Euclidean distance between the observations and their cluster's centroid [2, 7, 19].

$$WSS = \sum_{(k=1)}^{k} \sum_{(x_i \in C_k)} (x_i - \mu_k)^2 \tag{1}$$

where k is the total number of clusters, and x_i is an observation belonging to cluster i, while μ_k is the mean of all observations allocated within the cluster. The total

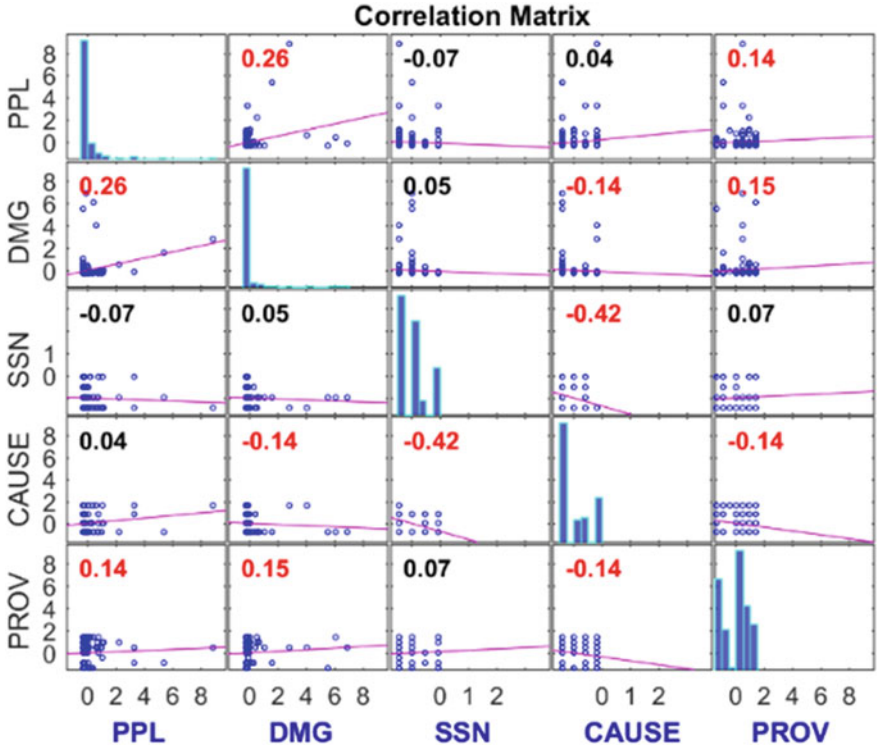

Fig. 3 The weight planes on each cluster of the SOM neural network algorithm

within cluster sum of squares *(WSS)* was inversely proportional to the value of k, and the rate of changed decreased as the value of k increased. For an optimum value for k to be chosen, the curve must have one edge -knee- where the slope of the curve changes. However, the graph in Fig. 4 does not possess this feature, but the optimum value is set between $k = 4$ and $k = 8$.

A model was created for number of clusters of 4, 6, and 8 as can be seen in Fig. 5. After inspecting all the clusters with different values of k, there was no clear distinction between the different clusters, or the basis on which they were divided as all datapoints of different clusters have intersecting features. As such, the decision to use Principal Component Analysis (PCA) was made. The PCA model projects the multidimensional space into a lower dimensional space, called the score space, considering the effect of all the different variables. The model explains a high portion of the variance within the data, and this portion increases as the number of components increase, with a minimum of 1, and a maximum of the total number of variables in the mode, which is 5 in this case. In the PCA analysis, a model with only two components was adequate. As can be seen in Fig. 6, the score plot, the model could be visually inspected for naturally clustered data, and as highlighted the 3 different circles indicate the different clusters, while all the outliers and those

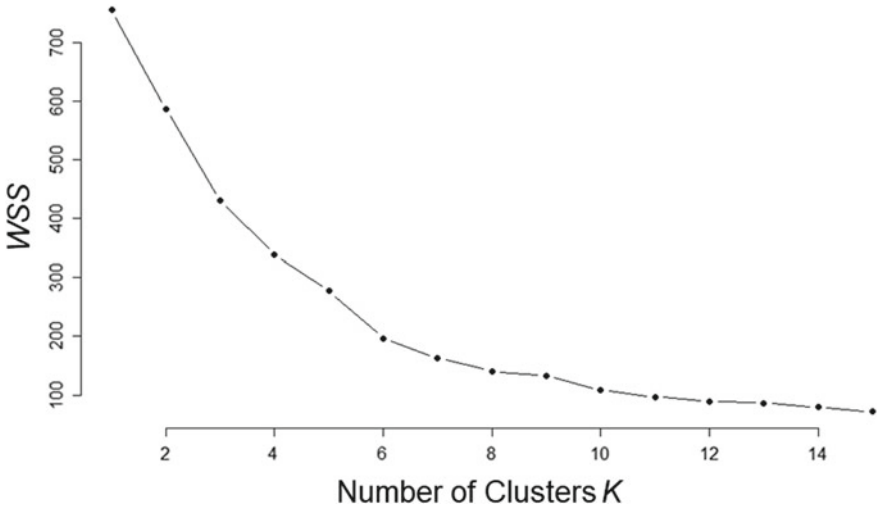

Fig. 4 The Total within-cluster sum of squares for different values of *K*

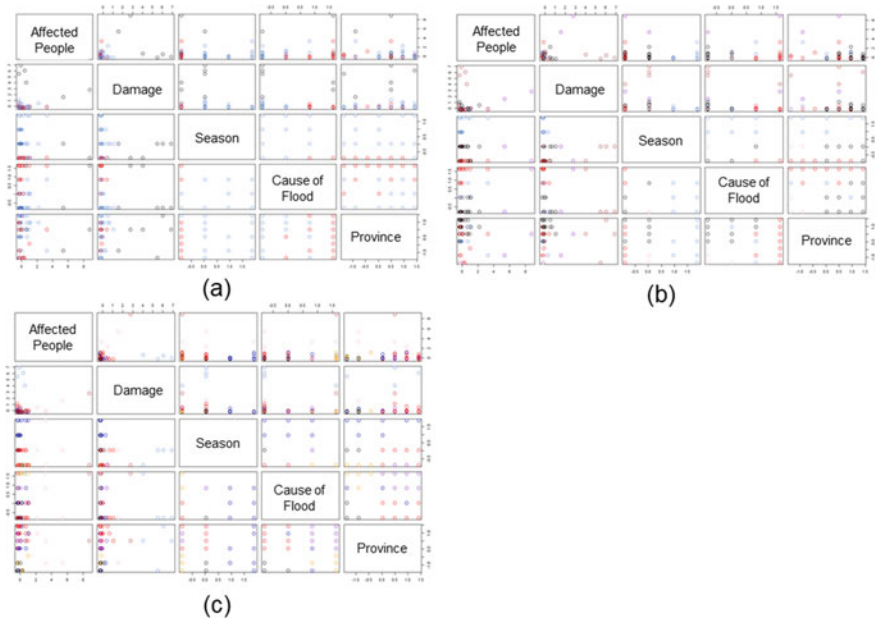

Fig. 5 K-means cluster Plots for different values of k where **a** is k-means clustering (k = 4), **b** is k-means clustering (k = 6), and **c** is k-means clustering (k = 8)

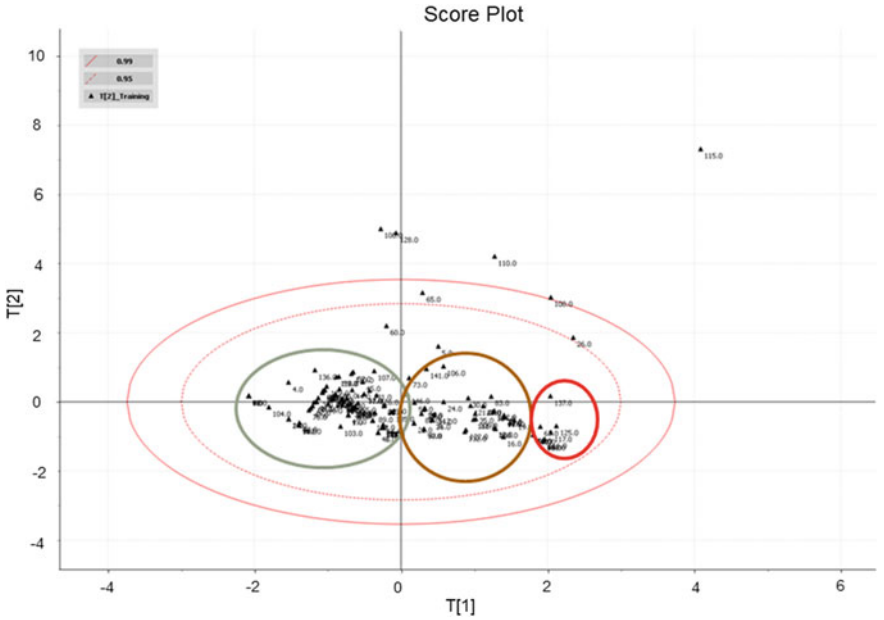

Fig. 6 PCA score plot using 2 scores with the circles indicating the different clusters

outside the 3 clusters would form the fourth cluster. Further inspection was made to infer more details outlining each cluster, to be able to find patterns and distinct traits in the separation algorithm. However, it was concluded that projecting the clusters in a two-dimensional space would limit the ability to distinguish the attributes of each cluster.

To overcome this problem, a third dimension was introduced to better visualize the attributes of each cluster. Instead of having a two-dimensional scatter plot between the Cause and Season, which were the two distinct features in the previous analysis, a third dimension that takes into account the affected people and the money losses was added by summation of the centered and scaled Money Losses vector and the Affected People vector. Figure 7 shows the three-dimensional scatter plot using the added dimension, where the different attributes of different clusters are clearly distinguishable as shown in Table 2. This third dimension introduced in this graph is proposed only for visualization purposes, as it was not part of the clustering algorithm.

After observing the created clustering models, four flood impact categories on cities were inferred. Looking closely at the numbers, the distinction was in seasonality, cause, affected people, and the money losses that happened during these events. The flood risk categories were named FR I, FR II, FR III, and FR IV as shown the attributes of each category in Table 3.

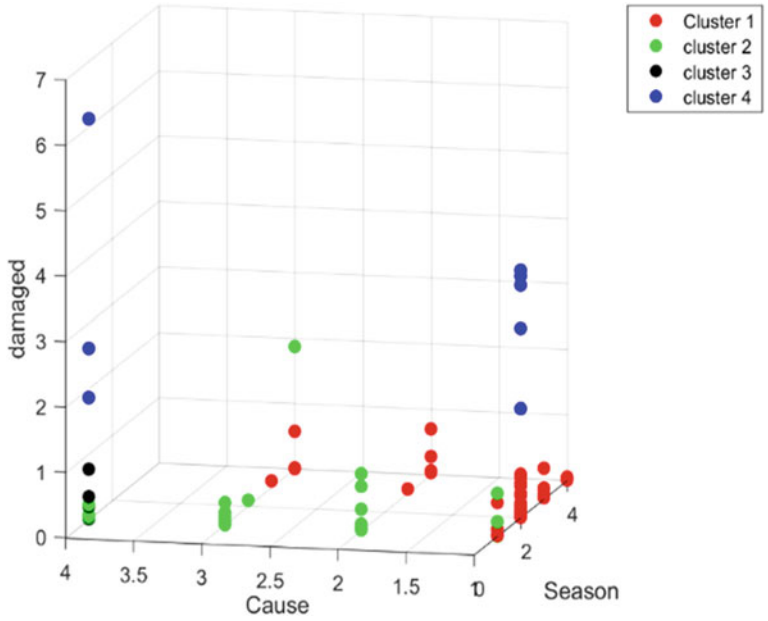

Fig. 7 Three-dimensional scatter plot of the clustered data

Table 3 Flood Risk Categories resulting from the unsupervised ML algorithm

Cluster number	Cluster description	FR
1	Events that happen in winter, summer, or fall, and affect less than 4000 people or caused less damage than 215 M $	I
2	Events that happen in the spring due to excessive rain, or snowfall/snowmelt, and affects less than 4000 people or caused less damage than 215 M $	II
3	Events that happen in the spring due to spring floods and affect less than 4000 people or caused less damage than 215 M $	III
4	Any event that affects more than 4000 people or caused more than 215 M $	IV

5 Conclusion

In this study, a new community flood resilience-based classification was developed using an unsupervised machine learning technique based on the different resilience components (i.e., the robustness and potential impacts on the exposed environment, and rapidity). Fatalities, Injured people, Cause of the flood, and seasonality of the flood were included in the dataset to represent Robustness and Rapidity, as Resilience metrics. A descriptive analysis was conducted that revealed the need for Machine learning techniques to be employed. Multiple Machine learning models were utilized

to achieve the goal of this framework. However, due to the size of the data and the interdependence of the variables, the Principal Component Analysis technique was most appropriate. The study presented herein resulted in 4 Resilience-based flood risk Categories that incorporate the features of the hazard (i.e. flood) and the robustness of the exposed community— represented by the number of affected people, fatalities, and monetary damage. Overall, the framework developed in this study paves the way for a resilience-based categorization that bypasses physics-based models and its complexity by adopting a data-driven approach, to categorize communities' resilience to flood hazard. Said categorization that focuses on the goals of resilience can be used in the development of flood projections that will aid decision makers in developing proactive policies that focus on mitigation and prevention for a comprehensive risk management plan.

Acknowledgements The work presented in this study supported by the Vanier Canada Graduate Scholarship (Vanier-CGS) awarded to the corresponding author, and the Natural Science and Engineering Research Council (NSERC) through the CaNRisk— Collaborative Research and Training Experience (CREATE) program. Additional support through the INViSiONLab and the INTERFACE Institute of McMaster university is also acknowledged.

References

1. Abdel-Mooty MN, Yosri A, El-Dakhakhni W, Coulibaly P (2021) Community flood resilience categorization framework. Int J Disaster Risk Reduction 61:102349. https://doi.org/10.1016/j.ijdrr.2021.102349
2. Alsabti K, Ranka S, Singh V (1997) An Efficient k-means clustering algorithm
3. Bertilsson L, Wiklund K, de Moura Tebaldi I, Rezende OM, Veról AP, Miguez MG (2019) Urban flood resilience–a multi-criteria index to integrate flood resilience into urban planning. J Hydrol 573(February 2016):970–982. https://doi.org/10.1016/j.jhydrol.2018.06.052
4. Bruneau M, Chang SE, Eguchi RT, Lee GC, O'Rourke TD, Reinhorn AM, Shinozuka M, Tierney K, Wallace WA, Von Winterfeldt D (2003) A framework to quantitatively assess and enhance the seismic resilience of communities. Earthq Spectra 19(4):733–752. https://doi.org/10.1193/1.1623497
5. Cimellaro GP, Fumo C, Reinhorn AM, Bruneau M (2009) Quantification of disaster resilience of health care facilities. Mceer-09–0009. http://mceer.buffalo.edu
6. Dunn K (2019) Process improvement using data. http://Learnche.Org/Pid, no. January: 381. http://learnche.org/Pid
7. Hartigan JA, Wong MA (1979) A k-means clustering algorithm. J R Stat Society Ser C (Appl Stat) 28(1):100–108.
8. Houghton JT, Jenkins GJ, Ephraums JJ (1990) Climate change: the IPCC scientific assessment
9. Leite C, Oliveira V, Miranda I, Pereira H (2020) Cork oak and climate change: disentangling drought effects on cork chemical composition. Sci Rep 10(1):1–8. https://doi.org/10.1038/s41598-020-64650-9
10. Levitus S, Antonov J, Boyer T, Baranova O, Garcia H, Locarnini R, Mishonov A et al (2017) NCEI ocean heat content, temperature anomalies, salinity anomalies, thermosteric sea level anomalies, halosteric sea level anomalies, and total steric sea level anomalies from 1955 to present calculated from in situ oceanographic subsurface profile data. Natl Centres Environ Inf Dataset. https://doi.org/10.7289/V53F4MVP

11. Lian J, Xu H, Xu K, Ma C (2017) Optimal management of the flooding risk caused by the joint occurrence of extreme rainfall and high tide level in a coastal city. Nat Hazards 89(1):183–200. https://doi.org/10.1007/s11069-017-2958-4
12. MathWorks (2019) Deep learning toolbox: User's guide (R2019b). Massachusetts. https://www.mathworks.com/help/pdf_doc/deeplearning/nnet_ug.pdf
13. Mcnicholas PD (2016) Model-based clustering. J Classif 373(November):331–373. https://doi.org/10.1007/s0035
14. Murdock HJ (2017) Resilience of critical infrastructure to flooding: quantifying the resilience of critical infrastructure to flooding in Toronto, Canada
15. Nerem RS, Beckley BD, Fasullo JT, Hamlington BD, Masters D, Mitchum GT (2018) Climate-change–driven accelerated sea-level rise detected in the altimeter era. Proc Natl Acad Sci USA 115(9):2022–2025. https://doi.org/10.1073/pnas.1717312115
16. Public Safety Canada (2019) The Canadian disaster database. https://www.publicsafety.gc.ca/cnt/rsrcs/cndn-dsstr-dtbs/index-en.aspx
17. Tsesmelis DE, Karavitis CA, Oikonomou PD, Alexandris S, Kosmas C (2019) Assessment of the vulnerability to drought and desertification characteristics using the standardized drought vulnerability index (SDVI) and the environmentally sensitive areas index (ESAI). Resources 8(1):1–19. https://doi.org/10.3390/resources8010006
18. USGCRP (2018) Fourth national climate assessment: report-in-brief, vol II. https://doi.org/10.1016/j.pbb.2008.09.016
19. Wagstaff K, Cardie C, Rogers S, Schrödl S (2001) Constrained k-means clustering with background knowledge. In: International conference on machine learning ICML, pp 577–84. http://citeseerx.ist.psu.edu/viewdoc/download?doi=10.1.1.90.4624&rep=rep1&type=pdf
20. Wilby RL, Beven KJ, Reynard NS (2007) Climate change and fluvial flood risk in the UK: more of the same? Hydrol Process 2309(December 2007):2300–2309. https://doi.org/10.1002/hyp
21. Wuebbles DJ, Fahey DW, Hibbard KA, Dokken DJ, Stewart BC, Maycock TK (eds) (2017) Climate science special report: fourth national climate assessment, vol I. Washington, DC. https://doi.org/10.7930/J0J964J6

Investigation of a Proposed Morphologic Change in the Squamish Estuary System

N. Asadollahi, G. Maciel-Jobb, and J. S. Readshaw

1 Introduction

The Squamish Training Berm is situated in the Squamish River estuary, at the head of Howe Sound in Squamish, BC Fig. 1. This study was undertaken to assess the impacts of the training berm removal as part of the Central Estuary Restoration Project. The intent of the removal is to restore and conserve the integrity of the Squamish River watershed by improving access and habitat in the central estuary for juvenile chinook. The scope of the study was to conduct a comparative assessment using a hydrodynamic and sediment transport model, coupled with wave modeling, for the existing and a future scenario, which reflects the plans for removal of the training berm.

2 Methodology

The methodology used consisted of a hydrodynamic/ sediment transport model coupled with a wave numerical model. The numerical model Delft-3D-FLOW and Delft3D-WAVE modules were used in conjunction with the Simulating WAves Nearshore (SWAN) wave model to model the wave forcing. Model setup and calibrations were conducted using local tidal stations water level measurements. Current speeds were validated using ADCP (Acoustic Doppler Current Profiler) data from February 16th, 2017 [3]. Coupled model was run for two scenarios (with and without

N. Asadollahi (✉)
Coastal Engineer (EIT), SNC-Lavalin Inc, Vancouver, Canada
e-mail: nora.asadollahi@snclavalin.com

G. Maciel-Jobb · J. S. Readshaw
Senior Coastal Engineer (PEng), SNC-Lavalin Inc, Vancouver, Canada

S. Walbridge et al. (eds.), *Proceedings of the Canadian Society of Civil Engineering Annual Conference 2021*, Lecture Notes in Civil Engineering 240,
https://doi.org/10.1007/978-981-19-0507-0_22

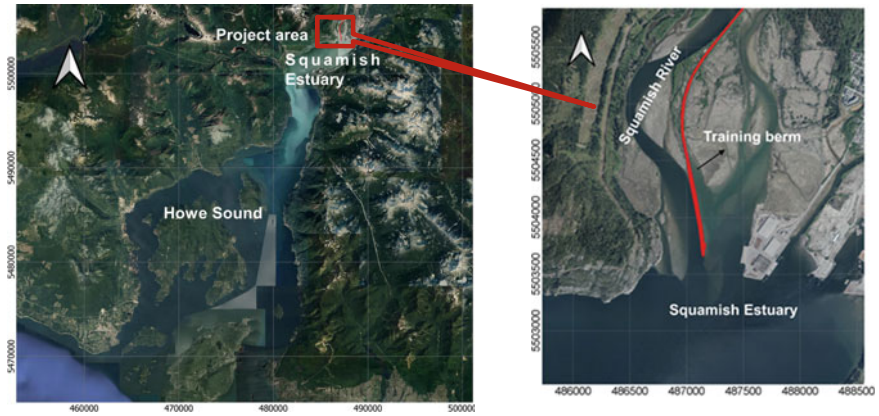

Fig. 1 Project location

the training berm), with a run duration of approximately 14 days each. The input for the modelling was based on existing operational conditions as a first identification of the removal consequences. The berm removal scenario includes a 1.1 km long berm removal, keeping the south end of the berm in place. Operational conditions include one typical storm and an average winter river discharge.

3 Metocean Input

A metocean assessment was conducted prior to determining the model input. The calculation of the sea state at the Squamish estuary requires a reliable estimate of the overwater winds, especially within the upper (north) reaches of Howe Sound. Wind data measured from three stations were analysed: Squamish Airport (10476F0), Squamish Wind Sports (SWS), and Pam Rocks (10459NN). The wind speeds at the Squamish Airport station are consistently lower when compared to Pam Rocks or the SWS station, mainly because the station is in-land. Even though the Squamish Airport wind data is the longest measured time series, it was not considered as a reliable source. Winds measured at the SWS station are predominantly from the southwest and higher, compared to Pam Rocks.

The tidal conditions are based on the water level height information for the Point Atkinson reference port (Station ID 7795). Storm surge influences were input to the model based on the measured residual water level data at Point Atkinson. Local storm surge effects, resulting of inflow and convergence effects in Howe Sound and Squamish Harbour, were estimated by comparing water levels measurements between the Point Atkinson and the new tidal station in the Lower Estuary.

River discharge was defined based on the available period of measured discharge from Water Survey of Canada at Squamish River station (08GA022). The associated

sediment flux at the upstream boundary was estimated based on the river flow—suspended sediment rating curve defined by [1] for this station.

4 Numerical Modelling

The modelling for this study was conducted in 2D mode (depth-averaged) using Cartesian grid co-ordinates.

The model was developed using a triple-nested configuration to account for the complexity of the area. The coarse model has a resolution of 100 × 100 m and covers Howe Sound. The wave climate and tidal induced currents were included in the 20 × 20 m nested model for the Squamish Estuary. The Squamish Estuary 20 × 20 m model in turn provides boundary condition to a fine resolution 5 × 5 m model of the study area.

The model was initially validated by comparing the water level at the Lower Estuary Station and results from the 5 × 5 m grid model. The currents were validated using the current speed measurements during ebb tide on February 16th. Limitations for calibration/validation are that the wind and water level inputs are hourly, discharge is daily, and currents were measured for less than one hour. The comparison concluded that the project circulation model provided a reasonable description of currents at the site.

5 Results and Discussion

The model results for the currents during existing and removal scenarios are presented, at the peak of a storm - on February 1st, 2010 at 10:00 AM, in Figs. 2 and 3. The cumulative sedimentation/erosion patterns are presented in Fig. 3 at the end of 14 days of model simulation.

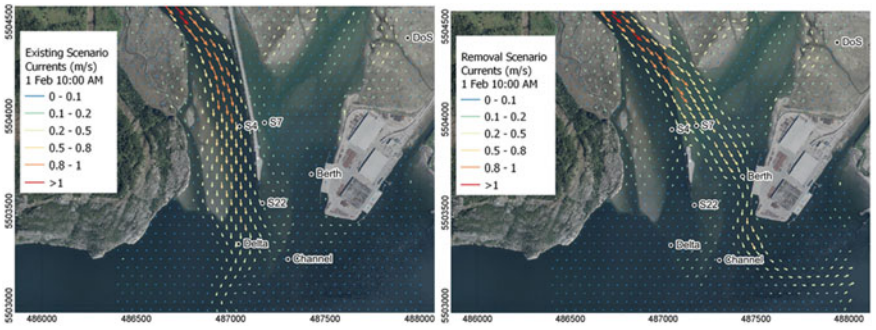

Fig. 2 Currents (m/s) at the peak of the modelled storm-existing scenario (left) and removal scenario (right)

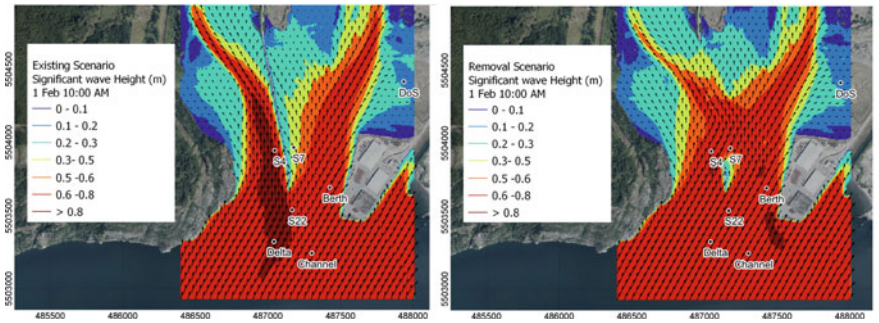

Fig. 3 Significant wave height on February 1st 10 AM (during Storm)-existing scenario (left) and removal scenario (right)

5.1 Currents

Removal of the berm results in higher currents at the east side of the existing berm footprint (S7) while the currents at the west side of the berm (S4) reduce from 0.8 m/s for the Existing scenario to 0.2 m/s for the Removal scenario (Fig. 2). The currents also diverge from the existing channel towards the Squamish Terminals and wrap around the remaining Windsports island. This results in stronger currents at the Squamish Terminal berth (approximately 0.4 m/s). Current in the remainder of the estuary essentially remain the same as the existing scenario.

5.2 Wave Field

There is no significant change in the sea state in the area between the existing and removal scenarios except on the east side of the berm (S7). The wave height increased from 0.5 m/s in the existing scenario to 0.7 m/s in the Removal scenario. This is a predictable change since the training berm is providing shelter Fig. 3: Significant wave height on February 1st 10 AM (during Storm) -Existing Scenario (left) and Removal Scenario (right).

for the immediate area. The removal of the berm allows the waves to propagate into the central channel and results in larger waves at the upper section of the channel adjacent to the berm (Fig. 3).

5.3 Sedimentation

For the removal scenario, the model shows overflowing of the removed berm footprint and subsequent sedimentation from the Squamish River, into the upper central

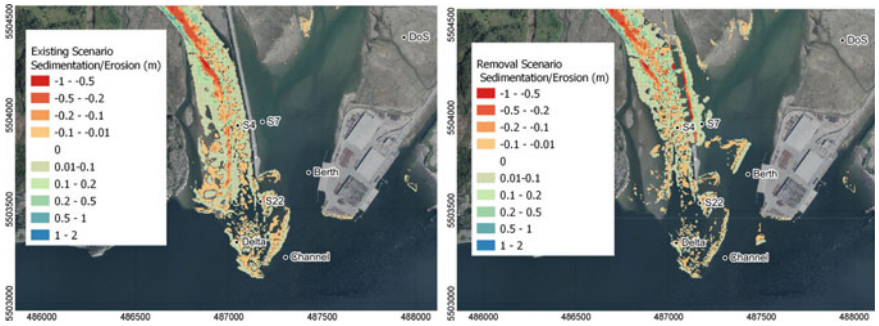

Fig. 4 Sedimentation/Erosion at the end of the simulation -Existing Scenario (left) and Removal Scenario (right)

channel area, sedimentation near the berm footprint on both sides and over the top of the removed berm (Fig. 4). No significant sedimentation/erosion took place around other points of interest including the existing channel, the Squamish Terminal or the perimeter of the estuary on the east side adjacent to the District of Squamish.

6 Conclusion

The objective of this study was to investigate the effect of the removal on the sedimentation processes in the area and provide a comparative assessment between the existing situation and the preferred berm removal scenario. The results suggest that the removal scenario could result in higher currents and waves in the vicinity of the upper central channel and the Squamish Terminal area. The removal scenario also allows currents and waves to carry sediments from the Squamish River into the upper central channel area and around and over the top of the remaining removed berm footprint surface.

This study presents the likely impacts of training berm removal on existing operational conditions. It represents a typical storm event and average winter river discharge. It is recommended that a sediment transport analysis to evaluate long term effects of severe storms or severe river discharges is undertaken prior to final design of any implementation process. It is also likely that further optimization of the Removal scenario could be considered, such as different lengths of berm removal.

The study purposefully did not assess differences during future sea level rise due to the complexity of defining future decisions regarding the fate of the training berm, Squamish Terminals and the many features running parallel to the District of Squamish lands on the east side of the estuary.

References

1. Clarke JEH (2016) First wide-angle view of channelized turbidity currents links migrating cyclic steps to flow characteristics. Nat Commun 7(1):1–13
2. Hickin EJ (1989) Contemporary Squamish River sediment flux to Howe Sound, British Columbia. Can J Earth Sci 26(10):1953–1963
3. Tetra Tech (2017) Squamish terminals hydrodynamic and sediment Transport modelling

Scenarios to Valorize Treated Spent Pot Lining in Cement and Concrete

N. Camara and C. Ouellet-Plamondon

1 Introduction

Cement and concrete are the most widely used materials in the construction sector and its production poses environmental and economic problems. Because of their large-scale uses, their production leads to significant emissions of greenhouse gases like CO_2, dust, particles [8] and mercury [10]. In addition global warming, there is also the local shortage of non-renewable resources, energy consumption [3] and water use [6]. To date, the demand for cement and concrete continues to increase so it would be important to implement strategies to limit their impact on the environment in order to reduce greenhouse gas (GHG) emissions [5]. Thus, to limit these problems, researchers have thought about the use of supplementary cementitious materials (SCMs) which will reduce the emissions of GHG. Among the supplementary cementitious materials, this paper considers treated spent pot lining (SPL), which is a waste of primary aluminum production. SPL is a hazardous material, which when mixed with cement has inert properties similar to quartz with a retarding effect below 7 days and a high alkali content [2]. However, Rio Tinto developed an industrial solution to remove hazardous properties of SPL and to produce industrial and valuable by-products [1]. Using the process called Low-Caustic Leaching and Liming (LCL&L), Rio Tinto's plant can produce from the refractory portion of the SPL, an inert material referred to internally as LCLL ash. This inert material is composed of 60–70% SiO_2 and Al_2O_3 and can be used as a raw material for clinker in the manufacture of cement when LCLL ash is calcinated at 1450 °C Fig. 1. Recent R&D projects conducted at ETS have shown that LCLL ash can be considered as a cementitious admixture in

N. Camara · C. Ouellet-Plamondon (✉)
Ecole de Technologie Supérieure, Department of Construction Engineering, Montreal, Canada
e-mail: claudiane.ouellet-plamondon@etsmtl.ca

N. Camara
e-mail: niakale.camara.1@ens.etsmtl.ca

S. Walbridge et al. (eds.), *Proceedings of the Canadian Society of Civil Engineering Annual Conference 2021*, Lecture Notes in Civil Engineering 240,
https://doi.org/10.1007/978-981-19-0507-0_23

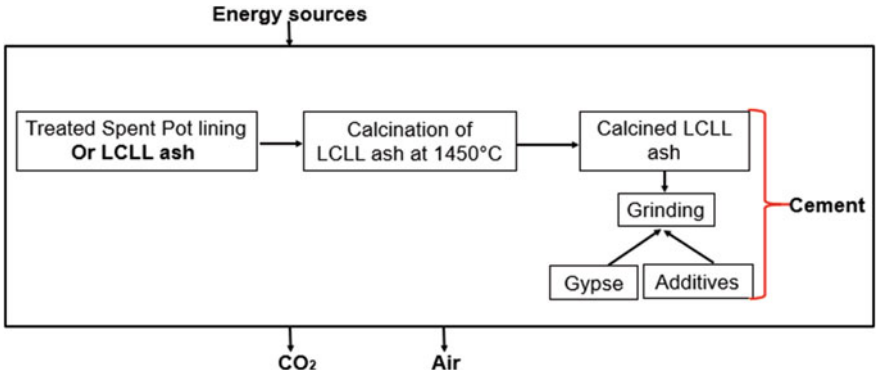

Fig. 1 Cement production with as raw material treated spent pot lining calcined at 1050 °C

concrete production if calcined at a temperature of 1050 °C. These calcined LCLL ash showed reaction properties similar to those of a calcined clay but no delay in hydration or expansion [2].

The objective of this research is to evaluate the potential to valorize the LCLL ash, by-product of the SPL treatment, in cement and in concrete. In order to evaluate the environmental impact, a life cycle analysis of this material will be conducted from cradle to grave and cradle to gate, depending on the valorization scenarios.

2 Valorization Scenario and Environmental Assessment

The first step is to define the analysis system and its limits. The materials used in this research are treated used tank linings, cement and concrete. The analysis is carried out from cradle to grave and gate to gate. The cradle to grave in LCA is the whole life of the material, until its end of life [11], so from the extraction of the raw materials to the production of the materials to be used, from the distribution to the landfill or recycling of the materials already used. The cradle-to-gate is an approach that has four-step process: the definition of goal and scope, the inventory analysis, the impact analysis and the interpretation [11]. On the other hand, the gate to gate only takes into account a single process in the entire production chain, so it concerns the entire production cycle of the product [9].

2.1 LCA to Assess the Environmental Impacts

The studies are defined according to the ISO 14040 and 14,044 standards by determining the inputs and outputs of the different material flows [4]. The raw material for this step comes from Rio Tinto SPL treatment plant, Usine de Traitement de

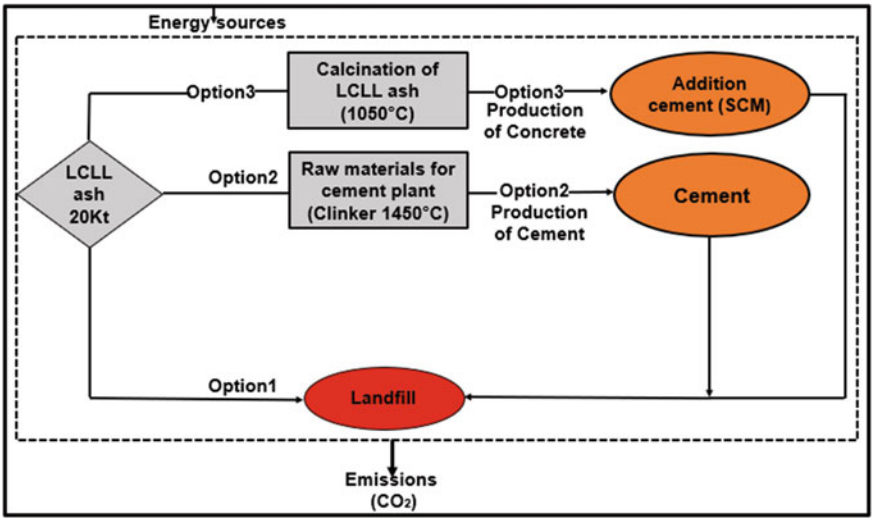

Fig. 2 Use of treated spent pot lining in cement and concrete's productions

la Brasque (UTB). Figure 2 shows the defined system with three different options. Option 1 concerns "cradle-to-grave" production where the treated SPL is sent to landfill and to know the CO_2's gain. Option 2 describes the second "cradle to grave" scenario where treated SPL is used as a raw material by a cement plant at 1450 °C to produce cement. Option 3 focuses on the "cradle to gate" scenario where the treated SPL is pre-calcined at 1050 °C to be used as a SCM to produce concrete.

2.2 Data Sources

The majority of the information sources come from the Ecoinvent database 3.10.1, which has made it possible to find disaggregated processes of the reference and elementary flows of each product. This database made it possible to obtain data on cement and concrete components more precisely in Quebec-Canada. The missing data was found on the Internet through articles and sites dedicated to construction materials, for example, electricity consumption for the manufacture of cement and concrete, for their transportation and for their burial. Data on electricity for municipal waste treatment was also found in the literature. The chemical compositions of LCLLash and calcined LCLLash are from the recent R&D projects conducted at ETS obtained by X-ray fluorescence bed fusion (XRF) [7].

2.3 Expected Results

The results will be calculated at the midpoint and damage level using the IMPACT 2002 + method as this model is one of the most widely used models in LCA analysis. Due to the ability to obtain data, midpoint categories including non-carcinogens, respiratory inorganics, respiratory organics, aquatic ecotoxicity, terrestrial ecotoxicity, terrestrial acidification/nitrification, aquatic acidification, aquatic eutrophication, global warming, and non-renewable energy, as well as human health, ecosystem quality, resource depletion, and climate change parameters will be selected in this study. In addition, normalization will be applied in this study to analyze the respective share of each median impact to the total impacts as well as to compare the median impacts with each other. The analysis will allow to know the environmental impacts generated by the treated pot lined products, cements and concretes on the one hand, but also the CO_2 gains obtained by using the treated pot lined products as raw material in the manufacturing of construction materials.

3 Expected Benefits and Industrial Impact

From a sustainable development perspective, this project will bring to light on the benefits of using treated spent pot lining in the production of cement and concrete, in a perspective of a circular economy. It will also contribute to the Aluminium stewardship commitment of the industry.

Acknowledgements This work was supported materially and financially by NSERC CRD grant program, CRITM consortium, Rio Tinto and Ciment Québec Inc. for their support for this project. The authors are also grateful for their various supports to conduct this project to achieve the determined objectives.

References

1. Birry L, Leclerc S, Poirier S (2016) The LCL&L process: a sustainable solution for the treatment and recycling of spent potlining. Light metals. Springer, pp 467–471
2. Brial V, Tran H, Sorelli L, Conciatori D, Ouellet-Plamondon C (2021) Evaluation of the reactivity of treated spent pot lining from primary aluminum production as cementitious materials. Resour Conserv Recycl 170:105584
3. Environment UN, Scrivener KL, John VM, Gartner EM (2018) Eco-efficient cements: potential economically viable solutions for a low-CO2 cement-based materials industry. Cem Concr Res 114:2–26
4. Finkbeiner M (2014) The international standards as the constitution of life cycle assessment: the ISO 14040 series and its offspring. Background and future prospects in life cycle assessment. Springer, pp 85–106

5. Habert G, Miller SA, John VM, Provis JL, Favier A, Horvath A, Scrivener KL (2020) Environmental impacts and decarbonization strategies in the cement and concrete industries. Nat Rev Earth Environ 1(11):559–573
6. Miller SA, Horvath A, Monteiro PJM (2018) Impacts of booming concrete production on water resources worldwide. Nat Sustain 1(1):69–76
7. Ouellet-Plamondon C, Brial V, Tran H, Sorelli L, Conciatori D, Birry L, Alamdari H (2020) AL18-valorization of treated spent pot lining by-product in concrete.In: Conference and exhibition of the international committee for study of Bauxite, alumina & Aluminium 9
8. Penrose B (2014) Occupational exposure to cement dust: changing opinions of a respiratory hazard. Health History 16(1):25–44
9. Tait MW, Cheung WM (2016) A comparative cradle-to-gate life cycle assessment of three concrete mix designs. Int J Life Cycle Assess 21(6):847–860
10. den Heede V, Philip, and Nele De Belie. (2012) Environmental impact and life cycle assessment (LCA) of traditional and 'green'concretes: literature review and theoretical calculations. Cement Concr Compos 34(4):431–442
11. Wu P, Xia B, Zhao X (2014) The importance of use and end-of-life phases to the life cycle greenhouse gas (GHG) emissions of concrete–a review. Renew Sustain Energy Rev 37:360–369

Deterioration Prediction Model Development and Analysis for Alberta's Provincial Highway Road Network's Pavement Condition

Foad Esmaeili, Mostafa Fadaeefath Abadi, and Fuzhan Nasiri

1 Introduction

The road network should provide a reliable platform for motorists to transport products and goods every day within the local, provincial, and national markets [1]. This feature highlights the importance of road and highway networks for society. As an essential factor related to the Pavement Management System (PMS), deterioration significantly impacts the infrastructure's performance. One of the essential elements of PMS is performance deterioration modelling [2, 3]. Hence, a trustworthy and accurate degradation and deterioration model needs to be obtained and applied to plan an appropriate network maintenance schedule. In addition, these maintenance plans have to be updated so that the desired targets considering cost optimization and other important factors could be addressed and achieved [4].

Valuable information and an overview of the road or highway network pavement condition could be provided by deterioration models. However, in individual pavement sections, the performance could not be understood well by these models [5]. There are many reasons which could cause road pavements to deteriorate. Some factors such as loads of traffic, the structure of pavement, type of surface or subgrade, environmental issues, and the level of maintenance impact pavement deterioration [2, 3].

Road agencies aim at providing a high service level for road networks by performing maintenance and rehabilitation works. In this regard, access to accurate deterioration information of the road segments, and on that basis, developing a proper prediction modelling method is essential to ensure the required level of service. Various details containing pavement condition information are gathered by the road agencies or the Transportation Departments, forming pavement condition

F. Esmaeili · M. Fadaeefath Abadi (✉) · F. Nasiri
Concordia University, Montréal, QC, Canada
e-mail: mostafa.fadaee@concordia.ca

S. Walbridge et al. (eds.), *Proceedings of the Canadian Society of Civil Engineering Annual Conference 2021*, Lecture Notes in Civil Engineering 240,
https://doi.org/10.1007/978-981-19-0507-0_24

datasets. However, these datasets may have high variance due to uncertainties in data collection, understating the road distress parameter and variables for specific segments [5].

This study's main objective is to investigate various deterioration models based on the literature and previous research works focusing on Artificial Neural Network (ANN) and regression models. A case study dataset of a highway network is then adopted to implement and compare these models and their performance concerning accurate predictions for the network pavement deterioration.

According to this paper's structure, in Sect. 2, an overview of previous research works and recent literature on different deterioration prediction models is discussed, and some of the critical applied models are presented. Section 3 provides information about the case study used in this research and details the dataset variables and attributes. A detailed data analysis has also been presented in this section. The types of models (ANN and regression) applied in this study to predict the IRI for the road network are presented in Sect. 4. The obtained results of IRI prediction are exposed and discussed in Sect. 5, and finally, Sect. 6 presents the conclusions.

2 Literature Review

Several studies have been conducted towards pavement deterioration modelling to predict road or highway pavements' future performance. Researchers use various methods and models to perform the prediction and obtain the results for further analysis. In this section, some of the most recent developments in this research area are presented. A prediction model has been developed to predict IRI following the structural parameters of the pavement. Structural number, asphalt layer thickness, subgrade strength, and environmental conditions are the parameters that were considered in this study. Empirical mechanistic and regressive empirical models are combined in the study to develop the IRI deterioration model. The researchers compared the obtained results and the measurements of road segments regarding different climate zones, and the results were obtained. According to the comparison results, most of the predicted and measured IRI data had a proper match, and their deviation was in the measurement error range [2].

A study on pavement condition prediction has been conducted by applying the Artificial Neural Network (ANN) method. The study's objective was to forecast several variables and parameters for Low Volume Roads (LVR) such as cracking, ravelling, rutting and roughness in India. In their research work, different ANN models were trained with various architectures. These models were tested to find the most suitable and optimized model. Their research demonstrated the accuracy of the applied ANN models in predicting cracking, ravelling, rut depth, and roughness parameters for the LVR network in India. The results are beneficial for maintenance planning and management [6].

Scholars have conducted model development to predict the Pavement Condition Index (PCI). First, the parameters were calibrated regarding the pavement features

related to its structure. These factors were the structural number of the pavement, the thickness of the asphalt layer, strength of subgrade and the environmental state. Then, a proper match and correlation were achieved by comparing the measured and predicted variables based on the results. Therefore, the developed model could be applied for PMS [3].

In another research, the pavement condition data has been obtained, and an investigation is performed to study and analyze the relationship between IRI and pavement damage parameters such as cracking, rutting, and ravelling. Based on the results, some factors like cracking and ravelling had a significant relationship with IRI [7].

3 Case Study

To study pavement performance, there are several measures and parameters to consider. The most important ones are permanent deformation (rutting), fatigue cracking (both bottom-up and top-down), thermal cracking and smoothness (International roughness index, IRI) [8].

To develop an accurate and reliable deterioration prediction model for road pavements, the model's aspects and applied dataset should meet some requirements. First, accurate data and measurements are needed as well as extended values and data points. Second, some essential attributes and variables related to the pavement performance level, such as traffic volume and axle load distribution and historical environmental parameters, climate, construction, and maintenance details, should be available. Finally, the applied deterioration prediction model should be acceptable and developed according to suitable standard engineering policies. In addition, the model should be easily adjusted to local engineering knowledge and historical data [3].

In this study, a dataset with sufficient data points has been selected to apply the relevant deterioration models for future condition prediction and perform training, testing and validating the results. In the following subsections, more information about the case study has been provided.

3.1 Dataset

The dataset selected for the case study has been obtained from Alberta's Government (Infrastructure and Transportation). This dataset is created and published by Alberta's Transportation Ministry and contains the annual International Roughness Index (IRI) and Rut Data parameters for provincial highways and other information collected in several years. The complete dataset can be found on the Alberta Government website (https://www.alberta.ca/international-roughness-index-and-rut-data.aspx). The IRI units are shown in mm/m, and Rut units are in mm. The pavement roughness and rut

depth parameters are measured and then summarized in 50 m segments within the lane that the measure was taken [9, 10].

The roughness of roads has been measured and applied as a sole measurement to categorize the overall physical condition. As mentioned, the average IRI value is measured for each 50 m segment of the Alberta highway network. Then, it has been averaged again for each one-kilometre section to provide a condition assessment. By having this information, the highway's quality has been carefully evaluated to support better traffic movement. Moreover, by planning proper maintenance or rehabilitation strategies, the Total Life Cycle Cost (LCC) of Alberta's highway network will be decreased, and the network's quality will be improved.

Although the dataset for some years had more than 30 attributes (variables), to have a more consistent dataset with the same data attributes for each year, the dataset was cleaned, and a portion of the whole dataset from years 2016 to 2018 has been chosen for this research. This dataset consists of 27 attributes for 1,048,576 assets (road segments). Among the attributes, 15 of them are selected for evaluation and modelling. The details of some main attributes are provided in the next section.

The maintenance and expansion of the provincial highway network are essential for Alberta Transportation as the leading responsible organization [1]. Therefore, this research aims to provide a deterioration model that could enhance maintenance scheduling and future road construction plans.

3.2 Data Dictionary (Attributes)

Alberta Transportation [11] has provided details and descriptions of each attribute in this dataset in their portal. As mentioned in the previous section, 15 attributes are selected for modelling, which were common for the years 2016 to 2018. The categorical data attributes are Road_No, Control_Section, Roadway_Code, Lane Type, Lane_Code, HR Rut DL, Vehicle ID. The Numerical Data attributes are listed below with their description.

- From_km_DMI and To_km_DMI (Numerical Data): The starting point or the endpoint of the corresponding road/highway segment.
- IRI_Inside and IRI_Outside (Numerical Data): The smoothness and comfort indicator measured for the inside (i.e. left) or outside (i.e. right) wheel paths of the lane of each road/highway segment.
- Avg_Rut_Inside and Avg_Rut_Outside (Numerical Data): The average rut for the inside (i.e. left) or outside (i.e. right) wheel paths of the lane of each road/highway segment which is calculated from continuous transverse profiles from the 3D sensors for every interval (50 m).
- Max_Rut_Inside and Max_Rut_Outside (Numerical Data): The deepest rut which is measured for the inside (i.e. left) or outside (i.e. right) wheel paths of the lane within each interval (50 m).

The wheel paths considered in the dataset are more precisely defined in accordance with AASHTO R85-18 designation, which is 1.0 m wide and centred 0.875 m from the centreline of the lane [11]. The "Lane Type", "HR Rut DL" and "Vehicle ID" attributes have not been considered in the final dataset and modelling process.

3.3 Data Analysis

A correlation matrix was first created with Python to present correlation coefficients between dataset attributes and variables in the data analysis process. Python is an interpreted, high-end programming language and areas of its application are numerous. In this study, Python and its data science libraries are used to perform analysis. In this matrix, the correlation between the two variables is shown in each cell. The correlation matrix is applied to evaluate the strength of the relationships between features and is considered as an input and a diagnostic tool for further and advanced data analysis [12]. It also assists in understanding the correlation among all attributes to select the most suitable variable for prediction modelling. The correlation matrix for Alberta's highway pavement is presented in Fig. 1.

In the second step of the dataset analysis, the k-means clustering technique is performed in Python. This technique could assist in creating a group of abstract objects that are clustered into categories of similar objects. When the model is applied to the whole dataset with no clustering, only one set of results is achieved. By applying

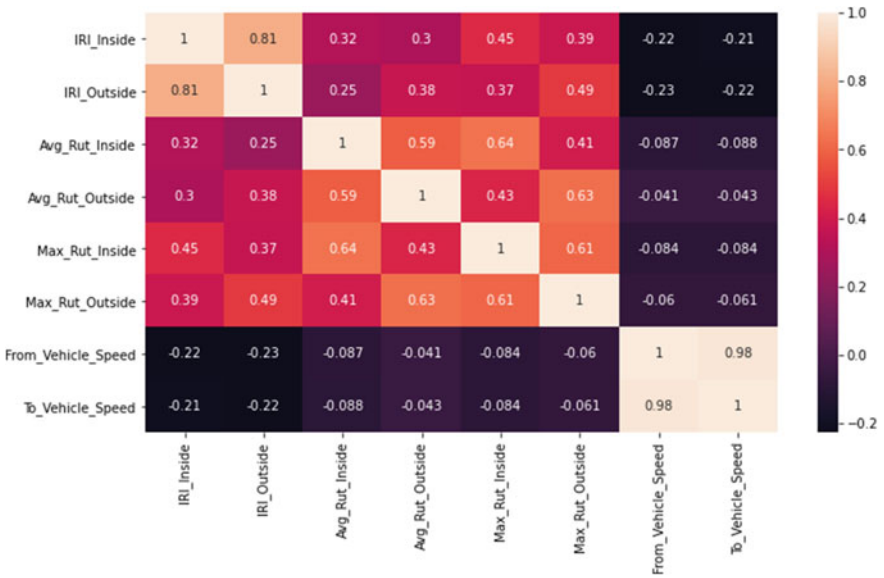

Fig. 1 Correlation matrix for the case study's dataset

the k-means clustering technique, the predictive model runs on different k clusters within the dataset; thus, the predictions for each cluster could become more or less accurate compared to the prediction dataset. If the accuracy of the results increases, this technique could be advantageous when a new data point is added. Once it is added to the whole dataset, its cluster will be identified, and then, the new data point is entered into its corresponding model, which could provide more accurate and better results.

Then, the Principal Component Analysis (PCA) has been conducted. This analysis is done to exclude the mutual impact of the evaluation. This method is also applied in other research works in civil engineering, including a study on Styrene–Butadiene–Styrene (SBS) block polymers modified asphalt. The research was performed to evaluate the ageing behaviour, including the pre and post ageing process of asphalt containing different SBS contents [13, 14].

To obtain insight regarding the distribution of dataset, the cluster analysis is considered in this research as a tool for evaluating each Cluster's features and specifications. As a principle step in an unsupervised algorithm and cluster analysis, the optimized number of dataset clusters should be evaluated. As a popular technique, the Elbow Method has been used in this study to obtain the optimal best value of k in the k-means clustering technique [15]. the Elbow Method is applied by Python's Scikit-learn library and it is concluded that the optimum number of clusters for the case study's dataset is 3 (Fig. 2).

When three principal components are considered regarding the PCA process, the variance results on non-standardized clustering are [0.765, 0.180, 0.037], and the variance results based on standardized clustering are [0.560, 0.138, 0.104]. Thus, the optimized number of clusters based on the Elbow method is three. The non-standardized clusters for three clusters in the case study's dataset are shown in Fig. 3, and the standardized clusters are presented in Fig. 4.

According to the PCA analysis results and further analysis, it is observed that the summation of variance numbers for three standardized clustering ($0.560 + 0.137 + 0.104$) hardly represents 80% of the total dataset. But for non-standardized clustering,

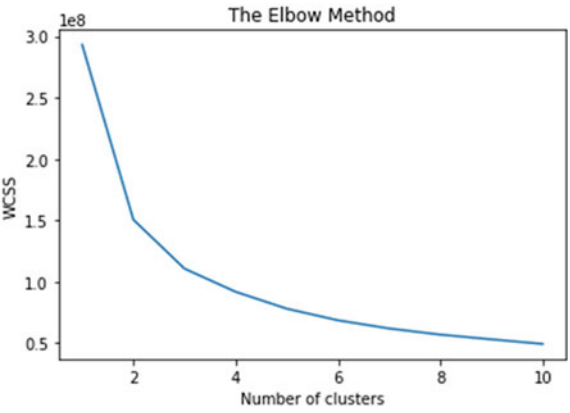

Fig. 2 Optimal number of clusters

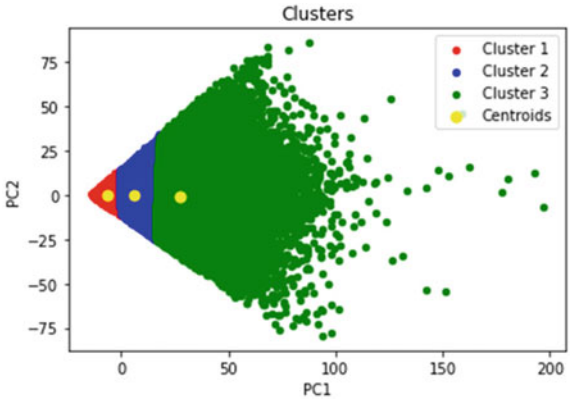

Fig. 3 Non-standardized clusters diagram with 2 principle components

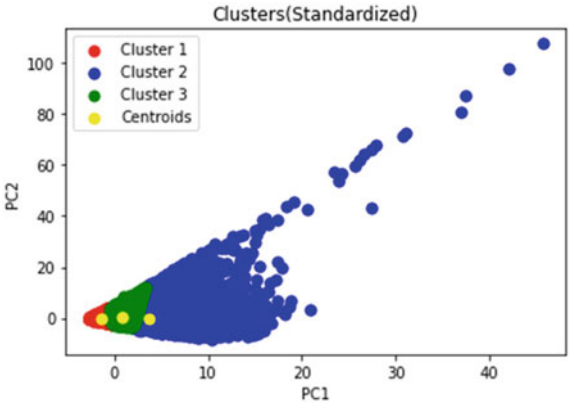

Fig. 4 Standardized clusters with 2 principle components

the variance results for two clusters (0.764 + 0.179) represent more than 94% and for three clusters (0.764 + 0.179 + 0.037) represent more than 98% of the total dataset. Therefore, non-standardized clustering is considered and selected as the appropriate option in this study.

The dataset has been divided into two different parts for training and testing purposes. As a general rule of thumb [16], the ratio of the training set to the testing set is set to four. Thus, one part of the dataset containing 80% of the data is used for network training, and the remaining 20% of the dataset is used for testing the network. Table 1 illustrates the variance results for the training set considering both non-standardized and standardized clustering. It should be noted that the objective

Table 1 Four highest variance variables for the training set

Variance of components for training set with four Components	
Non-standardized clustering	Standardized clustering
[0.765, 0.179, 0.037, 0.012]	[0.560, 0.137, 0.104, 0.087]

is to perform the prediction of pavement parameters based on numeric values and attributes. Table 1 consists of four components to show the trend of variance decrease after three main components. After the three main components, the variance decreases dramatically. In addition, the three main components have 98 percent and 80 percent of the total variance for non-standardized and standardized clustering, respectively. Therefore, some non-numerical variables such as Control Section, Roadway Code, Lane Type, Lane Code, etc., are eliminated from the dataset in the data analysis process.

3.4 Pavement Condition Parameters

In this section, the two main parameters (IRI and Rut) of the pavement condition (measured and available in the data) are elaborated.

The International Roughness Index (IRI) is an important factor for determining the performance of pavements. It has become a worldwide standard. It is a highly used pavement index to measure the roughness of the pavement [2]. The World Bank conducted the International Roughness Experiment not to be dependent on the longitudinal profile measurement device. The development of the International Roughness Index (IRI) was completed in 1982. Many road administrations and departments employ it as a valid and helpful index for measuring riding quality and helps to identify maintenance and rehabilitation tasks [17].

Rutting (rut depth) is the depression (lower levels of some pavement parts compared to surrounding areas) in pavements. The visibility of ruts will be more if they are filled with water after rain. Two main categories of rutting occur in the pavement. There two types are mix and subgrade rutting. In mix rutting, because of issues with the mix or compaction design, the depression will happen in the wheel path, but rutting does not occur for the subgrade. In subgrade rutting, the loading issues will cause exposed wheel path depressions in the road subgrade [18].

According to research works and analyzing the results, the values of rutting and IRI have a positive relationship with each other. However, there is uncertainty about the linear relationship between these two parameters. For example, a study conducted by M. Mubaraki shows a correlation coefficient of 0.464 between IRI and rutting density. Hence, based on correlation and regression coefficients studies, the research concludes that IRI does not represent rutting which could not be considered a ride-quality type of distress [7].

4 Methodology

Generally, the definition of a pavement performance prediction model is "a mathematical description of the expected value that a pavement attribute will take during a specified period of analysis". According to the research background and literature, the main categories of performance prediction models regarding their basis are Empirical (variables such as deflection, accumulated traffic loads, pavement age are usually analyzed with regression models), Mechanistic—empirical (subgrade strain, pavement layer stresses and strains etc. are analyzed and other calibrated models with determined coefficients could be used by regression analysis) and Subjective (are experience-based and some parameters such as serviceability loss are estimated using Markovian transition process models, Bayesian models etc.) [8]. In other studies conducted by scholars, deterioration models are divided into deterministic and probabilistic models. According to the pavement management guide of ASSHTO standard, these models could be categorized into deterministic, probabilistic, Bayesian and subjective (expert-based) models [2].

In the present study, different ANN and regression models have been considered and applied to predict pavement condition data. In this research, three regression models, which are Polynomial Regression, Support Vector Regression (SVR) or Support Vector Machine (SVM) and Random Forest Regression (RFR), have been applied for the prediction model.

The Polynomial Regression suits any dataset size and works appropriately on non-linear applications. However, the right polynomial degree selection is required to obtain a good bias/variance trade-off. SVM or SVR has the advantage of quickly adapting and working correctly on non-linear applications. But the feature scaling should be applied for this method, and the model is hard to understand and not well-known. RFR provides high power and accuracy and performs well on most problems (especially non-linear applications). However, it has some negative points, such as not being interpretable and having the over lifting issue. Also, the number of trees should be selected in the RFR model [19].

4.1 Model Development

Road agencies and organizations apply deterministic models when they have historical pavement condition datasets or enough survey information to identify statistically significant pavement deterioration trends. To develop these models, regression analysis is performed. First, an establishment between two or more variables is conducted. Because the relationship between the dependent variable (the predicted one) and the independent ones is not exact, applying the least square regression technique could be one of the best methods to obtain the statistical fit of the data [17].

4.2 Artificial Neural Network (ANN)

The application of ANN models has been increased recently due to its benefits for solving complex problems having intensive recourses. In an ANN model, a mathematical simulation of biological nervous systems is applied to process the collected information. These systems are used to perform the prediction process of data and to achieve the prediction outputs. To recognize the pattern, the process needs an appropriate training method [6].

In this research, ANN models with different architectures are used to predict one of the pavement condition parameters (IRI) based on other available data in the whole dataset. It should be noted that ANN architectures are selected based on trial and error with engineering judgment. The chosen ANN architectures are the final models used to predict the considered parameter. Two types of transfer functions are selected and used to train the ANN models. The Linear and ReLU (Rectified Linear Unit) Activation Functions are the ones used for different layers of the ANN models in this study.

ANN models are applied for the case study to validate the suitable model, which performs better to predict the "IRI_Inside" parameter. The trained ANN models are used to predict the "IRI_Inside" parameter based on the following variable available in the case study's dataset: IRI_Outside, Avg_Rut_Inside, Avg_Rut_Outside, Max_Rut_Inside, Max_Rut_Outside and HR_RUT_DL. In the final step of ANN model implementation, the R^2 Score and the Root Mean Square Error (RMSE) factors are calculated between the observed and predicted data for the case study to find the recommended ANN model. The results of applying ANN models are shown in Sect. 5.

4.3 Regression

Different regression models discussed earlier have been considered in this research to predict the case study's pavement condition parameters. Regarding the dataset's characteristics and size, the results show that the Random Forest Regression (RFR) model has the highest performance; therefore, it is selected as the primary predictive model for the case study's dataset. The RFR model results demonstrated the most accurate results for predicting the highway network's IRI parameter based on other variables in the dataset because this model captured the underlying patterns of the dataset better than other predictive models. It is noteworthily that because of the high memory required and the time needed for computing, applying the SVR or SVM model for this dataset was considered costly, and thus, the model was only used for one Cluster of the dataset and not for the whole dataset. Also, in the clustering mode, the Multiple Linear Regression (MLR) model was applied for all clusters of C1, C2 and C3 in the present study. These regression models are used to the "IRI_Inside" parameter based on the same variables mentioned for the ANN method. The results are shown in the next section.

5 Results and Discussion

IRI prediction results by applying ANN on the whole dataset for the model having 4 principle components and the one with no principle component are shown in Table 2. It should be noted that the standardization process is applied to the components to investigate how the prediction accuracy changes in comparison with the situation when the raw dataset is fed to the algorithms.

In the next part, in addition to the leading 13 attributes, two variables of "To_Vehicle_Speed", as an additional variable representing the minimum and maximum vehicle speed numbers, are also considered, and the ANN model is applied. The details and results are presented in Table 3.

In the next part of ANN modelling, the clusters of C1, C2 and C3 are created within the whole dataset, and the results are obtained based on these three clusters. Table 4 illustrates the ANN model results for all three clusters.

Table 2 ANN model results for IRI_Inside prediction

Number of components (PCA)	Root mean square error (RMSE)	R^2 score	Activation Function	Root mean square error (RMSE)
Four components	0.253	0.587	Linear	Yes
Four components	0.186	0.696	ReLU	Yes
All components	0.192	0.685	Linear	Yes
	0.177	0.711	ReLU	Yes
	0.193	0.685	Linear	No
	0.178	0.709	ReLU	No

Table 3 ANN results for IRI_Inside prediction considering "From/To Vehicle_Speed" (all components)

Root mean square error (RMSE)	R^2 score	Activation functions for different layers	Standardized
0.173	0.717	ReLU for all layers	No
0.173	0.718	Linear and ReLU	No

Table 4 ANN model results for IRI_Inside prediction for C1, C2 and C3 clusters

Cluster	Root mean square error (RMSE)	R^2 Score	Activation functions for different layers
C1	0.083	0.754	Linear and ReLU
C1	0.082	0.757	ReLU for all layers
C2	0.662	0.503	Linear and ReLU
C3	0.242	0.646	Linear and ReLU

According to the results of running ANN models, the one having both Linear and ReLU activation functions and considering additional variables of "From_Vehicle_Speed" and "To_Vehicle_Speed" show minimum RMSE and maximum R^2 Score, which are most suitable results in all ANN models. If the two addental variables are not considered, the model having all components (attributes) and using both Linear and ReLU activation functions and standardized data has the best results. When the dataset is classified based on clusters, the ANN model for the C1 Cluster and having ReLU for all layers had the best results (minimum RMSE and maximum R^2). In the first stage of regression modelling, the RFR model is applied to the whole dataset (no data clustering) to predict the IRI parameter. The obtained results are presented in Table 5.

The next stage of regression modelling contains applying regression models on three clusters of the dataset. Different regression models are tested for each Cluster of the dataset, and the acceptable results are presented. In addition to RFR as the primary regression model in this study, the Multiple Linear Regression (MLR) is also used for all three clusters. Also, only for the C2 Cluster, the SVM regression model was successfully applied, and results were achieved. Table 6 shows the prediction results of the IRI_Inside parameter obtained by applying MLR and SVM models and for C1, C2 and C3 clusters.

Based on the acceptable results of the MLR model (Table 6), it can be concluded that if a new observation is made and a new data point from the C1 Cluster is entered into the dataset, the prediction for the new data can be conducted by applying MLR method to reduce the computing costs. This approach assists decision-makers and maintenance planners in applying an efficient method for prediction. Table 7 presents the Random Forest Regression (RFR) model results for C1, C2 and C3 clusters.

Table 5 Random Forest Regression (RFR) model results for IRI_Inside prediction

Cluster	Root mean square error (RMSE)	R^2 score	Cluster	RMSE	R^2 score
1	0.349	0.430	5	0.227	0.630
2	0.272	0.556	6	0.222	0.637
3	0.247	0.597	7	0.218	0.644
4	0.234	0.617	8	0.215	0.648

Table 6 Results of IRI_Inside prediction for C1, C2 and C3 clusters

Cluster	Model type	Root mean square error (RMSE)	R^2 score
C1	MLR	0.083	0.754
C2	MLR	0.721	0.458
C2	SVM (radial basis function)	0.688	0.484
C3	MLR	0.253	0.630

Table 7 Random Forest Regression (RFR) model results for IRI_Inside prediction

No. of decision tree	C2 cluster		C2 cluster		C3 cluster	
	RMSE	R^2 score	RMSE	R^2 score	RMSE	R^2 score
1	0.143	0.576	1.407	0.054	0.526	0.232
2	0.122	0.638	1.055	0.208	0.405	0.407
3	0.116	0.655	0.925	0.306	0.364	0.467
4	0.112	0.669	0.864	0.352	0.345	0.496
5	0.109	0.676	0.825	0.381	0.335	0.510
6	0.107	0.682	0.802	0.398	0.325	0.524
7	0.105	0.689	0.783	0.412	0.321	0.531
8	0.104	0.692	0.773	0.420	0.316	0.538
9	0.103	0.695	0.765	0.425	0.313	0.542
10	0.102	0.696	0.760	0.429	0.310	0.547
11	0.102	0.697	0.756	0.433	0.307	0.551
12	0.102	0.697	0.751	0.436	0.304	0.555

6 Conclusions

In this research, efforts have been taken to run different models for predicting the pavement condition of a highway network. The results demonstrated that among ANN models, the one having two additional variables and the other ANN model for the C1 Cluster exposed the best outputs in RMSE and R^2. Regarding the regression models, the MLR model for the C1 Cluster exposed the minimum RMSE and maximum R^2. This model is also suggested for similar datasets to perform the prediction of IRI. In terms of practical implications, the results of this research could be a valuable resource for regions with similar road network characteristics. Finally, to achieve an accurate prediction of IRI in road and highway networks, the recommended prediction models could be used by practitioners such as road agencies, road pavement assessors and maintenance planners to calculate the deterioration time and conduct better recourse and budget allocation and capital planning. Therefore, this research's outputs could assist them in establishing more accurate road and highway maintenance planning.

References

1. Alberta Ministry of Transportation (2015) Transportation Annual Report
2. Sidess A, Ravina A, Oged E (2020) A model for predicting the deterioration of the international roughness index. Int J Pavement Eng 1–11. https://doi.org/10.1080/10298436.2020.1804062
3. Sidess A, Ravina A, Oged E (2020) A model for predicting the deterioration of the pavement condition index. Int J Pavement Eng 1–12

4. Mohammadi A, Amador-Jimenez L, Elsaid F (2019) Simplified pavement performance modeling with only two-time series observations: a case study of Montreal Island. J Transp Eng Part B: Pavements 145(4). https://doi.org/10.1061/JPEODX.0000138
5. Pantuso A, Flintsch GW, Katicha SW, Loprencipe G (2019) Development of network-level pavement deterioration curves using the linear empirical Bayes approach. Int J Pavement Eng 1–14
6. Thube DT (2012) Artificial neural network (ANN) based pavement deterioration models for low volume roads in India. Int J Pavement Res Technol 5(2)
7. Mubaraki M (2016) Study the relationship between pavement surface distress and roughness data. In: MATEC web of conferences, 2012, vol 81. EDP Sciences
8. Saba RG, Huvstig A, Hildebrand G, Sund E, Evensen R, Sigursteinsson H, Elsander J (2006) Performance prediction models for flexible pavements: a state-of-the-art report 62(Nr. 2477):1–54. https://doi.org/10.1093/sysbio/sys110
9. Government of Alberta (2020) International roughness index and rut data. Transportation. https://www.alberta.ca/international-roughness-index-and-rut-data.aspx
10. Alberta Government (2015) International roughness and rut dataset. Transportation. https://open.alberta.ca/opendata/international-roughness-and-rut-data-set#summary
11. Technical Standards Branch (2020) Alberta Transportation. http://www.transportation.alberta.ca/
12. Bock T (n.d.) What is a correlation matrix? Displayr. https://www.displayr.com/what-is-a-correlation-matrix/#:~:text=A correlation matrix is a,a diagnostic for advanced analyses. Accessed 7 Oct 2020
13. Xu M, Zhang Y, Zhao P, Liu C (2020) Study on aging behavior and prediction of SBS modified asphalt with various contents based on PCA and PLS analysis. Constr Build Mater 265:120732
14. Tutorials Point (n.d.) Data mining - cluster analysis. Tutorials Point. https://www.tutorialspoint.com/data_mining/dm_cluster_analysis.htm. Accessed 11 Oct 2020
15. Gupta A (2019) Elbow method for optimal value of k in K means. GeeksforGeeks. https://www.geeksforgeeks.org/elbow-method-for-optimal-value-of-k-in-kmeans/
16. The Data Detective (2020) The 80/20 split intuition and an alternative split method. Medium. https://towardsdatascience.com/finally-why-we-use-an-80-20-split-for-training-and-test-data-plus-an-alternative-method-oh-yes-edc77e96295d
17. Pérez-Acebo H, Linares-Unamunzaga A, Rojí E, Gonzalo-Orden H (2020) IRI performance models for flexible pavements in two-lane roads until first maintenance and/or rehabilitation work. Coatings 10(2).
18. Pavement Interactive (n.d.) Rutting. Pavement tools consortium. https://pavementinteractive.org/reference-desk/pavement-management/pavement-distresses/rutting/. Accessed 23 Sept 2020
19. Keerthi M (2020) How to choose the best regression model for your ML application? A medium corporation. https://medium.com/@mukul04.sk/how-to-choose-the-best-regression-model-for-your-ml-application-d1e60d6a98ad. Accessed 11 Oct 2020

Comparison of the Seismic Performance of Steel Moment-Resisting Frames and Moment-Resisting Knee Braced Frames

Mahdi Mokhtari, Abrar Islam, and Ali Imanpour

1 Frame Design

A five-storey office building with perimeter seismic force-resisting systems (SFRSs) that is located in Vancouver, British Columbia, Canada was selected in this study. The building is located on site class C. The plan of the building shown in Fig. 1 consists of five 9 m-long bays in the N-S direction and seven 9 m-long bays in the E-W direction. The height of the first storey and upper storeys are equal to 4.3 m and 4 m, respectively. The outermost bays of the exterior walls only carry gravity loads, while the rest of the bays are equipped with either MRFs or MRKBFs to resist lateral loads. The SFRS in the E-W direction is studied herein. Both MRFs or MRKBFs were designed in accordance with the National Building Code of Canada [7] and the Canadian Steel Design Standard [1]. In the first design, ductile MRF system was used to resist the lateral loads while MRKBF system was implemented in the second design.

1.1 Moment-Resisting Frame

The seismic performance of the MRF provides a baseline for comparison with the MRKBF. Beams and columns were selected from wide-flange sections conforming to ASTM A992 material with a yield strength of 345 MPa. It was assumed that plastic hinging occurs at the beams ends and the base of the first-storey column. Column splices were placed at the middle of the third storey. Reduced beam section (RBS) beam-to-column moment connections were utilized to ensure plastic hinging

M. Mokhtari (✉) · A. Islam · A. Imanpour
University of Alberta, Alberta, Canada
e-mail: mahdi5@ualberta.ca

S. Walbridge et al. (eds.), *Proceedings of the Canadian Society of Civil Engineering Annual Conference 2021*, Lecture Notes in Civil Engineering 240,
https://doi.org/10.1007/978-981-19-0507-0_25

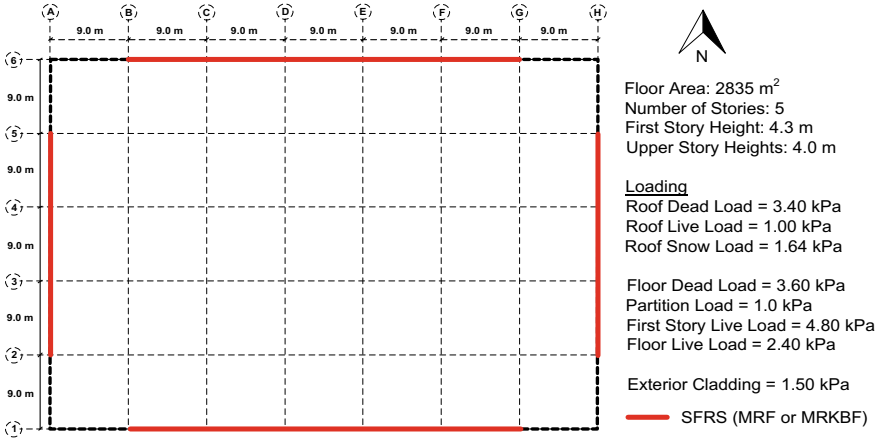

Fig. 1 Plan view of the selected building and loading information

Table 1 Summary of selected members for MRF

Storey	Beam	Interior column	Exterior column
5	W530X82	W610X195	W610X155
4	W610X101	W610X195	W610X155
3	W690X140	W610X217	W610X217
2	W690X170	W610X217	W610X217
1	W690X170	W610X217	W610X217

away from the face of the columns. Maximum allowable flange width cuts were used for the RBS since the NBCC drift requirement (i.e., 2.5%) governed member selection. Doubler plates were used as required at the column panel zones to increase shear resistance with the plate edges fillet welded to the column. Table 1 provides the selected members for the MRF. As shown, deep W610 column sections were selected to satisfy drift requirements as they offer larger flexural stiffness compared to sizes with square cross sections at similar weight. Deep column sections also contribute to minimizing the need for doubler plates, thus resulting in lower fabrication costs.

1.2 Moment-Resisting Knee Braced Frame

Figure 2 depicts the new MRKBF, which is composed of identical beam and column modules. Each beam module consists of a wide-flange section shop-welded to end plates at both ends. Covering up to three storeys, each column module comprises a wide-flange section to which beam stubs and knee braces are connected. Column modules also include shop-welded double-angles at every floor level to frame into the perpendicular gravity beams on site. As shown, beam stub-to-column as well as knee

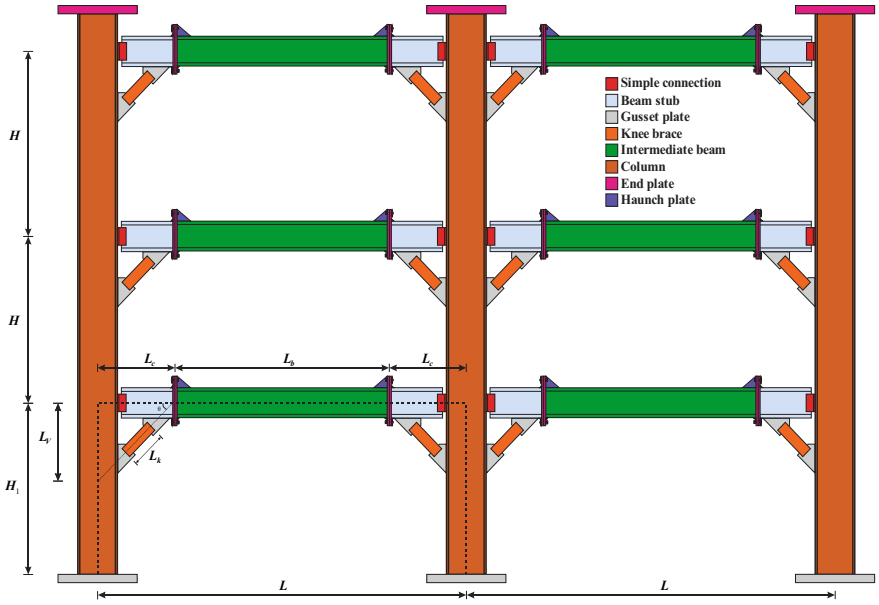

Fig. 2 Moment-resisting knee braced frame (First three storeys shown)

brace-to-beam/column connections are shop-welded simple connections. The beam modules are field-bolted to the column modules through stubs using shop-welded end plates, creating rigid beam-to-stub connections. The end-plate connection to stubs and intermediate beam segments are fabricated using partial-joint-penetration (PJP) groove welds reinforced by fillet welds. Moreover, haunch plates are welded to both ends of the intermediate beam segments in order to keep the plastic hinges away from the beam-to-brace connections.

The yielding mechanism of the MRKBF consists of flexural yielding of intermediate beam segments near the beam-to-stub connections and flexural plastic hinging at the base of the first-storey columns. Due to the similarity between the yielding mechanism of both frames, the seismic design parameters of ductile MRFs prescribed by NBCC 2015 were utilized to design the MRKBF in this study. Future performance evaluation studies should confirm this assumption. The braced length ratio (L_c/L) and the brace angle were considered 0.2 and 45˚, respectively [3]. Similar to the MRF, the member selection was governed by the NBCC drift requirements. The selected members for the MRKBF are summarized in Table 2. Wide-flange beams, beam stubs and columns confirming to ASTM A992 were selected, while the knee braces were made of ASTM A1085 Hollow Structural Sections (HSS).

Table 2 Summary of selected members for MRKBF

Storey	Beam	Beam sub	Knee brace	Interior column	Exterior column
5	W410X46.1	W410X67	HSS114.3X114.3X4.76	W610X125	W460X113
4	W610X82	W610X113	HSS152.4X152.4X9.52	W610X125	W460X113
3	W610X92	W610X140	HSS152.4X152.4X12.7	W610X217	W460X235
2	W610X92	W610X140	HSS152.4X152.4X12.7	W610X217	W460X235
1	W610X92	W610X140	HSS152.4X152.4X12.7	W610X217	W460X235

2 Results and Discussions

Nonlinear static and dynamic analyses were carried out to assess and compare the seismic performance of the designed frames. For the purpose of nonlinear time history analysis, 33 ground motions consisting of three suites of 11 records representing three different sources of seismicity expected in the region, i.e. shallow crustal, subduction intraslab and subduction interface, were selected and scaled to match on average the design response spectrum for the selected site as per the NBCC 2015 guidelines. The numerical models of the frames were developed in the *OpenSees* program [6]. To capture the effects of strength and stiffness deterioration, concentrated plasticity approach using the backbone curve parameters proposed by [4, 5] was implemented in the numerical models. The beam-to-column joint panel zones of the MRF were created using the parallelogram model proposed by [2]. A classical damping matrix was reproduced using the Rayleigh damping approach with a critical damping ratio of $\zeta = 2.0\%$ in the first and second modes of vibration. Mass-proportional damping was assigned to the nodes at column centrelines with point masses and stiffness-proportional term was assigned to elastic elements as recommended by [8]. To simulate member instability, nonlinear force-based elements were used to model the knee braces of the MRKBF.

The MRKBF offers a lighter structure compared to the MRF, leading to 7.35% reduction (49.77 tonnes vs. 53.72 tonnes) in steel tonnage excluding connections and reinforcing plates. The fundamental periods of the MRF and MRKBF were obtained as 1.83 and 1.70 s, respectively, suggesting that the MRKBF is slightly stiffer than the MRF. Figure 3a depicts the base shear versus roof drift curves for both frames. The elastic lateral stiffness of the MRKBF was 18% higher compared to the MRF. Moreover, the ultimate strength of the MRKBF was larger than that of the MRF by 17%, as shown in Fig. 3a. Figure 3b shows the envelope of the peak inter-storey drift ratios under the selected ground motions for the MRF and MRKBF. As shown, the peak drift ratios are always smaller in the MRKBF, except for the roof level. Although the seismic evaluation results prove the structural robustness of the proposed MRKBF system over conventional MRFs, additional connections, such as the shear tab and knee brace-to-beam/column connections, and fabrication costs can adversely affect the cost-efficiency of MRKBFs.

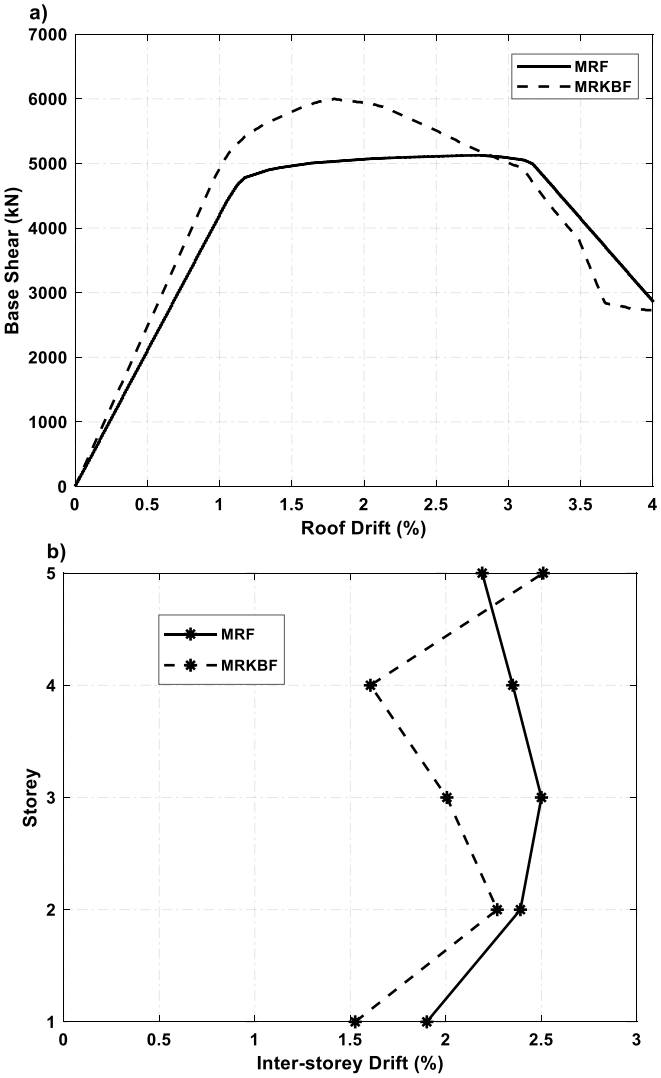

Fig. 3 Nonlinear analysis results: **a** Base Shear—Roof Drift curves from pushover analysis and **b** Maximum inter-storey drift profiles from dynamic analysis

3 Conclusions

A comparative study was carried out on the seismic performance of conventional Moment-Resisting Frames (MRFs) and an innovative modular steel lateral load-resisting system called Moment-Resisting Knee Braced Frame (MRKBF). A 5-story office building located in Vancouver, B.C. was designed once using MRFs and

then using MRKBFs according to the NBCC 2015 and CSA S16-19 guidelines. Detailed numerical models accounting for geometrical and material nonlinearities were developed for both frames. Nonlinear static and dynamic analyses proved the robustness and superiority of the seismic and structural performance of MRKBFs over MRFs. Additionally, the designed MRKBF was lighter in terms of the steel tonnage compared to the MRF. However, the costs associated with the fabrication of modules and additional connections in the MRKBF can lead to a lower level of cost-efficiency in the MRKBFs.

References

1. Canadian Standards Association. Design of Steel Structures CSA S16–19, CSA Group, Mississauga, ON, Canada
2. Gupta A, Krawinkler H (1999) Seismic demands for performance evaluation of steel moment resisting frame structures (SAC Task 5.4.3). In: Blume JA (ed) Earthquake engineering research center report no. 132, Department of Civil Engineering, Stanford University, Stanford, CA, USA
3. Leelataviwat S, Suksan B, Srechai J, Warnitchai P (2011) Seismic design and behavior of ductile knee-braced moment frames. J Struct Eng ASCE 137(5):579–588
4. Lignos DG, Krawinkler H (2011) Deterioration modeling of steel components in support of collapse prediction of steel moment frames under earthquake loading. J Struct Eng ASCE 137(11):1291–1302
5. Lignos DG, Hartloper AR, Elkady A, Deierlein GG, Hamburger R (2019) Proposed updates to the ASCE 41 nonlinear modeling parameters for wide-flange steel columns in support of performance-based seismic engineering. J Struct Eng ASCE 145(9)
6. Mazzoni S, McKenna F, Scott MH, Fenves GL (2006) OpenSees command language manual. University of California, Berkeley, CA, USA
7. National Research Council Canada (2015) National Building Code of Canada 2015, NRC Canada, Ottawa, ON, Canada
8. Zareian F, Medina RA (2010) A practical method for proper modeling of structural damping in inelastic plane structural systems. Comput Struct 88:45–53

A Canadian First: Developing a Climate Change Action Plan for Engineers and Geoscientists BC

Charling C. Li, Harshan Radhakrishnan, and Malcolm L. Shield

1 Introduction

In March 2021, Engineers and Geoscientists of British Columbia launched its first Climate Change Action Plan (CCAP) to guide its response to our changing climate. The development of the CCAP is a first in Canada for an engineering and geoscience regulator and is consistent with the regulatory body's guiding principle to act first and foremost in the public interest and to proactively plan for the future [8]. Engineers and Geoscientists BC undertook a wide-ranging engagement process to garner insights and opinions from its membership as well as a broader set of stakeholders to create a plan that meets the needs of its registrants in incorporating climate considerations in their professional practice. The challenge of the CCAP was to determine which types of climate actions are appropriate, effective, fitting within the regulatory mandate of Engineers and Geoscientists BC, to bring an appropriate organizational focus to the topic and to enable the regulatory body to dynamically respond to climate change.

This paper shares the process that the regulatory body and its consultant team took to develop the CCAP, which began in early 2019 and was approved and adopted unanimously by Engineers and Geoscientists BC's Council.

C. C. Li
City of Vancouver, Canada

H. Radhakrishnan (✉)
Engineers and Geoscientists BC, Burnaby, Canada
e-mail: hrad@egbc.ca

M. L. Shield
Associated Engineering, Edmonton, Canada

S. Walbridge et al. (eds.), *Proceedings of the Canadian Society of Civil Engineering Annual Conference 2021*, Lecture Notes in Civil Engineering 240,
https://doi.org/10.1007/978-981-19-0507-0_26

1.1 Climate Change and Professional Practice

Internationally and within Canada, there is a growing recognition that the earth's climate is changing at an unprecedented rate due to the emission of greenhouse gases resulting from human activity, and that recent historic climate trends are no longer a good indicator of the climate's future state. The Intergovernmental Panel on Climate Change (IPCC) made clear that warming of 1.5 °C or more increases the risks associated with long-lasting or irreversible changes to the earth's climate and ecosystems (IPCC 12). Recent Federal research indicates that Canada is warming at twice the global average rate; the impacts of which are already being felt and which are anticipated to increase in severity by mid-century (NRCan 2019). In British Columbia, independent research suggests that by 2050 most regions will experience hotter, drier summers; an increased intensity and frequency of precipitation and extreme events; warmer winters with lower snowpack; and longer growing seasons [10]. Such physical changes are already starting to have profound effects on the social, natural and built systems within which engineers and geoscientists hold many inherent responsibilities.

Although it is still possible to limit global average temperature rise to less than 1.5 °C (IPCC 2018), rapid and far-reaching transitions to land, energy, industry, buildings, transportation and cities will be necessary to achieve this target. Engineers and geoscientist need to respond to current climate change impacts and actively plan for the impacts that can be reasonably anticipated based on the latest climate science, traditional and cultural knowledge, while working to reduce the emission of greenhouse gases. In seeking to respond to climate change consistently, using a risk lens to understand the physical impacts and business or technology implications of reducing greenhouse gas emissions can be highly instructive. Such an approach aligns with the code of ethics for engineering and geoscience professionals, the first tenet of which is to "hold paramount the safety, health, and welfare of the public, including the protection of the environment and the promotion of health and safety in the workplace".

1.2 Engineers and Geoscientists BC's Regulatory Framework

Engineers and Geoscientists BC is the regulatory body for the engineering and geoscience professions and was established under the Province's *Engineers and Geoscientists Act*. In February 2021, Engineers and Geoscientists BC transitioned to operating under the new *Professional Governance Act* (PGA), a consolidated framework that sets consistent governance standards for British Columbia's self-regulated professions and introduces new regulatory tools, processes, and requirements. The PGA also provided a clear directive for the regulatory body to "…serve and protect the public interest with respect to the exercise of the profession, professional governance, and the conduct of registrants in the registrants' regulated practice, and to exercise

its power and discharge its responsibilities in the public interest" (S. 22.1 [11]). The regulatory body also has the responsibility to "…promote and enhance…the ability of its registrants to respond and adapt to changes in practice environments, advances in technology and other emerging issues" (S.22.2.k.iii [11]).

In 2019, the pending new legislative framework and the code of ethics illuminated the need for Engineers and Geoscientists BC to develop the CCAP in order to understand how to better support its registrants that serves the public interest and protects the environment. The development of the CCAP and its related engagement activities was the opportunity for the regulatory body to clearly identify its role as a regulator of professionals who have significant roles and responsibilities in the design, construction and maintenance of physical systems, development processes and decisions that are affected by a rapidly changing climate.

2 Development of the Climate Change Action Plan

2.1 Leading Up to the CCAP

Within Engineers and Geoscientists BC there had been a growing interest in understanding how to support registrants in responding to climate change. The regulatory body has led and supported many initiatives to advance its ability to address climate change in engineering and geoscience practice, including funding dedicated staff resources, developing practice guidelines on adapting to climate change and reducing greenhouse gas emissions, establishing a Climate Change Information Portal, engaging standard-setting bodies, and improving continuing education offerings related to climate change. Since 2012, Engineers and Geoscientists BC has also had a dedicated Climate Change Advisory Group (CCAG), a group of volunteers with cross-sector expertise to advise Engineers and Geoscientists BC. In 2017, the regulatory body released an on-line survey to all members in good standing to gauge their awareness of climate change and how professional practice should respond. The survey garnered a response rate amongst the regulatory body's highest for any survey and made clear that registrants understood the need to act on climate change, were unsure how to, and were seeking guidance from the regulatory body to integrate climate considerations into their work. At the 2018 Annual General Meeting, a general motion was brought forward to Council to consider undertaking and putting the necessary resources into the development of a comprehensive action plan that would provide direction on the roles and duties of registrants in addressing the changing climate. This motion catalyzed the process to develop the CCAP.

2.2 Plan Development and Engagement Process

Engineers and Geoscientists BC began by undertaking a desktop review to identify public-facing strategic climate plans for engineering and professional organizations. The review was extensive, although not exhaustive, touching mostly on English-language material from Europe, North America, and Australia. No outward-facing, strategic climate plans for engineering regulatory bodies were found, although many organizations were acting to meet their responsibilities in various ways. Most of the actions centered on knowledge dissemination and clear articulations on the need to consider climate change impacts in their respective fields; there was significantly less information on how the organizations themselves, or their membership, could act on climate change. Without any similar plans from peer regulatory bodies to reference or emulate, Engineers and Geoscientists BC tailored an engagement and development process to meet its unique organizational and regulatory needs.

The following objectives were identified in order to guide engagement with stakeholders internal and external to the regulatory body:

- Raise awareness about the potential impacts of climate change as they relate to the professional practice of engineering and geoscience;
- Increase registrants' awareness of the regulatory body's existing resources on climate change;
- Identify the issues, challenges, and opportunities experienced by registrants with respect to addressing climate change in professional practice; and
- Identify areas of practice that can contribute to climate change adaptation and mitigation.

An initial discussion paper was released to frame the conversation around the climate related challenges that registrants saw in their professional practice. The discussion paper laid out climate actions that the regulatory body was already taking alongside proposed new actions, and requested feedback as well as suggestions for other actions. The external engagement process began in late 2019 and included a presentation at the 2020 Annual Conference, a town-hall-style webinar, a series of focus groups with stakeholders in key disciplines and business sectors, and one-on-one interviews with subject matter experts in policy, academia, and professional practice. Written responses to the discussion paper were solicited from all registrants and stakeholders from February to June 2020. Internal engagement included workshops and presentations to Engineers and Geoscientists BC's leadership team and staff, and its volunteers within the Sustainability Advisory Group, the Climate Change Advisory Group, and the specifically formed Climate Change Action Plan Steering Group ('the Steering Group').

2.3 What We Heard

The external engagement process provided valuable insight into registrants' and stakeholders' experience of how climate change is affecting their work. In general, there was broad support for the regulatory body to strengthen its position on climate change in order to have practical effect. Only a few respondents felt that it should play a smaller role in climate action. Respondents identified the challenge of varying levels of awareness and knowledge around climate change in professional practice, as many registrants were unclear on how climate change impacted professional liability and their duty to uphold the safety and protection of the public and the environment. Registrants identified how climate impacts and related challenges differed across sectors and areas of practice and looked to Engineers and Geoscientists BC to provide more specific and actionable guidance. Registrants highlighted the need for the regulatory body to continue to foster collaboration with stakeholders across the public and private sectors and across disciplines to keep registrants up-to-date with climate-related policies, technology, science, and practice. Registrants were aware that many codes and standards are based on historical climate data and are becoming outdated in a rapidly changing climate. They were unsure of how to account for future climate risks in the meantime, as codes and standards can take a long time to be updated and released. Increased training and resources on identifying, communicating, and mitigating climate risk were highlighted as an important strategy for helping registrants manage professional liability concerns stemming from to climate change.

2.4 Developing Goals and Action Areas

The engagement process led Engineers and Geoscientists BC to establish twin goals to holistically address climate change in professional practice, committing it to:

- Support the effective assessment and management of climate risk in the practice of professional engineering and geoscience in British Columbia ('the adaptation goal'); and
- Support registrants to develop and implement solutions to reduce greenhouse gas emissions ('the mitigation goal').

A few respondents and stakeholders felt that the role of engineers and geoscientists was better suited to focus solely on the adaptation goal, while some felt that the mitigation goal was outside regulatory body's reach and mandate because emissions reduction goals and targets are dictated by public policy. Other participants, however, wanted Engineers and Geoscientists BC to encourage more aggressive climate mitigation efforts to advance global sustainability objectives. Engineers and Geoscientists BC's position on mitigation and the role of engineers and geoscientists is clear. In its 2016 position paper, Engineers and Geoscientists BC accepts there is

"strong evidence that human activities, in particular activities that emit greenhouse gases, are contributing to global climate change…[and that]…registrants have the potential to influence greenhouse gas emissions through their professional activities, and are expected to consider the impact of their work on the climate" (EGBC 2016). This position, coupled with strong evidence of the negative impacts of climate change to human and natural systems (IPCC 2018), culminated in the decision to hold the mitigation and adaptation goals on equal footing as twin goals in the CCAP.

With the two goals identified Engineers and Geoscientists BC's consultant team drafted key thematic areas through which to consider and evaluate the candidate actions solicited through the external engagement. These four themes also serve as objectives to advance climate goals that the regulatory body will pursue through the CCAP, as they align with the regulatory mandate that Engineers and Geoscientists BC has under the *Professional Governance Act*:

- Leadership and Collaboration: Lead the engineering and geoscience professions' response to climate change in BC and collaborate with others to leverage resources and enhance impact.
- Registration and Competency: Update the registration process for professional engineers and geoscientists to incorporate climate change competencies.
- Education and Knowledge Sharing: Build registrants' knowledge of and capacity to consider climate change in their professional practice.
- Practice Resources: Provide registrants with practical and relevant practice resources to help them deliver appropriate responses to a changing climate and reduce greenhouse gas emissions.

2.5 Developing the Actions

The input from the external engagement process, as well as additional insight from the volunteer committees, staff, and consultant teams had yielded a comprehensive list of more than 70 candidate actions for consideration. These were initially screened to see if they fit within, or were close to, Engineers and Geoscientists BC's regulatory mandate. Those that were too far outside the mandate were screened out. A theory of change wireframe was developed to ensure the selected actions would support either one of the CCAP's twin goals and achieve its objectives as identified by the four thematic areas (see Fig. 1).

The remaining candidate actions were scored by the volunteer Steering Group and staff for their effectiveness in achieving the regulatory body's climate goals, and by the staff team for the anticipated level of effort to execute the action. The combined score (which deliberately had no weighting) gave an overall rating for each action. This rating was not determinative; its purpose was to structure conversations at the Steering Group as they reviewed and shortlisted actions for further development. The shortlisted actions were further refined by Engineers and Geoscientists BC's staff, the consultant team and the Steering Group, to a consolidated, and more manageable, set of 10 actions included in the CCAP (see Fig. 1).

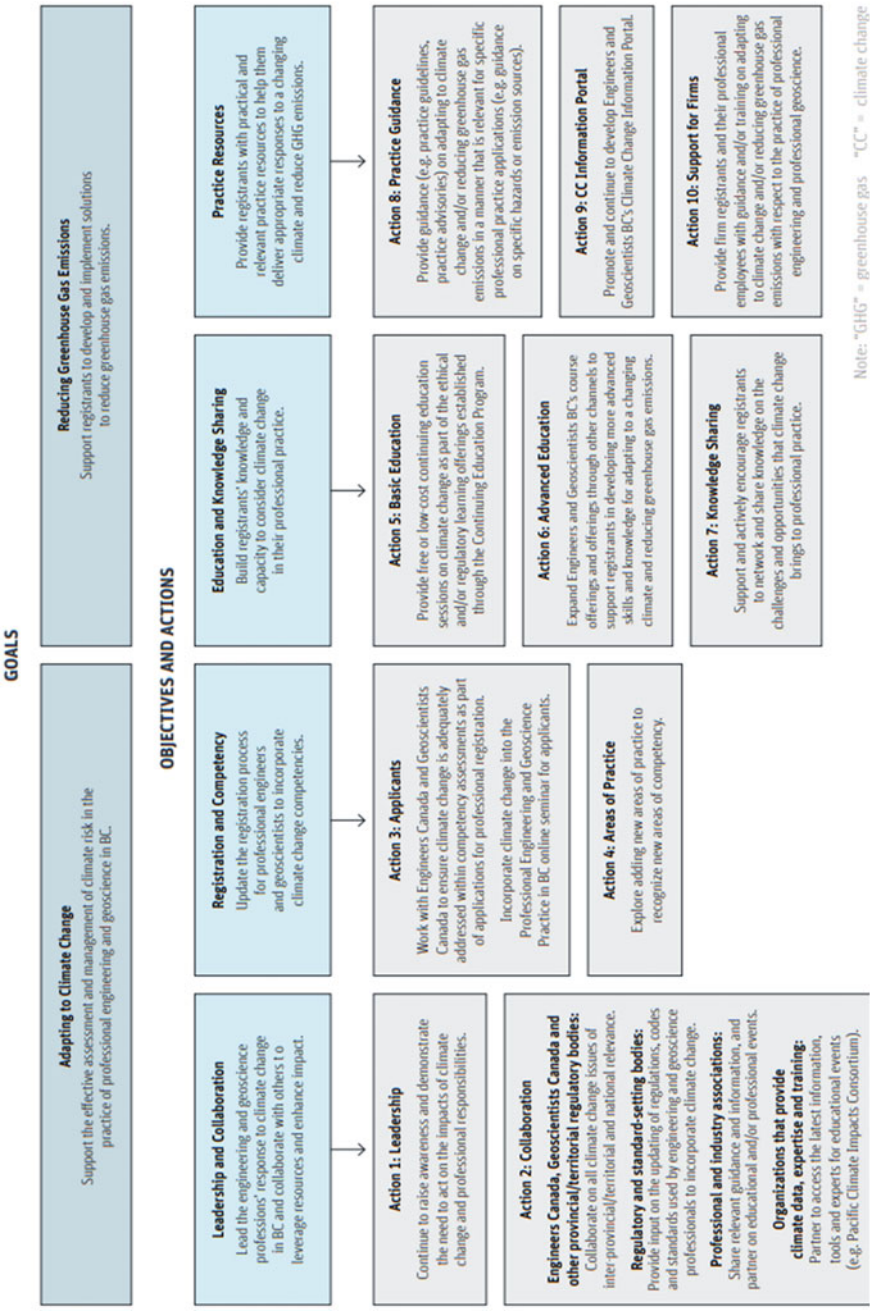

Fig. 1 Goals, Objectives and Actions of the Climate Change Action Plan, Engineers andd Geoscientists BC, 2021c. *Note* "GHG" greenhouse gas "CC" climate change

Implementing the CCAP will build on Engineers and Geoscientists BC's previous work in this space. Staff are making plans to track, evaluate and report on Engineers and Geoscientists BC's progress in delivering these actions to gauge success. The regulatory body will continue to assess progress towards the goals in the CCAP by engaging regularly with registrants to ensure they are receiving adequate support and will evaluate progress on an annual basis. The Action Plan will be reviewed and updated in three years.

3 Conclusion

Through the development of the CCAP, we heard that taking action on climate change presented both challenges and opportunities for the engineering and geoscience professions. While engineers and geoscientists are only a small group of actors considering the broad scope of climate change and the wide-ranging societal response that is necessary, we can play significant roles in advancing positive change and manage climate risk through our professional practice. No single profession or organization alone can make sense of, let alone mitigate, the multitude of risks posed by a rapidly changing climate. Interdisciplinary collaboration with professions working across all orders of government, academia, industry, and beyond can help engineers and geoscientists identify and manage such risks and meaningfully contribute to avoiding the worst effects of climate change.

The development of this plan has helped Engineers and Geoscientists BC identify new actions and build on existing practices to support registrants in fulfilling their professional responsibilities and meet the requirements of clients and owners to consider climate change. The CCAP's robust engagement and thorough development process helped Engineers and Geoscientists BC determine how to carry out its mandate to serve and protect the public interest as a regulatory body in responding to climate change. The Plan and development process is an example that other organizations may reference in their own activities to integrate climate change risk into their business, organizational or legislated objectives.

Acknowledgements The authors of this paper would like to acknowledge the efforts of volunteers and staff who guided the development of the CCAP, Pacific Institute for Climate Solutions for funding an internship position to support the engagement process as well as Sally Rudd of Compass Resource Management who led the CCAP development and engagement process on behalf of Engineers and Geoscientists BC. The role of the authors in the development of the CCAP are as follows: Charling Li is a volunteer with Engineers and Geoscientists BC who participated in the plan development process, Malcolm Shield is one of the lead consultants for the Plan's development, and Harshan Radhakrishnan is Engineers and Geoscientists BC's project manager for the Plan's development.

References

1. Engineers & Geoscientists British Columbia (EGBC). January 27, 2014 "Engineers and Geoscientists BC Climate Change Position Paper on evolving responsibilities for engineers and geoscientists." EGBC.ca. Accessed February 24, 2021. https://www.egbc.ca/getmedia/a39ff60e-80a1-4750-b6a5-9ddc1d75248a/APEGBC-Climate-Change-Position-Paper.pdf
2. Engineers & Geoscientists British Columbia (EGBC). September 8, 2016 "Engineers and Geoscientists BC Position Paper on Human-Induced Climate Change." EGBC.ca. Accessed February 24, 2021 https://www.egbc.ca/getmedia/33cce5c7-f7ab-4752-a398-4ca6e2c6dee3/Position-Paper-Final-2016.aspx
3. Engineers & Geoscientists British Columbia (EGBC) (2017a) Engineers and Geoscientists BC Climate Change Awareness Survey. EGBC.ca. Accessed February 24, 2021. https://www.egbc.ca/getmedia/412710a2-fa56-489b-9a0a-a6c7d560ec4b/Climate-Change-Survey-Findings-June-2017.pdf
4. Engineers & Geoscientists British Columbia (EGBC) (2017b) Engineers and Geoscientists BC Climate Change Awareness Survey Infographics." EGBC.ca. Accessed February 24, 2021. https://www.egbc.ca/getmedia/e7c4a71c-eda2-418d-bb7b-0af8ee226331/EGBC-CCAG-Survey-Infographic-FINAL.pdf
5. Engineers & Geoscientists British Columbia (EGBC) (2020) Discussion Paper - Climate Change Action Plan. EGBC.ca. Accessed February 24, 2021. https://www.egbc.ca/getmedia/7e48cabd-75d9-407b-a0be-d4bcb2d9d205/CCAP-Discussion-Paper-2020.pdf
6. Engineers & Geoscientists British Columbia (EGBC) (2021a) Climate Change Action Plan - What We Heard Report." EGBC.ca. Accessed February 24, 2021. https://www.egbc.ca/getmedia/fdcb28dd-39f3-4972-b838-34c09ad3b1c3/Climate-Change-Action-Plan-What-We-Heard-Report.pdf
8. Engineers & Geoscientists British Columbia (EGBC) (2021b) Strategic Plan & Core Values. Accessed March 1, 2021. https://www.egbc.ca/About/Governance/Strategic-Plan-Core-Values.
9. Engineers & Geoscientists British Columbia (EGBC) (2021c) Climate Change Action Plan. EGBC.ca. Accessed March 16, 2021. https://www.egbc.ca/getmedia/50e4e26b-30ad-46c8-8ca1-f06428af65dc/Engineers-and-Geoscientists-BC-Climate-Change-Action-Plan.pdf.aspx
10. Government of BC (2019) Preliminary Strategic Assessment of Climate Change. gov.bc.ca. Accessed February 24, 2021. https://www2.gov.bc.ca/gov/content/environment/climate-change/adaptation/risk-assessment
11. Government of BC (2021) Professional Governance Act (PGA)" Queen's Printer. Assented to November 27, 2018, effective February 5 2021." Bclaws.gov.bc.ca. Accessed February 24, 2021. https://www.bclaws.gov.bc.ca/civix/document/id/complete/statreg/18047#section22
12. Masson-Delmotte V, Zhai P, Pörtner HO, Roberts D, Skea J, Shukla PR, Pirani A, Moufouma-Okia W, Péan C, Pidcock R, Connors S (eds) (2018) International Panel on Climate Change (IPCC): Summary for Policymakers. In: Global Warming of 1.5°C. An IPCC Special Report on the impacts of global warming of 1.5°C above pre-industrial levels and related global greenhouse gas emission pathways, in the context of strengthening the global response to the threat of climate change, sustainable development, and efforts to eradicate poverty. World Meteorological Organization, Geneva, Switzerland, 32 pp
13. Natural Resources Canada (NRCan) (2019) Canada's Changing Climate Report" NRCan.gc.ca. Accessed February 24, 2021.https://www.nrcan.gc.ca/environment/impacts-adaptation/21177
14. Office of the Superintendent of Professional Governance (OSPG), February 5, 2021 OSPG Guidance: Advocacy Activity Evaluation Framework. Accessed February 24, 2021. https://professionalgovernancebc.ca/app/uploads/sites/498/2021/02/2020-GD-02-Advocacy-Framework-Web-20210205.pdf

Structural Defects Classification and Detection Using Convolutional Neural Network (CNN): A Review

P. Arafin and A. H. M. M. Billah

1 Introduction

With increasing amount of assets and business competition, owners and property managers are now more concerned with assessing the condition of their assets more efficiently to improve business performance and quality of work effectively to maintain their assets in operable condition [19]. In light of abrupt changes in our climate and natural disaster pattern, currently structures are in need of more frequent inspection and remediation plan. As a result, clients are more indulgent towards time-saving, effective, and economical solutions [1, 20, 28]. However, in the conventional inspection method, engineers physically perform a detailed condition assessment of the structure and prepare the final assessment on a remediation plan and, cost-estimation based on their experience. Unlike the traditional methods, computer-vision analysis offers a comprehensive solution that include detection, diagnosis and projection of the structural defects as well as remaining service life estimation [3]. Consequently, in Structural Health Monitoring system deep-learning models have become the most attractive approach showing significantly accurate performance [11, 29].

Surface defects, for instance- crack, surface deterioration, spalling, moisture damage, corrosion, are the most intimidating conditions that reflect the performance, durability, and soundness of the structure. To avoid the conventional human-based surface defects identification, various image processing techniques (IPTs) are developed. For instance, some of these IPTs are able to identify [8], and measure the width and localization of the cracks [17]. Despite being effective in detecting some specific

P. Arafin · A. H. M. M. Billah (✉)
Department of Civil Engineering, Lakehead University, Ontario, Canada
e-mail: habillah@lakeheadu.ca

P. Arafin
e-mail: parafin@lakeheadu.ca

S. Walbridge et al. (eds.), *Proceedings of the Canadian Society of Civil Engineering Annual Conference 2021*, Lecture Notes in Civil Engineering 240,
https://doi.org/10.1007/978-981-19-0507-0_27

image patterns, the overall accuracy of IPTs are not quiet appraisable. Different prevalent conditions such as, light, shadows, and rusty and rough surfaces can affect the images collected from a damaged concrete structure [16]. To overcome these shortcomings, Deep-learning was considered to be a great computer vision model to detect and classify the defect types from a vast set of labeled data. In recent years, a popular class of Deep-Learning methods known as Convolutional neural networks (CNNs), have been considered to be a strong candidate for damage detection due to their accuracy and ability in automatic feature extraction [22]. Later on, CNN was used by Gao and Mosalam [9]—for Multiple building systems and components damage classification, Kucuksubasia and Sorgucb [14]—for RC buildings cracks classification, where the performance evaluation was done based on confusion matrix and accuracy, respectively [23]. Over the last decade, significant advancement in artificial intelligence and IPTs have found their way in structural inspection and condition assessment. This paper aims to provide a summary of recent applications of CNN in structural damage detection with the following objectives:

1. To review the frontier CNN-based defect classification, detection process and working with pre-build CNN architecture models. The first segment summarizes the data preparation process, input methods, layers, parameters, and the classification output, and the second section outlines the advantages and performance criteria for pre-build CNN architecture models.
2. To study and summarize the existing CNN-based literature focusing on the structural defects classification and identification, address the significance and limitations of existing literature and identify the future scopes of CNN-based structural condition assessment.

2 Brief Description of CNN

2.1 How Convolutional Neural Network Works

Convolutional Neural Network (ConvNet/CNN) is a deep learning algorithm in Machine Learning (ML), which takes images as an input, learns the distinct features of an input image with training and validation through learnable parameters and hyper-parameters, and as an output classifies the images one from the other (Fig. 1).

2.2 General Process of Data Preparation and Data Input Method

Pre-labeled defect images are collected from various sources, including investigation reports, and image database, such as- ImageNet, DEEDS. The datasets are then divided into a Training set, Validation set, and Testing set for each type of defect,

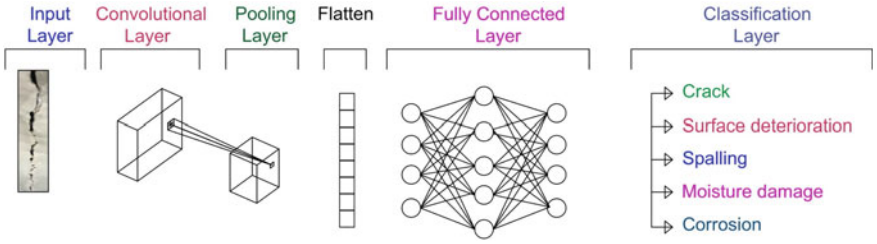

Fig. 1 Schematic diagram of basic CNN architecture

depending on the original size of the dataset and the number of hyper-parameters to train. Even though the original images can have different resolutions, the images are modified into lower resolution with RGB (Red–Green–Blue) channels (Fig. 2), and a close-cut image of defects is cropped out from the original image. When the network is trained on relatively small images, it can scan any desired feature quiet accurately larger than the designed size, but not vice-versa [7].

In data preparation, it is crucial to have an extensive amount of images as the performance of the CNN model tremendously depends on the size of the dataset, otherwise data augmentation-an artificial technique to create new datasets from existing datasets, can be an ultimate solution to optimize the model performance. Different techniques are typically employed for image manipulation, for instance-flips, zooms, shifts, crop, translations, brightness adjustment, rotations, resizing, and with a minor alteration to the existing dataset, neural network considers the manipulated image as a distinct image.

Depending on the image resolution, computers see the image as an assemblage of pixels such as—h x w x d, where h = Height, w = Width, d = Dimension of Channel (RGB channel) (Fig. 2). To reduce the computational time, CNN classifier transfers every Image from RGB channels to the grayscale level as the color feature is not an essential filter (Flah et al. 2020).

Fig. 2 Data input style

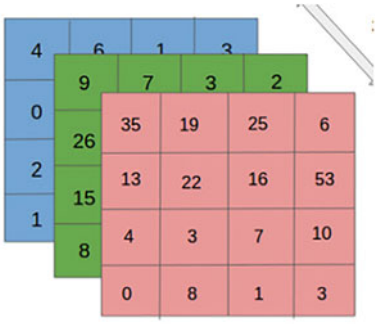

2.3 Layers of CNN Model

The CNN model consist of—(a) input layer, (b) hidden layer—(b.1) convolutional layer, (b.2) pooling layer, (b.3) fully connected layer, (c) classification layer (Fig. 3). In convolutional layer *'filter'* are used to extract certain feature from an input image. To explain- filter is a prespecified matrix which moves across the image in a consequent way and multiplied with the input value which enhances the output in a certain preferable manner. Filters are updated based on the best feature output with each forward-pass and backpropagation.

With each upcoming layer in deep neural network two problems are faced—(a) the image size shrinks, and (b) the pixels at edge side of the image are less used than the middle potion of pixels. So, technically a lot of informaton of the edge side is getting missed and to solve this Padding is introduced, which simply indicates to add layers containing value of "0" in both direction of the input matrix to keep the output size same as the input size. Padding, $P = \frac{f-1}{2}$, where f indicates the size of the filter. After the convolutional layer, pooling layer extraxts the specific feature of an image and helps with three things—(a) by having less spatial information, it helps to gain computation performance (Down sampling), (b) Less spatial information also means less parameters, which minimizes the chances of over-fit model, and (c) translation invariance can be gained. The most common type of pooling techniques are—(a) Max Pooling—Calculate the maximum value for each patch of the feature map, (b) Average Pooling—Calculate the average value for each patch on the feature map. Later on the fully connected layer works simply as a feed-forward neural networks. Fully connected (FC) input layer takes the 3D output of the previous convolutional layers or pooling layers, "flattens" them, and turns them into a single vector that can be an input for the next stage. When an input data is multiplied with its weight, the output data is verified through an activation function. The activation function works as a limit function, which sets a range to determine if the output data is within the limit. Each layer of the Convolutional Neural Network follows the $g\,(Wx + b)$ formulation, where x = input, W = weight, b = bias, g = activation function. The working principle of CNN is summarized in Fig. 4.

At the output layer, which is also called a classification layer typically considers a SOFTMAX activation function (a multi-classifier neural network), where a standanrd exponential fucntion of each element is devided by the sum of all the exponentials and the output is defined as a probability value for each of the classification labels which the network is trying to predict.

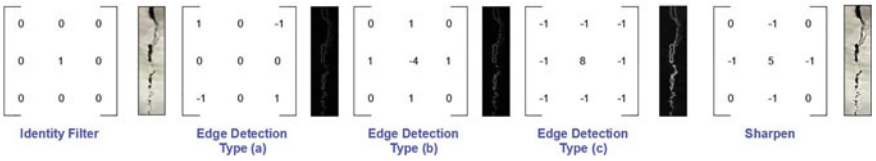

Fig. 3 Some examples of pre-defined filters

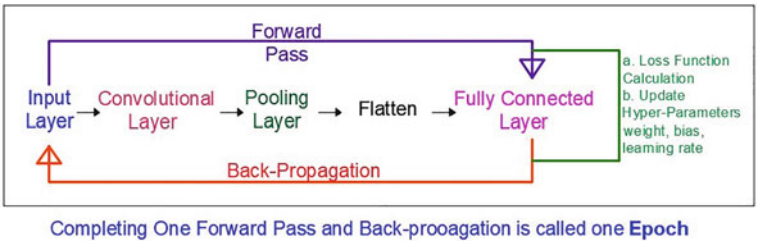

Fig. 4 Flow chart of CNN work procedure

During the trailing process at the end of each forward-pass and back-pass, which is called an epoch, the loss will be calculated using the network's output predictions and the true labels for the respective input.

Loss/Error = (model's prediction—(true label). Loss function optimizes the models' hyper-parameters ((weight, bias, learning rate).

2.4 Detection, Localization and Segmentation in CNN

In CNN, image classification labels the images based on a specific feature of an image and localization helps to identify the location of a single feature in an image. Some Object Localization algorithms such as—Sliding Window algorithm, YOLO (You Only Look Once), CAM (Class Activation Mapping), which works by putting a rectangular bounding box to show the existent defect area. Whereas the localization algorithm identifies a single object, object detection process identifies multiple objects present in an image. Image segmentation works as dividing an image into segments to focus only at the segments with certain features and to avoid processing the entire image at once (Fig. 5). U-NET, a profound segmentation method works in two steps-feature extraction and unsampling operations, also known as the encoder-decoder structure. U-NET is an end-to-end fully convolutional network, which can work with any sizes of images.

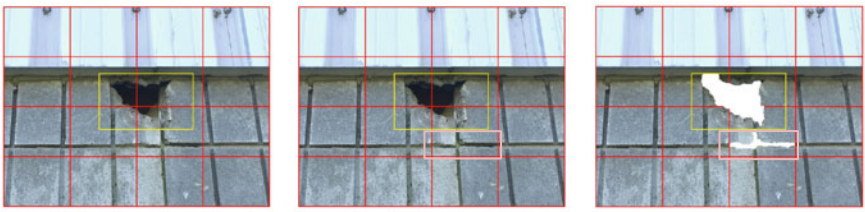

Fig. 5 **a** Classification and locatization **b** Object detection **c** Segmentation process of an image

3 Descriptions of Pre-build CNN Model

A pre-build or pre-trained model represents a fully trained filters, weights and bias features of a certain dataset and these learned features are often transferred to a different dataset to initialize the model, which is time-saving and beneficial for the modeller to easily identify the required features. This is introduced as Transfer Learning in CNN. In transfer learning, the pre-build model is adjusted to new model, for instance- the number of nodes in the input and output layers are adjusted to perform a similar task which is called fine tuning of the model.

AlexNet was one of the first deep learning CNN to achieve a considerable accuracy of 84.7%, consisting of five conv layers, three FC layer and ReLu (Rectified Liner Unit) as activation layer. Later on VGGNet was introduced to improve the training time while reducing the parameters of the conv layers, where each conv block is followed by a pooling layer [2]. In deep learning going deeper does not always results in more accuracy but in most of the cases the accuracy decreases by adding more layers to the network. To mitigate this vanishing gradient problem, ResNet architecture is introduced with the concept of skip connection to add the output from an earlier layer to a later layer. In CNN architecture Inception model is one of the latest upgradation, working with the concept of Inception layer, which is a combination of a block of parallel convolutional layers with multiple sized filters, a max pooling layer and as the output of the module the result is concatenated (Fig. 6). Till today Inception model is being considered a very simple but powerful architectural unit to learn both the same sized and different sized filters in parallel manner. Over the timeline different type of CNN architectures are built to improve the model performance, and a general timeline of introduction of CNN architectures are showed in Fig. 7.

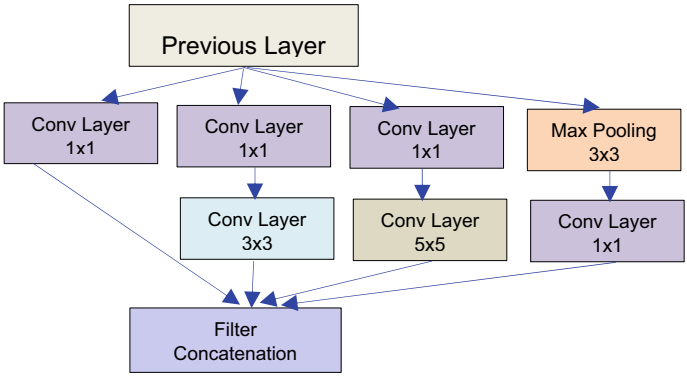

Fig. 6 Schematic diagram of inception layer

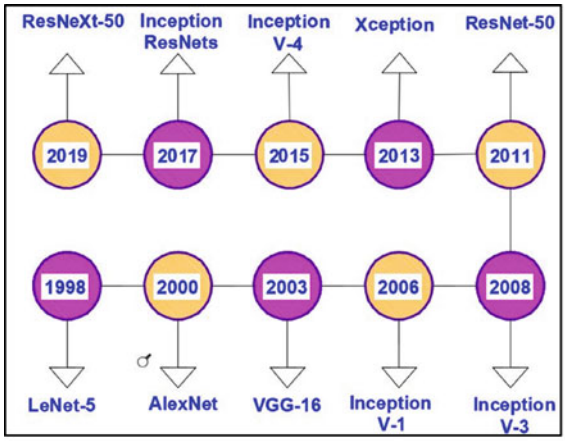

Fig. 7 CNN architechture over a timeline

4 Review of Prior Studies on Structural Defect Classification and Detection Using CNN

CNN, a sub-branch of deep learning has captured the focus of the researchers, as its' applications has successfully demonstrated the ability to classify and detect certain features of an image quiet accurately.

In recent times, Yang et al. [25] trained a fully convolutional network based on pre-build VGG-19 architecture to semantically identify and segment pixel-wise cracks at different scales. The author used 800 images with 224 × 224 pixels, where a split of 80 and 20% of images were used to train and test the model respectively, and the model performed an accuracy of 97.96%.

Yu et al. [27] utilized CNN to identify and localize the defects in a smart building structure, equipped with smart control devices (Magnetorheological-MR based device). In this study, the CNN models' performance is evaluated based on the damages due to external disturbance including vehicle loading and seismic loading, and model has shown A remarkable identification accuracy compared to the conventional signal processing methods and other Machine Learning methods. For data preparation Fast Fourier transform (FFT) is used to transform the time-sequence signals into frequency-domain features and a 2D feature matrix is designed as the input for CNN model. Also they proposed a 10-layer CNN model including an input layer, three convolutional layers and sub-sampling layer which are followed by two fully connected and one output layer, where Leaky rectified linear unit (LeReLu) and Cross entropy is considered as activation function and loss function respectively. Using the Root-Mean-Square (RMS) error validation their proposed model showed reasonable accuracy in predicting the damage severities and the location of the damage in most cases, and found to assign low severity values for undamaged section of the smart building.

With the real-time images, collected with unmanned aerial system (wireless data transmission system), Jiang and Zhang [10] applied CNN model- SSDLite-MobileNetV2 to assess the crack condition of structures. The proposed model SSDLite-MobileNetV2 was a combination of pre-build VGG-16 architecture based SSD model (Single Shot Multi-Box Detector), and MobileNet. The authors took 1330 crack images as input with the size of 640X480 pixel and divided into 1030 training images and 300 testing images. The study compared the average precision of the model with some other models and finally stated that the SSDLite-MobileNetV2 got the maximum average precision of 0.52.

Employing a Faster R-CNN build on the basic architecture of ResNet 101 [24] developed an automatic efflorescence and spalling detection process for historic masonry buildings. The orthophotos were taken from a certain area of the Palace Museum wall in Beijing, China with the initial resolution of 57,780 × 11,400 pixel, which was resized into 500 × 500 pixels. For,—input database 500 images were taken where 400 images were used as training dataset and rest of the 100 images were used for validation and testing dataset. They used a Faster R-CNN which starts with a convolutional layer and max-pooling layer, followed by three building blocks of conv layer, four building blocks of conv layer, twenty-three building blocks of conv layer, three building blocks of conv-layer which finishes with an average-pooling layer and a fully connected layer. The authors concluded that despite having some minor errors the developed model was able to obtain substantial success in predicting efflorescence and spalling.

For damage detection [6] accumulated images from hydro-junction infrastructure and utilized transfer learning method with pre-build CNN architecture Inception-v3. 435 real-time high resolutions (7952 × 5304 pixels) images were split into patches and prepared a dataset containing 18,605 images with 300 × 300 pixels each and a split of 8:1:1 was used for training, validation and testing respectively. The authors labelled the damages as- crack, spalling, seepage, rebar exposed and non-damage class. The performance of the model was based on confusion matrix to predict the damage types, accuracy, recall, precision and F-Score, and compared the value with Support Vector Machine (SVM) method. This study achieved a 96.8% accuracy in damage detection with the proposed method which is considerably higher than the SVM.

An improved crack detection and recognition process with Batch Normalized (BN) technique was adopted by [4] to detect crack on historical masonry buildings. The dataset of 20,000 images was gathered from Middle East Technical University Campus building and converted into 40,000 images the RGB pixels of 227 × 227. This study gained an average accuracy of 99.71% using the improved crack detection CNN model.

Ye et al. [26] proposed a fully convolutional network, Ci-Net for structural crack detection in their study. This proposed Ci-Net, consisted seven convolution layers, two max-pooling layers, two upsampling layers, six deconvolution layers, and a softmax layer. The study collected dataset from CrackForest and TITS 2016 and prepared 125,000 images with 80 × 80 pixels with a split of 70:30 for training and

validation process, and rest 500 unused images were used for testing. This model was able to achieve 93.6% accuracy at 40th epoch.

For defects at inaccessible area of concrete structures, Flah et al. [7], presented an inspection model for damage classification, detection and segmentation. This study prepared the dataset from real-time photoshoot and multiple database- SDNET2018, ImageNet, google and Baidu images. This dataset contained 20,000 cracked images and 20,000 undamaged surface images, and cropped into a resolution of 224 × 224 pixels from high-resolution of 4032 × 3024 pixels. The CNN model was trained with 10,000 images (5000 cracked + 5000 non-cracked images) and a split of 60:20:20 for training, validation and testing. This study adopted three CNN classifier models based on the different size of the input data size. They reported superior accuracy of 97.63% for training, 96.5% for validation and 96.17% for testing data.

To develop a deep-learning based automated inspection system of concrete structures, Kim et al. [13] adopted a three stage of image processing. In this study, the first two stages consisted 2D convolutional neural networks for crack classification and segmentation, and the final stage worked with a thinning and tracking algorithms to define the crack length and width. The dataset of images was collected from [18], with resolution of 4032 × 3024 pixels and resized into 227 × 227 pixels as input images. For- crack detection the network was built on 12 convolutional layers, and for segmentation work HiRes3DNet was adopted, consisting of 10 layers of convolutional layers and one dense layer. For classification stage- 36,000 input images are used for training and 4000 for testing, and the proposed model achieved the verification accuracy of 99.98%. For segmentation network-1751 images are used as training dataset and 249 images for evaluation, and the Intersection over Union (IoU) evaluation function obtained 87% of accuracy. For crack measurement the real-time crack length, minimum depth and maximum depth was quiet similar as the algorithm-based measurement.

Kim and Cho [12] employed a Mask R-CNN model to detect concrete damage. The model consisted of three stages- regional proposals, classification and segmentation. A dataset of total 765 real-time defect images (i.e., crack, efflorescence, rebar exposure and spalling) was taken from building and bridge structures. The authors successfully obtained an average of 90.41% precision and 90.81% recall for localization of defects, and 87.24% precision and 87.58% recall for segmentation of defects.

A multiscale convolutional neural network infused with different levels of semantic information to detect pavement crack damage, named as CrackSeg was proposed by Song et al. [21]. CrackSag was built on the basis of pre-trained model ResNet and a dilated network strategy. The pavement crack dataset was collected from 14 cities in the Liaoning Province, China, composed of 4736, 1036 and 2416 of images for training, validation and testing, respectively. Comparing with other CNN model, this study stated that the CrackSeg attained the high performance with an overall accuracy of 98.79%, precision of 98%, Recall 97.85%, F-Score 97.92% and mIoU 73.53%.

More recently, Dais et al. [5] utilized CNN and transfer learning for automatic crack classification and segmentation on brick masonry surfaces. They developed

an image dataset having 351 photos with cracks on the masonry surface and 118 images without any cracks. The dataset contained cracks of different shapes (i.e. zigzag, straight lines and combinations), length, width, and backgrounds. They used image patch classification for detecting cracks using transfer learning. The authors employed eight different deep learning (DL) networks for pixel-level crack segmentation on masonry surfaces. They found MobileNet to be the most accurate DL network with 95.3% accuracy. Similarly, Perez et al. [19] used pre-trained model (VGG-16, ResNet 50 and Inception model) and transfer learning to detect defects, e.g., mould, deterioration and stain. A dataset of 2622 images (1890 images as training dataset, 732 images as testing dataset) was used, and sliced into 224 × 224 pixels as input size. The study got a consistent overall accuracy of 87.50%, where 90%, 82%, 89% and 99% of images were classified correctly for mould, deterioration, stain and normal images respectively. Table 1 shows the summary of CNN-based literature mentioned in this study.

5 Limitations and Future Research Scope

With the introduction of Deep learning and studying the prior literatures, it is evident that the structural health assessment sector has a great future scope with the current limitations and major challenges, such as-

a. The datasets are very limited and mostly built on investigation reports, which raises the necessity to build an enormous resource of real-time investigation images. Also, the data preparation and data selection criteria are not centralized, mostly depending on the individual researcher's decision making capability, which can severely affect the precision of the model accuracy. Such standardization procedures should be addressed in future studies, including the expertise knowledge on significant defect types and conditions. Moreover, environment-related issues cannot be perfectly simulated via generalized numerical models; therefore, larger datasets can only be formed by acquiring data from the real world [3].
b. The defects type, significanctly vary considering the global structural context. As a result, considering only a few types of defects can not be counted or generalized as a performance evaluation assessment for any structure. Damage detection works with computer-vision will need to extended in future research work to classify and detect all types of defects in construction.
c. In all these research papers mentioned here, except for Kim et al. [13] a single image contains only one type of defect, while in the real infrastructure, typically multiple defects are prominently visible in a single area. Also, the images that are used mostly have high resolution without any background noise (shadow, extreme lightening, and orientation, etc.), which gives a significant research scope to perform a CNN analysis taking account of the extreme condition while achieving higher accuracy in training a model.

Table 1 Summary of CNN-based literature

References	Application	CNN architecture	Performance criteria
Yang et al. [25]	Automatic pixel-level crack detection	VGG-19	Accuracy, precision, recall, F-score
Yu et al. [27]	Damage identification and localization	10-layer CNN model	RMSE, SCC, AAD, ESR
Jiang and Zhang [10]	Crack condition of structures	SSDLite-MobileNetV2	Accuracy, mIoU
Wang et al. [24]	Concrete crack detection	Faster R-NN based on ResNet 101	Average precision, mean average precision
Feng et al. [6]	Damage detection at hydro-junction structures	Inceprion-v3	Accuracy, precision, recall, F-score
Chen et al. [4]	Crack detection and recognition of historic building	CNN model with Batch Normalized technique	Accuracy
Ye et al. [26]	Structural crack detection	Ci-Net	Accuracy, precision, recall, F-score, IoU
Flah et al. [7]	Concrete crack detection, segmentation, and density evaluation	11-layer CNN model	Accuracy, quantification error
Kim et al. [13]	Spalling detection for historic masonry structures	2D CNN model	Evaluation accuracy, intersection over union (IoU)
Kim and Cho [12]	Concrete damage detection	Mask R-CNN—instance segmentation, ResNet 101	Precision, recall
Song et al. [21]	Pavement crack detection	Multiscale Convolutional model, ResNet	Precision, Recall, F-Score, mIoU
Dais et al. [5]	Crack classification and segmentation	VGG-16, ResNet34, ResNet50, DenseNet121, DenseNet169, InceptionV3, MobileNet, MobileNetV2	Accuracy, precision, recall, F-score
Perez et al. [19]	Dampness of building. Criteria as—mould, stain or deterioration	VGG-16, RseNet-50, Inception	Accuracy

6 Conclusions

In the last couple of decades, the construction industry has faced and overcome an enormous amount of challenges regarding structural defects and damages with the expertise of engineers and researchers, but still, this sector is lacking in collaboration with the computer vision prospective. It is prevalent that with the rapid construction of gigantic structures, more environmental challenges and quality issues are at stack, which makes structures more susceptible to damages and defects. While identifying and decision making on solving these issues only by humans can be time-consuming, labor-intensive, dangerous, and inefficient, deep learning-based analysis, for instance, CNN can be the ultimate solution. With a long-term vision towards creating a vast, open-source database on different structural defect types can radically boost up the world-wide research works on condition assessment and redemption plan for any type of structure. In conclusion, the research in the future will concentrate on building an open-source standardized data source for civil structures, implementing the CNN algorithms to analyze the actual condition of the structure, and reducing the percentage of safety factors, making the construction sector more economical.

Acknowledgements The Natural Sciences and Engineering Research Council (NSERC) of Canada supported this study through the NSERC Alliance Grant in partnership with TBT Engineering. The financial support is highly appreciated.

References

1. Agdas D, Rice A, Martinez R, Lasa R (2015) Comparison of visual inspection and structural-health monitoring as bridge condition assessment methods. Perform Constr Facil 30(3):04015049
2. Anwar A (2019) Difference between AlexNet, VGGNet, ResNet, and Inception. Retrieved March 4, 2021. https://towardsdatascience.com/the-w3h-of-alexnet-vggnet-resnet-and-inception-7baaaecccc96
3. Azimi M, Eslamlou AD, Pekcan G (2020) Data-Driven Structural Health Monitoring and Damage Detection through Deep Learning: State-of-the-Art Review. Sensors 20(10):2778
4. Chen K, Yadav A, Khan A, Meng Y, Zhu K (2019) Improved crack detection and recognition based on convolutional neural network. Model Simul Eng 2019:8796743
5. Dais D, Bal I, Smyrou E, Sarhosis V (2021) Automatic crack classification and segmentation on masonry surfaces using convolutional neural networks and transfer learning. Autom Constr January 2021
6. Feng C, Zhnag H, Wang S, Li Y, Wang H, Yan F (2019) Structural damage detection using deep convolutional neural network and transfer learning. KSCE J Civ Eng 23:4493–4502
7. Flah M, Suleiman R, Nehd L (2020) Classification and quantification of cracks in concrete structures using deep learning image-based techniques. Cem Concr Compos (IF 6.257)
8. Fujita Y, Hamamoto Y (2011) A robust automatic crack detection method from noisy concrete surfaces. Mach Vis Appl 22(2):245–254
9. Gao Y, Mosalam K (2018) Deep transfer learning for image-based structural damage recognition. Comput-Aided Civ Infrastruct Eng 33(9):748–768

10. Jiang S, Zhang J (2019) Real-time crack assessment using deep neural networks with wall-climbing unmanned aerial system. Comput-Aided Civ Infrastruct Eng 35:6
11. Kaveh A, Dadras A (2018) Structural damage identification using an enhanced thermal exchange optimization algorithm. Eng Optim 50:430–451
12. Kim B, Cho S (2020) Automated multiple concrete damage detection using instance segmentation deep learning model. Appl Sci 10(22):8008
13. Kim J, Kim A, Lee S (2020) Artificial neural network-based automated crack detection and analysis for the inspection of concrete structures. Appl Sci 10(22):8105
14. Kucuksubasi F, Sorguc A (2018) transfer learning-based crack detection by autonomous UAVs. In: 2018 Proceedings of the 35th ISARC. Berlin, Germany, ISBN 978–3–00–060855–1, pp 593–600
15. Li S, Zhao X (2018) Convolutional neural networks-based crack detection for real concrete surface. In: Proceedings of the sensors and smart structures technologies for civil, mechanical, and aerospace systems. Berlin, Germany, 20–25 July 2018, pp 105983V
16. Li S, Zhao, X. Image-based concrete crack detection using convolutional neural network and exhaustive search technique, Vol 2019, Article ID 6520620.
17. Nishikawa T, Yoshida J, Sugiyama T, Fujino Y (2012) Concrete crack detection by multiple sequential image filtering. Computer-Aided Civil and Infrastructure Engineering 27(1):29–47
18. Özgenel R, Çaglar FO (2019) Concrete crack images for classification. Mendeley Data 02, Published: 23 July 2019 Version 2. https://doi.org/10.17632/5y9wdsg2zt.2
19. Perez H, Tah M, Mosavi A (2019) Deep learning for detecting building defects using convolutional neural networks. Sensors 19:3556
20. Shamshirband S, Mosavi A, Rabczuk T (2019) Particle swarm optimization model to predict scour depth around bridge pier. Preprints 2019, 2019050121
21. Song W, Jia G, Zhu H, Jia D, Gao L (2020) Automated pavement crack damage detection using deep multiscale convolutional features. J Adv Transp 2020(6412562):11
22. Sony S, Dunphy K, Sadhu A, Capretz M (2021) A systematic review of convolutional neural network-based structural condition assessment techniques. Eng Struct 226(1):111347
23. Sun H, Burton V, Huang H (2020) Machine learning applications for building structural design and performance assessment: state-of-the-art review. J Build Eng (IF 3.379) Pub Date: 2020–09–21
24. Wang N, Zhao X, Zhao P, Zhang Y, Zou Z, Ou J (2019) Automatic damage detection of historic masonry buildings based on mobile deep learning. Autom Constr 103:53–66
25. Yang X, Li H, Yu Y, Lua X, Huang T (2018) Automatic pixel-level crack detection and measurement using fully convolutional network. Comput-Aided Civ Infrastruct Eng 0(2018):1–20
26. Ye X, Jin T, Chen P (2019) Structural crack detection using deeplearning–based fully convolutional networks. Adv Struct Eng 22:16
27. Yu Y, Wang C, Gu X, Li J (2019) A novel deep learning-based method for damage identification of smart building structures. Struct Health Monit 18:143–163
28. Zhang Y, Anderson N, Bland S, Nutt S, Jursich G, Joshi S (2017) All-printed strain sensors: Building blocks of the aircraft structural health monitoring system. Sens Actuators, A 253:165–172
29. Zhao R, Yan R, Chen Z, Mao K, Wang P, Gao RX (2019) Deep learning and its applications to machine health monitoring. Mech Syst Signal Process 115:213–237

Nonlinear Buckling Analysis of Conical Steel Tanks Considering Field-Measured Imperfections—A Case Study

H. Zhang, A. M. El Ansary, and W. Zhou

1 Introduction

Steel tanks are widely used as containers of mass materials for industrial and civilian use. For water storage tanks, they are usually fabricated into cylindrical and conical shapes and located at a high elevation to provide pressure utilizing gravity. According to the steel water tank design standards published by the American Water Works Association (AWWA D100-11), loads from multiple sources are required to be considered in the design process of elevated steel tanks. Linearly varying hydrostatic pressure exerts hoop tensile stresses and meridional compressive and bending stresses on the wall. Superimposed roof load from additional structures on the top of tanks contribute to meridional stresses. The state of stresses in a liquid filled conical tank wall is shown in Fig. 1. Tanks with conical parts are more prone to buckling at the bottom part than the pure cylindrical ones since part of the meridional compression stress is contributed by hydrostatic pressure, which reaches a maximum amplitude at the base. Geometric imperfections formed during fabrication can have a nonnegligible impact on the buckling capacity of tanks. An elevated conical water tank in Seneffe, Belgium collapsed in 1972, initiated by buckling failure at the bottom. This generated attentions on the buckling problem of imperfect hydrostatically loaded steel tanks. After conducting experiments on hundreds of small-scale models, Ref. [16] proposed a series of design equations as the remedy of insufficient consideration of imperfections referenced later in The European Recommendations of Steel Construction (ECCS, 1984 edition), where a critical axisymmetric imperfection in the shape of sinusoidal waves was assumed along meridians.

Another incident happened in Fredericton, Canada in 1990, where a conical steel tank collapsed after being filled with water for the first time. Reports were published

H. Zhang (✉) · A. M. E. Ansary · W. Zhou
University of Western Ontario, London, Canada
e-mail: hzhan776@uwo.ca

S. Walbridge et al. (eds.), *Proceedings of the Canadian Society of Civil Engineering Annual Conference 2021*, Lecture Notes in Civil Engineering 240,
https://doi.org/10.1007/978-981-19-0507-0_28

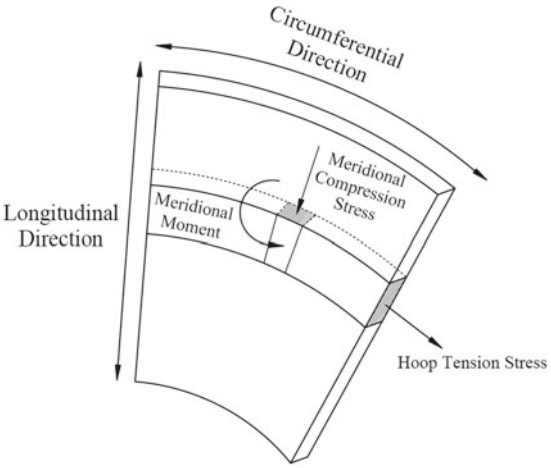

Fig. 1 Membrane stress in conical tank walls by Azabi et al. [2]

soon after the incident [4, 13, 17]. It was found that few measurements had been applied on geometric imperfections of the tank during fabrication nor the applied standards (AWWA D100, 1984 edition) have involved design tolerance about imperfections. Based on the axisymmetric meridional imperfections suggested by [5, 16] superimposed a circumferential wave on this assumption. El Damatty et al. [6] found that an axisymmetric circumferential pattern also has a critical impact on the buckling capacity of tanks. This imperfection was then introduced into a series of experiments on conical tanks with finite element analysis (FEA), where they were modelled with a sub-parametric triangular shell element. Similar studies have been carried out on pure conical tanks [5], stiffened conical tanks [8] and combined conical tanks with a cylindrical cap added at the top [11]. These assumed imperfections were also implemented in a simplified design approach by [7] as an alternative to the complex method in AWWA D100-05, standard which involves nonlinear analysis.

Compared to theoretical assumptions, few measurements and analyses have been carried out on geometric imperfections extracted from existing tanks. Hornung et al. [12] presented a series of investigation of cylindrical oil tanks. Geometric imperfections were measured from the inside surface, and the buckling test results showed conservativeness that despite real amplitude exceeded the tolerance in European codes (prENV1993-1–6 1999; prENV1993-4–2 1999), the capacity is much higher than predictions from codes. Another important investigation was carried out by Teng et al. [15] who studied the geometrical imperfections of a cylinder metal silo in Australia. A set of measurements were extracted and decomposed with 2D Fourier series. Results showed the relevance between imperfection wavelength and the panel size.

The current paper reports a novel investigation on the buckling capacity of existing liquid-filled steel conical tanks by considering in-situ measured geometric imperfections. A set of surface scan data of an imperfect combined conical tank is gathered and processed. Shapes of global and local imperfections are extracted and compared

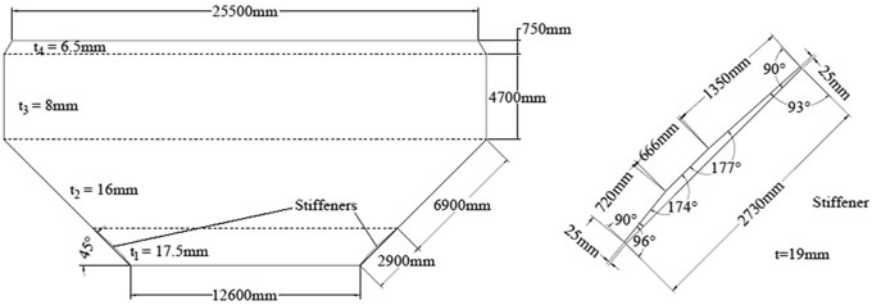

Fig. 2 Geometry of the tank and stiffeners (elevation view)

with tolerances in design codes and assumed patterns reported in the literature. A series of elastoplastic finite element analyses are carried out to obtain the impact of measured imperfections on the tank buckling capacity. Furthermore, the measured imperfections are then used to assess current geometric imperfection assumptions available in design codes and the literature.

2 Tank Geometry and Imperfection Data

A stiffened liquid-filled steel conical tank has been considered as a case study. The nominal geometry of the tank is shown in Fig. 2. This elevated water tank has been in service for many years. It is combined with a conical part sitting on the concrete shaft (not shown in Fig. 2) and a cylinder cap. A total of 48 stiffeners are distributed evenly around the tank circumference at the lower section of the cone, where the shell thickness $t_1 = 17.5$ mm.

Imperfection was captured by a laser scan on the exterior surface of the tank when it is empty. Since the conical part is the most critical component of the tank for buckling failure, the cloud points of the conical vessel were extracted from the laser scan data for further analyses. Figure 3 shows the cloud data of the conical vessel, which contains 3,250,386 scan points in the Cartesian coordinate system. Data points on the plane $z = 0$ m are aligned to the horizontal level of the cone bottom.

3 Imperfection Assumptions

An axisymmetric imperfection shape along the tank meridians is proposed by Vandepitte et al. [16], where the buckling wavelength L_b can be calculated as shown in Eq. 1. The imperfection amplitude is classified by [16] into two different levels reflecting the quality of tank construction. This amplitude, which is measured in a direction perpendicular to the tank surface, is assigned two values equal to 0.8 and 2% of half

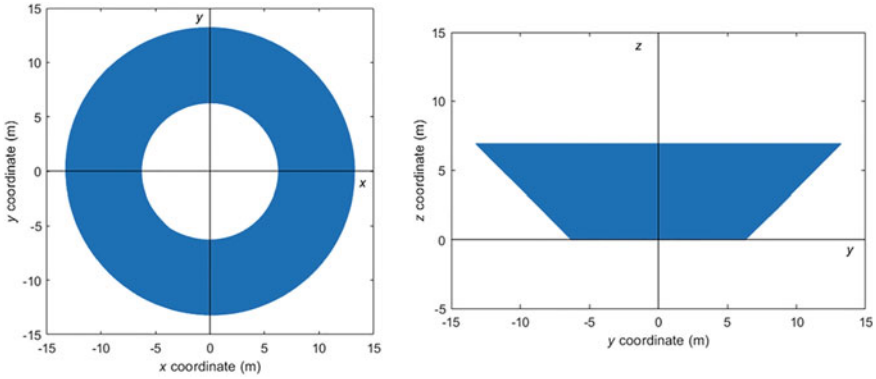

Fig. 3 Plan and elevation view of cloud data

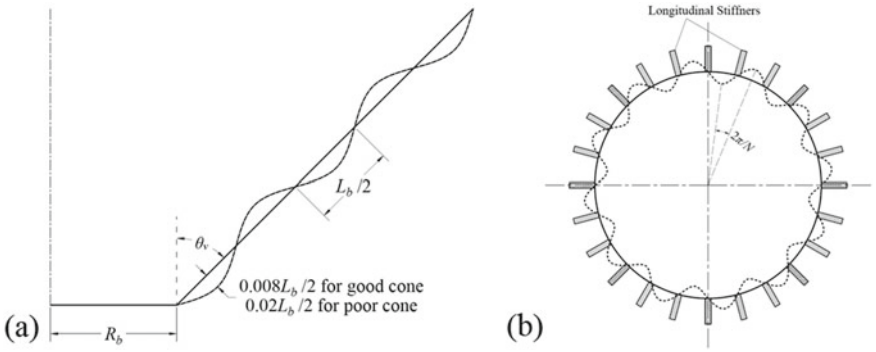

Fig. 4 Imperfection specification by **a** Vandepitte et al. [16] and **b** El Damatty et al. [8]

buckling wavelength, respectively (Fig. 4a).

$$L_b = 3.6\sqrt{R_b t/\cos_v} \tag{1}$$

where R_b is the radius at the tank base; θ_v is the angle between tank wall and vertical direction, and t is the thickness of the tank wall.

El Damatty et al. [8] specified a superimposed circumferential pattern on stiffened tanks (Fig. 4b), where the wave number can be calculated as half of the total number of evenly spaced longitudinal stiffeners N. The amplitude of the imperfection δ is given by Eq. 2:

$$\delta(s, \theta) = \delta_0 \sin(2\pi s/L_b)\cos(N\theta/2) \tag{2}$$

where δ_0 is the maximum imperfection amplitude; s is the distance measured on a generator of tank; L_b is the imperfection wavelength specified by Vandepitte et al. [16] and θ is the angular coordinate measured from the center of circumference.

4 Data Processing

According to design standards AWWA D100-11 and EN 1993–1-6, geometric imperfections can be classified as global and local imperfections. Global imperfections are usually defined as out-of-roundness (e.g. ovalization). Local imperfections include eccentricities between steel panels and local dimples. In this study, a least-square (LSQ) fitting approach is employed with an ellipse function, as shown in Eq. 3, and illustrated in Fig. 5.

$$\left[(x - x_0)\cos\theta + (y - y_0)\sin\theta\right]^2/A^2 + \left[(y - y_0)\cos\theta - (x - x_0)\sin\theta\right]^2/B^2 = 1 \tag{3}$$

where x_0 and y_0 are the coordinates of the centre of the ellipse; θ is the inclination angle of ellipse, and A and B are the lengths of semi-axes of the ellipse.

Deviation of the center (x_0, y_0) and twisted ovalization effect (θ, A and B) in the obtained results are considered as the global imperfections. The residual part is considered as the local imperfections. Since the calculated imperfections are planar,

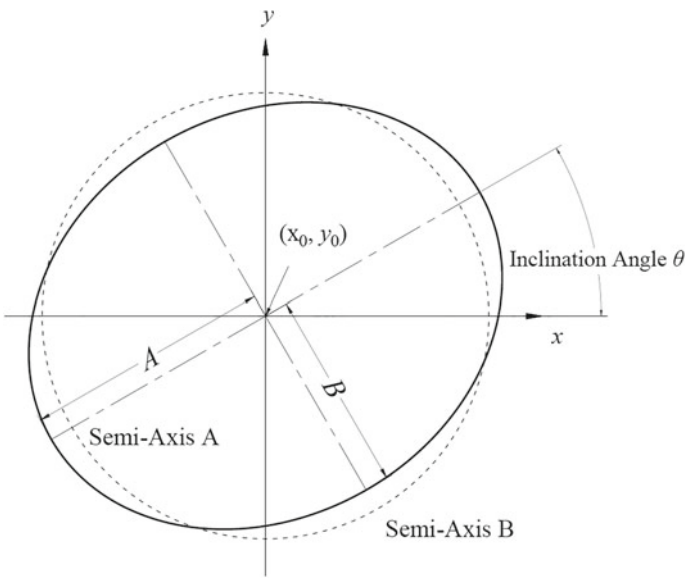

Fig. 5 Ellipse utilized in LSQ fitting

they are converted into imperfections perpendicular to the 45° tank wall with an approximation shown in Eq. 4. For demonstration purposes, part of the imperfections along meridians and circumferences extracted from the laser scan data are shown in Fig. 6.

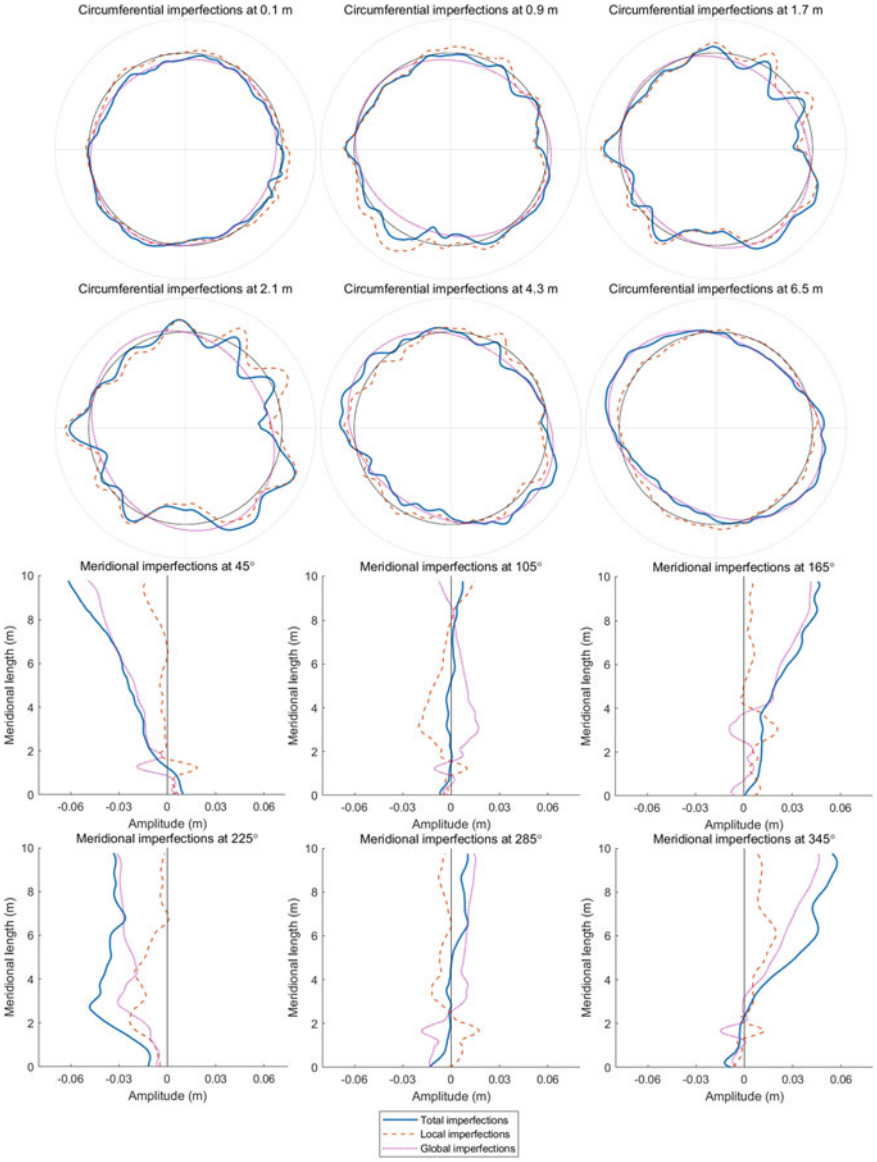

Fig. 6 Extracted imperfection shapes

$$\delta_{\text{planar}} = \sqrt{2}\delta_{\text{perpendicular}} \tag{4}$$

It is concluded from Fig. 6 that the amplitude of the circumferential imperfections is small close to the base of the tank. Local imperfections become dominant at one third of the height measured from the base, while global imperfections are dominant at the top. By studying varies meridians, the amplitude of total imperfections does not always show a larger amplitude than global or local components. At lower part, global and local imperfections sometimes have opposite directions, which makes the total imperfections have a smoother shape.

5 Finite Element Analysis of the Imperfect Tank

The studied tank is modelled in commercial FEM software ANSYS 16.1 using a four-node or three-node element SHELL181 element available in the ANSYS library. It has 6 degrees of freedom at each node: Translations Δx, Δy and Δz; Rotations θx, θy and θz. Triangular shape is adopted to enable the mesh grading between coarse and fine regions. A gist of the employment of SHELL181 element is its introduction of the reduced integration technique [18] where the shear locking phenomenon can be effectively avoided. The studied conical tank shown in Fig. 1 is examined with both measured imperfections (Fig. 6) and assumptions recommended in the literature [8, 16]. The accuracy of this commercial FEM package is also verified by simulating the tank located in Fredericton, Canada and comparing the results obtained from the FEM analysis with those reported by Vandepitte et al. [17], which are part of their investigation on the collapse incident of the Fredericton tank. Geometry of the tank and illustration of the SHELL181 element are shown in Fig. 7a, b.

Table 1 shows the material properties of both tanks. Bilinear strain hardening is applied in the studied conical tanks with isotropic hardening rule. The tangent modulus is assumed as 3% of Young's modulus [5]. No strain hardening is assumed in the work by Vandepitte et al. (1992).

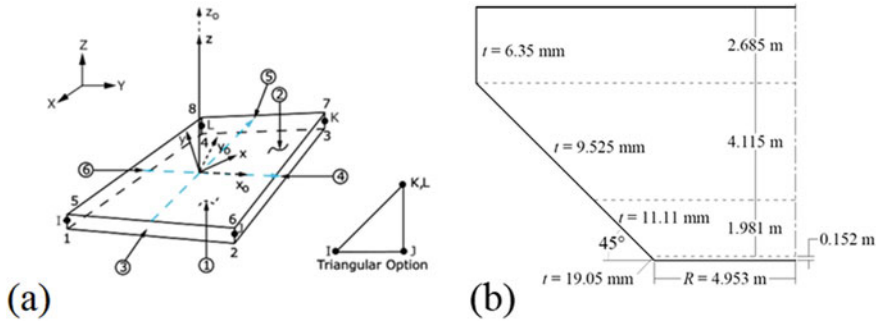

Fig. 7 Geometry of **a** SHELL181 element and **b** Fredericton tank (Symmetric)

Table 1 Material properties of tank models

Properties	Fredericton tank	Studied conical tank
Density (kg/m^3)	7850	7850
Young's modulus (MPa)	2×10^5	2×10^5
Poisson's ratio	0.3	0.3
Tensile yield strength (MPa)	250	270
Compressive yield strength (MPa)	250	270
Tangent modulus (MPa)	–	6000

Reference [16] assumed that the top edge of Fredericton tank is free to move. Translations of the lower edge are restrained. For the studied tank, the top rim is welded to a steel plate to support roof structures. The bottom edge is restrained to the top of concrete shaft. These physical constraints are simulated by boundary conditions in the finite element model. Bottom edges of stiffeners and lower rim of both tanks are simply supported where only rotations are allowed. Restrictions of translation along x and y directions are applied on the top rim of the cylindrical part of the studied tank.

Loads of both tanks are shown in Table 2. The design hydrostatic load in the studied tank is factored by multiplying water density as $1.25/0.9 \times 1000 \approx 1400$ kg/m^3. The factors 1.25 and 0.9 are the partial safety factors for the dead load and reduction factor for steel yield strength, respectively (NBCC 2015, AWWA D100-11). A line load is assumed at the top rim of Fredericton tanks; the main part of line load due to the roof structure and other part is the substitution of self-weight due to limitations of simulation program utilized by Vandepitte et al. [17].

Table 3 shows the element size of the mesh determined from preliminary sensitivity analysis. The solution reaches convergence by reaching the limit that the difference is within 0.5% when the mesh size decreases by 20%. The meshing process in both tanks is controlled by the local minimum element size. A coarse mesh is used in upper cylindrical part, and a more refined mesh is used in the lower part of the conical

Table 2 Loading conditions of tank models

Load parameters	Fredericton tank	Studied conical tank
Fluid density (kg/m^3)	1000	1400
Gravitational acceleration (m/s^2)	9.81	9.81
Elevation of free surface (m)	Top of the tank	12.1
Self-weight	Not included	Included
Line pressure (N/m)	9.236×10^{-3}	–

Table 3 Determined local minimum element size (m)

Section in the model	Fredericton tank	Studied conical tank
Cylindrical part	0.2	0.3
Top part of the cone	0.13	0.2
Bottom part of the cone	0.07	0.15
Stiffeners	–	0.15

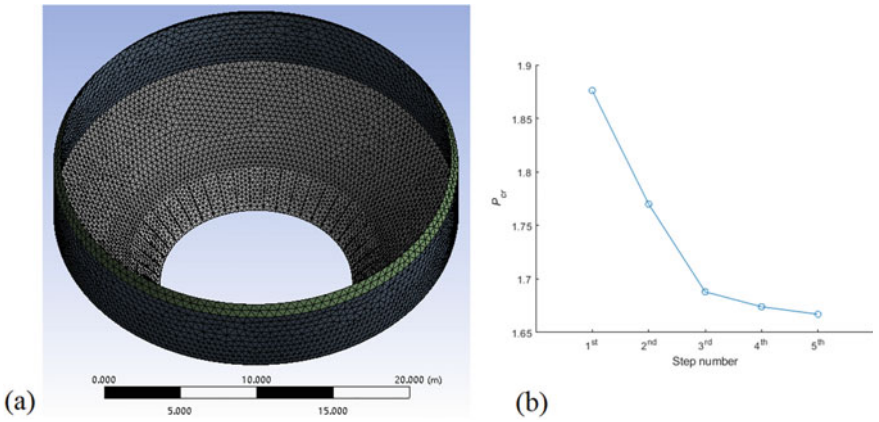

Fig. 8 **a** Mesh grading in FEM model **b** Calculated P_{cr} value for each step in mesh sensitivity analysis

vessel to yield towards more accurate prediction of the buckling capacity of the tank. The generated mesh is shown in Fig. 8a. The critical load factor (P_{cr}) is collected in the mesh sensitivity analysis to detect the convergence, where $P_{cr} = 1$ means a tank capacity that can just withstand the load levels applied on the model. Results of all steps are shown in Fig. 8b, where a convergence is shown by the variation of P_{cr} value reaching a plateau.

For the Fredericton tank, the imperfection shape suggested by [16] are simulated for verification. For the studied conical tank, the simplified imperfection patterns suggested by [8] is introduced. Each tank is assigned with two classifications of imperfection amplitude: 'good cone' and 'poor cone'. Additionally, the studied tank with measured imperfections is also analyzed as a comparison. Three extracted components: global imperfections, local imperfections, and total geometric imperfections (global and local imperfections) are assigned respectively to the FEM model.

The critical load factor (P_{cr}) is collected as a criterion for comparison. The von Mises yield criterion with associated flow rule is applied to the model, finite-strain configuration is adopted considering large strain may occur in the model. To get accurate solutions at buckling, the arclength method is utilized with the termination

Table 4 P_{cr} results from analyses

Case		Fredericton tank	Studied conical tank
Perfect			1.936
Global Imperfections			1.516
Local Imperfections			1.488
Total Imperfections			1.653
Verification with ANSYS 16.1	Good cone	1.705	
	Poor cone	1.184	

Table 5 P_{cr} reported in literatures

Case		Fredericton tank	Studied conical tank
Assumption by El Damatty et. al [8]	Good cone		1.705
	Poor cone		1.406
Report by Vandepitte et al. (1992)	Good cone	1.44	
	Poor cone	1.10	

at the point when stiffness matrix becomes singular. Tables 4 and 5 show the results from analyses conducted in the current study and those reported in the literature.

For verification with Fredericton tank, the calculated P_{cr} value is 18.403% and 7.636% larger than Vandepitte et al.(1992) results for the 'good cone' and 'poor cone', respectively. The possible reason for a larger difference in 'good cone' case is the difference in mesh, since Vandepitte et al. [16] utilized finite difference method in his analysis. This influence is more obvious for lower imperfection amplitude.

For the simplified imperfection pattern suggested by [5, 8], P_{cr} value obtained from FEA results is 88.07% (good cone) and 72.62% (poor cone) of the buckling capacity of the perfect tank. The tank assigned with total measured imperfections has 85.38% capacity of the perfect tank. It drops to 78.31% with global imperfections and 76.86% with local imperfections. These results suggest that local imperfections have the most significant effect on the reduction of the buckling capacity of such type of shell structures. The higher capacity associated with total imperfections might be attributed to the following reasons: (1) Counteraction between global and local imperfections plays a role in the coupling of individual components. Figure 7 shows that directions of global and local imperfections are sometimes opposite, which makes the amplitude of the total imperfection smaller than ossn e of its components. Furthermore, locations where the global imperfection are large are generally different from those where the local imperfections are large. This makes the total imperfection not necessarily the most critical case. (2) The imperfection shape has a significant effect on the buckling capacity. From meridional imperfections, shown in Fig. 7, compared to the smooth shape of total imperfections, sinusoidal waves with small wavelength are more obvious at the lower part of meridians ($z = 2$ m) with global or

local imperfections only. Such locations are critical where high meridional stresses are anticipated.

6 Conclusions

In this study, geometric imperfections extracted from laser scan cloud data on an existing stiffened conical water tank are implemented into a numerical model based on a verified FEA technique. The impact on the buckling capacity of a liquid-filled conical tank is compared with specifications in literature. Imperfection shape suggested by [8] for stiffened tanks leads to the most critical case with imperfection amplitude of 0.02 $L_b/2$ (classified as 'poor cone' by Vandepitte et al. [16], where the buckling capacity decreased to 72.62% of the perfect case. Measured local imperfections give a larger capacity (76.86% of perfect tank) even with the amplitude reaching 200% of the tolerance of classification 'poor cone'. In this case, more reduction in the buckling capacity of the tank with local imperfections has been noticed compared to the case with total measured imperfections or only global imperfections, where 85.38 and 78.31% capacity are reported in such cases, respectively. Based on the results, it is recommended that local imperfections can be deemed as the critical case. This introduces a conservative consideration in design procedures and help reducing complexity by ignoring global imperfections. Also, by comparing the buckling capacity while considering different imperfection assumptions and field measurements, it is shown that following current codes provisions for the assumed geometric imperfection will certainly lead to conservative design.

References

1. AWWA D100–11 Welded Carbon steel tanks for water storage, American Water Works Association, Denver, CO, USA
2. Azabi TM, El Ansary AM, El Damatty AA (2016) Analysis and Design of elevated liquid-filled reinforced concrete conical tanks. Adv Struct Eng 19(6):995–1008
3. D100–84: AWWA standard for welded carbon steel tanks for water storage, American Water Works Association, Denver, CO, USA
4. Dawe JL, Seah CK, Abdel-Zahr AK (1993) Investigation of the regent street water tower collapse. Manag Oper, AWWA J 34–47
5. El Damatty AA, Korol RM, Mirza FA (1997) Stability of imperfect steel conical tanks under hydrostatic loading. J Struct Eng 123(6):703–712
6. El Damatty AA, El-Attar M, Korol RM (1998) Inelastic stability of conical tanks. Thin-Walled Structures 31:343–359
7. El Damatty AA, El-Attar M, Korol RM (1999) Simple Design Procedure for Liquid-Filled Steel Conical Tanks. J Struct Eng 125(8):879–890
8. El Damatty AA, Marroquin EG, El Attar M (2001) Behavior of stiffened liquid-filled conical tanks. Thin-Walled Structures 39:353–373

9. El Damatty AA, Marroquin EG, El Attar M (1984) European recommendations for steel construction: buckling of shells, 3rd edn. European convention for constructional steelwork, Brussels, Belgium
10. El Damatty AA, Marroquin EG, El Attar M (2007) Eurocode 3—design of steel structures—part 1–6: strength and stability for shell structures. European Committee for Standardization, Brussels, Belgium
11. Hafeez G, El Ansary AM, El Damatty AA. (2010) Stability of Combined Imperfect Conical Tanks under Hydrostatic Loading. J Constr Steel Res 66(11):1387–1397
12. Hornung U, Saal H (2002) Buckling loads of tank shells with imperfections. International Journal of Nonlinear Mechanics 37:605–621
13. Korol RM (1991) An assessment of Fredericton's regent steel tower reservoir failure. Technical Report, McMaster University, Hamilton, Canada
14. National Building Code of Canada (2015) Ottawa: associate committee on the national building code, National Research Council
15. Teng JG, Lin X, Rotter JM, Ding XL (2005) Analysis of geometric imperfections in full-scale welded steel silos. Eng Struct 27(6):938–950
16. Vandepitte D, Rathe J, Verhegghe B, Paridaens R, Verschaeve C (1982) Experimental investigation of hydrostatically loaded conical shells and practical evaluation of the buckling load. In: Ramm E (ed) Buckling of shells. Springer-Verlag KG, Berlin, Germany, pp 375–399
17. Vandepitte D (1992) Report about the failure of a water tower, Fredericton, New Brunswick. Technical Report. Ghent University, Ghent, Belgium
18. Zienkiewicz OC, Taylor RL, Too JM (1971) Reduced integration technique in general analysis of plates and shells. Int J Numer Meth Eng 3(2):275–290

On the Analysis and Design of Reinforced Railway Embankments in Cold Climate: A Review

R. Desbrousses and M. Meguid

1 Introduction

With 41,757 km of track operated [10], Canada has a large railway network that transported over 88 million passengers and 341 million tonnes of freight in 2018 [10]. Due to their geographical location, many of the railway lines built on Canadian soil are exposed to seasonally cold climates. Such climatic conditions pose significant challenges to the stability and integrity of ballasted railway embankments that must be designed to maintain minimum track roughness and ensure optimal riding quality and safety. Issues associated with railway embankments in seasonally cold regions arise from the occurrence of frost action, which unfolds as a two-step process that consists of frost heave and thaw subsidence. This paper first describes the structure of conventional ballasted railway embankments and the role of their components in resisting frost action. The mechanisms by which frost action affects railway embankments are then reviewed. Finally, the design strategies used to mitigate frost action are examined with a particular focus on the incorporation of geosynthetics as reinforcement in the substructure of railway embankments.

2 Conventional Ballasted Railway Embankments

Ballasted railway embankments consist of a superstructure and a substructure (see Fig. 1). The superstructure is composed of the tracks, the fastening system and the ties. Its role is to guide the train and transfer the train wheel loads to the underlying substructure. The substructure is a multi-layer system made of a ballast layer, a subballast layer and a subgrade. The ballast layer consists of clean, coarse, angular

R. Desbrousses (✉) · M. Meguid
McGill University, Quebec, Canada
e-mail: romaric.desbrousses@mail.mcgill.ca

S. Walbridge et al. (eds.), *Proceedings of the Canadian Society of Civil Engineering Annual Conference 2021*, Lecture Notes in Civil Engineering 240,
https://doi.org/10.1007/978-981-19-0507-0_29

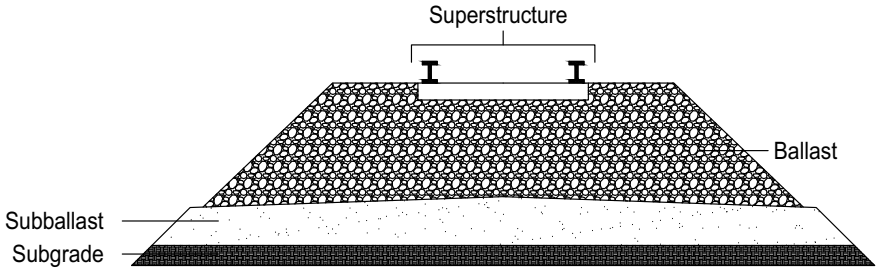

Fig. 1 Typical ballasted railway embankment

unbound aggregates and is tasked with reducing the stresses coming from the superstructure down to a level that can be withstood by the subballast. Besides acting as a bearing platform for the superstructure, the ballast layer also provides drainage, resiliency, void space for the storage of fouling material and frost protection [2, 3, 31, 41]. Frost protection is achieved by providing a layer of ballast material which, by virtue of being composed of coarse granular material is non-frost susceptible and thick enough to prevent the frost penetration depth from reaching a potentially frost susceptible subgrade. However, the ballast material degrades over time under the combined action of cyclic traffic loading, maintenance operations and weathering, leading to an increased fines content in the ballast layer [28, 41]. The fines content in heavily fouled ballast may increase its frost susceptibility and render it prone to suffering from frost heave [34].

Below the ballast layer lies the subballast. It is made of non-frost susceptible broadly graded sand-gravel mixtures and acts as an extension of the ballast layer. It is used to reduce the required thickness of the expensive ballast material. Its core functions are to reduce the magnitude of the vertical stresses down to a safe level for the subgrade, separate the ballast and subgrade layers, allow for water drainage and extend the frost protection offered by the ballast layer [34, 41]. The frost protection offered by the subballast is akin to that of the ballast with the layer acting as an insulator preventing subfreezing temperatures from reaching a potentially frost susceptible subgrade [41]. Nurmikolu [34] states than in Finland, the subballast is composed of two layers of non-frost susceptible material with one layer designed to reduce vertical stresses and act as a filter and separator while the second solely acts as an insulator for the underlying subgrade. In cold climates, the possibility of the subballast becoming frost susceptible due to fouling must be considered [34].

The subgrade is the bottommost layer of an embankment's substructure. It is typically made of the naturally existing soil or fill and acts as the bearing platform that supports the entire embankment. It plays a crucial role in maintaining satisfactory track performance. Subgrade problems are often the root cause of track failure or excessive maintenance needs [32]. In cold climates, the temperature is of concern when it causes freezing and thawing cycles in a frost susceptible subgrade that has access to water because it creates an environment where frost heave and thaw softening are likely to occur [32].

3 Impacts of Cold Weather on Ballasted Railway Embankments

Ballasted railway embankments located in seasonally cold regions are subjected to frost action, i.e., a phenomenon caused by the combined action of soil freezing and thawing. Frost action is detrimental to the integrity and stability of railway embankments due to the frost heaving and thaw softening that occur during freezing and thawing respectively [1, 4, 24, 36]. Freezing triggers a phase change in the water present in soil, leading to the formation of ice followed by the flow of water from unfrozen to frozen soil that accumulates in ice lenses. Ice lenses significantly increase the volume of the soil in which they form and cause it to heave. Correspondingly, when temperatures increase, the ice present in the soil starts to melt from the top down, increasing the amount of water in the soil. However, the melt water is not able to drain downward through frozen soil and contributes to increasing the pore water pressure, resulting in decreased soil strength and increased subsidence. Three conditions must be concurrently satisfied for frost action to take place: (1) freezing temperature and sufficient frost depth, (2) access to water, (3) frost susceptible soil [4, 36].

Frost heave and thaw subsidence are particularly detrimental to railway embankments given that they significantly disturb the track geometry and are the source of differential settlement. Increased track roughness results in poor riding conditions that may warrant the reduction of traffic speed on the affected portions of the train tracks or create a need for maintenance operations to restore the track geometry [34, 36].

3.1 Frost Heave Mechanism

Frost heave is characterized by the expansion of soil caused by the formation of ice lenses. It occurs in frost susceptible soils located within the frost penetration depth with an access to water [42, 44]. The frost susceptibility of a given soil is determined by its capillary rise, permeability and fines content, with soils having more than 10% passing No. 200 sieve assumed to be frost-susceptible [4]. When a frost susceptible soil with access to water freezes, part of the water undergoes a phase change and solidifies. The remaining water then flows from the unfrozen part of the soil to the frozen one through capillary rise, accumulating around the existing ice and leading to the formation of ice lenses [30]. The formation of ice lenses significantly increases the soil volume through the combined action of water accumulation at the freezing front and the expansion of water as it solidifies [1, 42, 44].

In a railway embankment, frost heave may occur as a result of the subgrade being frost susceptible, the ballast material being highly fouled and therefore prone to developing heave-causing ice, and issues with the subballast material such as

the subballast aggregate becoming too fouled or being too thin to prevent the frost penetration depth from reaching a frost susceptible subgrade [1, 34–36].

Particular attention must be paid to the cyclic train loading applied on railway embankments. This dynamic load generates excess pore water pressure in the foundation soil of railway embankments that can lead to the upward flow of water and fine, also known as pumping, from the subgrade to the ballast. Sheng et al. [42] defined pumping-enhanced heave as frost heave driven by the excess pore water pressure generated by cyclic train loads that becomes trapped below the frozen soil during the freezing period. The excess pore water being unable to dissipate then feeds the existing ice lenses and contributes to the existing heave [42]. Using numerical modeling, Sheng et al. [42] demonstrated that while the rate of frost heave increase stabilizes over time when there is no excess pore pressure, the rate of heave increase remains constant when excess pore pressure caused by dynamic train loads is generated, thereby indicating that pumping-enhanced frost heave occurs all winter long due to the frequent passage of trains on the tracks.

Frost heaving is a major contributor to the frost deterioration of ballasted railway embankments. The formation of ice lenses is not uniform in the substructure and leads to differential heave, thereby increasing track roughness [29]. Frost heave is also responsible for the thaw subsidence and softening that occur during warmer seasons when the ice lenses that formed during the cold season start to melt.

3.2 Thaw Subsidence and Softening

During the warmer months of the year, when temperatures cease to be subfreezing, the ice lenses that formed during the colder months start melting from the top downwards [24]. While the ice thaws, the water escapes through the space initially occupied by the ice, leaving behind a weakened soil with a high void ratio [4, 24]. As thawing takes place, the soil can be divided into three zones, i.e., the thawed zone, the thawing zone, and the frozen zone [46]. Given that thawing occurs from the top downwards, the melt water cannot initially drain because the soil below remains in a frozen state, resulting in an increased water content. This increased water content reduces the soil's strength and bearing capacity [27, 32, 46]. This weakening of the soil creates conditions where railway embankments can easily get damaged by train traffic loads that generate additional pore pressure in the supporting soil, further weakening the soil and increasing settlement.

4 Mitigating Frost-Induced Damage

The frost heave and thaw softening of railway embankment materials caused by freezing and thawing cycles considerably increase settlement and create dangerous train riding conditions. Different approaches to tackle frost-induced damage have

been described in the literature and involve either the insulation of frost susceptible material to prevent it from freezing, or the incorporation of reinforcement in the embankment structure to cope with the effects of freezing and thawing or a combination of the two approaches.

Based on an extensive survey of the railway network in Finland, Nurmikolu et al. [34–36] emphasized on the importance of preventing frost susceptible material from freezing. To do so, attention must be paid to ensure the ballast and subballast material are not heavily fouled to avoid the presence of frost susceptible material in these two layers. The ballast and subballast layers must also have sufficient thickness to act as an insulating system for the underlying subgrade. Additionally, the subballast must be designed to act as a filter and separator to prevent the migration of frost susceptible materials within the embankment.

Geosynthetic reinforcements have been introduced in railway embankments built in cold regions to mitigate the effects of freezing and thawing. Various geosynthetics were used on the Qinghai-Tibet Railway to reduce the detrimental effects of cold weather on railway embankments. Geogrids were used as subgrade reinforcement to reduce settlement and increase bearing capacity, while seepage-proof geomembranes, insulation materials, geocells and geotextiles were used to prevent water infiltration and insulate the subgrade [14]. The geogrids successfully reduced differential settlement, improved stability and led to a more uniform embankment deformation compared to unreinforced sections [14]. Geogrids have more generally been used in ballast railway embankments wherever excessive settlement and lateral spreading are identified as issues. As such, geogrids can be used to mitigate the loss of bearing capacity and subsequent increased settlement experienced during spring thaw as the ice water melts and softens the subgrade [37]. Following the introduction of geogrids in embankments on the Qinghai-Tibet Railway, the use of geotextiles in combination with a crushed rock layer to prevent frost damage was investigated [29]. It was reported that the assortment of geosynthetics and crushed rock successfully reduced the depth of frost penetration, prevented moisture migration and frost heave and resulted in smaller settlements [29].

5 Geosynthetic Reinforcement

Railway embankments located in seasonally cold regions are exposed to freezing and thawing cycles and experience significant weather-induced deformations that have a detrimental impact on track roughness. Additionally, the degradation of the ballast and subballast layers must be avoided such that they do not become frost susceptible and further contribute to frost heave and thaw subsidence. The cold weather-induced deformations and degradation of the unbound aggregate layers can be mitigated through the incorporation of geosynthetic reinforcement materials in railway embankments [8, 18]. The uses and functions of geogrids, geotextiles and geogrid composites are discussed in the following subsections and summarized in Table 1.

Table 1 Functions of geogrids, geotextiles and geogrid composites

	Geogrid	Geotextile	Geogrid composite
Reinforcement	✓		✓
Separation		✓	✓
Filtration		✓	✓

5.1 Geogrids

Geogrids are geosynthetic materials composed of large openings called apertures bordered by longitudinal and transverse ribs that are used as reinforcement materials in railway tracks [12, 25, 28]. As shown in Fig. 2, geogrids may typically be placed within the ballast layer, at the interface between the ballast layer or at the interface between the subballast and subgrade [12, 20, 40]. The reinforcing action of geogrids hinges of their ability to develop a strong mechanical interlocking with the soil they are placed in [28]. A geogrid's apertures allow for the surrounding aggregate or soil to strike through the plane of the geogrid, thereby reinforcing the soil or unbound aggregate layer by confining it laterally, increasing its stiffness and modulus and reducing the magnitude of stresses transferred to underlying strata [15, 16, 20, 22]. By providing additional lateral confinement to the ballast material, geogrids reduce the lateral spreading and vertical settlement that would normally occur in the ballast layer, reduce breakage of the ballast aggregate and diminishes the magnitude of the vertical stresses transferred to the subgrade [22].

In the context of railway embankments located in cold regions, geogrids can help reduce the rate of degradation of ballast material under regular service loads and prevent the increase in the content of fine particles in the voids between the ballast material that could render the layer susceptible to frost heave [38]. Geogrids may also lessen the magnitude of the deformations experienced by the embankment as a result of freeze/thaw cycles [14, 29]. The depth of placement and the aperture size of a geogrid have a significant impact on its ability to perform its functions. These two parameters are discussed in the following subsections.

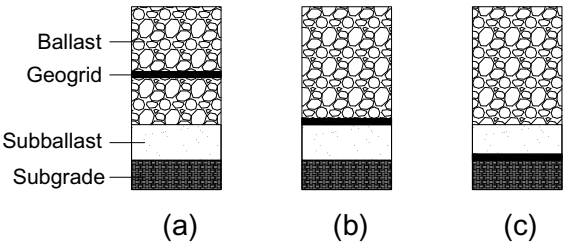

Fig. 2 Geogrid placed: **a** In the ballast, **b** Between the ballast/subballast, **c** Between the subballast/subgrade

5.1.1 Depth of Placement

Various recommendations exist on the desirable depth of placement of geogrid reinforcement in the ballast layer of a railway embankment. Bathurst and Raymond [5] and Raymond and Ismail [40] indicated that geogrids placed between 50 to 100 mm below the bottom of the ties are the most effective at reducing settlement but that for practical reasons, a depth of placement of 200 mm below the depth of the ties is appropriate. The depth of reinforcement placement to tie width ratio (D_r/B) was defined to characterize the depth of placement of geogrids in the ballast layer and acceptable values for the ratio were given as $0.2 < D_r/B < 0.4$ (Bathurst and Raymond 1987). Indraratna et al. [22] indicated that the effects of a geogrid are maximum in its immediate vicinity and quickly decrease with increasing vertical distance from the geogrid and concluded that there exists a threshold distance beyond which a geogrid loses its ability to restrain the lateral deflection of the ballast. The optimum depth of geogrid placement was found to be 130 mm above the subballast, but the recommended geogrid placement depth was set to 65 mm above the subballast due to practical considerations [22]. Similar findings were reported by Hussaini and Sweta [19] who determined that the geogrid placement depth that resulted in the maximum decrease in ballast particle damage was 130 mm above the subgrade but that the recommended placement depth was 65 mm due to practical considerations [19]. Additionally, Gedela and Karpurapu [15] reported that geogrids placed 125 mm below the ties were most effective at reducing vertical settlement.

5.1.2 Aperture Size

The reinforcing mechanism of a geogrid relies on the strong mechanical interlock between the geogrid and the soil that surrounds it. The effectiveness of the interlock is itself a function of the relative size of the geogrid apertures with respect to the average particle size of the surrounding soil. An extensive study conducted at the University of Nottingham comprising of a numerical modeling campaign [33] and laboratory experiments [9] on the geogrid reinforcement of railway ballast that an optimum ratio of aperture size to ballast particle diameter of 1.4 was needed to achieve maximum resistance, mobilize the greatest interlock and obtain the smallest displacement in the ballast layer when it is subjected to loads [33]. Laboratory experiments echoed the results of the numerical study, showing that for aggregates with a nominal size of 50 mm, a geogrid with an aperture size of 65 mm were very effective at reducing settlement while a geogrid with an aperture size of 38 mm yielded no improvements compared to the unreinforced case due to a lack of interlock with the surrounding aggregate [9]. The ratio of the geogrid aperture size (A) to average particle diameter (D_{50}) was related to the effectiveness of the mechanical interlock between the geogrid and the surrounding particles by Indraratna et al. [21]. The ratio A/D_{50} was divided into three zones: the feeble interlock zone where $A/D_{50} < 0.95$, the optimum interlock zone where $0.95 < A/D_{50} < 1.20$, and the diminishing interlock zone where $A/D_{50} > 1.20$ [21]. The relevance of these categories was validated by Indraratna et al.

[22] who demonstrated that a geogrid's ability to reduce the lateral spread of ballast increases when A/D_{50} increases from 0.60 to 1.20, but that a geogrid became less effective at reducing lateral spread when A/D_{50} exceeds 1.20. Similar findings were reported by Hussaini and Sweta [20] who showed that a geogrid is increasingly successful at preventing ballast material from spreading as its A/D_{50} ratio increases from 0.63 to 0.93 and described the existence of a threshold value for the A/D_{50} ratio beyond which a geogrid became unable to restrain ballast lateral displacement due to the free movement of ballast particles in its aperture. Gedela and Karpurapu [15] described direct shear and pull-out tests on geogrid-reinforced aggregates which indicated that the aperture size played a central role in a geogrid's ability to reinforce soil and that the range of aperture sizes to obtain an optimal reinforcing action is $0.9D_{50}$ to $2.5D_{50}$.

5.2 Geotextiles

Geotextiles are a type of geosynthetics that are made of non-woven, woven or knitted polymeric textile. In railroad applications, geotextiles are usually used to perform three functions: separation, filtration and reinforcement, with the third function being a consequence of the first two [15, 23, 39]. Geotextiles are typically installed at the interface between the ballast and subballast layers, within the subballast or between the subballast and the subgrade to act as a barrier against the migration of particles from one layer to another, improve drainage conditions and provide some degree of reinforcement [39]. A geotextile acts as a separator when placed over a layer of fine and soft materials (e.g., subgrade) and under a layer of coarser materials (e.g., subballast) by preventing the upward migration of fine particles into the voids of the coarse materials [25]. Filtration is a necessary complement of a geotextile's separation ability. In the presence of water in the track structure and under repeated loading generated by the passage of trains, high pore pressures are induced in the track roadbed and may force fine particles from the subgrade and sub-ballast to migrate upwards into the ballast layer [39]. A geotextile placed at the bottom of the ballast layer prevents the mixing of fines with the ballast materials by retaining the fine particles while allowing water to pass through it [39].

In seasonally cold regions, a geotextile's ability to improve the internal drainage conditions of the track support structure and to separate its various components are of particular interest. During the spring, thaw occurs from top to bottom in a frozen track embankment, with the bottom frozen soil preventing the downward dissipation of the melt water which then becomes trapped in the embankment, creating conditions where high pore water pressure may arise under train traffic loading [39]. A geotextile's filtration ability may help drain the melt water away from the track support structure and into the side ditches. A geotextile may also act as a barrier to prevent capillary rise and reduce frost heave during the winter [18]. Additionally, a

geotextile may mitigate the extent of ballast fouling by separating it from the underlying subgrade and/or subballast which contain smaller particles, thereby preventing potentially frost-susceptible materials from reaching the ballast layer [11, 38].

5.3 Geogrid Composites

The reinforcing property of geogrids can be combined with the separation and filtration properties of geotextiles with a geosynthetic product called a geogrid composite. A geogrid composite consists of a geogrid bonded to a geotextile that acts as a separator, filter and reinforcement. This type of geosynthetic has been used in the construction of railway embankments in Canada [6, 7] over weak saturated subgrades. The use of geogrid composites rolled over the subgrade improved drainage conditions and allowed excess pore pressures generated by train traffic to be dissipated while also separating the subgrade soil from the rest of the embankment and reinforcing the entire track support structure [6].

6 Conclusion

Seasonally cold regions akin to those found in Canada impose harsh environmental conditions on railway embankments. The subfreezing temperatures that characterize the coldest months of the year can adversely impact the geometry of railway tracks through frost heave. Frost heave occurs when frost susceptible materials found in the subgrade and fouled subballast/ballast layers of a railway embankment are exposed to subfreezing temperatures and have access to water, leading to the formation of ice lenses that significantly increase the volume of the soil and results in the heaving of the embankment's surface. Frost heaving is followed by thaw softening and subsidence that take place during warmer months. As the ice lenses start to melt from the top down, melt water becomes trapped in the embankment substructure, being unable to drain downward through the frozen soil, and causes a reduction in the soil's strength, leaving it vulnerable to damages caused by ongoing train traffic. Several approaches are used to either prevent frost action from occurring in a railway embankment through the use of sufficiently thick, non-frost susceptible ballast and subballast layers, or to reduce the deformations caused by frost action through the incorporation of geosynthetic reinforcement in the embankment substructure. Commonly used geosynthetic reinforcements include geogrids, geotextiles and geogrid composites. Geogrids are typically placed within or at the bottom of the ballast layer and reinforce it by developing a strong mechanical interlock with the ballast aggregates, thereby reducing ballast breakage, deformation and the magnitude of stresses transferred to underlying layers. Geogrids help reduce the frost action-induced deformations and prevent the ballast from becoming frost susceptible by reducing its fouling. Geotextiles are primarily used for their separation and filtration functions. They inhibit the

upward migration of frost susceptible fine soil particles coming from the subgrade into the subballast and ballast layers and drain water away from the embankment's substructure. Finally, geogrid composites combine the properties of both geogrids and geotextiles and effectively reinforce an embankment while providing filtration and separation.

References

1. Akagawa S, Hori M, Sugawara J (2017) Frost heaving in ballast railway tracks. Transportation Geotechnics and Geoecology, TGG 2017. Saint Petersburg, Russia. 189:547–553
2. Alabbasi Y, Hussein M (2019) Geomechanical modelling of railroad ballast: a review. Arch Comput Methods Eng. https://doi.org/10.1007/s11831-019-09390-4.WOS:000507791500001
3. Alemu AY (2011) Survey of railway ballast. Master, Department of Transport Science, Royal Institute of Technology
4. Barker J, Howard T (2013) Geotechnical engineering in cold regions. In: 10th International symposium on cold regions development, vol 1, Anchorage, AK, pp 204-214
5. Bathurst RJ, Raymond G (1986) Geogrid reinforcement of ballasted track. Transp Res Rec 1153:8–14
6. Bhat S, Thomas J (2015) Use of polymer geogrid composite to support rail track over weak saturated clay subgrade—a case study. Geo-Environ Eng Montreal, QC, 1:1–5
7. Bhat S, Thomas J2017) Railroad stabilization using biaxial geogrid-geotextile composite—a case study. In: First international conference on technology and application of geotextiles, vol 1, Santiago, Chile, pp 1–7
8. Bonthron B, Jonsson C (2017) Geogrids in cold climate: temperature controlled tensile tests and half-scale installation tests at different temperatures. Lulea University of Technology (Lulea, Sweden)
9. Brown SF, Kwan J, Thoma NH (2007) Identifying the key parameters that influence geogrid reinforcement of railway ballast. Geotext Geomembr 25(6):326–335. https://doi.org/10.1016/j.geotexmem.2007.06.003.WOS:000251893500002
10. Canada, Railway Association (2019) 2019 Rail trends. Railway Association of Canada, Ottawa, ON, Railway Association of Canada
11. Christopher BR (2016) Geotextiles used in reinforcing paved and unpaved roads and railroads. In: Koerner RM (ed) Geotextiles: from design to applications. Woodhead Publishing, pp 305–335
12. Das BM (2016) Use of geogrid in the construction of railroads. Innov Infrastruct Solut 1(1)
13. Ge JJ, Wei J, Bao LM, Shi XM, Xuan LH, Li XL (2008) Introduction and application of geosynthetic in qinghai-tibet railway construction. Geosynthetics in Civil and Environmental Engineering, Shanghai, China. pp 817–822
14. Gedela R, Karpurapu R (2021) A review on the role of geosynthetics in preventing the excessive settlement and mud pumping of ballasted railway track. Geohazards, Singapore, 86:715–726
15. Gobel CH, Weisemann UC, Kirschner RA (1994) Effectiveness of a reinforcing geogrid in a railway subbase under dynamic loads. Geotext Geomembrs 13(2): 91–99. https://doi.org/10.1016/0266-1144(94)90041-8. WOS:A1994MY00400002
16. Graham J, Au VCS (1985) Effects of freeze thaw and softening on a natural clay at low stresses. Can Geotech J 22(1):69–78. https://doi.org/10.1139/t85-007. WOS:A1985AEJ5600007
17. Han J, Jiang Y (2013) Use of geosynthetics for performance enhancement of earth structures in cold regions. Sci Cold Arid Regns 5(5):517–529. https://doi.org/10.3724/SP.J.1226.2013.00517
18. Hussaini SKK, Indraratna B, Vinod JS (2016) A laboratory investigation to assess the functioning of railway ballast with and without geogrids. Transp Geotech 6:45–54. https://doi.org/10.1016/j.trgeo.2016.02.001.WOS:000377793700005

19. Hussaini SKK,Sweta K (2020) Application of geogrids in stabilizing rail track substructure. Front Built Environ 6. https://doi.org/10.3389/fbuil.2020.00020. WOS:000548325300001
20. Indraratna B, Hussaini SKK, Vinod JS (2012) On the shear behavior of ballast-geosynthetic interfaces. Geotech Test J 35(2): 305–312. WOS:000302849900009
21. Indraratna B, Hussaini SKK, Vinod JS (2013) The lateral displacement response of geogrid-reinforced ballast under cyclic loading. Geotext Geomembrs 39:20–29. https://doi.org/10.1016/j.geotexmem.2013.07.007. WOS:000325388400003
22. Indraratna B, Shrawan Nimbalkar S (2013) The role of geosynthetics in improving the behaviour of ballasted rail tracks. In: Indraratna B, Shrawan Nimbalkar S (eds) Geosynthetics in railway track, New Delhi, India, Central Board of Irrigation and Power, pp 59–85
23. Jackson N, Dhir RK (1996) Civil Engineering Materials. 5th, Edition. Palgrave, London
24. Koerner RM (2005) Designing with Geosynthetics. Upper Saddle River, NJ, Pearson Prentice Hall
25. Koerner RM (2016) Geotextiles Used in Separation. In: Koerner RM (ed) Geotextiles: from design to applications. Woodhead Publishing, pp 239–256
26. Krzewinski TG, Wachholz MJ, Miller D, Lotakis G (2006) ARRC rail alignment improvements birchwood, alaska railroad design—construction in marginally frozen relic ice and soil. In: 13th International conference on cold regions engineering. Orono, ME, pp 1–10
27. Kwan J (2006) Geogrid reinforcement of railway ballast. Ph.D., Department of Civil Engineering, University of Nottingham
28. Lai YM, Zhang SM, Yu WB (2012) A new structure to control frost boiling and frost heave of embankments in cold regions. Cold Reg Sci Technol 79–80:53–66. https://doi.org/10.1016/j.coldregions.2012.04.002.%3cGotoISI%3e://WOS:000305201300006
29. Le Borgne V, Roghani A, Hiedra Cobo J, Thivierge S-É (2019) Design and installation of a geotechnical monitoring system for monitoring freeze-thaw cycles on a railway track. In: 18th International Conference on cold regions engineering and 8th canadian permafrost conference. Quebec City, QC, pp 153–160
30. Li D, Hyslip J, Sussmann T, Chrismer S (2016) Railway Geotechnics. CRC Press, Boca Raton, FL
31. Li D, Selig ET (1995) Evaluation of railway subgrade problems. Transp Res Rec 1489:17–25
32. McDowell GR, Harireche O, Konietzky H, Brown SF, Thom NH (2006) Discrete element modelling of geogrid-reinforced aggregates. Proc Inst Civ Eng-Geotech Eng 159(1): 35–48. https://doi.org/10.1680/geng.2006.159.1.35. WOS:000235910000005
33. Nurmikolu A (2012) Key aspects on the behaviour of the ballast and substructure of a modern railway track: research-based practical observations in Finland. J Zhejiang Univ-Sci A 13(11):825–835. https://doi.org/10.1631/jzus.A12ISGT1.WOS:000311204600004
34. Nurmikolu A, Kolisoja P (2005) Extruded polystyrene (XPS) foam frost insulation boards in railway structures. In: Proceedings of the 16th international conference on soil mechanics and geotechnical engineering, vol 1–5, pp 1761–1764. WOS:000246615102141
35. Nurmikolu A, Silvast M (2013) Causes, effects and control of seasonal frost action in railways. Sci Cold Arid Regns 5(4):363–367. https://doi.org/10.3724/SP.J.1226.2013.00363
36. Petriaev A, Ganchits V, Chetina M, Kozlov I, Petrenko S (2020) Stamp test of railway ballast, stabilized by geogrids. Transp Soil Eng Cold Regns, Singapore, 2:45–53
37. Raymond GP (1986) Installation factors that affect performance of railroad geotextiles. Transp Res Rec 1071:64–71
38. Raymond GP (1999) Railway rehabilitation geotextiles. Geotext Geomembrs 17(4):213–230. https://doi.org/10.1016/S0266-1144(99)00002-3
39. Raymond GP, Ismail I (2003) The effect of geogrid reinforcement on unbound aggregates. Geotext Geomembrs 21(6):355–380. https://doi.org/10.1016/S0266-1144(03)00044-X
40. Selig ET, Waters JM (1994) Track geotechnology and substructure management. ICE Publishing, London
41. Sheng D, Zhang S, Niu F, Cheng G (2014) A potential new frost heave mechanism in high-speed railway embankments. Geotechnique 64(2):144–154. https://doi.org/10.1680/geot.13.P.042.WOS:000333526000005

42. Stenstrom C, Famurewa FM, Aditya P, Galar D (2012) Impact of cold climate on failures in railway infrastructure. In: PMM 2012: the 2nd international congress on maintenance performance measurement and management conference proceedings, Lulea, Sweden, pp 1–9
43. Wang TL, Liu YJ, Yan H, Xu L (2015) An experimental study on the mechanical properties of silty soils under repeated freeze-thaw cycles. Cold Reg Sci Technol 112:51–65. https://doi.org/10.1016/j.coldregions.2015.01.004.%3cGotoISI%3e://WOS:000352748500006
44. Zhang S, Sheng DC, Zhao GT, Niu FJ, He ZY (2016) Analysis of frost heave mechanisms in a high-speed railway embankment. Can Geotech J 53(3):520–529. https://doi.org/10.1139/cgj-2014-0456.%3cGotoISI%3e://WOS:000375426000012
45. Zhdanova S, Edigarian A, Gorshkov N, Neratova O (2020) Soil research for strengthening railroad bed design in cold regions of far east. TransSiberia 2019: VIII International Scientific Siberian Transport Forum. Novosibirsk, Russia. 1116:49–59

Applications of Flow-Drilled Connections in Modular Construction

L. Kalam, J. Dhanapal, S. Das, and H. Ghaednia

1 Introduction

A proprietary method of steel modular building construction currently exists that uses modules made from hollow structural steel (HSS) members. These HSS members are used to form both the beam and column members of the modules [5]. Making a traditional bolt and nut connection on the HSS members is difficult due to access limitations resulting from its geometry, thus holes are required to be made on the face of the HSS to allow access for the nut to connect to the bolt. Such a method impedes the speed and efficiency of the modular construction method; thus, the flow drilling method is preferred.

Flow drilling and flow tapping allow bolted connections to only require access to one side of the HSS member. This method involves using a quick rotating drill bit that displaces the work metal as the screw hole is drilled. The displaced metal forms a bush that extends two to four times the thickness of the work metal from the metal face. Threads are made on the bush using a technique called flow tapping, which uses a special drill bit that does not cut into the bush metal. Traditional tapping techniques can also be used on the bush to form threads as well. The extension of the bush from the work metal face increases surface space to allow for more threads to increase screw engagement. This study focuses on the experimental testing of single flow drilled connections made on HSS members under tension and shear loads. The ultimate strength and behavior at failure were studied and compared to standard drilling and tapping techniques. The effect of the number of threads per inch (TPI)

L. Kalam (✉) · S. Das
University of Windsor, Windsor, Canada
e-mail: kalaml@uwindsor.ca

J. Dhanapal · H. Ghaednia
Z-Modular, Toronto, Canada

S. Walbridge et al. (eds.), *Proceedings of the Canadian Society of Civil Engineering Annual Conference 2021*, Lecture Notes in Civil Engineering 240,
https://doi.org/10.1007/978-981-19-0507-0_30

was explored, and analytical equations to predict the mode and sequence of failure of the flow drilled connection are presented.

2 Experimental Setup

Four parameters were considered in this study, resulting in fifteen different connections. The parameters were HSS wall thickness and geometry, TPI, drilling technique, and tapping technique. The parametric combinations and their respective connection notations are presented in Table 1. The diameter of the screw hole was kept constant throughout the specimens at 0.75 inch. Five specimens for each connection and loading type (tension and shear) were manufactured, resulting in a total of 150 specimens. The HSS specimens used in this study conform to ASTM A500 Grade C [1] and the socket head cap screws (SHCS) used conform to ASTM A574 [2].

2.1 Tension Setup

The tension test specimen contained an HSS section with its bottom face welded to a steel T section and a single screw hole on one wall. A SHCS with a diameter of 0.75″

Table 1 Test matrix

HSS Section (b × h × t)	TPI	Drilling technique	Tapping technique	Connection notation
6″ × 3″ × 1/8”	10	FD	ST	1-10FDST
			FT	1-10FDFT
		SD	ST	1-10SDST
6″ × 3″ × 3/16”	10	FD	ST	2-10FDST
			FT	2-10FDFT
		SD	ST	2-10SDST
	16	FD	ST	2-16FDST
			FT	2-16FDFT
		SD	ST	2-16SDST
5″ × 2″ × 1/4”	10	FD	ST	3-10FDST
			FT	3-10FDFT
		SD	ST	3-10SDST
	16	FD	ST	3-16FDST
			FT	3-16FDFT
		SD	ST	3-16SDST

FD—Flow drilling; SD—Standard drilling; FT—Flow tapping; ST—Standard tapping

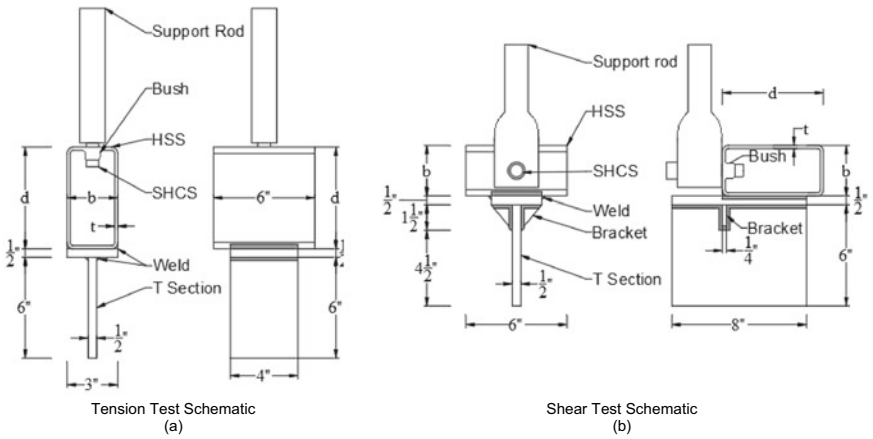

Fig. 1 Test schematic

was connected to the screw hole on the HSS wall on one end and a steel support rod on the other. The entire specimen was installed on a universal testing machine (MTS) by clamping the end of the support rod and the web of the T-section. The displacement control method was used to apply the pure tension load. A schematic of the tension setup can be seen in Fig. 1a.

2.2 Shear Setup

The shear test specimen was similar to the tension specimen, composing of an HSS section with a screw hole welded to a steel T section; however, the orientation of the screw hole and support rod differs. The T section was strengthened using two 0.25″ brackets due to a higher predicted capacity of the connection in shear over tension. The same MTS machine was used by clamping the end of the support rod and the web of the T section and the displacement control method was used. A schematic of the shear setup can be seen in Fig. 1b.

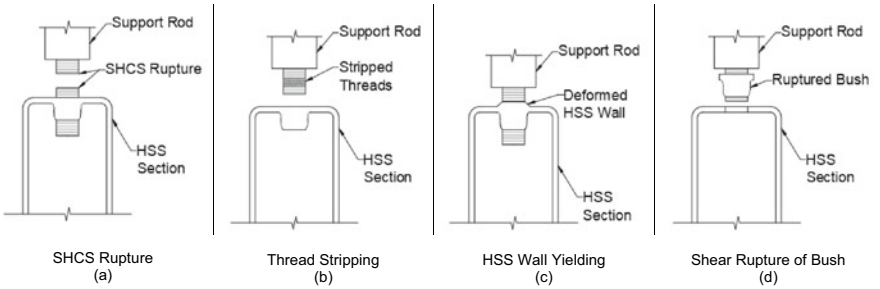

Fig. 2 Tension failure modes

3 Analytical Equations for Failure Sequence

3.1 Tension Failure Modes

3.1.1 SHCS Rupture

The equation used to calculate the capacity associated with the SHCS rupture was based on the equation from the Canadian design standard, CSA S16-14 (CSA S16-14 2014). In Eq. 1, $\emptyset_b$ is the bolt resistance factor, A_b is the nominal bolt cross-sectional bolt area, and F_u is the ultimate tensile strength of the bolt material. A diagram of this failure mode can be seen in Fig. 2a.

$$T_{r,1} = 0.75\phi_b A_b F_u \tag{1}$$

3.1.2 HSS Hole Thread Stripping

Thread stripping refers to the shear rupture of bending deformation of the threads in the screw hole. The load at which thread stripping occurs was calculated using Eq. 2 [7]. A diagram of the thread stripping failure mode can be seen in Fig. 2b.

$$T_{r,2} = \text{Min}\left(\sum F_{S,1,Rd}, \sum F_{S,1,Rd}\right) \tag{2}$$

In Eq. (2), $F_{s,1,Rd}$ and $F_{s,2,Rd}$ refers to the shear and bending strength of a single thread, respectively. They are calculated as shown:

$$F_{s,1,Rd} = \frac{\pi D h F_y}{\sqrt{3}} \tag{3}$$

$$F_{s,2,Rd} = \frac{\pi D h^2 F_{y,p}}{4b} \tag{4}$$

In Eqs. 3 and 4, Fy, p refers to the yield strength of the HSS material, D is the SHCS outer diameter, h is the thickness of a thread, and b is the height of a thread. The values of h and b were calculated based on the thread profile provided in ASTM B1.1 [3].

As Eqs. 3 and 4 are for the strength of a single thread, the summation in Eq. 2 is to account for the strength of the total number of threads in the connection. The length of the bush was determined to be 3t for HSS wall thicknesses of 1/8″ and 3/16″. The length of the bush was assumed to be 2.3t for HSS wall thickness of 1/4″, which was determined by measuring the bushes of the test specimens.

3.1.3 HSS Wall Yielding

The yielding of the HSS wall section around the screw hole is of a circular pattern similar to the way a concrete slab yields around a column. As such, the yield line analysis results of the circular yield pattern of slabs [6]. was used to determine the required tensile load to cause yielding in the wall. The required load is given in Eq. 5, where m_1 and m_2 are the plastic moment capacities in the circumferential and radial direction. For isotropic materials such as steel, m_1 and m_2 are equal, so the plastic moment capacity per unit width is given by Eq. 6. Substituting Eqs. 5 and 6, the required tension load to cause yielding of the HSS section is given by Eq. 7. A diagram of this failure mode can be seen in Fig. 2c.

$$T_{r,3} = 2\pi(m_1 + m_2) \tag{5}$$

$$m = m_1 = m_2 = \frac{F_{y,p}t^2}{4} \tag{6}$$

$$T_{r,3} = \pi t^2 F_{y.p} \tag{7}$$

3.1.4 Shear Rupture of Bush

A diagram of the failure mode in which the bush ruptures is shown in Fig. 2d. In this failure mode, the bush ruptures along a shear plane. The equation for the tension load required to cause this failure is given by Eq. 8.

$$T_{r,4} = \frac{\pi Dt F_{y,p}}{\sqrt{3}} \tag{8}$$

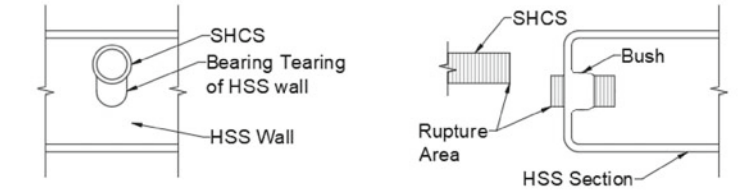

Fig. 3 Shear failure modes

3.2 Shear Failure Modes

3.2.1 Bearing-Tearing of HSS Wall

Since the shear load applied to the connection is transverse to the screw hole, the bearing capacity of the flow drilled connection and the standard drilled connection was expected to be the same. The required shear load to cause the bearing-tearing of the HSS wall was calculated from Eq. 9, which was provided in CSA S16-14 (CSA S16-14 2014). In this equation, $\emptyset_{br}$ is the bearing resistance factor of value 0.8 and $F_{u,p}$ is the HSS material tensile strength. A diagram of the bearing tearing of the HSS wall can be seen in Fig. 3a.

$$S_{r,1} = 3_{\phi \mathrm{br}} t D F_{u,p} \tag{9}$$

3.2.2 Shear Rupture of SHCS

The required load to cause the shear rupture of the SHCS was calculated from Eq. 10, which was provided in CSA S16-14 (CSA S16-14 2014). This equation assumed that the rupture occurs at the thread of the SHCS, thus the reduced cross-sectional area at the thread root for different TPI was not considered in Eq. 10. A diagram showing the shear rupture of the SHCS can be seen in Fig. 3b.

$$S_{r,2} = 0.42_{\phi \mathrm{b}} A_b F_u \tag{10}$$

4 Results of Experimental Tests

4.1 Tension Tests

The ultimate load for the tensile tests was considered as the peak or highest load reached by the specimen. The average ultimate load reached, standard deviation, and coefficient of variation for each connection configuration is presented in Table 2. The coefficient of variation is under 5% for each connection, showing consistency of the test results. The increase in the ultimate capacity of the flow drilled connections in comparison to standard drill and standard tapping connections is also shown in Table 2.

The load–displacement curves of the connections made on the 6″ × 3″ × 1/8″, 6″ × 3″ × 3/16″, and 5″ × 2″ × 1/4″ HSS sections are presented in Fig. 4a–c respectively. Each curve in Fig. 4 represents the results of all the specimens for the respective connection. It can be observed from Fig. 4a that the flow drilled (FD) connections reached a higher ultimate load than standard drilled (SD) connections. Also, flow tapped (FT) connections exhibited a higher ultimate load than standard tapped (ST) connections and it can be observed from Table 2 that FDFT connections had a 90% increase in ultimate load capacity when compared to SDST connections for the 6″ × 3″ × 1/8″ HSS section.

Figure 4b shows that FD connections again have a higher ultimate load capacity than SD connections for the 6″ × 3″ × 3/16″ HSS section; however, the percent

Table 2 Tension test results

Connection	Average ultimate load (kN)	Coefficient of variation (%)	Increase in ultimate load over SDST connection (%)
1-10FDST	29.3	2	77
1-10FDFT	31.6	2	90
1-10SDST	16.7	2	0
2-10FDST	53.1	3	55
2-10FDFT	58.2	2	70
2-10SDST	34.3	3	0
2-16FDST	54	2	71
2-16FDFT	58	1	84
2-16SDST	31.5	1	0
3-10FDST	99.2	4	23
3-10FDFT	119.2	1	48
3-10SDST	80.5	2	0
3-16FDST	98.9	2	21
3-16FDFT	104.4	1	28
3-16SDST	81.4	2	0

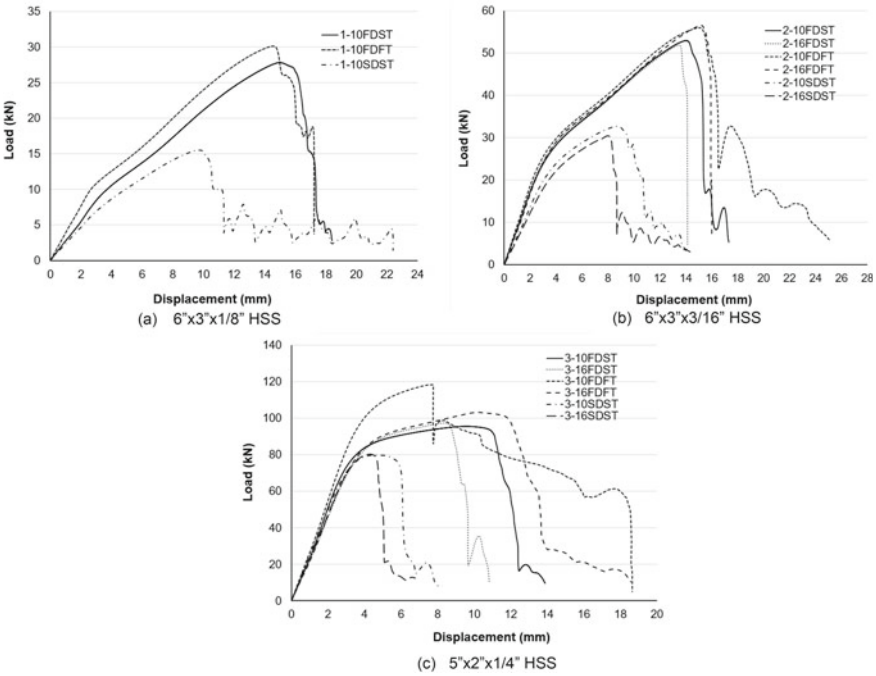

Fig. 4 Tension load displacement curves

increase in ultimate load capacity from FDFT to SDST connections is 20% less than the improvement observed on the 6″ × 3″ × 1/8″ HSS section. This indicates that the improvement in ultimate load capacity of FD connections decreases for increased wall thickness. No distinction could be made on the impact of TPI for FD connections. However, the 10 TPI screw hole had a 9% decrease in ultimate load capacity from the 16 TPI screw holes in SD connections. The yielding of the HSS wall was observed in all the tests for each HSS section. For the 6″ × 3″ × 1/8″ HSS section, yielding occurred earlier for SD connections at approximately 7 kN in comparison to the 10 kN observed in the FD connections. Yielding of the HSS wall began at approximately 20 kN for all of the connections on the 6″ × 3″ × 3/16″ HSS section. At the point of yielding, the HSS wall containing the screw hole began to deform plastically as shown in Fig. 2c. The connections continued to carry increased loads beyond the point of yielding due to the SHCS holding it together. Bush rupture, shown in Fig. 2d, was observed at failure for FDFT connections, while thread stripping, shown in Fig. 2b, was observed at failure for SDST connections. For FDST connections, inspection after failure showed the SHCS was still securely attached to the bush, indicating that the failure occurred due to the beginning of bush rupture. Figure 4c shows that the ultimate load reached for FD connections is significantly higher than the SD connections. For the FDFT connection with the 10

TPI screw hole, the ultimate load capacity is significantly higher than the rest of the connections on the 5″ × 2″ × 1/4″ HSS section.

4.2 Shear Test Results

The ultimate load for the shear tests was considered as the peak or highest load reached by the specimen. The average ultimate load reached, standard deviation, and coefficient of variation for each connection configuration is presented in Table 3. Table 3 also shows the change in the ultimate capacity of the flow drilled connections in comparison to standard drill and standard tapping connections is also shown in Table 3.

Similar to the shear tests, the ultimate load for the tensile tests was considered as the peak or highest load reached by the specimen. The change in the ultimate capacity of the flow drilled connections in comparison to standard drill and standard tapping connections is also shown in Table 3. The load–displacement curves of the connections made on the 6″ × 3″ × 1/8″, 6″ × 3″ × 3/16″, and 5″ × 2″ × 1/4″ HSS sections are presented in Fig. 5a–c, respectively. Each curve in Fig. 5 represents the results of all five test specimens for the respective connection.

It can be observed from Fig. 5a, b that the connections exhibited similar initial behavior irrespective of the type of drilling, tapping, and TPI used. It can be seen

Table 3 Shear test results

Connection	Average ultimate load (kN)	Coefficient of variation (%)	Change in ultimate load over SDST connection (%)
1-10FDST	56.7	2	11
1-10FDFT	55.7	2	9
1-10SDST	51.3	4	0
2-10FDST	97.2	3	−2
2-10FDFT	96.9	3	−2
2-10SDST	98.7	1	0
2-16FDST	104.4	2	2
2-16FDFT	98	3	−4
2-16SDST	102.3	4	0
3-10FDST	120.9	3	0
3-10FDFT	127.5	13	5
3-10SDST	121.2	2	0
3-16FDST	123.4	2	2
3-16FDFT	125.5	2	3
3-16SDST	121.4	1	0

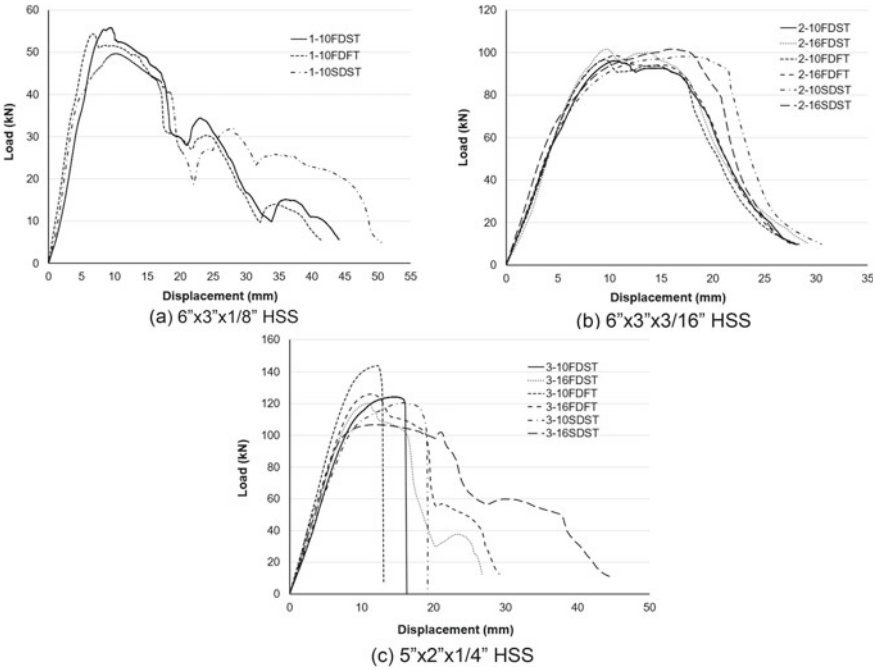

Fig. 5 Shear load displacement curves

from Table 4 that there is an 11% increase in ultimate load for FDST connections over SDST connections for the 6″ × 3″ × 1/8″ HSS section; however, no significant change was observed in the 6″ × 3″ × 3/16″ HSS section. At the point where the nonlinear behavior begins is when the HSS wall began to deform plastically, ultimately resulting in the bearing tearing failure shown in Fig. 3a as the loading increased. A drop in the load can also be seen in Fig. 5a, b at the ultimate load, which may be due to the rupture of the bush.

Figure 5c shows that the FD connections have a higher ultimate load capacity than SD connections on the 5″ × 2″ × 1/4″ HSS section. The 10FDFT connection has a much higher ultimate load capacity than the other FD connections; however, the remainder of the FD connections exhibited more similar results. Bush rupture occurred at the ultimate load for the FD connections on the 5″ × 2″ × 1/4″ HSS section. Sudden fracture occurred on the edges of the HSS wall with the screw hole at ultimate load for the 10FDFT connection. The sudden drop in load after the ultimate load seen in Fig. 5c can be attributed to this failure. The major nonlinear behavior of the SD connections indicates slight plastic deformation in the HSS wall, after which thread stripping was observed.

Table 4 Tension analytical results

	Analytical findings					Test results		
Connection	1 Bolt rupture (kN)	2 Thread stripping (kN)	3 HSS wall yielding (kN)	4 bush rupture (kN)	Predicted first mode of failure	Observed first mode of failure	Failure mode at ultimate load	Average ultimate load (kN)
1-10FDST	200	63	9	***34***	3	3	4	29.3
1-10FDFT	200	63	9	***34***	3	3	4	31.6
1-10SDST	200	***21***	9	–	3	3	2	16.7
2-10FDST	200	94	20	***51***	3	3	4	53.1
2-10FDFT	200	94	20	***51***	3	3	4	58.2
2-10SDST	200	***31***	20		3	3	2	34.3
2-16FDST	200	94	20	***51***	3	3	4	54
2-16FDFT	200	94	20	***51***	3	3	4	58
2-16SDST	200	***31***	20	–	3	3	2	31.5
3-10FDST	200	96	35	***68***	3	3	4	99.2
3-10FDFT	200	96	35	***68***	3	3	–	119.2
3-10SDST	200	***42***	35	**–**	3	3	2	80.5
3-16FDST	200	96	35	***68***	3	3	4	98.9
3-16FDFT	200	96	35	***68***	3	3	4	104.4
3-16SDST	200	***42***	35	–	3	3	2	81.4

5 Analytical Test Results

5.1 Tension

The capacity of the connections for the different failure modes under tension is presented in Table 4. In the calculation for these capacities, the thickness of the HSS wall was taken to be 90% of the nominal thickness to account for the allowable variation in HSS wall thickness. The first mode of failure was predicted to be the lowest calculated capacity among the four identified failure modes and marked the beginning of nonlinear behavior. The predicted first mode of failure matched the observed first mode of failure for all the connections, which was HSS wall yielding. The ultimate failure occurred due to a different subsequent failure mode, however, which is shown in Table 4. This subsequent mode of failure was predicted to be the second lowest calculated capacity among the modes identified. The predicted subsequent mode of failure is highlighted in bold in Table 4 and matches with the observed mode of failure at ultimate load for all the connections. This indicates that the sequence of failure can accurately be predicted using the identified analytical equations. Table 4 also shows that the predicted ultimate load was overestimated for certain connections, namely all the connections on the $6'' \times 3'' \times 1/8''$ HSS section and the SD connections on the $6'' \times 3'' \times 3/16''$ HSS section. This could be attributed to the influence of the first mode of failure on the connection which the analytical equations do not consider. Despite this, safety factors can be applied to the equations to get a reasonable estimate of the ultimate capacity of the connections.

5.2 Shear

The capacity of the connections for two failure modes under shear is presented in Table 5. The mode of failure in the connection was predicted based on the lowest calculated capacity corresponding to the two failure modes. It can be observed from Table 5 that the predicted failure mode matched with the observed failure mode for all of the connections apart from the 10 TPI connections on the $5'' \times 2'' \times 1/4''$ HSS section. This could be due to the load capacity associated with the two failure modes being very close (111 kN for bearing tearing of the HSS wall and 112 kN for shear rupture), thus shear rupture was observed in some specimens. From Table 5 it can be observed that the analytical equation yields slightly overestimated capacities of the connections on the $6'' \times 3''1/8''$ HSS section; however, the equations yield conservative estimates for the remainder of the connections. Thus, the equations can be used to estimate the ultimate shear capacity of the connection; however, safety factors are required for thinner walled HSS sections.

Table 5 Shear analytical results

Connection	Analytical findings			Test results	
	1. Bearing tearing (kN)	2. Shear rupture (kN)	Predicted failure	Observed first failure	Avg. ultimate load (kN)
1-10FDST	56	112	1	1	56.7
1-10FDFT	56	112	1	1	55.7
1-10SDST	56	112	1	1	51.3
2-10FDST	83	112	1	1	97.2
2-10FDFT	83	112	1	1	96.9
2-10SDST	83	112	1	1	98.7
2-16FDST	83	112	1	1	104.4
2-16FDFT	83	112	1	1	98
2-16SDST	83	112	1	1	102.3
3-10FDST	111	112	1	1/2	120.9
3-10FDFT	111	112	1	1/2	127.5
3-10SDST	111	112	1	1/2	121.2
3-16FDST	111	112	1	1	123.4
3-16FDFT	111	112	1	1	125.5
3-16SDST	111	112	1	1	121.4

6 Conclusion

This study presents the findings of a parametric study of flow drilled and standard drilled connections on HSS sections that are used in the modules of modular buildings. The connections were subject to axial tension and shear and the parameters considered were HSS wall thickness, screw threads per unit length, screw hole drilling technique, and tapping technique. The results of this study showed that under axial tension, the connections exhibit initial failure through deformation of the HSS wall; however, the full failure of the connection occurs due to a subsequent failure mode. This full failure was due to bush rupture in flow drilled connections and thread stripping in standard drilled connections. An improvement of up to 90% in the ultimate capacity was observed in flow drilled connections over standard drilled connections on the $6'' \times 3'' \times 1/8''$ HSS section; however, this improvement was lower with increased wall thickness. No significant impact of the threads per inch of the screw was observed on the tension capacity of the connection; however, a 9% reduction in the ultimate capacity from 10 to 16 TPI was observed for standard drilled connections on the $6'' \times 3'' \times 3/16''$ HSS section. The analytical equations developed in this study for tension can be used with safety factors to estimate the ultimate load capacity of the connections and can predict the sequence of failure modes. The method of drilling did not have a significant impact on the shear capacity of the connection and the analytical equations developed for shear can be used to estimate

the shear capacity of the connections; however, safety factors are required for the 6″ × 3″ × 1/8″ HSS section.

References

1. A500/A500M (2018) Standard specification for cold-formed welded and seamless carbon steel structural tubing in rounds and shapes. ASTM International, pp 1–6
2. A574 (2017) Standard specification for alloy steel socket-head cap screws. ASTM International, pp 1–7
3. ASME B1.1 (2004) Unified inch screw threads (UN and UNR thread form). American Society of Mechanical Engineers, pp 1–178
4. CSA S16–14 (2014) Design of steel structures. CSA Group
5. Jothiarun D, Ghaednia H, Das S, Velocci J (2019) Structural performance of state-of-the-art VectorBloc modular connector under axial loads. Eng Struct 496–509
6. Kurobane Y, Packer JA, Wardenier J, Yeomans N (2004) Design Guide for Structural Hollow Section Column Connections. TUV
7. Zhu X, Wang P, Liu M, Tuoya W (2017) Behaviors of one-side bolted T-stub through thread holes under tension strengthened with backing plate. J Constr Steel Res 134:53–65

Behavior of Vectorbloc Beam-Column Connections

L. Kalam, J. Dhanapal, S. Das, and H. Ghaednia

1 Introduction

Modular construction is on the rise due to the increased speed, efficiency, and quality control it provides in comparison to traditional construction practices. Modular construction involves the offsite construction of elements, panels, and modules in a factory before onsite installation [1]. Among the many types of modular construction, structural steel-based modular construction is of particular interest in high-rise buildings [2]. A key component in modular construction is the connection between the individual modules, which hold the building together against applied loads such as gravity, snow, and wind.

A state-of-the-art cast steel connector, named the VectorBloc connector, is presently used in the connections between steel modules of modular buildings. These modules are made using hollow structural steel (HSS) members. The novelty of this connector is that it provides both beam-column connection in a module and intermodular connection between modules with a construction tolerance of 1/16 inches. This study focuses on the VectorBloc connector used in the corner connection of these modules under the design loads of a mid-rise building that was in development.

L. Kalam (✉) · S. Das
University of Windsor, Windsor, Canada
e-mail: kalaml@uwindsor.ca

J. Dhanapal · H. Ghaednia
Z-Modular, Toronto, Canada

S. Walbridge et al. (eds.), *Proceedings of the Canadian Society of Civil Engineering Annual Conference 2021*, Lecture Notes in Civil Engineering 240,
https://doi.org/10.1007/978-981-19-0507-0_31

2 Test Specimen

Four full-scale specimens were manufactured for experimental testing. Two of the specimens were used for axial tension and compression testing and the remaining two were used for bending testing. The specimens were composed of the VectorBloc corner connector, two 18 in long HSS 4″ × 4″ × 3/8″ upper and lower columns, two 50 in long HSS 3″ × 8″ × 1/5″ floor beams, and two 48 in long HSS 3″ × 3″ × 3/8″ ceiling beams. The columns, floor, and ceiling beams were connected to the connector via full penetration fillet welds all around.

2.1 Vectorbloc Connector

The VectorBloc corner connector comprises a upperbloc, lowerbloc, two 0.75 in diameter flat head cap screws (FHCS), two 1 in diameter socket head cap screws (SHCS), a 0.5 in thick gusset plate, and a 2 in diameter registration pin. The lower bloc connects the top HSS column to the HSS floor beam and the upper block connects the bottom HSS column to the HSS ceiling beam. The gusset plate is connected to the upper bloc with the FHCS, and the registration pin is threaded into the lower bloc. The upper bloc and lower bloc are vertically connected via the SHCSs, which thread into holes in the upper bloc. Details of the corner VectorBloc connector can be seen in Fig. 1.

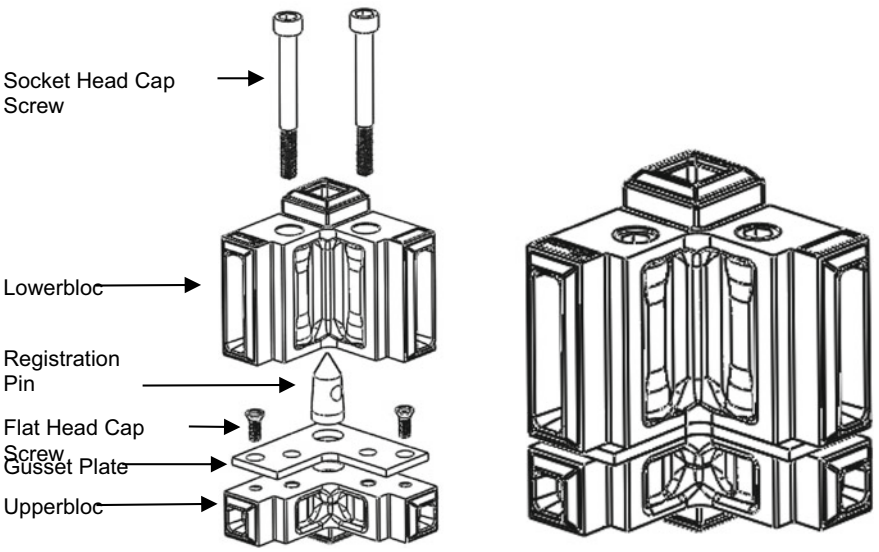

Fig. 1 Vectorbloc connector

3 Test Overview and Setup

3.1 Experimental Test

Three types of tests were conducted on the specimen: axial tension, axial compression, and bending. The experimental test setup for the axial tension and compression tests were identical, while the setup for the bending test differed. The maximum loads applied to the specimen were determined based on the maximum design loads expected on a corner connection of a mid-rise building that was in development. Loading the specimens until failure would cause damage to the loadcells, loading jacks, and potentially other parts of the test setup. As the development of the test setup was very expensive and time-consuming, it was determined that loading until failure should be avoided to protect the equipment. Loads to the specimen for all of the tests were applied using a displacement control method until the desired design load was reached.

3.1.1 Axial Tension and Compression

Two full-scale specimens representing a typical corner connection were used: one for the axial tension test and one for the axial compression test. The axial loads were applied with a load jack and loadcell located at the end of the top column. The column ends were given a pin-roller boundary condition. The bottom column was restrained in translation in all three axes and the top column was restrained in translation in the horizontal axes and free to translate in the vertical axes to allow for movement of the load jack. Two linear variable transducers (LVDTs) were placed on the specimen to measure the displacement between the sections of the specimen to which they were connected. The first LVDT was connected to the top column and lower bloc, while the second column was connected to the bottom column and upper bloc. The details of the axial tension and compression setup can be seen in Fig. 2a.

3.1.2 Bending

Two full-scale specimens representing a typical corner connection were used for the bending tests. The free ends of the floor beams were reinforced with 0.5″ plates to prevent local deformation under the applied loads. The reinforced ends of the floor beams were beared on the ceiling beams to allow the load to be transferred between them. The top and bottom columns were given a pin-roller boundary condition and restrained in translation in all directions. Two load cells were placed at the end of each floor beam in this test setup. Bending loads were applied to the connection by applying vertical loads on the ends of the floor beams. Four LVDTs were placed on the floor beams to measure its deflection at different points along its length. The labeling and location of these LVTDs can be seen in the schematic of the test

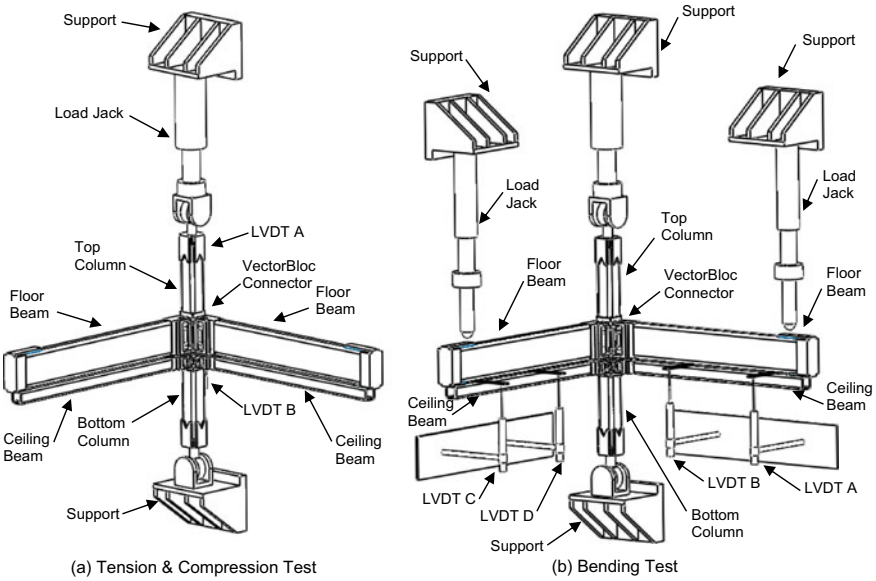

Fig. 2 Test schematics

specimen in Fig. 2b. As the floor beam beared on the ceiling beam, it was assumed that the deflection for both would be the same, hence only the deflection of the floor beam was measured.

3.2 Finite Element Analysis

Full-scale experimental tests are useful in obtaining information on the overall behavior of the connection under axial and bending loads. However, they are very expensive and do not provide certain information, such as stress and strain distribution, that is important to understand the structural behavior of the connection. Finite element (FE) models of the specimen were developed using a commercially available finite element code, ABAQUS/Standard version 6.13 [3]. Three models were developed to simulate the axial tension, axial compression, and bending tests that were experimentally conducted. These models were used to conduct further tests on the connection and collect information that could not be obtained from the experimental testing.

The welded joints of the connection, the threaded screw connection between the SHCSs and upperbloc, and the connection between the gusset plate and upperbloc were modeled using surface-to-surface tie constraints. Surface-to-surface frictionless hard contact was used on all areas where contact occurred between the components of the connection. The ends of the upper and lower columns were kinematically coupled

to points corresponding to the center of the column end fixture. Boundary conditions of the corresponding supports were applied to these points. Coupon testing of the components of the specimen was performed and the results were used to determine the material properties used in the models.

4 Test Results

4.1 Axial Compression

The maximum compression load applied to the specimen was 400 kN. The load was gradually increased using the displacement control method until the maximum design load of 400 kN was reached. The axial load-deformation results of this test are shown in Fig. 3. It can be seen that the behavior of the connection is linear under the applied load, indicating that it is still in the elastic range and the connection is safe under the design load. The load was eccentric at the lower bloc and gusset plate contact due to the difference in the cross-sections of the blocs and columns. This resulted in the columns and cross-section of the bloc being subjected to both axial compression and bending, causing a small relative rotation of the blocs which was resisted by the SHCSs.

Figure 3 also shows the axial load-deformation results of the finite element analysis (FEA) that was conducted on the specimen. From this figure, it can be observed that the FEA results are in good alignment with the experimental test

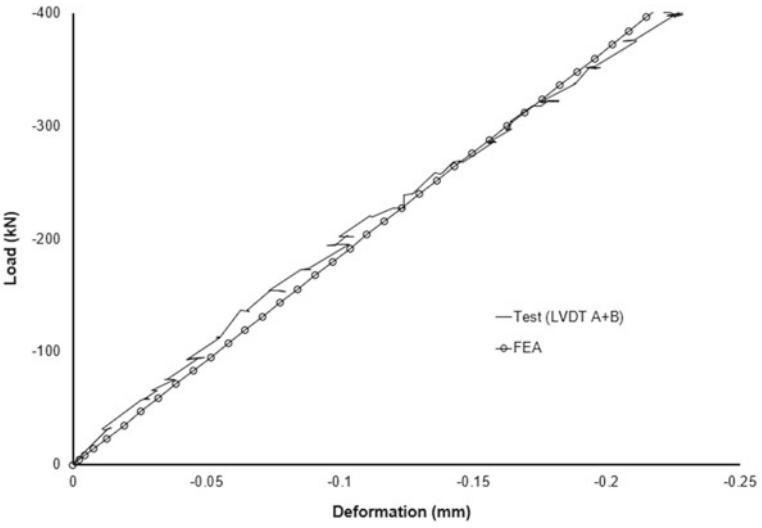

Fig. 3 Axial compression load deformation

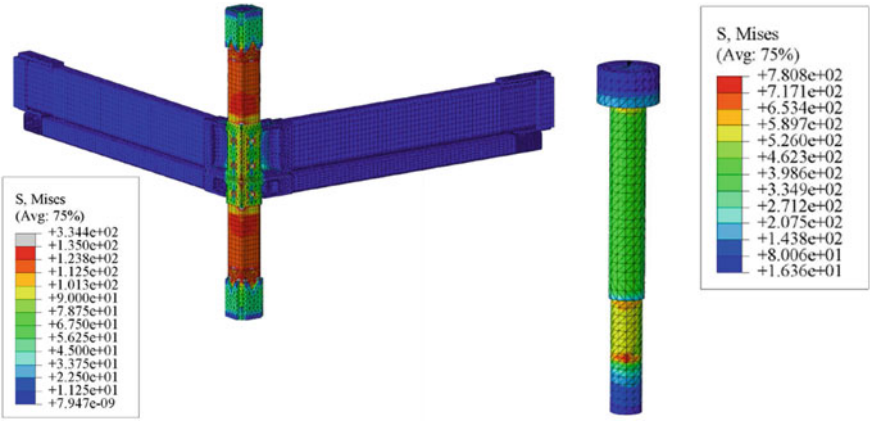

(a) Compression Von Mises Stress (b) Tension Von Mises Stress

Fig. 4 Von Mises Stress Distribution

results. Observing the von Mises stress distribution of the specimen in Fig. 4a, the maximum stress occurred at the columns. At the maximum applied compressive load, the equivalent plastic strain (PEEQ) is zero. This confirms that the specimen under an axial compressive load of 400 kN remains within the elastic limit and if the specimen were loaded to failure, the failure would most probably occur at the columns.

4.2 Axial Tension

The maximum tension load applied to the specimen was 200 kN. The displacement control method was used to gradually apply tension load to the specimen until the maximum design load was reached. The axial load-deformation results of this test are shown in Fig. 5, which also shows the results of the FEA that was conducted on the specimen. Like the compression test results, the behavior of the specimen under the design load was linear. The SHCSs primarily resist the loads under axial tension. Due to the eccentricity of the SHCSs with the center of the applied load, there was a relative rotation between the upper and lower blocs which caused a separation between the blocs on one side and bearing on the other.

Comparing the FEA data with the data collected from the experimental testing, it can be seen that they are in good agreement. Observing the von Mises stress distribution of the SHCS shown in Fig. 4b, it can be seen that the maximum stress occurred at the threaded region of the SHCSs. The PEEQ measure on the SHCSs is zero at the maximum design load of 200 kN, which shows that the SHCSs stayed within the elastic limit. If the load was increased beyond 200 kN until failure, the ultimate failure would likely occur due to the rupture of the SHCSs.

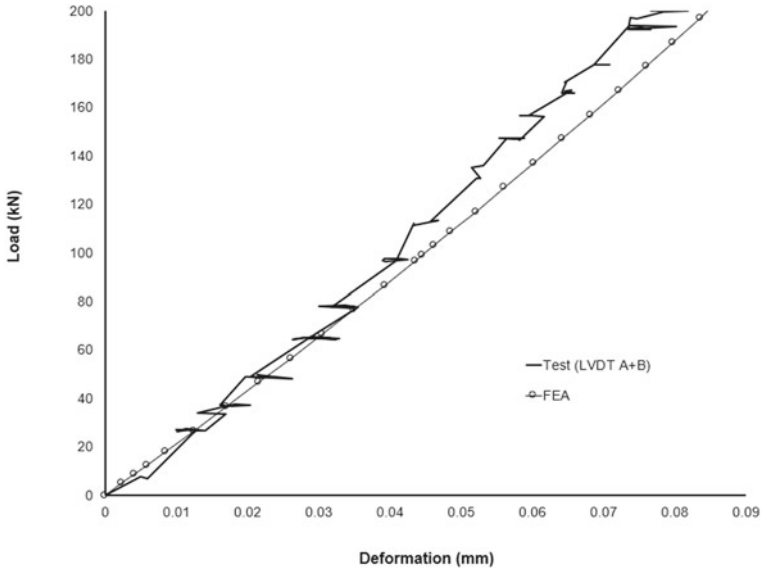

Fig. 5 Axial tension load deformation

Table 1 Bending load summary

Specimen	Applied load			
	Left Plane (kN)	Moment (kNm)	Right plane (kN)	Moment (kNm)
Uniaxial bending	40	50	–	–
Biaxial bending	40	50	40	50

4.3 Bending

Two types of bending tests were conducted, uniaxial bending and biaxial bending. The bending load was applied to the connector by applying a vertical load to the end of one floor beam for the uniaxial test and the ends of both floor beams for the biaxial bending test. The maximum vertical load applied to the ends of the floor beams was 40 kN. A summary of the applied vertical loads and resulting moments can be seen in Table 1. The moment values in this table were calculated using a moment arm of 1.25 m, which is the distance from the location of the applied load to the face of the column.

4.3.1 Uniaxial Bending

As shown in Table 1, the applied bending load to the floor beam end for the uniaxial bending test was 40 kN. The results of the uniaxial bending test are shown in Fig. 6.

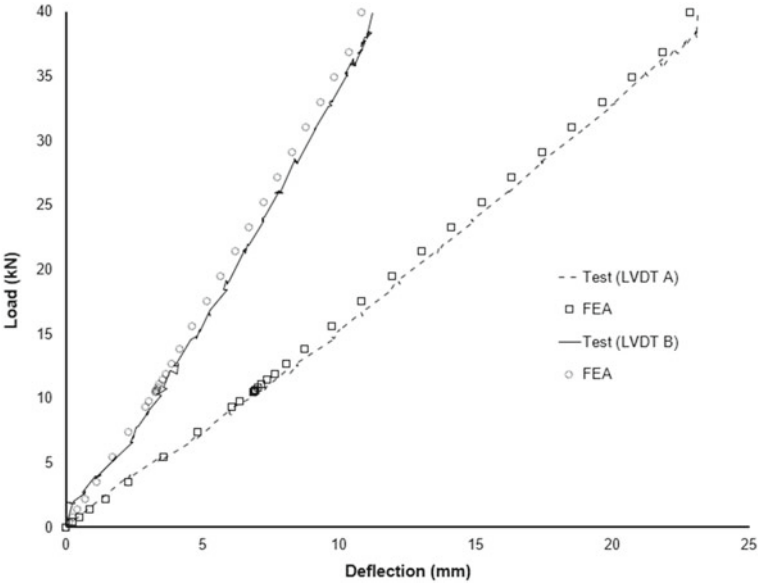

Fig. 6 Uniaxial bending load deformation

which also shows the results of the FEA that was conducted. The applied bending load caused the floor and ceiling beams to flexural defect, causing deformation on the columns. These deformations caused a separation between the upper and lower blocs, but this was resisted by the SHCSs which held them together. The deflections in Fig. 6 are the deflections measured from the LVDTs A and B shown in Fig. 2 (b). From the load-deformation plot, it can be observed that the behavior of the connection is linear under the applied load.

It can be seen from Fig. 6 that the FE analysis results are in good agreement with the results obtained from experimental testing. The von Mises stress distribution of the specimen showed that the columns experienced the maximum stress under the applied design load. The FE analysis also confirmed that the specimen remained well within the elastic limit, which indicates that the connection is safe under the maximum bending design load.

4.3.2 Biaxial Bending

The bending load applied to both floor beams was 40 kN. Both loads were applied at the same time to the two beams. The load-deformation curve of the biaxial bending test can be seen in Fig. 7. The deflections in Fig. 7 are the deflections measured from LVDTs A, B, C, and D, as shown in Fig. 2b. The deflections of the floor beams under the applied loads show that the behavior of the connection under the design bending loads was linear.

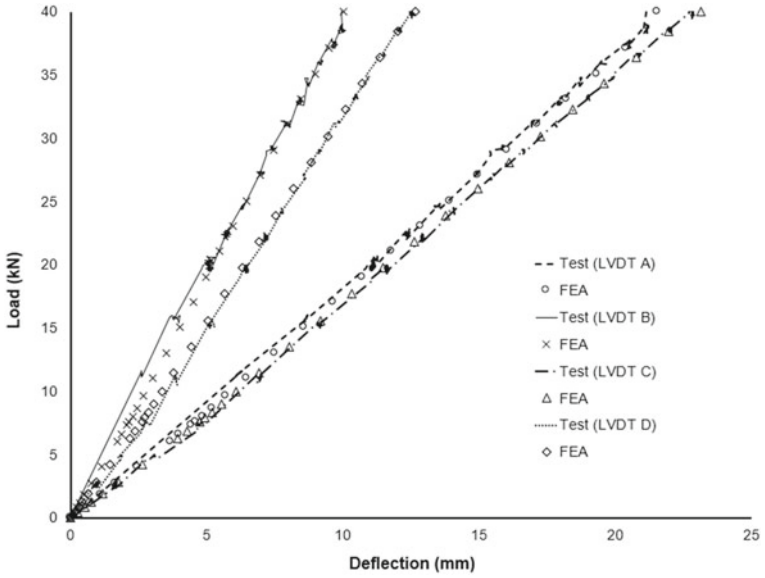

Fig. 7 Biaxial bending load deformation

From Fig. 7, it can be seen that the FEA results are in good agreement with the experimental test results. The von Mises stress distribution of the specimen under the biaxial design loads showed a high concentration of stress in the columns where the column and VectorBloc connector intersect. The FE analysis revealed local plastic deformation in this area. These local stress concentrations and plastic deformation in the columns were not large enough to cause any nonlinearity in the overall global behavior of the specimen under the bending loads, which is in line with what was observed in the experimental tests.

5 Parametric Study

A parametric study was conducted on the specimen using FEA. The parameters considered were the weight of the upper and lower blocs and the location of the SHCSs. The models were tested under axial compression and tension. The results of the parametric study were compared with that of the reference model, which is the model used in the experimental tests in this study. The varied weights of the blocs were calculated based on the percent weight reduction with respect to the reference model. The weight reductions considered were 5%, 10%, 15% and 20%. The locations of the SHCSs varied from that of the reference model by $\pm$ 0.5 inches and are shown along with their respective notations in Fig. 8. In this parametric study, the models were loaded until failure, and the ultimate load is considered to be the

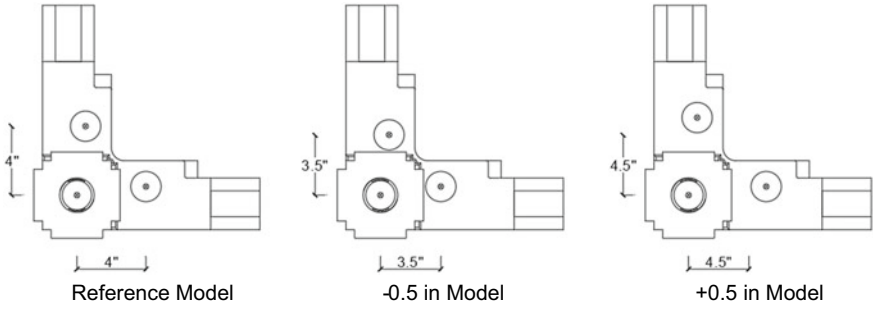

Fig. 8 SHCS locations

maximum load capacity of the model. The yield load is considered to be the load at which the model begins to show plastic strain.

In all of the FE models under axial compression, the plastic strain initially occurred in the columns. The columns underwent axial deformation with increased compressive loading and experienced inelastic bucking after the ultimate load was reached. All the models were also subjected to the maximum compressive design load of 400 kN and remained well within the elastic region at this load.

The yield and ultimate loads of the reference model with varying weights under axial compression are shown in Fig. 9. The specimen had an ultimate compression capacity of approximately 1440 kN. It can be observed that a reduction in the weight reduces the ultimate load capacity of the connection. The reduction in capacity compared to the reference model was calculated to be 2%, 6%, 13%, and 21% for the

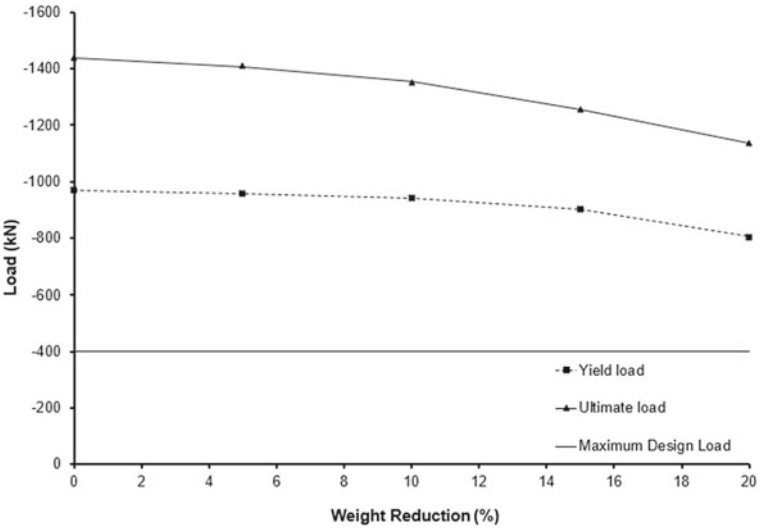

Fig. 9 Ultimate and yield loads under compression

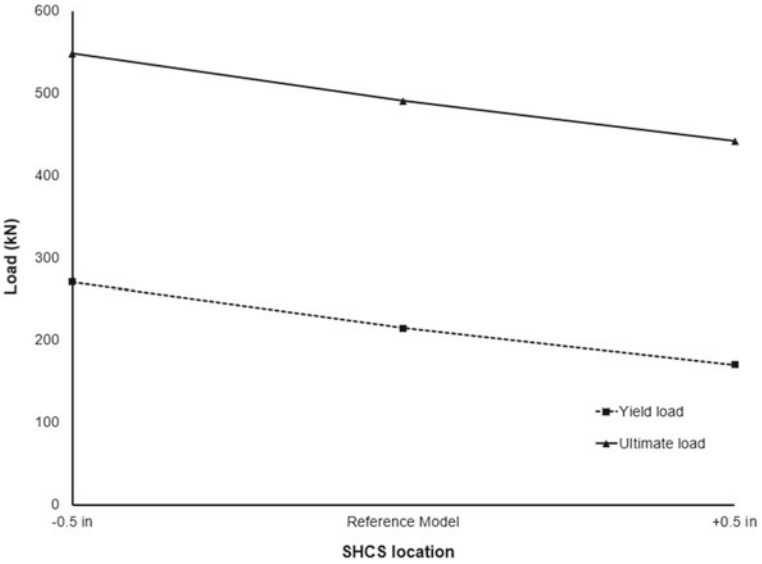

Fig. 10 Ultimate and yield loads under tension

5%, 10%, 15%, and 20% weight reductions, respectively. The reduction in capacity may be acceptable due to the maximum design load of 400 kN being much lower than the yield load, as shown in Fig. 9. Reducing the weight would decrease the cost of the connector and make it lighter. The parametric study showed that the location of the SHCS did not have an effect on the axial compressive behavior of the connection.

The yield and ultimate load capacities of the reference model with varying SHCS locations are shown in Fig. 10. It can be seen from this figure that the locations of the SHCSs affect the capacity of the connection. As the eccentricity of the SHCSs from the column increases, the capacity of the connection decreases. Thus, the highest capacity was seen in the model with 0.5 in eccentricity. The increase in the ultimate load capacity for the −0.5 in SHCS location was calculated to be 25%. It is thus recommended that the SHCSs are moved towards the column to increase the load-carrying capacity of the connection under axial tension. It can also be seen from this figure that the reference specimen has an ultimate tensile capacity of approximately 490 kN.

6 Conclusion

The main objective of this study was to determine the structural performance of the VectorBloc connector under design axial compression, tension, and bending loads. Full-scale experimental testing and finite element analysis were conducted. A

parametric study of the connector was also conducted. The following conclusions were made based on the analysis of the results of these tests.

i. The connection is within the elastic limit under the applied axial compression, axial tension, and uniaxial and biaxial design loads.
ii. The failure of the connection occurs due to plastic deformation of the columns, which are the critical members.
iii. The weight of the connector affects the compression capacity of the connection and the location of the socket head cap screws affect the tension capacity of the connection.
iv. Up to 20% of the weight of the current connector can be reduced while still maintaining its ability to safely carry the design loads.
v. The socket head cap screws can be moved up to 0.5 inches towards the column to increase its tensile capacity by 25%.
vi. The failure loads of the connection are much higher than the maximum design loads.

References

1. Goodier C (2007) Future opportunities for offsite in the UK. Constr Manag Econ 25(6):585–595
2. Lawson RM, Ray GO, Rory Bergin (2012) Application of modular construction in high-rise buildings. J Arch Eng 18(2)
3. SIMULIA (2017) Analysis user's manuals. Providence: Dassault Systemes

Step Through the Noise: Insight into Resilience-Driven Power Asset Management

E. Goforth, W. El-Dakhakhni, and L. Wiebe

1 Introduction

Power infrastructure systems offer critical service to the operation of society. The ability of power systems to return to operation following an outage is crucial to ensure customers do not experience a long power disruption. Over the past few decades, there has been an increasing frequency and severity of outages affecting power infrastructure systems [3]. This has led to an increased focus on the resilience of power systems to such unplanned outages [6]. Resilience is defined as the ability of a system to prepare for, absorb, and recover from external adverse events [5], and can be quantified in terms of resilience goals (i.e., robustness and rapidity) and means (i.e., resourcefulness and redundancy) [7]. The resilience goals are presented in Fig. 1 showing the resilience triangle indicating the loss of operation and outage duration due to an adverse event [7].

In order to improve the response of utilities that own and operate power infrastructure assets, several data-driven methods have been deployed to derive insight into the resilience goal metrics [3]. Data-driven modeling involves collecting, cleaning, processing, and analyzing related datasets and subsequently gaining informative insights [1]. Data-driven models have been developed to handle the ever increasing volume and variety of data being collected by sensors and maintenance reports in power infrastructure systems [8]. Data-driven models, such as machine learning methods, have been shown to identify patterns within large and diverse datasets that would have been previously hidden from standard analysis techniques (e.g., figures and tables) [8]. Specifically, association rule analysis has shown promise in deriving insights into power asset performance in several applications. Bashkari et al. [2] investigated patterns in outage causes for distribution network components using

E. Goforth (✉) · W. El-Dakhakhni · L. Wiebe
McMaster University, Hamilton, Canada
e-mail: goforte@mcmaster.ca

S. Walbridge et al. (eds.), *Proceedings of the Canadian Society of Civil Engineering Annual Conference 2021*, Lecture Notes in Civil Engineering 240,
https://doi.org/10.1007/978-981-19-0507-0_32

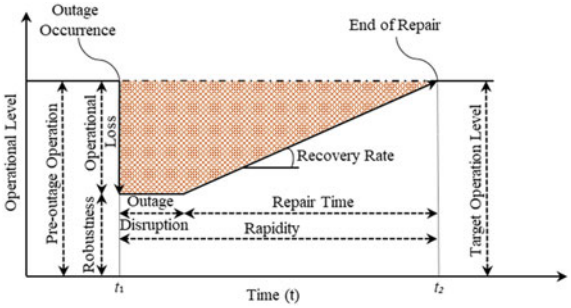

Fig. 1 Resilience concept including metrics robustness and rapidity [7]

association rules and Doostan and Chowdhury [4] used association rules to identify correlated features to fault code occurrences in the distribution network. These studies presented a detailed analysis of outage and fault cause dependent features using association rules, but their studies lacked an application to transmission infrastructure and the connection of resilience to the insights gained from feature association. This study tackles those elements where a transmission line outage dataset is analyzed to find feature associations related to long-duration outage events to identify the key features that affect rapidity.

2 Methodology

All data-driven models require the use of a clean data set (e.g., no missing values) that can be used as a direct input into a machine learning model. This study used a data set that includes transmission line outages from 2005 to 2018. The original data set included outages from 1978 to 2018 but in 2005 additional features were added that describe the primary outage cause and location of each outage event. The dataset from 2005 to 2018 included 16,792 transmission line outage events. Each outage event had input features that described the voltage, primary cause group, primary cause name, subcomponent group, subcomponent name, type of failure, type of fault, structure, conductors per phase, ground wires, circuits per tower, month, day, and hour. The output feature was the duration class. The duration class feature was based on the duration of the corresponding outage and was split based on that duration into one of three different classes (i.e., *short* (1–5 min), *moderate* (5–240 min), and *long* (greater than 240 min)). The long-duration outage class is the output feature for this study, to provide feature associations to characterize the resilience metric of rapidity.

Utilities would benefit from knowing which combinations of features commonly lead to long-duration outage events in order to assign appropriate repair crews. The goal would be to improve the rapidity of a utility to unplanned outage events. This study uses association rule analysis to evaluate feature associations. Association rule analysis is a machine learning method that generates frequent feature sets from data in the form of $X \rightarrow Y$ where X is a set of input features and Y is a set of output

feature(s) [1]. Metrics used to evaluate the importance and significance of a generated association rule are support, confidence, and lift, as shown in Eqs. (1–3) respectively.

$$Support(X \rightarrow Y) = P(X \cap Y) \tag{1}$$

$$Confidence(X \rightarrow Y) = \frac{P(X \cap Y)}{P(X)} \tag{2}$$

$$Lift(X \rightarrow Y) = \frac{P(X \cap Y)}{P(X)P(Y)} \tag{3}$$

Support is a metric of feature set frequency among all occurrences in the data set. Confidence is a metric of output feature likelihood given that the input features are in the feature set. Lift is a metric that compares the frequency of a feature set occurrence with the occurrence of input and output features. The lift metric indicates the likelihood that a generated rule is not a coincidental occurrence. The metrics from Eqs. 1–3 were calculated for each generated association rule.

3 Results

All the association rules for long-duration outages are shown in Fig. 2. The confidence metric is shown by the colour of the point on the figure. Confidence is directly correlated to the lift of each rule. This corresponds to Eq. 3 where lift is calculated using the base from Eq. 2 accounting for the likelihood of the output feature occurrence. In this study, the output feature was specified, therefore the correlation between confidence and lift is expected. Figure 2 shows the number of rules decreases with increasing lift value and as the lift increases, the support for each rule decreases. This indicates that there are few important rules (i.e., rules with high lift values) that occur among the reviewed transactions, but when these rules do occur, there can be high confidence in their association to long-duration outages. Also of note are rules that fall along the Pareto front in Fig. 2. These rules indicate associations that occur more frequently among the transactions (i.e., high support) and because the lift is still greater than 1, they are important to take note of to indicate long-duration outage events.

The top five association rules by lift are shown in Table 1. These rules allow an asset manager to see the key input features that lead to long-duration outages and plan accordingly. Among the association rules shown in Table 1, common input features (i.e., features that occur three or more times in Table 1) include subcomponent group = 1 (i.e., outage occurred in the integral subcomponent), equipment failure as the primary cause name, and two ground wires on the transmission line asset. The long-duration outage events are closely associated with equipment failures, specifically to the structure of the transmission line. An asset manager can use this information to inform their decision-making regarding allocation of resources towards repair and

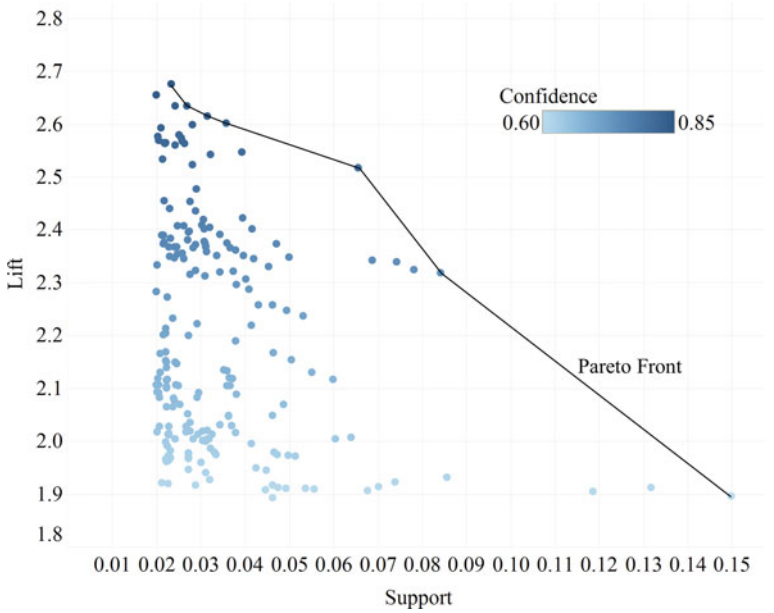

Fig. 2 Long-duration outage association rules

Table 1 Top five association rules by lift to determine long-duration outages

LHS	RHS	Support (%)	Confidence (%)	Lift
{Primary cause name = Equipment failure, subcomponent group = Integral, Conductors/phase = 1, Ground wires = 2}	{>240 min}	2.3	84.8	2.67
{Primary cause group = Defective equipment, Subcomponent name = Structure, Failure type = Normal operation}	{>240 min}	2.0	84.2	2.65
{Primary cause name = Equipment failure, Subcomponent group = Integral, Ground wires = 2}	{>240 min}	2.6	83.5	2.63
{Primary cause group = Defective equipment, Subcomponent group = Integral, Conductors/phase = 1, Ground wires = 2}	{>240 min}	2.4	83.5	2.63
{Primary cause name = Equipment failure, Subcomponent name = Structure}	{>240 min}	3.1	82.9	2.61

maintenance of these assets. This knowledge and insight would improve the future performance of a utility to long-duration outage events therefore improving their rapidity to unplanned outage events.

4 Conclusion

This study developed association rules to find sets of input features that led to long-duration outage events. These association rules would allow asset managers to review the important features commonly leading to long duration outage events. The association rules were generated based on a transmission line outage data set from 2005–2018. The study revealed that equipment failures, specifically in the transmission line structure, were important features of long-duration outages. An asset manager could take this information and deploy additional resources in maintenance and repair to minimize these long-duration outage events, therefore improving the rapidity of the utility to unplanned outages. Future work would include prediction of outage duration based on similar input features to attempt to classify outages to proactively manage long-duration outage events.

Acknowledgements The data for this study was provided by the Canadian Electricity Association (CEA). Financial support was provided through the CaNRisk—Collaborative Research and Training Experience (CREATE) program of the Natural Science and Engineering Research Council (NSERC). The support of the INTERFACE Institute and the INViSiONLab is also acknowledged in the development of this study.

References

1. Aggarwal CC (2015) Data mining: the textbook. Springer, New York, USA
2. Bashkari MS, Sami A, Rastegar M (2021) Outage cause detection in power distribution systems based on data mining. IEEE Trans Industr Inf 17(1):640–649
3. Bhusal N, Abdelmalak M, Kamruzzaman M, Benidris M (2020) Power system resilience: Current practices, challenges, and future directions. IEEE Access 8:18064–18086
4. Doostan M, Chowdhury BH (2017) Power distribution system fault cause analysis by using association rule mining. Electr Power Syst Res, Elsevier BV., 152: 140–147
5. Panteli M, Mancarella P (2015) The grid: stronger, bigger, smarter? IEEE Power Energy Mag, IEEE, 13(May/June): 58–66
6. Preston BL, Backhaus SN, Ewers M, Phillips JA, Dagle JE, Tarditi AG, Looney J (Pat), King TJJ (2016) Resilience of the U.S. electricity system: a multi-hazard perspective. Springfield, VA
7. Salem S, Siam A, El-Dakhakhni W, Tait M (2020) Probablistic resilience-guided infrastructure risk management. J Manag Eng 36(6):1–15
8. Zhou K, Fu C, Yang S (2016) Big data driven smart energy management: from big data to big insights. Renew Sustain Energy Rev Elsevier 56:215–225

Shell Analysis of Steel Frames Considering Low-Cycle Fatigue Within the Continuum-Damage-Plasticity Framework

S. Delir, E. Erkmen, and L. Tirca

1 Introduction

Low-cycle fatigue failure under cyclic loading is one of the common causes of failure in structures. Cyclic loading causes crack initiation and propagation in steel material which then cause changes in structural stiffness and load carrying capacity. Among different modelling strategies that can capture fatigue effect in the material behaviour, the Continuum Damage Plasticity (CDP) framework is one of the widely used approaches especially for multi-axial loading situations [1, 9–13]. Using CDP, Murakami et al. [15] studied the loss of ductility due to low-cycle fatigue damage. They have related the effect of small cracks that are present in the material with the loss of ductility and limited life due to fatigue. Their experiments showed the correlation of crack length present in the surface and the fatigue life. They also showed that by removing surface cracks, ductility and fatigue life could be extended. Zhan et al. [19] used Continuum Damage Mechanics-based approach to predict the fatigue life of aluminum alloy. In their study, Lemaitre's plasticity damage model (1994) was used to evaluate the damage accumulation and accordingly the fatigue life of aluminum alloy that has undergone foreign object impact. Springer and Pettermann [18] developed a multi-axial damage model to predict fatigue life under low-cycle loading. Martinez et al. [12] presented an evolution law for the hardening parameter. One dimensional beam-type element are frequently used for structural analysis purposes in which uniaxial material models are often adopted. Bosco and Tirca [3] used fibre-based uniaxial damage accumulation modelling to simulate the damage evolution in I-shaped steel beams. Their model is based on Miner's Law to predict

S. Delir · E. Erkmen (✉) · L. Tirca
Concordia University, Montreal, Quebec, Canada
e-mail: Emre.erkmen@concordia.ca

S. Walbridge et al. (eds.), *Proceedings of the Canadian Society of Civil Engineering Annual Conference 2021*, Lecture Notes in Civil Engineering 240,
https://doi.org/10.1007/978-981-19-0507-0_33

fatigue damage due to cyclic loading and had good agreement with related experiment results. However, to capture local buckling effects on thin-walled steel sections shell element modelling is required e.g., Fafard et al. [7].

In this study we employ a shell element formulation by combining the 4 Node–3 DOF per node quadrilateral plate element of Batoz and Tahar [2] and the quadrilateral 4-Node membrane element with drilling DOF of Ibrahimbegovic et al. [9]. Second-order geometrical nonlinearities are considered in the strain-deflection relations by adopting Green–Lagrange strains. When shell elements are used, multi-axial material models are needed and for this purpose Continuum Damage Plasticity (CDP) framework is used to build an inelastic multi-axial stress–strain relationship. We employ the multi-axial Continuum Damage Plasticity (CDP) framework introduced by [1]. The damage evolution law for fatigue effects was adopted from [18]. The yield surface of von Misses and the associated flow rule were adopted for the evolution of plastic deformations. We have included the isotropic softening of the yield surface due to fatigue according to Martinez et al. [12].

2 Continuum Damage Plasticity

Following [1], the coupled damage and plasticity constitutive equations can be built on 3 basic hypotheses: additive decomposition of the total strain field, the strain energy and finally the plasticity and damage initiation criteria.

- The additive decomposition implies that the total deformation can be decomposed into elastic part $\boldsymbol{\varepsilon}_e$, plastic part $\boldsymbol{\varepsilon}_p$ and damage part $\boldsymbol{\varepsilon}_d$ as

$$\boldsymbol{\varepsilon} = \boldsymbol{\varepsilon}_e + \boldsymbol{\varepsilon}_p + \boldsymbol{\varepsilon}_d. \tag{1}$$

- The strain energy stored during deformation can be written as the sum of elastic and damage strain energies plus the energies due to hardening effects of plastic and damage parts as:

$$\Psi\left(\boldsymbol{\varepsilon}, \boldsymbol{\varepsilon}_p, \kappa_p, \phi, \boldsymbol{\varepsilon}_d, \right) = \Psi^e(\boldsymbol{\varepsilon}_e) + \Psi^d(\boldsymbol{\varepsilon}_d, \phi) + \Xi^p(\kappa_p) + \Xi^d(\kappa_d) \tag{2}$$

  where hardening effects can be accounted with the hardening potentials for the plastic behaviour $\Xi^p(\kappa_p)$ and damage behaviour $\Xi^d(\kappa_d)$, which are functions of hardening variables κ_p and κ_d for plasticity and damage, respectively. The $\Psi^e(\boldsymbol{\varepsilon}_e)$ parameter is the elastic strain energy and the $\Psi^d(\boldsymbol{\varepsilon}_d, \phi)$ is the damage strain energy. The damage parameter ϕ can be written in terms of the reduction factor as $\phi = \varphi/(1-\varphi)$, where $\varphi \in [0, 1]$ is a measure of reduction in the load carrying area.
- The elastic domain can be specified as the domain in stress space where no change of internal variables, i.e. $\boldsymbol{\varepsilon}_p, \kappa_p, \phi, \boldsymbol{\varepsilon}_d, \kappa_d$, takes place. The boundaries

of the domain is determined by the plastic failure criterion and the damage failure criterion with:

$$\Phi^p\left(\boldsymbol{\sigma}, \kappa_p\right) \leq 0 \text{and} \Phi^d(\boldsymbol{\sigma}, \kappa_d) \leq 0 \tag{3}$$

The plastic and damage failure criteria are generally independent from each other. However, an a-priori assumed partitioning of the strain tensor in the form of $\mathrm{d}\boldsymbol{\varepsilon}_d = \varphi \mathrm{d}\boldsymbol{\varepsilon}$, simplifies the selection of the failure surfaces as it permits the use of single failure criterion, i.e., $\Phi^p\left(\boldsymbol{\sigma}, \kappa_p\right) = \Phi^d(\boldsymbol{\sigma}, \kappa_d)$ and $\mathrm{d}\kappa_d = \phi \mathrm{d}\kappa_p$ Therefore, the coupled elastoplastic-damage model can be easily calibrated to fit to the observed behaviour. The proposed approach also simplifies the numerical procedure, details of which can be found in Sarikaya and Erkmen [16].

2.1 Effect of Fatigue on the Stiffness

Change in material properties due to fatigue can be introduced as an evolution equation for the damage parameter. Following Springer and Pettermann [18], we update damage parameter ϕ in a cycle that produces plastic deformations. The plastic work in a closed cycle can be written as provided in:

$$\Delta w = \int_{1cycle} \sigma \varepsilon^p \mathrm{d}\varepsilon^p \tag{4}$$

As the plastic strains are only deviatoric in associated von Misses plasticity, a volumetric term is also introduced additional into the energy term in each cycle as per.

$$\Delta w_m = \Delta w + \alpha \sigma_h^{max} \tag{5}$$

Herein, x is a material parameter and σ_h^{max} is the maximum hydrostatic pressure that occurs during a cycle. Accordingly, the evolution of the damage parameter can be written as in:

$$\varphi = \int \frac{x_1}{l} (\Delta w_m)^{x_2} \mathrm{d}N \tag{6}$$

where x_1, x_2 are material properties, l is the characteristic element length and $\mathrm{d}N$ is a measure of cycle increment.

2.2 Hardening

Fatigue not only reduces the stiffness of the material it also reduces the maximum load carrying capacity. In order to consider that effect, fatigue should cause an isotropic strain softening effect on the yield surface. The functions used for hardening/softening effects due to fatigue are adopted from Martinez et al. [12]:

$$K = K_0 + H_s \sqrt{1 - \left(\frac{\kappa_p - \kappa_{pt} + 1}{\left(1 + \kappa_{pt}\right)^2} \right)} if \kappa_p < \kappa_{pt} \tag{7}$$

$$K = K_0 + H_s + H_{ss} \sqrt{1 - \left(\frac{\kappa_p - \kappa_{pt}}{\left(1 + \kappa_{pt}\right)^2} \right)} if \kappa_p \geq \kappa_{pt} \tag{8}$$

where K_0, H_s, and H_{ss}, are material related hardening parameters. The parameter κ_p is the total plastic work and κ_{pt} is a plastic work-related threshold which separates the hardening and softening stage of material. Thus, the hardening potential can be expressed as $\Xi^p(\kappa_p) = 0.5K{\kappa_p}^2$. The parameters $\alpha, x_1, x_2, l, K_0, H_s, H_{ss}, \kappa_{pt}$ should be calibrated from material and structural tests.

3 Finite Element Modelling of Thin-Walled Beams and Frames

The shell element is a combination of a membrane element with drilling degree of freedom and Discrete Kirchhoff Quadrilateral (DKQ) plate element. The strains in the shell element formulation can be decomposed into three parts which are strains due to plate bending ε_b, membrane deformations ε_m, and second order terms in Green–Lagrange strains considering both membrane and plate bending actions ε_N, i.e.

$$\varepsilon = \varepsilon_b + \varepsilon_m + \varepsilon_N \tag{9}$$

$$\varepsilon_b = -z \left\{ \frac{\partial \hat{\theta}_x}{\partial x}, \frac{\partial \hat{\theta}_y}{\partial y}, \frac{\partial \hat{\theta}_x}{\partial y} + \frac{\partial \hat{\theta}_y}{\partial x} \right\} \tag{10}$$

$$\varepsilon_m = \left\{ \frac{\partial \hat{u}_0}{\partial x}, \frac{\partial \hat{v}_0}{\partial y}, \frac{\partial \hat{u}_0}{\partial y} + \frac{\partial \hat{v}_0}{\partial x} \right\} \tag{11}$$

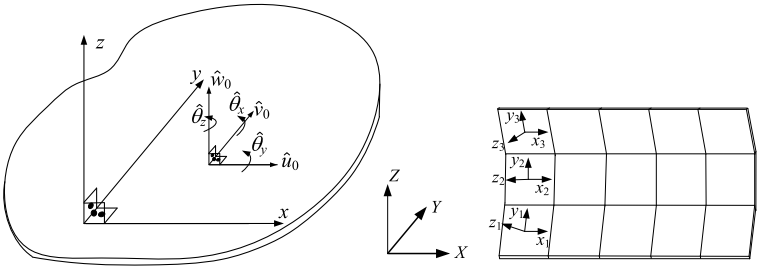

a) Local deflections of the shell element (b) Global vs. local coordinate system

Fig. 1 Deflections and coordinate systems for the shell element formulation. **a** Local deflections of the shell element **b** Global versus local coordinate system

$$\varepsilon_N = \left\{ \frac{1}{2}\left(\frac{\partial \hat{w}_0}{\partial x}\right)^2 + \frac{1}{2}\left(\frac{\partial \hat{v}_0}{\partial x}\right)^2, \frac{1}{2}\left(\frac{\partial \hat{w}_0}{\partial y}\right)^2 + \frac{1}{2}\left(\frac{\partial \hat{u}_0}{\partial y}\right)^2, \frac{\partial \hat{w}_0}{\partial x}\frac{\partial \hat{w}_0}{\partial y} \right\} \tag{12}$$

in which $\hat{u}_0$ and $\hat{v}_0$ are deflections in the mid-surface of local x–y plane, respectively and $\hat{w}_0$ is the out of plane deflection in the local z-direction, as shown in Fig. 1. The bending rotations $\hat{\theta}_x$ and $\hat{\theta}_y$ are defined within local x–z and y–z planes, and the drilling rotation $\hat{\theta}_z$ is around z-direction.

The displacements are interpolated according to the shape functions of Batoz and Tahar [2] and Ibrahimbegovic et al. [9], accordingly, the virtual work can be written in algebraic form and the equilibrium equation obtained can be solved iteratively. Details of the shell element formulation and its implementation for nonlinear analysis can be found in Erkmen [5]. Closest-Point Projection algorithm was used for the stress update considering inelastic deformations. Details of the stress update can be found in Erkmen and Saleh [6].

4 Model Validation

The I-shaped cantilever beam which was introduced by Engelhardt et al. [4] was chosen in Bosco and Tirca [3] as a case for validation. Herein, the obtained results are compared with that found by Bosco and Tirca [3]. The type of analysis performed in this case is under quasi-static cyclic loading. The information for the material and the structural properties are provided in Table 1 and the system setup and boundary conditions are presented in Fig. 2 (Figs. 3 and 4).

Table 1 Mechanical properties of the specimen 7A as per Engelhardt et al. [4]

Specimen number	Cross-section	F_y Flange (MPa)	F_y Web (MPa)	Elasticity modulus (MPa)	Lv (mm)
7A	W36 × 150	301.3	362.3	2.1×10^5	2985

The model considered without fatigue effect and the hardening function values are $K_0 = 100MPa$, $H_s = 200MPa$, with $\kappa_{pt} = 0.1MPa$. (We do not use the second part isotropic hardening $H_{ss} = 0$)

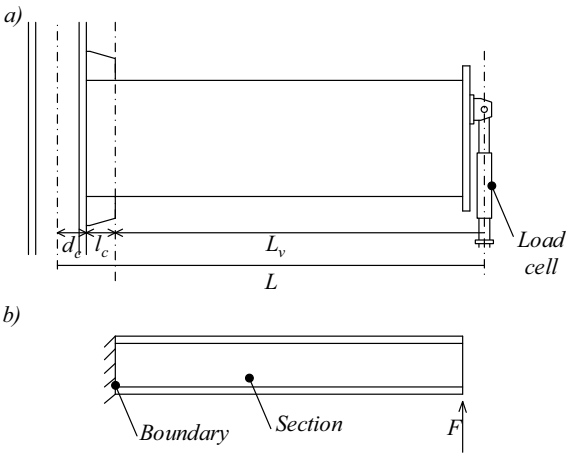

Fig. 2 Cantilever beam **a** Experimental test setup [3] **b** modelling of I-shaped specimen in the setup

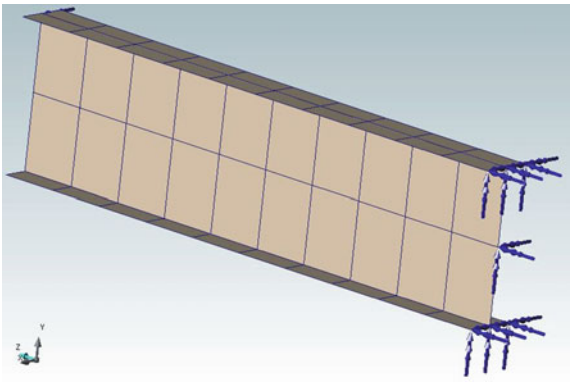

Fig. 3 Finite element modelling of the cantilever beam using 60 shell elements

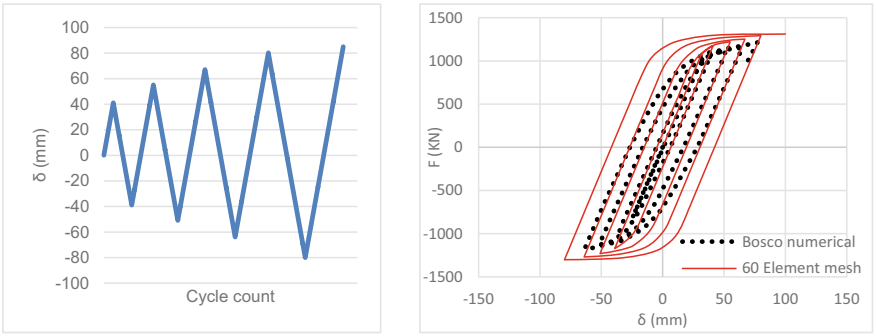

Fig. 4 **a** The quasi-static cyclic displacement loading protocol **b** Hysteresis loops from nonlinear analysis using beam theory in shell element without stiffness degradation against the results obtained by Bosco and Tirca [3]

5 Case Studies

5.1 Details of the Analysed Frame

For the purpose of investigating fatigue effects on the load deflection relations, a single story one bay moment frame is modelled using the proposed material model and the shell element. Sections for columns and beam are W14 × 176 (W360 × 162) and W21 × 44 (W530 × 66) respectively and dimensions are presented in Table 2. The schematic view and dimensions of the frame is also provided in Fig. 5. The shell modelling of each section consists of 6 elements in transversal and 20 elements in longitudinal directions. To capture the effects of fatigue damage, the parameters introduced in Eq. 6 are taken as $\alpha = 0.006$, $l = 300mm$ and x_1, x_2 are considered as 3.75 mm/cycle (MPa), 0.45 and 0.45, respectively. The hardening parameters presented in Eq. 7 and Eq. 8 are taken as $K_0 = 100MPa$, $H_s = 200MPa$, $H_{ss} = 0.09MPa$, MPa with $\kappa_{pt} = 10.0MPa$. For the steel material, the yield stress limit was taken as $Fy = 317.1MPa$.

Table 2 Dimensions and characteristics of beam and columns sections

Element	Area mm^2	Ix 10^3 mm^3	Zx 10^3 mm^3	Iy 10^3 mm^3	Zy 10^3 mm^3	d mm	b mm	tf mm	tw mm
W530 × 66	8390	351	1560	8.57	166	525	165	11.4	8.9
W360 × 162	20,600	515	3140	186	1520	364	371	21.8	13.3

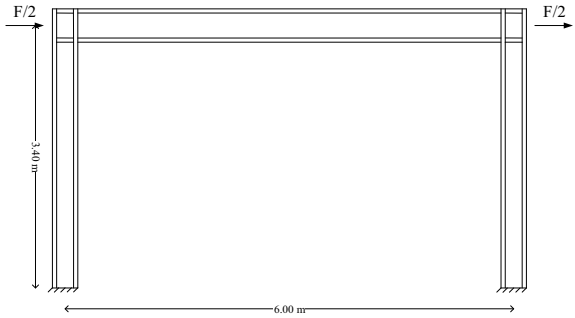

Fig. 5 The geometry of investigated one–storey moment frame

5.2 Pushover Analysis

Three case studies are considered under different kinematic assumptions. In the first case, constraint conditions are imposed to prevent local, as well as, lateral-torsional buckling behaviour, which is called as Case 1. The kinematic behaviour in Case 1, is similar to conventional beam element-based models. To impose such beam element behaviour, we have used Multiple-Point Constraints (MPC) and lateral supports on the shell model. In Case 2, we have prevented local buckling only by using MPCs but allowed lateral-torsional buckling behaviour and Case 3 is completely free to locally buckle or move laterally. As initial imperfections, the mode shapes based on the first elastic mode were introduced (e.g. [17]). The first buckling mode shapes are shown in Fig. 6.

A displacement control pushover analysis is performed, and the results are presented in Fig. 7. As it is shown in Fig. 7, different restrictions on the same system can lead to different responses. In this example, the results based on Case 3 is more conservative than the other results which is due to the fact that plasticity occurs in an earlier stage compared to other cases with restrictions.

5.3 Cyclic Pushover Analysis

Because the fatigue effects appear only under cyclic loading, a cyclic pushover analysis is performed to compare the response under different kinematic assumptions. Again, three cases are used; Case 1 is prevented against local and lateral-torsional buckling using MPCs and lateral supports; Case 2 is prevented against local buckling using MPCs but allowed to deform laterally; and Case 3 is completely free to locally buckle or move laterally. Again, as initial imperfections the first buckling mode shapes were imposed in each case. The cyclic loading protocol is presented in Fig. 8. From Fig. 9, by comparing the responses in each kinematic case, it can be seen

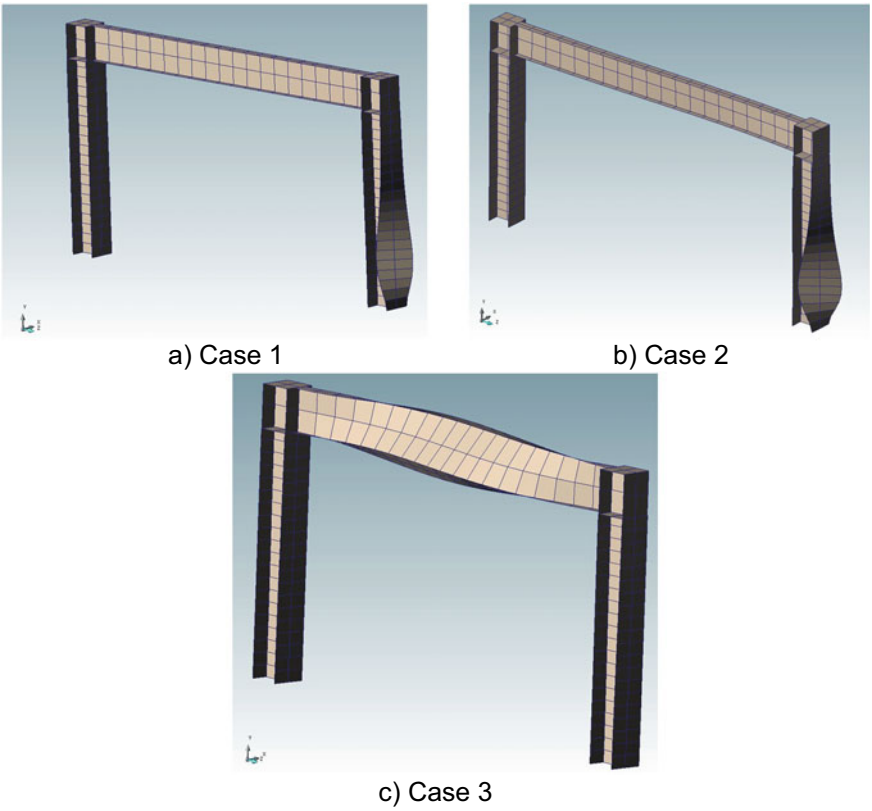

Fig. 6 Buckled shapes based on the first mode

Fig. 7 Pushover analysis results

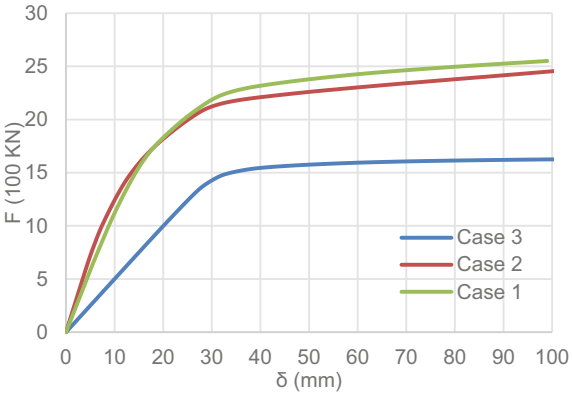

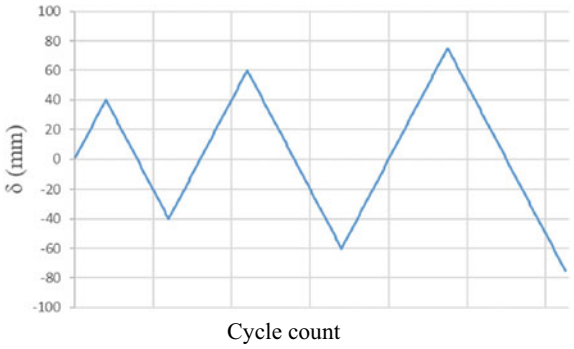

Fig. 8 Loading protocol for quasi-static cyclic pushover analysis

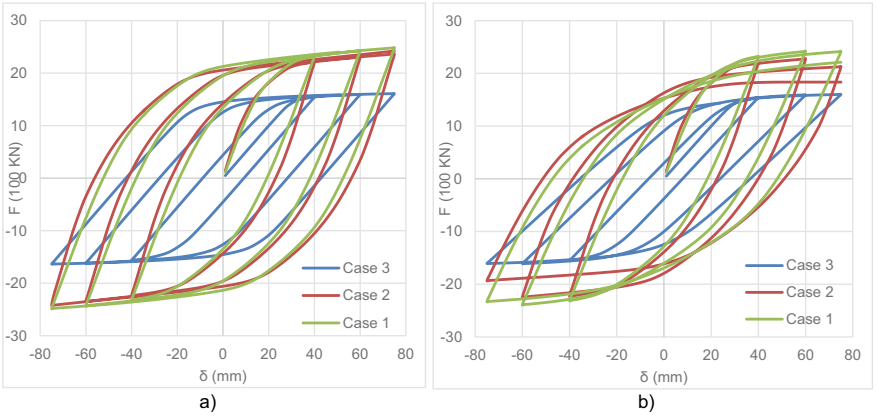

Fig. 9 Hysteresis loops **a** for the cases without fatigue, **b** for the cases with fatigue

that the load carrying capacity reduces in each cycle when fatigue effects are considered. Figure 9 also shows that the stiffness also reduces in each cycle. Comparison of each individual case with and without fatigue effects is also presented in Fig. 10.

6 Conclusions

This paper mainly focused on validation and applicability of a 3D elasto-plastic damage model for the analysis of steel frames under cyclic loads. It was shown that the developed analysis tool based on the Continuum Damage Plasticity framework can capture the low-cycle fatigue effects in the constitutive behaviour of the steel material. The parameters of the steel constitutive model were introduced in detail. Early yielding and stiffness degradation of the material due to low-cycle fatigue

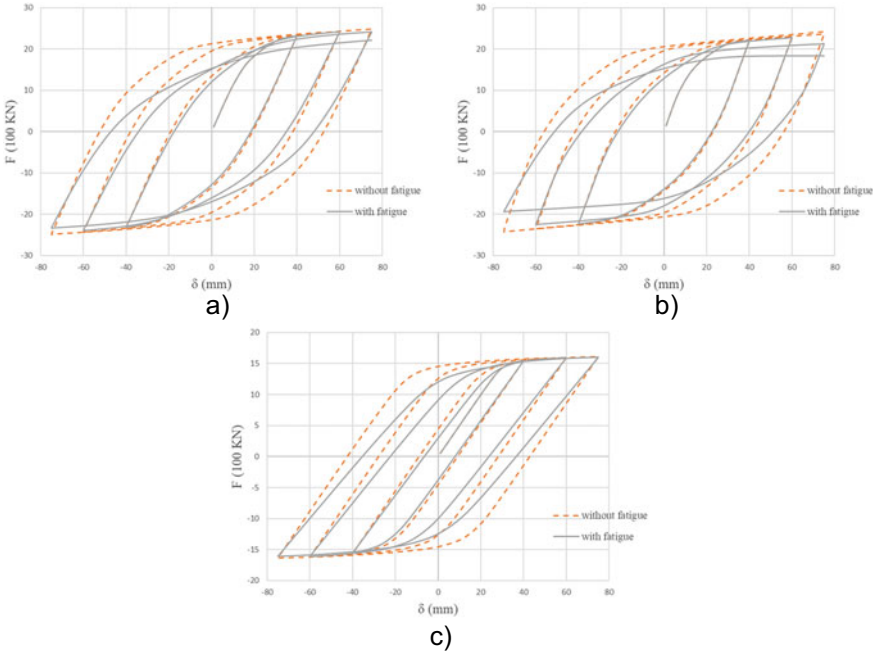

Fig. 10 Hysteresis loops resulted with and without fatigue subjected to quasi-static cyclic loading using cyclic-pushover analysis **a** Case 1 **b** Case 2 **c** Case 3

effects were captured by adopting a suitable hardening/softening and damage accumulation criteria from literature specific to the low-cycle fatigue behaviour of metals. As the material model is multi-axial, it is particularly suitable for the shell-type analysis of steel frames. By using Multiple-Point-Constraints some of the possible buckling modes were avoided and it was shown that when the model is not capable of capturing the kinematic behaviour properly, significant over-estimation of the capacity may occur in the predicted behaviour of steel frames. Such sophisticated modelling approaches might be required especially when local buckling of steel frame components and connections is a major concern due to reduction of stiffness and load carrying capacity under cyclic loads.

References

1. Armero F, Oller S (2000) A general framework for continuum damage models. I. Infiniterimal plastic damage models in stress space. Int J Solids Struct 37:7409–7436
2. Batoz JLT (1982) Evaluation of a new quadrilateral thin plate-bending element. Int J Num Methods Eng 18:1655–1677
3. Bosco M, Tirca L (2017) Numerical simulation of steel I-shaped beams using a fiber-based damage accumulation model. J Constr Steel Res 133:241–255

4. Engelhardt MD, Sabol TA (1994) Testing of welded steel moment connections in response to the Northridge Earthquake, Progress Report to the AISC Advisory Subcommittee on Special Moment Resisting Frame Research
5. Erkmen RE (2013) Bridging multi-scale approach to consider the effects of local deformations in the analysis of thin-walled members. Comput Mech 52:65–79
6. Erkmen RE, Saleh A (2017) Iterative global-local approach to consider the effects of local elasto-plastic deformations in the analysis of thin-walled members. Int J Multiscale Comput Eng 15:143–173
7. Fafard M, Beauliu D, Dhatt G (1987) Buckling of thin-walled members by finite elements. Comput Struct 25(2):183–190
8. Ibrahimbegovic A, Jehel P, Devanne L (2008) Coupled damage-plasticity constitutive model and direct stress interpolation. Journal of Computational Mechanics 42:1–11
9. Ibrahimbegovic A, Taylor RL, Wilson EL (1990) A robust quadrilateral membrane finite element with drilling degrees of freedom. Int J Num Methods Eng 30:445–457
10. Inglessis P (1999) Model of damage for steel frame members. Journal of Engineering Structures 21:954–964
11. Krajcinovic D (1996) Damage mechanics. North-Holland Series
12. Martinez X, Oller S, Barbu LG, Barbat AH, du Jesus AMP (2015) Analysis of ultra-low cycle fatigue problems with the Barcelona plastic damage model and a new isotropic hardening law. Int J Fatigue 73:132–142
13. McClintock FA (1968) A criterion for ductile fracture by the growth of holes. J Appl Mech 35:363–371
14. Miner MA (1954) Cumulative Damage in Fatigue. Transactions ASME – Journal of Applied Mechanics, 12 A159.
15. Murakami S (2012) Continuum damage mechanics: a continuum mechanics approach to the analysis of damage and fracture. Springer. https://doi.org/10.1007/978-94-007-2666-6
16. Sarikaya A, Erkmen RE (2019) A plastic-damage model for concrete under compression. Int J Mech Sci 150:584–593
17. Shayan S, Rasmussen K, Zhang H (2014) On the modelling of initial geometric imperfections of steel frames in advanced analysis. J Constr Steel Res 98:167–177
18. Springer M, Pettermann HE (2018) Fatigue life predictions of metal structures based on low-cycle, multi-axial fatigue damage model. Int J Fatigue 116:355–365. https://doi.org/10.1016/j.ijfatigue.2018.06.031
19. Zhan Z, Hu W, Meng Q, Shi S (2016) Continuum damage mechanics-based approach to fatigue life prediction for 7050-T7451 aluminum alloy with impact pit. Int J Damage Mech 25(7):943–966

Basis of Sustainable Infrastructure Project Decisions

V. Ferrer, P. Pradhananga, and M. ElZomor

1 Introduction and Background

Sustainability is an important worldwide concern; addressing climate change and global warming is becoming an emerging necessity in the construction industry, which introduces a new challenge not only in the design of projects but also in the construction and operation phases. Low awareness of a project's societal and environmental impacts and a lack of standardized procedures to quantify these impacts are often roadblocks to achieving sustainability [25]. Infrastructure projects play a critical role in the built environment, but these projects also tend to reduce the ability of the natural environment (i.e., pervious soils), its habitats, and species to adapt to climate change [1]. Despite such an impact of infrastructure projects, sustainable materials that have lower cost and environmental implication are seldom integrated during the construction of infrastructures [20]. To ensure sustainable development and mitigate environmental damage, it is critical to adopt sustainable design elements early in the design phase such that it meets people's need as well as improves the resilience of infrastructures [25]. Sustainable design aims to improve the built environment's performance through a suite of economic, social, and environmental aspects, or as it is usually called: "The Triple Bottom Line (TBL)". It is known that most of the

V. Ferrer
Construction Management, Florida International University (FIU), Miami, USA
e-mail: vferrerr@fiu.edu

P. Pradhananga
Department of Civil and Environmental Engineering, Florida International University (FIU), Miami, USA

M. ElZomor (✉)
Department of Construction Management, Moss School of Construction Infrastructure and Sustainability, College of Engineering and Computing, Florida International University, Miami, USA
e-mail: melzomor@fiu.edu

S. Walbridge et al. (eds.), *Proceedings of the Canadian Society of Civil Engineering Annual Conference 2021*, Lecture Notes in Civil Engineering 240,
https://doi.org/10.1007/978-981-19-0507-0_34

natural resources are finite and community development has consequences that affect the TBL, thus the construction of infrastructures should not only be robust, but it must also be sustainable [15]. The construction industry has spotlighted green buildings as an approach to creating a more sustainable built environment. However, infrastructure projects have typically been left out of sustainable construction efforts, which maybe because of the many challenges that stakeholders must encounter resulting in increased difficulty assessing sustainability.

Infrastructure projects play a critical role in the built environment; they provide the basis for personal security and public health, influence the economic growth and competitiveness of communities, provide drinking water and handle waste, and, most importantly, allow building and industrial projects to connect with all main utilities. In comparison to building projects (vertical construction), infrastructure projects are "horizontal" and act as vectors that connect residential and industrial nodes as well as provide services and goods within the built environment. According to ISI [15], massive investments in infrastructure are now needed due to decades of negligence and outdated infrastructure around the world. The American Society of Civil Engineers (ASCE) rates the U.S. infrastructure every 4 years; in 2017 ASCE reported a score of D + for infrastructure, confirming that the U.S infrastructure systems are declining as a result of negligence, overuse, insignificant investment, and poor construction [2]. Furthermore, proper planning for infrastructure projects, or better-called infrastructure management (IM), is often not met due to the complexity of such projects, thus causing schedule overruns and failure to meet the forecasted budgets. Research shows that, despite the usual practices, the best way to deliver a project is focusing on the Front-End Planning (FEP) phase, prior to authorizing its funding and subsequent construction [7, 7]. Infrastructure projects may present unique planning and sustainability challenges (i.e. right-of-way (ROW) acquisitions or adjustments, underground, more interface with the public and the environment). Thus, there is an existing need for infrastructure projects with improved project performance and low environmental and social impacts. Incorporating traditional planning is vital to address the additional efforts during the planning, design, construction, and operation phases of sustainable projects, yet FEP remains paramount.

Front-End Planning is a critical process that establishes a suitable scope definition and a structured approach for a project while uncovering any project's unknowns and risks [3]. FEP comprises all the tasks between project commencement and the initiation of the detailed design [25]. The FEP of a project helps stakeholders addressing and minimizing risks to accomplish improved project outcomes [11]. Applying FEP practices to infrastructure projects is vital for the development of these projects, and thus, maintain access to critical goods and services throughout the nation. Previous research has demonstrated the significance of FEP tools on capital projects and how they correlate with a project's success [10, 21]. Hansen et al. [12] compiled 30 years of valuable FEP literature review in response to the low general understanding of FEP and how it differs from traditional project planning. Their research included the strong need for implementation of FEP, a concise differentiation between FEP and traditional planning, the benefits and challenges of implementing FEP, and more. The CII [6] indicated that despite the requirement for initial investment for FEP even

higher savings can be achieved on a project. According to Bingham and Gibson [3], the FEP process aid in recognizing and mitigating risks on infrastructure projects related to issues such as environmental hazards, permits, right-of-way concerns, utility adjustments, and logistic problems. CII [6] also highlighted that proper FEP can help achieve project objectives such as improved scheduling, cost, and operating characteristics, as well as social and environmental goals.

Nowadays, construction companies need to shift from focusing on the cost, time, and quality performance of a project, to also include the Triple Bottom Line (TBL) impacts by incorporating sustainability into project management [23]. Sustainable Infrastructure (SI) and infrastructure management (IM) are typically seen as two different and distinct topics, and yet these are strongly related. Mneimneh et al. [19] and Weerasinghe et al. [25] have demonstrated that sustainability can be properly accomplished if coupled with Front-end Planning (FEP) tools. Weerasinghe et al. [25] piloted a framework that correlated a green building rating system and a scope definition tool (FEP tool) and concluded that both systems complement each other. Their findings indicated that this synergy assists in (1) the overall FEP process, (2) the decision-making process; (3) setting adequate costs and procurement requirements; (4) quality management; and (5) ensuring the sustainability of the project. Additionally, Silvius and Schipper [23] concluded that sustainability can influence the entire process of project management. The authors identified three different changes in the integration of sustainability into project management: (1) a fluctuation in the scope of the project, from managing cost and schedules to managing the TBL, (2) a variation in the common practices of project management by including resilience and opportunity; and (3) a change-of-mind for the project manager of also considering sustainable development in their projects. In fact, existing sustainable rating systems may provide a standardized pre-project planning process that takes into account the TBL [15, 25]. However only a few research studies have connected FEP tools to sustainability purposes, and none of them have had a focus on infrastructure projects specifically. Therefore, this research fills in the literature gap by providing a sustainable framework that addresses horizonal infrastructure rather than vertical projects.

Despite the variety of sustainable rating systems, there is only one that addresses sustainability for all types of civil infrastructure projects: The Envision™ Rating System, created by the Institute for Sustainable Infrastructure (ISI) and the Zofnass Program for Sustainable Infrastructure at the Harvard University Graduate School of Design. Based on ISI [14] and Huang [13], there are higher probabilities of achieving increased long-term profitability on Envision™ projects, particularly in regards to anticipating limited maintenance activities as well as controlled operational requirements and running costs. Vandebergh et al. [24] highlighted that it is critical to start pursuing a sustainability certification as early as possible i.e., during the Front-End Planning (FEP) phases, so there is more broad and effective collaboration between stakeholders and higher ability to make changes at little to no cost. Likewise, Weerasinghe et al. [25], recommended that the overall cost of the project, including any sustainability rating system certification, must be identified and mitigated during FEP. Although Envision™ is applicable at any point during an infrastructure project's

lifecycle, to date it has not been integrated nor aligned with any of the evidence-based Front-End Planning tools. Klakegg [18] listed some of the reasons why sustainability is seldom integrated into construction project management: faulty economic benefits, high investments, lack of stakeholder commitment, multiple changing conditions, and poor scope definition. Moreover, when construction companies do decide to pursue a sustainable project, they are mostly focused on vertical construction (residential and commercial projects), leaving civil infrastructure projects behind. Despite the large investments needed for infrastructure projects, enhanced performance can be reached if sustainability criteria are integrated as part of the entire project management process [17]. To this end, this study aims to help infrastructure stakeholders better assess the sustainability of their projects by demonstrating how FEP, jointly with sustainable design, can maximize the possibilities of a successful infrastructure project.

2 Methodology

This study aims to investigate the existing synergies between sustainability criteria for infrastructure projects and the scope definition elements of the FEP process. To this end, the research analyzed the most important (i.e. highest-weighted) section in one of the effective FEP tools for infrastructure projects: The Project Definition Rating Index (PDRI) [8]. This section, Basis of Project Decision (BPD), is the process where the project team decides the project strategy, its objectives, and requirements [7]. It is divided into five major categories: (1) Project Strategy, (2) Owner/Operator Philosophies, (3) Project Funding and Timing, (4) Project Requirements and (5) Value Analysis. This study investigated the nexus between the FEP phase, such as Basis of Project Decision for infrastructure projects, and 59 sustainability credits (*derived from Envision™ Rating System*) divided into five major categories: (1) Quality of Life (QL), (2) Leadership (LD), (3) Resource Allocation (RA), (4) Natural World (NW), and (5) Climate and risk (CR) through a conceptual matrix analysis. A conceptual matrix is an analytical tool that provides a logical and reliable framework [9, 25] and easily demonstrate the relationship between sustainability credits and BPD decisions. The BPD section is manually correlated to the selected Envision™ sustainability credits to determine when, during the BPD phase, the appropriate sustainability decisions need to be made. The matrix approach adopted for correlation analysis is partially based on the research finding of Weerasinghe et al. [25], who developed a LEED-FEP matrix framework for green buildings. This research highlighted that the matrix provides a logical and reliable framework that support team members in planning, assessing risks, and managing sustainable projects. Given that infrastructure projects are more complex and require advanced tools, this research addresses the gap by defining a similar matrix framework that connects the sustainability criteria of the Envision™ Rating System and the elements of the FEP process.

The authors also conducted more than a hundred case-studies to assess the importance of establishing synergies of FEP practices with sustainability criteria for infrastructure projects. The case-studies utilized in this paper included only those infrastructure projects with sustainability certification (i.e. Envision™). The analysis was based on online surveys conducted to 109 stakeholders that have been involved in at least one SI project, which represents more than 60% of the number of projects awarded by Envision™ to date in the U.S. The case-study surveys entailed information about the overall planning process of the projects and how the sustainability certification process relates to the BPD elements. Some of the questions included information regarding the approximate value of the project, the rate of success, the financial and change management performance, the strengths and weaknesses of the sustainable rating system, the challenges presented during the certification, and in which stages of the project life cycle they applied all sustainability criteria.

3 Results and Analysis

The analysis of this study is divided into two phases, to determine the correlations between the sustainable criteria of infrastructure projects and the Basis of Project Decision (BPD) during FEP phase. Phase 1 presents the developed framework that shows the sustainability-related decisions corresponding to the BPD elements. While Phase 2 serves as a validation approach to the developed framework and is based on the surveying case-study analyses.

3.1 Phase 1: Developing Framework for Basis of Project Decision and Sustainability Criteria

This segment describes in detail the matrix presented in Fig. 1 for FEP Basis of Project Decision of infrastructure projects, diving deeper into how the framework supports proper scope definition for sustainable infrastructure projects. The potential correlation decisions between Envision™ criteria and FEP tool are marked with an "X" in Fig. 1 and are chosen based on the BPD elements descriptions identified by Bingham et al. (2010). Each sustainability criteria have been analyzed, and the corresponding FEP elements have been identified. This comprehensive analysis demonstrates that sustainability certification criteria can aid in the scope definition process of sustainable infrastructure projects. For instance, the analysis of three credits from the sustainability Climate and Risk (CR) category was selected to provide an example of the analysis. This category was chosen because it includes credits with the highest points in the Envision™ Rating System.

- ***CR2.1 Avoid Unsuitable Development***. The intent of this credit is to minimize construction on hazardous sites to avoid site-related risks [15]. This credit needs

Sustainability Criteria / Basis of Project Decision			PROJECT STRATEGY				OWNER / OPERATOR PHILOSOPHIES				PROJECT FUNDING AND TIMING			PROJECT REQUIREMENTS									VALUE ANALYSIS			
			A.1 Need & Purpose Documentation	A.2 Investment Studies & Alt. Assessm.	A.3 Key Team Member Coordination	A.4 Public Involvement	B.1 Design Philosophy	B.2 Operating Philosophy	B.3 Maintenance Philosophy	B.4 Future Expansion & Alteration Consid.	C.1 Funding & Programming	C.2 Preliminary Project Schedule	C.3 Contingencies	D.1 Project Objectives Statements	D.2 Functional Classification & Use	D.3 Evaluation of Compliance Req.	D.4 Existing Environmental Conditions	D.5 Site Characteristics Available vs. Req.	D.6 Dismantling & Demolition Req.	D.7 Determination of Utility Impacts	D.8 Lead/Discipline Scope of Work	E.1 Value Engineering Procedures	E.2 Design Simplification	E.3 Material Alternatives Considered	E.4 Constructability Procedures
QUALITY OF LIFE	QL1.1	Improve Community Quality of Life	X	X	X	X	X	X	X	X	X		X	X					X		X					
	QL1.2	Enhance Public Health and Safety	X			X	X	X	X	X				X					X		X					
	QL1.3	Improve Construction Safety	X		X	X							X	X		X			X		X					
	QL1.4	Minimize Noise and Vibration	X	X		X	X	X			X	X		X		X			X		X					
	QL1.5	Minimize Light Pollution	X	X		X	X	X			X	X		X		X			X	X	X					
	QL1.6	Minimize Construction Impacts	X	X		X	X	X			X	X		X		X			X	X	X	X	X	X	X	X
	QL2.1	Improve Community Mobility	X		X	X	X			X			X	X							X					
	QL2.2	Encourage Sustainable Transportation	X	X	X	X	X	X	X	X	X		X	X							X					
	QL2.3	Improve Access & Wayfinding	X		X		X			X			X	X			X				X					
	QL3.1	Advance Equity and Social Justice	X		X	X					X		X	X							X					
	QL3.2	Preserve Historic and Cultural Resources	X	X		X	X	X	X	X	X			X			X				X					
	QL3.3	Enhance Views and Local Character	X			X					X			X			X	X			X					
	QL3.4	Enhance Public Space & Amenities	X			X					X			X				X			X					
LEADERSHIP	LD1.1	Provide Effective Leadership & Commitment	X	X	X	X	X	X	X	X	X	X	X	X	X	X	X	X	X	X	X	X	X	X	X	X
	LD1.2	Foster Collaboration and Teamwork	X	X	X						X			X					X		X	X				
	LD1.3	Provide for Stakeholder Involvement	X	X	X	X					X			X							X					
	LD1.4	Pursue By-Product Synergy	X	X			X				X	X	X	X							X	X	X	X	X	
	LD2.1	Establish a Sustainability Management Plan	X	X	X	X	X	X	X	X	X	X	X	X	X	X	X	X	X	X	X	X	X	X	X	X
	LD2.2	Plan for Sustainable Communities	X			X	X			X	X			X					X		X					
	LD2.3	Plan for Long-Term Monitoring & Mainten.	X		X				X	X	X		X	X					X		X	X			X	
	LD2.4	Plan for End-of-Life	X		X				X	X	X			X					X		X					
	LD3.1	Stimulate Economic Prosperity & Develop.	X	X			X			X	X	X	X	X							X					
	LD3.2	Develop Local Skills & Capabilities	X	X	X	X								X							X					
	LD3.3	Conduct a Life-Cycle Economic Evaluation	X	X			X	X	X	X	X	X	X	X							X					
RESOURCE ALLOCATION	RA1.1	Support Sustainable Procurement Practices	X		X		X	X	X	X				X	X	X	X		X		X	X	X	X	X	X
	RA1.2	Use Recycled Materials	X			X	X	X			X	X	X	X		X		X			X	X	X	X		
	RA1.3	Reduce Operational Waste	X	X				X			X			X					X		X	X				
	RA1.4	Reduce Construction Waste	X	X				X	X		X			X							X	X				
	RA1.5	Balance Earthwork On Site	X											X		X	X	X			X	X	X			X
	RA2.1	Reduce Operational Energy Consumption	X	X				X			X			X					X	X	X		X			X
	RA2.2	Reduce Construction Energy Consumption	X	X			X	X			X			X						X	X		X			X
	RA2.3	Use Renewable Energy	X	X			X	X	X		X	X	X	X		X	X	X		X	X	X	X	X	X	X
	RA2.4	Commission & Monitor Energy Systems	X	X	X		X	X	X					X		X	X	X	X	X	X					
	RA3.1	Preserve Water Resources	X			X								X		X	X				X					
	RA3.2	Reduce Operational Water Consumption	X	X				X			X			X						X	X		X			X
	RA3.3	Reduce Construction Water Consumption	X	X			X	X			X			X						X	X		X			X
	RA3.4	Monitor Water Systems	X	X	X		X	X	X				X	X			X	X			X					

Fig. 1 Basis of project decision and sustainability criteria framework

to be considered during A.1 Need and Purpose Documentation since this BPD element aids in identifying and selecting alternatives, i.e. a proper location of the project. The CR2.1 credit also requires decisions under A.2 Investment Studies since it may need investment in preliminary surveys, such as geographic information systems (GIS), satellite imaging, site and environmental conditions, safety and social studies, and more. The B.1 Design Philosophy element should also consider this credit since it includes issues such as environmental sustainability, safety improvement requirements, hazard mitigation strategies, and compliance with applicable jurisdictional requirements. All these issues may need to be considered while deciding the project site to avoid unsuitable development. D.1

Sustainability Criteria / Basis of Project Decision			PROJECT STRATEGY				OWNER / OPERATOR PHILOSOPHIES				PROJECT FUNDING AND TIMING			PROJECT REQUIREMENTS								VALUE ANALYSIS			
			A.1 Need & Purpose Documentation	A.2 Investment Studies & Alt. Assessm.	A.3 Key Team Member Coordination	A.4 Public Involvement	B.1 Design Philosophy	B.2 Operating Philosophy	B.3 Maintenance Philosophy	B.4 Future Expansion & Alteration Consid.	C.1 Funding & Programming	C.2 Preliminary Project Schedule	C.3 Contingencies	D.1 Project Objectives Statements	D.2 Functional Classification & Use	D.3 Evaluation of Compliance Req.	D.4 Existing Environmental Conditions	D.5 Site Characteristics Available vs. Req.	D.6 Dismantling & Demolition Req.	D.7 Determination of Utility Impacts	D.8 Lead/Discipline Scope of Work	E.1 Value Engineering Procedures	E.2 Design Simplification	E.3 Material Alternatives Considered	E.4 Constructability Procedures
NATURAL WORLD	NW1.1	Preserve Sites of High Ecological Value	X	X		X	X	X			X		X	X			X	X			X				
	NW1.2	Provide Wetland & Surface Water Buffers	X	X		X	X	X						X			X	X			X				
	NW1.3	Preserve Prime Farmland	X	X		X	X	X						X			X	X			X				
	NW1.4	Preserve Undeveloped Land	X	X		X	X	X		X				X			X	X			X				
	NW2.1	Reclaim Brownfields	X										X	X			X				X				
	NW2.2	Manage Stormwater	X	X		X	X	X	X	X	X			X	X	X	X	X	X		X	X			X
	NW2.3	Reduce Pesticide & Fertilizer Impacts	X			X	X							X		X	X				X		X		X
	NW2.4	Protect Surface & Groundwater Quality	X			X		X						X		X	X				X				
	NW3.1	Enhance Functional Habitats	X	X		X	X				X		X	X			X				X				
	NW3.2	Enhance Wetland & Surface Water Funct.	X	X	X	X	X							X		X	X				X	X			
	NW3.3	Maintain Floodplain Functions	X	X			X	X	X	X				X			X				X	X			
	NW3.4	Control Invasive Species	X	X		X	X	X	X		X	X	X	X		X	X				X	X			X
	NW3.5	Protect Soil Health	X	X		X	X	X	X		X			X			X				X				
CLIMATE AND RISK	CR1.1	Reduce Net Embodied Carbon	X	X			X	X	X	X	X			X			X			X	X	X		X	
	CR1.2	Reduce Greenhouse Gas Emissions	X	X			X	X			X			X		X	X		X	X	X	X		X	
	CR1.3	Reduce Air Pollutant Emissions	X	X		X	X							X		X	X			X	X	X		X	
	CR2.1	Avoid Unsuitable Development	X	X			X							X				X			X	X	X		
	CR2.2	Assess Climate Change Vulnerability	X	X			X							X		X	X				X				
	CR2.3	Evaluate Risk and Resilience	X		X	X	X			X	X	X		X		X					X				
	CR2.4	Establish Resilience Goals and Strategies	X	X	X	X	X							X		X					X				
	CR2.5	Maximize Resilience	X	X	X	X	X	X	X	X	X	X		X		X					X		X		
	CR2.6	Improve Infrastructure Integration	X	X			X				X			X				X	X		X	X			X

Fig. 1 (continued)

Project Objectives Statement was correlated to this credit because it considers any limitation placed on the project and multiple performance objectives, i.e. sustainability and security. Element D.5 Site Characteristics was also considered to be correlated to this credit. After all, it aids in considering any site-related characteristics including uncertainty and investigation of existing conditions. D.8 Lead/Discipline Scope of Work was correlated to all sustainability credits because it includes a complete description of the project, including background information and sequencing of work. Lastly E.1 Value Engineering and E.2 Design Simplification were connected to CR2.1 because they assess a project's overall effectiveness and may help in identifying alternatives without compromising safety, function, and security.

- ***CR2.3 Evaluate Risk and Resilience***. The intent of this credit is to identify risk and resilience-related risks and hazards [15]. This credit helps to identify vulnerabilities of the infrastructure's critical functions, which is considered during the A.1 Need and Purpose Documentation of the BPD. The risk evaluations may be done through collaborative work between all stakeholders including the community affected by the project (A.3 Key Team Member Coordination and A.4 Public

Involvement). Additionally, the project needs to be designed following sustainability and safety guidelines, which are included in the B.1 Design Philosophy of BPD. And, if there are possibilities of expansion in the project, risk and resilience evaluation should also be considered for those future stages (B.4 Future Expansion Considerations). Similarly, all risk assessment activities need to be included in the project's cost and schedule estimates (C.1 Funding, C.2 Preliminary Project Schedule), and in the project objectives (D.1 Project Objectives statements). Besides, while identifying threats and hazards, the project team must consider all possible compliance with national, regional, and local requirements, including design and control standards (D.3 Evaluation of Compliance Requirements). Finally, as with all other sustainability criteria, the evaluation of risk and resilience must be included in the project's scope of work (D.8 Lead/Discipline Scope of Work)

- ***CR2.5 Maximize Resilience***. The objective of this credit is to maximize the project's durability to increase its ability to withstand hazards [15]. In order to do so, the project team needs to establish resiliency goals and strategies, as well as to define the need of the project which may include site visits and stakeholders and public input (A.1 Need and Purpose Documentation, A.3 Key Team Member Coordination, and A.4 Public Involvement). In some cases implementing resiliency strategies may result in additional costs and time, which is why the CR2.5 credit should be considered during investment analyses, and cost and schedule estimates (A.2 Investment Studies, C.1 Funding and Programming, and C.2 Preliminary Project Schedule). Resiliency is critical to a project's entire lifecycle, thus, it must be considered during design, operation, and maintenance phases as well as possible future activities (B.1 Design, B.2 Operating, and B.3 Maintenance Philosophies, and B.4 Future Expansion). Additionally, all resiliency goals and approaches need to be included in the project objectives and scope of work (D.1 Project Objectives statements, and D.8 Lead/Discipline Scope of Work) as well as comply with national, regional, and local standards and codes (D.3 Evaluation of Compliance Requirements). Finally, when considering possible resiliency strategies, the project team may identify and document activities that optimize the project's performance (E.2 Design Simplification)

The sustainability rating system developed for infrastructure projects also provides a comprehensive project planning framework to help stakeholders pursue infrastructure projects in the 'right' way [15]. Integrating sustainability principles, including social and environmental aspects, can influence the entire project management process, i.e. the requirements of the project's final output [23]. Research findings of Shivakumar et al. [22] and Weerasinghe et al. [25] as well as results obtained from this study demonstrate that implementing sustainability criteria at the FEP phases of a project can reduce risks and uncertainties while increasing the possibilities of a successful and resilient project. Additionally, previous investigations have indicated that sustainable projects may focus more on proper FEP than conventional projects, resulting in better cost performance and reduced change orders [16]. Thus, the additional efforts that sustainable projects implicate can be better justified since

they can result in better cost performance than traditional projects. To this end, the framework developed in this study, aids in the FEP process of sustainable projects for all stakeholders.

3.2 Phase 2: Multiple Case-Study Analysis

To validate the conceptual correlation matrix developed in Phase 1, the research team surveyed industry professionals with more than 10 years of experience in sustainable infrastructure projects. All surveyed professionals agreed that the sustainability certification process serves as a project planning outline and has improved the overall performance of their projects. The respondents mentioned that, although sustainability can be applied throughout the entire project life cycle, including the end-of-useful-life activities, it begins at the early stages of planning and design. This connects sustainability criteria with the processes of FEP on infrastructure projects. Respondents also agreed that the FEP tools (i.e. the PDRI) can support a better and smoother process towards sustainability certification.

The survey resulted in qualitative and quantitative data, which was later analyzed and evaluated to support Fig. 1. Figure 2 summarizes some of the FEP processes that the respondents followed during a sustainability certification and these are separated according to the corresponding categories. Based on the survey responses, the majority of the case-study projects would have benefited from a standardized FEP process or tool during the sustainability certification, i.e. a similar framework to the one developed in this research. The activities they pursued throughout the project to accomplish the sustainability credits were strongly related to FEP, as can be seen from the examples given in Fig. 2. Many infrastructure projects in which the stakeholders contributed seldom integrated sustainability in an early phase, i.e. during FEP. Consequently, there were not only uncertainty and barriers to its successful operation but also unexpected costs to address environmental implications after the design phase had been initiated. The respondents agreed that to pursue a sustainability certification, all credits and procedures should be analyzed prior to project initiation, i.e. during FEP. This early design work includes defining the owner's requirements and including them in the overall project strategy [25]. It involves more than basic design, like the selection of the location, the right materials and systems, innovative technology, risk management, and so forth. This way, the case-study survey responses and the presented Fig. 2 serve as a supporting document to the framework developed in Fig. 1.

SUSTAINABILITY CRITERIA	FRONT-END PLANNING
QUALITY OF LIFE	• Community demographic studies. • Overall planning and basic design in resource area • Defining and selecting project alternatives • Improve economies and enhance livability throughout the region • Alternative Technical Concept (ATC) to pursue better improvement in the wellbeing of the community • Innovative construction methodologies to protect and improve public health and safety • Implementation of energy efficient lightning • Analysis of types of conveyance, and products to be conveyed • Cultural resource surveys (historical preservation, archeological sites)
LEADERSHIP	• Project fund and budget details • Effective collaboration between owner and project team • Planning for sustainability • Stakeholder identification and management • Commissioning and decommissioning strategies • Stablish controlling legal terms and conditions • Profitability analyses • Sustainability objectives; sustainable certification process
RESOURCE ALLOCATION	• Zoning and ecological design ideas • Value engineering procedures • Site surveying • Life cycle cost studies • Technological needs assessment • Operation requirements • Maximize the use of durable materials with recycle content • Sustainability objectives; sustainable certification process • Hazardous materials studies
NATURAL WORLD	• Ecological design ideas • Running water and sewage design • Water conservancy ideas • Contamination Management Plans and Spill prevention • Remediation in areas of contamination within the project's right-of-way • Selection of non-invasive species • Environmental assessment and conservation programs • Analysis of environmental and mitigation costs • Sustainability objectives; sustainable certification process • Natural resource surveys
CLIMATE AND RISK	• Water treatment requirements • Analysis of site conditions • Conform plans to necessary standards and codes • Environmental assessment • Site Surveys and Visits • Project management plan to mitigate risks • Application of innovative chemical materials to protect air quality during construction • Interface with other future infrastructure projects • Analysis of environmental and mitigation costs • Sustainability objectives; sustainable certification process

Fig. 2 Case-study-based results of sustainability criteria applied during the FEP phase

4 Conclusions and Future Work

This study explained how sustainable infrastructure criteria complement the Front-End Planning of infrastructure projects, specifically during the Basis of Project Decision (BPD) phase. A matrix framework was developed, which correlates 59 of Envision™'s sustainability credits and 23 scope definition elements of FEP tools. This framework helps stakeholders to seamlessly transition from pre-planning to design and construction while considering the entire sustainable Triple Bottom Line of infrastructure projects. Stakeholders can easily identify from Fig. 1 when, during FEP, each sustainability criteria should be considered to further support the planning decisions for infrastructure projects. Thus, the developed framework may reduce

uncertainty and risks while improving resiliency and overall sustainability as well as allows project stakeholders to set achievable schedule and costs estimates, as well as procurement requirements.

According to the matrix developed in this study, the scope definition elements from the BPD section are highly correlated with all presented sustainability credits. Sustainable infrastructure goals like the improvement of the community's life quality, the engagement of stakeholders, and the pursuit of the best project solution can be accomplished by properly defining the scope of the project at FEP phases. The existing synergies between BPD and SI have been demonstrated and supported through case-study analysis. 109 stakeholders were surveyed to support the developed framework by investigating the sustainability and planning process of case-study projects. All respondents indicated that applying sustainability to their infrastructure projects has improved their overall performance, including reduced costs and shorter schedules. They agreed that the sustainability certification process serves as a project planning outline, but that following an FEP tool would have been much more helpful. The scope definition elements presented in this study, together with all sustainability criteria, can aid project managers in determining adequate estimates and requirements. Overall, the framework presented in this paper forms the foundation of an FEP tool for sustainable infrastructures. In addition, the matrix advises project stakeholders to focus more on elements that have a higher impact on the performance of a project and aids in a detailed scope definition by reducing uncertainty and risks associated with the project. Thus, as future studies, it is recommended to investigate how all phases of infrastructure project management can complement sustainability requirements, and vice versa.

References

1. ASCE (2007) The vision for civil engineering in 2025. Am Soc Civil Eng 18(4):651–660
2. ASCE (2017) America's infrastructure report card 2017 | GPA: D+. Accessed July 28, 2020. https://www.infrastructurereportcard.org/
3. Bingham E, Gibson GE (2017) Infrastructure project scope definition using project definition rating index. J Manag Eng 33(2)
4. Bingham E, Gibson Jr. GE (2010) Development of the project definition rating index (PDRI) for infrastructure projects. Arizona State University
5. Cho C, Gibson GE Jr (2000) Development of a Project Definition Rating Index (PDRI) for general building projects. American Society of Civil Engineers, Reston, VA, Construction Congress VI, pp 343–352
6. CII (2006) Front end planning: break the rules, pay the price. Res Summary 213–1. Construction Industry Institute, Austin, TX
7. CII (2013) Project definition rating index—infrastructure projects. Implement Resour 268–2. Construction Industry Institute, Austin, TX
8. Elzomor M, Burke R, Parrish K, PhD., Asce AM, Gibson GE, PhD, Asce M (2018) Front-end planning for large and small infrastructure projects: comparison of project definition rating index tools. 34(4):1–12
9. Fernández-Sols JL, Pathak R, Lavy S, Beltrán LO, Son K, Kim K (2011) Framework for selecting performance assessment tools for achieving leed 3.0 credits. Arch Eng Des Manag 7(4):236–250

10. Gibson GE, Wang Y-R, Cho C-S, Pappas MP (2006) What Is preproject planning, anyway? J Manag Eng 22(1):35–42
11. Hamilton MR, Gibson GE (1996) Benchmarking pre-project planning effort. J Manag Eng 12(2):25–33
12. Hansen S, Too E, Le T (2018) Retrospective look on front-end planning in the construction industry: A literature review of 30 years of research. Int J Construct Supply Chain Manag 8(1):19–42
13. Huang C (2014) Sustainable pedestrian bridge design: a discussion of the envision rating system. ICSI 2014, American Society of Civil Engineers, Reston, VA, pp 722–734
14. ISI (2016) Runway 4L/22R and Associated Taxiways Reconstruction | Institute For Sustainable Infrastructure. https://sustainableinfrastructure.org/project-awards/dtw-runway-reconstruction/ (July 19, 2020)
15. ISI (2018) Envision: sustainable infrastructure framework guidance manual. Washington, DC
16. Kang Y, Kim C, Son H, Lee S, Limsawasd C (2013) Comparison of preproject planning for green and conventional buildings. J Constr Eng Manag 139(11):1–9
17. Kivilä J, Martinsuo M, Vuorinen L (2017) Sustainable project management through project control in infrastructure projects. Int J Project Manag, Elsevier Ltd, APM and IPMA 35(6):1167–1183
18. Klakegg OJ (2009) Pursuing relevance and sustainability: Improvement strategies for major public projects. Int J Manag Proj Bus 2(4):499–518
19. Mneimneh F, Srour I, Kaysi I, Harb M (2017) Eco-City projects: incorporating sustainability requirements during pre-project planning. J Urban Technol, Taylor & Francis 24(1):47–74
20. Pradhananga P, Elzomor M (2020) Environmental implications of quarry rock dust: a sustainable alternative material to sand in concrete. Construction Research Congress 2020, American Society of Civil Engineers, Reston, VA, pp 916–924
21. Sherif MA, Price ADF (1999) A framework for pre-project planning. In: Proceedings 15th annual ARCOM conference. Association of Researchers in Construction Management, vol 2, pp 435–444, Liverpool, UK (15–17 September 1999)
22. Shivakumar S, Pedersen T, Wilkins S, Schuster S (2014) Envision: a measure of infrastructure sustainability. Pipelines 2014, American Society of Civil Engineers, Reston, VA, pp 2249–2256
23. Silvius AJG, Schipper RPJ (2014) Sustainability in project management: a literature review and impact analysis. Social Business 4(1):63–96
24. Vandebergh K, Augustus N, Peterson C (2016) Ridgewood view park reservoir and pump station: a case study on envision verification. J Am Water Works Assoc 108(6):51–56
25. Weerasinghe G, Soundararajan K, Ruwanpura J (2007) LEED – PDRI framework for preproject planning. J Green Build 2(3):123–143

Assessing Suitability of Geopolymer Composites Under Chloride Exposure

M. J. Hasan and K. M. A. Hossain

1 Introduction

In modern age, concrete is one of the most widely used construction materials and the most conventional form concrete is produced from Portland cement (PC) [14]. However, the production of cement often leads to almost 8% of total global carbon-dioxide emissions along with substantial amounts of nitrogen oxides, particulate matter, and other pollutants [2]. This, eventually, contributes to the increase in global greenhouse gas emissions up to about 7–9%, creating sustainability issues [9]. In order to address this growing environmental concern, geopolymer was introduced as an alternative binder option to PC. Unlike traditional concretes, Geopolymer Concrete (GC) releases 5–6 times lower amount of CO_2 [11] along with the advantages of reduced energy consumption [17] and utilization of waste by-product [18]. Geopolymer, the environment friendly alternative to Portland cement (PC), is an amorphous aluminosilicate material, composed of cross-linked alumina (AlO_4^{5-}) and silica (SiO_4^{4-}) tetrahedra forming polysialates [10, 19, 25]. Geopolymer is the by-product of the reaction between aluminosilcate source material (such as: fly ash, metakaolin and other waste materials) and alkaline activator [34] and unlike conventional cement, it hardens and develop strength through polycondensation [10, 12]. Moreover, numerous research studies have shown the advantages of geopolymers over conventional concrete in terms of better strength gain, thermal and chemical stability, strong adhesion to any surface and low permeability [29]. Despite of these advantages, there are some limitations confining its application for small-scale usage till date. As suggested by [13, 23, 27], the conventional approach of producing "two part" geopolymer mix using solution-based activator often leads to issues such as-difficulties in proper quality control during mass production due to highly corrosive

M. J. Hasan (✉) · K. M. A. Hossain
Ryerson University, Toronto, Canada
e-mail: jihan.hasan@ryerson.ca

S. Walbridge et al. (eds.), *Proceedings of the Canadian Society of Civil Engineering Annual Conference 2021*, Lecture Notes in Civil Engineering 240,
https://doi.org/10.1007/978-981-19-0507-0_35

and viscous alkaline solution, complex rheology and inadequate field level aid to control it, alkali to available silicate ratio sensitivity of the system, efflorescence, high permeability etc. Therefore, it will be prudent to consider "one part (just add water)" approach in developing geopolymer mixes considering the ease and prospect for large-scale application, similar to the conventional PC concrete.

The geopolymer mixes assessed during the current study, were developed following "one part mix" technique due to its possible future implications. Also, Polyvinyl alcohol (PVA) fiber was incorporated as reinforcing material within the mix to develop engineered geopolymer composites (EGCs). The brittle characteristics of the geopolymer mix necessitates studying the impact of fiber incorporation within concrete to improve its flexure and tensile performance. This study is primarily focused on assessing the performance of EGCs when subjected to aggressive chloride environment. One of the severe and costly deterioration mechanisms hampering serviceability of reinforced concrete structures is chloride-ion induced corrosion of steel reinforcement [20, 32]. In a well compacted and properly cured concrete, reinforcement steel is unlikely to corrode owing to a firmly adhering passive oxide film of γ-ferric hydroxide with pH = 12.5 which can impede ingress of corrosion inducing agents [3, 33]. However, such ideal conditions are usually difficult to ensure resulting in intrusion of corrosion inducing agents which abolishes the passive oxide film at low pH and induces corrosion [15, 21, 30]. Thus, it is imperative to assess the chloride susceptibility of the developed concrete mix as an indicator of long-term durability. Recently, few researches attempted to study the chloride and corrosion susceptibility of geopolymer composites [4, 16, 24] but the number is, still, limited.

This paper presents with the performance evaluation of the fiber reinforced engineered geopolymer composites when subjected to aggressive chloride environment. The developed geopolymer composites were prepared following "one part mix" technique using powder-based activator with aluminosilicate source materials. Also, an oil-coated Polyvinyl Alcohol (PVA) fiber was incorporated within concrete as reinforcing material. The chloride susceptibility of these composites was evaluated from Rapid Chloride Permeability Test (RCPT). RCPT provides with rapid testing opportunity for otherwise time-consuming chloride penetration testing. In addition to the RCPT, surface resistivity, sorptivity, compressive strength and UPV values of the developed mixes were evaluated and are presented. The findings and recommendations of this ongoing research will provide a base guideline for any future research endeavour to evaluate the long-term durability performances of "one part" geopolymer composites.

2 Experimental Program

2.1 Materials and Mix Proportions

A number of fiber reinforced engineered geopolymer composite mixes were prepared using combinations of three types of aluminosilicate source materials: Fly Ash-Type C (FA-C), Fly Ash-Type F(FA-F) and Ground Granulated Blast Furnace Slag (GGBFS). As for activator reagents, two different combinations of powder-based alkaline reagents designated as A1 made of Calcium Hydroxide with Sodium Metasilicate (A1: $Ca(OH)_2 + Na_2SiO_3{\cdot}5H_2O$) and A2 made of Calcium Hydroxide with Sodium Sulphate (A2-$Ca(OH)_2 + Na_2SO_4$) were used to activate the source materials. The activator component ratios were: $Na_2SiO_3{\cdot}5H_2O$: $Ca(OH)_2 = 2.5{:}1$ and $Ca(OH)_2$: $Na_2SO_4 = 2.5{:}1$. The silica modulus (SiO_2/Na_2O) of Sodium Metasilicate was 1. The specific gravity for these three basic reagents $Na_2SiO_3{\cdot}5H_2O$, $Ca(OH)_2$ and Na_2SO_4 were 1.81, 2.24 and 2.70, respectively.

The geopolymer composite mixes were prepared following "one-part mixing/dry mixing" by adding water to the powder-based alkaline activators and aluminosilicate source materials. Four different mixes were prepared following the mix proportions as outlined in Table 1.

M1 and M2 mixes are binary blends (FA-C and GGBFS) whereas M3 and M4 are ternary blend. As superplasticizer, a polycarboxylate based high range water reducing admixture (HRWRA) was used. In order to produce engineered geopolymer composites, Polyvinyl Alcohol (PVA) fiber was mixed within the matrix. These fibers were of 8 mm in length and 40 μm in diameter and the surface was coated with 2% oil by weight to reduce fiber/matrix frictional bond. Silica sand was used as fine aggregate.

2.2 Sample Preparation and Curing

As mentioned earlier, the mixes were prepared following "one-part mix" technique. At the start of the mixing, the different activator components were mixed to produce a uniform mix of activator. This activator powder was then added to the source materials and dry mixed in a shear mixer for about 5 min. After the dry mix, water was added gradually followed by superplasticizers to make a flowable enough paste for sand addition. Next in sequence comes addition of silica sand followed by addition of 2% PVA fiber. The total mixing procedure was finished within 20–25 min. For each mix, three cube specimens (50 mm × 50 mm × 50 mm) and three cylindrical specimens (dia-100 mm and height-200 mm) were prepared and kept in a curing room maintained at 23 ± 3 °C and 95 ± 5% relative humidity (RH). After 24 h, the specimens were demolded and then, kept in the same curing condition till the day of testing.

Table 1 Mix design of fiber reinforced geopolymer composites

Mix ID	Source material (SM)	Activator	Activator/SM	Water/Binder*	SP	Silica Sand/binder	PVA fibers
M1	FA-C + GGBFS	A1: $CaOH_2 + Na_2SiO_3 \cdot 5H_2O$	0.09	0.34	2% wt of Binder	0.3	2% wt of Binder
M2	FA-C + GGBFS	A2: $CaOH_2 + Na_2SO_4$	0.09	0.35			
M3	FA-C + GGBFS + FA-F	A1: $CaOH_2 + Na_2SiO_3 \cdot 5H_2O$	0.09	0.34			
M4	FA-C + GGBFS + FA-F	A2: $CaOH_2 + Na_2SO_4$	0.09	0.35			

* Binder = source material + alkaline activator and SP = superplasticizer

2.3 Testing Methodology

The cube specimens were tested for compressive strength as per [5] at the age of 28 days. The cylindrical specimens were used for the measurement of different transport and durability related properties. The transport properties of the developed geopolymer composites were measured in terms of chloride permeability, water absorption and initial sorptivity and surface resistivity (SR) values. Additionally, Ultrasonic Pulse Velocity (UPV) measurement was conducted to correlate with the transport property values. Both UPV and surface resistivity measurements were conducted on the 100 × 200 mm cylinders and the average values were reported. UPV of the specimens were measured in terms of pulse velocity using a Portable Ultrasonic Non-Destructive Digital Indicating Tester as per ASTM C597 [6] during which the time taken by the ultrasonic waves to pass through the 200 mm length of the cylinders. The SR testing was performed as per directives of [1] and it involved measuring resistivity of a saturated 100 × 200 mm cylinders using 4-pin Wenner probe array (Fig. 1a). During testing, the surface was wetted to ensure a conductive medium and an alternate current potential difference was applied between two outer pins. The resultant potential difference between inner pins is, eventually, used to measure the resistivity of the specimen (Eq. 1).

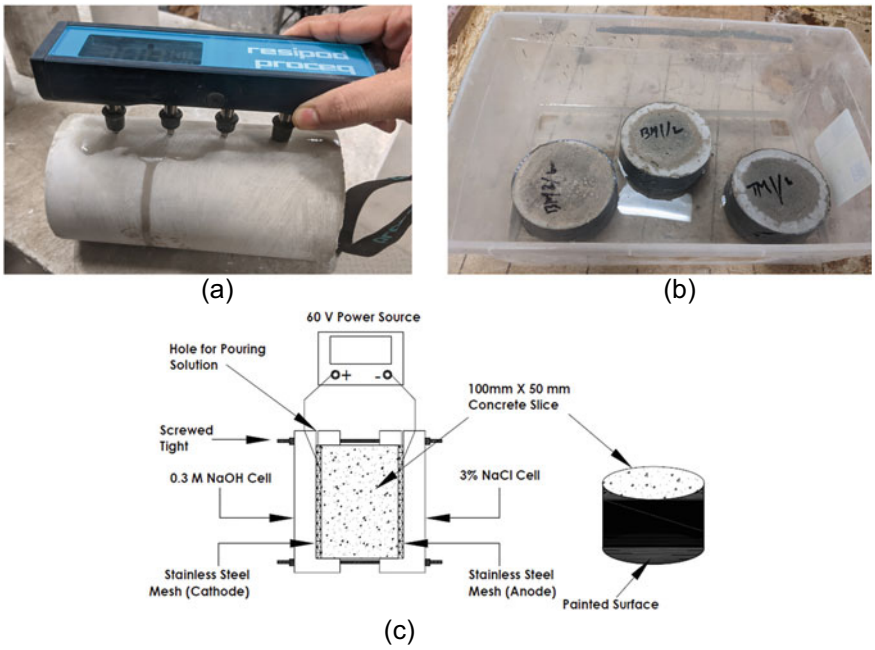

Fig. 1 **a** Surface resistivity measurement, **b** sorptivity test, and **c** schematic of RCPT setup as per ASTM C1202

Table 2 Degree of chloride penetrability based on RCPT [7] and SR [1] values

Chloride penetrability	Total charges passed (Coulomb)	Surface resistivity (kΩ/cm)
High	>4,000	<12
Moderate	2,000–4,000	12–21
Low	1,000–2,000	21–37
Very low	100–1,000	37–254
Negligible	<100	>254

$$\rho = 2\pi a \frac{V}{I} \tag{1}$$

where, ρ = resistivity, V = potential difference, I = applied current through outer probe, a = spacing of the probes.

As for water absorption and chloride permeability measurements, the cylindrical samples were sawed into three pieces of 50 mm depth and tested. The absorption and initial sorptivity of the specimens were measured as per [8] which involved measuring difference of the initial mass of the oven dry sample and mass after immersing in water to a depth of 5–10 mm (Fig. 1b). The mass gain was measured at the interval of 30 min for 2 h followed by 1 h interval up to 6 h of testing. From the straight-line plot of the cumulative volume of penetrated water per unit surface the slope is measure and reported as initial sorptivity. The chloride permeability values were determined following Rapid Chloride Permeability Test (RCPT) as per ASTM C1202 [7] where 50 mm sawed concrete specimen was subjected to an accelerated testing (Fig. 1c) under a specific DC voltage and the value of total charge passed indicated the chloride permeability of the tested specimen. Both ASTM C1202 and AASHTO TP 95 have categorised concrete chloride permeability from high to negligible for certain ranges of observed RCPT and SR values, respectively (Table 2).

3 Results and Discussions

3.1 Chloride Permeability and Other Transport Properties

During this study, the suitability of four developed engineered geopolymer composite mixes had been assessed in terms RCPT values and the results are presented in tabular form (Table 3). The surface resistivity and initial sorptivity results are also provided in Table 3 to further complement the findings from RCPT.

Based on the observed transport properties of the geopolymer composites, as outlined in Tables 3 and 4, the mix type M4 (ternary blend with activator type A2) is observed to be more durable as compared to other three mixes. However, general trend of the RCPT values and surface resistivity (as shown in Fig. 2 and Tables 3 and

Table 3 RCPT, Initial Sorptivity and Surface Resistivity of the developed geopolymer composites

Mix ID	Density (kg/m^3)	RCPT-total charges passed (Coulomb)	Surface resistivity (kΩ/cm)	Chloride penetrability	Initial sorptivity ($\times 10^{-3}$ cm/min$^{1/2}$)	UPV	
						Velocity (m/s)	Time (μs)
M1	2038.45	1233	22.4	(Low)	1.75	3202.4	62.5
M2	2024.44	1667	15.67	(Low)	3.0	3225.5	63
M3	1928.95	2007	10.67	(Moderate to high)	2.55	3122.2	64.08
M4	2023.67	988	39.117	(Very low)	1.5	3492.5	57
Ganeshan et al. [16]							
– Normal GP	–	1321	–	(Low)	2.85	–	–
– GP with steel fiber	–	1392–1762	–	(Low)	2.11–2.74	–	–
Noushini [24]							
– GP (50% GGBFS)	–	2272	–	(Moderate)	3.1	–	–
– GP (75% GGBFS)	–	1041	–	(Low)		–	–
– GP(100% GGBFS)	–	930	–	(Very low)	4.0	–	–
Noushini and [26]							
– Concrete with PC		–	10–11	(High)		3675 ~ 3800	
– Concrete with GP		–	1.5–4	(High)		3200 ~ 3950	

Table 4 Water absorption

Mix ID	Density (kg/m^3)	Dry mass (gm)	Absorbed water (gm) after immersing in water for			
			30 min	60 min	90 min	120 min
M1	2038.45	695.02	13.31	15.735	17.87	19.145
M2	2024.44	649.05	26.19	33.045	39.76	43.155
M3	1928.95	641.09	18.81	22.625	25.985	27.96
M4	2023.67	645.35	11.25	13.37	15.025	16.11

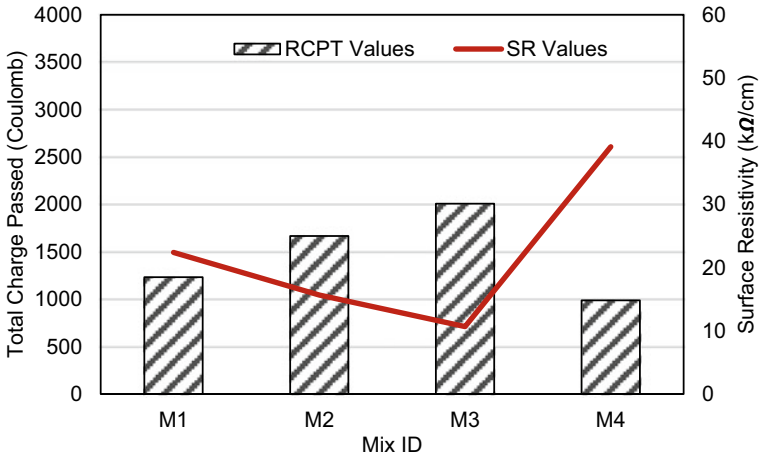

Fig. 2 Variation of RCPT and Surface Resistivity (SR) of different geopolymer composites

4) shows better durability performance of binary blend (M1 and M2) as compared to ternary counterpart (M3). Both binary mixes (M1 and M2) exhibited "low" chloride penetrability based on ASTM and AASHTO classifications as specified in Table 2. This can be attributed to the presence of high calcium content in the source material (about $CaO/SiO_2 = 0.82$). As per [24, 28], geopolymer produced from source material containing high calcium often leads to finer pore structure with higher tortuosity due to the pore filling effect of calcium silicate hydrate gel which is formed due to the presence of slag or high calcium fly ash in the blended matrix. The findings of [24] shows with increasing slag content in the geopolymer blend, the calcium content is expected to increase and thus, results in lower RCPT values. Similarly, in terms of water absorption, binary mix -M1 shows about 31% lower absorption rate as compared to its ternary counterpart-M3. Mix type M4 (ternary blend with activator type A2) shows better resistance against chloride permeability ("very low") than mix type-M3 (ternary blend with activator type 1) due to densified pore structure. This can be attributed to the formation of additional binding phase of C–S–H due to larger amount of Ca^{2+} ions from activator type A2 ($Ca(OH)_2/Na_2SO_4 = 2.5{:}1$) and FA-F's intrinsic high silica content [31]. Apart from better chloride resistance, M4 mix shows about 41% lower initial sorptivity and thus, lower rate of water absorption than the mix M3. As compared to the performances of steel fiber reinforced geopolymers as studied by [16], the findings of the current study on engineered geopolymer composites with PVA fiber were found to be comparable or in some cases better. However, long term chloride testing using RCPT as well as measuring diffusion coefficient of the geopolymer composites are necessary and thus, recommended to further solidify the observed facts.

3.2 *Correlation of RCPT, Surface Resistivity and Initial Sorptivity Values*

Figure 3 represents correlation between RCPT (total charges passed) and Surface Resistivity (SR) values with initial sorptivity/water absorption rate. It is known that concrete or composite mixes with higher chloride susceptibility are likely to show higher coulomb values during RCPT measurement. Similarly, a high initial sorptivitty value signifies a mix with higher porosity, higher rate of water absorption and thus, has proportional relation to corrosion susceptibility. The plot in Fig. 3 of RCPT vs sorptivity values is based on the findings of the current study and exhibits a correlation supporting the above-mentioned facts. The correlation equation between RCPT and sorptivity values can be expressed as: RCPT = 542.68 (Initial Sorptivity) + 279.85 with R2 value of about 0.7 signifying a moderate correlation.

As for correlation between surface resistivity (SR) and sorptivity values, the trend is observed to follow the equation: SR = −14.565 (Initial Sorptivity) + 54.006 with a R2 value of 0.67 indicating a moderate correlation. The negative slope of the equation signifies the inverse relation between surface resistivity and sorptivity. As described by [22], concrete with less interconnected pores is more likely to impede electron flow through the system resulting higher electrical resistivity. Therefore, the variation of the sorptivity values with respect to surface resistivity will be inversely proportional. Mixes M1 and M4 are expected to form a denser and less porous microstructure, as mentioned earlier and thus, show higher surface resistivity and comparatively lower initial sorptivity values (Table 3).

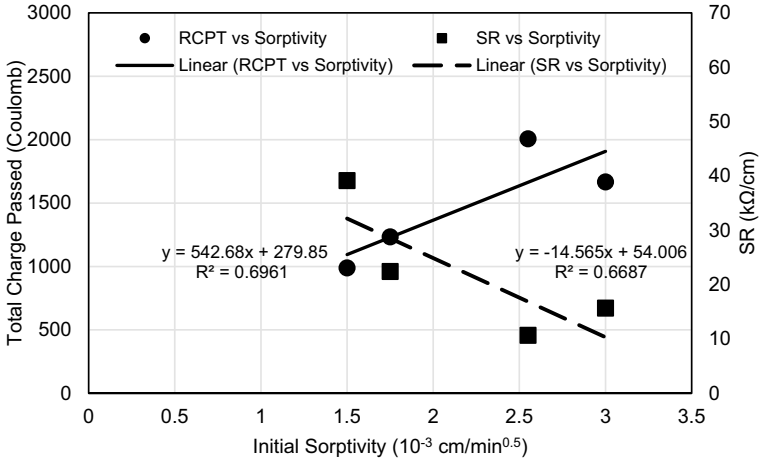

Fig. 3 Correlation of initial sorptivity with RCPT and SR values

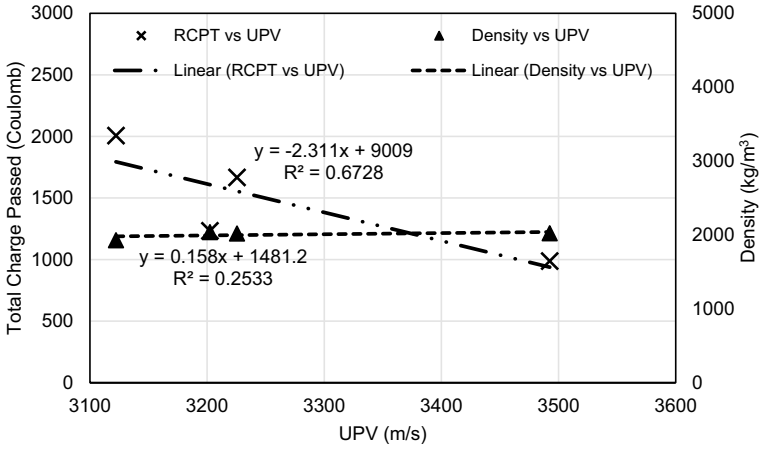

Fig. 4 Correlation of UPV measurements with RCPT and density

3.3 Correlation of UPV with RCPT and Density

The UPV primarily measures the material characteristics. The velocity of the ultrasonic pulse will vary as a function of the density of the material with high UPV for denser material signifying a proportional correlation similar to Fig. 4. This high density and UPV value will eventually, correspond to the better resistance to chloride permeability associated with lower RCPT values. This similar inverse relation can also be observed for the mixes considered for this study (Fig. 4).

3.4 Compressive Strength

The observed 28-day compressive strengths for mixes M1, M2, M3 and M4 were 31.5, 24, 28.5, 37 MPa, respectively. These values again, points out the better performance of mixes M1 and M4 as compared to the other two counterparts. This can also be attributed to the presence of high Ca^{2+} content in the matrix of these two mixes coming from FA-C, GGBFS and for M4 also from component of the activator $Ca(OH)_2$ and forming denser microstructure with lower chloride permeability. Figure 5 shows the correlation of compressive strength with RCPT and surface resistivity values. Although further long term and big scale observations are recommended to confirm the correlation pattern. It further validates the fact that mixes with better strength and pore refinement will show lower chloride susceptibility and therefore, high resistivity.

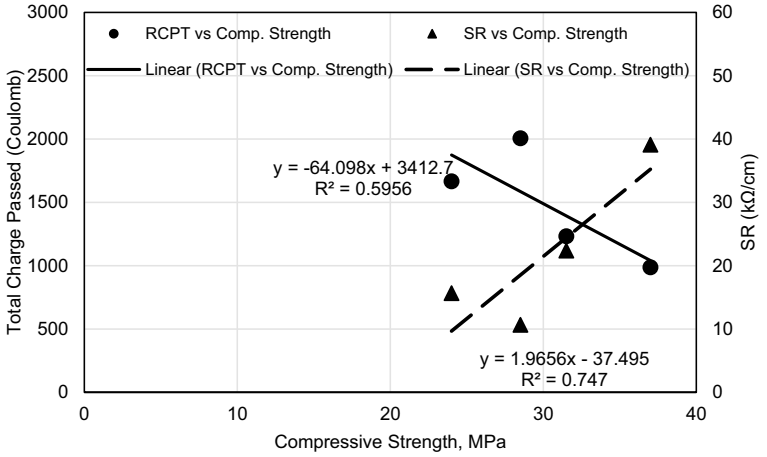

Fig. 5 Correlation of compressive strength with RCPT and SR values

4 Conclusions and Recommendations

The prime objectives of the current study were to assess the suitability of developed "one part" fiber reinforced engineered geopolymer composites when subjected to chloride exposure using Rapid Chloride Permeability Test (RCPT). In order to augment the findings from RCPT, water absorption, initial sorptivity, surface resistivity, compressive strength and UPV measurements were also conducted. Based on the test results of four developed geopolymer composite mixes (M1, M2, M3 and M4), the following conclusions are drawn:

(a) In general, binary blends of geopolymer composites (mixes M1 and M2) exhibit "low" chloride susceptibility. The reason attributing to the fact is pore refinement by C–S–H gel formed due to high Ca^{2+} content presence in source materials: fly ash class C (FA-C) and ground granulated blast furnace slag (GGBFS) used in the binary mixes.

(b) Unlike the other ternary (source materials: FA-C + GGBFS + fly ash class F) mix M3, mix M4 shows the lowest rapid chloride permeability (RCP) and the highest surface resistivity values due to the densified pore due to additional Ca^{2+} from activator and silica from FA-F.

(c) In terms of water absorption and UPV measurements, mixes M1 and M4 perform better considering the less interconnected pore network and thus, densified matrix. This eventually aids in establishing the observed correlation pattern and facts from RCPT and surface resistivity (SR) measurements.

(d) Correlations of the compressive strength with RCPT and SR values, further, validate the fact that the mixes (M1 and M4) with denser matrix can be expected to perform better in terms of both strength development and chloride susceptibility.

These findings present the prospect of the developed fiber reinforced geopolymer composites with better performance under chloride exposure. However, a long-term durability study along with mechanical properties is recommended before ensuing field application and production of such composites.

Acknowledgements The authors acknowledge the financial support from Natural Sciences and Engineering Research Council (NSERC) Canada.

References

1. AASHTO TP 95 (2014) Standard method of test for surface resistivity indication of concrete's ability to resist chloride ion penetration. American Association of State Highway and Transportation Officials, USA
2. Andrew RM (2018) Global CO_2 emissions from cement production. Earth Syst Sci Data 10:195–217
3. Angst U (2011) Chloride induced reinforcement corrosion in concrete: concept of critical chloride content-methods and mechanisms. Ph.D. thesis, Department of Structural Engineering, Norwegian University of Science and Technology
4. Al-Majidi MH, Lampropoulos A, Cundy A, Meikle S (2016) Development of geopolymer mortar under ambient temperature for in situ applications. Constr Build Mater 120:198–211
5. ASTM C109 (2016) Standard test method for compressive strength of hydraulic cement mortars. In: American society for testing and materials, West. Conshohocken, PA, USA
6. ASTM C597 (2006) Standard test method for pulse velocity through concrete. In: American society for testing and materials, West Conshohocken, PA, USA
7. ASTM C1202-12 (2019) Standard test method for electrical indication of concrete's ability to resist chloride ion penetration. In: American society for testing and materials. West Conshohocken, PA, USA
8. ASTM C1585 (2013) Standard test method for measurement of rate of absorption of water by hydraulic-cement concretes. In: American society for testing and materials. West Conshohocken, PA, USA.
9. Bildirici M (2017) Impact of militarization and economic growth on biofuels consumptions and CO_2 emissions. Environ Prog Sustain Energy 37(3):1121–1131
10. Davidovits J (1993) Geopolymer cements to minimize carbon dioxide greenhouse warming. Ceram Trans 37(1993):165–182
11. Davidovits J (2008) Geopolymer chemistry and applications, 2nd edn. Inst. Geopolymer, Saint Quentin, Fr
12. Duxson P, Fernández-Jiménez A, Provis JL, Lukey GC, Palomo A, van Deventer JSJ (2007) Geopolymer technology: the current state of the art. J Mater Sci 42(9):2917–2933
13. Duxson P, Provis JL (2008) Designing precursors for geopolymer cements. J Am Ceram Soc 91(12):3864–3869
14. El-Wafa MA, Fukuzawa K (2018) Early-age strength of alkali-activated municipal slag-fly ash-based geopolymer mortar. J Mater Civ Eng 30(4):04018040, 1–9
15. Etman ZA (2012) Reinforced concrete corrosion and protection. Concr Res Lett 3(1)
16. Ganesan N, Abraham R, Raj SD (2015) Durability characteristics of steel fibre reinforced geopolymer concrete. Constr Build Mater 93:471–476
17. Gulshan ME, Alzeebaree R, Rasheed AA, Nis A, Kurtoglud AE (2019) Development of fly ash/slag based self-compacting geopolymer concrete using nano-silica and steel fiber. Constr Build Mater 211:271–283
18. Hardjito D, Wallah SE, Sumajouw DM, Rangan BV (2004) On the development of fly ash-based geopolymer concrete. Mater J 101(6):467–472

19. Komnitsas KA (2011) Potential of geopolymer technology towards green buildings and sustainable cities. Procedia Eng 21:1023–1032
20. Lizarazo-Marriaga J, Claisse P (2009) Determination of the concrete chloride diffusion coefficient based on an electrochemical test and an optimization model. Mater Chem Phys 117(2–3):536–543
21. Moreno M, Morris W, Alvarez MG, Duffo GS (2004) Corrosion of reinforcing steel in simulated concrete pore solutions—Effect of carbonation and chloride content. Corros Sci 46:2681–2699
22. Nadelman EI, Kurtis KE (2014) A resistivity-based approach to optimizing concrete performance. Concr Int 36(5):50–54
23. Nematollahi B, Sanjayan J, Shaikh FUA (2015) Synthesis of heat and ambient cured one-part geopolymer mixes with different grades of sodium silicate. Ceram Int 41(4):5696–5704
24. Noushini A (2018) Durability of geopolymer concrete in marine environment. Ph.D. thesis, School of Civil and Environmental Engineering, The University of New South Wales, Sydney, Australia
25. Noushini A, Castel A, Aldred J, Rawal A (2020) Chloride diffusion resistance and chloride binding capacity of fly ash-based geopolymer concrete. Cement Concr Compos 105(2020):103290
26. Noushini A, Castel A (2015) A resistivity-based approach to indicate chloride permeability of geopolymer concrete. In: 27th concrete institute of Australia conference, Melbourne, Australia.
27. Provis JL (2009) Activating solution chemistry for geopolymers. In: Provis JL, van Deventer JSJ (eds) Geopolymers: structures, processing, properties and industrial applications. Woodhead, Cambridge, UK, pp 50–71
28. Provis JL, Myers RJ, White CE, Rose V, van Deventer JSJ (2012) X-ray microtomography shows pore structure and tortuosity in alkali-activated binders. Cem Concr Res 42(6):855–864
29. Provis JL, Bernal SA (2014) Geopolymers and related alkali-activated materials. Annu Rev Mater Res 44:299–327
30. Pradhan B, Bhattacharjee B (2009) Half-cell potential as an indicator of chloride-induced rebar corrosion initiation in RC. J Mater Civ Eng 21(10):543–552
31. Sood D, Hossain KMA (2021) Optimizing precursors and reagents for the development of alkali-activated binders in ambient curing conditions. J. Compos Sci 5(59):1–20
32. Samson E, Marchand J, Snyder KA (2003) Calculation of ionic diffusion coefficients on the basis of migration test results. Mater Struct 36:156–165
33. Verma SK, Bhadauria SS, Akhtar S (2014) Monitoring corrosion of steel bars in reinforced concrete structures. Sci World J 2014:1–9
34. Zhang YJ, He PY, Zhang YX et al (2018) A novel electroconductive graphene/fly ash-based geopolymer composite and its photocatalytic performance. Chem Eng J 334:2459–2466

Integrated Project Delivery Perception and Application in Washington State

D. Martin, H. Dang, and W. Plugge

1 Introduction

The traditional Design-Bid-Build (DBB) project delivery system dates to the late nineteenth century. As design and construction methods have become more complex, the contractual relationships between construction stakeholders require more collaboration and innovation. As a result, alternative project delivery methods continue to evolve as the industry takes on more complex projects. Specifically, Integrated Project Delivery (IPD) strives to maximize collaboration and optimize resources for all parties in a complex project. The IPD process reduces rework, design changes and iterations, construction duration, project costs, including materials, labor, and equipment.

IPD is defined as "a method of project delivery distinguished by a contractual arrangement among a minimum of the owner, constructor, and design professional that aligns business interests of all parties" [1]. It has eight contractual and three behavior principles [2]. These eight contractual principles are (1) key participants being bounded together as equals, (2) shared financial risk and reward based on project outcomes, (3) liability waivers between key participants, (4) fiscal transparency between key participants, (5) early involvement of key participants, (6) intensified design, (7) jointly developed project target criteria, and (8) collaborative decision marking. These three behavior principles are (1) mutual respect and trust, (2) willingness to collaborate, and (3) open communication. IPD principles can be applied to various contractual arrangements, and IPD teams can include members well beyond the basic triad of the owner, architect, and contractor. In all cases, IPD projects are uniquely distinguished by highly effective collaboration among the

D. Martin (✉) · H. Dang · W. Plugge
Central Washington University, Ellensburg, USA
e-mail: david.martin@cwu.edu

S. Walbridge et al. (eds.), *Proceedings of the Canadian Society of Civil Engineering Annual Conference 2021*, Lecture Notes in Civil Engineering 240,
https://doi.org/10.1007/978-981-19-0507-0_36

owner, the prime designer, and the prime constructor, commencing at early design and continuing through to project handover [3].

A desire to improve everyone's position and align all participants' interests involved while increasing one's position and interest is the central theme of IPD. It is the foundation for integrating peoples' labor, talents, and investments. "Two are better than one, because they have a good return for their labor: If either of them falls down, one can help the other up. But pity anyone who falls and has no one to help them up" (Ecclesiastes 4: 9–10, New International Version). As the Wisdom of Solomon suggests, two working together is better than two working separately, as each acts as a support structure for the other. IPD contracts are structured in such a way as to embody the spirit of Ecclesiastes 4 that elicits devotion to not only the entity that each project participant represents but also to each other's welfare. In the end, the sacrifices made to lift the other up yields greater returns for everyone.

The IPD approach typically stands in opposition to the entrenched philosophy in the construction industry, established through decades of distrust. IPD contracts deviate from many other collaborative contracts, which are emblematic of a distrustful industry, that attempts to modify behavior. IPD contracts are structured to resemble the Mayflower Compact that attempts to modify attitude and is a critical and necessary first step toward acknowledging Solomon's wisdom. However, attitudes are unlikely to change based on structural changes alone. A cultural shift toward collaboration is required to realize the benefits of a collaboratively structured contract.

Through an initial investigation, a significant amount of information exists regarding IPD but is still a relatively unknown concept to many in the industry. Projects in all sectors of the construction industry are becoming more complicated. So, as the project's level of difficulty increases, the complexity in the network of people also increases. Whether the contract is Design-Bid-Build, Design-Build, CM at Risk, or IPD, there are always similar people that take on important roles in the project [4]. Coordinating all these people is overwhelming but essential to all projects. When the people involved in a project can communicate ideas and work together, all other pieces of the project can come together with much more efficiency.

2 Literature Review

Comparing the structures of the DBB (Fig. 1) and IPD (Fig. 2) project delivery methods, it is clear to recognize their differences, even though they consist of the same personnel. For example, the DBB method requires several separate individual contracts at different project phases. On the other hand, IPD operates under the auspice of a single contract that all parties are signatory to execute at all project phases.

One of the most significant contributions to establishing IPD as a mainstream project delivery system is using contracts that encourage collaboration. Arguably, traditional arrangements in the construction industry do not foster collaboration.

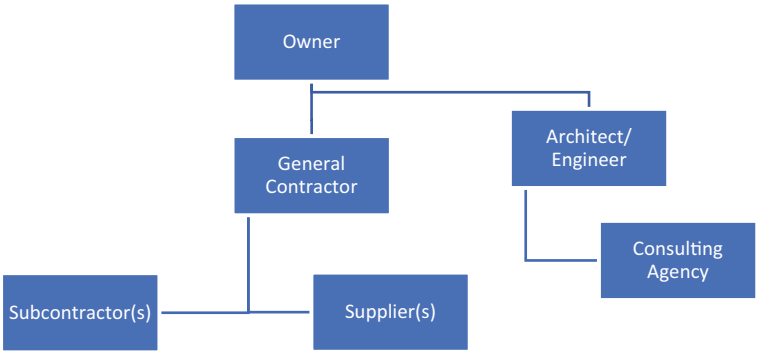

Fig. 1 Basic breakdown structure of the contracting parties in the traditional DBB system [5]

Fig. 2 The basic breakdown structure of contracting parties in IPDs [5]

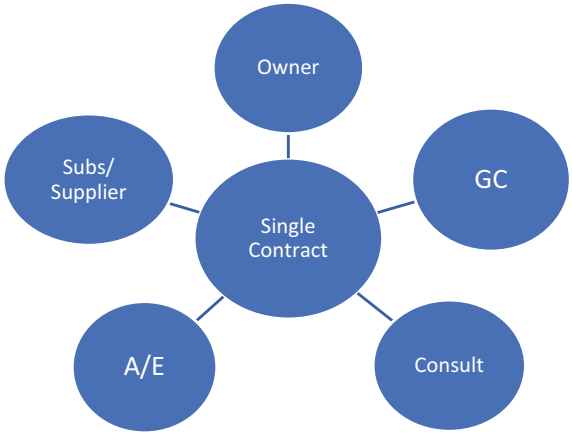

Collaboration requires participants to understand each other regarding specific technologies, financing techniques, and operations of the respective participants [6]. In addition, sharing information requires a significant level of trust among project participants.

A joint-venture construction company in central Florida provided a blueprint for an IPD definition and is credited as the first organization to employ IPD. As observed and reported, the fundamental changes to the organizational structure, administrative procedures, design processes, field operations, and the use of technology were the impetus behind this collaborative approach [7]. The delivery mechanism developed represents compact-like characteristics and is structured as shown in Fig. 1. The organizational structure consists of individual companies that work as one contract party to design, procure, and construct the project. The firms include an architecture and engineering firm, a mechanical–electrical–plumbing engineering firm, a general contractor, a design-build electrical contractor, a mechanical contractor, a plumbing

contractor, and a fire protection contractor. The individual has assumed responsibilities for both the individual scope of work and the project's overall performance in a homogenous organization. Each member signs the primary contract. This contract is framed similarly to a covenant-like contract (compact) that requires each member to be a co-indemnitor to the performance of the entire project, not just the area each is responsible for, as is the case in most traditional contracts [7].

Administrative procedures are also different from traditional contracts. Each member is a joint-venture company's proportional owner with shared costs and profits, planning, budgeting, and decision-making. Each member is reimbursed for direct job costs at the end of each month, and then at the end of the project, the gross profit is distributed among the primary team members. Also, planning and coordination of the work become the responsibility of each member. To a large extent, this is relegated to the people who perform the work to plan and coordinate amongst themselves. Furthermore, budgets are established by combining individual estimates from each portion of the work. Because of the co-ownership of cost overruns and shared profits, decisions are generally made in the field. Problems are identified, solved, and then documented instead of the traditional identified, documented, negotiated, and then solved. There are no change orders within the team or back-charges since any additional cost is allocated proportionately among the members [7].

The design process is the responsibility of the contractors who have expertise in technical areas. Along with the designers, the entire team develops and analyzes alternatives. Once the design is selected, the budget is then developed. The contractors work with the designers to produce the project documents, and they sign off on every design document. In short, the project documents become fabrication drawings rather than engineering drawings. Designers, engineers, and construction personnel are all located on-site to provide immediate responses to questions and concerns and to develop coordination documents as necessary [7].

Besides, regarding field procedures, participants perform activities that are outside their original scope of work (provided no safety regulations are violated) to streamline construction and make work easier for the other team members. For example, if a plumber can spend an additional $5,000 to save the electrician $20,000, they will do it. As mentioned previously, all direct costs are reimbursable, and all the team members share profit. A significant factor that helps improve field procedures is the use of composite teams. For example, during the renovation of a dormitory, a fire sprinkler system, central hot water, data terminals, cable television, and a telephone system for each room were needed to be added to the contract. Instead of having each subcontractor perform all the tasks separately, a composite crew was formed to complete each room [7].

The behavior of the project participants must be clearly specified when attempting to approach construction with more collaborative project delivery systems [8]. Contracts need to identify how project participants should behave to pursue a common goal. These are common beliefs that most experts adhere to as a requirement for fostering collaborative construction projects. However, this approach reverses the causal order of the variables. Contracts cannot establish trust. Contracts are based on established trust. Underlying all contracts is an unstated established level of trust

that the other party will meet their responsibilities. Attempting to instill trust through a contract heightens the expectation that one party will not fulfill their responsibilities, let alone act collaboratively outside contractual requirements. Therefore, some practitioners think that more clauses in contracts are required to spell out what is and what is not collaborative, again making situations more and more distrustful, ultimately spiraling down to an inability to collaborate.

While laying the groundwork for research on organizational behavior, Katz states that "an organization which depends solely upon its blueprints for prescribed behavior is a fragile social system" [9]. To protect the rights of individuals, contracts inherently divide the project participants and encourage individuals only to be concerned with their individual self-interest [10], defined by roles, responsibilities, and behaviors. Contracts provide rather prescriptive formulas that disrupt collaborative relationships. In lieu of being inspired to work collaboratively, fear of the consequences of breaching the contract then becomes the primary motivating factor for collaboration. Fear may generate obedience, but it rarely generates collaboration.

Regarding commitment, traditional approaches continue to focus on behavior versus attitude. In each of the aforementioned theses, the focus is on defining appropriate behavior and its enforcement through contracts or other legal means. Little regard is given to commitment. The predominant motivating factor (fear) ultimately leaves the project participants' commitment level unchanged from the traditional approach. In lieu of being inspired to work collaboratively, fear of the consequences of breaching the contract is still the motivating factor. Respecting the rights of individuals is unquestionably a noble endeavor; however, contracts have little to do with respect. Contracts merely safeguard against disrespect. Therein lies one of the problems with contracts. Behavior modification effectively ensures individual conformity to a prescribed method of behavior; contracts attempt to ensure the same result. However, commitment levels remain low, and behavior is limited to the scope of the contract. Contracts do not inspire a sense of commitment since they are imposed upon project participants thus, restricting individual freedom.

On the other hand, the compact understanding establishes a common identity with people of a certain ilk that have a deep loyalty toward the cause of the common good [11]. In compacts, the behavior is not stressed as much as attitude. Instead, it is assumed that appropriate behavior is a by-product of the compact attitude. Specifically, ensuring appropriate behavior is accomplished through an obligatory, elective commitment by subjecting one's interest to the benefit of the goal. In this environment, the predominant motivating factor, and ultimately the project participants' behavior, is drastically changed from traditional construction project relationships. Instead of being inspired by fear, a compact generates commitment by rewarding more significant benefits to the individual and the whole group. To benefit the project by subjecting oneself to the goal, compacts inherently unite the project participants and encourage individuals to support each other. Therein lies the benefit of compacts. Each partner is benefited greater in the long term by each project participant subjecting themselves to the project (goal) than if each individual pursued their self-interest.

This is not to say that compacts require complete self-sacrifice whenever other project participants request it. Sometimes, a project participant might sacrifice too much to the point that other project participants begin to take advantage of them [12]. Rather it is understood that when one member of a project team is negatively affected, all participants absorb this impact, therefore, they willingly agree to support each other in difficult times. In this environment, compacts have a purpose. To consider the well-being of others and to work together for the benefit of all involved, compacts establish commitment rather than modify behavior. Compacts help unite project participants to act responsibly toward other project participants to benefit everyone willingly. Compacts establish a structure where stakeholders are in partnership, whereas contracts perpetuate separation. Consequently, compacts employed in collaborative environments structurally unite collaborative forces to work for the project, as shown in Fig. 2 [5] as well as act in the best interest of all the project participants.

In response to the need for establishing more collaborative environments in the construction industry, leaders in the construction industry are beginning to use contracts that mirror compacts, which is referred to as Integrated Project Delivery (IPD). Through research and real-world applications in the early to mid-2000s, a definition of IPD was developed, and the principles behind IPD contracts are outlined in the Integrated Project Delivery: A Guide publication [5]. IPD principles include mutual respect and trust, mutual benefit and reward, collaborative innovation and decision making, early involvement of key participants, early goal definition, intensified planning, open communication, appropriate technology, and relational contracting [5].

In an IPD project, the owner, designer, consultants, constructor, subcontractors, and suppliers commit to collaboration and work towards the project's best interests. Using IPD requires earlier involvement by more of the project participants. IPD compensation structures recognize and reward early involvement. Compensation is based on the value-added by an organization, and it rewards behavior tied to achieving project goals. IPD business models are designed to support collaboration. The key participants are involved from the earliest possible time. Their combined knowledge and expertise are most valuable during the early stages, where informed decisions have the most significant effect. Decision-making considers the knowledge and expertise of all key participants, key decisions are evaluated by the project team, and to the greatest practical extent, decisions are made unanimously. Project goals are developed early and agreed upon by all participants. Finally, conflicts are recognized as they occur and are promptly resolved.

Communication should be open, direct, and honest among all participants in a no-blame culture leading to the identification and resolution of problems rather than determining liability. The use of specific technologies is specified at project initiation to aid functionality and interoperability. Because open standards allow for more efficient communications between all participants, the technology that is compliant with open standards is used whenever possible. The project team is an organization in its own right and follows the project's goals and values. Leadership is assumed by the team member most capable with regard to specific work and services. Often, design

professionals and contractors lead in their areas of expertise. However, specific roles are determined on a project-by-project basis [5].

3 Research Method

Researchers at Central Washington University (CWU) distributed a short survey to various construction contractors in the Pacific Northwest. This research aims to determine the familiarity of IPD amongst these contractors and which characteristics make a successful IPD project. The authors used open-ended questions to collect qualitative data from contractors in the survey. The survey also consisted of a few short answers to determine the use of IPD and project characteristics. A series of survey emails were sent to several contractors, as shown in (Appendix A). Another email was sent to follow up to ensure a significant number of responses were provided for analysis.

Researchers at CWU contacted a variety of general contractors throughout Washington state. The data set focused on mid-to-large-sized general contractors. Although the questions in the Appendix A survey were broad and straightforward, they were selected to answer the following research questions:

1. Question 1 attempts to determine which construction sectors have a relationship to IPD use.
2. Question 2 attempts to determine the types of contracts most commonly used across all sectors. By identifying the most common contracts, companies can reflect the contract aspects that do not work. If their most commonly used contracts still put too much risk on the contractors, they may be more inclined to try an alternative delivery method.
3. Question 3 aims to answer a company's exposure to IPD?
4. Question 4 focuses on time, money, and resource constraints in construction.
5. Question 5 addresses the common themes among general contractors, jobs, and people and if these relate to IPD.

4 Results, Discussion, and Conclusions

It is clear from Fig. 3 that the most responses (i.e., 36%) came from commercial contractors who would most frequently be engaged in the IPD project delivery system. It was surprising to see such a low representation of heavy civil contractors because the program at CWU focuses on the commercial and heavy civil sectors. One possible reason is that many heavy civil contractors engage in public projects requiring the design-bid-build project delivery to determine the most qualified bidders for the project based on the lowest bid. Therefore, this would explain why IPD has not been widely adopted into the heavy-civil construction project arena. Also, there

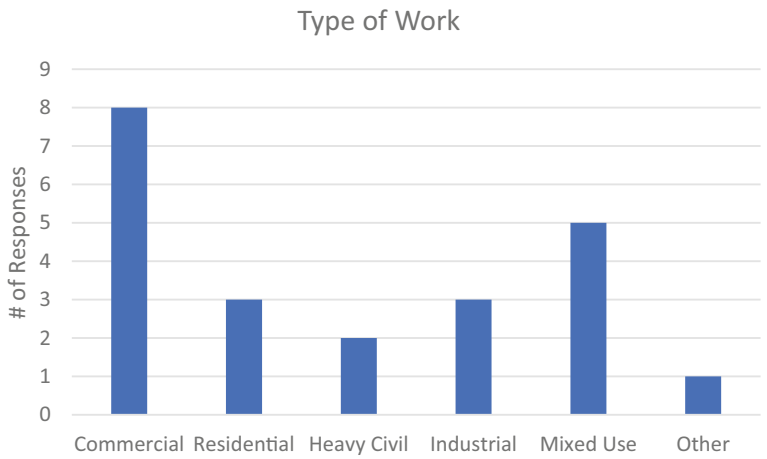

Fig. 3 Question 1 results

is a significant amount of mixed-use work projects taking place in the state of Washington. Mixed-use construction combines both vertical (i.e., general construction) and horizontal work (i.e., heavy civil), much like how integrated project delivery combines project delivery processes from other delivery methods. Although this correlation would require further and more extensive research, it still poses some of the following questions: What type of contract(s) have been most utilized to deliver mixed-used projects? Would the IPD project delivery method be most effective for mixed-use projects?

Figure 4 demonstrates that the D-B-B method is one of the most common in

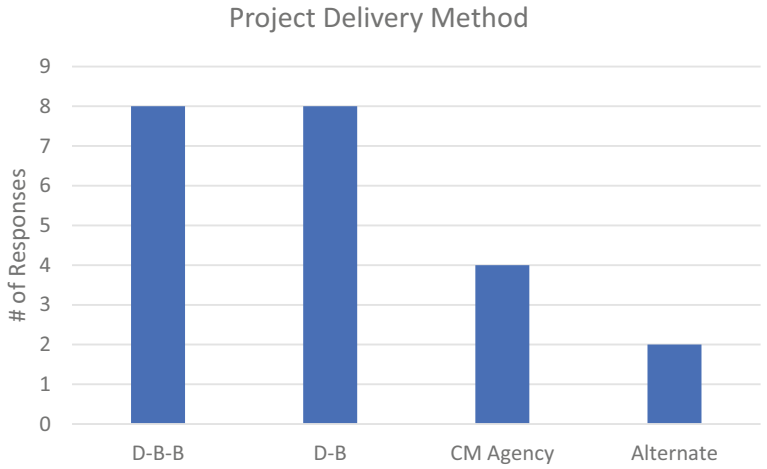

Fig. 4 Question 2 results

Fig. 5 Question three results

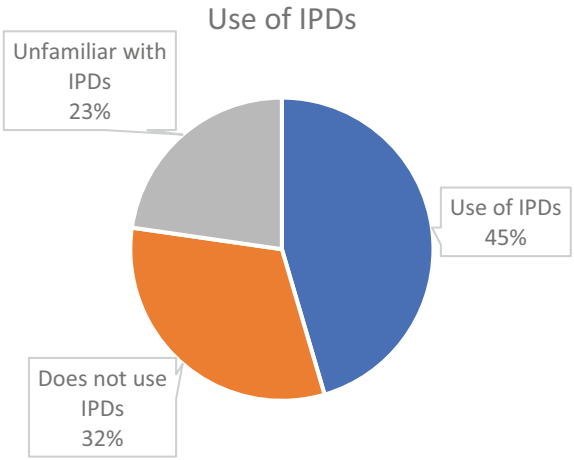

this sample, along with Design-Build. While only two of the 22 responses selected alternate delivery methods, that does not mean those companies are implementing integrated project delivery. Another way to interpret this data is to compare the two traditional methods to the two newer contracting models, including the CM Agency and Alternate project delivery models. Construction Manager Agency and Alternate delivery make up approximately 27% of the sample, while design-bid-build makes up 36%. This is important because it shows that there is a portion of Washington contractors using newer methods, and the gap between older and more recent methods is beginning to close.

Figure 5 reveals that 23% of the responses were unfamiliar with IPD. This lack of familiarity shows how little the state of Washington recognizes IPD. On the other hand, this data also indicates that there is a large percentage of projects that have been procured under the IPD delivery method. Almost half of the sample has been on at least one or more projects using this contracting method. This large percentage shows that contractors in the state of Washington recognize and use IPD.

Researchers were interested in the effectiveness of IPD as a project delivery method. The literature review suggests all the positive theoretical remarks, reviews, and successes of IPDs, but are they as good as what common research proposes? Table 1 summarizes the responses to question 4. The collected data provides support for IPD as being both efficient and inefficient. Only 50% of the IPD projects were

Table 1 Question four results

Question 4	Yes	No
On time?	5	5
Within Budget	5	5
	Less	Same
Change orders	6	4

completed on time, while the other 50% did not. Also, only 50% of the IPD projects were completed within budget. Change orders showed the most benefit as none indicated that there were more change orders; 40% reported a similar amount, whereas 60% showed improvement. This was the most interesting piece of data because zero response stated there were more change orders on their IPD job. It should be noted that the number of responses was limited, which could skew these results.

Question 5 was an open-ended question that provided an understanding of the most important aspects of a construction project. The most common answers to question 5 were (1) communication, (2) planning/scheduling, and (3) trust. Communication and planning are generally accepted as key to project success. However, the third aspect, "trust," is central to IPD processes and lends insight into some of the successes associated with IPD.

5 Limitation

One of the most impactful limitations this study reveals was the number of participants and the response rate. The sample size should have been larger to reflect all the general contractors in Washington better. The response was at approximately 41%. Perhaps more time and persistence would have improved the response rate.

COVID-19 impacted the ability to ensure agreement to complete the surveys. This has limited their work, causing dramatic changes in their practices. In addition, with so many changes occurring on a day-to-day basis, companies likely did not have time to answer the survey questions.

6 Future Research

To conduct similar research for the state of California. California is more IPD established, and it would be interesting to collect data on how many general contractors are using it. The sample size for this research would have to be much larger than Washington because of the large population of people and projects.

Furthermore, conducting more surveys to general contractors across all the states could provide results that better reflect the construction industry. By asking the same questions to a larger sample of general contractors, you would be able to see the trends of each state, region, and country. In addition, recognizing the areas that most commonly use IPD would allow researchers to have a more excellent comprehension of the effectiveness of IPD.

Appendix A

Dear Contractor.

The construction management program at Central Washington University is conducting a study on Integrated Project Delivery. The program has created a short survey in which your response is completely voluntary and answers the questions that pertain to your company. It is your preference on how you provide your responses. Please answer the questions shown below and email them back to the program at cwucmgt@cwu.edu.

Survey Questions:

1. What type of projects does your company typically work on? Select the best answer.
    a. Commercial
    b. Residential
    c. Heavy Civil
    d. Industrial
    e. Mixed-Use
    f. Other
2. What type of project delivery do you most often work with? Select the best answer.
    a. Design-Bid-Build
    b. Design-Build
    c. Construction Manager Agency
    d. Alternate Project Delivery
3. Has your company ever used Integrated Project Delivery (IPD)? Select the best answer.
    a. Yes
    b. No
    c. I am unfamiliar with IPD
4. If yes, please answer the following regarding the IPD.
    a. Was the project completed on time?
    b. Was the project completed within budget?
    c. Were there more, less, or about the same amount of change orders?
5. In your opinion, what are the 3–5 most essential items that must take place for a successful project?

We sincerely appreciate your response. Your answers will significantly contribute to my final project.

Central Washington University

Construction Management

manningal@cwu.edu

References

1. AIA (American Institute of Architects), and AGC (American General Contractors) (2011) Primer on project delivery. Washington, DC
2. Hanna AS (2016) Benchmark performance metrics for integrated project delivery. J Constr Eng Manag 142(9)
3. Integrated Project Delivery: A Guide (PDF). American Institute of Architects 2007 version 1. Accessed 13 Nov 2008
4. Dang H, Shane J (2018) Construction manager general contractor (CMGC) characteristics and effective practices in transportation sector. Constr Res Congr. https://doi.org/10.1061/9780784481271.072
5. AIA National, AIA California Council (2007) Integrated project delivery: a guide. AIA, AIA CC
6. Ibbs WC, Kwak YH, Ng T, Odabasi AM (2003) Project delivery systems and project change: quantitative analysis. J Constr Eng Manag 382(6)
7. Martin D, Songer A (2004) Contracts versus covenants in integrated project delivery systems. ChartEd Inst Build 6:51–55
8. Flora G, Ernzen J, Schexnayder C (1998) Field-level management's perspective of design build. Pract Period Struct Des Constr 180(6)
9. Katz D (1964) Motivational basis of organizational behavior. Behav Sci 9:131–146
10. Clegg SR (1992) Contracts cause conflicts. In: Fenn P, Gameso R (eds) Construction conflict management and resolution, pp 128–144
11. Shin K (2001) The covenantal interpretation of the business corporation. University Press of America, Lanham, MD, p 29
12. Lazar F (2000) Project partnering: improving the likelihood of win/win outcomes. J Manag Eng 16(2):71–83
13. Kanter RB (1994) Collaborative advantage. Harv Bus Rev 96(13)

Earthquake-Induced Damage Assessment of Segmental Post-tensioned Precast Concrete Bridge Pier

Chanh Nien Luong, Cancan Yang, and Mohamed Ezzeldin

1 Introduction and Literature Review

It has been widely recognized that 'Accelerated Bridge Construction' (ABC) can reduce construction time, minimize traffic interruption, reduce construction and maintenance cost, improve work safety, and enhance concrete quality [1]. As such, the implementation of precast concrete elements and systems, as an important ABC technique, has been facilitated in Canada in the past two decades. However, most of the current precast concrete bridge pier applications in Canada are limited in low seismicity regions due to the lack of seismic code provisions [2]. Previous studies on non-emulative precast concrete system with unbonded post-tensioning tendons have shown prominent seismic response [3–10]. This non-emulative precast pier outperforms the conventional cast-in-place pier in terms of the self-centering ability of the former that allows the structure to undergo large lateral deformations with small residual drifts. To enhance the energy dissipating (ED) capacity of the bridge pier, researchers have investigated different systems including ED steel bars [5–7, 9, 11], bearing elastomers [12], external energy dissipaters [3, 4, 13], shear slips [8, 14], and friction dampers [15, 16].

Despite research efforts on segmental post-tensioned precast concrete (SPPC) bridge pier, engineers are reluctant to adopt segmental precast bridge construction in moderate-to-high seismic regions without well-established seismic design provisions. The current seismic bridge design philosophy is shifting from a conventional Force-Based Seismic Design to Performance-Based Seismic Design (PBSD) for the objective of predictable structural performance in the event of an earthquake. The

C. N. Luong (✉) · C. Yang · M. Ezzeldin
McMaster University, Hamilton, Canada
e-mail: luongcn@mcmaster.ca

S. Walbridge et al. (eds.), *Proceedings of the Canadian Society of Civil Engineering Annual Conference 2021*, Lecture Notes in Civil Engineering 240,
https://doi.org/10.1007/978-981-19-0507-0_37

structure is designed not only to prevent collapse, but also to increase life safety, minimize economic loss, reduce post-earthquake traffic disruption, and decrease emergency needs. Currently, PBSD has been adopted in highway bridge design codes [17, 18] based on extensive studies on reinforced concrete bridge column [19–23].

The essence for the implementation of PBSD is high-fidelity modelling techniques for the prediction of structural performance and well-defined damage measures. Prior studies have only focused on the performance-based seismic performance assessment [24–27]. However, limited attention has been directed toward the damage state quantification for SPPC pier, which is an inherent requirement for PBSD. This study fills this gap. Canadian Highway Bridge Design Code [17] defines four performance levels (immediate service, limited service, service disruption, and life safety) according to the material strain limits. However, these definitions of damage/limit states cannot be directly used for SPPC piers due to the particular seismic response mechanisms of the latter. Large-scale experiments have been performed to evaluate the damage states particular to SPPC piers [5, 6, 8, 28]. However, an experimental investigation is typically based on limited number of SPPC specimens due to the high cost and time consumption. Numerical models are introduced as an alternative for evaluating the damage of SPPC piers. Two modelling techniques are frequently used to simulate the SPPC piers: simplified model and finite-element (FE) model. Simplified models are used to understand the global behavior, such as the lateral force-displacement relationship [3, 29, 30]; while FE models allow for local structural damage assessment [24, 25, 31]. This paper focuses on evaluating potential damage and failure modes for SPPC piers, therefore a nonlinear FE approach is used.

The primary objectives of the current paper include (1) development of a FE model capable of capturing not only global responses, including lateral stiffness versus displacement, post-tension force versus lateral displacement, but also the strain responses of concrete, ED bars and post-tension (PT) strands of SPPC columns; (2) validation of the FE model against the experimental data obtained from quasi-static testing of SPPC piers tested in previous experimental programs [5, 6, 10]; (3) evaluation of the effect of ED bar on the global behaviour and limit states of SPPC piers.

2 Finite Element Model

Finite element software ABAQUS/Standard was used to develop a 3D non-linear FE model for the SPPC bridge pier in this study. The developed FE model features the ability to assess both the global behaviour and local damages of SPPC piers. Figure 1 shows a typical SPPC bridge pier assembly in ABAQUS.

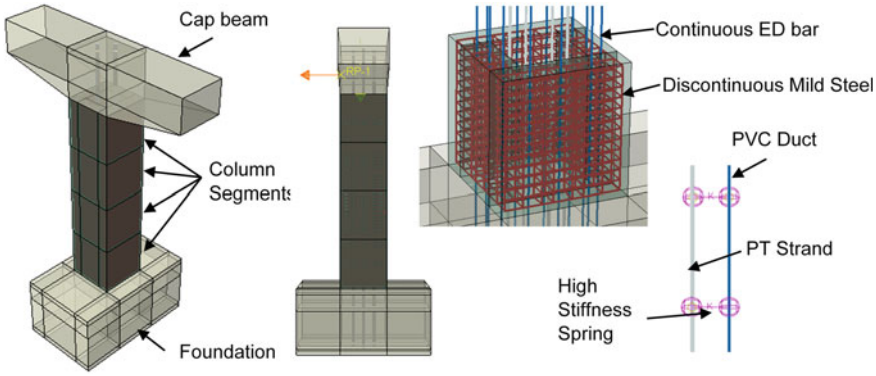

Fig. 1 Typical SPPC bridge pier assembly

2.1 Geometry, Element Modeling, and Meshing

The model consists of a cap beam, column segments, foundation, PT strands, PVC ducts, mild steel rebars and optional ED bars. The cap beam, column segments and foundation were modelled using first-order 8-node, 3D hexahedral linear elements with reduced integration and hourglass control (C3D8R). The beam and foundation were expected to behave elastically throughout the loading process and were defined using elastic concrete properties. On the other hand, column segments were assigned both elastic and plastic concrete properties in order to analyze the damage due to rocking. Post-tensioning strands and PVC ducts were modelled using 2-node linear beam elements (B31). PT strands were assigned with material properties as will be discussed later, while PVC ducts were given a small elastic modulus. 2-Node linear truss elements (T3D2) were used to simulate mild steel reinforcement and ED bars. They were both defined using the corresponding steel properties.

All concrete elements were meshed with a mesh size of 50.8 mm, except for the bottom column segment which used the mesh size of 25.4 mm. The finer mesh in the bottom column segment was used to better capture the concrete damage near the rocking surface. The mesh size for all reinforcement bars, ED bars, post-tensioning strands and PVC ducts were selected to be 25.4 mm.

2.2 Material Constitutive Modeling

2.2.1 Concrete

The elasticity limit for compression was assumed to be 45% of the concrete design strength (50 and 35 MPa) as per ACI 318-19. The tensile stress–strain relationship is assumed linear up until the tensile strength (4.3 and 3.2 MPa) was reached. The

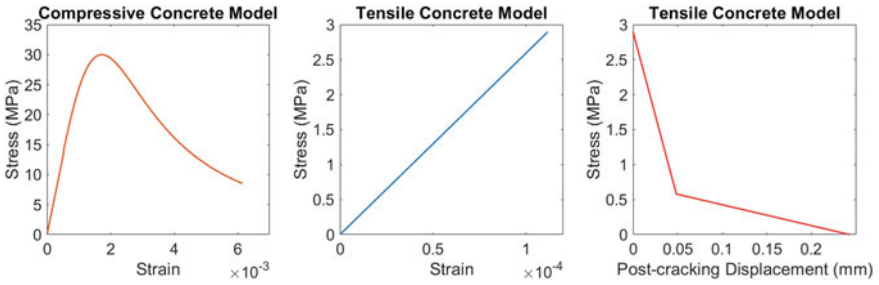

Fig. 2 Concrete model

Young's modulus of concrete was calculated as per ACI 318-19 [32]. The unconfined concrete constitutive model developed by Popovics [33] was selected to define the inelastic compression stress–strain relationship [33]. Figure 2a shows the stress–strain curve for 30 MPa compressive strength concrete. Tension softening behaviour was denied as a function of crack opening as per FIB [34]. Figure 2b, c show the tensile concrete model for 30 MPa compressive strength concrete.

Concrete damaged plasticity (CDP) was selected to model the nonlinearity of concrete in *ABAQUS/Standard* [35]. The CDP model uses isotropic hardening and non-associated flow rule. The yield criterion proposed by Lubliner et al. [36] with the modifications of Lee and Fenves [37] was adopted. The ratio of initial equibiaxial compressive yield stress to initial uniaxial compressive yield stress, f_{bo}/f_{co}, and the tensile-to-compressive meridian stress ratio, K_c were determined as 0.65 and 0.64 per Lim et al. [38]. The dilation angle, eccentricity, and viscosity parameter were set to be 37°, 0.1, and 0.001, respectively.

2.2.2 Non-continuous and Energy Dissipation Bars

The nonlinear tensile constitutive models for both non-continuous and ED bars were defined by Mander [39]. The Young's modulus and Poisson's ratio for steel were set to be 200,000 MPa and 0.3, respectively. Figure 3 shows the stress–strain relationship for Grade 60 steel bar. The fracture strain limit was set to be 0.09 as per ASTM A615/A615 [40].

2.2.3 Post-Tension Strand-Anchorage Assembly

PT strands were 7-wire 15.2 mm, 1,860 MPa low-relaxation strands. A constitutive model for the PT strand was developed by [31] to consider the pre-stress loss due to anchorage wedge-seating and strand inelasticity. Although the ultimate strain is 0.035 as per ASTM A416/A416M-18 [41], the recommended design strain for PT strand is 0.01, considering the premature failure due to stress concentration at anchorage [31]. Figure 4 shows the stress–strain relationship of one PT strand with an initial stress of 635 MPa.

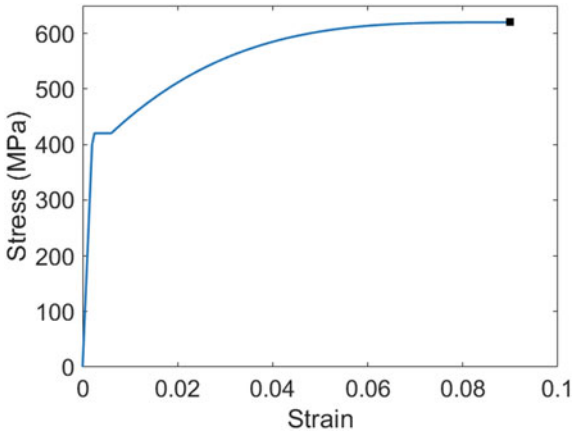

Fig. 3 Stress–strain relationship of grade 60 steel bar

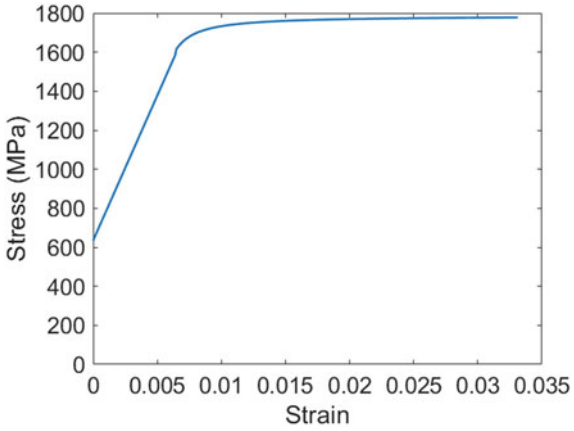

Fig. 4 Stress–strain relationship of 15.24 mm PT strand with 635 MPa initial stress

2.3 Contact Interactions and Constraints

Both cap beam and foundation were considered as a rigid body with reference points located on the surface of the cap beam and the bottom edge of the foundation, respectively. A small region near the contact-interfaces with column segments was excluded when the rigid body constraint is defined. The depth of the non-rigid region was set to be 101.6 mm for the model without ED bars, whereas it was set to be equal to the length of unbonded ED bars for the model with ED bars. Embedded constraints were used between concrete segments/reinforcement bars and PVC ducts. For ED bars, a portion near the rocking surface was left unbonded to reduce the

stress concentration, which would cause a premature fracture. The unbonded portions remained unconstrained by the surrounding concrete. To unbond PT strands from concrete, a small portion on each end of PT strands was embedded to the cap beam to model the anchorage system. The anchorage slip was included when defining the constitutive model of the PT strand anchorage assembly. The unbonded length of PT strands was kept as same as in the experiments. To mimic the hard contact between PT strand and PVC ducts (i.e., limit the lateral movement of strands within the ducts), rigid links/springs with high stiffness were used to connect PVC ducts and PT strands at a number of discrete points along the length of PT strands, as shown in Fig. 1. Surface-to-surface contact formulation was used to allow finite sliding between concrete segments. The behaviour in the tangential direction was modelled using the Coulomb friction model with a constant friction coefficient of 0.5. For the normal direction, the hard contact, pressure-overclosure relationship was selected because it can avoid tensile stress to be created once separation occurs and can minimize penetration.

2.4 Boundary and Loading Conditions

Fix-end boundary condition was applied on the bottom face of the foundation, which restrained the translations and rotations in all directions. Axial load was applied to the structure as per the experimental set-up [5, 6, 10]. Lateral displacement was applied to a reference point on the cap beam at the height that matches with the experimental setup, as shown in Fig. 1. The initial post-tension force was applied on each strand in the form of predefined tensile stress.

2.5 Analysis Methods and Loading Steps

The analysis was conducted using the standard solver provided by *ABAUQUS/Standard* [35]. Two loading steps were used for the analysis in the FE model. During the first step, gravity loads, initial post-tension force and fixed-end constraint were applied. In the second step, the displacement-controlled lateral loading was applied at the mid-height of the rigid cap beam.

3 Model Validation

Two sets of test data from Ou et al. [5, 6] and Yang and Okumus [10] were used to examine the effectiveness of the developed FE modelling techniques to simulate the behaviour of SPPC piers. Table 1 summarizes the design parameters of the two experiments. The predicted damage conditions, such as concrete spalling, concrete

Table 1 Summary of design parameters used in the tested specimens

Reference	Designation	Compressive strength of concrete	Aspect ratio	Gravity load	Initial PT force	PT strand ratio	ED bar ratio	Yield strength of ED bar	Transverse volumetric reinforcing ratio
		$f_c^{'}$	L/D	$P/f_c^{'}A_g$	$f_{pu}A_{pt}$	–	–	f_{yED}	ρ_v
		MPa	–	%	%	%	%	MPa	%
Ou et al. [5, 6]	C5C	55	4.2	5	47	0.276	0.5	434	2.46
Yang and Okumus[10]	Specimen 1	35.2	4.8	2	34	0.434	0	–	2.64

crushing, yielding of PT strands were examined against the experiments. The lateral force-drift ratio relationship and the variation of post-tension force versus drift ratio were also compared between FE models and experimental measurements.

3.1 Damage Assessment

In general, the developed FE model was capable of predicting the damage conditions of SPPC piers. For the test conducted by Ou et al. [5, 6], the first spalling of cover concrete was observed at a drift ratio of 4% during the experimental test. In the numerical analysis, the ultimate unconfined concrete strain is assumed to be the strain when compression stress decreases to 50% in the softening portion [31]. Using this method, the concrete spalling occurred at the drift ratio of 3.5% as per the FE analysis results, which is similar to the experimental observation. The first ED bar fracture was reported at the drift ratio of 5%. The calculated drift ratio when the first ED bar fracture was approximated 5.4% based on FE analysis results, and this is similar to the experimental observation. For Specimen 1 [10], both the experiment and FE analysis results showed that concrete spalling was concentrated at the bottom segment near the rocking edge. The minor concrete spalling that occurred at upper segments observed during the test was mainly due to the sudden shear slip, therefore was not captured in the FE model. No PT strand fracture was observed using FE analysis results, which match the experimental observation.

3.2 Lateral Force and Drift Ratio Relationship

A comparison between the predicted and measured lateral forces versus drift ratios of the aforementioned pier specimens are presented in Fig. 5. It is found that the FE model over-estimated the lateral strength by 13.4% and 13.8% for specimens C5C and 1, respectively. This overprediction is mainly because the static pushover analysis does not account for the accumulated damages due to cyclic loading. The difference may also stem from the uncertainties in material properties. In general,

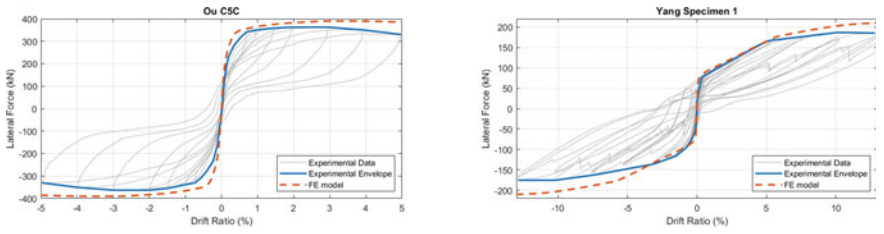

Fig. 5 Lateral force versus drift ratio for tested SPPC specimens: **a** C5C and **b** Specimen 1

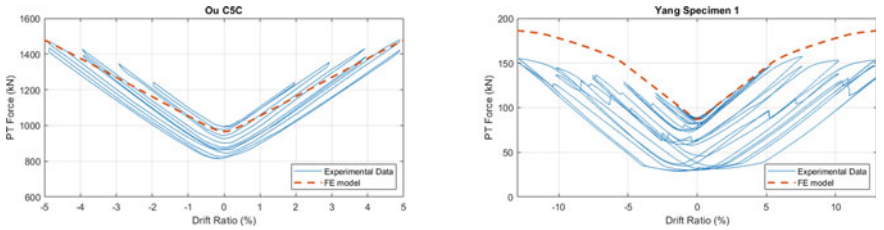

Fig. 6 Average post-tension force of strands for tested SPPC specimens: **a** C5C and **b** Specimen 1

the FE model is capable to predict the overall load-displacement response obtained from testing with acceptable errors.

3.3 Post-tension Force and Drift Ratio Relationship

Figure 6 shows a comparison between the FE and experimental post-tension forces. For the C5C specimen, the predicted post-tension forces match quite well with their experimental counterparts. The percentage of error ranges from −5.5 to +3.1%. For Specimen 1, the post-tension force was in good agreement with the experimental measurement up to 5% drift ratio. However, the FE model over-estimated the post-tension force for drift ratios larger than 5%. The difference between the FE model and experimental measurement can be explained by the fact that the FE model did not account for concrete loss at the rocking edge due to concrete crushing, which reduces the cross-section depth and shifts the rocking toe towards the inside of the cross section. The post-tension loss due to anchorage seating and strand inelasticity also contributed to this difference.

4 Effects of Energy Dissipation Bars on Damage States

This section selected specimen C5C as a reference to understand the influence of ED bars on the behaviour of SPPC structures. Two models were considered, one including ED bars (i.e., specimen C5C) and the other one without ED bars (i.e., specimen C5C with ED bars excluded). The analysis results are presented until the failure of the bridge pier occurs. The failure point is defined when any of three limit states is reached: confined concrete crushing, first ED bar fracture and first PT strand fracture. Five damage states were considered in this study, and they are first ED bar yield, concrete cover spalling, first PT strand yield, first ED bar fracture and first PT strand fracture. Figure 7a compares their force-drift ratio relationships. The inclusion of ED bars leads to an up to 44% increase in the lateral strength. The failure of the model with ED bar occurred at 5.5% drift ratio and is due to ED bar fracture;

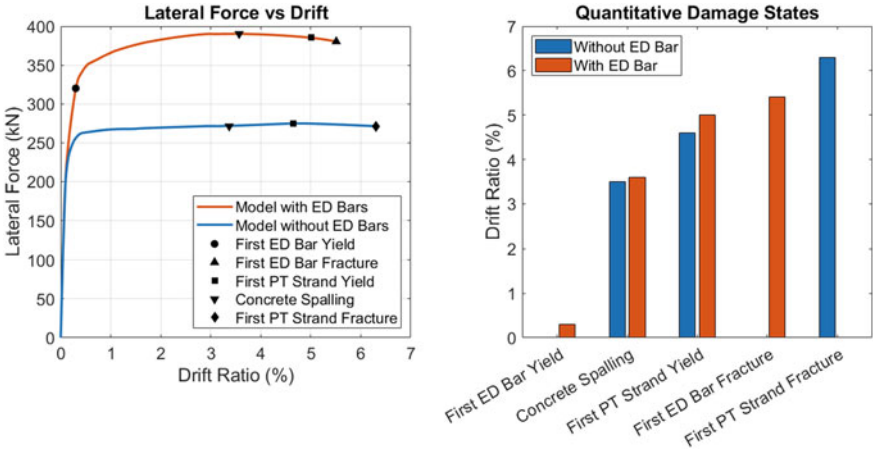

Fig. 7 Damage state comparison for SPPC pier with and without ED bars

whereas the failure of the model without ED bar was caused by PT strand fracture and concrete crushing, both occurred at 6.3% drift ratio. The addition of ED bars results in a lower ductility, which is consistent with the experimental observation of [42]. Figure 7b shows the drift ratio, at which five damage states occur. In general, including ED bars can enhance the damage tolerance of SPPC piers by postponing the PT strand yielding by 0.5% drift ratio. However, the influence of ED bars on concrete spalling is negligible.

Figures 8 and 9 show the principal compressive and tensile strain at the interface between the bottom segment and foundation, as obtained from the FE analysis. Concrete cover spalling occurred at the rocking side of the segment. It was observed that the presence of ED bars could help to reduce the strain concentration in concrete and spread over the contact surface. From the principal tensile strain plot, the tensile crack occurred near the location of the ED bar. This is because unlike the discontinuous mild steel, the ED bar is continuous between the bottom column segment and foundation.

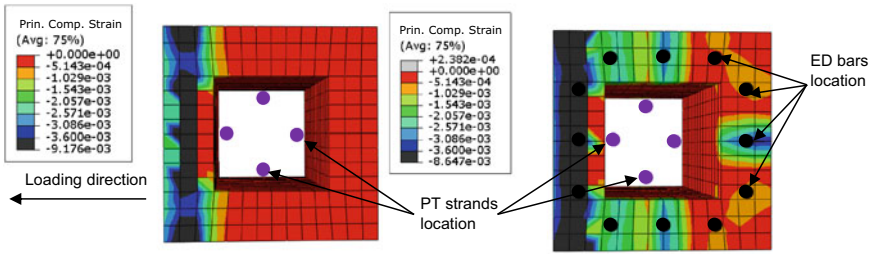

Fig. 8 Comparison of principal compressive strain at bottom interface at 5% drift ratio for SPPC pier with and without ED bars

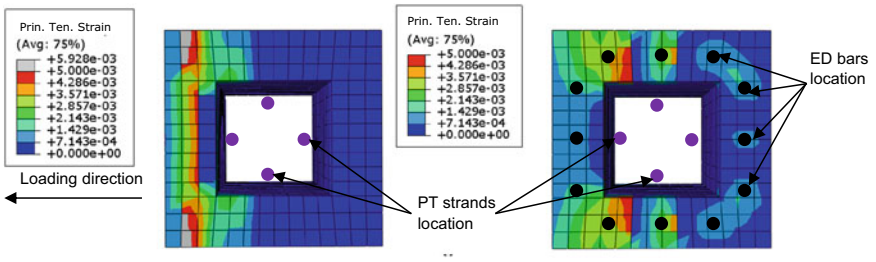

Fig. 9 Comparison of principal tensile strain at bottom interface at 2% drift ratio for SPPC pier with and without ED bars

5 Conclusion and Future Work

This paper first developed a non-linear FE model to understand the damage states of SPPC piers. Next, previous laboratory test results are used to validate the accuracy of the developed modelling techniques. Finally, the validated FE model is used to investigate the influence of energy dissipation bars on the damage condition and failure modes of SPPC piers. The major conclusions are as follows:

- The FE model exhibits good agreement with the experimental results in terms of damage condition, lateral force and drift ratio relationship, and post-tension force.
- The analysis results show that adding ED bars to the SPPC piers enhance the damage tolerance of SPPC piers by delaying the PT strand yielding and concrete spalling for SPPC piers.

Acknowledgements This research was supported by the Faculty of Engineering at McMaster University. The results, conclusions and opinions given in this paper are the ones of the authors and do not necessarily reflect the views of the funding agencies and the parties acknowledged.

References

1. Marsh ML, Stanton JF, Wernli M, Eberhard MO, Garrett BE, Weinert MD (2011) Application of accelerated bridge construction connections in moderate-to-high seismic regions. In: Application of accelerated bridge construction connections in moderate-to-high seismic regions. https://doi.org/10.17226/14571
2. Zhang Q, Alam MS (2020b) State-of-the-art review of seismic-resistant precast bridge columns. J Bridg Eng 25(10):03120001. https://doi.org/10.1061/(asce)be.1943-5592.0001620
3. ElGawady MA, Asce M, Sha'lan A (2011) Seismic behavior of self-centering precast segmental bridge bents. https://doi.org/10.1061/(ASCE)BE.1943-5592.0000174
4. Marriott D, Pampanin S, Palermo A (2009) Quasi-static and pseudo-dynamic testing of unbonded post-tensioned rocking bridge piers with external replaceable dissipaters. Earthq Eng Struct Dyn 38:331–354. https://doi.org/10.1002/eqe.857
5. Ou Y-C, Tsai M-S, Chang K-C, Lee GC (2010) Cyclic behavior of precast segmental concrete bridge columns with high performance or conventional steel reinforcing bars as energy dissipation bars. Earthq Eng Struct Dyn 39:1181–1198. https://doi.org/10.1002/eqe.986
6. Ou YC, Wang PH, Tsai MS, Chang KC, Lee GC (2010) Large-scale experimental study of precast segmental unbonded posttensioned concrete bridge columns for seismic regions. J Struct Eng 136(3):255–264. https://doi.org/10.1061/(ASCE)ST.1943-541X.0000110
7. Palermo A, Pampanin S, Marriott D (2007) Design, modeling, and experimental response of seismic resistant bridge piers with posttensioned dissipating connections. J Struct Eng 133(11):1648–1661. https://doi.org/10.1061/(asce)0733-9445(2007)133:11(1648)
8. Sideris P, Aref AJ, Filiatrault A (2014) Quasi-static cyclic testing of a large-scale hybrid sliding-rocking segmental column with slip-dominant joints. J Bridg Eng 19(10):04014036. https://doi.org/10.1061/(asce)be.1943-5592.0000605
9. Wang Z, Wang J, Zhu J, Zhao G, Zhang J (2020) Energy dissipation and self-centering capacities of posttensioning precast segmental ultra-high performance concrete bridge columns. Struct Concr 21(2):517–532. https://doi.org/10.1002/suco.201900024
10. Yang C, Okumus P (2017) Ultrahigh-performance concrete for posttensioned precast bridge piers for seismic resilience. J Struct Eng (U S) 143(12):1–13. https://doi.org/10.1061/(ASCE)ST.1943-541X.0001906
11. Bu Z, Guo J, Zheng R, Song J, Lee GC (2016) Cyclic performance and simplified pushover analyses of precast segmental concrete bridge columns with circular section. Earthq Eng Eng Vib 15(2):297–312. https://doi.org/10.1007/s11803-016-0323-3
12. Motaref S, Saiidi MS, Sanders DH (2010) Experimental study of precast bridge columns with built-in elastomer. Transp Res Rec: J Transp Res 2202:109–116. https://doi.org/10.3141/2202-14
13. Chou CC, Chen YC (2006) Cyclic tests of post-tensioned precast CFT segmental bridge columns with unbonded strands. Earthquake Eng Struct Dynam 35(2):159–175. https://doi.org/10.1002/eqe.512
14. Yang C, Okumus P, Ren R (2019) A hysteretic model for self-centering precast concrete piers with varying shear-slip between segments. Eng Struct 188:350–361. https://doi.org/10.1016/j.engstruct.2019.01.053
15. Cheng C-T, Chen F-L (2014) Seismic performance of a rocking bridge pier substructure with frictional hinge dampers. Smart Struct Syst 14(4):501–516. https://doi.org/10.12989/SSS.2014.14.4.501
16. Guo W, Zeng C, Gou H, Hu Y, Xu H, Guo L (2019) Rotational friction damper's performance for controlling seismic response of high speed railway bridgetrack system. CMES-Comput Model Eng Sci 120(3):491–515. https://doi.org/10.32604/cmes.2019.06162
17. CSA (2019) Canadian highway bridge design code. Canadian Stadards Association
18. NZT (2016) New Zealand bridge manual. Transit New Zealand
19. Billah AHMM, Alam MS (2016) Performance-based seismic design of shape memory alloy-reinforced concrete bridge piers. I: development of performance-based damage states. J Struct Eng 142(12):04016140. https://doi.org/10.1061/(asce)st.1943-541x.0001458

20. Kim TH, Kim YJ, Kang HT, Shin HM (2007) Performance assessment of reinforced concrete bridge columns using a damage index. Can J Civ Eng 34(7):843–855. https://doi.org/10.1139/L07-003
21. Lehman D, Moehle J, Mahin S, Calderone A, Henry L (2004) Experimental evaluation of the seismic performance of reinforced concrete bridge columns. J Struct Eng 130(6):869–879. https://doi.org/10.1061/(ASCE)0733-9445(2004)130
22. Mackie KR, Stojadinovic B (2007) Performance-based seismic bridge design for damage and loss limit states. Pac Conf Earthq Eng 36(13):1953–1971. https://doi.org/10.1002/eqe
23. Sheikh MN, Tsang HH, McCarthy TJ, Lam NTK (2010) Yield curvature for seismic design of circular reinforced concrete columns. Mag Concr Res 62(10):741–748. https://doi.org/10.1680/macr.2010.62.10.741
24. Dawood H, ElGawady M, Cofer W (2011) Seismic behavior and design of segmental precast post-tensioned concrete pier (64)
25. Kwan W-P, Billington SL (2003) Unbonded posttensioned concrete bridge piers. I: monotonic and cyclic analyses. J Bridg Eng 8(2):92–101. https://doi.org/10.1061/(asce)1084-0702(2003)8:2(92)
26. Lee WK, Billington SL (2010) Performance-based earthquake engineering assessment of a self-centering, post-tensioned concrete bridge system. Earthquake Eng Struct Dynam 40(8):887–902. https://doi.org/10.1002/eqe
27. Zhang Q, Alam MS (2020a) Performance-based seismic design of hybrid rocking precast performance-based seismic design of hybrid rocking, pp 1–12
28. Wang H-C, Ou Y-C, Chang K-C, Lee GC (2008) Large-scale seismic tests of tall concrete bridge columns with precast segmental construction. Earthq Eng Struct Dyn 37(12):1449–1465. https://doi.org/10.1002/eqe
29. Hewes JT, Priestley MJN (2002) Seismic design and performance of precast concrete segmental bridge columns
30. Wang Z, Wang J, Tang Y, Gao Y, Zhang J (2019) Lateral behavior of precast segmental UHPC bridge columns based on the equivalent plastic-hinge model. J Bridg Eng 24(3):04018124. https://doi.org/10.1061/(asce)be.1943-5592.0001332
31. Yang C (2019) Reducing earthquake-induced damage to precast concrete bridge piers. University at Buffalo, The State University of New York
32. ACI 318-19 (2019) Building code requirements for structural concrete (ACI 318-19). In: 318-19 Building code requirements for structural concrete and commentary. American Concrete Institute. https://doi.org/10.14359/51716937
33. Popovics S (1973) A numerical approach to the complete stress-strain curve of concrete. Cement and Concrete Research, 3(5):583–599. https://doi.org/10.1016/0008-8846(73)90096-3
34. FIB (2010) fib model code for concrete structures 2010. International Federation for Structural Concrete. https://doi.org/10.16309/j.cnki.issn.1007-1776.2003.03.004
35. Dassault Systèmes Simulia (2018) ABAQUS/Standard
36. Lubliner J, Oliver J, Oller S, Oñate E (1989) A plastic-damage model for concrete. Int J Solids Struct 25(3):299–326. https://doi.org/10.1016/0020-7683(89)90050-4
37. Lee J, Fenves GL (1998) Plastic-damage model for cyclic loading of concrete structures. J Eng Mech 124(8):892–900. https://doi.org/10.1061/(asce)0733-9399(1998)124:8(892)
38. Lim JC, Ozbakkaloglu T, Gholampour A, Bennett T, Sadeghi R (2016) Finite-element modeling of actively confined normal-strength and high-strength concrete under uniaxial, biaxial, and triaxial compression. J Struct Eng 142(11):04016113. https://doi.org/10.1061/(asce)st.1943-541x.0001589
39. Mander JB (1983) Seismic design of bridge piers. University of Canterbury, New Zealand
40. ASTM A615/A615-20 (2020) Standard specification for deformed and plain carbon-steel bars for concrete reinforcement. https://doi.org/10.1520/A0615_A0615M-20
41. ASTM A416/A416M-18 (2018) Standard specification for low-relaxation, seven-wire steel strand for prestressed concrete. https://doi.org/10.1520/A0416_A0416M-18
42. Wang J, Wang Z, Tang Y, Liu T, Zhang J (2018) Cyclic loading test of self-centering precast segmental unbonded posttensioned UHPFRC bridge columns. Bull Earthq Eng 16(11):5227–5255. https://doi.org/10.1007/s10518-018-0331-y

Analysis of Retrofitted Concrete Columns Using 3D Elastic-Plastic-Damage Modelling

Z. Al-Maadhidi and R. E. Erkmen

1 Introduction

The performance of the concrete columns is the primary factor affecting the structural response under extreme loadings such as earthquakes or blasts. Upgrading the columns during their lifetime may be required due to damage or deterioration or to improve the performance. Inadequate column behaviour can happen due to inappropriate design or construction, and due to durability-related issues. Confining concrete is a common practice in structural retrofitting applications and the use of Fiber Reinforced Polymer (FRP) composites as wraps or jackets for concrete columns has become a very popular technique [7, 9, 18]. Moreover, its installation is simple which makes FRP jacketing an efficient technique for retrofitting columns. FRP is superior in many aspects compared to other types of jacketing such as steel jacketing and concrete jacketing due to their high strength, non-corrosive nature for external surfaces and durability.

For design purposes, numerical modelling is often necessary to predict the behaviour of columns. For finite element structural modelling purposes several uniaxial stress–strain relationships have been developed for confined concrete including the works of [2, 8, 20]. Such models require an a-priori estimate of the confinement pressure which however depends on the local stress distribution. On the other hand, elastic-plastic-damage based constitutive laws have been applied extensively for the description of progressive failure of concrete. 3D elasto-plastic damage models have the capability of capturing the confined concrete behaviour naturally as a result of the stress distribution as the stress–strain relations are developed considering the multi-axial states. Furthermore, the evolution of the internal parameters

Z. Al-Maadhidi · R. E. Erkmen (✉)
Department of Building, Civil and Environmental Engineering, Concordia University, Montreal, QC, Canada
e-mail: emre.erkmen@concordia.ca

S. Walbridge et al. (eds.), *Proceedings of the Canadian Society of Civil Engineering Annual Conference 2021*, Lecture Notes in Civil Engineering 240,
https://doi.org/10.1007/978-981-19-0507-0_38

in phenomenological plasticity and damage models can be related to underlying mechanisms within the material in a thermodynamically consistent manner, e.g., development of slip bands and dislocation systems causing plastic deformations or void nucleation and crack development causing stiffness degradation. Initial attempts to merge elastoplastic and damage constitutive models can be found in [13, 23]. Other coupled plasticity and damage models include the works of [3, 5, 9, 14, 16, 24, 25]. An efficient coupled elastoplastic damage model that is capable of simulating the behaviour of plain concrete was also developed by [12]. Recently [22], showed that the [12] model can be captured as a special case within the framework of [1] by imposing a kinematic condition between the strain components. In both [12, 22] a single failure surface, potential function and hardening/softening criterion can be adopted in order to characterize the inelastic behaviour of concrete, providing an efficient computational framework. Some other attempts for Elasto-Plastic-Damage modelling of concrete can be found in [5, 6, 17]. ABAQUS has included Elasto-Plastic-Damage models developed by [10, 14] as modelling options. In this paper, we implement the model developed in [22] for the behaviour of FRP jacketed confined concrete and compare it with the model of [11] that is implemented in ABAQUS.

2 Methodology

2.1 Finite Element Types, Boundary Condition and Loading

The concrete column models contain the concrete bulk, FRP jacketing as well as steel reinforcement which requires different types of elements to work together as they will be connected at the nodes. In the software developed, a four-node orthotropic shell-type element is used for the FRP sheets, a two-node beam-type element is used for the steel reinforcement and an 8-node solid element is used for the concrete bulk. The shell and solid elements contain drilling degrees of freedom so that all elements have compatible 6-DOFs. All FE-types have been implemented and assembled in FORTRAN.

In ABAQUS the bulk concrete is modelled as a homogeneous 8-node 3D brick element (C3D8R) and the longitudinal and transverse steel are modelled as linear truss element (T3D2). To model the CFRP jacket, the S8R shell element is used. To model the interaction between the concrete and the reinforcement, an embedded region constraint is used. The embedded contact region is used to make sure that the number of translational degrees of freedom at a node on the embedded element is identical to the number of translational degrees of freedom at a node on the host element (Compatible DOF). The reinforcement was embedded in the concrete, which is considered the host region. Therefore, the concrete and reinforcement share the same node where a perfect bond was assumed. The interaction between the concrete and the FRP jacket was considered as cohesive contact behaviour.

Mesh refinement studies were conducted for both FORTRAN and ABAQUS models to eliminate any significant effects of numerical errors due to spatial discretization. All the modelled columns were fixed in the bottom in all directions and released in the top except the top middle point where the loads were applied. In order to obtain the load-deflection behaviour of the modelled columns, a static monotonic load was placed on the mid-top of the column. The loading was applied until failure using the displacement control technique. Displacement increments were adjusted to 3 mm in each step.

2.2 Description of Material Models and Parameters

2.2.1 Concrete Compression Model Implemented in FORTRAN

The plastic model that determines the envelope curve for the stress–strain relationship consists of a potential surface, hardening law, which describes the deformation capacity in multiaxial compression, and a yield surface. We employ the yield surface proposed by [15] which is given as:

$$\Phi^p\left(\xi, \rho, \theta, \kappa_p\right) = \left(\sqrt{1.5}\rho\right)^2 + q_h(\kappa_p)m\left(\frac{\rho}{\sqrt{6}}r(\theta) + \frac{\xi}{\sqrt{3}}\right) - q_h(\kappa_p)q_s\left(\kappa_p\right) \leq 0 \tag{1}$$

where q_h and q_s controls the shape and location of the loading surface and m can be written as:

$$m = 3\frac{{f_c}^2 - {f_t}^2}{f_c f_t}\frac{e}{e+1} \tag{2}$$

in which f_c is the uniaxial compressive strength, f_t is the uniaxial tensile strength taken herein as $0.09 f_c$. Both the plastic potential and the yield surface are constituted by using the unified coordinates in the Haigh-Westergaard stress space, which are based on the stress invariants. The three coordinates ξ, ρ and θ can be expressed as:

$$\xi = \frac{I_1}{\sqrt{3} f_c} \tag{3}$$

$$\rho = \frac{\sqrt{2J_2}}{f_c} \tag{4}$$

$$\cos 3\theta = \frac{3\sqrt{3}}{2}\frac{J_3}{J_2^{3/2}} \tag{5}$$

where:

$$I_1 = \sigma_{11} + \sigma_{22} + \sigma_{33} \tag{6}$$

$$J_2 = \frac{1}{6}\left[(\sigma_{11} - \sigma_{22})^2 + (\sigma_{22} - \sigma_{33})^2 + (\sigma_{33} - \sigma_{11})^2\right] + {\tau_{12}}^2 + {\tau_{23}}^2 + {\tau_{31}}^2 \tag{7}$$

$$\begin{aligned} J_3 = &-\left(\frac{I_1}{3}\right)^3 + \left(\frac{I_1}{3}\right)^2 (\sigma_{11} + \sigma_{22} + \sigma_{33}) \\ &+\left(\frac{I_1}{3}\right)(\tau_{12}\tau_{12} + \tau_{13}\tau_{13} + \tau_{23}\tau_{23} - \sigma_{11}\sigma_{22} - \sigma_{11}\sigma_{33} - \sigma_{22}\sigma_{33}) \\ &-\tau_{13}\tau_{13}\sigma_{22} - \tau_{23}\tau_{23}\sigma_{11} - \tau_{12}\tau_{12}\sigma_{33} + 2\tau_{12}\tau_{13}\tau_{23} + \sigma_{11}\sigma_{22}\sigma_{33} \end{aligned} \tag{8}$$

The eccentricity e defined in the [15] model can be written as:

$$e = \frac{1+\epsilon}{2-\epsilon} \tag{9}$$

in which

$$\epsilon = \frac{f_t}{f_b}\frac{f_b^2 - f_c^2}{f_c^2 - f_t^2} \tag{10}$$

where f_b is the equibiaxial compressive strength taken herein as $1.5\,{f_c}^{-0.925}$. In Eq. 1, $r(\theta)$ is the polar radius as:

$$r(\theta) = \frac{v(\theta)}{s(\theta) + t(\theta)} \tag{11}$$

In which:

$$v(\theta) = 4\left(1 - e^2\right)\cos^2\theta + (2e-1)^2 \tag{12}$$

$$s(\theta) = 2\left(1 - e^2\right)\cos\theta \tag{13}$$

$$t(\theta) = (2e-1)\left[4\left(1 - e^2\right)\cos^2\theta + 5e^2 - 4e\right]^{1/2} \tag{14}$$

Hardening and softening of concrete can be simulated by varying the shape and location of the loading surface during plastic flow. The variation is controlled by the hardening/softening parameter κ_p. During the hardening range q_h in Eq. 1 for concrete can be selected as [17].

$$q_h(\kappa_p) = k_o + (1 - k_o)\sqrt{1 - \left(\frac{\varepsilon_{vo}^p - \kappa_p}{\varepsilon_{vo}^p}\right)^2} \tag{15}$$

where:

$$k_o = \sigma_{co}/f_c \tag{16}$$

in which σ_{co} is the uniaxial concrete stress at the onset of plastic flow. In Eq. 15, ε_{vo}^p is the threshold value for the volumetric plastic strain at uniaxial concrete strength defined as:

$$\varepsilon_{vo}^p = \frac{f_c}{E_c}(1 - 2\upsilon) \tag{17}$$

where E_c and υ are the Young's modulus and Poisson ratio for concrete, respectively. During softening range q_s in Eq. 1 for concrete can be selected as [17]:

$$q_s(\kappa_p) = \left(\frac{1}{1 + \left(\frac{n_1 - 1}{n_2 - 1}\right)^2}\right)^2 \tag{18}$$

where $n_1 = \frac{\kappa_p}{\varepsilon_{vo}^p}$, $n_2 = \frac{\varepsilon_{vo}^p + t}{\varepsilon_{vo}^p}$ and $t = \frac{f_c}{15000}$. Note that f_c is considered in MPa. The potential function is again written in Haigh-Westergaard stress space and adopted herein from [6] expressed as:

$$\Theta^p(\xi, \rho, q_p) = -A\left(\frac{\rho}{\sqrt{q_h(\kappa_p)q_s(\kappa_p)}}\right)^2 - B\frac{\rho}{\sqrt{q_h(\kappa_p)q_s(\kappa_p)}} + \frac{\xi}{\sqrt{q_h(\kappa_p)q_s(\kappa_p)}} \tag{19}$$

in which:

$$A = \frac{\psi_2 - \psi_1}{2(\rho_1 - \rho_2)} \tag{20}$$

$$B = \rho_1\frac{\psi_1 - \psi_2}{(\rho_1 - \rho_2)} - \psi_1 \tag{21}$$

In Eqs. 20 and 21, ρ_1 and ρ_2 are the normalized deviatoric stress indicators at uniaxial and triaxial compressive strength, respectively as:

$$\rho_1 = \sqrt{\frac{2}{3}} \tag{22}$$

and

$$\rho_2 = \sqrt{\frac{2}{3}} \frac{\left| f_{cc} - \sigma_{pc} \right|}{f_c} \tag{23}$$

where f_{cc} is the triaxial compressive strength taken herein as 4.333 f_c and σ_{pc} is the lateral stress taken herein as f_c. On the other hand, ψ_1 and ψ_2 are the inclinations of the plastic strain vector under uniaxial and triaxial compressive strength, respectively given as:

$$\psi_1 = \sqrt{2} \frac{\left| \varepsilon_{3pu} - \varepsilon_{1pu} \right|}{\varepsilon_{vo}^p} \tag{24}$$

and

$$\psi_2 = \sqrt{2} \frac{\left| \varepsilon_{3pc} - \varepsilon_{1pc} \right|}{\varepsilon_{vo}^p} \tag{25}$$

In the above equation ε_{3pu} is the axial plastic strain component at uniaxial compressive strength, which can be calculated as:

$$\varepsilon_{3pu} = \varepsilon_c - \frac{f_c}{E_c} \tag{26}$$

and ε_{1pu} is the lateral plastic strain component at uniaxial compressive strength, which is calculated as:

$$\varepsilon_{1pu} = \varepsilon_{2pu} = \frac{\varepsilon_{vo}^p - \varepsilon_{3pu}}{2} \tag{27}$$

In the equation above, ε_c is the total strain in the axial direction at uniaxial compressive strength and ε_{3pc} is the axial plastic strain component at triaxial compressive strength, which is defined as:

$$\varepsilon_{3pc} = \varepsilon_{cc} - \frac{1}{E_c}(f_{cc} - 2\upsilon\sigma_{pc}) \tag{28}$$

and ε_{1pc} is the lateral plastic strain component at triaxial compressive strength, that is obtained from:

$$\varepsilon_{1pc} = \varepsilon_{2pc} = \frac{\varepsilon_{vo}^{p} - \varepsilon_{3pc}}{2} \tag{29}$$

For concrete, it can be assumed that $\varepsilon_{cc} = \varepsilon_c\left(1 + 17\frac{\sigma_{pc}}{f_c}\right)$, e.g., [17] and generally σ_{pc} is taken as $\sigma_{pc} = f_c$, and thus in Eq. 28 ε_{cc} becomes $\varepsilon_{cc} = 18\varepsilon_c$. The damage parameter ϕ is updated after every converged step. For this purpose, we have adopted the relationship given in [5] defined as:

$$\varphi = \left(1 - e^{-C\frac{\kappa_p}{\varepsilon_{vo}^{p}}}\right) \tag{30}$$

In which C is a parameter that is to be calibrated based on stiffness degradation.

2.2.2 Concrete Compression Model Implemented in ABAQUS

To define the plasticity model of concrete in ABAQUS, there are some fundamental parameters that need to be defined. Those parameters are the dilation angle (ψ), the plastic potential eccentricity (e), the ratio of initial equibiaxial compressive yield stress to initial uniaxial compressive yield stress (fb_o/fc_o), the ratio of the second stress invariant on the tensile meridian which controls the shape of the yield surface (K_c), and the viscosity (μ). The dilation angle was used as 31 based on calibration. The eccentricity e, (fb_o/fc_o),K_c and μ were defined as 0.1, 1.16, 2/3, and zero respectively [4].

In order to obtain the compressive behaviour for confined concrete, a design-oriented stress–strain model is used [11]. The first part of the stress–strain curve is a parabolic line and the second part is a straight line. The slope of the parabola line is the modulus of elasticity of the unconfined concrete. The parabolic line meets the straight line smoothly so there is no change in slope between the two portions. For simplicity, the intersection point of the two lines represents the unconfined compressive strength $f_{co}^{'}$. The stress–strain curve ends at a point where both the ultimate compressive strength $f_{cc}^{'}$ and the ultimate axial strain ε_{cu} of the confined concrete are reached.

In 3D Elasto-Plastic Damage models, the behaviour is imposed according to yield-surface, potential surface, hardening etc. However, these imposed conditions can be adjusted to follow certain stress–strain behaviour.

The uniaxial stress–strain behaviour in [10] model satisfies the following equations:

$$\sigma_c = \begin{pmatrix} E_c\varepsilon_c - \frac{(E_c - E_2)^2}{4f_{co}^{'}}\varepsilon_c^2 (0 \le \varepsilon_c \le \varepsilon_t) \\ f_{co}^{'} + E_2\varepsilon_c (\varepsilon_t \le \varepsilon_c \le \varepsilon_{cu}) \end{pmatrix} \tag{31}$$

where:

$$\varepsilon_t = \frac{2f_{co}^{'}}{E_c - E_2} \tag{32}$$

and

$$E_2 = \frac{f_{cc}^{'} - f_{co}^{'}}{\varepsilon_{cu}} \tag{33}$$

In the equation above σ_c is the axial stress, ε_c is the axial strain of confined concrete, E_c is the elastic modulus of unconfined concrete, ε_t is the axial strain at the transition point, and E_2 is the slope of the straight line of the curve. In this model $f_{cc}^{'}$ is obtained from [21] as:

$$\frac{f_{cc}^{'}}{f_{co}^{'}} = 1 + k_1 \frac{f_l}{f_{co}^{'}} \tag{34}$$

where f_l is the confining pressure. Also, the value of K_1 is considered as 3.3 [11]. To calculate the ultimate axial strain of uniformly confined concrete ε_{cu}, the following equation is utilized:

$$\frac{\varepsilon_{\text{cu}}}{\varepsilon_{\text{co}}} = 1.75 + K_2 \frac{f_l}{f_{co}^{'}} \left(\frac{\varepsilon_{h,\text{rup}}}{\varepsilon_{\text{co}}}\right)^{0.45} \tag{35}$$

In which ε_{co} is the axial strain at the compressive strength of unconfined concrete, and K_2 is the strain enhancement coefficient. The value of those two parameters is 0.002 and 12 respectively [10].

2.2.3 Reinforcement

For the steel reinforcement, a simpler elastic-perfectly plastic model without strain hardening behaviour is employed. A uniaxial associated plasticity model was used accordingly.

2.2.4 FRP Jacket

FRP is modelled in both FORTRAN and ABAQUS models as unidirectional lamina composites. A unidirectional Lamina is considered as a homogenous body and consisting of continuous fibres strongly bonded in a matrix. The FRP jacket is modelled as linear elastic orthotropic material, which means that the mechanical properties of the material are different in different directions. Modulus of elasticity, shear modulus and Poisson ratio respectively are 260 MPa, 100 MPa and 0.3 respectively.

3 Case Study

In order to evaluate the performance of the numerical model before and after retrofitting, experimental data reported in [19] was used. This experimental program consisted of 42 prismatic concrete columns. Most of the columns were strengthen by internal steel reinforcement and external FRP wrapping. All the tested columns have the same geometry of square cross-section of 200 mm, 320 mm height, and 30 mm corner radius. The specimens that were selected in this research for validation purposes were subjected to monotonic compression load until failure. The compressive strength and the elastic modulus of concrete are 25.5 MPa and 19.3 GPa respectively. The steel nominal yield stress is 500 MPa and the elastic modulus is 200 GPa. For the FRP, the thickness of each layer is 0.117 mm and the tensile modulus is 240 GPa.

The reinforced concrete columns contained transverse and longitudinal reinforcement. The longitudinal reinforcement has a 14 mm diameter. Whereas the transverse reinforcement has a diameter of 8 mm. The spacing distance was 95 mm for transverse stirrups that was symbolized as S2 (Table 1).

3.1 Validation of the Numerical Model

The numerical model implemented in FORTRAN was validated against experimental results and the ABAQUS model. Figures 1, 2 and 3 illustrate the stress–strain curve at mid-span for retrofitted columns. The model was tested for three different

Table 1 Details and notation of the specimens that used for the numerical validations

Specimen label	Steel bars & stirrups	CFRP sheet layers	Jacket nominal thickness mm
BS2	4∅14&8∅/95	–	–
BC5	–	5	0.585
BS2C5	4∅14&8∅/95	5	0.585

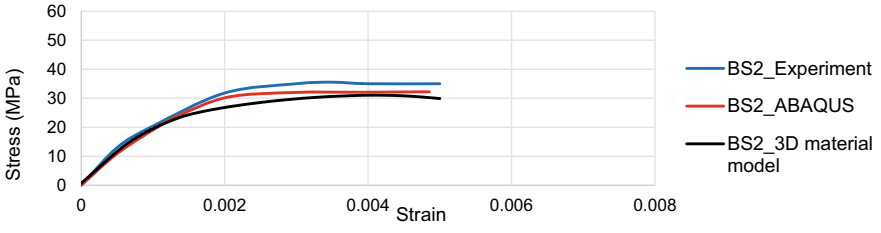

Fig. 1 Stress–strain curve for Reinforced concrete column (S2)

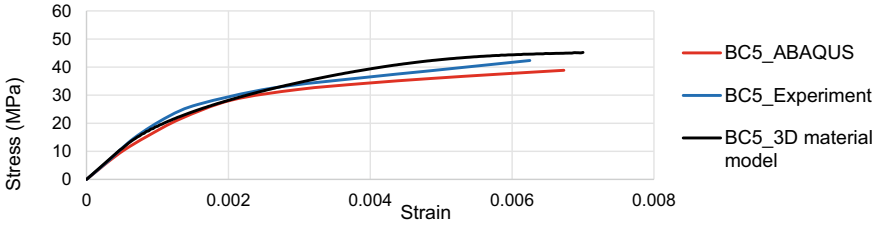

Fig. 2 Stress–strain curve for concrete column wrapped with five layer of FRP jacket (BC5)

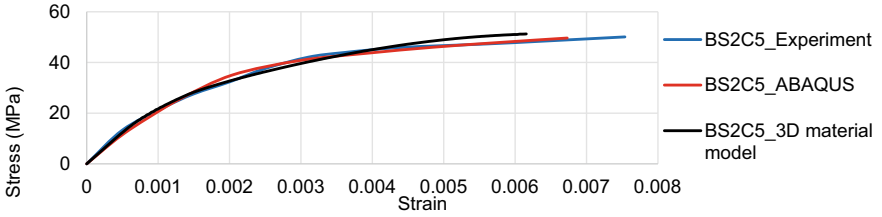

Fig. 3 Stress–strain curve for reinforced concrete column wrapped with five layers of FRP jacket (BS2C5)

column types; reinforced columns, confined columns with FRP jackets, and reinforced columns with FRP jackets. It is clear from the figures that the finite element numerical model has the ability to capture the behaviour of concrete columns before and after FRP retrofitting.

3.2 Parametric Study

A parametric study was conducted to test the sensitivity of the mesh size on the stress–strain curve of a confined reinforced concrete column with FRP layers. In Fig. 4, the numerical results of the stress–strain curve for BS1C5 are illustrated with

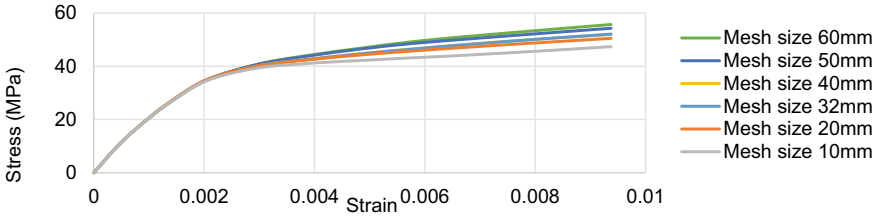

Fig. 4 Stress–strain curve of FE analysis response for BS1C5 when using different mesh size in ABAQUS

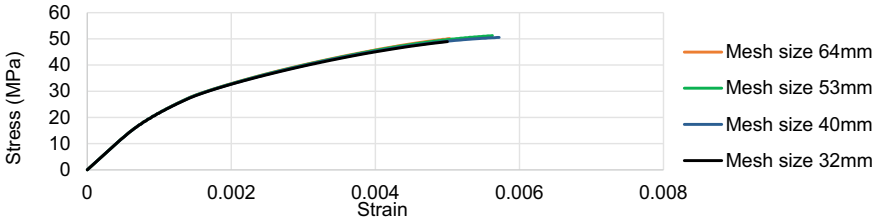

Fig. 5 Stress–strain curve for BS2C5 when using different mesh size using 3D material model

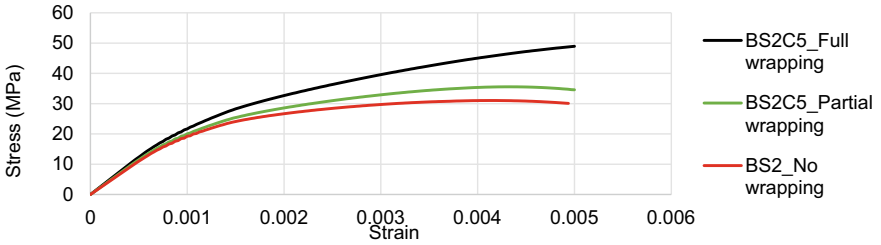

Fig. 6 Comparing the behaviour of partially wrapped reinforced concrete column (BS2C5) with fully wrapped and not wrapped cases using 3D material model

60, 50, 40, 32, 20, and 10 mm using ABAQUS software. Whereas, Fig. 5 shows the mesh sensitivity for BS2C5 using the 3D material model with 64, 53, 40, and 32 mm. As the mesh sensitivity depends on the finite element types the discrepancies between ABAQUS results can also be attributed to differences in element types. On the other hand, our 3D material model was also employed for a partially wrapped reinforced concrete case (BS2C5) and the behaviour was compared with fully and unwrapped cases in Fig. 6. The width of the FRP was 32 mm and the vertical spacing of the FRP strips was 32 mm which started from the bottom of the column.

4 Conclusion

3D elasto-plastic damage models are particularly suitable for the modelling and analysis of retrofitted concrete columns as confinement pressure is generally unknown before the analysis, which depends on the size, shape, loading, boundary conditions as well as material properties. This paper mainly focused on the validation and applicability of a 3D elasto-plastic damage model. It was shown that in simulating the behaviour of retrofitted columns with FRP composites under monotonic axial compressive loading, the results of the 3D elasto-plastic damage model proposed in this study agree well with those of the ABAQUS model and the experimental results. Such sophisticated 3D modelling approaches are required especially when

design guidelines are not sufficient to address the specifics of the designed cases. To illustrate the applicability of the proposed concrete constitutive model a partially wrapped column case was analyzed, and its performance was compared against full wrapping and no wrapping cases. The parameters of the elasto-plastic damage-based concrete model were presented in detail. It is of interest to note that the calibration parameters of the model such as modulus of elasticity, the peak uniaxial compressive stress and the corresponding peak strain as well as hardening parameters of the yield surface and the slope of the potential surface in the rendulic plane are consistent with those reported in literature based on the corresponding concrete grade. Those parameters are pretty much agreed upon in literature and thus the proposed model can be used for general purpose analysis of concrete structural members.

Acknowledgements The authors acknowledge the financial support from Canadian Standards Association (CSA group).

References

1. Armero F, Oller S (2000) A general framework for continuum damage models. I. Infinitesimal plastic damage models in stress space. Int J Solids Struct 37(48–50):7409–7436
2. Attard MM, Setunge S (1996) Stress-strain relationship of confined and unconfined concrete. Mater J 93(5):432–442
3. Benallal A, Billardon R, Doghri I (1988) An integration algorithm and the corresponding consistent tangent operator for fully coupled elastoplastic and damage equations. Commun Appl Numer Methods 4(6):731–740
4. Demir A, Caglar N, Ozturk H, Sumer Y (2016) Nonlinear finite element study on the improvement of shear capacity in reinforced concrete T-Section beams by an alternative diagonal shear reinforcement. Eng Struct 120:158–165
5. Grassl P, Jirasek M (2006) Damage plastic model for concrete failure. Int J Solids Struct 43:7166–7196
6. Grassl P, Lundgren K, Gylltoft K (2002) Concrete in compression: a plasticity theory with novel hardening law. Int J Solids Struct 39:5205–5223
7. Ilki A, Peker O, Karamuk E, Demir C, Kumbasar N (2008) FRP retrofit of low and medium strength circular and rectangular reinforced concrete columns. J Mater Civ Eng (ASCE) 20(2):169–188
8. Isleem HF, Wang D, Wang Z (2018) Modeling the axial compressive stress-strain behavior of CFRP-confined rectangular RC columns under monotonic and cyclic loading. Compos Struct 185:229–240
9. Klisiński M, Mroz Z (1988) Description of inelastic deformation and degradation of concrete. Int J Solids Struct 24(4):391–416
10. Lam L, Teng JG (2003b)Design-oriented stress-strain model for FRP-confined concrete in rectangular columns. J Reinf Plast Compos 22(13):1149–1186
11. Lam L, Teng JG (2003) Design-oriented stress–strain model for FRP-confined concrete. Constr Build Mater 17(6–7):471–489
12. Lee J, Fenves GL (1998) Plastic-damage model for cyclic loading of concrete. J Eng Mech ASCE 124:892–900
13. Lemaitre J (1985) A continuous damage mechanics model for ductile fracture 83–89
14. Lubliner J, Oliver J, Oller S, Oñate E (1989) A plastic-damage model for concrete. Int J Solids Struct 25(3):299–326

15. Menetrey P, Willam KJ (1995) Triaxial failure criterion for concrete and its generalization. Struct J 92(3):311–318
16. Meschke G, Lackner R, Mang HA (1998) An anisotropic elastoplastic-damage model for plain concrete. Int J Numer Meth Eng 42(4):703–727
17. Papanikolaou VK, Kappos AJ (2007) Confinement-sensitive plasticity constitutive model for concrete in triaxial compression. Int J Solids Struct 44:7021–7048
18. Parvin A, Brighton D (2014) FRP composites strengthening of concrete columns under various loading conditions. Polymers 6(4):1040–1056
19. Rousakis TC, Karabinis AI (2012) Adequately FRP confined reinforced concrete columns under axial compressive monotonic or cyclic loading. Mater Struct 45(7):957–975
20. Saatcioglu M, Razvi SR (1992) Strength and ductility of confined concrete. J Struct Eng 118(6):1590–1607
21. Samaan M, Mirmiran A, Shahawy M (1998) Model of concrete confined by fiber composites. J Struct Eng 124(9):1025–1031
22. Sarikaya A, Erkmen RE (2019) A plastic-damage model for concrete under compression. Int J Mech Sci 150:584–593
23. Simo JC, Ju JW (1987) Strain-and stress-based continuum damage models—I. Formulation. Int J Solids Struct 23(7):821–840
24. Voyiadjis GZ, Taqieddin ZN, Kattan PI (2008) Anisotropic damage-plasticity model for concrete. Int J Plast 24(10):1946–1965
25. Yazdani S, Schreyer HL (1990) Combined plasticity and damage mechanics model for plain concrete. J Eng Mech 116(7):1435–1450

Exploratory Investigation on Diversity and Inclusion Programs in Large Construction Companies from the Private Sector in the United States of America

H. Dang

1 Introduction

The construction industry plays a major role in the economy and provides a wide range of business opportunities to various contractors, manufacturers, and vendors in the United States. The construction industry is projected to have a compound annual growth rate of 4.9% to reach $1,804.8 billion by 2023 in the United States. The commercial building construction market is projected to rise by 6.8% in value over the forecast period [1]. The promising and booming construction industry needs to implement and improve processes and programs to improve performance and efficiency to keep up with workforce demand, particularly in the case of private commercial projects. The programs analyzed in this study are the Diversity and Inclusion Programs for Subcontractors in Construction Firms, which focus specifically on commercial projects in the Northwest Pacific and East Coast regions of the United States. This study analyzes the impact of these programs on the performance of the construction firm and the minority and under-represented subcontractors and their experience in the procurement of contracts with large construction companies.

Diversity is a range of human differences, including, but not limited to, race, ethnicity, gender identity, sexual orientation, age, social class, physical ability or attribute, the system of religious or ethical values, national origin and political beliefs. Inclusion is involvement and empowerment, where the inherent value and dignity of all people are recognized [2]. Construction firms implementing programs for diversity and inclusion promote a sense of belonging and respect for the beliefs, backgrounds, and other social aspects of subcontractors.

One of the government's initiatives to promote diverse, equal, and inclusive contracting opportunities is the Disadvantaged Business Enterprise (DBE) program.

H. Dang (✉)
Central Washington University, Ellensburg, USA
e-mail: Hongtao.Dang@cwu.edu

S. Walbridge et al. (eds.), *Proceedings of the Canadian Society of Civil Engineering Annual Conference 2021*, Lecture Notes in Civil Engineering 240,
https://doi.org/10.1007/978-981-19-0507-0_39

The DBE program was established to provide a fair opportunity for small businesses owned and managed by socially and economically disadvantaged individuals to compete on federal transport contracts and to contribute to the diversity of subcontractors and integration efforts in the construction industry. The DBE program was established in 1980 as a minority/women business enterprise program and is regulated under Title VI of the Civil Rights Act of 1964, which prohibits discrimination of racial, ethnic, and national origin [3]. Due to the previously inconsistent use of DBE and ongoing discrimination and barriers, there are significant barriers to federally financed transportation contracts for minority and women-owned enterprises. In 2015, Congress passed the "Fixing America's Surface Transportation Act" (FAST-ACT) to ensure that the DBE program was permanently and consistently implemented by the States Department of Transportation.

Little or no effort was made to address the lack of subcontractor diversity and inclusion in federal projects prior to 1980. It was unheard of for private sector commercial projects. Although the DBE program is needed for federally funded highway projects, Subcontractor Diversity and Inclusion is optional for private sector projects. It is often not even discussed or needed. According to a telephone interview with a local construction firm, some educational institutions (e.g., the University of Washington) and some corporations (e.g., Microsoft) have made it necessary for prime contractors to reach targets for minority and disadvantaged subcontractors hired to successfully complete the contract. However, other companies, including Amazon, do not mention or request the goal of subcontracting diversity or the requirement for prime contractors to win the contract.

It is not easy to implement a Subcontractor Diversity and Inclusion program thoroughly and effectively. However, it is crucial, and the payoff is substantial, if the company follows a thorough and intentional approach to implementation. Companies that focus on diversification are companies that tend to see more sales and revenues. Gender diversity can help revenue to grow by 40% in the first year of this effort [4]. Conversely, women are not being hired equitably. In a study funded by Harvard and Princeton, managers received a set of applications and qualifications that did not reveal any gender. In this blind process, women were preferred over male counterparts when gender was not part of the recruitment process. However, more than 50% of women are still under-represented in the workforce [5].

To implement and promote a company culture of diversity and inclusion, regional construction companies such as Sellen Construction and Lease Crutcher Lewis have set up a dedicated subcontractor diversity and inclusion department, setting them ahead of the Pacific Northwest curve. National firms such as Hensel Phelps, Messer Construction, Knutson Construction and the Gilbane Group have been recognized for their economic inclusion initiatives. This umbrella encompasses the diversity and integration of subcontractors. These efforts have set them as examples of successful Subcontractor Diversity and Inclusion programs in the industry.

The construction firm benefits the dedicated subcontractor Diversity Department in construction firms. The dedicated Subcontractor Diversity and Inclusion Department demonstrates the firm's commitment to change, diversity and improved business

practices. As a result, it empowers minority-owned companies, gives them confidence, and enables growth by creating opportunities. Creating a larger and more talented pool for prime contractors reduces the problem of insufficient subcontractors to fill projects on time. If large construction firms dedicate a Department solely for subcontractor diversity and inclusion, then their performance and efficiency for project procurement and completion have higher chances of success. This research aims to analyze firms that currently have a Department dedicated to subcontractor diversity and inclusion and the impact on potential minority and underrepresented subcontractors.

2 Literature Review

The importance of establishing the Diversity and Inclusion Subcontractor Program in construction firms is a positive benefit to the company. This initiative also contributes to the growth of smaller businesses in each community, resulting in a stronger supply pool for prime contractors. Building a culture with Subcontractor Diversity and Inclusion as a priority gives more opportunities for innovation that deliver positive results for companies applying this principle. The few companies that set up these programs in their organizations have seen positive results. These firms and their performance metrics have been analyzed for this study and the results are presented in the research section. Minority- or women-owned diverse businesses are owned by individuals from an underrepresented minority group-including people of color, women, veterans, people with disabilities, and members of the LGBTQ community.

The analysis of construction firms with a dedicated subcontractor diversity and inclusion program has not yet been researched or identified, nor has an analysis been conducted of companies that apply subcontractor diversity and inclusion guidelines for all commercial projects. Due to this lack of research, the long-term impact or benefits are not known. Most of the published studies on any type of subcontractor diversity and integration guidelines for construction are about the Disadvantaged Business Enterprises (DBE) program for federal transport projects; however, the program can be controversial and applies only to a small sector.

Diversity and inclusion of subcontractors have positive effects at the level of employees. According to a study of diversity, inclusion and commitment in organizations, the employee's perception of acceptance and belonging transcends cultural differences but finds similarities in the employee's commitment and performance to the organization [6]. Not only did performance and commitment to the organization have a positive effect, but lower stress levels were indicated for all group samples tested. The study had limitations due to the size of the sample being studied and the significant cultural differences, as one sample group was from California and the other from Israel. Nonetheless, the study highlights the importance of distinguishing between an organization that is "diversity tolerant" versus a truly inclusive organization.

A similar concept of diversity and integration at the organizational level has been applied in the construction sector, at the subcontractor level, with the introduction of the Disadvantaged Business Enterprise (DBE) program. A recent study on the performance of certified minority and women-owned enterprises (MBE/DBE/WBE) in transport projects reveals significant differences in the performance of MBE/DBE/WBE and non-MBE/DBE/WBE firms [7]. The age of the companies was a key factor affecting underperformance of MBE/DBE/WBE since most of them were younger and working with less capital than their counterparts. This study has many limitations since the opinions of the participants are subjective and the performance tool used was based on previous models that need improvement. Aside from this study's limitations, the DBE program is controversial and only focuses on a niche of federal transportation projects.

A study on inclusive procurement and contracting in the construction industry explains the industry's problems with the MBE/DBE/WBE system. The findings of this study point to the root of the problem on the demand side, indicating that initiatives for inclusion and diversity are not being implemented effectively. The study concludes that if the demand-side system is broken, the supply-side infrastructure is broken. MBE/DBE/WBE companies cannot compete effectively for large-scale infrastructure projects operating within a rapidly changing construction industry that is plagued by discrimination [8].

The research conducted by the Massachusetts Gaming Commission is another study on the overall diversity and inclusion mandated by the state. This study shows the risk outcomes of using the workforce, supplier, and subcontractor diversity for three casino projects. Based on the Diversity Performance Studies, the stakeholders for these projects overwhelmingly supported the implementation of this program and the use of the Access and Opportunity Committee (AOC) program [9]. The AOC was the basis of several strategies implemented to achieve diversity in their casino development projects by providing transparent progress monitoring and collaborative problem-solving at stakeholder level. The study points out that the initiative on subcontractor diversity and inclusion had to be a combined effort of the advocacy groups and the AOC. The AOC acted as a venue for facilitating the acquisition of information by MBE/DBE/WBE firms on demand for services, communication of contract procurement issues and conflict resolution. Although this study is an excellent example of overall diversity and integration in the construction sector, it does not focus solely on subcontractor diversity and inclusion. Another limitation in the study is that the initiative is a legal requirement, such as the DBE program in federal transport projects, rather than a natural core value for the organization.

The Association of General Contractors (AGC) conducted the most direct research on this subject. The study highlights the importance of an intentionally diverse and inclusive culture in maintaining a competitive advantage in the construction industry. One of the benefits identified is the opportunity to expand market share by forming and maintaining collaborative partnerships with MBE/DBE/WBE subcontractor firms [10].

Finally, the research carried out in this study analyzes the impact of the various diversity and inclusion programs and initiatives implemented by local and national

construction companies. These firms are pioneers in the process of diversity and inclusion and have opened the argument for the need to implement a dedicated Subcontractor Department for Diversity and Inclusion. The primary objective of some of the firms interviewed is to promote diversity and inclusion as their core value. These firms began their journey of diversity and inclusion, seeking financial gain, changing the industry, bridging the gap with historically underutilized subcontractors, and promoting social justice. Minority subcontractors interviewed indicated how, for some, these programs are flawed and have the potential for improvement. This critical study exposes the opportunity for construction firms to improve their programs to equally benefit the construction firm and the minority and under-represented subcontractors.

3 Research Design

This research explores the hypothesis that Subcontractor Diversity and Inclusion Programs improve project procurement and completion objectives for construction firms and provide equal opportunities for minority and under-represented subcontractors. These programs bridge the gap between construction companies and historically underutilized subcontractors. As there is a lack of prior research on the impact of the Subcontractor Diversity and Inclusion Programs, this study aims to maximize findings by using a mixed research design consisting primarily of exploratory qualitative research and quantitative research.

The primary research tool used in this study is an electronic survey distributed to general construction firms with Subcontractor Diversity and Inclusion programs for both qualitative and quantitative surveys. Minority and under-represented subcontractors were interviewed by telephone with a list of open-ended questions. The qualitative portion of the survey for construction firms consists of five-point Likert Scale questions. The perceived benefits and challenges of Subcontractor Diversity and Inclusion Programs for both minority and under-represented subcontractors and general construction firms, as well as the impact of Subcontractor Diversity and Inclusion Programs on the project performance of general construction firms. (For the study, project performance is defined as procurement and completion of projects). The quantitative portion of this survey consists of questions exploring expenditure and revenue trends before and after the launch of the Diversity and Inclusion Programs for Subcontractors. The findings of this survey are used to analyze the perceived impact of the Diversity and Inclusion Programs of Subcontractors. The research study explores if Subcontractor Diversity and Inclusion Programs increase the revenue of minority and underrepresented subcontractors.

As mentioned above, this voluntary study consists of two groups. The first group includes senior managers overseeing Subcontractor Diversity and Inclusion Programs in 10 companies with a large market share of commercial projects in the private sector. The author has recruited general contractors with established subcontractors or suppliers of diversity and inclusion programs with a large market share in

commercial projects in the private sector. The author has thoroughly researched and asked the participants to participate in this study.

The second group includes minority and under-represented owners of subcontractors or representatives of firms providing services in the state of Washington. Minority and under-represented subcontractors were recruited from the Washington State Office of Minority and Women's Business Enterprises Certified Firm Directory, including through formal e-mail or telephone calls. The parameters used to search for subcontractors or suppliers were firms with MBE, MWBE and WBE certifications in Pierce, Thurston, King, Snohomish counties and a select few in the eastern part of Washington State.

The survey protocol sent to senior managers of general construction firms and minority and under-represented subcontractors required participants to keep their responses as objective and honest as possible with the option of maintaining anonymity. The study used the following procedure to achieve the intended research objective:

(1) Obtained and interpreted data collected in surveys sent to senior managers of general construction firms and minority and underrepresent subcontractors.
(2) Classified data into complete and objective data, and data with missing or biased information. The latter was removed, and the completed and objective data were analyzed.
(3) Assessed and evaluated project procurement and completion of general construction firms before and after establishing a Subcontractor Diversity and Inclusion program.
(4) Assessed and evaluated the impact experienced by minority and underrepresent subcontractors' firms based on attempts to procure contracts with general contractors.
(5) Sent surveys to senior managers of general construction firms with established Subcontractor Diversity and Inclusion Programs had different questions than the surveys sent to minority and underrepresented subcontractors.

Apart from the basic questions on the size of the construction firm surveyed, the survey questions on general construction firms were as follows:

(1) How much has the utilization of Minority Business Enterprise (MBE), Minority Women Business Enterprise (MWBE), and Women Business Enterprise (WBE) firms impacted project procurement since the inception of the Subcontractor Diversity and Inclusion Program?
(2) How many private sector clients have required your firm to utilize MBE/MWBE/WBE subcontractors for their projects in the past five years?
(3) Does your firm require the utilization of MBE/MWBE/WBE subcontractors in all projects regardless of client requirements?
(4) How much has the utilization of MBE/MWBE/WBE firms impacted project completion goals since the inception of the Subcontractor Diversity and Inclusion Program?

(5) In terms of spending, what is the percentage of increase allocated to MBE, MWBE, and WBE firms before and after a Subcontractor Diversity and Inclusion Program was established?
(6) Besides financial, what are other benefits that justified the cost of implementing a diversity and inclusion program?

The survey questions targeting minority and under-represented subcontractors were open-ended and concerned issues related to their trade, company information, their involvement with construction firms in general, and construction firms with diversity and inclusion initiatives.

(1) What are some of the positive things you've experienced working with general contractors with diversity and inclusion initiatives?
(2) What are the challenges you have experienced working with general contractors with subcontractor diversity and inclusion initiatives?
(3) In your experience, do you find that a general contractor with a Subcontractor Diversity and inclusion program makes an overall difference in the future of your business?
(4) Is there any additional information you would like to share on Subcontractor Diversity and inclusion programs or initiatives?

In conclusion, this methodology is designed to provide data and insight to general contractors interested in pursuing or improving the dedicated Subcontractor Diversity and Inclusion Program and to minority and under-represented subcontractors seeking to form or improve partnerships with general construction firms.

4 Results and Discussion

The analysis of the data collected demonstrates the consistent theme that Subcontractor Diversity and Inclusion Programs strengthen innovative capacity and increase potential from the perspective of the construction firm. Another finding was that minority and under-represented subcontractors view Subcontractor Diversity and Inclusion Programs as project-by-project initiatives rather than as a dedicated programme.

The results for construction firms mostly showed a positive effect on the procurement of projects. Most construction firms have had a moderate impact on project procurement, while fewer firms have had a higher positive impact. The trend shows that more clients require a minority and under-represented subcontractor objective to be achieved for the construction firms to be awarded the project. The work of Subcontractor Diversity and Inclusion Programs helps to establish, establish and maintain relationships with minority subcontractors. This makes the process of procurement of projects with minority subcontractor requirements easier. The result is an increase in the rate of project procurement by construction companies (Fig. 1).

Construction firms also rated better project completion rates as a positive result of subcontractor Diversity and Inclusion programs. The results were evenly spread to

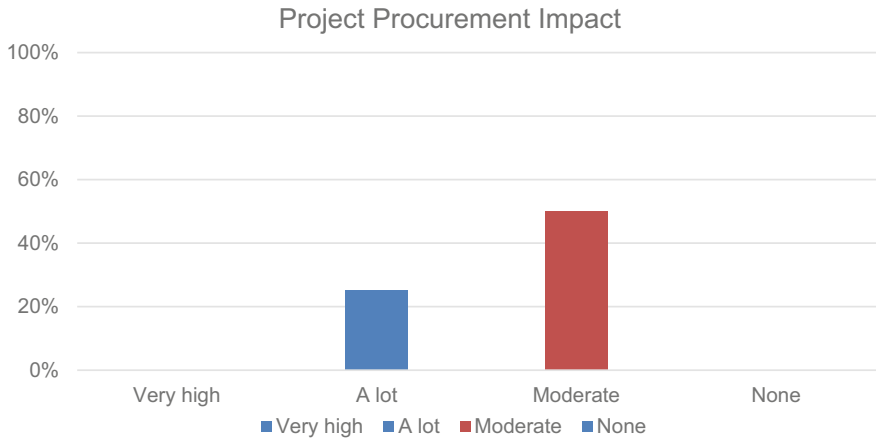

Fig. 1 Project procurement impact

the completion of the project, between a moderate amount of impact, a high amount and a very high amount. By having a larger pool of subcontractors to choose from, construction firms are more likely to choose a subcontractor that will fit better on the basis of their schedule and availability of resources. Having a limited number of subcontractors to use increases the dependence of the construction firm on the existing pool of resources that could have an impact on the project completion schedule (Fig. 2).

The increase in minority subcontractor spending each year is a common measure used to determine the successful Subcontractor Diversity and Inclusion Program. The data collected suggest that most construction firms allocate between 11 and 20% of expenditure to minority subcontractors. A quarter of the construction firms surveyed reported spending between 6 and 10% on minority subcontractors. Construction firms

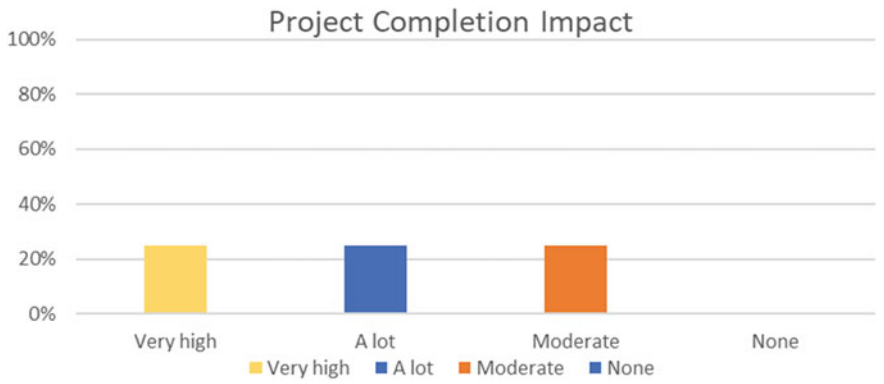

Fig. 2 Project completion impact

use this metric to analyze the dollar spent on minority subcontractors against the objectives they set as a company or as required by contract requirements depending on the project (Fig. 3).

A few firms have expressed passion and have proved themselves to be a driving force for minority subcontractors to perform and remain consistent and reliable. The feedback received by construction firms with Subcontractor Diversity and Inclusion Programs was mostly positive, with challenges that could not be quantified.

Construction firms have stated that the main challenge is the resistance to change from within the industry. Parties in a position of power tend to want to use the same subcontractors because they trust them, fear risks, and are unable to overcome the myths of minority subcontractors that do not get the job done and are not responsive. There appears to be a bias not only on the basis of race or gender, but also on the basis of the size of the business. With the inability to overcome the bias of smaller enterprises not being able to perform, minority and under-represented subcontractors cannot demonstrate their potential. Without this opportunity, there is no way to find out if the business could have been successful.

On the other hand, the challenge presented by construction firms supports the results of data collected by interviewing minority and under-represented subcontractors who have been awarded or attempted to win contracts for large projects. The minority and under-represented subcontractors interviewed for this research did not work with the construction firms analyzed in this study. Their experience is limited to building projects with diversity and inclusion quotas and misleading diversity and inclusion initiatives.

The data supports the fact that most subcontractors experience a false sense of diversity and integration presented by construction firms. Minority and under-represented interviews with subcontractors concluded that the procurement system is often unattainable for minority subcontractors due to the disproportionate amount of risk allocated to the subcontractor.

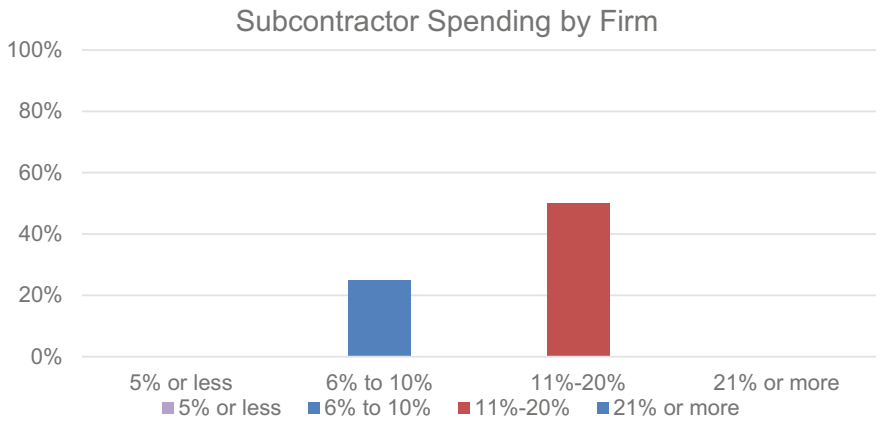

Fig. 3 Subcontractor spending by firm

The agreement of all minority subcontractors on the effect of a delay in payment by construction firms was a compelling finding. The average payment delay is thirty days, with some construction firms waiting for sixty to ninety days to submit payment to the subcontractor after the work has been completed. This is particularly difficult for small subcontractors who usually do not have a substantial cash flow to undertake projects where they will not receive payment until ninety days after completion. For this reason, many minority and under-represented subcontractors agree that the system is in place to exclude them as there is an economic disparity in the minority and under-represented communities.

Another common theme was the lack of significant opportunities for minority subcontractors. According to the minority subcontractor interviewed, the quota allocated to minorities is typically assigned to work that nobody wants to do, such as flagging and erosion control. Some large construction firms advertise subcontractor diversity and inclusion opportunities to present the company in a good light but to fill the minimum requirement with scopes of lesser importance in order to check the diversity and inclusion box required for the project. Significant scopes of work are unattainable for minorities, as large construction firms assign this work to larger subcontractors with an established relationship with the construction firm, exposing the known ethical issue of cronyism in the construction industry.

Minority subcontractors have shown that the only positive outcome of diversity and inclusion of outreach events coordinated by construction firms has been networking opportunities to find legal and professional resources. These resources may help minority subcontractors to carry out contract reviews and risk assessments. The excavating minority subcontractor interviewed indicated that this process saved her thousands of dollars and helped her assess the significant risk that her company would have to undertake to complete the scope of the work presented.

This study shows a discrepancy between what diversity and inclusion programs in construction firms perceive as important and what minority subcontractors need from them. Most of the results show a benefit to the construction firm rather than to the minority and under-represented subcontractors.

5 Conclusion

After analyzing the data collected from both the construction firm and the minority and under-represented subcontractor, it is essential to note the limitations of this study. The sample size of the construction companies interviewed was limited. Most of the construction firms contacted had limited knowledge of what diversity and inclusion meant to subcontractors. Of the few companies that did so, even fewer had the Subcontractor Diversity and Inclusion Program in place; therefore, the sample size for this study was small. Some of the construction firms interviewed included suppliers in their diversity and inclusion programmes. Consequently, their results may not accurately interpret the diversity and inclusion of subcontractors.

From a minority and under-represented subcontractor perspective, the size of the sample was also limited. Most minority and under-represented subcontractors also objected to interviews due to lack of faith in diversity and inclusion programs based on their experience. The few who agreed to be interviewed had mostly negative experiences with construction firms with subcontractor diversity and inclusion initiatives on a per-project basis rather than as established programs.

Although the results are not reliable as the sample size was small, it is important to note the valuable insight into the benefits and challenges of subcontractor diversity and integration programs for the construction industry. Construction firms with established Subcontractor Diversity and Inclusion Programs are taking an important first step towards equity. These programs are a concept that will evolve, have an immense growth potential and the power to transform the construction industry into a more equitable place of opportunity. The few companies that have adopted programs and initiatives in the field of diversity and inclusion are pioneers in their field and are taking on a challenging task of improving the sector with systemic issues.

References

1. Woods L (2019) Research and markets. Bus Wire. https://www.businesswire.com/news/home/20190923005677/en/United-States-Construction-Industry-Databook-Market-Size#:~:text=In%20first%20half%20of%202018,US%24%201%2C804.8%20billion%20by%202023
2. Association, Canadian Construction (2019) The value of diversity and inclusion in the canadian construction industry. https://www.cca-acc.com/wp-content/uploads/2020/01/CCA_13413_Business_Case_EN.pdf. Accessed 20 May 2020
3. Department of Transportation (2014) Disadvantaged business enterprise program final. Transportation.gov. https://www.transportation.gov/osdbu/disadvantaged-business-enterprise/disadvantaged-business-enterprise-program-final
4. Miller K (2020) Future of working. 20 advantages and disadvantages of diversity in the workplace. https://futureofworking.com/11-advantages-and-disadvantages-of-diversity-in-the-workplace/.
5. Johnson SK, Kirk JF (2020) Research: To reduce gender bias, anonymize job applications. Harv Bus Rev. https://hbr.org/2020/03/research-to-reduce-gender-bias-anonymize-job-applications
6. Barak EM, Findler L, Wind LH (2001) Diversity, inclusion, and commitment in organizations: international empirical explorations. Inst Appl Behav Manag 71–96
7. Kim A, Arditi D (2010) Performance of MBE/DBE/WBE construction firms in transportation projects. J Constr Eng Mang 136(7):768–777
8. Fairchild D, Rose K (2018) Inclusive procurement and contracting: building a field of policy and practice. In: Emerald cities collaborative America empowered, pp 1–59
9. Barringer P (2019) Built to last: best practices for diversity in the construction industry. The massachusetts casino development experience. The Massachusetts Gaming Commission, pp 1–32
10. AGC Diversity & Inclusion Council (2020) The business case for diversity & inclusion. In the construction industry. In: Huneke B, Brown R (eds) AGC of America, pp 1–12

Current Trends and Future of Advanced Simulations in Facility Management—An Owner's Perspective

Z. Ghorbani and C. Dubler

1 Introduction

Building Information Management (BIM) for facilities management (FM) has reached an inflection point within owner organizations. There are many examples of BIM for FM implementations within the design and construction phase of a project with a focus on what data is needed for post construction operations and maintenance. However, there is little evidence of success in using BIM or operations and maintenance data for advanced analysis or advanced simulation within facilities management. This paper provides a literature review on the status of national and international implementation of advanced simulations, such as digital twins and augmented reality in facilities management. Additionally, a large university organization is used as a potential future case study for a framework of advanced simulation and analysis implementation. Both challenges and keys to success are identified for The Pennsylvania State University to implement advanced BIM simulations referencing current examples of success from related industries.

1.1 Facilities Management: Operations and Maintenance

Facilities management is a broad term that classifies multiple disciplines covering everything from real estate and financial management to maintenance and janitorial services. The International Facilities Management Association (IFMA) defines facility management (FM) as "a profession that encompasses multiple disciplines to ensure functionality, comfort, safety, and efficiency of the built environment by

Z. Ghorbani (✉) · C. Dubler
The Pennsylvania State University, University Park, USA
e-mail: zxg120@psu.edu

S. Walbridge et al. (eds.), *Proceedings of the Canadian Society of Civil Engineering Annual Conference 2021*, Lecture Notes in Civil Engineering 240,
https://doi.org/10.1007/978-981-19-0507-0_40

integrating people, place, process, and technology." This paper focuses mainly on the operations and maintenance aspect of facilities management when reviewing current trends in BIM implementation and future strategies for advancement. Operations and maintenance (O&M) encompass the day-today activities that are necessary to ensure that the facility performs the functions as intended in design after completion of construction. Estimates show that O&M lifecycle cost are five to seven times higher than the initial investment costs [28] and three times the total construction cost. Therefore, owners have the most to gain on efficiencies in operation and maintenance and have a vested interest in the implementation of advanced technologies in facilities management.

1.2 The Pennsylvania State University

The Pennsylvania State University (Penn State) is a land-grant research institution with multiple campuses throughout the state of Pennsylvania in the United States. While remaining deeply rooted in tradition, the Penn State's mission is to stay on the cutting edge of knowledge, diversity, and technology. They pride themselves on their creative endeavors to generate, disseminate, integrate, and apply relevant and valuable knowledge to industry. The facilities representative for Penn State is called the Office of Physical Plant (OPP). Acting as an owner, as well as professional and construction manager on most university projects, the OPP has an opportunity to diversely implement BIM processes. Due to this position, the OPP has the ability to research, test, and create processes which allow for an uninterrupted flow of facilities information beginning at project conception. To date, OPP has been very successful at implementing BIM within design and construction and procuring valuable operations and maintenance data from each project for use in operations and maintenance. However, like many other larger owners, Penn State struggles to implement advanced BIM/simulation technology such as augmented reality, virtual reality, and digital twins.

Penn State owns an extensive and multifaceted building inventory across 24 campuses. Penn State's University Park campus contains approximately 950 buildings over 2,000 gross square foot (gsf). The campus buildings encompass over 22 million gsf with a very diverse portfolio from barns, research labs to nuclear reactors. The current capital renewal plan for University Park campus is approximately $4 billion over the next ten years. The Penn State commonwealth campuses (all other campuses) contain approximately 790 buildings across the state of Pennsylvania. Most of the projects the OPP works on are minor renovations, rehabilitations, and major maintenance projects. The OPP is involved during all stages of a project life cycle for new construction on campus. There were 425 projects across all campuses in 2019/2020, approximating for over $600 million in cost. Because of the extent of facility and asset inventory, Penn State has a tremendous backlog of projects, estimated to be over $2.5 billion. This backlog requires a considerable amount of

effort and resources to complete, without even considering the incorporation of a BIM implementation strategy.

2 Research Methodology

The methodology for this paper focuses on providing a comprehensive analytical review of the existing research on advanced simulations in facilities management (FM). Three main areas of advanced technology in facilities management were chosen, including augmented reality (AR), virtual reality (VR), and digital twins. Two databases, namely Compendex and Inspec, were used to search for related articles, both nationally and internationally. To that end, three different searches were conducted using the combination of facilities management and each selected technology (i.e., FM + AR, FM + VR, FM + digital twins). Three papers focused on both AR and VR in facilities management. In those cases, the paper was included in both categories. Therefore, the categories are not mutually exclusive.

2.1 Selection Criteria

Since this paper focuses on a specific market and current trends, it was important to develop rigorous paper criteria prior to literature search. The following criteria were used to determine papers' eligibility for the study:

1. To ensure currency, only articles published from 2011 to 2020 were considered.
2. Selected papers were required to address advanced simulations within facilities management related to virtual reality, augmented reality, and digital twins. Articles that concentrated solely on design and construction were excluded. For instance, articles that focused on the implementation of AR for improvements in design and construction for FM were excluded.
3. Journal papers from peer-reviewed journals were selected to ensure papers' quality and rigour. Peer-reviewed conference papers were also included from relevant conference proceedings and were labeled accordingly.

If the articles did not meet these criteria, they were not used for literature review analysis. However, the research team took the amount of non-academic (lack of peer-review) publications related to advanced technologies in FM into perspective when summarizing the current state of industry advancement.

2.2 Article Extraction and Classification Procedure

After the articles were narrowed based on defined criteria, two additional steps were taken to ensure the research team identified pertinent articles. First, the abstract for each article was read to ensure that the article focused on the advanced simulations in FM. During this step, articles that did not focus on the FM were excluded. As an example, some articles included the word "facility management" in an introductory sentence of the abstract. However, the main focus of the article was advanced simulations in design or construction, which made them ineligible for our study. Second, full articles were read to identify their purpose and methodology, followed by classification of the articles based on their content. In this stage, the framework proposed by Kim et al. [25] was adopted and modified. Figure 1 presents the developed framework including categories and subcategories. This framework consists of three tiers, including concept and theory, implementation, and industrial application. Concept and theory tier includes papers that introduce the topic and look at the theory behind the implementation of advanced simulations but fail to implement the concept. Implementation tier includes articles that implement a solution (either a software/application or a framework). The most advanced tier, industrial application, includes papers that document how these advanced simulations can be implemented within a facilities owner.

The first tier, concept and theory, was broken down into three subcategories, including conceptual framework, review, and others. Papers in the conceptual framework subcategory include high-level frameworks for applying these advanced technologies. However, they do not include any implementation details or suggestions. Reviewed papers in this category mostly include literature review and focus on outlining what other researchers have accomplished in this research area. The second tier, implementation was divided into two subcategories, including implementation framework and application design. Papers in the first subcategory focus on providing a framework for implementing these technologies in FM. The main difference between the implementation framework and the conceptual framework is that the former is a very high-level framework and does not get into the implementation details. The second subcategory, application design, comprises of articles that focus on designing

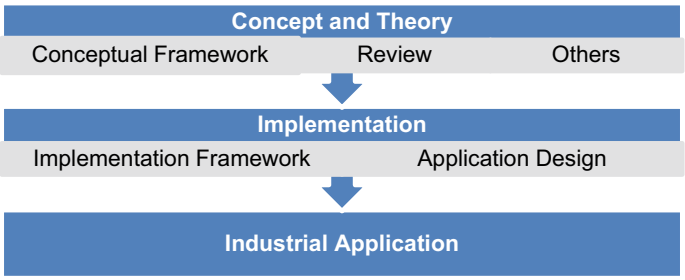

Fig. 1 Proposed framework for categorizing the studied articles

an application or an interface that uses these technologies in supporting FM on an experimental level. The third tier does not include any subcategories. Papers in this tier provide a framework for industrial application. Specifically, these articles include a framework that explains how these technologies can be implemented in the industry with some level of rigor that can be repeated on a future project.

3 Results and Discussion

This section focuses on the results from the authors' extensive literature search. Figure 2 presents the number of articles in each technology category between 2011 and 2020. Based on this chart, the number of articles published on these advanced technologies have increased in the past ten years, which implies they have gained more popularity. Moreover, AR seems to be the most studied and documented advanced technology among all. Digital twins have gained popularity since 2017; although there are examples of prototyping, this article is focusing on the advanced level that is encompassed by the term digital twin.

Table 1 presents the number of articles in each category based on the defined classification framework. According to this Table, 65.3% of the articles focused on the implementation of advanced simulation technologies in AR. 30.8% of the articles focused on concept and theory of these technologies. More importantly, only 3.8% of the papers focused on the industrial application, which could be an indication of either of these two scenarios: (1) these technologies are not being implemented in the industry or (2) they are being implemented but not published. According to some industry reports such as the report by Campbell et al. [6], AR is being implemented

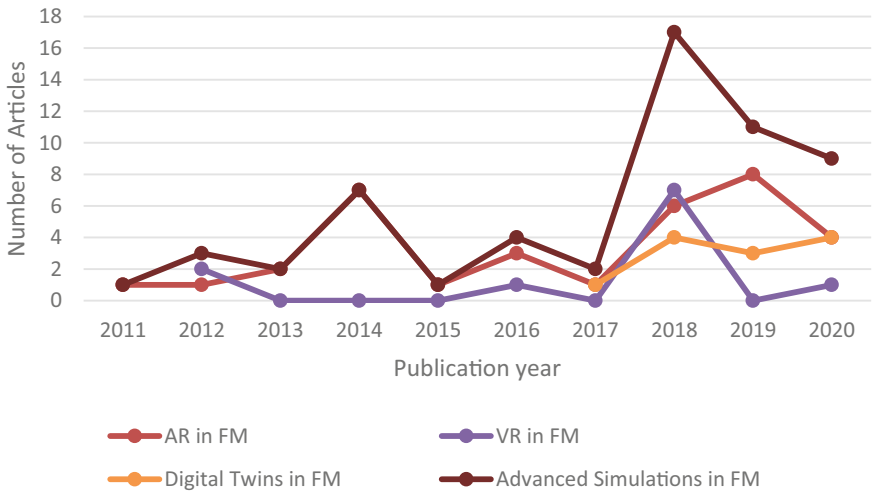

Fig. 2 Number of articles in each technology category between 2011 and 2020

Table 1 Number of articles by each subject from the classification framework

Classification category	# of articles (augmented reality)	# of articles (virtual reality)	# of articles (digital twins)	# of articles (total)	Relative percentage (%)	Global percentage (%)
Concept and theory	7	2	7	16	100	**30.8**
Conceptual framework	2	1	2	4	25	7.7
Review	2	0	3	5	31	9.6
Others	3	1	2	7	44	13.5
Implementation	23	6	5	34	100	**65.3**
Implementation framework	5	3	5	13	38	25
Application design	18	3	0	21	62	40.4
Industrial application	1	0	1	2	100	**3.8**

in Facilities management to some extent. Although these types of reports are not pee-reviewed and could potentially be biased, they still indicate that the industry case studies are not being published. Therefore, there seems to be a gap between industry adoption and academic publications in this area.

Tables 2, 3, and 4 provide the list of references in each category and subcategory for the application of the three studied advanced simulation technologies in facilities management, namely virtual reality, augmented reality, and digital twins. According to Table 2, 75% of the papers that focused on VR in FM (six papers), were under the second tier (i.e., implementation). Among those papers, three of them focused on implementation framework and three papers included application design. The remaining 25% (two papers) were under the first tier (i.e., concept and theory). One paper focused on conceptual framework and the other one focused on defining BIM

Table 2 Articles on virtual reality in facility management

Classification category	Subcategory	References
Concept and theory	Conceptual framework	Renforth et al. [38]
	Review	–
	Others	Zou et al. [52]
Implementation	Implementation framework	Chung et al. [10], Moon et al. [32], Naticchia et al. [33]
	Application design	Carreira et al. [7], Shi et al. [41], Soria et al. [43]
Industrial application		–

Table 3 Articles on augmented reality in facility management

Classification category	Subcategory	References
Concept and theory	Conceptual framework	Schumann et al. [39], Wang and Piao [48]
	Review	Gheisari et al. [15], Siegele et al. [42]
	Others	Gheisari and Irizarry [17], Jalo et al. [22], Ortega et al. [37]
Implementation	Implementation framework	Chung et al. [10], Götze et al. [18], Koch et al. [26], Neges and Koch [34]
	Application design	Bae et al. [1, 2], Baek et al. [3], Chen et al. [8, 9], Corneli et al. [11], Diao et al. [12], El Ammari and Hammad [14], Gheisari et al. [16], Irizarry et al. [21], Ji et al. [23], Kahn et al. [24], Liu and Seipel [29], Mahmood et al. [31], Nguyen et al. [35], Soria et al. [43], Uimonen and Hakkarainen [47], Williams et al. [50]
Industrial application		Hou et al. [20]

Table 4 Articles on digital twins in facility management

Classification category	Subcategory	References
Concept and theory	Conceptual framework	Bolshakov et al. [5], Konchenko et al. [27]
	Review	Love and Matthews [30], Nixon [36], Stojanovic et al. [45]
	Others	Sharma et al. [40], Wei and Akinci [51]
Implementation	Implementation framework	Baskaran et al. [4], Eilers et al. [13], Hlady et al. [19], Vorobyeva [44], Wei and Akinci [49]
	Application design	–
Industrial application		Føllesdal Tjønn [46]

model characteristics that enables using BIM models for VR environments. There were no papers under industrial application tier on this topic.

Observing Table 3, from the 31 papers that focused on AR in FM, 23% of them (seven papers) were under the first tier, concept and theory. Among them, two papers focused on conceptual framework, two papers focused on reviews. From the remaining three papers, one focused on facility managers' perspective on mobile AR applications, one focused on exploring benefits of collaborative AR in FM, and the other one included designing data models for managing hidden facilities, in which AR was also included. The second tier, implementation, included 74% of papers (23 papers). Four of these papers provided an implementation framework and the other 19 papers focused on application design. Under the third tier, industrial application,

there was only one paper (3% of the articles) that focused on providing an industrial framework for implementing AR in FM. This paper focused on the Oil & Gas industry. However, the same concepts can be used in the AEC industry.

As specified by Table 4, from 13 papers that focused on digital twins in FM, 54% of them (seven papers) were under the concept and theory tier. Among those papers, two of them focused on providing a conceptual framework and three of them were review papers. The remaining two papers focused on explaining digital twinning concept and benefits in FM. 38% of the papers (five papers) fell under the implementation tier, all of which focused on providing an implementation framework for applying digital twinning in FM. The remaining 8% (one article) fell under the industrial application tier.

3.1 Conceptual Implementation Framework for Penn State

Upon completion of the literature review, the research team focused on applying the results to a conceptual framework to advance the implementation of advanced simulation at Penn State University. Specifically, findings were analyzed for keys to success based on previously developed concepts and theory, documented implementation frameworks and any case study applications. Based on the literature review findings, the research team has identified the following key points for future implantation strategies for Penn State's advanced implementation of BIM workflows (AR, VR, and digital twins):

(1) There are limited examples of academic-published success. It was clear throughout the literature review process on the limited examples of advanced simulations in FM based on peer-reviewed journal and conference papers. Therefore, owners need to rely on internal research and development until further examples of success are published.

(2) Non-academic (industry) case studies are available. While searching for related peer-reviewed journals, it was evident that there is an abundance of non-academic (industry) publications on the success of advanced simulations in FM. Through initial research, it was determined that there is a substantial consulting market in this area. However, with little examples of academic-published success, owners need to be careful to not waste money on unproven benefits and should not be sold on consultants offering successful implementations without a detailed business plan.

(3) Planning is important to advanced technology success. The majority of peer-reviewed papers documented an implementation framework and discussed a key for advanced technology implementation is early planning. Therefore, it is important for owners to develop a business plan using applicable qualitative and quantitative methods; document the scope and implementation phase; and develop a financial return on their investment.

Future work for the research team includes applying the defined key points into a rigorous implementation strategy for Penn State facilities management for advanced simulation. Penn State has already seen success of advanced BIM methods in design and construction projects and is ready to see a return on investment into facilities management.

4 Summary and Conclusion

This paper focused on analyzing the existing research on advanced simulations in facilities management. First, a comprehensive search was completed on the existing papers on three advanced simulation technologies in FM, including AR, VR, and digital twins. Relevant peer-reviewed conference and journal papers were then selected based on the authors' suggested criteria to make sure they meet the objectives of this research. Afterwards, a framework was developed to categorize the selected papers based on their content. The proposed framework consisted of three tiers, including concept and theory, implementation, and industrial application. Furthermore, each tier was divided into subcategories. The concept and theory tier included three subcategories, namely conceptual framework, review, and others. The implementation tier was broken down into implementation framework and application design subcategories. Papers in each studied technology area (i.e., VR in FM, AR in FM, and digital twins in FM) were then categorized based on the proposed framework.

In the first technology area (i.e., VR in FM), 25% of the papers were under the first tier (i.e., concept and theory), and 75% of them were under the second tier (i.e., implementation). 23% of the papers that focused on the second technology area (i.e., AR in FM), were under the first tier, 74% of them were under the second tier, and only 3% of them were under the third tier (i.e., industrial application). Among papers that focused on the third technology area (i.e., digital twins in FM), 54% of them were under the first tier, 38% of them fell under the second tier, and only 8% of them were under the third tier. Based on the observations from the studied literature, a conceptual framework was then introduced for Penn State (or other large institutional owners) to move towards implementing these advanced technologies.

In summary, owners have the most to gain through the implementation of BIM in FM, specifically operations and maintenance, due to the long life of a facility and the total cost of ownership. Although there has been documented success in BIM data being developed for O&M during design and construction, the implementation of advanced simulations (virtual reality, digital twins, and augmented reality) has seen little documentation of actual industry-based implementation. Therefore, owners are left to rely on non-academic publications of success and academic publications of framework to develop their implementation strategy and push towards advancing BIM in FM. Future work includes defining a successful framework for owners to follow to advance their implementation from BIM in FM to advanced simulations that further increase efficiencies in operations and maintenance.

References

1. Bae H, Golparvar-Fard M, White J (2013) High-precision and infrastructure-independent mobile augmented reality system for context-aware construction and facility management applications. In: International workshop on computing in civil engineering. ASCE, Los Angeles, CA, USA, pp 637–644
2. Bae H, Golparvar-Fard M, White J (2014) Rapid image-based localization using clustered 3D point cloud models with geo-location data for AEC/FM mobile augmented reality applications. In: Computing in civil and building engineering. ASCE, Orlando, FL, USA, pp 841–849
3. Baek F, Ha I, Kim H (2019) Augmented reality system for facility management using image-based indoor localization. Autom Constr 99:18–26
4. Baskaran V, Singh S, Reddy V, Mohandas S (2019) Digital assurance for oil and gas 4.0: role, implementation and case studies. In: SPE/IATMI Asia pacific oil & gas conference and exhibition. society of petroleum engineers, Bali, Indonesia, SPE-196292-MS
5. Bolshakov N, Badenko V, Yadykin V, Celani A, Fedotov A (2020) Digital twins of complex technical systems for management of built environment. IOP conference series: materials science and engineering, vol 869, 6th edn. IOP Publishing, Hanoi, Vietnam, p 62045
6. Campbell M, Kelly S, Lang J, Immerman D (2019) The state of industrial augmented reality 2019. PTC, pp 1–7
7. Carreira P, Castelo T, Gomes CC, Ferreira A, Ribeiro C, Costa AA (2018) Virtual reality as integration environments for facilities management: application and users perception. Eng Constr Archit Manag 25(1):90–112
8. Chen K, Chen W, Li CT, Cheng JC (2019) A bim-based location aware ar collaborative framework for facility maintenance management. ITcon 24:360–380
9. Chen K, Yang J, Cheng JC, Chen W, Li CT (2020) Transfer learning enhanced AR spatial registration for facility maintenance management. Autom Constr 113:103135
10. Chung SW, Kwon SW, Moon DY, Ko TK (2018) Smart facility management systems utilizing open BIM and augmented/virtual reality. In: Proceedings of the international symposium on automation and robotics in construction, vol 42. IAARC Publications, Berlin, Germany, pp 1–8
11. Corneli A, Naticchia B, Carbonari A, Bosché F (2019) Augmented reality and deep learning towards the management of secondary building assets. In: Proceedings of the international symposium on automation and robotics in construction, vol 36. IAARC Publications, Banff, Canada, pp 332–339
12. Diao PH, Shih NJ (2019) BIM-based AR maintenance system (BARMS) as an intelligent instruction platform for complex plumbing facilities. Appl Sci 9(8):1592
13. Eilers J, Jacquin S, Burgos Basile N (2020) Asset reliability in practice: an effective combination of APM, AI and simulation solutions within a one stop environment. In: Abu Dhabi international petroleum exhibition & conference. Society of Petroleum Engineers, Abu Dhabi, UAE, SPE-202985-MS
14. El Ammari K, Hammad A (2019). Remote interactive collaboration in facilities management using BIM-based mixed reality. Autom Constr 107:102940
15. Gheisari M, Williams G, Walker BN, Irizarry J (2014) Locating building components in a facility using augmented reality vs. paper-based methods: a user-centered experimental comparison. In: Computing in civil engineering. ASCE, Orlando, FL, USA, pp 850–857
16. Gheisari M, Goodman S, Schmidt J, Williams G, Irizarry J (2014) Exploring BIM and mobile augmented reality use in facilities management. In: Construction research congress: construction in a global network. ASCE, Atlanta, GA, USA, pp 1941–1950
17. Gheisari M, Irizarry J (2016) Investigating human and technological requirements for successful implementation of a BIM-based mobile augmented reality environment in facility management practices. Facilities 34(1/2):69–84
18. Götze J, Schumann CA, Müller E (2014) Context awareness and augmented reality in facility management. In: International conference on engineering, technology and innovation (ICE). IEEE, Bergamo, Italy, pp 1–5

19. Hlady J, Glanzer M, Fugate L (2018) Automated creation of the pipeline digital twin during construction: improvement to construction quality and pipeline integrity. In: 12th international pipeline conference. American society of mechanical engineers digital collection, Calgary, Alberta, Canada, IPC2018-78146, V002T02A004
20. Hou L, Wang Y, Wang X, Maynard N, Cameron IT, Zhang S, Jiao Y (2014) Combining photogrammetry and augmented reality towards an integrated facility management system for the oil industry. Proc IEEE 102(2):204–220
21. Irizarry J, Gheisari M, Williams G, Roper K (2014) Ambient intelligence environments for accessing building information: a healthcare facility management scenario. Facilities 32(3/4):120–138
22. Jalo H, Pirkkalainen H, Torro O, Kärkkäinen H, Puhto J, Kankaanpää T (2018) How can collaborative augmented reality support operative work in the facility management industry? In: 10th international conference on knowledge management and information sharing (KMIS). Seville, Spain, pp 39–49
23. Ji SY, Kim MK, Jun HJ (2017) Campus space management using a mobile BIM-based augmented reality system. In: 22nd international conference on computer-aided architectural design research in Asia (CAADRIA): protocols, flows and glitches. The Association for Computer-Aided Architectural Design Research in Asia (CAADRIA), Suzhou, China, pp 105–114
24. Kahn S, Olbrich M, Engelke T, Keil J, Riess P, Webel S, Graf H, Bockholt U, Picinbono G (2012) Beyond 3D 'as-built' information using mobile AR enhancing the building lifecycle management. In: International conference on cyberworlds. IEEE, Darmstadt, Germany, pp 29–36
25. Kim M, Wang X, Love P, Li H, Kang SC (2013) Virtual reality for the built environment: a critical review of recent advances. J Inf Technol Constr 18:279–305
26. Koch C, Neges M, König M, Abramovici M (2014) Natural markers for augmented reality-based indoor navigation and facility maintenance. Autom Constr 48:18–30
27. Konchenko A, Chatar C, Doronichev S, Saetern D, Bruns J (2020) Oilfield virtual twin. In: SPE annual technical conference and exhibition. Society of Petroleum Engineers, Denver, CO, USA. SPE-201745-MS
28. Lee SK, An HK, Yu JH (2012) An extension of the technology acceptance model for BIM-based FM. In: Proceedings of the construction research congress: construction challenges in a flat world. ASCE, West Lafayette, IN, USA, pp 602–611
29. Liu F, Seipel S (2018) Precision study on augmented reality-based visual guidance for facility management tasks. Autom Constr 90:79–90
30. Love PE, Matthews J (2019) The 'How' of benefits management for digital technology: from engineering to asset management. Autom Constr 107:102930
31. Mahmood B, Han S, Lee DE (2020) BIM-based registration and localization of 3D point clouds of indoor scenes using geometric features for augmented reality. Remote Sensing 12(14):2302
32. Moon HS, Kim HS, Moon SY, Kim HW, Kang, LS (2012) Prototype model of wireless maintenance operation system for bridge facility using VR and ubiquitous technology. In: Proceedings of the 11th ACM SIGGRAPH international conference on virtual-reality continuum and its applications in industry (VRCAI '12). Association for Computing Machinery, Singapore, p 350
33. Naticchia B, Corneli A, Carbonari A, Bonci A, Pirani M (2018) Mixed reality approach for the management of building maintenance and operation. In: Proceedings of the international symposium on automation and robotics in construction (ISARC), vol 35. IAARC Publications, Berlin, Germany, pp 1–8
34. Neges M, Koch C (2016) Augmented reality supported work instructions for onsite facility maintenance. In: 23rd international workshop of the European group for intelligent computing in engineering, UK, pp 1–10
35. Nguyen TB, Tran AB, Nguyen MT, Le-Nguyen K (2020) Application of building information modelling, extended tracking technique and augmented reality in building operating management. In: CIGOS 2019, innovation for sustainable infrastructure. Lecture Notes in Civil Engineering, Springer, Singapore, pp 1247–1252

36. Nixon J (2020) Digitalization deployed: lessons learned from early adopters. In: Offshore technology conference. Houston, TX, USA, OTC-30794-MS
37. Ortega LM, Jurado JM, Ruiz JLL, Feito FR (2020) Topological data models for virtual management of hidden facilities through digital reality. IEEE Access 8:62584–62600
38. Renforth L, Giussani R, Mendiola MT (2018) Smart condition monitoring system for HV networks with artificial intelligence, augmented reality and virtual reality: copyright material IEEE, Paper No. PCIC-2018-37. In: Petroleum and chemical industry technical conference (PCIC), IEEE, Cincinnati, OH, USA, pp 325–332
39. Schumann CA, Forkel E, Otto F, Müller E, Clauß M, Lanka A (2016) Knowledge acquisition and representation in facility management: facility management with semantic technologies and augmented reality. In: International conference on computational science and computational intelligence (CSCI). IEEE, Las Vegas, NV, USA, pp 1005–1009
40. Sharma P, Hamedifar H, Brown A, Green R (2017) The dawn of the new age of the industrial internet and how it can radically transform the offshore oil and gas industry. In: Offshore technology conference. OnePetro, Houston, TX, USA, OTC-27638-MS
41. Shi Y, Du J, Lavy S, Zhao D (2016) A multiuser shared virtual environment for facility management. Procedia Eng 145:120–127
42. Siegele D, Di Staso U, Piovano M, Marcher C, Matt DT (2020) State of the art of non-vision-based localization technologies for AR in facility management. In: International conference on augmented reality, virtual reality and computer graphics. Lecture notes in computer science. Springer International Publishing, Lecce, Italy, Cham, pp 255–272
43. Soria G, Ortega Alvarado LM, Feito FR (2018) Augmented and virtual reality for underground facilities management. J Comput Inf Sci Eng 18(4):041008
44. Vorobyeva D (2019) Stages of design of digital twin for local enterprise. In: Data analytics and management in data intensive domains: XXI international conference DAMDID/RCDL. Kazan, Russia, p 103
45. Stojanovic V, Trapp M, Richter R, Hagedorn B, Döllner J (2018) Towards the generation of digital twins for facility management based on 3D point clouds. In: Proceedings of the 34th annual ARCOM conference. Association of researchers in construction management conference, Belfast, UK, pp 270–279
46. Føllesdal Tjønn A (2018) Digital twin through the life of a field. In: Abu Dhabi international petroleum exhibition & conference. Society of Petroleum Engineers, Abu Dhabi, UAE, SPE-193203-MS
47. Uimonen M, Hakkarainen M (2018) Accessing BIM-related information through AR. In: International symposium on mixed and augmented reality adjunct (ISMAR-adjunct). IEEE, Munich, Germany, pp 399–400
48. Wang TK, Piao Y (2019) Development of BIM-AR-based facility risk assessment and maintenance system. J Perform Constr Facil 33(6):04019068
49. Wei Y, Akinci B (2019) A vision and learning-based indoor localization and semantic mapping framework for facility operations and management. Autom Constr 107:102915
50. Williams G, Gheisari M, Chen PJ, Irizarry J (2015) BIM2MAR: an efficient BIM translation to mobile augmented reality applications. J Manag Eng 31(1):A4014009
51. Yusen XU, Bondaletova NF, Kovalev VI, Komrakov AV (2018) Digital twin concept in managing industrial capital construction projects life cycle. In: Eleventh international conference "Management of Large-Scale System Development" (MLSD). IEEE, Moscow, Russia, pp 1–3
52. Zou Z, Arruda L, Ergan S (2018) Characteristics of models that impact transformation of BIMS to virtual environments to support facility management operations. J Civ Eng Manag 24(6):481–498

Effect of Using Alternative Stress–Strain Definitions on the Buckling Load Predictions of Thin-Walled Members

R. E. Erkmen, H. Moradpoor, and A. Bhowmick

1 Introduction

The use of fibre-reinforced polymer composite-laminated thin-walled members as a construction material has increased in recent years. The primary reason for this increase is their non-corrosive nature and long-term durability, high tensile strength-to-weight ratio, electromagnetic neutrality, and resistance to chemical attack. Because of their high strength-to-weight ratios, slender structural components may be formed by using composite laminates. One of the primary design concerns for such components, however, is their susceptibility against buckling due to their slenderness; therefore, it is important to predict their buckling loads accurately for a reliable design. For fibre reinforced laminates, a thin-walled beam formulation was developed by Bauld and Tzeng [1], which also includes geometrically nonlinear analysis. Closed-form analytical solutions for various cases of flexural and lateral-torsional type buckling were developed by researchers including [2–6]. However, these formulations are limited to certain boundary and loading conditions. On the other hand, finite element method can be used to obtain solutions that are applicable to general cases. For the buckling analysis of thin-walled composite beams, finite element formulations were developed by [7–11].

The effect of shear deformation can gain significance in the buckling behaviour of beams when materials with low shear modulus are used, such as FRP pultruded beams. The effect of shear deformation on buckling behaviour of thin-walled members was investigated in displacement-based formulations by [12–15]. In [16] a complementary energy-based finite element formulation was developed for torsional buckling analysis of thin-walled columns and in [17, 18] shear deformation effects

R. E. Erkmen (✉) · H. Moradpoor · A. Bhowmick
Department of Building, Civil and Environmental Engineering, Concordia University, Montreal, QC, Canada
e-mail: emre.erkmen@concordia.ca

S. Walbridge et al. (eds.), *Proceedings of the Canadian Society of Civil Engineering Annual Conference 2021*, Lecture Notes in Civil Engineering 240,
https://doi.org/10.1007/978-981-19-0507-0_41

were included in lateral-torsional buckling analysis by using a complementary energy-based finite element formulation. Based on a Hellinger-Reissner principle adopted for thin-walled beams, hybrid finite element formulations that can capture shear deformation effects in the buckling analysis were developed in [19, 20].

One important aspect that is often overlooked in buckling analysis is that the material description for nonlinear strains depends on the choice of strain definition even when the material is elastic. An accurate hyperelastic material description leads to complicated expressions because the material parameters depend on finite deformations. To avoid complications in the material description, a direct adaptation of the generalized Hooke's material, where deformation independent moduli are used, is often justified by assuming that deflections are large, but strains are small. However, literature has shown that when shear deformations are involved, contradictory buckling predictions can be produced by adopting Hooke's material directly, as in the case of Engesser versus Haringx column buckling formulas. The difference between the two methods has been attributed to different assumptions for the internal force orientations at the deformed state of the column (e.g., [21]). Engesser assumes that the axial force is parallel to the beam axis in the loading state whereas, in Haringx theory, the axial force is assumed to be perpendicular to the cross section of the beam. This difference in the assumption of force directions can indeed be traced down to differences in the definitions of adopted strains within the Doyle-Ericksen family of strains and conjugate stresses (e.g., [22]).

In this study, we develop a shear-deformable finite element formulation that is applicable for the buckling analysis of thin-walled composite beams. The element can be used in the modelling of composite beams of any open section. The element consists of various laminates with different mechanical properties and unidirectional continuous fibres directed in arbitrary directions. The effect of fibre orientation on the buckling behaviour of thin-walled composite beams is illustrated using the developed finite element formulation for the analysis. The formulation is developed in terms of a generic member of the Doyle-Ericksen family of strains, while elastic Hooke's material is adopted for the constitutive relations. As such, the developed formulation is an extension of both Engesser and Haringx buckling formulas to thin-walled beams.

2 Methodology

2.1 Strains

The strain components can be written in terms of deflections $u(z)$, $v(z)$ and $w(z)$ of the beam axis that are parallel to x, y, z directions respectively, and the angle of twist $\phi_z(z)$ of the cross-section (Fig. 1a) and additionally $\phi_x(z)$ and $\phi_y(z)$ are rotation angles around the x and y axes respectively and $\psi(z)$ is the Vlasov warping function for thin-walled beams.

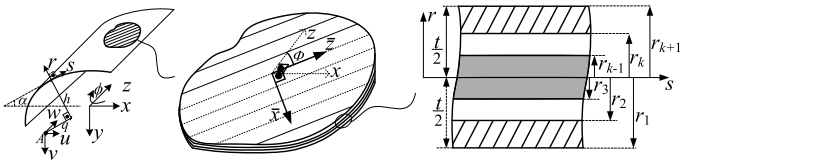

Fig. 1 Thin-walled beam composed of fibre-reinforced laminates

For the Doyle-Ericksen finite strain tensor definition in continuum, we refer to [23], i.e.$\boldsymbol{\varepsilon}_m = \frac{(\mathbf{U}^m - \mathbf{I})}{m}$, where m is a real parameter deciding on which member of the family, $\mathbf{I}$ is the unit tensor, and $\mathbf{U}$ is the right-stretch tensor of polar decomposition of the deformation gradient. In particular, $m = 2$ produces the commonly used Green-Lagrange strain tensor, $m = 1$ produces the Biot strain tensor, $m = 0$ produces Hencky strain tensor and $m = -2$ produces the Almansi strain tensor. For calculating the critical loads in buckling, only the second-order approximations to the strain tensor matters. Therefore, we limit ourselves to second order accuracy in which case the strains can express as $\boldsymbol{\varepsilon}_m = \boldsymbol{\varepsilon} + \boldsymbol{e} - \eta \boldsymbol{\varepsilon}^T \boldsymbol{\varepsilon}$ which consists of six components in 3D and contains a first order strain tensor $\boldsymbol{\varepsilon}$, a second order strain tensor $\boldsymbol{e}$, and $\boldsymbol{\xi} = \boldsymbol{\varepsilon}^T \boldsymbol{\varepsilon}$ where $\eta = 1 - 0.5$ m determines which member of the Doyle-Erickson family is chosen. The formulation is restricted to prismatic thin-walled members of arbitrary cross-sections and it is based on the kinematic assumptions that; cross-section does not change its shape during deformation. Therefore, some of the strain components that causes deformations within the plane of the cross-section can be eliminated directly, i.e. $\varepsilon_{xy} = 0$, $\varepsilon_{xx} = 0$, $\varepsilon_{yy} = 0$. As a result, only the axial strain in the z direction ε_{zz} and the shear strains γ_{xz} on the flanges and γ_{yz} on the web survive. We define a common shear strain considering the orientation of the thin-walled segments, $\gamma = \gamma_{xz}\cos\alpha + \gamma_{yz}\sin\alpha$ where a is shown in Fig. 1. Accordingly, the non-zero components of the linear strain $\boldsymbol{\varepsilon} = \langle\, \varepsilon_{zz} \;\; \gamma \,\rangle^T$ can be written as

$$\varepsilon_{zz} = w' - x\phi_y' + y\phi_x' - \omega\psi' \tag{1}$$

$$\gamma = \Big(u' - \phi_y\Big)\cos\alpha - \Big(v' + \phi_x\Big)\sin\alpha + h\Big(\phi_z' - \psi\Big) - 2r\phi_z' \tag{2}$$

In Eqs. (1) and (2), x and y identifies coordinates of a point on the cross-section, and r is the normal distance from the mid-surface (Fig. 1a). Sectorial area coordinate of the Vlasov theory was used, i.e. $\omega = \int h ds$ in which h is the normal distance to the tangent of the point on the section contour from the arbitrarily located pole A with x and y coordinates(a_x, a_y), i.e., $h = (x - a_x)\sin\alpha - \big(y - a_y\big)\cos\alpha$ (Fig. 1a), where α is the angle between x and s axes. As shown in Fig. 1a, s axis is tangent to the mid-surface of the cross-section and directed along the contour line. In Eqs. (1) and (2), prime denotes derivative with respect to the axial coordinate z, i.e. $()' = d()/dz$. The non-zero components of the nonlinear strain tensor $\boldsymbol{e} = \langle\, e_{zz} \;\; g \,\rangle^T$ can be

written as

$$e_{zz} = \frac{1}{2}\left(u'^2 + v'^2\right) - xv'\phi_z - a_{Gx}v'\phi'_z + yu'\phi_z + a_{Gy}u'\phi'_z + \frac{1}{2}\left[(x - a_{Gx})^2 + \left(x - a_{Gy}\right)\right]\phi'^2_z \tag{3}$$

$$g = \left(v'\phi_z - \phi_z w'\right)\cos\alpha - \left(u'\phi_z - \phi_x w'\right)\sin\alpha + q\phi_z\phi'_z \tag{4}$$

where $q = (x - a_x)cos\alpha + (y - a_y)sin\alpha$. The non-zero components of the nonlinear strain tensor $\boldsymbol{\xi} = \langle\, \xi_{zz}\ \varphi \,\rangle^T$ can be written as

$$\xi_{zz} = \frac{1}{4}\left(u' - \phi_y\right)^2 + \frac{1}{4}\left(v' + \phi_x\right)^2 \tag{5}$$

$$\varphi = w'\left(u' - \phi_y\right)\cos\alpha + w'\left(v' + \phi_x\right)\sin\alpha \tag{6}$$

2.2 Constitutive Relations

For a laminate composed of n orthotropic layers, the orientation of the local $\overline{x}_k\overline{z}_k$-plane with respect to the global xz-plane is determined by angle ϕ about the y-axis (Fig. 1b). Assuming that perfect interlaminar bond exists between the layers, the stress–strain relationship for the kth layer can be written as follows;

$$\boldsymbol{\sigma}^{(k)} = \begin{Bmatrix} \sigma_z{}^{(k)} \\ \tau^{(k)} \end{Bmatrix} = \overline{Q}^{(k)}\boldsymbol{\varepsilon}_m \tag{7}$$

where

$$\overline{Q}^{(k)} = \begin{bmatrix} \overline{Q}^{*(k)}_{11} & \overline{Q}^{*(k)}_{16} \\ \overline{Q}^{*(k)}_{16} & \overline{Q}^{*(k)}_{66} \end{bmatrix} \tag{8}$$

in which

$$\overline{Q}^{*(k)}_{11} = \overline{Q}^{(k)}_{11} - \frac{\overline{Q}^{(k)}_{12}{}^2}{\overline{Q}^{(k)}_{22}} \tag{9}$$

$$\overline{Q}^{*(k)}_{16} = \overline{Q}^{(k)}_{16} - \frac{\overline{Q}^{(k)}_{12}\overline{Q}^{(k)}_{26}}{\overline{Q}^{(k)}_{22}} \tag{10}$$

$$\overline{Q}^{*(k)}_{66} = \overline{Q}^{(k)}_{66} - \frac{\overline{Q}^{(k)2}_{26}}{\overline{Q}^{(k)}_{22}} \tag{11}$$

$$\overline{Q}^{(k)}_{11} = Q^{(k)}_{11}\cos^4\phi_k + 2\left(Q^{(k)}_{12} + 2Q^{(k)}_{66}\right)\sin^2\phi_k\cos^2\phi_k + Q^{(k)}_{22}\sin^4\phi_k \tag{12}$$

$$\overline{Q}^{(k)}_{16} = \left(Q^{(k)}_{11} - Q^{(k)}_{12} - 2Q^{(k)}_{66}\right)\sin\phi_k\cos^3\phi_k + \left(Q^{(k)}_{12} - Q^{(k)}_{22} + 2Q^{(k)}_{66}\right)\sin^3\phi_k\cos\phi_k \tag{13}$$

$$\overline{Q}^{(k)}_{66} = \left(Q^{(k)}_{11} + Q^{(k)}_{22} - 2Q^{(k)}_{12} - 2Q^{(k)}_{66}\right)\sin^2\phi_k\cos^2\phi_k + Q^{(k)}_{66}\left(\sin^4\phi_k + \cos^4\phi_k\right) \tag{14}$$

and

$$Q^{(k)}_{11} = \frac{E^{(k)}_1}{1 - v^{(k)}_{12}v^{(k)}_{21}} \tag{15}$$

$$Q^{(k)}_{12} = \frac{v^{(k)}_{12}E^{(k)}_2}{1 - v^{(k)}_{12}v^{(k)}_{21}} \tag{16}$$

$$Q^{(k)}_{22} = \frac{E^{(k)}_2}{1 - v^{(k)}_{12}v^{(k)}_{21}} \tag{17}$$

$$Q^{(k)}_{66} = G^{(k)}_{12} \tag{18}$$

where $E^{(k)}_1$ and $E^{(k)}_2$ are Young's moduli of the kth layer in the local $\overline{z}_k$ and $\overline{x}_k$ directions, respectively, $G^{(k)}_{12}$ is the shear moduli in $\overline{x}_k\overline{z}_k$ plane of the kth layer, $v^{(k)}_{12}$ is the Poisson's ratio defined as the ratio of the transverse strain in the $\overline{x}_k$ direction to the axial strain in $\overline{z}_k$ direction, and $v^{(k)}_{21}$ is the Poisson's ratio defined as the ratio of the transverse strain in the $\overline{z}_k$ direction to the axial strain in $\overline{x}_k$ direction. The laminate configuration is limited to symmetric angle-ply stacking sequence with respect to mid-plane (Fig. 1c).

3 Energy Functional for Static and Buckling Analyses

For the buckling analysis herein the pre-buckling deformations are neglected. In this case the analysis can be performed in two steps. Firstly; linear static analysis is performed under applied loads for which the equilibrium equations can be obtained from the first variation of the total potential energy functional, i.e., $\delta\Pi = 0$. Secondly; the internal forces obtained from the linear static analysis are used in the stability

condition, which can be obtained from the second variation of the total potential energy functional, i.e., $\delta^2\Pi = 0$.

3.1 Energy Functional for Static Analysis

The equilibrium equations for linear static analysis can be obtained in the weak form using the total potential energy functional, i.e.,

$$\delta\pi = \int_L \int_A \delta\varepsilon_m^T \underbrace{\overline{Q}^{(k)}\varepsilon}_{\sigma^{(k)}} dA dz - \int_L \delta\Delta^T p dz \tag{19}$$

where the first integral term is due to strain energy stored, $\boldsymbol{p}$ is the vector of applied loads, $\boldsymbol{\Delta}$ is the displacement vector of the load application point and δ denotes variation. Note that in Eq. (19), only the linear part of the strain tensor was used and based on which the stress distribution $\boldsymbol{\sigma}^{(k)}$ can be obtained.

3.2 Energy Functional for Buckling Analysis

The neutral equilibrium equations for buckling analysis can be obtained from the vanishing of the second variation of the total potential energy functional Eq. (17), i.e., $\delta^2\Pi = 0$, where

$$\delta^2\pi = \int_L \int_A \delta\varepsilon^T \overline{Q}^{(k)} \delta\varepsilon dA dz + \int_L \int_A \delta^2 e^T \underbrace{\overline{Q}^{(k)}\varepsilon}_{\sigma^{(k)}} dA dz - \eta \int_L \int_A \delta^2\xi^T \underbrace{\overline{Q}^{(k)}\varepsilon}_{\sigma^{(k)}} dA dz \tag{20}$$

in which pre-buckling deformations are ignored. Note that $\boldsymbol{\sigma}^{(k)}$ has been obtained from the linear static analysis in Eq. (19) and substituted into Eq. (20). The first term in Eq. (20), leads to the elastic stiffness matrix, while the second and third terms leads to the geometric stiffness matrix.

4 Finite Element Formulation

The finite element formulation is obtained by interpolating the displacement fields u, v, w, rotation fields ϕ_x, ϕ_y and ϕ_z and the warping function ψ using polynomial functions of the axial coordinate z, i.e.,

$$\begin{Bmatrix} w(z) \\ v(z) \\ \phi_x(z) \\ u(z) \\ \phi_y(z) \\ \phi_z(z) \\ \psi(z) \end{Bmatrix} = \begin{bmatrix} \boldsymbol{N} & 0 & 0 & 0 \\ 0 & \boldsymbol{L}_f & 0 & 0 \\ 0 & \boldsymbol{M}_f & 0 & 0 \\ 0 & 0 & \boldsymbol{L}_t & 0 \\ 0 & 0 & \boldsymbol{M}_t & 0 \\ 0 & 0 & 0 & \boldsymbol{L}_t \\ 0 & 0 & 0 & \boldsymbol{M}_t \end{bmatrix} \begin{Bmatrix} \boldsymbol{w} \\ \boldsymbol{\Omega} \\ \boldsymbol{\Lambda} \\ \boldsymbol{\Gamma} \end{Bmatrix} \tag{21}$$

where, $\boldsymbol{w} = \langle\, w_1 \; w_2 \,\rangle^T$, $\boldsymbol{\Omega} = \langle\, v_1 \; \phi_{x1} \; v_2 \; \phi_{x2} \,\rangle^T$, $\boldsymbol{\Lambda} = \langle\, u_1 \; \phi_{y1} \; u_2 \; \phi_{y2} \,\rangle^T$, $\boldsymbol{\Gamma} = \langle\, \phi_{z1} \; \psi_1 \; \phi_{z2} \; \psi_2 \,\rangle^T$ are the vectors of nodal values and $\boldsymbol{N} = \langle\, N_1 \; N_2 \,\rangle$, $\boldsymbol{L}_f = \langle\, L_{f1} \; L_{f2} \; L_{f3} \; L_{f4} \,\rangle$, $\boldsymbol{M}_f = \langle\, M_{f1} \; M_{f2} \; M_{f3} \; M_{f4} \,\rangle$, $\boldsymbol{L}_t = \langle\, L_{t1} \; L_{t2} \; L_{t3} \; L_{t4} \,\rangle$, $\boldsymbol{M}_t = \langle\, M_{t1} \; M_{t2} \; M_{t3} \; M_{t4} \,\rangle$ are the vectors of corresponding interpolation functions in which

$$N_1 = \frac{L - z}{L} \tag{22}$$

$$N_2 = \frac{z}{L} \tag{23}$$

$$L_{f1} = 1 - \frac{z\alpha_f}{L\left(1+\alpha_f\right)} - \frac{3z^2}{L^2\left(1+\alpha_f\right)} + \frac{2z^3}{L^3\left(1+\alpha_f\right)} \tag{24}$$

$$L_{f2} = \frac{z(1+0.5\alpha_f)}{\left(1+\alpha_f\right)} - \frac{2z^2(1+0.25\alpha_f)}{L\left(1+\alpha_f\right)} + \frac{z^3}{L^2\left(1+\alpha_f\right)} \tag{25}$$

$$L_{f3} = \frac{z\alpha_f}{L\left(1+\alpha_f\right)} + \frac{3z^2}{L^2\left(1+\alpha_f\right)} - \frac{2z^3}{L^3\left(1+\alpha_f\right)} \tag{26}$$

$$L_{f4} = -\frac{0.5z\alpha_f}{\left(1+\alpha_f\right)} + \frac{z^2(0.5\alpha_f - 1)}{L\left(1+\alpha_f\right)} + \frac{z^3}{L^2\left(1+\alpha_f\right)} \tag{27}$$

$$M_{f1} = -\frac{6z}{L^2\left(1+\alpha_f\right)} + \frac{6z^2}{L^3\left(1+\alpha_f\right)} \tag{28}$$

$$M_{f2} = 1 - \frac{z\left(4+\alpha_f\right)}{L\left(1+\alpha_f\right)} + \frac{3z^2}{L^2\left(1+\alpha_f\right)} \tag{29}$$

$$M_{f3} = \frac{6z}{L^2\left(1+\alpha_f\right)} - \frac{6z^2}{L^3\left(1+\alpha_f\right)} \tag{30}$$

$$M_{f4} = \frac{z\left(\alpha_f - 2\right)}{L\left(1+\alpha_f\right)} + \frac{3z^2}{L^2\left(1+\alpha_f\right)} \tag{31}$$

where α_f is a shear parameter approximated as $\alpha_f = \frac{12EI_x}{GA_yL^2}$ where EI_x is the bending rigidity of the composite cross-section around the x axis and GA_y is the shear rigidity in direction y. Components of the vectors $\boldsymbol{L}_t$ and $\boldsymbol{M}_t$ in Eq. (22) are identical to those given for $\boldsymbol{L}_f$ and $\boldsymbol{M}_f$ in Eqs. (24)–(31) except the fact that α_f should be replaced with α_t which is approximated as $\alpha_t = \frac{12EI_y}{GA_xL^2}$. As a result of the interpolation scheme, one obtains Eq. (20) in the discretised form as

$$[\boldsymbol{K} + \lambda \boldsymbol{K}_G]\delta \boldsymbol{d}_b = 0 \tag{32}$$

in which λ is the buckling load factor, $\boldsymbol{K}$ and $\boldsymbol{K}_G$ are the assembled elastic stiffness and geometric stiffness matrices, respectively, and $\delta \boldsymbol{d}_b$ is the vector of buckle mode shape. It should be noted that the solution for λ and the corresponding $\delta \boldsymbol{d}_b$ depends on the selected strain parameter η.

5 Applications

5.1 *Lateral-Torsional Buckling of Mono-Symmetric Thin-Walled Beam Under Uniform Moment*

A simply supported mono-symmetric section under uniform bending moment is analysed herein for validation purposes. Figure 2 shows the loading and boundary conditions of a 4 m span beam, and the dimensions of the cross-section of the analysed beam.

Flanges and the web are laminated symmetrically with respect to their mid-plane using 16 layers of equal thickness. For the examples considered herein the material of the beams is glass-epoxy and the values of material properties are provided in Table 1.

Stacking sequence of the layers and the corresponding buckling moments based on the current study and those based on ABAQUS shell element model used in [4] are shown in Table 2. It can be verified that the results are in good agreement and

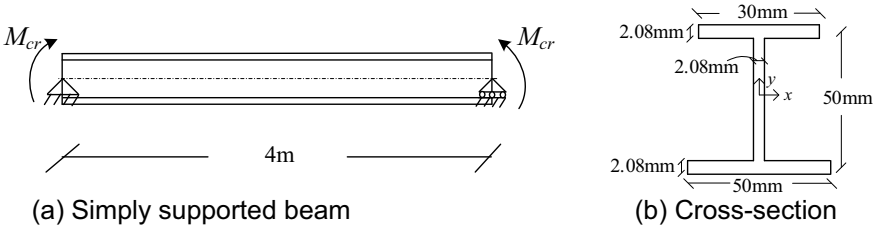

Fig. 2 Mono-symmetric beam under uniform bending moment. **a** Simply supported beam. **b** Cross-section

Table 1 Values of material properties for glass-epoxy composite (GPa)

E_1	E_2	G_{12}	ϑ_{12}	ϑ_{21}
53.78	17.93	8.96	0.25	0.25

Table 2 Critical moments for the simply supported beam in Fig. 2 (Nmm)

Stacking sequence	This study sixteen elements-No shear effect	This study sixteen elements-Shear effect with $m = 2$	This study sixteen elements-Shear effect with $m = -2$	Ref. [4]
$[0]_{16}$	47.30	47.30	47.30	46.560
$[15/-15]_{4S}$	46.76	46.76	46.76	48.794
$[30/-30]_{4S}$	42.9	42.90	42.90	49.624
$[45/-45]_{4S}$	36.57	36.57	36.57	44.611
$[60/-60]_{4S}$	32.6	32.6	32.6	37.730
$[75/-75]_{4S}$	30.1	30.1	30.1	31.359
$[0/90]_{4S}$	39.48	39.48	39.48	38.792
$[0/-45/90/45]_{2S}$	38.44	38.44	38.44	41.970

thus lateral buckling behaviour can be captured with the proposed finite element formulation without requiring sophisticated shell element models.

It should be noted that by selecting $m = 2$ or $m = -2$, one obtains Green-Lagrange or Almansi strains, respectively. Effect of fibre-orientation on the buckling moment predictions of both simply supported beam is illustrated in Fig. 3.

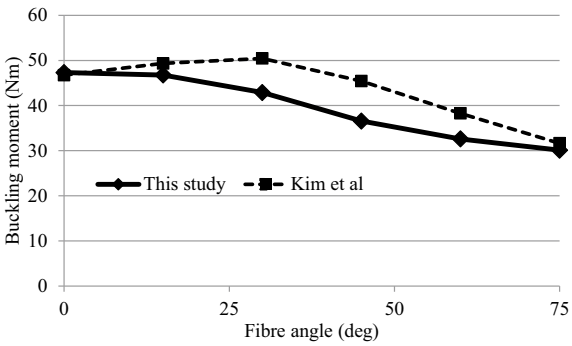

Fig. 3 Critical buckling moments according to lay-up $[\pm\Phi]_{4S}$

5.2 *Lateral-Torsional Buckling of Simply Supported Symmetric I-section Under Uniform Load*

In this example the buckling predictions are illustrated by using the developed formulation for the analysis of a simply supported symmetric I-section under uniform distributed load as shown in Fig. 4.

The material properties are same as in the previous example and given in Table 1. The distributed load is applied at the beam's centroidal axis. Results are compared with those based on [3] in which a formulation was suggested as

$$q_{cr} = \frac{8}{L^2} \times 1.13 M_{yz} \tag{33}$$

where $M_{yz} = \sqrt{(\pi^2 E I_y / L^2)(G J_d + \pi^2 E I_w / L^2)}$. Results are shown for various different stacking sequences in Table 3.

Effect of fibre orientation is shown in Fig. 5.

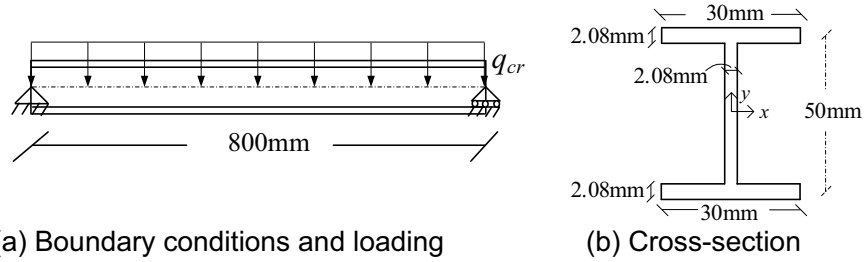

Fig. 4 Symmetric simply supported beam under distributed load. **a** Boundary conditions and loading. **b** Cross-section

Table 3 Critical uniform loads for the simply supported beam in Fig. 4 (N/m)

Stacking sequence	This study sixteen elements-No shear effect	This study sixteen elements-Shear effect with $m = 2$	This study sixteen elements-Shear effect with $m = -2$	Eq. (33)
$[0]_{16}$	3.60	3.59	3.59	3.88
$[15/-15]_{4S}$	3.35	3.35	3.35	3.78
$[30/-30]_{4S}$	2.70	2.70	2.70	3.42
$[45/-45]_{4S}$	2.06	2.06	2.06	2.85
$[60/-60]_{4S}$	1.76	1.76	1.76	2.26
$[75/-75]_{4S}$	1.63	1.63	1.63	1.85
$[0/90]_{4S}$	2.61	2.61	2.61	2.81
$[0/-45/90/45]_{2S}$	2.34	2.34	2.34	2.80

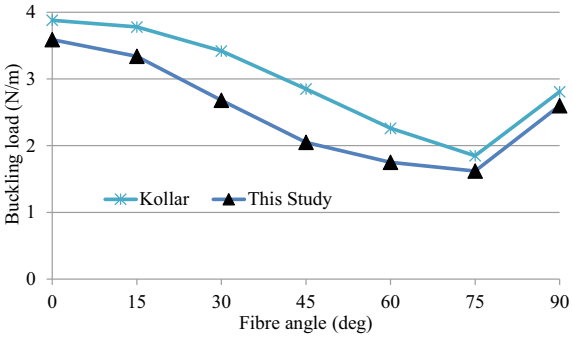

Fig. 5 Critical buckling loads according to lay-up $[\pm\Phi]_{4S}$

5.3 *Flexural Buckling of Simply Supported Symmetric I-section Under Compressive Load*

In the literature one can find two different classical formulas suggested for the buckling analysis of shear deformable columns, namely by Engesser and Haringx. The buckling predictions based on Engesser P_E and Haringx P_H can be expressed, respectively as follows:

$$P_E = \frac{P_s P_b}{P_s + P_b} \tag{34}$$

and

$$P_H = \frac{1}{2}\left(\sqrt{P_s^2 + 4P_s P_b} - P_s\right) \tag{35}$$

in which

$$P_b = \pi^2 EI/L^2 \tag{36}$$

is the Euler buckling load where EI is the flexural rigidity and L is the effective length, and $P_s = GA$ is the shear buckling load in which GA is the shear rigidity. For very large shear rigidity cases, the critical load will approach P_b in both methods. However, in shear-weak cases, Engesser solution yields $P_E = P_s$ and Haringx theory obtains a significantly different result as $P_H = \sqrt{P_s P_b}$.

In this example, the simply supported beam shown in Fig. 6 below is analysed under compressive load. The material properties are the same as in the previous examples as given in Table 1. The span is 100 mm and buckling occurs around the y axis. The flexural buckling load predictions based on the proposed solution strategy herein are compared with those based on Euler, Engesser and Haringx column buckling solutions in Table 4.

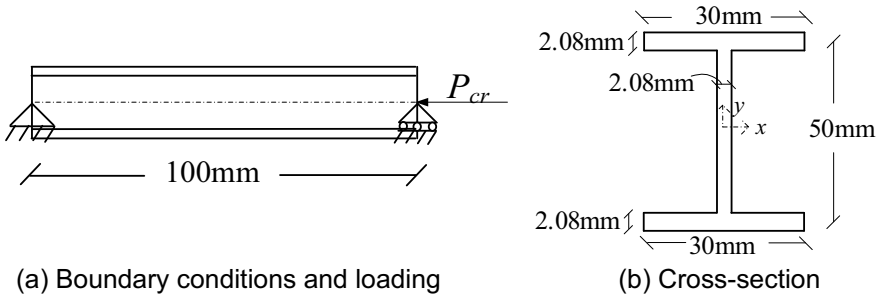

Fig. 6 Symmetric simply supported beam under compressive load

Table 4 Critical compressive loads for the simply supported beam in Fig. 6 (N)

Stacking sequence	This study-sixteen elements-shear effect with $m = 2$	This study-sixteen elements-shear effect with $m = -2$	This study-sixteen elements-no shear effect	Engesser P_E Eq. (34)	Haringx P_H Eq. (35)	Euler P_b Eq. (36)
$[0]_{16}$	352.24	383.03	513.77	351.97	382.69	513.68
$[15/-15]_{4S}$	333.38	356.34	462.50	333.11	356.03	462.16
$[30/-30]_{4S}$	269.38	279.48	338.85	269.23	279.30	338.80
$[45/-45]_{4S}$	197.40	201.27	231.40	197.35	201.21	231.43
$[60/-60]_{4S}$	161.79	164.05	184.51	161.70	163.95	184.45
$[75/-75]_{4S}$	150.92	153.13	172.75	150.84	153.04	172.71
$[0/90]_{4S}$	262.34	275.08	342.48	262.15	274.87	342.46
$[0/-45/90/45]_{2S}$	232.74	240.18	286.94	232.60	240.02	286.89

The effect of fibre orientation is shown in Fig. 7.

Fig. 7 Critical buckling loads according to lay-up $[\pm\Phi]_{4S}$

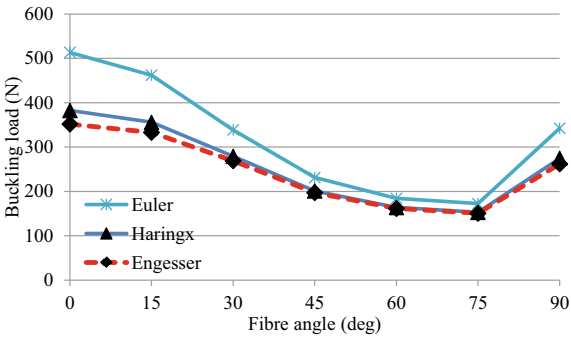

6 Conclusion

The proposed formulation for buckling analysis of thin-walled beams was validated against known solutions from the literature. In the case of long slender beams under uniform bending moment loading the results agree well with those of a shell-type model from literature and including shear deformations have not effect on the results. The effect of shear deformation and stress–strain definitions in buckling load predictions were not significant in the analysed lateral-torsional buckling problems. However, in the case of a short column problem, it was shown that Engesser and Haringx solutions lead to significantly different result. In the finite element analysis context, this difference is due to differences in the definitions of adopted stresses which affect the geometric stiffness matrix within the linearized eigenvalue problem. The finite element results based on the proposed methodology exactly match with those based on the analytical results of Engesser, Haringx, and Euler when corresponding stress–strain definitions are used. That confirms that the formulation is capable of capturing the shear deformation effects very accurately. The Engesser's formula provided more conservative results comparison to that of the Haringx and as Euler's formula neglects shear deformation effects, it is unconservative when shear deformations are significant. The effect of the fibre orientation on the buckling predictions was also illustrated in all three cases studied herein.

References

1. Bauld NR Jr, Lih-Shyng T (1984) A Vlasov theory for fiber-reinforced beams with thin-walled open cross sections. Int J Solids Struct 20(3):277–297
2. Pandey MD, Kabir MZ, Sherbourne AN (1995) Flexural-torsional stability of thin-walled composite I-section beams. Compos Eng 5(3):321–342
3. Sapkás Á, Kollár LP (2002) Lateral-torsional buckling of composite beams. Int J Solids Struct 39(11):2939–2963
4. Kim NI, Shin DK, Kim MY (2007) Exact lateral buckling analysis for thin-walled composite beam under end moment. Eng Struct 29(8):1739–1751
5. Roberts TM (2002) Influence of shear deformation on buckling of pultruded fiber reinforced plastic profiles. J Compos Constr 6(4):241–248
6. Roberts TM, Masri HMKJAH (2003) Section properties and buckling behavior of pultruded FRP profiles. J Reinf Plast Compos 22(14):1305–1317
7. Omidvar B, Ghorbanpoor A (1996) Nonlinear FE solution for thin-walled open-section composite beams. J Struct Eng 122(11):1369–1378
8. Lee J, Kim SE, Hong K (2002) Lateral buckling of I-section composite beams. Eng Struct 24(7):955–964
9. Lee J (2006) Lateral buckling analysis of thin-walled laminated composite beams with monosymmetric sections. Eng Struct 28(14):1997–2009
10. Back SY, Will KM (2008) Shear-flexible thin-walled element for composite I-beams. Eng Struct 30(5):1447–1458
11. Cardoso JB, Benedito NM, Valido AJ (2009) Finite element analysis of thin-walled composite laminated beams with geometrically nonlinear behavior including warping deformation. Thin-Walled Struct 47(11):1363–1372

12. Saadé K, Espion B, Warzée G (2004) Non-uniform torsional behavior and stability of thin-walled elastic beams with arbitrary cross sections. Thin-walled struct 42(6):857–881
13. Kim M-Y, Nam K II, Hee-Taek Y (2003) Exact dynamic and static stiffness matrices of shear deformable thin-walled beam-columns. J Sound Vib 267(1):29–55
14. Wu L, Mohareb M (2011) Buckling formulation for shear deformable thin-walled members—II Finite element formulation. Thin-Walled Struct 49(1):208–222
15. Erkmen RE, Attard MM (2011) Lateral-torsional buckling analysis of thin-walled beams including shear and pre-buckling deformation effects. Int J Mech Sci 53(10):918–925
16. Erkmen RE, Mohareb M, Bradford MA (2009) Complementary energy based formulation for torsional buckling of columns. J Eng Mech 135(12):1420–1426
17. Erkmen RE, Mohareb M (2008) Buckling analysis of thin-walled open members—A complementary energy variational principle. Thin-walled struct 46(6):602–617
18. Erkmen RE, Mohareb M (2008) Buckling analysis of thin-walled open members—A finite element formulation. Thin-walled struct 46(6):618–636
19. Erkmen RE (2014) Shear deformable hybrid finite-element formulation for buckling analysis of thin-walled members. Finite Elem Anal Des 82:32–45
20. Erkmen RE, Niki V, Afnani A (2021) Shear-deformable hybrid finite-element formulation for lateral-torsional buckling analysis of composite thin-walled members. Can J Civ Eng 48. https://doi.org/10.1139/cjce-2019-0560
21. Attard (2003) Finite strain beam theory. Int J Solids Struct 40:4563–4584
22. Bazant ZP (2003) Shear buckling of sandwich, fiber-composite and lattice columns, bearings and helical springs: paradox resolved. ASME J Appl Mech 70:75–83
23. Bazant ZP, Cedolin L (2010) Stability of structures. Oxford University Press, Inc., New York

An Experimental Design Approach for the Design of Two-Lift Concrete Pavements

Surya T. Swarna and Kamal Hossain

1 Introduction

Various types of plain jointed concrete pavement are in use in different countries depending upon the climate, availability of materials, soil types, experience, and traffic. As per construction practice, the following three types of plain concrete pavements are most common.

- Single concrete pavement—A concrete layer directly paced over a granular subgrade/subbase.
- Unbonded concrete pavement—Two layers concrete construction with a separation (plastic sheet) layer between the concrete layers.
- Bonded concrete pavements/Two-Lift Concrete Pavement (TLCP)—Two layers concrete construction with a high bond interface.

A Bonded concrete pavement, also known as two-lift concrete pavement (2LCP) involves placing two layers of concrete 'wet-on-wet' rather than the traditional method of using a single, homogeneous layer of concrete. The bottom layer is generally thicker and consists of lower quality concrete mixtures or aggregate, in many cases recycled aggregate or local aggregates that are not suitable for use in surface courses exposed to the abrasive action of traffic. 2LCP will reduce material costs

S. T. Swarna (✉)
Faculty of Engineering and Applied Science, Memorial University of Newfoundland, St. John's, Canada
e-mail: stswarna@mun.ca

K. Hossain
Pavement Engineering, Carleton University, Ottawa, Canada

Department of Civil Engineering, Advanced Road & Transportation Engineering Lab (ARTEL), Memorial University of Newfoundland, St. John's, Newfoundland A1B 3X5, Canada

S. Walbridge et al. (eds.), *Proceedings of the Canadian Society of Civil Engineering Annual Conference 2021*, Lecture Notes in Civil Engineering 240,
https://doi.org/10.1007/978-981-19-0507-0_42

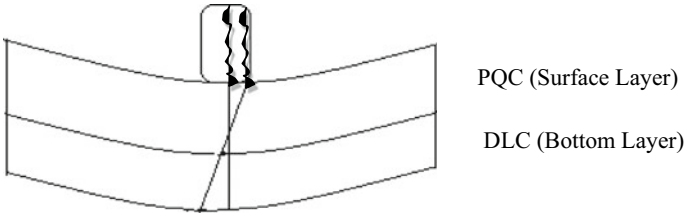

Fig. 1 Concrete pavement and subbase act monolithically

by being able to consume more local materials including low-quality aggregates, recycled concrete aggregate (RCA), and reclaimed asphalt pavement (RAP).

The surface layer bonds with the fresh lean concrete subbase, which will result in a monolithic action of the two layers, which will reduce stresses in pavement layers. The strain variation for the monolithic pavement is shown in Fig. 1.

2 Past Studies

Greene et al. [4] investigated three test section of 2-Lift Concrete Pavement (2LCP) for performance. This study concluded that there is no significant performance differences between subsections with differing econocrete strength. Therefore, these type of 2LCP sections are more feasible alternative for the conventional concrete pavements. Bentsen et al. [1] stated that the two-lift paving is a possible and practical application, Economic paving sections can be obtained using recycled aggregate bottom layer. On the other hand, additional care has to be taken on bonding between two layers in the construction of 2LCP. Bonding between two layers depends on the time gap for the lay surface layer over econocrete layer. The time lag between two layers' placement is very important in terms of achieving a good bond. But there are other factors that should be considered while selecting time lag. These factors include wind speed, temperature, relative humidity, and requirements of the contractor. Use of recycled aggregates is thought to be the cause of delamination between two layers of time delay in construction (30 min to 2 h) and separation. No data on the coefficient of thermal expansion (CoTE) of concrete were available, which can be another reason of the distresses. To avoid these types of distresses, no recycled aggregate was allowed in 2LCP project in 2012 was presented by Hu et al. [5].

Although 2LCP is becoming a technically feasible technique, successful implementation of the technique will require more demonstration projects to promote the practice and to eliminate difficulties and challenges for 2LCP implementation demands laboratory and field studies to determine optimum time lag between the two lifts under different conditions, minimum bond strength, and CoTE on debonding issues and/or thermal deformation. Several full-scale demonstration projects [2, 3, 5, 10] report that two-lift construction offers an economic solution with almost similar performance as the conventional.

The main factors governing the design of concrete pavements are design period, volume of commercial traffic, composition of commercial traffic in terms of single, tandem, tridem, and multi-axle, axle load spectrum, tire pressure, lateral placement characteristics, directional distribution, strength of pavement foundation layer and climatic factors.

Huang [6] found stresses in bonded concrete pavements using the principle of equivalent stiffness method which fails to estimate the interface stresses in bonded concrete pavements. Published literature for the analysis of TLCP are very limited. In the available literature, the non-linear temperature variation is not taken into consideration. In addition, analytical solutions are not available to compute the interfacial stresses in two-lift concrete pavements.

Kandil and Lye [7] performed a statistical design of experiment to minimise the number of the runs, and also to take the possible quadratic or curvature effects into the model, a one-half fraction of a 2^7-experiment coupled with a face centred central composite response surface design was adopted to predict the response of asphalt pavement.

3 Objective of the Study

The objective of this study is to compute the stresses in Two-Lift Concrete Pavements (TLCP) under various environmental and loading conditions. In addition, it is also aimed to quantify the influence of various factors on flexural stresses in TLCP. The factors include temperature differential, modulus of subgrade reaction, wheel load, LC thickness, and PQC thickness.

4 Structural System

The factors and the levels considered for the statistical design of experiments are presented in Table 1. Form the past studies, it is clearly described why the following factors and the levels considered in the analysis.

Table 1 Summary of experimental design

Factors	Name	Units	Low level	Mid-level	High level
A	Temperature differential	°C	9.0	15.0	21.0
B	Modulus of subgrade reaction	kg/cc	5.0	7.5	10.0
C	Wheel load	kN	120	160	200
D	LC thickness	mm	150	200	250
E	PQC thickness	mm	150	200	250

For Factor A, temperature differentia is selected based on the maximum and minimum temperature gradient which is possible to occurs during daytime and night-time. In addition, temperature differential is selected in such a way that the minimum temperature influences the response. Temperature is one of the critical factors which can be influenced by other factors such as modulus of subgrade reaction. The lower level of factor A is 9.0 °C and high level is at 21.0 °C.

For Factor B, modulus of subgrade reaction is the main factor where the pavement layers are resting on. As the concrete pavements are more elastic in nature, Modulus of subgrade reaction won't affect the flexural stress much compared to other factors. But it interacts with other factors such as temperature and wheel load, it varies drastically. The lower level of factor B is 5.0 kg/cc and high level is at 10 kg/cc.

For Factor C, wheel load is the basic factor which highly influence the flexural stress in concrete pavements. The levels are selected based on the legal limit of axle load provided by the Department of Transportation and Works of all the provinces in north America.

Factor D and E are the main factors which is are responsible for the pavement performance. The final outcome of the pavement design is the thickness of LC and PQC. The levels of these factors considered in such a way that, the design must be suitable for low volume traffic and high-volume traffic recommended by Department of Transportation and Works of all the provinces in North America.

The response from this experiment is flexural stress in lean concrete layer and pavement quality concrete layer. As the two layers are bonded flexural stress in PQC layer gives the interfacial stresses. In the design of TLCP, these flexural stresses place an important role in selecting the appropriate thickness of LC and PQC thickness based on cumulative fatigue of concrete pavement.

To minimise the number of experimental runs to be performed, and to take into account possible quadratic or curvature effects, a face centred central composite response surface design will be used for this study.

5 Modeling in Finite Element

The paper presents an analysis of stresses in bonded concrete pavement considering axle loads as well as temperature gradients acting simultaneously to model the realistic condition. A finite element software named ANSYS is used to determine the stress in two-lift concrete pavements. In addition, interfacial stresses are also computed.

A two-layer bonded concrete pavement system of the top layer is in blue colored elements, the bottom layer is in pink colored elements as solid 185, 8 noded brick elements were selected in ANSYS Package. The 3D FEM elements are capable enough to take tension, compression, torsion under adverse conditions. Such elements rest on a subgrade modeled as a set of discrete linear springs, also known as Winkler foundation, as shown in Fig. 2. Combination spring dampener 14 is considered for the modelling bed of linear springs. The foundation is designated by its modulus

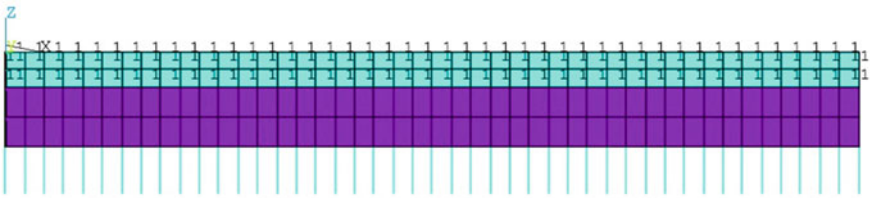

Fig. 2 Two lift monolithic concrete slab on Winkler foundation

Table 2 Material properties considered for modelling

Properties	Top layer	Bottom layer
Modulus of elasticity (MPa)	30,000	15,000
Poisson's ratio	0.15	0.25
Coefficient of thermal expansion (°C)	1 × 10–5	1 × 10–5
Reference temperature (°C)	35	35
Density (kg/m^3)	2,400	2,000

of subgrade reaction, K in MPa/m. Intense care was taken during the selection of boundary conditions to cope with practicality. The material properties considered in the analysis are presented in Table 2.

Figure 3a, b shows the placement of an axle at the edge and corners which are critical for pavement design. Over 20 different loading conditions are iterated and found the two critical loading conditions. The first loading condition is an axle

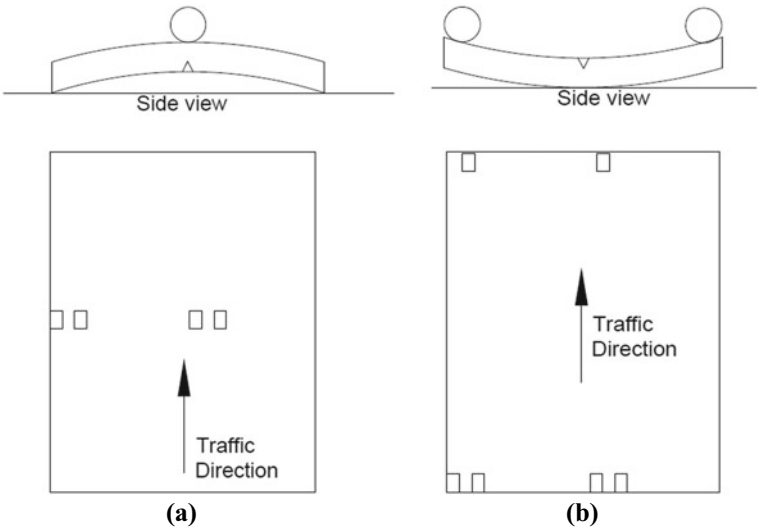

Fig. 3 Wheel loading condition during, **a** day-time, **b** night-time

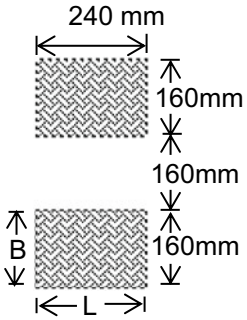

Fig. 4 Tyre imprint on a concrete pavement

load at the edge of the slab while the slab is restrained in the high curling portion during daytime as illustrated in Fig. 3a. This loading condition predominantly causes bottom-up cracking in the pavement. Another loading condition is a combination of two axles (front and rare) in both edges of the slab while the slab is in curl up position during nighttime as exhibited in Fig. 3b. This loading condition causes top-down cracking in the TLCP.

If the effect of the tyre wall is ignored, the contact pressure between the tyre and pavement must be equal to the tyre pressure. The assumption is made that contact pressure are uniform over the imprint area. Past studies show the tyre imprints of commercial vehicles with tyre pressure between 0.7 and 0.8 MPa is closer to a rectangle than to a circle. Hence an equivalent rectangular contact area, of dimension 240 (L) $\times$ 160 mm (W) (corresponding to 120 kN wheel load and 0.8 MPa tyre pressure) was considered for each wheel and kept constant for all the loads (i.e. as loads are varying, their respective tyre pressures are also varying due to constant contact area). The geometry of the imprint is as shown in Fig. 4.

The temperature gradient in a concrete pavement is non-linear [8, 9]. The non-linear temperature variation across the depth of pavement slab was close to a parabola and can be approximated by a bilinear distribution across the depth as shown in Fig. 4. The difference of temperature between mid-depth and the pavement surface is about double of that between the mid-depth and the bottom as shown in Fig. 5.

Using Finite element analysis, flexural stresses in both the layers of two-lift concrete pavement are computed for different combinations of loads, temperature gradients, and for various modulus of subgrade reaction values (Fig. 6).

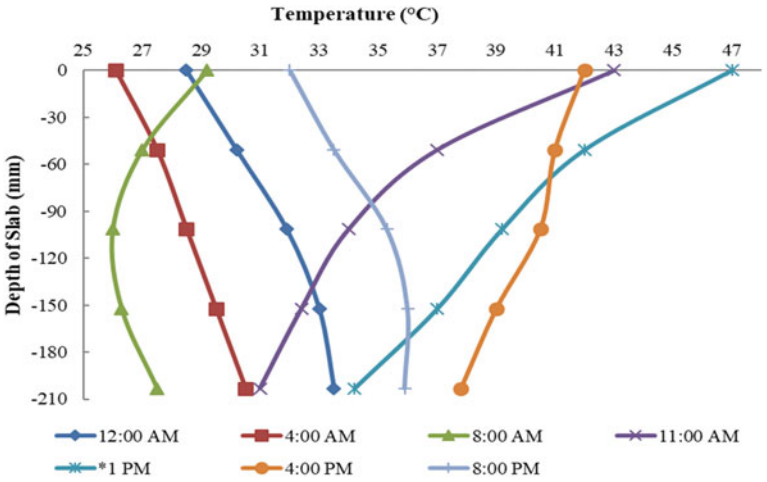

Fig. 5 Temperature distribution in an existing concrete pavement from field data [8]

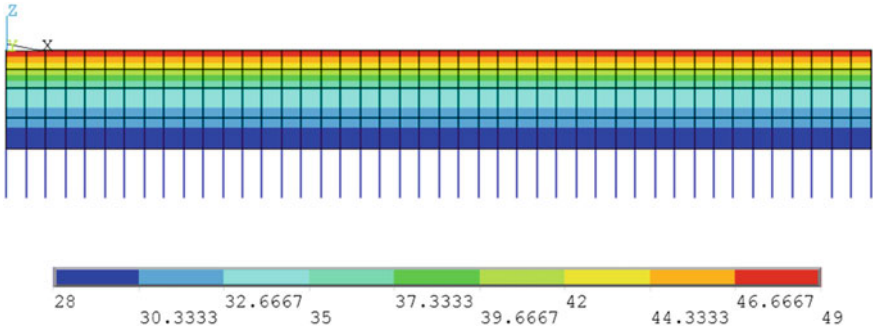

Fig. 6 FEM model with non-linear temperature gradient

6 Data Analysis

6.1 Central Composite Design

It is clearly observed that the Design-Expert suggests Quadratic model. So, in selecting the terms for ANOVA, process order is taken as Quadratic and auto selected the significant factors using AICc criterion and forward selection. For response 1, from this auto selection, it is witnessed that the Factors such as B, C, D, E, AC, AD, AE, BE, CD, DE and A^2 are significant. Since AB and A^2 are significant, A is considered into the model which makes the model hierarchical. In addition, it is also noticed that the quadratic terms are significant. Which concludes that the model is purely Quadratic. For response 2, From this auto selection, it is witnessed that the

Factors such as A, B, C, D, E, AB, AC, AD, AE, CD, CE, DE and A^2 are significant. In addition, it is also noticed that the quadratic terms are significant. Which concludes that the model is purely Quadratic.

From Table 3, it is clearly observed that the factor A and B are insignificant but when it interacts with other factor, the interaction became highly significant.

For flexural stress in LC, all assumptions (Normality, constant variance and Independence) are checked and found that all assumptions are ok. No transformation is needed.

Table 3 ANOVA table for both the models

Source	Flexural stress in PQC			Flexural stress in LC		
	RC	*F*-value	*P*-value	RC	*F*-value	*P*-value
Model	0.096279	98.95814	1.03E−20	1.106713	210.4149	4.79E−25
A-temperature	0.00245	2.51864	0.122993	4.749802	903.0607	2.1E−23
B-modulus of subgrade reaction	0.003789	3.894805	0.057709	0.116708	22.18918	5.67E−05
C-wheel load	0.229844	236.2394	9.16E−16	1.356003	257.8114	5.73E−16
D-DLC thickness	0.515689	530.0386	1.27E−20	4.679052	889.6093	2.59E−23
E-PQC thickness	0.167794	172.4625	5.67E−14	1.10088	209.3059	8.5E−15
AB	–	–	–	0.094178	17.90568	0.000213
AC	0.035463	36.45005	1.26E−06	0.14824	28.1843	1.08E−05
AD	0.024886	25.57892	1.98E−05	0.632813	120.3141	7.78E−12
AE	0.086289	88.69017	1.82E−10	1.057058	200.9742	1.43E−14
BE	0.003056	3.14108	0.0865	–	–	–
CD	0.008748	8.991058	0.00541	0.098568	18.74034	0.000163
CE	–	–	–	0.019405	3.689299	0.064644
DE	0.011155	11.46491	0.001996	0.147153	27.97763	1.13E−05
A^2	0.066186	68.02754	3.31E−09	0.187408	35.63116	1.73E−06
Residual	0.000973			0.00526		
Cor total						
R^2	0.975359			0.989509		
Adj-R^2	0.965503			0.984807		
Pre-R^2	0.955483			0.977283		

Note For flexural stress in PQC, all assumptions (Normality, constant variance and Independence) are checked and found that all assumptions are ok, but box-cox suggested to transform the both models to square root. So, the model is transformed to square root

$$\begin{aligned}\text{Sqrt (Flexural Stress in PQC)} &= 1.02096 + 0.00848954 * \text{A} \\ &+ 0.0105571 * \text{B} \\ &+ 0.0822199 * \text{C} - 0.123156 * \text{D} - 0.0702503 * \text{E} \\ &- 0.0332901 * \text{AC} + 0.0278873 * \text{AD} \\ &+ 0.0519282 * \text{AE} + 0.00977248 * \text{BE} \\ &- 0.0165337 * \text{CD} + 0.0186703 * \text{DE} \\ &+ 0.0964398 * \text{A}^2 \left[\text{R}^2 = 0.9754\right]\end{aligned} \tag{1}$$

$$\begin{aligned}\text{Flexural Stress in LC} &= 1.36922 + 0.373765 * \text{A} \\ &+ 0.0585882 * \text{B} + 0.199706 * \text{C} \\ &- 0.370971 * \text{D} - 0.179941 * \text{E} \\ &+ 0.05425 * \text{AB} + 0.0680625 * \text{AC} - 0.140625 \\ &* \text{AD} - 0.18175 * \text{AE} - 0.0555 * \text{CD} - 0.024625 * \text{CE} \\ &+ 0.0678125 * \text{DE} - 0.162281 * \text{A}^2 \left[\text{R}^2 = 0.9895\right]\end{aligned} \tag{2}$$

6.2 For Response 1

From Fig. 7, at 15 °C, the stresses are reduced, it occurs mainly because of built in curl in the concrete pavements. It is also witnessed that the stresses are almost similar for lower and higher thickness at high temperature. At lower temperature the stresses are high in lower PQC and LC thickness.

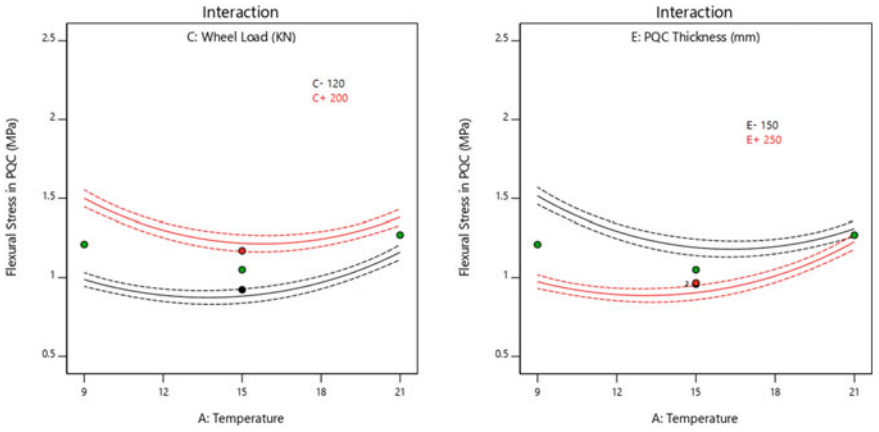

(a) (b)

Fig. 7 Interaction plots for the response 1

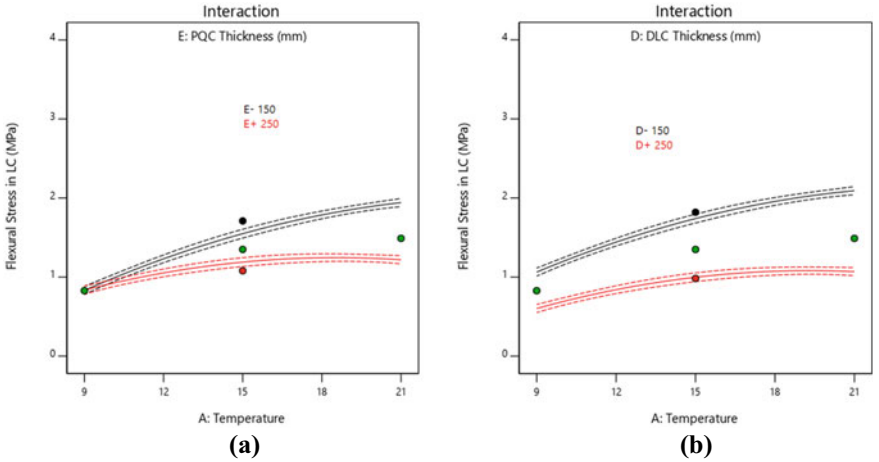

Fig. 8 Interaction plots for the response 2

6.3 For Response 2

From Fig. 8, it is observed that with the increase in temperature differential, stresses increase with a decrease in thickness for different loads at lower thickness of LC and vice versa. For lower temperature differential, stress is same and variant at higher temperature differential.

The models are validated using 3 random points, it is witnessed that the model predicts very accurately. All the three points are with in 95% PI level and very close to Predicted mean.

7 Conclusions

The paper indicates that the stresses in PQC and the lower concrete layer can be made to be low by selecting appropriate combinations of the thickness of the two layers for bonded concrete pavements. This conclusion is made based on the thorough FEM analysis. From this analysis, following conclusions are made:

- Two lift constructions can offer an eco-friendly solution for a concrete pavement at a lower life cycle cost as it gives higher life compared to unbonded concrete pavements.
- At 15 °C, the stresses are reduced; it occurs mainly because of built in curl in the concrete pavements. It is also witnessed that the stresses are almost similar for lower and higher thickness at high temperature. At lower temperature the stresses are high in lower PQC and LC thickness.

- For the lower thickness of the bottom lift, the stresses are less for lower modulus of subgrade reaction (k) due to higher temperature differential and it increases with an increase in modulus of subgrade reaction for similar temperature condition.
- Factors such as temperature and modulus of subgrade reaction are insignificant but when it interacts with other factor such as temperature differential and PQC thickness, the interaction became highly significant.
- With the increase in temperature differential, stresses increase with an increment in k-value for different loads at lower thickness of LC and vice versa.
- The analysis presented in this paper can be used for the design of two lift concrete pavements.
- The models developed for the flexural stresses are useful for the stress predication in cumulative fatigue damage analysis.

8 Limitations

- Subgrade is considered as Winkler foundation in the finite element analysis. Winkler foundation assumes zero shear strength for the subgrade.
- This study also assumes that the Winkler foundation is attached to the concrete layers. This applies a tension force when the concrete slab curls up and applies a compressive force when the concrete slab curls down.

References

1. Bentsen RA, Vavrik WA, Roesler JR, Gillen, SL (2013) Ternary blend concrete with reclaimed asphalt pavement as an aggregate in two-lift concrete pavement. In: Proceedings of the 2013 international concrete sustainability conference, pp 6–8
2. Brand A, Amirkhanian A, Roesler J (2014) Flexural capacity of full-depth and two-lift concrete slabs with recycled aggregates, transportation research record. J Transp Res Board (2456):64–72 (Washington DC). https://doi.org/10.3141%2F2456-07
3. Cable JK, Frentress DP, Williams JA (2004) Two-lift portland cement concrete pavements to meet public needs. Final Report. Iowa State University
4. Greene J, Nazef A, Choubane B (2011) A 30 year performance evaluation of a two layer concrete pavement system. Technical Report FL/DOT/SMO/10-540. Florida Department of Transportation, Tallahasse, FL
5. Hu J, Siddiqui MS, David Whitney PE (2014) Two-lift concrete paving-case studies and reviews from sustainability, cost effectiveness and construction perspectives. In: TRB 93rd annual meeting compendium of papers
6. Huang YH, Pavement analysis and design, 2nd edn
7. Kandil K, Lye L (2005) Experimental design approach to pavement response evaluation. In: 6th transportation specialty conference. CSCE
8. Subramanian VV (1964) Investigation on temperature and friction stresses in bonded cement concrete pavement, doctoral dissertation. Ph.D. thesis transportation engineering section. Civil Engineering Department, IIT Kharagpur

9. Swarna S, Reddy KS, Reddy MA, Pandey BB (2018) Analysis of stresses due to traffic and thermal loads in two-lift bonded concrete pavements by finite element method. Adv Civ Eng Mater 7(2):207–222. https://doi.org/10.1520/ACEM20170028
10. Swarna S, Hossain K, Reddy MA, Pandey BB (2019) A mechanistic and economic analysis of two-lift concrete pavements. Road Mater Pavement Des 1–19. https://doi.org/10.1080/14680629.2019.1620843

Experimental Investigation of Tornado Induced Pressures on Residential Buildings

J. Williams and E. Dragomirescu

1 Introduction

An average of 172 windstorms occurs each year in Canada. Of these, 62 have been reported as tornadoes according to a Northern Tornadoes Project Survey [5]. Until recently, most of the tornado activity occurred in southern Saskatchewan and Alberta, but in the light of the recent climate changes, tornado activity has expanded to southwestern and southeastern Ontario. The design recommendations for structures that can withstand tornado wind speeds are still under development in Canada. The main challenge for determining tornadoes design procedures lays in the difficulty to predict and track a tornado occurrence; also, it is nearly impossible to obtain data from the full-scale tornadic event [7]. Parameters such as velocity, tornado path diameter can be determined, however, parameters like the swirl ratio, Reynolds number and tornado vector field are much more difficult to obtain. Thus, producing tornado simulation models allow engineers and scientists to control these parameters, test models, and learn the shapes tendencies of tornadoes formations. This can allow for a better testing of wind-induced pressures on various types of house models, necessary for optimization of building codes. Currently the pressure coefficients available in NBCC'15 are determined based on boundary layer wind tunnels tests, while for tornado events it is not possible to use a straight wind speed profile as a mean to measure the forces, as the surface pressures measured during experiments are 3–5 times higher in a vortex formation with the same velocity as for a straight wind. Therefore, it is important to be able to accurately model a tornado vortex to obtain accurate pressure coefficients results on structures [8]. Several experimental

J. Williams · E. Dragomirescu (✉)
University of Ottawa, Ottawa, ON, Canada
e-mail: elndrag@uottawa.ca

J. Williams
e-mail: jwill132@uottawa.ca

S. Walbridge et al. (eds.), *Proceedings of the Canadian Society of Civil Engineering Annual Conference 2021*, Lecture Notes in Civil Engineering 240,
https://doi.org/10.1007/978-981-19-0507-0_43

facilities for simulating tornadoes effects on structures were developed for large-scale testing [1] and others for small-scale testing [4] and results for internal and external pressures induced by tornadoes of different intensities were investigated.

A study performed by [2] tested 7 residential house models using the Tornado Simulator Facility at the Iowa State University, where the effect of the house geometry on the tornado wind-induced pressures was investigated. The simulated tornado had a core diameter of 0.56 m and a wind speed of 11.6 m/s, which corresponds to a scaled EF3 tornado and the tested model was scaled by a factor of 1/100 from a full-scale residential house. Also, [6] has studied the dynamics of the internal pressure for a 1:100 scaled model with one opening tested in the large-scale simulator WindEEE Dome and compared the results with the pressure coefficients obtained from a boundary layer wind tunnel and found that both these facilities can replicate internal pressure testing models, within a 0.1 difference between the measured coefficients. The internal pressure built inside a house, due to displaced sections of the roof during a tornado was also investigated by Wang et al. [9], for different gable roof corner-opening ratios and was found that the mean pressure coefficient inside the tornado core decreases with the opening ratio increase of up to 8% and the mean internal pressure coefficient registered minimum value when the building location was 0.75 of the tornado radius.

2 Experimental Setup

Recently, a Wind Damage Simulator (WDS) was built at the University of Ottawa which can simulate turbulent winds, shear winds and tornadic wind flows. With a varying fan RPM ranging from 350 to 3600RPM, the WDS can simulate low wind speeds necessary for small-scale experiments on model structures or can replicate full-scale turbulent winds capable of displacing roofs shingles and mock-ups. The WDS testing section has dimensions of 3.0 m $\times$ 3.6 m $\times$ 3.6 m. The fan outlet positioned in the middle of the ceiling has a diameter of 31 cm and draws the air upwards. To create different flows and vortices, 5 circular inlets, each with diameter of 20 cm are found on each wall of the WDS box. Depending on the experimental purposes, these inlets can be opened or closed to produce different flow patterns. To produce the tornado vortex required for this set of experiments, one inlet from each of the four corners of the WDS were opened, thus creating a rotating vortex in the center of the room (Fig. 1).

The goal of the current experiment is to assess the external pressures on a scaled house model, caused by a tornadic wind. The experimental program was conducted in two phases: the first part of the experiment consisted in measuring the tangential wind speed at different distances from the vortex center, based on a similar procedure as the one used in the experiments performed by Haan et al. (2010).

A 12-hole Omniprobe, by Aeroprobe, attached to an L bracket that was anchored to a threaded rod mounted beneath the floor, was used to find the velocity parameters of the tornado flow. Standard tubing connected the probe to a DSA3217 pressure

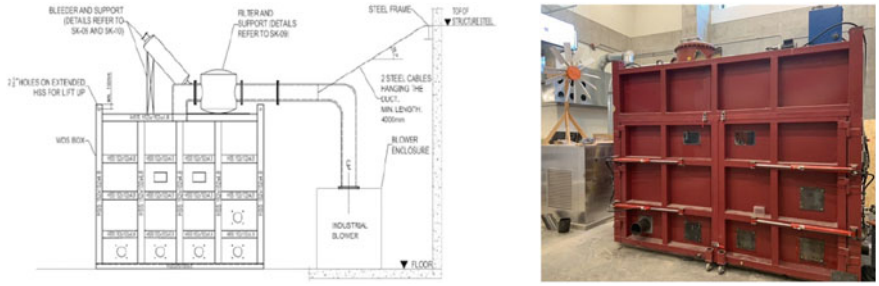

Fig. 1 **a** Wind induced damage simulator dimensions **b** Wind damage simulator facility

scanner, and data was acquired at a sampling rate of 40 Hz for 30 s at each 5 cm intervals to a range of 45 cm from the center of the tornado. The tornado was assumed to be symmetric about the center of the floor which was directly under the fan outlet and the Omniprobe was positioned facing the tangential velocity component of the tornado. The Aeroflow computer software, which transforms the pressure data and produces three velocity vectors on x, y, z directions. The tangential velocity component was used for this experiment. The tangential velocity data obtained during these tests have some fluctuation with short high and low velocity peaks. To avoid errors caused by the sensors, the velocities were averaged every 0.1 s. The maximum 0.1 s average tangential velocity was the taken for each 5 cm interval. Multiple tests were done to determine an adequate tornado tangential velocity and each test was repeated three times. The tornado wind speed cross-section measurements were taken for fan speeds of 750RPM, 825RPM and 900RPM. With the velocity data, the location of maximum tangential wind speed was found for three different tornadoes generated by three different fan RPM's. Using the tangential velocity and tornado radius data, a choice was made for the test locations tests to subject the house model to different velocity zones of the tornado: max velocity, mid velocity and low velocity, in the second phase of the experiment. The 1:100 scaled house model tested had dimensions of 145 mm × 100 mm × 74 mm for length, width and roof ridge respectively, as also used by Haan et al. (2018) and [2]. The eave height was 60 mm and the roof pitch angle was 16°. The house model was instrumented with a total of 96 pressure taps on the roof and on the lateral walls, as represented in Fig. 2b, and was anchored to the floor along three different locations in the simulated tornadic vortex.

Also, the house model was tested at three different locations and at three different angles 0°, 45° and 90°, for a total of 9 tests, refer Table 1. Locations along the radius are based on the maximum, mid and minimum tangential velocities measured in the Phase 1 of the experiment. The 0 and 90° angle orientation were chosen as these represent a perpendicular incident wind relative to the windward wall and roof. The 45° angle orientation was chosen to represent to test a condition where the incident wind could be split by the corner of the house (Fig. 3a). For the 3 different house angles tested, 0, 45 and 90°, the house wall A was facing the center of the tornado at

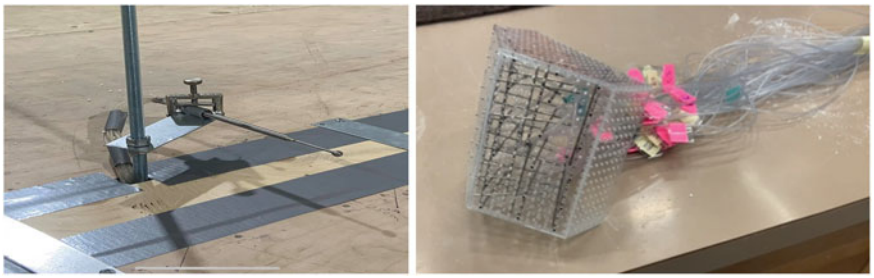

(a) **(b)**

Fig. 2 **a** Omniprobe used for Phase 1 experiments **b** Pressure taps residential house model used for Phase 2 experiments

Table 1 Test cases for different angles and model locations

Tornado zone	Max velocity			Mid velocity			Min velocity		
Case	1	2	3	4	5	6	7	8	9
Angle (°)	0	45	90	0	45	90	0	45	90
Location (cm)	10	10	10	25	25	25	40	40	40

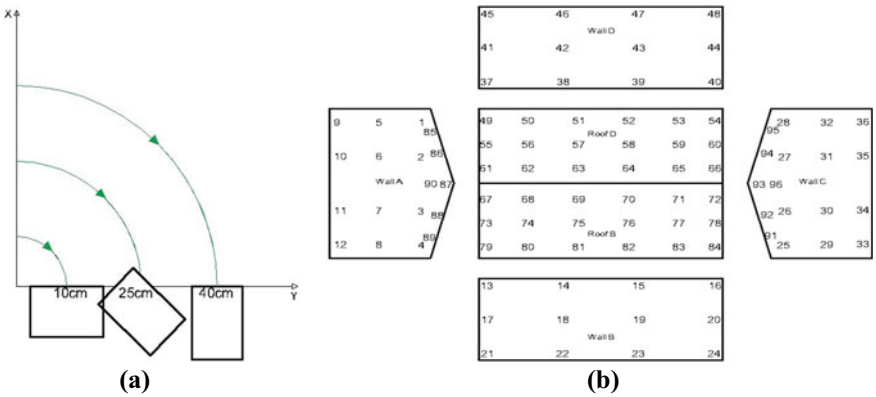

(a) **(b)**

Fig. 3 **a** Top view of a quarter of the tornado showing model locations and orientations for case 1 at 10 cm, case 5 at 25 cm and case 9 at 40 cm **b** Pressure tap approximate locations on model surface

0° and for the 90° orientation the wall A is parallel to the Y axis radius, thus receiving the tangential velocity perpendicularly as it can be seen in Fig. 3a.

The three ranges of tangential velocity correspond to three radii as positions where the house model was placed: the 10 cm radius as the location of maximum tangential velocity, the 25 cm as a mid velocity location, and the 40 cm as the low velocity location. As the tornado simulated in the current experiment is stationary, these three

model locations give a better understanding of the peak pressures on the house model at different locations in the tornado.

Three DSA3217 pressure scanners recorded pressure measurements at a rate of 400 Hz relative to a reference pressure. Each of the scanners has an individual reference pressure input. A total of three DSA3217 pressure scanners connected to 48 pressure tap sensors through individual 40 cm tubing. As space inside the model was limited for placement of all required pressure taps, the experiment was conducted in 2 stages. The first stage consisted of 48 pressure taps affixed in all the rectangular sections of the walls. For the second stage, the 48 pressure taps were removed from the walls and were affixed to the roof and to the triangular gable at the ends of the house. Data from the 2 stages were compiled and grouped to represent the condition for which all house surfaces were tested for the same wind conditions. Thus, pressure data was registered for 96 pressure tap locations on the house surfaces. The pressure tap layout can be seen in Fig. 3b.

Every case scenario was run for 30 s and repeated three times. The peak pressure value was taken from each of the three repeated tests and the peak pressure coefficients were calculated. The maximum average pressure coefficient ($C_{p\_max\_avg}$) was calculated by averaging the C_{p_max} (Eq. 1) values for each of the three repeated tests. This was done for every pressure tap for all the 9 cases.

$$Cp_{\max} = \frac{(p_{\max} - p_{ref})}{\frac{1}{2}\rho(V_{t.0.1s.avg})^2_{\max}} \tag{1}$$

where ρ is the air density, $p_{\max}$ is the peak pressure measured at the pressure tap, p_{ref} is the atmospheric pressure measured outside of the windbox in a static bottle, $V_{t.0.1s.avg}$ is the maximum tangential velocity from the 0.1 s intervals found at the radius where the model was tested.

3 Tangential Velocity Profiles of the Tornado

Tangential velocity measured in the Phase 1 of the experiment, at nine locations along the tornado radius, at 5 cm intervals, is reported in Fig. 4, for the three fan velocity RPM tested. As expected, higher velocities, of up to 16.00 m/s and 16.5 m/s, were recorded for higher RPM, of 900RPM and 825RPM and lower velocities were noticed for 750 RPM. Also, as a general trend, high velocities were noticed in the central region of the tornado, up to 15 cm, however these decreased gradually with the distance from the center reaching a common value of 3.0 m/s for all tested RPMs. Similar evolutions of tangential wind speed in a tornadic flow were pointed out by previous studies [4], thus the tornado simulated in the WDS facility is considered adequate for testing pressure taps house models. The tangential velocities for 750RPM and 900RPM were more unstable within the 15 cm radius from the center and no distinct single peak velocity was registered therefore, the 825RPM test, which

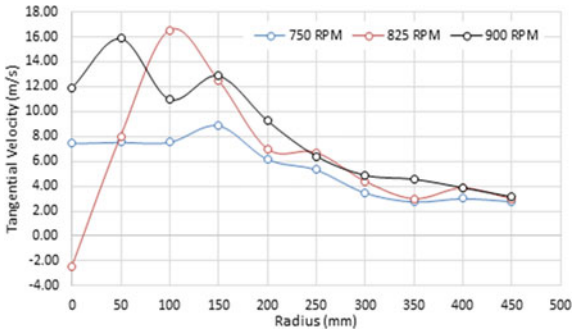

Fig. 4 Maximum tangential velocity versus radius for different RPMs

had the closest agreement with the normalized tangential velocity curves obtained by [4] was considered adequate for simulating the tornadic flows for the phase 2 of the experiments. In the first 5 cm from the center of the tornado, the wind velocity decreases significantly, and this is a common feature for the tornadic flows simulated in laboratory conditions, which rely on a central outlet for suction.

4 Wind-Induced Pressure Coefficients

For the 1:100 scaled residential house model, the tornado-induced pressure was measured for the 825RPM, which generates the highest tangential velocities of 16.5 m/s at 10 cm, 6.7 m/s at 25 cm and 3.86 m/s at 40 cm from the center of the tornado. The walls A, B, C and D and the roof sides B and D were instrumented with pressure taps, as represented in Fig. 3b, however only the pressure windward wall D and roof side D are depicted below, due to space limitations.

4.1 Wall Pressure Coefficients

When the model was placed at 10 cm, it was noticed that the highest negative pressure coefficients for the wall D exposed to the incoming tornado flow were due to the higher tangential velocity, and gradually decreased for 25 cm and 40 cm, where the tangential velocities are lower (Fig. 5a). In general, the pressure coefficients along the wall D were lowest near the right edge of the wall, due to the influence of the velocity near the center of the tornado, they increased thereafter towards the middle of the wall D, where the model was impacted directly by the tangential velocity and decreased slightly thereafter up to −0.35 towards the left edge of the wall D, as it can be noticed in Fig. 5a. A similar trend was noticed for the pressure coefficients measured for 45° orientation shown in Fig. 5b, especially for 10 and 25 cm from the center, while at 40 cm radius the pressure coefficients were more constant along the wall. For 90°

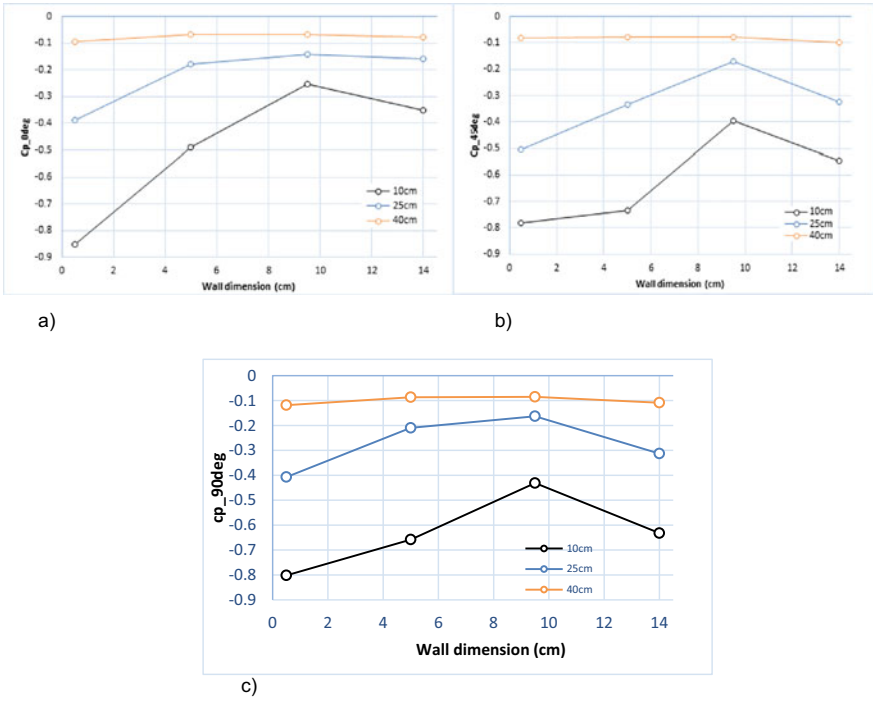

Fig. 5 Tornado-induced pressure coefficients for the wall D at 825RPM for **a** 0°, **b** 45° and **c** 90°

orientation, the pressure coefficients had a similar trend with the lowest pressure coefficient at the earliest point of contact with the wind. This indicates the lowest pressure coefficient at the initial contact with the wind. The pressure coefficient then increases until the far edge of the wall where the coefficient because more negative again (Figs. 5 and 6).

Fig. 6 Average pressure coefficient along the wall at different angle orientation

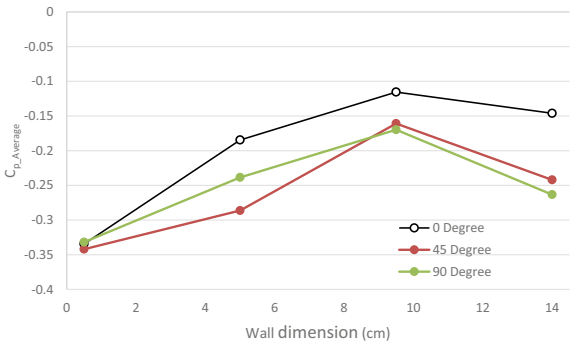

When the pressure coefficients were averaged for all the three locations, 45 and 90° showed a more consistent evolution, while 0° case registered a higher pressure coefficients than the rest of the cases.

4.2 *Roof Pressure Coefficients*

The relative position of the roof dimensions' change depending on the model orientation. For the Fig. 7a the pressure coefficient nearest the center of the tornado has the lowest pressure coefficient. The coefficient increases as the distance from the peak tangential velocity increases. A similar trend can be seen at the center portion of the roof for the Fig. 7b. Orientation tap array at the dimension 0 cm is closest to the core of the tornado. For the 45° orientation, the array at the dimension 0 cm is also the closest array to the center, however it is less close than the dimension 0 array from the 0° orientation. For the 90° orientation, the arrays at the 0 and 14 cm dimension are the same distance from the core of the tornado. However, the 14 cm dimension array is downwind from the 0 cm dimension array due to the direction of the tornado wind. The Fig. 7c, has a higher pressure coefficient nearest the wall that receives the incoming wind first. As the wind progresses past the wall and towards the middle of

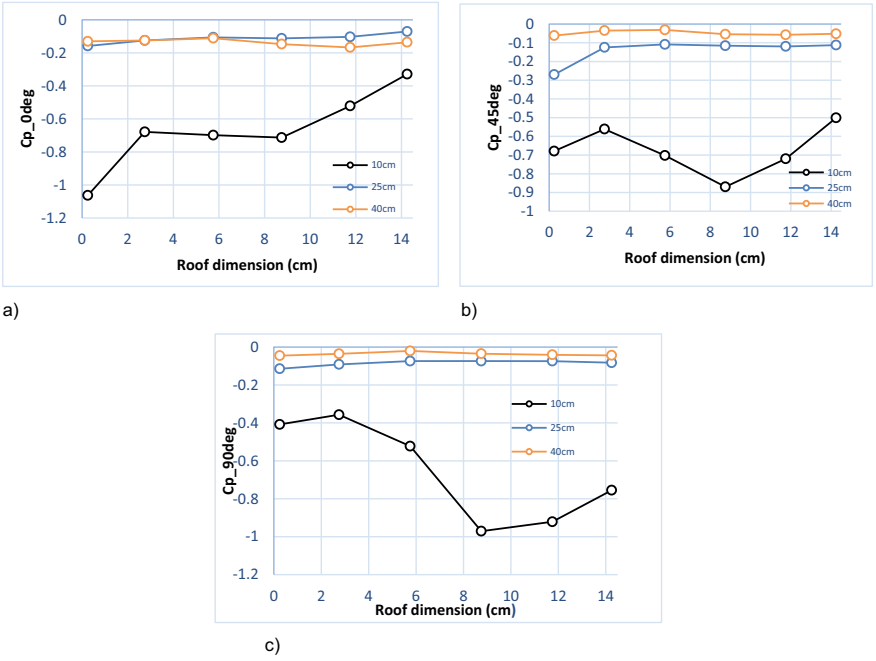

Fig. 7 Tornado-induced pressure coefficients for the wall D at 825RPM for **a** 0°, **b** 45° and **c** 90°

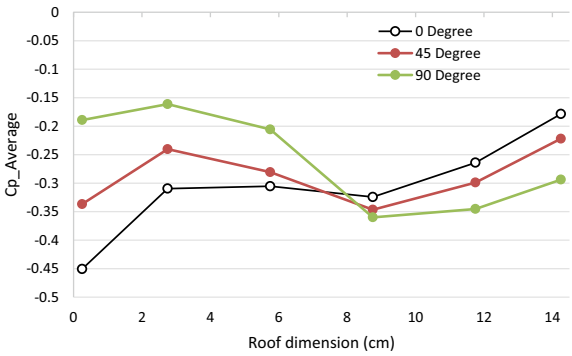

Fig. 8 Average pressure coefficient along the wall at different angle orientation

the roof, the pressure coefficient become more negative and significant. The gable at wall A could be causing the oncoming wind to be diverted over the first two arrays of pressure taps. The pressure coefficient then becomes more negative at the center array, at 8 cm, with a slight increase at end of the roof edge. The pressure coefficients obtained for the mid and low velocity zones, 25 and 40 cm radius respectively, have much higher pressure coefficients than the coefficient obtained from the model in the peak velocity zone. This is expected due to the significant decrease in tangential velocity.

Averaged pressure coefficients for all the three locations (Fig. 8), representing the overall pressure induced by one tornado passage showed an inflection point at 8.75 cm along the roof, where the pressure coefficients increased for 0 and 45° and decreased for 90°. This could be caused y the symmetry of the house model and by the parallel exposure to the tangential velocity for the case of 90°.

5 Conclusion

Wind-Induced Damage Simulator (WDS) Facility was employed for simulating tornadic flows and their effect on the wind-induced pressure measured for a 1:100 scaled pressure taps models of a residential house. As the WDS has a square test section, preliminary studies were necessary to determine the tangential velocity profiles achieved when opening one inlet at each corner of the wind box, in a symmetric configuration and by operating the wind flow in the WDS by the aid of an industrial fan with velocities of 750RPM, 820RPM and 900RPM, connected to the ceiling central outlet this providing uplift flow circulation. By comparing the tangential velocities obtained at different radii across the testing section, the 820RPM tornado was selected for testing the 1:100 scaled model of a house with 91 pressure taps installed along the walls and the roofs. The current experiment was performed for a stationary tornado, however for simulating the passage of the tornado, the house model was tested at 3 different locations from the center: 10 cm, 25 cm and 40 cm, where the velocities were tangential velocities were maximum, medium and

minimum. Also, three different angles between the house and the tangential velocity vector were tested, namely 0, 45 and 90°. For the wall exposed to the incoming tangential velocity of the tornado, the highest suction was obtained at 10 cm, the closest distance from the center of the tornado and the lowest was at the furthest point from the center of the tornado tested at 40 cm, for all angles investigated. A significant decrease in suction was noticed for the 90° inclination, for which the tangential wind becomes parallel to the tested wall.

The pressure coefficients obtained in the current experiments were lower than the ones reported by [8] for a similar model, who reported highest negative pressure coefficients on the exposed wall and exposed side of the roof, of up to −1.5 for the 90° inclination, compared with −0.9 measured in the current study. [3] has measured up to −1.43 peak pressure coefficients for a stationary vortex and up to -1.89 when the tornado was translated vortex. Therefore, tornadic flows of different parameters should be further investigated in the WDS, for determining the optimum combination of inclination angles and locations to be used for testing the tornado-induced peak pressure coefficients on scaled residential house models.

Acknowledgements The authors would like to acknowledge the support of the NSERC funding project 210715 and would like to express their gratitude for the continuous support offered by Dr. Muslim Majid and Dr. Gamal Elnabelsy.

References

1. Ashrafi A, Romanic D, Kassab A, Hangan H, Ezami N (2021) Experimental investigation of large-scale tornado-like vortices. J Wind Eng Ind Aerodyn 208. Elsevier
2. Case J, Sarkar P, Sritharan S (2014) Effect of low-rise building geometry on tornado-induced loads. J Wind Eng Ind Aerodyn 113:124–134
3. Haan FL (2017) An examination of static pressure and duration effects on tornado-induced peak pressures on a low-rise building. Wind Eng Sci Front Built Environ 3:20
4. Haan FL, Sarkar P, Gallus WA (2008) Design, construction and performance of a large tornado simulator for wind engineering applications. Eng Struct 30:1146–1159. Elsevier
5. ICLR Report (2018) The-Ottawa-Gatineau-Tornado-Outbreak. https://www.iclr.org/wp-content/uploads/2018/10/The-Ottawa-Gatineau-Tornado-Outbreak-v9.pdf
6. Jaffe AL, Kopp GA (2021) Internal pressure modelling for low-rise buildings in tornadoes. J Wind Eng Ind Aerodyn 209. Elsevier
7. Mishra AR, James DL, Letchford CW (2008) Physical simulation of a single-celled tornado-like vortex, Part A: Flow field characterization. J Wind Eng Ind Aerodyn 96:1243–1257. Elsevier
8. Roueche DB, Prevatt DO, Haan FL (2020) Tornado-induced and straight-line wind loads on a low-rise building with consideration of internal pressure. Wind Eng Sci Front Built Environ 6:18
9. Wang M, Cao S, CaoJ (2020) Tornado-like-vortex-induced wind pressure on a low-rise building with opening in roof corner J Wind Eng Ind Aerodyn 205. Elsevier

Drought Proneness Analysis of Southern Saskatchewan Province Using Markov Chain Model

U. Sumaiya, M. Ghaith, S. Hassini, and W. El-Dakhakhni

1 Introduction

Drought is a complex natural disaster that impacts more people than any other natural calamities; however, it is the least understood phenomenon [26]. It is considered the costliest disaster concerning geographical and temporal distribution [9, 26]. Drought has several specific definitions depending on the sector of interest (e.g., hydrology, meteorology, water management, agriculture, and wildlife-biology) as the impacts of droughts may differ significantly among these sectors [21]. The general definition of drought is reached after studying the nature of the water deficiency [6]. Therefore, the United States Weather Bureau states drought as "*a lack of rainfall so great and long-continued as to affect injuriously the plant and animal life of a place and to deplete water supplies both for domestic purposes and for the operation of power plants, especially in those regions where rainfall is normally sufficient for such purposes*" [8]. The causes, impacts, and extents of drought may differ significantly spatially and temporally; It has become difficult to define drought in a specific definition [9].

On the other hand, drought is considered a relative condition that could not be adequately quantified using physical variables [5, 23]. Since drought events highly vary in space and time, it is difficult to identify each event's specific duration, intensity, and geographical distribution [4]. The classification of drought entirely depends on the regional variability of climatic parameters (e.g., wind, temperature, humidity, duration, and intensity of precipitation) [5, 13]. The American Meteorological Society classified droughts into four groups—climatological, agricultural, hydrological, and socio-economical drought based on the causes, duration, intensity, and geographical distribution [5, 9, 10, 14, 21, 22]. Different drought indices, such as Standard Precipitation Index and Palmer Drought Index, were formulated

U. Sumaiya (✉) · M. Ghaith · S. Hassini · W. El-Dakhakhni
McMaster University, Hamilton, ON, Canada
e-mail: sumaiyau@mcmaster.ca

S. Walbridge et al. (eds.), *Proceedings of the Canadian Society of Civil Engineering Annual Conference 2021*, Lecture Notes in Civil Engineering 240,
https://doi.org/10.1007/978-981-19-0507-0_44

and applied by climatologists and meteorologists. The Standard Precipitation Index (SPI) is widely used as it requires only one variable (precipitation) and produces statistically relevant results [5, 12, 13]. Over the years, drought has been studied using different techniques such as data mining techniques, neural network methods, and time series methods. Combining Markov Chain Model and SPI can improve drought analysis. This technique was applied in several studies, such as drought forecasting [1, 15], drought propagation concept [18], and drought interval simulation [2]. However, Markov Chain Model incorporating SPI was not previously employed to analyze severity, duration, recurrence time, and the probability of drought to the authors' best knowledge.

The region of Canadian prairies is susceptible to agricultural and meteorological droughts, where the most remarkable events occurred during the 1890, 1910, 1960, and 1980s [3], Elaine [25]. Southern Saskatchewan is also highly prone to drought, and the number of droughts is expected to double by 2099 with higher magnitude, frequency, and duration [24]. The purpose of this study is to develop a methodology to estimate drought severity, probability of drought occurrence, expected drought duration, mean-time of drought first-passage, and mean-time of drought recurrence in southern Saskatchewan. A first-order Markov chain model with five states is applied in this study, and the states are identified based on drought classifications of SPI [12].

2 Methodology

2.1 Markov Chain Model

It is a memoryless (solely dependent on the present state and independent of the past) stochastic model where space and time, two states of Markov chain, are discrete. Similarly, the transition probability matrix (TPM) derived from this model is constant for space and time [11]. this particular characteristic of Markov model is beneficial for estimating the probability of an event. The TPM of Markov chain model is formulated by using the maximum likelihood method, and the TPM in between the states carries the significant characteristics of the model [11, 27]. From this TPM, steady-state matrix (SSM), and drought parameters (mean first passage time (MFPT), mean recurrence time (MRT), and mean drought duration (MDD)) have been calculated. These drought parameters are explained below with the SSM:

Steady State Matrix: The steady-state or stationery or equilibrium matrix is mainly a probability vector following equations where π symbolizes the equilibrium probabilities for j states and steady states are connected to eigenvalues (P) equal to 1 [16, 19]. Equation (1) shows the corresponding relation.

$$0 \leq \pi \leq 1 \tag{1}$$

Table 1 Drought intensities resulting from the SPI [12]

Drought categories	SPI values
No Drought (ND)	> 0.00
Mild Drought (MiD)	0 to −0.99
Moderate Drought (MoD)	−1.00 to −1.49
Severe Drought (SD)	1.50 to −1.99
Extreme Drought (ED)	≤ −2.00

$$\sum_{j \in S} \pi_J = 1$$

$$\pi . P = 1$$

Mean First Passage Time: The total number of estimated steps needs to be covered before reaching another step in an irreducible Markov chain [17, 20].

Mean Recurrence Time: Total number of expected states needs to be passed before reaching the starting state [17, 20].

Mean Drought Duration: Total time duration of each of the states [28].

Based on the guidelines [5, 7], a minimum of 20–30 years of monthly precipitation data is preferred for SPI calculation. Considering this, Broadview, Last Mountain CS, and Swift Current CDA stations were chosen, with precipitation data available for more than 30 years. Another significant criterion was maintained that each of these stations has less than 10% of missing data imputed using the regression method. The daily precipitation data were converted into monthly data, and SPI values were calculated for 12 months scale. The SPI values were classified by drought severity based on the study of [12] and is shown in Table 1.

Based on the SPI values, the Markov model was developed for each station, and the corresponding transition probability matrices (TPM) were calculated. These matrices were finally used for estimating drought proneness by setting drought parameters (SSM, MFPT, MRT, and MDD). Figure 1 summarizes the data preparation methodology used to estimate the drought in this study.

2.2 Study Area and Data

Saskatchewan is experiencing extreme temperature and weather events with a continental climate which means relatively low precipitation and considerable sunshine during the summer months. This province is in the center of the continent—far from any moderating oceanic influences. Temperatures can range from −40 °C in the dead of a northern winter to +35 °C during summer in the southern regions. The extreme nature of the climate extends to severe climate events: from drought to flooding downpours, thunderstorms to blizzards, and calm to tornadoes. Saskatchewan has

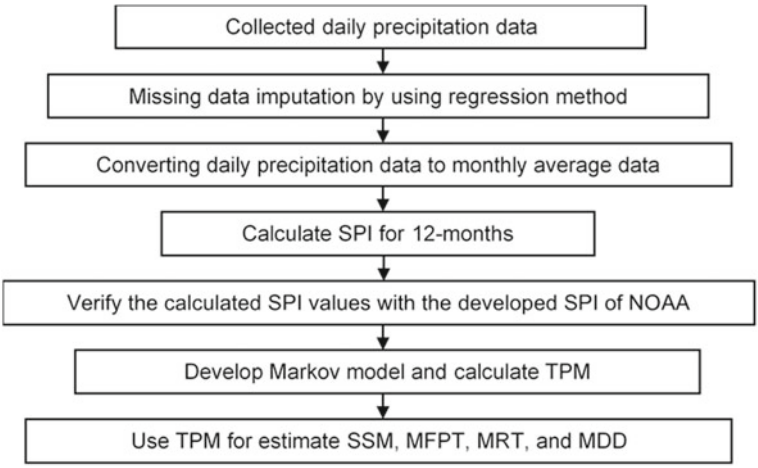

Fig. 1 Schematic diagram of the methodology

one of the world's most variable climates across seasons, years, and decades. Annual precipitation varies even more than temperature. Precipitation levels and variability tend to decrease from north to south. Yearly precipitation is lower by 200 mm between the Taiga and the Prairie Ecozones zones. Across Saskatchewan, summer brings the most significant percentage of annual rainfall (SaskAdapt, 2020). The study area consists of the southern part of Saskatchewan, which includes Saskatoon, Regina, Swift Current, and other major cities. Figure 2 shows the study area and the selected climate stations of this study. The three stations' date range and characteristics are summarized in Table 2.

3 Result and Discussions

3.1 Performance Testing of the Model

At the very beginning, the calculated SPI values were compared with the SPI values formulated by the National Centers for Environmental Information (NOAA) to check the performance and reliability of the method. Four different goodness of fit tests were performed: Nash–Sutcliffe Model Efficiency Coefficient (NSE), Root Mean Square Error (RMSE), Standard Error (STDER), and Coefficient of Determination (R^2). The perfect fit for NSE and R^2 is 1, and for STDER and RMSE, the value is 0. Apart from these, a graphical comparison was made for R^2 in between the observed (NOAA) and calculated SPI values. The inspection showed that both NSE and R^2 values are very close to the perfect value (1). The other two goodness of fit tests also showed satisfactory results. The values of the goodness of fit tests are provided in

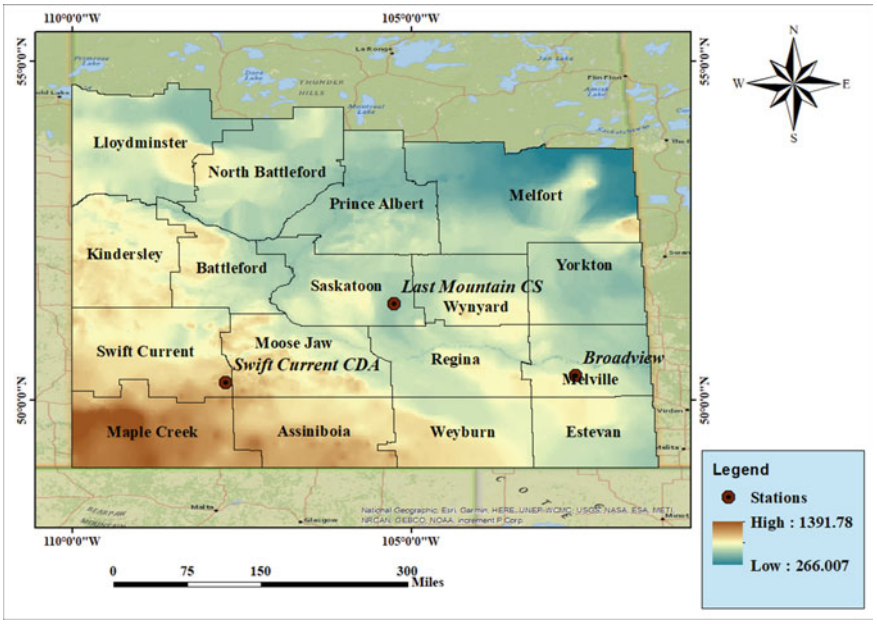

Fig. 2 Study area with the selected stations

Table 2 Characteristics of the stations analysed for the study

Climate id	Station name	Latitude	Longitude	Elevation (m)	Missing data (%)	Recorded year
4,010,879	Broadview	50.37	−102.57	599.8	1.3	1965–2019
4,014,156	Last mountain CS	51.42	−105.25	497	1.3	1976–2019
4,028,060	Swift current CDA	50.27	−107.73	825	0.6	1960–2019

Table 2. Considering values for all of the goodness of fit tests indicated that R^2 has significantly performed for this analysis. In conclusion, the result implies that the calculation process of SPI for this study works efficiently. Thus this method can be applied to the rest of the stations of the Saskatchewan province (Table 3).

3.2 Drought Parameter Analysis

Based on the analysis of steady-state matrices of three of the stations, it is evident from Fig. 3 that even though the probability of happening ED is low, however, the chances of MiD, MoD, and SD are significantly high. The probability of occurrence

Table 3 Goodness of fit tests

Stations	NSE*	RMSE**	STDER***	R^{2****}	R^2 (Graphical)
Broadview	0.89	0.30	1.31	0.91	0.907
Last mountain CS	0.96	0.21	0.66	0.97	0.961
Swift current CDA	0.92	0.29	0.78	0.92	0.917

*Nash–Sutcliffe Model Efficiency Coefficient, **Root Mean Square Error, ***Standard Error, and ***Coefficient of Determination

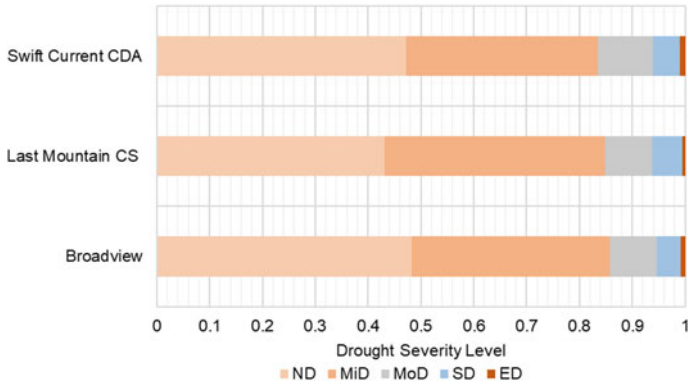

Fig. 3 Probability of drought severity

of MiD is more than 35% in three of the stations. In Swift Current CDA station, the chances of MoD are more than 10%. Furthermore, Swift Current CDA and Last Mountain CS both have more than 5% chances of SD. The alarming part is that three stations are susceptible to drought, varying from mild to extreme intensity, for more than 50%. Thus, all of the constructions, infrastructures, agricultural decisions need to be taken considering the possibilities of droughts.

The mean drought duration (MDD) analysis was quantified for all of the stations, which is depicted in Fig. 4. The figure revealed that MiD lasts longer in all of the stations. However, other drought classes showed some variations. The station Swift Current CDA experiences a longer duration of MoD and ED than the rest of the stations, which is more than 2.4 and 1.4 months, respectively. However, it has the lowest drought duration for SD. The MiD condition stays for almost 4.4 months, and ND lasts longer than 8 months. Last Mountain CS is in the most favorable state of having the highest ND duration. However, the MiD and SD duration is 5.6 and 2.6 months, respectively. A significant finding is that both Last Mountain CS and Broadview stations experience longer SD duration than MoD and ED.

In conclusion, Fig. 4 demonstrated that three stations are susceptible to experience MiD, MoD, SD and, ED for more than 4 months, 2 months, 2.1 months, and 1 month, respectively on average.

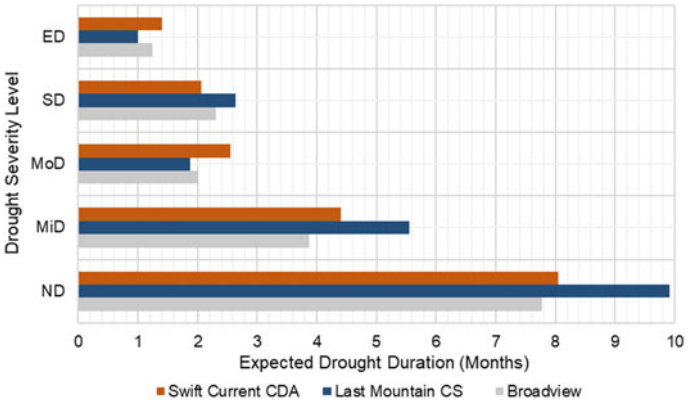

Fig. 4 Expected drought duration in months

The mean recession time (MRT) study showed that both ND and MiD take two months to change from one state to another. For MoD, Last Mountain CS and Broadview both have more than 11 months of recession time, greater than Swift Current CDA station. The recession time of SD is the highest for Broadview station (21.70 months). The variation of ND, MiD, MoD, and SD in the three stations is minimal. However, drastic variations occurred for ED among the stations. Table 4 depicts that MRT for ED is the longest for Last Mountain CS stations and shortest for Swift Current CDA stations. This situation indicates that Last Mountain CS will be advantageous compared to the rest of the stations. This also implies that Broadview and Swift Current CDA will be prioritized while taking drought measures for ED.

Based on the results displayed in Table 4, the mean first passage time (MFPT) reveals an interesting indication that Last Mountain CS has the highest MFPT for all categories of droughts ranging from 12 to 21 months. This means the fluctuations of changing the drought severity states are steadier for this station than other stations. Table 4 also reveals that this value is lowest for Broadview stations ranging from

Table 4 MRT (months) and MFPT (months) analysis

Stations	ND	MiD		MoD		SD		ED	
	MRT*	MFPT**	MRT*	MFPT**	MRT*	MFPT**	MRT*	MFPT**	MRT*
Broadview	2.07	8.43	2.67	12.07	11.22	14.37	21.70	14.47	130.20
Last mountain CS	2.32	12.95	2.40	16.11	11.27	19.20	17.48	20.20	168.85
Swift current CDA	2.12	8.71	2.76	14.82	9.66	16.66	19.31	16.47	102.09

*mean recurrence time, and **mean first passage time

8 to 15 months. So, the drought may change their states frequently in this station comparing to the other two stations.

Furthermore, the result of MFPT showed that all of the stations might face drought (MiD) after almost 8.43 to 12.95 months interval of ND, whereas this value is nearly 14.47 to 20.20 months for ED. So, there will be a time gap between ND to droughts to take the necessary steps.

4 Conclusion

In southern Saskatchewan, drought has become a usual natural calamity as this region has been facing droughts all year round in different severity levels. A heads-up on drought parameters is a practical and smart approach to tackle droughts at different levels. In this study, the authors figured out a simplified method using Markov chain model and SPI, which can indicate drought severity, expected drought duration, mean recurrence time of drought, and mean first passage of drought. This study has been done to develop a technique that will be eventually applied to more considerable extents and in higher number of stations, which do not have publicly available SPI values. Thus, verifying this method is very crucial for this study.

In this study, the SPI values were validated with NOAA by using four different statistical goodness of fit tests—the Nash–Sutcliffe model efficiency coefficient (NSE), the root mean square error (RMSE), the standard error (STDER), and the coefficient of determination (R^2). At the same time, the coefficient of determination (R^2) was also estimated by using the graphical method. The results were significant to use this technique on other stations for the whole Saskatchewan region. The analysis for three of the stations indicated that the probability of drought is more than 50% for all of the stations in different drought intensities, and the chances of mild drought (MiD) is the highest (more than 35%) among the other groups of draught. In the same way, the expected drought duration for all of the stations is greater than 4, 2, 2.1, and 1 month for mild drought (MiD), moderate drought (MoD), severe drought (SD) and extreme drought (ED), respectively. Among these, Last Mountain CS has the highest drought duration for MiD and SD; Swift Current CDA possesses the highest expected drought duration for MoD and ED. The mean recurrence time of drought and the mean first passage of drought can be varied between 2–169 months and 8–21 months, respectively, depending on the stations and severity of the drought.

These actions demonstrate that planners, engineers, decision-makers, agricultural policymakers, and other professionals can prepare themselves for taking necessary measures against droughts by understanding the drought parameters and severity level. This study can be further extended to the stations which are not active in NOAA, and thus a complete understanding of the drought parameters can be obtained. In the same way, this method can be applied to the different periods of SPI to identify the drought characteristics of meteorological, agricultural, and hydrological drought.

References

1. Barua S, Perera BJC, Ng AWM, Tran D (2010) Drought forecasting using an aggregated drought index and artificial neural network. J Water Clim Change 1(3):193–206
2. Beyaztas U, Yaseen ZM (2019) Drought interval simulation using functional data analysis. J Hydrol 579:124141
3. Bonsai, B. R., & Wheaton, E. E. (2005). Atmospheric circulation comparisons between the 2001 and 2002 and the 1961 and 1988 Canadian prairie droughts. Atmosphere-Ocean, 43(2), 163-172
4. Burton I (1993) The environment as hazard. Guilford Press
5. Desert Action JRC, IES (2011) SPI: Standardized Precipitation Index 1–6
6. Dracup JA, Lee KS, Paulson EG (1980) On the definition of droughts. Water Resour Res 16(2):297–302. https://doi.org/10.1029/WR016i002p00297
7. Guttman NB (1998) Comparing the palmer drought index and the standardized precipitation index 1. JAWRA J Am Water Resour Assoc 34(1):113–121
8. Havens AV (1954) Drought and agriculture. Weatherwise 7(3):51–68. https://doi.org/10.1080/00431672.1954.9930320
9. Heim Jr RR (2002) A review of twentieth-century drought indices used in the United States. Bull Am Meteor Soc 83(8):1149–1166
10. Kamruzzaman M, Kabir ME, Rahman ATMS, Jahan CS, Mazumder QH, Rahman MS (2018) Modeling of agricultural drought risk pattern using Markov chain and GIS in the western part of Bangladesh. Environ Dev Sustain 20(2):569–588
11. Lazri M, Ameur S, Brucker JM, Lahdir M, Sehad M (2015) Analysis of drought areas in northern Algeria using Markov chains. J Earth Syst Sci 124(1):61–70. https://doi.org/10.1007/s12040-014-0500-6
12. McKee TB, Doesken NJ, Kleist J (1993) The relationship of drought frequency and duration to time scales. Proc Conf Appl Climatol 17(22):179–183
13. Mishra AK, Singh VP (2010) A review of drought concepts. J Hydrol 391(1–2):202–216. https://doi.org/10.1016/j.jhydrol.2010.07.012
14. Palmer WC (1965) Meteorological drought, vol 30. US Department of Commerce, Weather Bureau
15. Rezaeianzadeh M, Stein A, Cox JP (2016) Drought forecasting using Markov chain model and artificial neural networks. Water Resour Manage 30(7):2245–2259
16. Ross SM (2002) Introduction to probability models. Academic Press. Se Prohibe Comer Y Beber En El Salon De Clase
17. Sanusi W, Jemain AA, Zin WZW, Zahari M (2015) The drought characteristics using the first-order homogeneous Markov Chain of monthly rainfall data in Peninsular Malaysia. Water Resour Manage 29(5):1523–1539. https://doi.org/10.1007/s11269-014-0892-8
18. Sattar MN, Jehanzaib M, Kim JE, Kwon H-H, Kim T-W (2020) Application of the hidden Markov bayesian classifier and propagation concept for probabilistic assessment of meteorological and hydrological droughts in South Korea. Atmosphere 11(9):1000
19. Spedicato GA, Kang TS, Yalamanchi SB, Yadav D, Cordón I (2016) The Markovchain package: a package for easily handling Discrete Markov Chains in R. Accessed Dec.
20. Spedicato GA, Signorelli M (2014) The markovchain package: a package for easily handling discrete Markov Chains in R. Cran, Spedicato 2017. http://cran.r-project.org/web/packages/markovchain/
21. Svoboda M, Hayes M, Wood D (2012) Standardized precipitation index user guide. World Meteorological Organization Geneva, Switzerland
22. Vicente-Serrano SM, Beguería S, López-Moreno JI (2010) A multiscalar drought index sensitive to global warming: the standardized precipitation evapotranspiration index. J Clim 23(7):1696–1718. https://doi.org/10.1175/2009JCLI2909.1
23. Vicente-Serrano SM, Beguería S, Lorenzo-Lacruz J, Camarero JJ, López-Moreno JI, Azorin-Molina C, Revuelto J, Morán-Tejeda E, Sanchez-Lorenzo A (2012) Performance of drought

indices for ecological, agricultural, and hydrological applications. Earth Interactions 16(10). https://doi.org/10.1175/2012EI000434.1
24. Wheaton E, Bonsal B, Wittrock V (2013) Future possible dry and wet extremes in Saskatchewan, Canada
25. Wheaton E, Kulshreshtha S, Wittrock V, Koshida G (2008) Dry times: hard lessons from the Canadian drought of 2001 and 2002. Canadian Geographer/Le Géographe Canadien 52(2):241–262
26. Wilhite DA (2016) Droughts: a global assesment. Routledge
27. Woolhiser DA, Pegram GGS (1979) Maximum likelihood estimation of Fourier coefficients to describe seasonal variations of parameters in stochastic daily precipitation models. J Appl Meteorol Climatol 18(1):34–42
28. Yeh H-F, Hsu H-L (2019) Using the Markov Chain to analyze precipitation and groundwater drought characteristics and linkage with atmospheric circulation. Sustainability 11(6):1817. https://doi.org/10.3390/su11061817

Development of a Virtual Visit Model Based on a Bim Model and a Game Engine

Mouhamadou Moustapha Gueye and Conrad Boton

1 Introduction

In recent years, the construction sector has shown a productivity lag relative to the industrial sector. Add to this the fact that construction projects are becoming more and more difficult, resulting in more complex and dynamic construction environments. To remedy this, the construction industry is increasingly implementing Bulding Information Modeling (BIM) to foster collaboration and data sharing among the various trades involved in construction projects. Besides, this approach relies on models of objects in the built environment and metadata defining their semantics, to produce a multidisciplinary and intelligent 3D model of the facility, to document and improve its design and to facilitate its operation throughout its whole lifecycle. While BIM has many benefits such as increased constructability, reduced conflicts, reduced cost estimation times and many other opportunities, there are many challenges associated with adopting this approach within the construction industry. Not all companies can adopt the associated technologies and use them in an effective way. In fact, the main BIM software are currently limited in terms of the realism of visualization, general immersion, and proposed interactions, especially for newbies [11]. In this context, to overcome these difficulties, the integration of 3D BIM models with Virtual Reality (VR) technologies is a promising alternative, to provide the non-specialist stakeholders with more intuitive visualization and interaction mechanisms [2]. Thus, according to Sidani et al. [15], researches on immersive systems and interfaces and

M. M. Gueye (✉) · C. Boton
Département du génie de la construction, École de Technologie Supérieure, Université du Québec, Montréal, Québec, Canada
e-mail: mouhamadou-moustapha.gueye.1@ens.etsmtl.ca

C. Boton
e-mail: Conrad.Boton@etsmtl.ca

S. Walbridge et al. (eds.), *Proceedings of the Canadian Society of Civil Engineering Annual Conference 2021*, Lecture Notes in Civil Engineering 240,
https://doi.org/10.1007/978-981-19-0507-0_45

BIM have produced favourable results for construction-related applications, thus improving the design, the team collaboration and the decision-making.

However, very little research has been devoted to interoperability between BIM and VR environments. Also, despite notable evolution through some commendable efforts, Virtual Reality support software such as game engines are quite inflexible and seem poorly suited to fully integrating data from BIM models. The work presented in this article is part of more comprehensive research aiming at developing and evaluating intuitive interoperability workflow between BIM tools and Virtual Reality environments. The purpose of this article is to present, as preliminary results, the development of an intuitive visualization and interaction tool based on the interoperability between a BIM authoring tool and a game engine. The article is organized into 4 main sections. The first section presents the related works, including the use of VR in construction and its association with BIM. The second section describes the methodology adopted for this research, including the main steps followed in the development and the evolution of the artefact. The third section presents the results of the research with a description of the functionalities and user navigation of the virtual tour model created. The fifth section discusses the results and presents the future works before concluding the article.

2 Related Works

2.1 Virtual Reality in Construction

Whether for the world of video games or industrial simulation, virtual reality has a major place on the innovation scene [5]. Virtual reality is defined by Arnaldi et al. [1] as a scientific and technical field exploiting computer science and behavioural interfaces to simulate in a virtual world the behaviour of 3D entities, which interact in real-time with each other and with one or more users in pseudo-natural immersion via sensor-motor channels. [5] believes that virtual reality is a mediated experience that plunges one or more users into the heart of an artificial environment in which the user can feel and interact in real-time via sensor-motor interfaces. The user finds the experience credible, accepts to take part in the game and in response feels a sense of presence. Virtual reality has no defined limits, from electronics to computer vision, which gives several possibilities in its use and exploitation.

Several design areas are interested in the use of virtual reality. Now, as the prices of this technology become accessible to the public and especially with the use of 3D digital mock-ups by various disciplines, the use of virtual reality is becoming more and more necessary given all the possibilities that this technology can offer. Jimeno and Puerta [10] have proposed virtual reality as a computer-aided design tool. Several studies have been conducted to understand and exploit the potential of this technology within the construction industry. Firstly Cruz-Neira et al. [6] have implemented the Cave system, which is a visualization system that offers an innovative point of view.

Researchers have tried to determine an effective and productive strategy for the use of virtual reality as a design tool [9]. In the same vein, [11] proposed a study on the visualization of business knowledge and interaction with immersive devices for construction. Dawood et al. [7] have presented through their work an application of virtual reality to Islamic architecture. Others such as Yan and Culp [17] have developed a new design process with a BIM support tool to improve architectural design and visualization by combining Microsoft XNA Framework software as a game engine and Autodesk Revit Architecture as a BIM authoring application.

Other studies have gone even further by using virtual reality as a simulation tool for building evacuation situations. This is the case of Rüppel and Schatz [13] who have designed a simulation of the evacuation of building occupants in the case of fire. This simulation uses the interactivity of a game engine to identify the decisions made by these users at a given time and the paths chosen by them.

In the future, virtual reality could help to improve the collaboration and mainly the communication of the different participants in a construction project, as virtual reality offers the possibility for architects and engineers to get together to pool their work and possibly make decisions regarding possible interferences and conflicts that might exist.

2.2 Association Between Virtual Reality and BIM

Virtual reality is recognized as a promising method that can improve workflow in the construction industry [15]. For example, a link between BIM models and virtual reality may be feasible with the advent of game engines such as Unity or Unreal Engine. Some works such as Boton [4] or Younes et al. [18] have addressed in their research the issue of BIM integration in virtual reality environments. Edwards et al. [8] show through their study the feasibility of using game engines to include end-users in the BIM design process. They used an Autodesk Revit plugin to communicate with the Unity game engine allowing collaboration via a network connection. Similarly, in their study, Shengyi and Jia [14] tried to propose a method for integrating BIM models into a virtual environment from the game engine by designing a virtual interactive roaming simulation. To facilitate and improve the integration processes of BIM models in virtual reality environments, several major software publishers such as Unity, Epic, Autodesk and Trimble are currently trying to develop solutions such as plugins that enable the link between BIM modelling software and game engines.

The link between BIM and virtual reality environments is a technological difficulty in this approach. Previous studies have shown that there is a problem related to the management of data flows and the transfer of information between BIM software and game engines in general. For example, 4D [4] has highlighted difficulties related to the preparation and transfer of data to a game engine such as Unity with a problem of preserving the metadata of the 3D model. Moreover, due to the different steps involved in exporting a BIM model to a virtual reality environment,

these processes often present errors such as missing material information (textures, building elements, etc.) leading to additional steps that may be necessary to complete the exported model [3]. These additional steps may be modifications that can be made in the game engine or the modeling software for a new export, complicating the entire workflow. Others, such as Tulke and Hanff [16], have found that additional developments are needed about visualization, for example, the addition of support for scaling and moving building elements in the game engines.

Despite the rapid development of virtual reality in the construction industry, there are not many models that link BIM and virtual reality, but more importantly, the industry has not yet been able to take full advantage of the potential of this approach. Moreover, virtual reality is not yet widely used in design processes in general, particularly in the BIM approach.

3 Research Methodology

The objective of this study is to develop a method for designing a virtual tour model that allows its users to experiment, analyze and interact in an immersive environment. The methodology proposed in this study consists of 4 main steps: statement of needs, choice of the technological tools, development of the VR model and evaluation of the results.

3.1 Statement of Needs

Because of the difficulties noted in the association between virtual reality and BIM, this research project aims to propose: To propose more integrative approaches, with ease of understanding and capable of accommodating different profiles and academic backgrounds, both for the actors in construction projects and for "the general public". In this perspective, the virtual visit model created should offer an immersive experience with the possibility of being able to go through a building in all its spaces in real-time, to be able, for example, to access closed rooms thanks to interaction mechanisms and animation games, but above all to be able to make changes in real-time such as changes in texture.

3.2 Choice of the Technological Tools

Within the framework of this research, we used the Revit software from the Autodesk editor. This software also allows us to make an architectural design and to be able to directly integrate structural, electrical, and mechanical graphic elements into the same model. In this logic, we were able to integrate an architectural and structural

model into a federated model. Then, we chose the Unreal Engine game engine for the design of the virtual environment considering all the possibilities and functionalities that this game engine could offer. Nevertheless, workflow management seemed to be a challenge at first, as importing a BIM model into a game engine was previously problematic for many users. Thanks to the plugin Datasmith we were able to cleanly import the model into the game engine.

3.3 Development of the VR Model

As indicated, the objective of this research is to design a virtual visit model based on a BIM model. As a result, the different steps leading to the design of the model constitute a work process method explored by Natephra et al. [12] as shown in Fig. 1. We will see in more detail in the following chapter the method, but above all the different steps that have been proposed to integrate a BIM model in a virtual reality environment.

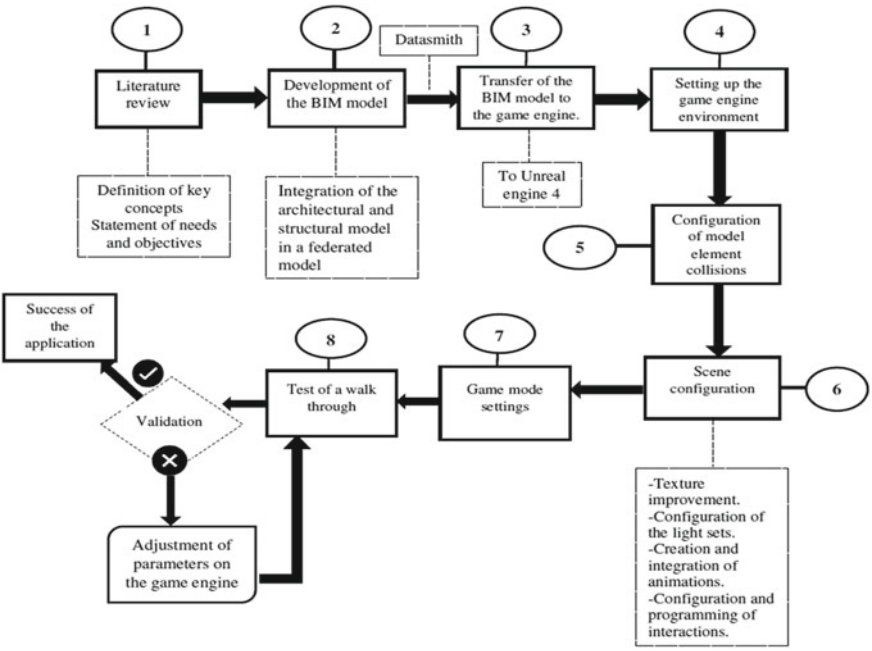

Fig. 1 Process of integrating a BIM model in an VR environment

3.4 Evaluation of the Results

At the end of the design of the model, to bring an evaluation to the created application, we will be able to consider three main criteria. The first would be whether the application meets the desired needs. The second criterion would be that the model should include functionalities (animations, interactions, etc.) that are functional to meet the expectations of future users. And the third criterion would be the ease of use and navigation in the model for different users.

4 Development of a Virtual Visit Model Based on a Bim Model and a Game Engine

Figure 1 summarizes the different stages that enabled us to design the virtual visit model. After defining the objectives and potential needs of this research, we had to develop a BIM model that would contain not only an architectural model but also a structural model, thus constituting a federated model. This could be done using the Revit software.

Figure 2 illustrates the federated model that was designed on Revit and its import on the Unreal Engine 4 game engine thanks to the plugin Datasmith.

After importing the BIM model on the game engine, it was necessary to configure the game engine environment. The main task was to configure the visual aspect of the main character proposed by Unreal into an invisible camera that can simulate all the movements of a user in full navigation. This step makes navigation and visualization more realistic since in the standard form of the character, it is made up of bionic hands and a weapon as shown in Fig. 3.

In the next step, it was necessary to represent the physical properties and parameters that make a user's immersion more realistic. To do this, we had to parameterize collisions of each element (slab, staircase, walls, doors, fittings, etc.) of the model using the "Collision mesh" tool of the game engine, which allowed us to simulate certain physical properties such as gravity and collision, making a walkthrough more

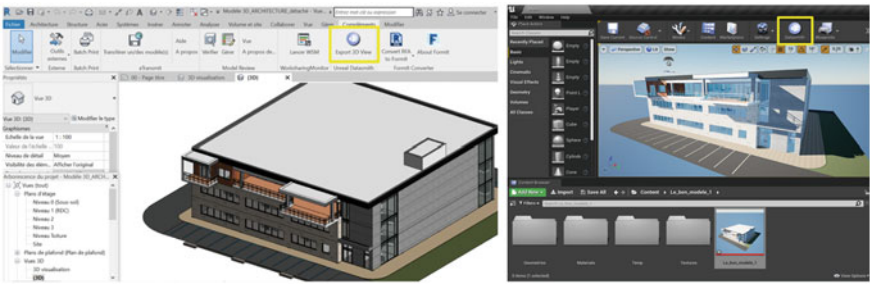

Fig. 2 Validation of the import process on Unreal Engine

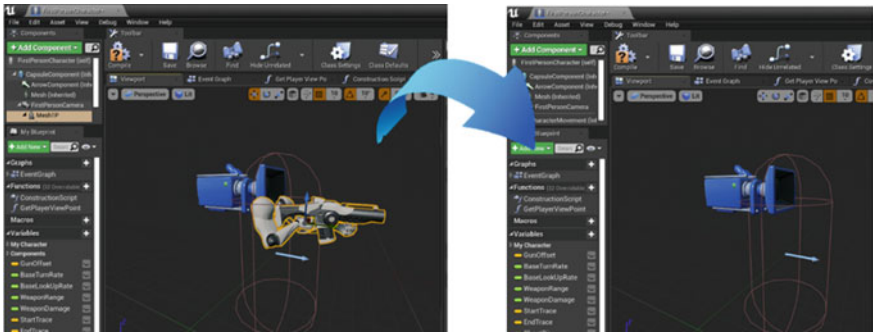

Fig. 3 First-person configuration for game mode

natural. To obtain a good visual rendering, visual treatment of the play of lights of the scene and the improvement of the textures of certain elements of the model were necessary. In this step, it was, therefore, necessary to improve the lighting of the scene by using functions on the game engine such as Lightmass Importance Volume, Directional Light or the Reflection Environment function which allowed for more realistic and natural light effects.

The integration of video animations and interactions in the model was necessary because in a virtual reality model, a user must be able to interact in an immersive environment. After setting up the model scene and the different light effects, we set up interactions that are functional when the game starts. With the Interaction Widget tool, we can create on Unreal various interactive "accessories" such as cursors, combined boxes, and many other interactions in a virtual reality environment. Thanks to the Interaction Widget, we have therefore created various interactions to give a user the possibility of customizing different components of the model such as tiles, walls or even furniture. One of these interactions gives for example the possibility for a user to change materials for a tile in the game.

To do so, different materials (wood, ceramic, marble …) have been set up to be connected to switch buttons that allow a user to be able to change the base material of a tile in real-time during a walk-through. For these created and parameterized interactions to be functional, the application of these interactions must be programmed in the level blueprint which makes them functional during a walk-through as shown in Fig. 4.

Once the model was developed, it had to be tested to see if it met the objectives and needs that had been established. The main objectives were to improve visualization, to create new interaction mechanisms that could make design review easier. To do this, we tested the model on Unreal. Indeed, Unreal mainly offers five active play modes that allow generating visualization modes to perform a walk-through. These active play modes are Selected viewport, the Simulate mode, the two PIE modes (Mobile Preview ES3. 1 and the New Editor Window) and the Standalone Game mode. We had identified two interesting game modes that allow integrating the character in the first person (First-person), but also to be able to support the different high-resolution

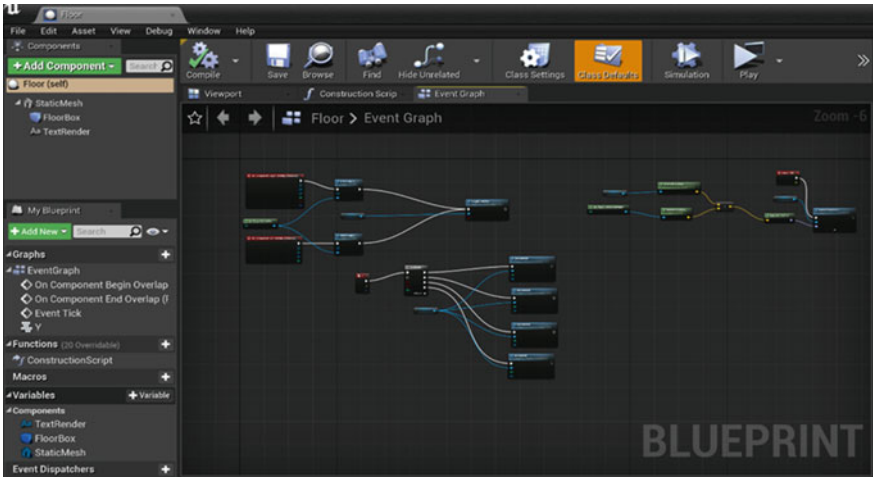

Fig. 4 Interaction programming of material change interaction of a slab

textures that are in the model. We, therefore, had to choose between the PIE module (New Editor Window) and Standalone Game mode. In the end, the choice went to Standalone Game mode as it supports all the textures that were used in the model and brings a better visual rendering.

So during the virtual visit test of the model, we could realize that the various functionalities and interactions created and integrated into the gameplay from the Level Blueprint were present and working. From the First Person who simulates the representation of the first person in Standalone Game mode, it is possible to move around the building, to be able to access rooms thanks to the door opening animations by simply getting closer to the doors and to be able to access the different levels of the building by going up and down the stairs. It is also possible to interact on elements of the scene by clicking on combined box buttons as shown in the screenshots in Fig. 5.

This makes it possible to change in real-time the basic materials of the objects in the scene such as furniture or even elements according to the different materials offered and to see these visual changes in relation to the whole scene.

5 Conclusion and Future Works

Virtual reality is a developing technology that is attracting the interest of several disciplines such as simulation, teleoperation, audiovisual and collaborative work. Indeed, it is characterized by a better visualization, the immersion of these users and the possibilities of interaction in a virtual environment. From a technical point of view, BIM is based on the use of a 3D digital model. It is therefore open to the use

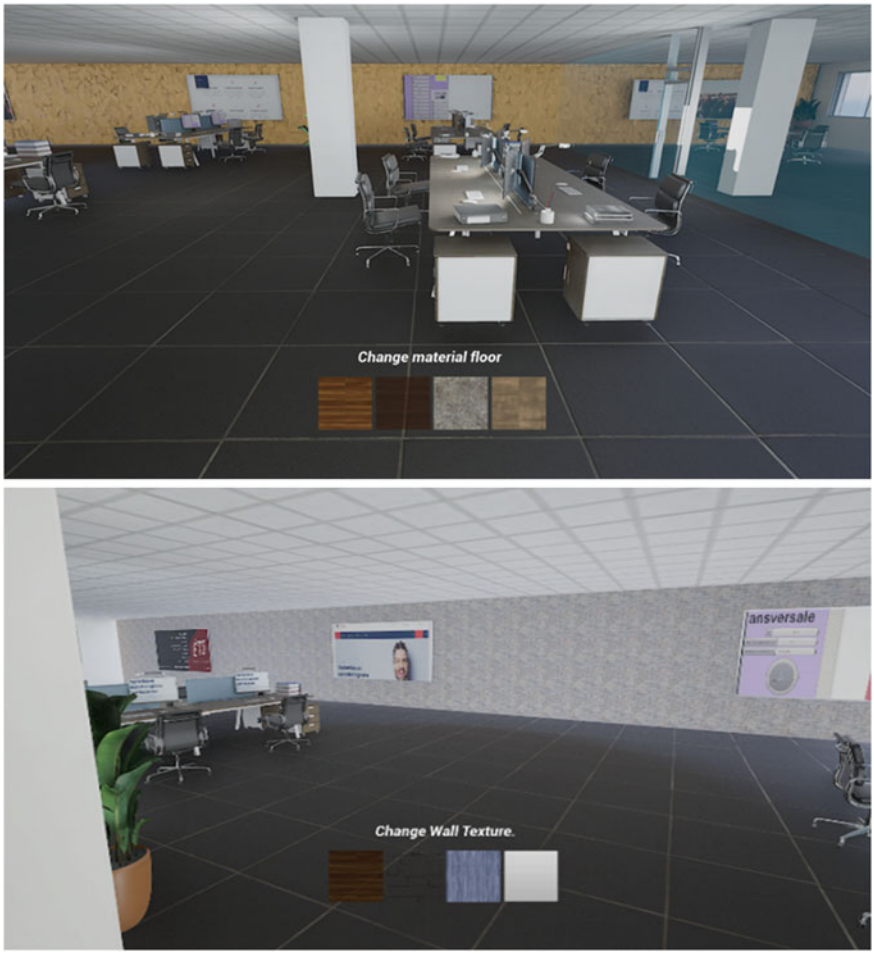

Fig. 5 Screenshots of the interactions offered to a user during a walk-through

of new tools. In this context, the integration of 3D BIM models in RV environments would be a plus for BIM players given the advantages and possibilities offered by this technology. However, linking BIM with virtual reality environments has always been a technological challenge in the past, as the processes of transferring 3D digital models into RV support software such as game engines remain an ambiguous task due to the various errors that can be generated.

The objective of this research was to be able to suitably integrate a 3D BIM model into a game engine to create a virtual visit model that should offer an immersive experience with the possibility of being able to go through a building in all its spaces in real-time, for example, to be able to access closed rooms thanks to interaction mechanisms and animation games. In this perspective, we first presented,

through a literature review, the different applications of virtual reality within the construction industry with an analysis of the limits interfering with the link between BIM and virtual reality. Then, based on a research methodology, we presented the different steps and methods that allowed us to design a virtual visit model from the Unreal Engine game engine. The final model designed allows navigating realistically in an environment where a user can interact on objects in the scene thanks to created interactions. This research was able to provide interaction tools that could be implemented in future work in the context of 4D. However, this research was unable to link these interaction tools developed in the framework of the virtual visit model and previous work on 4Ds focused on the use of virtual reality. Future work can therefore focus on the integration of these interactions with regard to 4D, the creation of other tools such as conflict detection tools for example on game engines to further support design reviews and constructability and study meetings.

As previously mentioned, the functionalities developed in the model are all functional. It can also be seen that the model is visually more attractive than before importing from Revit. This can be explained by a clear improvement in textures and a configuration of the play of light, which may have made the model more realistic. A feeling of immersion is present when navigating through the model. Besides, during a walk-through, the camera movements follow the directions given by the user via the system controls with a certain fluidity of movement. It is also possible to observe a lack of latency between the interaction of a user on a button during the simulation and the display of the expected visual result. From the point of view of use, the model is easy for a user to use, but also allows a novice user, for example, to easily assimilate the navigation and interaction techniques available in the model. However, in the preview mode, it can sometimes be seen that certain textures are not properly supported by the system, unlike the Standalone Game visualization mode which gives it a better visual rendering. On the other hand, the model does not give the possibility to a user to select and move elements in the gameplay. The addition of this functionality could be considered as part of the possible improvement tracks.

To support future research focused on the use of virtual reality and game engines per se as Unreal, this research provides a methodology for the design of interactions and the detailed configuration of Unreal's environment. Indeed, difficulties concerning the integration of textures and the creation of certain interactions have been noted in previous work on the use of virtual reality on 4D BIM models. The use of the created model would therefore allow giving an added value to the 4D simulation prototypes already available. This would make it possible to meet the needs of project owners or clients, even more, to involve them in the design process by using the BCF (BIM Collaboration Format), for example using screenshots and comments, and to go even further in the context of supporting study and constructability meetings.

On the other hand, this study is limited by the lack of external evaluation by qualified practitioners and experts in the construction industry and to further adjust and enrich this research. Thus, in the context of future research, to validate the model's performance and functionalities with practitioners and professionals in the construction industry, the model should be applied in a real case, thus making it possible to conceptualize the expression of real needs. Therefore, based on feedback

from potential users, the latter will first be able to improve the functionalities and interactions present in the model, to recalibrate them according to the needs of the projects in particular and, above all, to compare the method used for the design of the model and the combinations of software used for the design of other models or prototypes.

References

1. Arnaldi B, Tisseau PF, Tisseau J (2003) Le traité de la réalité virtuelle. Les Presses de l'Ecole des Mines de Paris, p 8
2. Bednarz T, James C, Widzyk-Capehart E, Caris C, Alem L (2015) Distributed collaborative immersive virtual reality framework for the mining industry. In: Machine vision and mechatronics in practice. Springer, Berlin, pp 39–48
3. Boeykens S (2011) Using 3D design software, BIM and game engines for architectural historical reconstruction. CAAD Futures
4. Boton C (2018) Supporting constructability analysis meetings with immersive virtual reality based collaborative BIM 4D simulation. Automat Construct 1–15
5. Bouvier P (2009) La Présence En Réalité Virtuelle, Une Approche Centrée Utilisateur. PhD thesis. Paris-Est: Université Paris-Est, 4 décembre
6. Cruz-Neira C, Sandin DJ, DeFanti TA (1993) Surround-screen projection-based virtual reality: the design and implementation of the cave. In: Proceedings of the 20th annual conference on computer graphics and interactive techniques, pp 135–142
7. Dawood NN, Alkass S et al (2014) Applications of virtual reality and islamic architecture. In: Proceedings of the 14th international conference on construction
8. Edwards G, Li H, Wang B (2015) BIM based collaborative and interactive design process using computer game engine for general end-users. Vis Eng 3–4
9. Greenwood D, Horne M et al (2008) Strategic perspectives on the use of virtual reality within the building industries of four countries. Arch Eng Des Manag 85–98
10. Jimeno A, Puerta A (2007) State of the art of the virtual reality applied to design and manufacturing processes. Int J Adv Manuf Technol 9–10
11. Martin H (2016) Maquette numérique 3D pour la construction: visualiser les connaissances métier et interagir avec des dispositifs immersifs. PhD thesis. Paris: Interface homme-machine [cs.HC]. Université Paris-Saclay
12. Natephra W, Ali M, Tomohiro F et al (2017) Integration de la modelisation des informations du batiment et des moteurs de developpement de realite virtuelle pour la conception d'eclairage interieur des batiments. Visualisation en ingenierie
13. Rüppel U, Schatz K (2011) Designing a BIM based serious Game for fire safety evacuation simulations. Adv Eng Inform 600–611
14. Shengyi L, Jia W (2016) Research on integrated application of virtual reality technology based on BIM. In: Chinese Control and Decision Conference (CCDC), pp 2865–2868
15. Sidani A, Dinis FM, Sanhudo L et al (2019) Recent tools and techniques of BIM-based virtual reality: a systematic review. Arch Comput Methods Eng 5–6
16. Tulke J, Hanff J (2007) 4D construction sequence planning new process and data model. In: Proccedings of CIB—W78 24th international conference on information technology in construction, pp 79–84
17. Yan W, Culp C (2011) Integrating BIM and gaming for real time interactive architectural visualisation. Automat Construct 20:446–458
18. Younes G et al (2017) Virtual and augmented reality for rich interaction with cultural heritage sites: a case study from the Roman Theater at Byblos. DAACH 5:1–9

A Damage Detection Procedure Using Spectral Element Method

M. Delpasand, R. Erkmen, and R. Ganesan

1 Introduction

Dynamic analysis of structures to detect and quantify the effect of damage is an important area of research e.g. [2]. For example, impact hammer testing is often used to investigate the effect of damage in composite laminates. The effect of such damage often reveals itself in high frequency modes [10]. For spatial discretization of structures finite element technique has often been a popular choice which is often used for model updating in damage detection problems. However, finite element method produces fair estimation of natural frequencies only to the low frequency part of the spectrum. One can only expect from a discrete model of degree-of-freedom n to produce fewer than $n/3$ eigenvalues with reasonable accuracy [8]. The reason is conventional finite element treats the distributed load induced by the mass as lumped at the nodes of the finite element model. Therefore, many elements must be used if the mass distribution is to be modeled accurately [6].

Using the spectral element method, a beam element can be formulated which exactly considers the distributed mass effect, which may significantly reduce the model size [6]. Spectral element formulation adopts an exact dynamic stiffness matrix for each frequency based on which a spectral analysis method for steady-state response was developed in [5]. In Doyle's spectral element method, the response is first obtained for each discrete frequency content of the load function in the frequency domain using Fourier Transform. The solution is then re-constructed in time-domain using Inverse Fourier Transform. As the dynamic stiffness matrix is exact for each frequency, the accuracy of the steady-state solution depends only on the Discrete Fourier Transform conditions. On the other hand, determination of the free-vibration

M. Delpasand · R. Erkmen (✉) · R. Ganesan
Department of Building, Civil and Environmental Engineering, Concordia University, Montreal, Canada
e-mail: emre.erkmen@concordia.ca

S. Walbridge et al. (eds.), *Proceedings of the Canadian Society of Civil Engineering Annual Conference 2021*, Lecture Notes in Civil Engineering 240,
https://doi.org/10.1007/978-981-19-0507-0_46

modes and frequencies of the dynamic stiffness matrix generally results in a transcendental eigenvalue problem, which is necessary to determine the transient component of the general solution. A method based on counting the number of natural frequencies exceeded by any arbitrary value for ω^*, a trial threshold, has been suggested in Wittrick and Williams [12]. Lee and Cho [9] attempted to develop a pseudo force method to add the transient response due to non-null initial conditions. Veletsos and Kumar [11] proposed an approach to build the transient response using initial conditions and the steady-state response of a single degree of freedom system as well as multi-degree of freedom systems if vibration mode shapes and mass matrix of the system is available.

In this paper Veletsos' method was adopted to determine the Transient response within the spectral element analysis procedure. Both steady-state and transient responses were considered in the analysis to develop a tool for damage detection in elastic beams. The analysis tool is then used for the model updating procedure within a genetic algorithm [7] that optimizes the cost function based on relative changes in frequencies and mode shapes as a metric for damage detection. Dong and Wang [4] used the same cost function with an ordinary finite element based model update procedure.

2 Spectral Element Formulation

In Spectral Element Method (SEM) the exact solution of the homogenous Helmholtz equation is used for the shape functions. Those exact shape functions are used to formulate the exact dynamic stiffness matrix. As the Helmholtz equation is frequency dependent, the dynamic stiffness matrix is also frequency dependent which can be considered as a mixture of inertia and stiffness related terms. As such the dynamic stiffness matrix considers continuous mass and stiffness distributions. Consequently, the frequency dependent displacement solution based on the exact dynamic stiffness matrix is exact at the nodes. Therefore, the need for mesh refinement is kept to a minimum.

2.1 Exact Dynamic Stiffness of Euler–Bernoulli Beam Element

The free bending vibration of an Euler–Bernoulli beam is governed by

$$EI\frac{\partial^4 w}{\partial x^4} + \rho A\frac{\partial^2 w}{\partial t^2} = 0 \tag{1}$$

where $w(x,t)$ is the transverse displacement, E is the Young's modulus, A is the cross-sectional area, I is the moment of inertia of the cross-section about the neutral axis and ρ is the mass density. Assuming a general solution in the form $w(x,t) = \widehat{w}(x)e^{i\omega t}$ or Fourier Transform leads to a frequency dependent differential equation, i.e.

$$EI\frac{\partial^4 \widehat{w}}{\partial x^4} - \omega^2 \rho A \widehat{w} = 0 \tag{2}$$

From the above equation in frequency domain the solution for $\widehat{w}(x)$ can be obtained as

$$\begin{aligned} \hat{w}(x) &= C_1 e^{-ikx} + C_2 e^{-kx} + C_3 e^{-ik(L-x)} + C_4 e^{-k(L-x)} \\ &= \hat{g}_1 \hat{w}_0 + \hat{g}_2 \hat{\theta}_0 + \hat{g}_3 \hat{w}_L + \hat{g} \hat{\theta}_L \end{aligned} \tag{3}$$

where $k = \sqrt{\omega}\left(\frac{\rho A}{EI}\right)^{\frac{1}{4}}$, $\widehat{w}_0 = \widehat{w}(0)$, $\widehat{\theta}_0 = \widehat{w}'(0)$, $\widehat{w}_L = \widehat{w}(L)$ and $\widehat{\theta}_L = \widehat{w}'(L)$ are the nodal displacements and rotations, and $\hat{g}_1$ to $\hat{g}_4$ are the exact shape functions obtainable after determining the coefficients C_1 to C_4 in terms of nodal values. By expressing the moment and shear forces in terms of the differentiations of the displacement field, i.e., $M(x,t) = EI\frac{\partial^2 w(x,t)}{\partial x^2}$ and $V(x,t) = EI\frac{\partial^3 w(x,t)}{\partial x^3}$, one obtains [6]:

$$\begin{Bmatrix} \widehat{V}_0 \\ \widehat{M}_0 \\ \widehat{V}_L \\ \widehat{M}_L \end{Bmatrix} = \frac{EI}{L^3} \begin{bmatrix} \alpha & \overline{\gamma} L & -\overline{\alpha} & \gamma L \\ \overline{\gamma} L & \beta L^2 & -\gamma L & \overline{\beta} L^2 \\ -\overline{\alpha} & -\gamma L & \alpha & -\overline{\gamma} L \\ \gamma L & \overline{\beta} L^2 & -\overline{\gamma} L & \beta L^2 \end{bmatrix} \begin{Bmatrix} \widehat{w}_0 \\ \hat{\theta}_0 \\ \widehat{w}_L \\ \hat{\theta}_L \end{Bmatrix} \tag{4}$$

where:

$\alpha = [\cos(kL)\sinh(kL) + \sin(kL)\cosh(kL)]\frac{(kL)^3}{\Delta}$, $\bar{\alpha} = [\sin(kL) + \sinh(kL)]\frac{(kL)^3}{\Delta}$, $\beta = [-\cos(kL)\sinh(kL) + \sin(kL)\cosh(kL)]\frac{(kL)}{\Delta}$, $\bar{\beta} = [-\sin(kL) + \sinh(kL)]\frac{(kL)}{\Delta}$,

$\gamma = [-\cos(kL) + \cosh(kL)]\frac{(kL)^2}{\Delta}$, $\bar{\gamma} = \sin(kL)\sinh(kL)\frac{(kL)^2}{\Delta}$, $\Delta = 1 - \cos(kL)\cosh(kL)$, $\hat{V}_0 = \hat{V}(0)$, $\hat{M}_0 = \hat{M}(0)$, $\hat{V}_L = \hat{V}(L)$, and $\hat{M}_L = \hat{M}(L)$ are introduced in Fig. 1.

The above matrix is the frequency dependent dynamic stiffness matrix of the Euler–Bernoulli beam element. As shown above the displacement field $\hat{w}(x)$ can be obtained from the nodal values by using exact shape functions in $\hat{g} = \{\hat{g}_1, \hat{g}_2, \hat{g}_3, \hat{g}_4\}$ for each frequency ω. The assemblage procedure of the element stiffness matrices is identical to that of the standard displacement-based FEM. As a result of the assemblage the structural dynamic equilibrium can be obtained as $\widehat{\boldsymbol{K}}\widehat{\boldsymbol{d}} = \widehat{\boldsymbol{f}}$, in which $\widehat{\boldsymbol{K}}$ is the dynamic structural stiffness matrix, $\widehat{\boldsymbol{d}}$ nodal displacement vector component

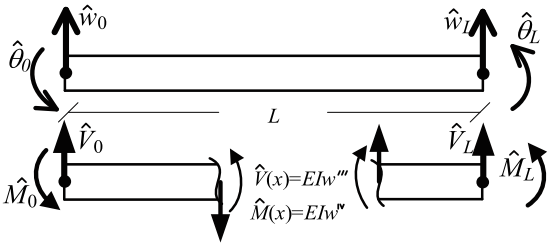

Fig. 1 Beam element

in the frequency domain and $\widehat{\boldsymbol{f}}$ is the Fourier Transform of the excitation. After the displacement field is obtained for each frequency content the time behaviour can be re-constructed as the synthesis of the frequency dependent solutions, i.e., $\boldsymbol{d}(x,t) = \widehat{\boldsymbol{d}}(x)e^{i\omega t}$. As a general solution would span the whole frequency range, i.e., $-\infty < \omega < \infty$, the solution in time-domain is obtained from the IFT, i.e.,

$$\boldsymbol{d}(t) = \sum_{n=-\infty}^{\infty} \widehat{\boldsymbol{d}}_n e^{in\omega t} \tag{5}$$

The essentials of the spectral element solution scheme are to first replace the input by its spectral form obtained from the application of the Fourier Transform to determine the frequency content. By doing this the problem can be solved in the frequency domain to obtain the output also in the frequency domain. The reconstructions in the time domain are then done by application of the inverse Fourier Transform. Note that because of the discrete nature of the Fourier transform the result of inverse FFT is only valid up to the Nyquist frequency. As suggested in [5], the inverse transform is evaluated only up to the Nyquist, half the sampling frequency, and the remainder is considered as the complex conjugate of the initial part. This ensures that the reconstructed history is real in time domain.

A summary of the Spectral Element solution procedure is shown in Fig. 2, which does not include the damage detection component. Damage detection algorithm that employs the results of the Spectral Element analysis is discussed in Sect. 3. In Spectral Element Analysis, it is essential to replace the external excitation by its

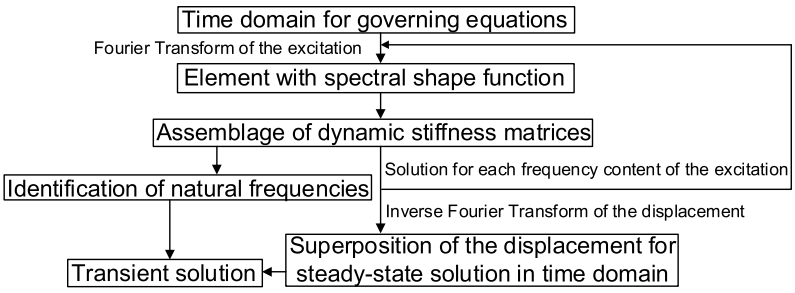

Fig. 2 Solution procedure

spectral form using the Fourier Transform to determine its frequency content. By doing this the problem can be solved in the frequency domain to obtain the output also in the frequency domain. The reconstructions in the time domain are then done by application of the inverse Fourier Transform and this completes the Steady-State solution. However, to obtain the Transient response, the natural frequencies of the system needs to be identified.

2.2 *Identification of the Natural Frequencies Using the Wittrick-Williams Algorithm*

In Wittrick-Williams algorithm eigenvalue separation property based on max–min criteria on the Rayleigh's quotient is used as a tool to count number of eigenvalues exceeded by a trial eigenvalue. The procedure employs the upper triangular matrix $\widehat{\boldsymbol{K}}_{\Delta}$ that is obtained from $\widehat{\boldsymbol{K}}$ by using the usual form of Gauss elimination, in which rows are taken as pivotal in order, and appropriate multiples of the pivotal row are added to succeeding rows, making all elements below the pivot zero. The number of negative elements in this factorized form based on a selected frequency $\bar{\lambda}$ is equal to the number of eigenvalues smaller than $\bar{\lambda}$. Conversely if $\lambda_i < \bar{\lambda} < \lambda_{i+1}$, where λ_i and λ_{i+1} are two consequtive eigenvalues of $\widehat{\boldsymbol{K}}$, there are exactly i negative diagonal elements in $\widehat{\boldsymbol{K}}_{\Delta}$. In Wittrick-Williams algorithm this fact is used as a tool to make sure no eigenvalue is skipped. The key step of the method is to calculate J at successive trial values of $\bar{\lambda}$, where J is the number of natural frequencies lying between zero, i.e. $\bar{\lambda} = 0$ and the trial value. Thus, the amount by which J changes between successive trial values equals to the number of natural frequencies lying between the trial values. J is calculated from the equation $J = J_0 + s\left\{\widehat{\boldsymbol{K}}\right\}$ in which $s\left\{\widehat{\boldsymbol{K}}\right\}$ is the 'sign count' of $\widehat{\boldsymbol{K}}$, which is readily calculated as the number of the negative leading diagonal elements of $\widehat{\boldsymbol{K}}_{\Delta}$.

In Wittrick-Williams algorithm applied in the context of spectral element formulations, J_0 is the value on fully constraints structure in which all the active degrees-of-freedoms are nullified so that $\boldsymbol{d} = 0$. When $\boldsymbol{d} = 0$ the the eigenvalues can still be counted for component members as if they are in isolation with their ends clamped, i.e. $J_0 = \sum J_m$ in which summation extends over all the members and J_m is the number of natural frequencies lying between zero and the trial value of $\bar{\lambda}$, for a member with its ends clamped.

2.3 *Addition of the Transient Part*

A significant gap in literature exists regarding the transient solution within the context of Spectral Element Method. Lee and Cho [9] attempted to introduce the Pseudo

Force approach to identify the contribution of the transient solution based on a previously obtained steady-state solution. However, his solution procedure is based on the assumption that the unit impulse response function is the inverse Fourier transform of the frequency response function which clearly does not involve the transient solution. For single degree-of-freedom systems, however, Veletsos and Kumar [11] developed a procedure based on the solution of the dynamic differential equation, in which the steady-state solution can be used to identify the additional transient contribution for systems that are starting from at rest state. This method can simply be extended to multi-degree-of-freedom systems using modal analysis as each mode can be treated to constitute a single-degree-of-freedom system. Herein, the Veletsos method has been adopted on an ad-hoc basis by using the shape functions obtained from the spectral method within the mode shapes.

In a single-degree-of-freedom system the general solution of the below differential equation

$$m\ddot{x} + kx = p \sin \overline{\omega},\ x(0) = 0,\ \dot{x}(0) = 0 \tag{6}$$

consists of the particular solution, that is:

$$x_p(t) = \frac{p}{k} \frac{1}{1 - \left(\frac{\overline{\omega}}{\omega_n}\right)^2} sin\overline{\omega}t \tag{7}$$

and the complementary solution, which is the free vibration response, where ω_n is the natural frequency of the system:

$$\mathrm{x}_c(\mathrm{t}) = \mathrm{A}\sin\omega_n\mathrm{t} + \mathrm{B}\cos\omega_n\mathrm{t} \tag{8}$$

By imposing the initial conditions, the constants A and B are determined, and the total solution can be obtained as

$$x(t) = \frac{p}{k} \frac{1}{1 - \left(\frac{\overline{\omega}}{\omega_n}\right)^2} sin\overline{\omega}t + \frac{p}{k} \frac{\frac{\overline{\omega}}{\omega}}{1 - \left(\frac{\overline{\omega}}{\omega_n}\right)^2} sin\omega_n t \tag{9}$$

If the result from spectral analysis is shown with y(t) and the total response is shown with x(t). The difference between these two can be written as a corrective function ϵ(t) as (Veletsos, Kumar, 1983):

$$\varepsilon(t) = x(t) - y(t) \tag{10}$$

ϵ(t) represents the effect of unsatisfied initial conditions. Consequently, one can write:

$$\epsilon(t) = \epsilon(0)cos\omega t + \frac{\dot{\epsilon}(0)}{\omega}\sin\omega t \tag{11}$$

Using Eq. 10, one can write for the system introduced in Eq. 6:

$$\varepsilon(0) = x(0) - y(0) = 0,\ \dot{\varepsilon}(0) = \dot{x}(0) - \dot{y}(0) = -\frac{p\overline{\omega}}{k}\frac{1}{1-\left(\frac{\overline{\omega}}{\omega n}\right)^2} \tag{12}$$

For multi-degree-of-freedom systems, the steady-state response, i.e. y(t), can be expressed in terms of modes of vibration as:

$$\{y(t)\} = \sum_{i=1}^{n}\{\phi_i\}r_i(t) \tag{13}$$

where $\{\phi_i\}$ is the vector of ith mode of displacement and $r_i(t)$ is the modal coordinate.

Also, one can write:

$$\{x(t)\} = \sum_{i=1}^{n}\{\phi_i\}[r_i(t) + \alpha_i(t) \tag{14}$$

where $\alpha_i(t)$ is the modal coordinate for the transient part. Considering that structure is initially at rest, i.e.,

$$\{\dot{\epsilon}(t)\} = \sum_{i=1}^{n}\{\phi_i\}\frac{\dot{\alpha_i}(0)}{\omega}\sin\omega t(t) \tag{15}$$

Hence one can calculate $\dot{\alpha_i}(0)$ as:

$$\dot{\alpha_i}(0) = \frac{\{\phi_i\}^T[M](\{\dot{x}(0)\} - \{\dot{y}(0)\})}{\{\phi_i\}^T[M]\{\phi_i\}} \tag{16}$$

Note that the mode shapes and frequencies are calculated from the dynamic stiffness matrix and M is the lumped mass matrix, which introduces some spatial discretization error to the transient solution.

2.4 Case Studies and Validation

To demonstrate the performance of the mentioned method a simple case study is done. A uniform simply supported beam made of aluminum with elastic modulus of 10^6 psi and a density of $0.26 * 10^{-3}\frac{lbs^2}{in^4}$ is considered. The length of the beam is

$60in$. In the first case, the beam is under a concentrated transverse step load in the middle for 1 s with the amplitude of 1000 lb. In the second test, the beam is under a sine load with the amplitude of 100 lb and frequency of 1 Hz.

The lateral displacement of the middle point of the beam is captured using spectral elements and compared with the results from analytical solutions in Fig. 3.

To calculate the natural frequencies and vibration mode shapes, the beam is modelled once with spectral elements and another time with conventional finite elements. The Wittrick-Williams method explained above is applied to the spectral element model and linear eigenvalue analysis is applied to the finite element model. The results are compared with the analytical results as shown in Table 1.

Using the Wittrick-Williams method explained in Sect. 2.2, the natural frequencies are obtained and the corresponding modes of vibration are then obtained using the equation of motion:

$$\left[\hat{K}(\omega)\right]\{d\} = 0 \tag{17}$$

Substituting each natural frequency into the dynamic stiffness matrix and solving for {d}, gives the modes of vibration. The rows or the columns of the $\widehat{K}(\omega)$ are

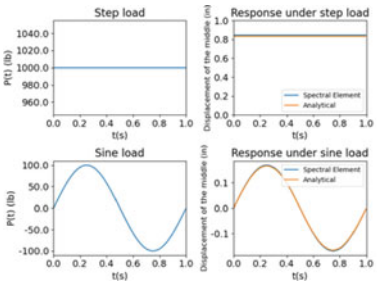

a: Excitation function and the steady state response.

b: A simply supported b eam with a concentrated load applied in the middle.

Fig. 3 Lateral vibration of the middle point of a simply supported beam under step and sine load

Table 1 Natural frequencies

Bending mode number	Analytical (Hz)	Finite element [2 elements] (Hz)	Finite element [3 elements] (Hz)	Finite element [4 elements] (Hz)	Finite element [5 elements] (Hz)	Finite element [6 elements] (Hz)	Spectral element [2 elements] (Hz)
1	31.24	31.36	31.26	31.24	31.24	31.24	31.24
2	124.95	138.68	126.42	125.44	125.15	125.05	124.95
3	281.13	348.58	312.03	286.27	283.36	282.24	281.13
4	499.79	635.51	580.20	554.72	511.30	505.69	499.79

linearly dependent. So, the eigenvector is determined by assuming an arbitrary value for one of the terms in {d} and solving for the rest. The same procedure is used for the first four modes and the results are compared with analytical results in Table 2.

If number of modes is set to 1 in Eq. 16, the displacement of the middle point of the beam under the previous sine and step loads will be as plotted in Fig. 4.

3 Damage Detection Using Vibration Data

As shown in the previous section, SEM provides a computationally efficient tool to calculate as many vibration modes and frequencies as desired. The efficiency is due to the fact that there is no need for mesh refinement to get access to higher modes. Structural damage usually causes stiffness reduction, which is reflected as a decrease in natural frequencies and change in vibration mode shapes. Furthermore, measuring natural frequencies and mode shapes is easily applicable through sensor measurements since they are global characteristics of the structure.

3.1 Modeling Damage

Consider the simply supported beam in Fig. 5, with a cracked element inside. The properties of the cracked element can be addressed using the following parameters:

L: Location of the damaged element.

L_w: Length of the damaged element.

D: Damage index.

D is the reduction ratio in E due to cracks and has a value between 0 and 1. Elasticity modulus of the cracked element is related to the elasticity modulus of the healthy element through Eq. 18:

$$E_{Cracked} = (1 - D)E \tag{18}$$

3.2 Damage Cost Function

Assume that the first n natural frequencies and corresponding mode shapes of a cracked structure are measured:$(\{\lambda\}^{exp}, \{\Phi\}^{exp})$. The purpose of the damage detection tool is to incorporate a damaged element inside the healthy structure in a way that the location, the length, and the damage index matches that of the real structure.

Table 2 Modes of vibration of the simply supported beam

	Mode1		Mode2		Mode3		Mode4	
	Spectral Element	Analytical	Spectral element	Analytical	Spectral element	Analytical	Spectral element	Analytical
v1	0.00	0.00	0.00	0.00	0.00	0.00	0.00	0.00
Theta1	−1.00	−1.00	1.00	1.00	−1.00	−1.00	1.00	1.00
v2	−19.10	−19.10	0.00	0.00	6.37	6.37	0.00	0.00
Theta2	0.00	0.00	−1.00	−1.00	0.00	0.00	1.00	1.00
v3	0.00	0.00	0.00	0.00	0.00	0.00	0.00	0.00
Theta3	1.00	1.00	1.00	1.00	1.00	1.00	1.00	1.00

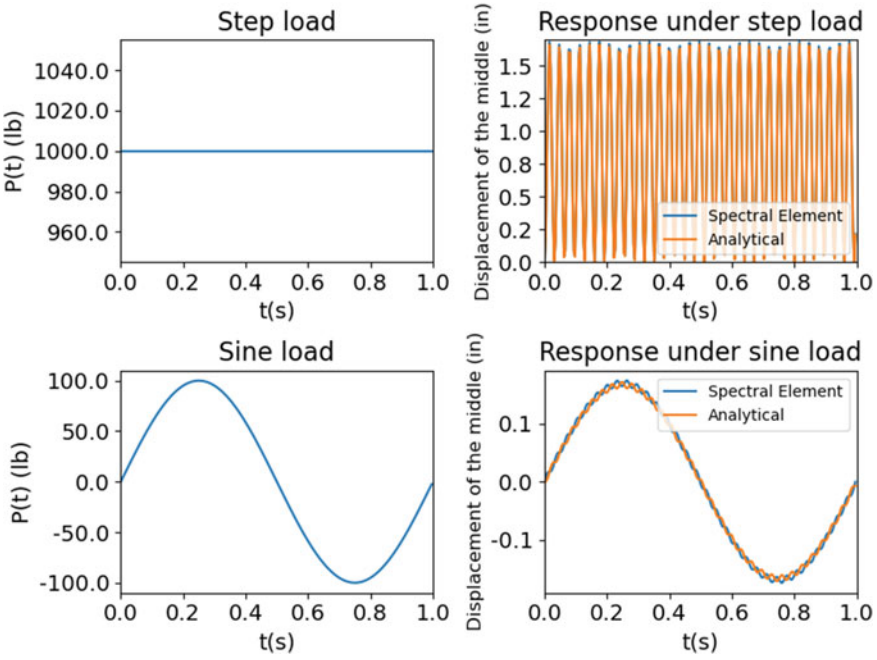

Fig. 4 Vibration of the middle point considering the transient response under step and sine loads

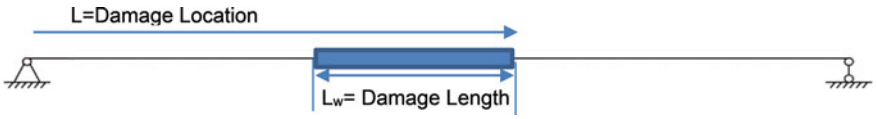

Fig. 5 Damage Model

So, a trial damaged model is created, and the first n natural frequencies and mode shapes are calculated using spectral element analysis and they are: $\left(\{\lambda\}^{trial}, \{\Phi\}^{trial}\right)$

As suggested in Dong and Wang [4], the cost function in Eq. 19, gives a comparison metric indicating how close the trial structure is to the real structure. The first term gives the relative difference in natural frequencies. The second term takes in two vectors at each step, the ith mode shape from measurement and the ith mode shape from the trial structure. The MAC (Modal Assurance Criterion) takes on values from zero- representing no consistent correspondence, to one- representing a consistent correspondence. So, if the modal vectors exhibit a consistent linear relationship, the modal assurance criterion should approach unity. Note that the MAC value is normalized by the magnitude of input vectors and is bounded by zero and one. [1]

$$Cost(\{\lambda\}^{trial}, \{\Phi\}^{trial}, \{\lambda\}^{exp}, \{\Phi\}^{exp}) = \sum_{i=1}^{n} \left(\frac{\lambda_i^{exp} - \lambda_i^{trial}}{\lambda_i^{exp}} . w_{\lambda_i} \right)^2$$

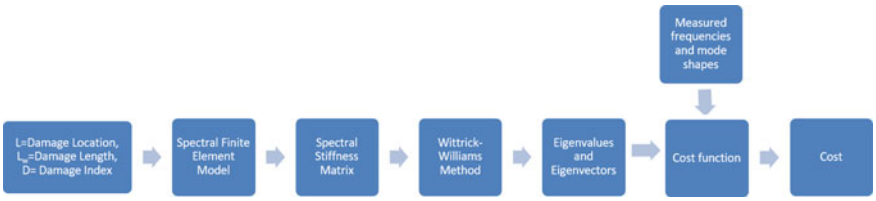

Fig. 6 Calculation of the cost value of each trial structure

$$+\left(\frac{1-\sqrt{MAC_i\left(\left\{\phi_i^{exp}\right\},\left\{\phi_i^{trial}\right\}\right)}}{\sqrt{MAC_i\left(\left\{\phi_i^{exp}\right\},\left\{\phi_i^{trial}\right\}\right)}}.w_{\phi_i}\right)^2 \tag{19}$$

$$\{\lambda\}^{\exp}=\left\{\lambda_1^{\exp},\lambda_2^{\exp},\ldots,\lambda_n^{\exp}\right\},\{\lambda\}^{trial}=\left\{\lambda_1^{trial},\lambda_2^{trial},\ldots,\lambda_n^{trial}\right\}.$$
$$\{\Phi\}^{\exp}=\left\{\left\{\phi_1^{\exp}\right\},\left\{\phi_2^{\exp}\right\},\ldots,\left\{\phi_n^{\exp}\right\}\right\},\{\Phi\}^{trial}=\left\{\left\{\phi_1^{trial}\right\},\left\{\phi_2^{trial}\right\},\ldots,\phi_n^{trial}\right\}$$

$$MAC_i\left(\{\phi_i^{exp}\},\left\{\phi_i^{trial}\right\}\right)=\frac{\left(\left\{\phi_i^{exp}\right\}^T.\left\{\phi_i^{trial}\right\}\right)^2}{\left(\left\{\phi_i^{exp}\right\}^T.\{\phi_i^{exp}\}\right)^2\left(\left\{\phi_i^{trial}\right\}^T.\{\phi_i^{trial}\}\right)^2} \tag{20}$$

The weights w_{λ_i} and w_{ϕ_i} are set to 1 in this study. However, depending on the location of damage some modes will change noticeably more than others. Thus, it will be beneficial to consider higher values for those modes. This will be investigated in future works.

The diagram in Fig. 6 shows how for each set of $\{L^{trial}, L_w^{trial}, D^{trial}\}$, a cost value is found. The problem that is tried to be solved is minimizing the cost function by changing $\{L^{trial}, L_w^{trial}, D^{trial}\}$ within the given constraints given in Eq. 21:

$$\begin{aligned} &minimize\left[Cost\left(\{\lambda\}^{trial},\{\Phi\}^{trial}\right)\right] \\ &\text{subjectedto}: 0<L_w^{trial}<L_w^{\max},0<L^{trial}<L_{beam},0<D<1.0 \end{aligned} \tag{21}$$

3.3 Genetic Algorithm (GA)

GAs are based on principles of evolutionary theory such as natural selection and evolution. Each possible solution is called a chromosome and consists of multiple genomes. Fitness function indicates how close the candidate solution is to the real solution. The cost function in Eq. 19 is taken as the fitness function in this study. Obviously, since we are solving a minimization problem, the lower the fitness value is, the better the solution for the corresponding chromosome is. A generation includes a set

of chromosomes. The population size can differ depending on the problem. Reproduction is the process of creating a new generation based on the previous generation. Reproduction is done through crossover and mutation [7]. In this study the generation size was taken as 8. The first generation is produced randomly within the constraints in Eq. 21. The population is sorted based on the fitness of candidates in it. The two best candidates in the first generation are moved directly to the next generation. The rest of the next population is generated through pair selection, crossover, and mutation.

Pair selection: In a population of size n like $[x_1, x_2, x_3, \ldots, x_n]$ with the corresponding fitness values $[f_1, f_2, f_3, \ldots, f_n]$, the candidate with a lower fitness value, has a better chance of entering the next generation. So, the possibility of each chromosome entering the reproduction process is shown as $[p_1, p_2, p_3, \ldots, p_n]$ and calculated as in Eq. 22:

$$P_i = 1 - \frac{fitness_i}{\sum_{i=1}^{populationsize} fitness_i}, i = 1, 2, 3, .., n \tag{22}$$

Cross-over: Assume two chromosomes selected after pair-selection like, $x_i = [x_{i1}, x_{i2}, x_{i3}, \ldots, x_{im}]$ and $x_j = [x_{j1}, x_{j2}, x_{j3}, \ldots, x_{jm}]$. If the elements after the kth element on x_i are swapped with the ones on x_j, the new chromosomes will be, $x_i = [x_{i1}, x_{i2}, x_{i3}, \ldots, x_{ik}, x_{j(k+1)}, \ldots, x_{jm}]$ and $x_j = [x_{j1}, x_{j2}, x_{j3}, \ldots, x_{jk}, x_{i(k+1)}, \ldots, x_{im}]$. In this study multi-point crossover was used.

Mutation: Sometimes the solution gets trapped around a local minimum instead of the global minimum. During mutation one of the genomes is randomly selected and its value is changed from 0 to 1 or from 1 to 0. This brings new solutions to evolution that might have better answers than what is already in the population. The probability of mutation was taken as 0.5 in this study.

3.4 Case Study

Consider a damaged structure as shown in Fig. 5 with the following properties $\{L = 20in, L_w = 5in, D = 25\%\}$. The first three natural frequencies and mode shapes are calculated using spectral analysis. The results are taken as $\{\lambda\}^{exp}, \{\Phi\}^{exp}$ in Eq. 19 as simulation of a vibration test.

The GA computes 8 trial solutions for each generation. The algorithm stops when the cost function of the best solution becomes zero or when the number of generations reaches a certain limit. The trial solution with the lowest cost in each generation is plotted in Fig. 7.

The exact values for $\{L^{trial}, L_w^{trial}, D^{trial}\}$ were predicted in the 356th generation. This means 356*8 = 2848 possible cases were investigated until the right solution was found. Considering the constraints in Eq. 21 and with regards that L_w^{max} was

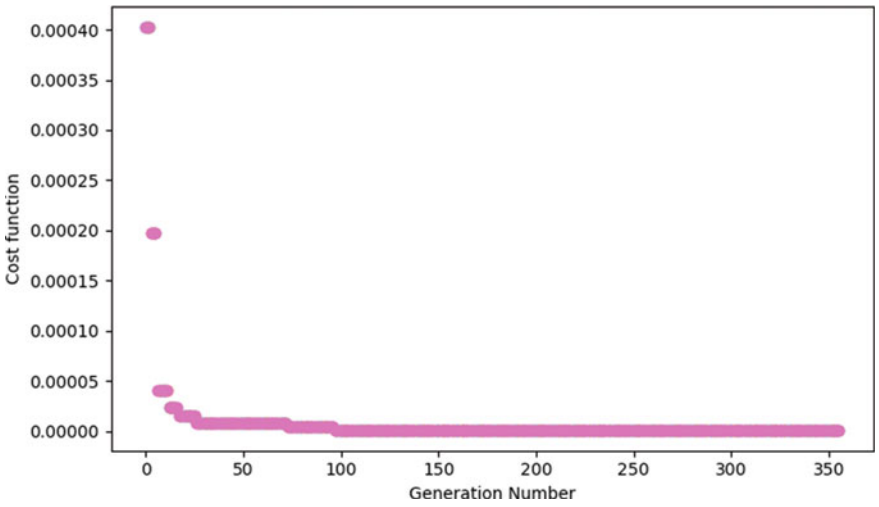

Fig. 7 Performance of the GA in optimization

taken as 20 as a simplifying assumption, 20 * 60 * 100 = 20,000 possible cases of damage exist. This means the GA found the exact location of damage and its severity by considering only $\left(\frac{2848}{120000} * 100\right)2.37\%$ of all possible cases.

4 Conclusion

A transient solution procedure was developed within the context of spectral element method and implemented for the analysis of Euler–Bernoulli beams. As Spectral Element procedure is originally developed for the steady-state dynamic solution, the developed procedure utilizes the steady-state solution to determine the transient solution. The numerical efficiency of the Spectral Element Method over the finite element method, in obtaining the free vibration frequencies and mode shapes, was illustrated in case studies. The efficiency gained by the Spectral Element Method gains more significance in higher frequencies which is especially important as in many cases damage effects reveal themselves only at high frequencies. Results of the dynamic analysis were employed in a genetic algorithm-based damage detection procedure. The genetic algorithm searches for the optimum of a cost function that employs the frequencies and mode shapes of the spectral element model to identify the damaged configuration, including damage location and size. A case study was designated to show the success of the overall damage detection algorithm developed.

References

1. Allemang RJ (2003) The modal assurance criterion—twenty years of use and abuse. J Sound Vib 37(8):14–23
2. Bagchi A (2005) Updating the mathematical model of a structure using vibration data. J Vib Control 11(12):1469–1486
3. Clough RW, Penzien J (1995) Dynamics of structures. Computers & Structures Inc., Berkeley, CA, USA
4. Dong X, Wang Y (2018) Formulation and optimization algorithm comparison for the FE model updating of large-scale models. https://github.com/ywang-structures/Structural-Model-Updating
5. Doyle JF (1997) Wave propagation in structures. Springer, New York, NY, USA
6. Doyle JF, Farris TN (1990) A spectrally formulated finite element for flexural wave propagation in beams. Int J Anal Exp Modal Anal 5(2):99–107
7. Hong H, Yong X (2002) Vibration-based damage detection of structures by genetic algorithm. J Comput Civ Eng 16(3):222–229
8. Kumar V, Yitshak M (2002) Transcendental eigenvalue problem and its applications. AIAA J 40(7):1402–1407
9. Lee U, Cho J (2008) FFT-based spectral element analysis for the linear continuum dynamic systems subjected to arbitrary initial conditions by using the pseudo-force method. Int J Numer Methods Eng 74(1):159–174
10. Pardoen GC (1989) Effect of delamination on the natural frequencies of composite laminates. J Compos Mater 23(12):1200–1215
11. Veletsos AS, Kumar A (1983) Steady-state and transient responses of linear structures. J Eng Mech 109(5):1215–1230
12. Wittrick WH, Williams FW (1970) A general algorithm for computing natural frequencies of elastic structures. Q J Mech Appl Math 24(3):263–284

Effective Bond Length of FRP Sheet Bonded to Concrete

M. F. Qureshi and S. A. Sheikh

1 Introduction

Amongst the available strengthening techniques, retrofit with FRP has offered better ease of application and in many cases better performance especially with respect to the conventional techniques. The de-bonding failure, however, is still one of the major issues in the application of external FRP that needs to be dealt with. This premature de-bonding hinders to achieve full effectiveness of the bonded FRP sheets over time. Different testing practices have investigated the bond between concrete and FRP, but huge discrepancies exist in the available bond results. To date, no standard procedure is available for testing the FRP to concrete bond which is one of the reasons of vast scatter in the bond test results. Based on the cost and the time to do the tests and symmetry of load application, double shear tests are usually preferred for the bond tests compared to other setups. Effective bond length (L_e), bond length corresponding to the FRP sheet de-bonding load, is measured from bond tests to calculate average bond stress and bond slip.

Nakaba et al. [8] tested 36 double shear bond specimens with 300 mm bond length. The specimens consisted of a concrete prism with dimension of 100 × 100 × 600 mm cracked at mid-length using a hammer after FRP laminates application. The variables examined were: (1) type of fiber, and (2) substrate type, (3) substrate strength, and (4) influence of putty thickness. The study investigated three types of fibers: standard carbon fiber, high stiffness carbon fiber, and aramid fiber, and two types of substrate: mortar and concrete. The substrate strength was in the range of 23.8–57.6 MPa. The failure happened by peeling of the FRP laminates in all the specimens. About 1 mm substrate surface was adhered to the peeled FRP laminates, which reduced with higher substrate strength. The comparison of the test results

M. F. Qureshi (✉) · S. A. Sheikh
University of Toronto, Toronto, ON, Canada
e-mail: faizan.qureshi@mail.utoronto.ca

S. Walbridge et al. (eds.), *Proceedings of the Canadian Society of Civil Engineering Annual Conference 2021*, Lecture Notes in Civil Engineering 240,
https://doi.org/10.1007/978-981-19-0507-0_47

showed greater failure load for stiffer FRP laminates, where stiffness was defined as laminate thickness multiplied by elastic modulus of FRP laminate. Like failure load, a direct relation was found between the effective bond length and FRP laminates stiffness. The maximum local bond stress was not affected by the type of fiber but increased as compressive strength of concrete increased. The substrate type and putty thickness did not significantly influence failure load or effective bond length.

A couple of research programs at the University of Toronto investigated the effective bond length using FRP to concrete bond specimens. In 2001, Sato and Vecchio tested six CFRP bond specimens cracked at middle region, 150 × 150 × 800 mm, with variable bond lengths to evaluate bond length and developed a bond-slip relation. All specimens failed by de-bonding of CFRP sheets with large concrete pieces attached to the de-bonded sheet at specimen crack location. An effective bond length of 150 mm was observed in this study.

Parvathy and Sheikh [9] studied the effective bond length of FRP-concrete specimens, 76 × 76 × 305 mm, under double shear. The variables considered in this study were bond length and types of FRP. Based on the results of fifty specimens, it was concluded that the effective bond length is directly proportional to the FRP sheet stiffness. A similar study was carried out by Homam and Sheikh [5] to investigate the bond behaviour. The only variable was the FRP sheet type, CFRP and GFRP. The failure was reported in the epoxy-concrete interface with little concrete pieces chipped off from the substrate. The findings of the research demonstrated lower average bond stress in the GFRP-concrete bond specimens compared to the CFRP-concrete bond specimens, it was attributed to the lower stiffness of the GFRP sheets. Tam and Sheikh [12] conducted FRP-concrete bond study with the same setup as Parvathy and Sheikh [9] with two variables, bond length and types of FRP. 40 and 100 mm effective bond lengths were inferred for GFRP and CFRP, respectively, from the test outcomes. The failure was observed between FRP and concrete interface.

Serbescu et al. [11] tested 20 double shear bond specimens as part of international Round Robin Test (iRRT) to assess the feasibility of double shear tests. Each specimen consisted of two concrete prisms with dimensions of 150 × 150 × 400mm, embedded with two 16 mm diameter steel bars and bonded with 600 mm FRP plates on two faces of the specimen. One hundred mm length of FRP plates was left unbonded in the mid-span of specimens to avoid shearing of concrete corners. Two variables were studied: types of FRP plate and levels of concrete surface roughness. The test findings showed an increase in the effective bond length for FRP plates with higher stiffness. Slightly higher effective bond length was measured for specimens with rougher concrete surface. All specimens failed due to de-bonding by shear-induced peel-off. The specimens with higher surface roughness failed with a thicker layer of concrete attached to the FRP plate due to better adhesion and greater mechanical interlock. The results showed the bond strength was dependent on the surface roughness of concrete substrate.

The study presented here was conducted as part of a comprehensive program to study the effects of climate change on the FRP reinforced structures. This paper presents the results of FRP to concrete bond specimens studied to evaluate the effective bond length and investigate analytical models for effective bond length. The

results of this study will also be used to investigate the effects of the climate change on bond behaviour.

2 Test Program

Twelve bond specimens were manufactured and tested in this experimental program. The variables studied were bond length and types of FRP. The specimens were subdivided into six groups, each group comprised of two specimens. The details of the specimens are presented in Table 1.

2.1 Materials

Commercially available unidirectional GFRP and CFRP products were used in this research. A two-component epoxy was used as the polymer matrix for the composite comprising of a resin (Part A) and hardener (Part B) in the ratio of 100:42 by volume. The resin and the hardener were mixed at a speed of 400–600 rpm for 5 min as suggested by the supplier. The manufacturer reported FRP and epoxy properties are listed in Table 2. The ready-mix concrete (class C-1) supplied by a local supplier was used for the specimens following the CSA A23.2–19 code specifications. The average 28 days compressive strength of the concrete was tested at 50.8 MPa. The average

Table 1 Test program

Group No	Number of specimens	Specimen ID	Type of FRP	Bond length (mm)
1	2	FCC-L-100	CFRP	100
2	2	FCC-L-125	CFRP	125
3	2	FCC-L-150	CFRP	150
4	2	FCG-L-75	GFRP	75
5	2	FCG-L-100	GFRP	100
6	2	FCG-L-125	GFRP	125

Table 2 Manufacturer reported properties of the FRP and Epoxy

Material	Ultimate tensile strength	Elongation at rupture	Nominal thickness of the fabric	Tensile modulus
	(MPa)	(%)	(mm)	(MPa)
GFRP	575	2.2	1.3	26,100
CFRP	986	1.0	1.0	95,800
Epoxy	72.4	5		3,180

compressive strength increased to 59 MPa when the bond study was conducted. A two-component epoxy was used to bond the LVDT holders and targets to the bond specimen.

2.2 Specimen Details

All the specimens comprised of 100 × 100 × 400 mm concrete prism with 800 mm long steel rebar (20 M) centered in the concrete cross-section. The rebar protruded 200 mm from both ends for load application as shown in the Fig. 1. Wooden formwork was used to cast FRP-concrete bond specimens. The molds were filled with concrete and vibrated using the handheld concrete vibrator. After 24 h, all the concrete prisms were demolded and shifted to the curing chamber. Concrete prisms were taken out of the chamber three weeks before the test day and cut into two halves using the wet saw. A wooden frame was constructed to hold the two halves of the specimens together. A 100 × 100 mm flame-retardant Garolite oiled sheet was inserted between the two halves of the specimens to remove any friction between the concrete surfaces. Then, wooden frame was secured tight using the screws ensuring the alignment of the specimen. All gaps between specimen and wooden frame were then filled with silicone caulking to avoid epoxy penetration in the gaps. The bond surfaces were prepared using a handheld rotary-bristle tool to meet concrete surface profile 3 (CSP3) requirements i.e., 0.01–0.025 mm profile depth (ICRI 310.2R 2013) to simulate the surface preparation in the field. ACI 440.2R 2017R also recommends minimum surface preparation of CSP3 for bond-critical applications. However, CSA suggests

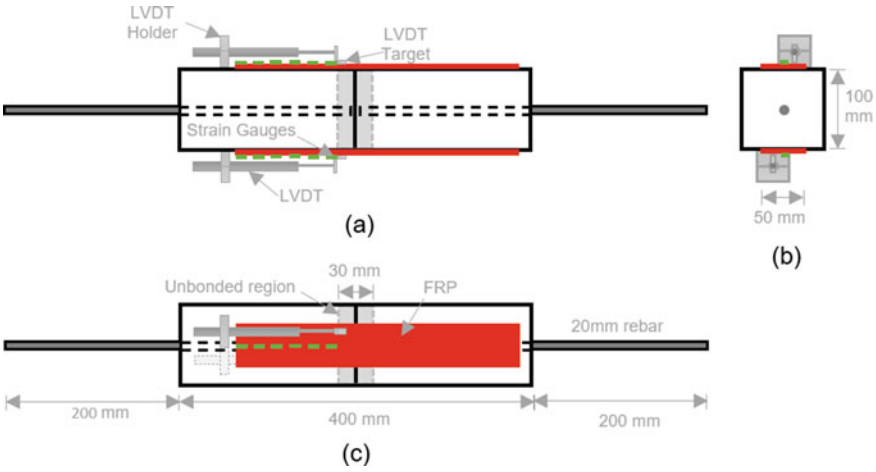

Fig. 1 Schematic of FRP-concrete bond specimen: **a** Longitudinal side view, **b** Transverse side view, and **c** Top/bottom view

dry concrete surface prepared by abrasive method with maximum surface irregularities of 1 mm. After surface preparation, the specimen was cleaned using compressed air to remove dust particles and wiped with acetone to ensure a clean surface. Markings were drawn on the concrete surface for the bonded and un-bonded region. Duct tape was adhered to the central un-bonded region to break the bond between FRP and concrete surface. The un-bonded region (30 mm) was provided to avoid stress concentration at the loaded ends. Epoxy was prepared using resin and hardener as briefed in Sect. 2.1. Using a roller, epoxy was applied to the concrete surface and the FRP sheet with a vinyl backing. About 30 min later, when the epoxy became sticky, FRP sheet was applied to the specimen with vinyl backing. An aluminum grooved roller was used in the fiber direction to remove extra epoxy and entrapped air bubbles. Next day, FRP sheet was bonded to the other side of the specimen following the same procedure. After 7 days of curing of the FRP application, a pre-coating agent was applied to create a smooth surface for strain gauge application. It was cured for 24 h before the strain gauges were applied (15 mm apart). Lastly, two LVDT holders and two targets were adhered to the specimen using epoxy as illustrated in Fig. 1. One LVDT was used on each instrumented side to measure total bond slip.

To evaluate the effective bond length, three bond lengths were selected for both types (GFRP and CFRP) specimens. These lengths were decided based on the available code equations as detailed in Table 3. For the GFRP specimens, the code-determined bond length values were in the range of 37–98 mm, two values were selected within the range i.e., 75, 100 mm and third value (125 mm) was selected slightly higher than the range to ensure effective bond length can be captured. Same procedure was followed for the CFRP specimens and three bond lengths selected were 100, 125, and 150 mm.

A 1000-kN servo-controlled universal testing machine was used for loading the bond specimens as illustrated in Fig. 2. For the first bond specimen, the initial loading rate used was 0.2 mm/min which was found to be too fast, so the loading rate was reduced to 0.08 mm/min. This lower loading rate was used for all the subsequent specimens. The specimen was placed in the machine with the wooden frame on and after fixing the specimen in the machine, specimen alignment was checked with an auto-leveling laser. Two clamps were applied on the specimen to ensure failure on the instrumented side. The wooden frame was loosened before load application to avoid any resistance offered by the frame. The specimen was monotonically loaded to failure considering de-bonding of the FRP sheet as the ultimate failure.

3 Test Results

3.1 Effective Bond Length

Force in the concrete generated by the applied load is transferred to FRP sheet through shear stresses in an active bond length which is part of the total bond length. The active

Table 3 FRP-concrete effective bond length calculations

Code	Equation	Factors*	Le (mm)	
			GFRP	CFRP
ACI 440.2R-17	$L_e = \frac{23,300}{(nt_fE_f)^{0.58}}$	n= number of FRP layers t_f= thickness of FRP per layer E_f=FRP tensile modulus	56	31
CSA S806-12 (R2017)	$L_e = k * L_{ea}$ $L_{ea} = \frac{25,350}{(t_fE_f)^{0.58}}$	k ranges from 0.6 to 1.6 with an interval of 0.2	61	34
	$L_e = 0.6 * \frac{25,350}{(t_fE_f)^{0.58}}$		37	20
	$L_e = 1.6 * \frac{25,350}{(t_fE_f)^{0.58}}$		98	54
FIB B14 Approach 1 (2001)	$l_{b,max} = \sqrt{\frac{E_f t_f}{c_2 f_{ctm}}}$	c_2=calibration constant = 2.0 f_{ctm}=mean concrete tensile strength	80	133
CS TR55 (2012)	$l_{t,max} = 0.7 * \sqrt{\frac{E_{fd} t_f}{f_{ctm}}}$	E_{fd}=design tensile modulus of FRP laminate	79	132
CNR-DT 200 (2013)	$l_{ed} = \min\left\{\frac{1}{\gamma_{Rd} f_{bd}}\sqrt{\frac{\pi^2 E_f t_f \Gamma_{Fd}}{2}}, 200\right\}$	Γ_{Fd}=design fracture energy = $\frac{k_b k_G}{FC}\sqrt{f_{cm} f_{ctm}}$ $k_b = \sqrt{\frac{2-b_f/b}{1+b_f/b}} \geq 1$ $k_G = 0.037$ (wet lay-up) FC = confidence factor $f_{bd} = \frac{2\Gamma_{Fd}}{s_u}$, $s_u = 0.25$ $\gamma_{Rd} = 1.25$ (corrective factor)	59	99

*n =1; t_fE_f=32,370 MPa-mm (GFRP); t_fE_f=90,100 MPa-mm (CFRP); f_{ctm}=2.53 MPa; $E_{fd}t_f = E_ft_f$;f_{cm}= 59 MPa; b_f= 50 mm; b=100 mm; FC = 1.0

bond length increases with the applied load until the de-bonding of FRP. Beyond the de-bonding load level, the FRP sheet starts to peel off without further increase in the load or the active bond length. FRP sheet de-bonding causes shifting of the active bond length away from the loaded end until FRP sheet is completely de-bonded. The active bond length corresponding to the de-bonding load is termed as the effective bond length 'L_e'. This length can be determined by using the strain variation in the FRP sheet and is defined as the distance in which the peak strain of the FRP sheet drops to almost zero. For every load level, second degree polynomial was used to

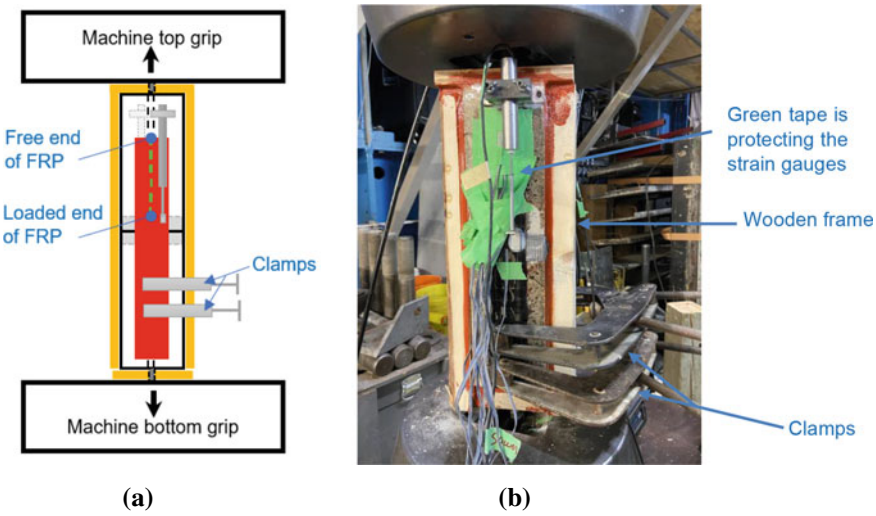

Fig. 2 **a** FRP-Concrete Bond Setup Schematic, **b** FRP-Concrete Bond Test Setup

represent strain variations in the FRP. As an example, consider the FCG-L-125.2 specimen plots (Fig. 3) which show the strain variations along the bonded length at different load levels. At 50% ultimate load (50%P_u), only two strain gauges near the loaded end showed any strain indicating that the load was transferred only within the 30 mm active bond length region. Active bond lengths of around 47 and 60 mm were measured corresponding to 75% and 95% of the ultimate loads which increased to 70 mm at ultimate load. It is important to note that in a few specimens, strain

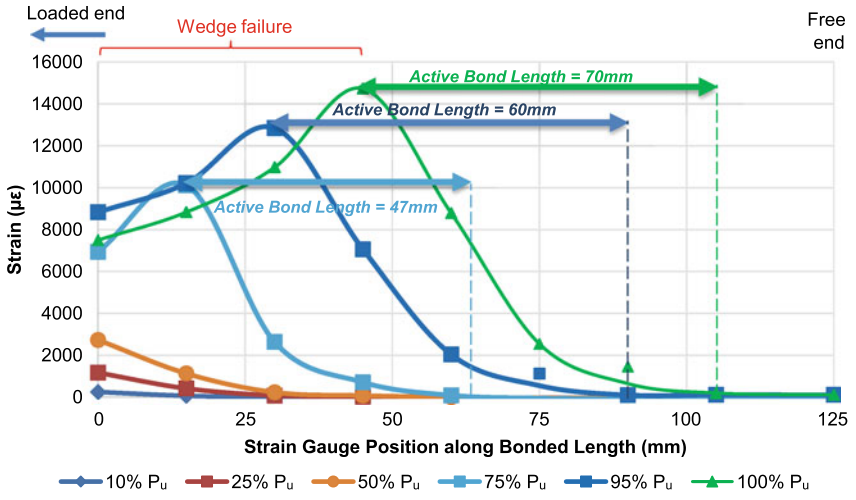

Fig. 3 Strain versus strain gauge position along bonded length plot (FCG-L-125.2)

gauges near the loaded end recorded higher values than expected after de-bonding initiated. For example, at ultimate load, the strain gauge 30 mm away from loaded end measured strain value of 10,969 μ ε which is greater than the elastic strain (9330 μ ε) calculated using that load and FRP elastic modulus. This was caused by the unexpected wedge failure near the loaded end causing strain concentration. Ideally, the strain values in the first few gauges at the loaded end should give similar strain after de-bonding.

As for other bond lengths, two FCC-L-100 specimens were constructed. One of these specimens was the first tested in this series for which the failure occurred prematurely on the un-instrumented side due to unavoidable bending. For this reason, results from only one 100 mm bond length specimen are presented. Table 4 presents the ultimate load, average bond stress at ultimate load, effective bond length and slip for all the specimens. For specimens with bonded length greater than the effective bond length, the observed ultimate load was higher than the de-bonding load. After initiation of the FRP sheet de-bonding, the load kept increasing with the shift of active bond length from FRP loaded towards the free end. This load increase was likely due to the additional friction forces generated between the de-bonded FRP sheet and concrete surface. Two bond stress values were calculated for each bond specimen, average effective bond stress from Eq. 1, and average bond stress from Eq. 1a. Average effective bond stress increased with increasing bonded length due to higher contribution of friction forces. However, the average bond stress reduced with longer bond lengths because the ultimate load did not increase in proportion to the bonded length. Higher average bond stress was observed for CFRP sheets compared to that for less stiff GFRP sheets for the same bonded length. The effective bond length for CFRP was estimated to be 100 mm as compared to a lower value of 70 mm for GFRP. Specimen FCC-L-100 was excluded from the average effective bond length calculations because of the erroneous strain data due to wedge failure. The concrete wedge was almost 30 mm long leaving only 70 mm bonded length for load transfer between FRP sheet and concrete at ultimate load. Average effective bond length measured for CFRP sheet was greater than the GFRP sheet indicating the effect of higher stiffness.

$$\tau_{avg,eff} = \frac{Q_u}{2 * b_f * L_{e,avg}} \tag{1}$$

$$\tau_{avg,tot} = \frac{Q_u}{2 * b_f * L_{tot}} \tag{1a}$$

where $\tau_{avg,eff}$= average effective bond stress; Q_u= ultimate load; b_f = FRP sheet width; $L_{e,avg}$= average effective bond length of each group corresponding to ultimate load; $\tau_{avg,tot}$= average bond stress; and L_{tot}= total bond length of each specimen.

Table 4 FRP-concrete bond length test results

Sr #	Specimen ID	Bond length (mm)	Ultimate load (kN)	Average effective bond stress (MPa)	Average bond stress (MPa)	Effective length (mm)	Average effective length (mm)	$Slip_{SG}$(mm)	$Slip_{LVDT}$(mm)	$Slip'_{SG}$(mm)
1	FCC-L-100	100	29.8	4.26	2.98	70	70.0	0.48	0.45	0.28
2	FCC-L-125.1	125	37.0	3.66	2.96	96	101.0	0.40	0.64	0.25
3	FCC-L-125.2	125	35.2	3.49	2.82	106		0.36	0.47	0.23
4	FCC-L-150.1	150	38.7	3.91	2.58	95	99.0	0.34	0.57	0.22
5	FCC-L-150.2	150	38.7	3.91	2.58	103		0.36	0.65	0.19
6	FCG-L-75.1	75	20.6	2.86	2.75	75	72.0	0.26	0.32	0.26
7	FCG-L-75.2	75	19.9	2.76	2.65	69		0.37	–	0.26
8	FCG-L-100.1	100	25.5	3.75	2.55	68	68.0	0.34	0.38	0.21
9	FCG-L-100.2[1]	100	23.3	3.43	2.33	55		0.29	0.38	0.27
10	FCG-L-125.1	125	28.8	4.18	2.31	68	69.0	0.72	0.76	0.26
11	FCG-L-125.2	125	30.2	4.38	2.42	70		0.77	0.71	0.31

[1]Epoxy leakage joined the two concrete prisms and concrete substrate acted as a single prism up till 90% of the de-bonding load. Prisms separated abruptly at 90% de-bonding load, therefore, results from this test were neglected for calculating average effective length, bond stress and bond slip i.e. $Slip'_{SG}$

– = LVDT's did not work

3.2 Slip

The total bond slip measured between concrete and FRP sheet at ultimate load is presented in Table 4 for each specimen. In the current test program, total bond slip was measured using two approaches: (1) using strain gauge data (SG's) and (2) using data from linear variable differential transducers (LVDT's). Total bond slip is comprised of three components: (1) δ_b = bond slip between bonded FRP sheet and concrete, (2) δ_c = deformation of concrete and (3)δ_{FRP} = elongation of the de-bonded FRP sheet. The second component 'δ_c' was neglected in the first approach considering the large concrete stiffness (EA) in comparison with the stiffness of FRP sheets. The total bond slip was determined by plugging strain gauge values in Eq. 2. The equation integrates the strain values along the bonded length using Simpson's rule. The LVDT's measured deformation that included the bond slip and the elastic elongation of the FRP along with concrete elongation (Eq. 3). Comparable slips were observed from both approaches as shown in Table 4. The difference between the two approaches was due to several reasons such as (a) LVDT's measured the elastic concrete elongation which was not measured by the strain gauges and (b) assumption of linear strain variation between the strain gauges to calculate total bond slip. The bond slip value (δ_b) corresponding to the ultimate load was also calculated for each specimen to evaluate the effect of longer bonded length and FRP stiffness. Equation 4 was used for this purpose which integrated the strain values only along the effective bond length region. As Table 4 shows, the longer bonded length did not affect the bond slip in the effective bond length region. Moreover, almost similar bond slip values were calculated for both type of FRP sheets regardless of the FRP stiffness and the bonded length.

$$\text{Slip}_{SG} = \delta_b + \delta_{FRP} = \sum_{i=1}^{n-1} \left(\frac{\varepsilon_i + \varepsilon_{i+1}}{2} \right) \cdot (x_{i+1} - x_i) \tag{2}$$

where n = number of strain gauges; i = 1, 2, 3, …, n − 1; ε_i = strain value at ith strain gauge; ε_{i+1} = strain value at (i + 1)th strain gauge; x_i = distance of ith strain gauge from loaded end; and x_{i+1} = distance of (i + 1)th strain gauge from loaded end

$$\text{Slip}_{LVDT} = \delta_b + \delta_c + \delta_{FRP} \tag{3}$$

$$\text{Slip}'_{SG} = \delta_b = \sum_{i=j}^{n-1} \left(\frac{\varepsilon_i + \varepsilon_{i+1}}{2} \right) \cdot (x_{i+1} - x_i) \tag{4}$$

where n = number of strain gauges; i = j, j + 1, j + 2,…n − 1; j = first strain gauge on bonded (as opposed to de-bonded) FRP sheet towards the free end; ε_i = strain value at ith strain gauge; ε_{i+1} = strain value at (i + 1)th strain gauge; x_i = distance

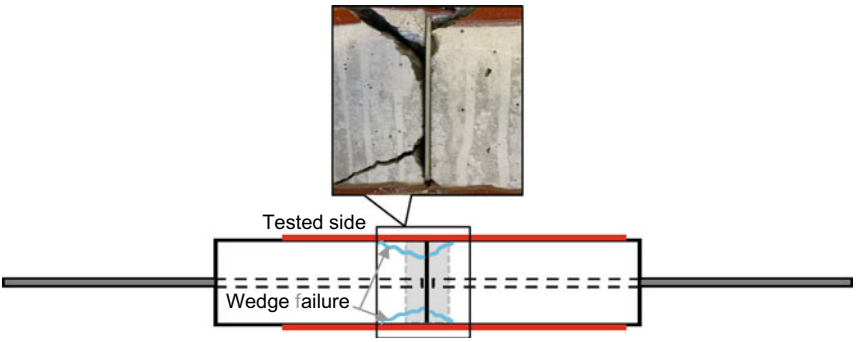

Fig. 4 FRP-concrete wedge failure

of ith strain gauge from loaded end; and x_{i+1} = distance of (i + 1)th strain gauge from loaded end.

3.3 Failure

Failure occurred in an abrupt manner by de-bonding of the FRP sheet in all the specimens with a wedge failure near the loaded end. As mentioned earlier, an un-bonded length (15 mm) was provided on each concrete prism to avoid wedge failure of the concrete, but the wedge failure (Fig. 4) was still observed in the tested specimens due to stress concentration near the loaded end. The FRP sheet de-bonding initiated with a cracking sound at around 80–90% of the ultimate load and continued until the failure. Three possible failure modes can be observed for the bond specimens; (1) Rupture of the FRP; (2) Adhesive and concrete interface failure; and (3) Shearing of the concrete surface. In all the tested specimens, the failure was due to concrete shearing. A thin layer of concrete was found attached to FRP sheet after de-bonding failure.

4 Proposed Model

Based on the findings of the FRP-concrete tests, the average effective bond length was inferred to be 70 mm for the GFRP sheets and 100 mm for the CFRP sheets. In addition to the current test results, data gathered from literature [8, 11] and previous University of Toronto studies [5, 9, 10, 12] were also used to plot effective bond length vs stiffness plot as shown in Fig. 5. The FRP stiffness used (Fig. 5) is defined as a product of FRP thickness and modulus since it is difficult to maintain epoxy thickness in the wet lay-up technique. The curves based on the available FRP standards are also shown on the same figure to assess their applicability. For the current study, all

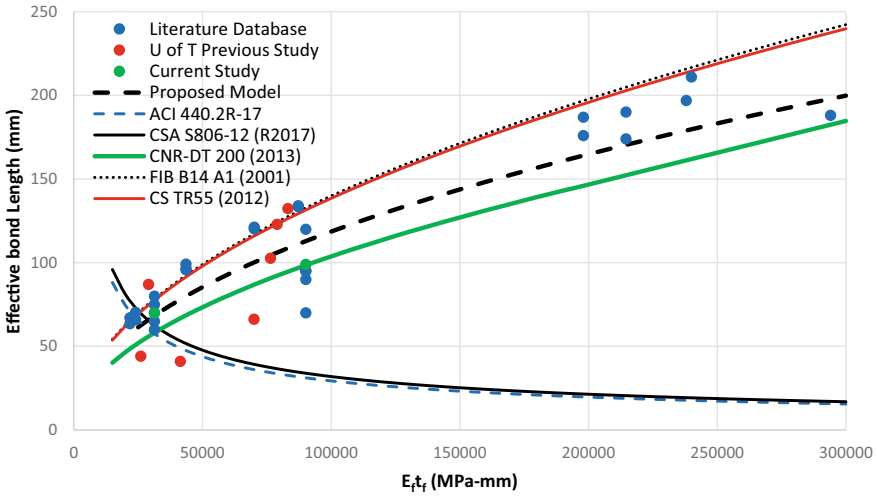

Fig. 5 Effective bond length comparison using FRP codes/guides and proposed model

codes/standards predicted reasonable effective bond length value for GFRP, however, for CFRP only CNR DT-200 2013 predicted reasonably accurate value. All code equations seem to predict correct effective bond length for a few data points but not all. It is important to mention that the CSA effective bond length equation was quite inaccurate especially for the CFRP sheets. Using the current test data and data gathered from literature, Eq. 5 is proposed for effective bond length. The power function was found to be best suited to define the relationship between the effective bond length and FRP sheet stiffness.

$$L_e = \frac{(E_f t_f)^{0.475}}{2} \tag{5}$$

where L_e = effective bond length; $E_f t_f$ = FRP sheet stiffness.

The predicted effective length for CFRP and GFRP is 112.8 and 69.4 mm using the proposed model. The reason for the difference between the analytical effective bond length values and the estimated experimental values is the large scatter in the bond specimen's database as well as a lack of strain data due to malfunctioning of strain gauges in the tests. This can partially be improved by standardizing the test method and defining concrete surface preparation details.

5 Conclusions

Twelve FRP-concrete bond specimens, carefully constructed and instrumented, were tested with varying bond lengths to study the effective bond length of GFRP and CFRP sheets with normal concrete. Effective bond length of around 70 and 100 mm were inferred for the GFRP and CFRP bond specimens, respectively. A direct relation was observed between the effective bond length and the FRP sheet stiffness. CFRP sheets showed higher average bond stress compared to GFRP sheets for same bonded length. However, almost similar bond slips were calculated for both FRP types. The findings also confirmed the total bond slips measured using LVDT's and strain gauges were greater than the bond slip ($Slip'_{SG}$) mainly due to the elastic elongation of de-bonded FRP sheet. An analytical model based on the available test data was developed to estimate the effective bond length and a comparative study was done to evaluate the available relevant equations from the FRP codes. Contrary to the CSA S806-17 model, the effective bond length was found to be proportional to the FRP stiffness. The proposed equation predicted the effective length values reasonably well and offered an improvement over the available models. However, additional bond specimen test results are needed with standardized test method and concrete surface preparation to improve the model.

Acknowledgements The authors acknowledge funding from the National Research Council of Canada (NRC) for this project. Thanks are also due to FYFE Co. for donating the FRP materials. The experimental work was conducted at the Structures Laboratories of the University of Toronto, Toronto, Canada.

References

1. American Concrete Institute Committee 440 (2017) Guide for the Design and Construction of Externally Bonded FRP Systems for Strengthening Concrete Structures, ACI 440.2R-17, Farmington Hills, MI, USA
2. Canadian Standards Association (2017). Design and Construction of Building Structures with Fiber-Reinforced Polymers, CSA S806–12 (reaffirmed 2017), Mississauga, Ontario, Canada
3. CAN/CSA-A23.3–14 (2014) Design of Concrete Structures. Canadian Standards Association, Rexdale, Ontario, Canada
4. Federation Internationale du Beton Task Group 9.3 (2001) Externally Bonded FRP Reinforcement for RC Structures, Technical Report, Fib Bulletin 14, CEB-FIP, Lausanne, Switzerland
5. Homam SM, Sheikh S (2005) Fiber Reinforced Polymers (FRP) and FRP-Concrete Composites Subjected to Various Loads and Environmental Exposures, PhD's Thesis, University of Toronto, Toronto, Canada
6. International Concrete Repair Institute (2013) Selecting and specifying concrete surface preparation for sealers, coatings, polymer overlays, and concrete repair, ICRI Guideline No. 310.2R-2013, Rosemont, IL, USA
7. Italian National Research Council (2013) Guide for the design and construction of externally bonded frp systems for strengthening existing structures. CNR-DT 200 R1/2013. Italy, Rome, p 2013

8. Nakaba K, Kanakubo T, Furuta T, Yoshizawa H (2001) Bond Behavior between Fiber-Reinforced Polymer Laminates and Concrete. ACI Struct J Title no 98–S34, 1–9
9. Parvathy U, Sheikh S (2003) Behaviour of FRP-to-FRP and FRP-to-concrete bond, Master's Thesis, University of Toronto, Toronto, Canada
10. Sato Y (2001) Report on FRP bond sheet test. University of Toronto, Toronto, Canada
11. Serbescu A, Guadagnini M, Pilakoutas K (2013) Standardised double-shear test for determining bond of FRP to concrete and corresponding model development. Compos Part B 55:277–297
12. Tam SSF, Sheikh S (2007) Durability of Fiber Reinforced Polymer (FRP) and FRP Bond Subjected to Freeze-Thaw Cycles and Sustained Load, Master's Thesis, University of Toronto, Toronto, Canada
13. The Concrete Society (2012) Design guidance for strengthening concrete structures using fibre composite materials, concrete society, CS-TR-55-UK, Technical Report No. 55, 3rd edn. Report of a Concrete Society Committee, Berkshire, UK

Self-Sensing Properties of Engineered Geopolymer Composites

M. A. Hossain and K. M. A. Hossain

1 Introduction

Developed as a novel, environment-friendly, and promising alternative to Portland cement (PC), geopolymers are inorganic polymer by-products formed from the reaction of solid aluminosilicate source materials and alkaline activators [10, 12, 17]. As per [10], unlike PC, geopolymers are developed through polycondensation by utilizing silica and alumina from the source materials and high alkaline activators which eventually, gain strength. The advantage of geopolymer over PC concrete includes better mechanical strength at early and final ages, stability under thermal and chemical conditions, strong adhesion to various surfaces, low permeability, and low carbon emission [26]. However, geopolymer concrete shows brittle characteristics justifying the necessity to study the prospect of introducing different reinforcing materials (fibers, nanomaterials, etc.) to improve flexural and fracture performances.

The recent developments in nanotechnology have enabled the incorporation of nanosized particles/fibers/tubes such as nano-silica, carbon nanotubes, nano TiO_2, etc., as reinforcing elements within the matrix of cementitious materials. Previous research has shown the effectiveness of these nanoparticles/fibers/tubes compared to other reinforcing materials such as steel bar, PVA fibers, etc. in impeding initiation and propagation of the nanosized cracks that eventually form micro-cracks [30, 35]. Another option can be the use of nano-silica particles. Fine additives like nano-silica particles have a filler effect and can densify the concrete microstructure [14, 25, 28, 32]. Moreover, nano-silica also contributes to cement hydration as these particles have a high specific surface area (300 m^2/g) [19, 27]. However, these particles lack the ability to prevent nanosized crack formation due to its low aspect ratio (spherical shape) [25], bringing the use of carbon-based nanofillers. Unlike nano-silica, carbon

M. A. Hossain (✉) · K. M. A. Hossain
Ryerson University, Toronto, ON, Canada
e-mail: ahossain@ryerson.ca; mohammadali.hossain@ryerson.ca

S. Walbridge et al. (eds.), *Proceedings of the Canadian Society of Civil Engineering Annual Conference 2021*, Lecture Notes in Civil Engineering 240,
https://doi.org/10.1007/978-981-19-0507-0_48

nanotubes (CNTs) have a high aspect ratio (from 1000:1 to 2,500,000:1) [18, 20, 21] in addition to its high strength and high modulus of elasticity [29, 38]. Owing to these benefits of high aspect ratio and mechanical performance, CNTs have been found to be significantly effective in enhancing mechanical strength and crack resisting performance of the cementitious composites. However, research outcomes related to the large-scale application of CNT within reinforced cement composite is still scarce.

Another important aspect of the civil structure is ensuring and improving its safety and serviceability by controlling and monitoring structural vibration, load, and structural health. One of the best options to address this issue is Intrinsic self-sensing concrete (ISSC) which provides a new approach to maintain sustainable development in concrete materials and structures [7]. Self-sensing is the ability of structural materials to sense changes in its own condition, such as strain, stress, damage, and temperature [8, 9]. Self-sensing concrete can be fabricated by incorporating some functional fillers such as carbon fiber (CF), carbon nanotube (CNT), carbon black, graphene nanomaterials, etc. [33]. An extensive conductive medium within the concrete can be achieved through the dispersion of these fillers. Due to deformation or stress development under external force or environmental action, this medium will undergo changes affecting its electrical properties (such as conductivity). Based on the changes in the electrical properties, any change under external force or environmental action can be sensed and identified [9, 39]. One of the major challenges, as described by [23], still remains to be proper utilization of these nanoparticles in order to bring their electrical properties effectively onto the macroscopic level for sensing purposes, to be specific for a larger application.

The main purpose of this article is to present a brief overview of the developments, properties, and applications of CNT-based fiber reinforced engineered geopolymer composites (EGCs). The CNTs used for this study were multi-wall carbon nanotubes (MWCNTs). A comparative analysis of electrical behavior for the increase in CNT content has also been presented. Primarily, the fresh state and mechanical properties of developed MWCNT based EGC mixes are described along with the variation in electrical behavior (such as resistivity) of specimens under progressive compressive loading to failure for assessing self-sensing performance. However, the focus is primarily given on challenges and prospects of self-sensing performance of nanofiber reinforced EGC specimens under external compression loading. The findings of this paper will help researchers and engineers to develop and evaluate MWCNT-based conductive geopolymer composites with self-sensing ability.

2 Materials and Methodology

Three types of source materials, i.e., Ground Granulated Blast Furnace Slag (GGBFS), class F-Fly Ash (FA-F) and class C Fly Ash (FA-C) were used as source materials to develop EGCs. The binary (BM) (FA-C + slag) and ternary TM (FA-C + slag + FA-F) EGC mixtures were developed by incorporating FA-C, slag, and FA-F

Table 1 Details of binary and ternary EGC mixes

Mix ID	Source Materials (SMs)	SM (mass)	WCNT*	Activator*	Silica Sand*	SP*	PVA**	Water/SM (W/S)
BM	FA-C + slag	1	0%,0.3%,0.6%	0.1	0.3	0.02	0.02	0.35
TM	FA-C + slag + FA-F	1	0%,0.3%,0.6%	0.1	0.3	0.02	0.02	0.35

*Weight proportion with respect to SM; **Volume proportion with respect to the total volume of the mix; FA-C: fly ash class C; FA-F: fly ash class F. slag: ground granulated blast furnace slag

as reactive aluminosilicate solids, fine silica sand (SS), water, and polycarboxylate based high range water reducing admixture (HRWRA). As an alkaline activator, a particular combination of powder form of Na_2SiO_3 and Ca $(OH)_2$ was used for this study. Commercially available Polyvinyl Alcohol (PVA) fiber with 8 mm in length and 40 μm in diameter was used to produce EGCs. The surface of PVA fiber was coated with 2% oil by weight to reduce fiber/matrix frictional bond. In addition, to evaluate self-sensing behavior, 0–0.6% of multi-wall carbon nanotubes (MWCNTs) with 20–30 nm diameter, 10–30 μm length, 95% (wt %) purity were used in both mixes in order to get conductive properties. The specimens were cured at ambient temperature (23 ± 3°C) and 95 ± 5% relative humidity in the moisture room till the testing date (28 days). The details of prepared binary (BM) and ternary (TM) EGC mixes with MWCNTs are provided in Table 1.

Setting time, slump flow, and fresh state /hardened density of EGCs with MWCNTs were evaluated. The slump flow (Fig. 1a) and fresh density were measured as per ASTM C1611 [3] and ASTM C138 [2], respectively. Setting times (initial and final) were measured following ASTM C807 [5] as shown in Fig. 1b. Compressive and direct tensile strength of EGC specimens were determined by testing 50 mm cube and Dogbone specimens as per ASTM C109 [1] and ASTM E8 [6] with specimens neck size 100 mm × 25 mm × 25 mm, respectively. Flexural strength of EGC mixes were also determined using simply supported beam specimens (310 mm × 76 mm × 50 mm) subjected to four-point loading following ASTM C651 [4] standard (Fig. 1c). The hardened density of EGC was evaluated following conventional procedure.

Two prove-probe electrodes [15, 22, 37] made of copper meshes embedded near the two opposite faces of cubic specimens were used for measurement of electrical resistance (using 5 V DC current) during compressive loading to failure to study piezoresistive effect for self-sensing property assessment. A computer-aided data acquisition system was used to record load-resistivity response during loading history until failure of the specimen (Fig. 1d). Electrical resistivity or conductivity was also measured using cube specimens by applying 5 V DC current as shown in Fig. 1e.

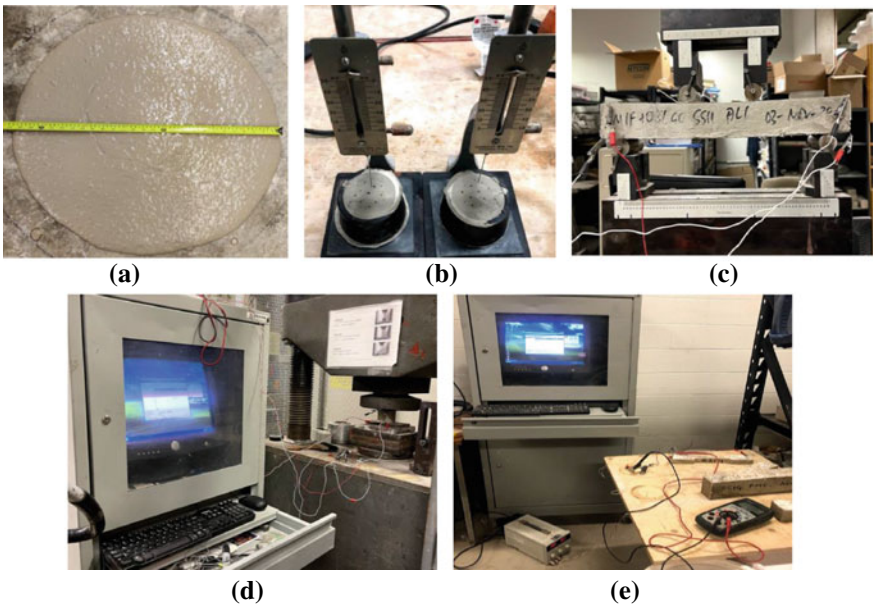

Fig. 1 Test set-ups: **a** Slump flow, **b** Setting times **c** Flexural strength **d** Piezoresistive test **e** Conductivity/resistivity test

3 Results and Discussion

3.1 Setting Time, Slump Flow and Densities of the EGC Mixes

The initial and final setting times of MWCNT based EGC mixes are provided in Table 2. It is evident binary (BM) EGC mixes experienced a relatively early setting as compared to their ternary (TM) counterparts. The initial and final setting times of BM mixes were observed to be about 60 and 30 min less than those of TM mixes, respectively. The presence of FA-F in the ternary mixes was responsible for such delay in setting times since it increased the SiO_2/Al_2O_3 ratio [30]. BM mixes

Table 2 Summary of setting time, fresh and hardened density

Sample name	Setting time (mean values)		Mean fresh density (kg/m^3)	Mean hardened density (kg/m^3)
	Initial (min)	Final (min)		
BM: 0%, 0.3%, 0.6% MWCNT	150	260	1935	1970
TM: 0%, 0.3%, 0.6% MWCNT	210	290	1905	1988

experienced slump flow of around 720 mm within 5 s, whereas TM mixes exhibited slump flow of about 725 mm within 3 s. Hence, the ternary mixes were found to be more flowable than the binary mixes. The fresh state and hardened densities of EGC mixes are also provided in Table 2. The fresh state density of BM and TM EGC mixes ranged from 1905 to 1935 kg/m^3 while 28-day hardened density ranged from 1970 to 1988 kg/m^3.

3.2 *Compressive, Flexural and Direct Tensile Strengths*

The 28-day compressive strength of the developed MWCNT-based BM EGC mix was 24–26 MPa compared to 22–24 MPa of TM mixes. The relative lower strength of the ternary mixes was due to comparatively lower activation of FA-C [34]. From previous studies, it was found that the compressive strength of fly ash-based geopolymer with solution-based activator ranged from 10 to 80 MPa, depending on water to geopolymer solid (source materials) ratio and curing temperature [11, 31]. On the other hand, compressive strengths of EGCs were found to be in the range of 17.4–54.6 MPa in previous research studies conducted by Nematollahi et al. [24] using fly ash as source materials and combinations of NaOH and Na_2SiO_3 as activators. The maximum compressive strength was achieved by the geopolymer mixes with water to source materials (W/S) ratio between 0.18 and 0.20. W/S ratios were significantly less than the ratio used in the current study. Hence, there is scope for further improvement in the compressive strength of EGCs with MWCNT by reducing the water content.

Figure 2 compares the flexural stress vs. mid-span deflection variation of beam

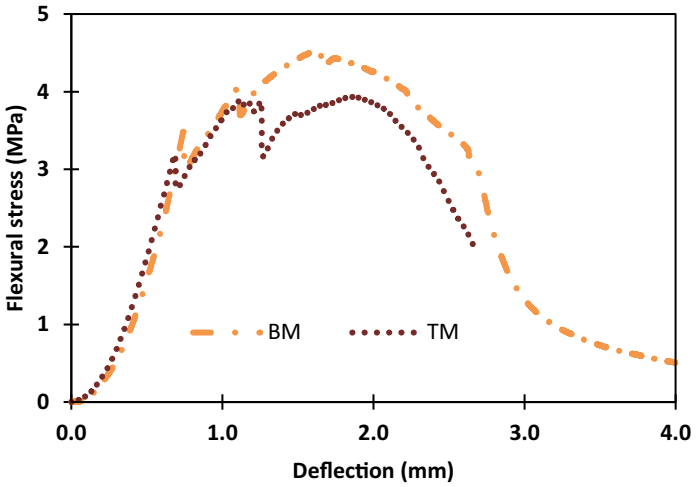

Fig. 2 Flexural stress versus mid span deflection responses of beams made of EGC-MWCNT mixes

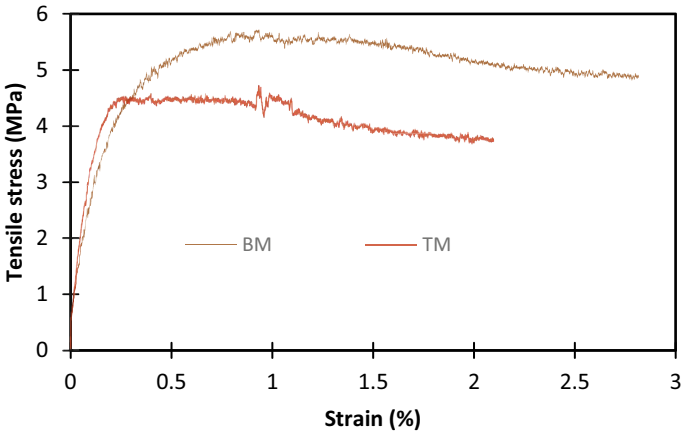

Fig. 3 Tensile stress versus strain relationship of EGC-MWCNT mixes

specimens made of BM and TM mixes with 0.3% MWCNT at the age of 28 days. The maximum flexural strength values of BM- MWCNTand TM-MWCNT EGC mixes were 4.7 and 3.7 MPa, respectively, with TM mixes showing lower strength. Flexural toughness were observed 8.182(BM-MWCNT), 7.538(TM-MWCNT) and the ductility factor were found BM 3.01 and TM 3.1. BM mixes showing better toughness and both mixes showing similar ductility factor. The tensile stress–strain responses of EGC-MWCNT mixes with 0.3% MWCNT at 28 days are compared in Fig. 3. Maximum tensile strength of 4.5 and 4.7 MPa were achieved by the binary (BM-MWCNT) and ternary (TM-MWCNT) EGC mix, respectively. It can be noted from Fig. 3 that specimens made of both BM and TM EGC mixes with MWCNT exhibited strain hardening (ductile) behavior with the formation of micro-cracking showing more than 2% strain before failure. Moreover, both flexural and tensile strengths of BM and TM EGC mixes are comparable with those found from previous research studies. Uni-axial tensile strength of EGC mixes developed by Nematollahi et al. [24] ranged from 2.9 to 3.4 MPa and 3.9 to 5.2 MPa, respectively.

3.3 Piezoresistive Characteristics of EGC Mixes

Figure 4 shows the variation of electric resistivity with progressive compressive stress in cube specimens during loading as an indicator of self-sensing performance. Both BM and TM EGC cube specimens showed sensitive properties showing a decreasing trend of resistivity with increase in compressive stress/load. The change in resistivity with the change in compressive stress (above 10 MPa) was observed to be noteworthy and, thus, present with the significant prospect for MWCNT incorporation for self-sensing purposes. As the specimen underwent increasing compressive load, the MWCNT layers can be expected to come closer (better interconnection),

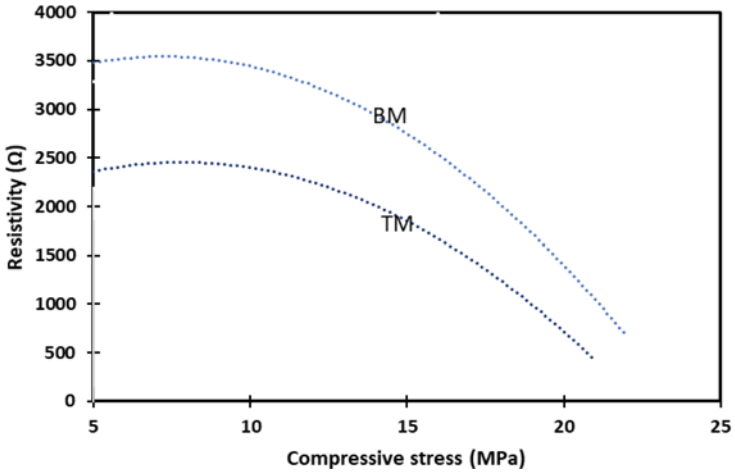

Fig. 4 The piezoresistive effect showing a variation of resistivity with compressive stress during loading

resulting in a better conductive media and, thus, reduced resistivity value [36]. Also, this finding presents the self-sensing prospect of MWCNT based EGC mixes from the variation of electrical property due to change in external loading condition. During field application, this decreasing trend of resistivity value will indicate increase in developed stress resulting from the change in external compression loading and thus, signify the self-sensing characteristics/performances of developed EGC-MWCNT mixes.

3.4 Influence of MWCNT Content on Electrical Resistivity/conductivity Properties of EGC Mixes

Figure 5 shows the effect of MWCNT concentration on the resistivity/conductivity of BM and TM EGC mixes. It can be noted that mix with 0% MWCNT exhibited a non-conductive medium showing very low conductivity. However, with the incorporation of 0.3% MWCNT, the conductivity increased to 0.0198–0.021 S/m. The conductivity values further increased with the increase in MWCNT content from 0.3% to 0.6%, up to a limit of around 0.026 S/m for binary BM-MWCNT mix and 0.029 S/m for TM-MWCNT. The conductivity of BM-MWCNT and TM-MWCNT mixes were found to be 19.80×10^{-3} S/m and 21.0×10^{-3} S/m, respectively, and these values are in agreement with the previously observed values of 10^{-1} S/cm–10^{-6} S/cm from former research studies [13]. In general, conductivity increased with the increase of MWCNT content and ternary (TM) EGC mix exhibited higher conductivity compared its binary (BM) counterpart at higher MWCNT content. This can be attributed to the formation of better conductive EGC media/matrix resulting from the addition of increased

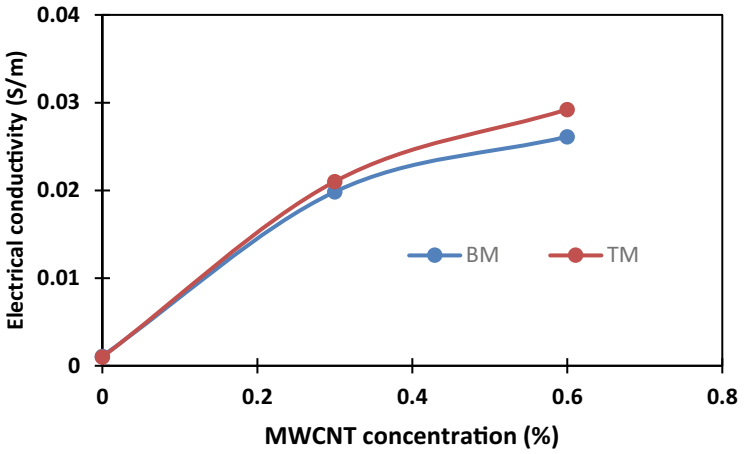

Fig. 5 Variation of electrical resistivity/conductivity of EGC mixes with MWCNT concentration

MWCNT content. Moreover, these observed trends of conductivity variations and the trend of increase in conductivity with the increase of MWCNT addition was confirmed from previous research studies where MWCNT addition of up to 1% increased the conductivity [16].

4 Conclusions

This paper presents findings of an ongoing comprehensive investigation on engineered geopolymer composites (EGCs) having varying contents of multi-wall carbon nanotube (MWCNT), binary and ternary combinations of source materials such as fly ash F (FA-F), fly ash C (FA-C) and ground granulated blast furnace slag (slag), combination of alkaline reagents as activators and polyvinyl alcohol fibers. Based on the results of fresh state (such as slump flow and setting times), mechanical (flexural and tensile strength) and coupled piezoresistive-electrical conductivity (for self-sensing evaluation) tests, the following conclusions are drawn:

- The binary mixes (BM) made of FA-C and slag exhibited relatively quicker initial and final setting times as compared to their ternary (TM) counter parts made of FA-C, slag and FA-F. In addition, binary and ternary EGC mixes experienced comparatively slower setting times in comparison with conventional geopolymer mixes.
- The binary mixes achieved higher compressive strength at 28 days in comparison with the ternary mixes. Both BM and TM EGC mixes experienced compressive strengths that are comparable to the strengths of geopolymer mixes from previous research studies having similar water to source material ratios.

- The binary mixes achieved almost similar tensile strengths compared to their ternary counterparts and mix. All mixes exhibited strain herding tensile stress–strain responses (showing > 2% strain) with micro-cracking characteristics However, for flexural performance, the binary mixes produced about 27% increase in maximum flexural strength compared to their ternary counterparts.
- The variation in electrical resistivity value of MWCNT based EGC cube specimens with progressive compression loading to failure (during piezoresistive testing) implies MWCNT as prospective filler material for inducing self-sensing properties in geopolymer composites and confirmed the self-showed better conductive media/matrix with increasing stress due to better interlayer connection between MWCNT layers. Both BM and TM mixes had shown reasonable conductivity that supported the findings from previous research studies.
- The increase in MWCNT content from 0.3%wt to 0.6%wt showed an increase in conductivity from about 0.019–0.026 S/m to 0.021–0.029S/m.
- The outcomes of this experimental investigation are quite promising and exhibit potential for developing EGC-MWCNT mixes with powder based activators under ambient curing conditions as sustainable and conductive construction materials for the self-sensing purpose. However, further studies will be required to develop design specifications for EGC-MWCNT mixes.

Acknowledgements The authors acknowledge the financial support from Natural Sciences and Engineering Research Council (NSERC) Canada.

References

1. ASTM C109/C109M (2016) Standard test method for compressive strength of hydraulic cement mortars (using 2-in. or [50-mm] cube specimens). ASTM International, West Conshohocken, PA
2. ASTM C138/C138M (2017) Standard test method for density (unit weight), yield, and air content (gravimetric) of concrete. ASTM International, West Conshohocken, PA
3. ASTM C1611/C1611M (2018) Standard test method for slump flow of self-consolidating concrete. ASTM International, West Conshohocken, PA
4. ASTM C651–20 (2020) Standard test method for flexural strength of manufactured carbon and graphite articles using four-point loading at room temperature
5. ASTM C807 (2018) Standard test method for time of setting of hydraulic cement mortar by modified vicat needle. ASTM International, West Conshohocken, PA
6. ASTM E8/E8M (2016) Standard test methods for tension testing of metallic materials. ASTM International, West Conshohocken, PA
7. Banthia N (2009) Fiber reinforced concrete for sustainable and intelligent infrastructure. In: First international conference on sustainable built environment infrastructures in developing countries. Algeria, pp 337–350
8. Chung DD (1998) Self-monitoring structural materials. Mater Sci Eng R Rep 22(2):57–78
9. Chung DDL (2004) Electrically conductive cement-based materials. Adv Cem Res 16(4):167–176
10. Davidovits J (1991) Geopolymers: inorganic polymeric new materials. J Therm Anal Calorim 37(8):1633–1656

11. Diaz-Loya EI, Allouche EN, Vaidya S (2011) Mechanical properties of fly-ash-based geopolymer concrete. ACI Mater J 108(3):300
12. Duxson P, Fernández-Jiménez A, Provis JL, Lukey GC, Palomo A, van Deventer JSJ (2007) Geopolymer technology: the current state of the art. J Mater Sci 42(9):2917–2933
13. Feng C, Jiang L (2013) Micromechanics modeling of the electrical conductivity of carbon nanotube (CNT)–polymer nanocomposites. Compos A Appl Sci Manuf 47:143–149
14. Gupta M, Kumar M (2019) Effect of nano silica and coir fiber on compressive strength and abrasion resistance of concrete. Constr Build Mater 226:44–50
15. Hou T-C, Lynch JP (2005) Conductivity-based strain monitoring and damage characterization of fiber reinforced cementitious structural components. In: Smart structures and materials 2005: sensors and smart structures technologies for civil, mechanical, and aerospace systems, vol 5765. International Society for Optics and Photonics, pp 419–429
16. Jittabut P, Horpibulsuk S (2019) Physical and microstructure properties of geopolymer nanocomposite reinforced with carbon nanotubes. Mater Today: Proc 17:1682–1692
17. Komnitsas KA (2011) Potential of geopolymer technology towards green buildings and sustainable cities. Procedia Eng 21:1023–1032
18. Konsta-Gdoutosa MS, Metaxa ZS, Shah, & S.P. (2010) Multi-scale mechanical and fracture characteristics and early-age strain capacity of high performance carbon nanotube/cement nanocomposites. Cement Concr Compos 32:110–115
19. Li W, Li X, Chen SJ, Liu YM, Duan WH, Shah, & S.P. (2017) Effects of graphene oxide on early-age hydration and electrical resistivity of Portland cement paste. Constr Build Mater 136:506–514
20. Makar J, Margeson J, Luh J (2005) Carbon nanotube/cement composites-early results and potential applications. In Proceedings of the 3rd international conference on construction materials: performance, innovations and structural implications. Vancouver, Canada, pp 1–10
21. Manzur T, Yazdani N, Emon MAB (2016) Potential of carbon nanotube reinforced cement composites as concrete repair material. J Nanomater Article ID 1421959, 2
22. Qizhen M, Bingyuan Z, Darong S, Zhuoqiu L (1996) Resistance changement of compression sensible cement speciment under different stresses. J Wuhan Univ Technol Mater Sci
23. Marinho B, Ghislandi M, Tkalya E, Koning CE, de With G (2012) Electrical conductivity of compacts of graphene, multi-wall carbon nanotubes, carbon black, and graphite powder. Powder Technol 221:351–358
24. Nematollahi B, Sanjayan J, Shaikh FUA (2015) Synthesis of heat and ambient cured one-part geopolymer mixes with different grades of sodium silicate. Ceram Int 41(4):5696–5704
25. Pan Z, He L, Qiu L, Korayem AH, Li G, Zhu JW, Collins F, Li D, Duan WH, Wang, & M. C. (2015) Mechanical properties and microstructure of a graphene oxide–cement composite. Cement Concr Compos 58:140–147
26. Provis JL, Bernal SA (2014) Geopolymers and related alkali-activated materials. Annu Rev Mater Res 44:299–327
27. Sanchez F, Sobolev K (2010) Nanotechnology in concrete—a review. Constr Build Mater 24(11):2060–2071
28. Senff L, Labrincha JA, Ferreira VM, Hotza D, Repette WL (2009) Effect of nano-silica on rheology and fresh properties of cement pastes and mortars. Constr Build Mater 23(7):2487–2491
29. Shi T, Li Z, Guo J, Gong H, Gu C (2019) Research progress on CNTs/CNFs-modified cement-based composites—a review. Constr Build Mater 202:290–307
30. Siad H, Lachemi M, Sahmaran M, Mesbah HA, Hossain KA (2018) Advanced engineered cementitious composites with combined self-sensing and self-healing functionalities. Constr Build Mater 176:313–322
31. Singh B, Gupta Ishwarya M, Gupta, & S. K. Bhattacharyya. (2015) Geopolymer concrete: a review of some recent developments. Constr Build Mater 85:78–90
32. Singh LP, Karade SR, Bhattacharyya SK, Yousuf MM, Ahalawat S (2013) Beneficial role of nanosilica in cement based materials—a review. Constr Build Mater 47:1069–1077

33. Singh NP, Gupta VK, Singh AP (2019) Graphene and carbon nanotube reinforced epoxy nanocomposites: a review. Polymer 180, ID 121724
34. Sood D, Hossain KMA, Manzur T, Hasan MJ (2019) Developing geopolymer pastes using dry mixing technique. In: Proceedings of the CSCE annual conference: growing with youth–Croître avec les jeunes, pp 12–15
35. Xie T, Fang C (2019) Nanomaterials applied in modifications of geopolymer composites: a review. Aust J Civ Eng 17(1):32–49
36. Yoo DY, You I, Lee SJ (2017) Electrical properties of cement-based composites with carbon nanotubes, graphene, and graphite nano-fibers. Sensors 17(5):1064
37. Xin C, Shoude W, Lingchao L, Shifeng H (2011) Influence of preparation process on piezo-conductance effect of carbon fiber sulfoaluminate cement composite. J Compos Mater 45(20):2033–2037
38. Zheng LX, O'connell MJ, Doorn SK, Liao XZ, Zhao YH, Akhadov EA, Peterson DE (2004) Ultralong single-wall carbon nanotubes. Nat Mater 3(10):673–676
39. Zhu S, Chung DDL (2007) Numerical assessment of the methods of measurement of the electrical resistance in carbon fiber reinforced cement. Smart Mater Struct 16(4):1164

Analysis of Reinforced Concrete Shear Walls Using Elastic–Plastic-Damage Modelling

R. E. Erkmen, A. Sarikaya, O. Arat, and K. Galal

1 Introduction

Shear walls are useful structural tools in redistributing the loads and controlling the damage in reinforced concrete buildings under earthquake loads. Due to their comparatively large cross-sections, they carry significant portion of the base bending moment and shear under lateral load. Bending mode of behaviour also improves ductility when the reinforcement arrangements are sufficient. Analysis of shear walls requires incorporation of inelastic material models as often the stresses the elastic threshold under extreme lateral loading such as earthquake. For finite element structural modelling purposes elastic–plastic-damage based constitutive laws have been applied extensively for the description of progressive failure of concrete. The evolution of the internal parameters in phenomenological plasticity and damage models can be related to underlying mechanisms within the material in a thermodynamically consistent manner, e.g., development of slip bands and dislocation systems causing plastic deformations or void nucleation and crack development causing stiffness degradation. Initial attempts to merge elastoplastic and damage constitutive models can be found in Lemaitre [6], Simo and Ju [12] and recently by Armero and Oller [1]. An efficient coupled elastoplastic damage model, that is capable of simulating the behaviour of plain concrete, was also developed by Lee and Fenves [5]. Recently, Sarikaya and Erkmen [11] showed that the Lee and Fenves [5] model can be captured

R. E. Erkmen (✉) · O. Arat · K. Galal
Department of Building, Civil and Environmental Engineering, Concordia University, Montreal, Canada
e-mail: emre.erkmen@concordia.ca

A. Sarikaya
School of Civil and Environmental Engineering, University of Technology Sydney, Sydney, NSW 2007, Australia

S. Walbridge et al. (eds.), *Proceedings of the Canadian Society of Civil Engineering Annual Conference 2021*, Lecture Notes in Civil Engineering 240,
https://doi.org/10.1007/978-981-19-0507-0_49

as a special case within the framework of Armero and Oller [1] by imposing a kinematic condition between the strain components. In both [5, 11] a single failure surface, potential function and hardening/softening criterion can be adopted in order to characterise the inelastic behaviour of concrete, providing an efficient computational framework.

On the other hand, analysis and design tools used for buildings often employ beam-type one-dimensional finite element formulations for shear walls as well as beams and columns as such models are computationally faster which is especially important in nonlinear time-history analysis and the results are easier to interpret for design purposes. Accordingly, uniaxial stress–strain relations or lumped springs providing nonlinear moment-rotation relations have been used for the analysis of buildings under lateral loads. Such one-dimensional generalized force–deflection or stress–strain relations depends on a-priori assumed conditions such as confinement pressures and failure modes. In this paper we propose to use a multi-axial material model that can capture the effect of shear as well as the axial stresses on the cross-section in the evolution of inelastic deformations. As the model is multi-axial the stresses in other surfaces and directions are either assumed zero or tied to the calculated cross-sectional stresses by a calibration factor so that confinement effects can be incorporated within the material model. The adopted a multi-axial concrete model is based on multi-surface plasticity which is applicable for both tension and compression behaviour. The inelastic material behaviour of steel reinforcements bars has also been considered in the analysis. In the following the details of the proposed concrete model is introduced and employed within a beam type 1D finite element. Cross-sectional properties and stress resultants consider the reinforcements locations and difference in their material properties under the kinematic assumption of plane cross-section remains plane. Such formulations are often called fibre elements in literature e.g., Spacone et al. [13], Erkmen and Attard [2]. However, adaptation of a multi-axial material model within a fibre element formulation so that shear effects can be considered in the material behaviour is the novelty introduced herein. The beam finite element formulation and the associated interpolation functions are based on the Timoshenko theory so that the shear deformation effects are also considered in the analysis. The numerical formulation is then used for pushover analysis of shear walls and compared with experimental results from literature for validation purposes.

2 Continuum Damage Plasticity

Following Armero and Oller [1], the coupled damage and plasticity constitutive equations can be built on 3 basic hypotheses: additive decomposition of the total strain field, the strain energy and finally the plasticity and damage initiation criteria.

- The additive decomposition implies that the total deformation can be decomposed into elastic part $\boldsymbol{\varepsilon}_e$, plastic part $\boldsymbol{\varepsilon}_p$ and damage part $\boldsymbol{\varepsilon}_d$ as $\boldsymbol{\varepsilon} = \boldsymbol{\varepsilon}_e + \boldsymbol{\varepsilon}_p + \boldsymbol{\varepsilon}_d$.

- The strain energy stored during deformation can be written as the sum of elastic and damage strain energies plus the energies due to hardening effects of plastic and damage parts:

$$\Psi\left(\varepsilon, \varepsilon_p, \kappa_p, \phi, \varepsilon_d, \kappa_d\right) = \Psi^e(\varepsilon_e) + \Psi^d(\varepsilon_d, \phi) + \Xi^p\left(\kappa_p\right) + \Xi^d(\kappa_d)$$

  where hardening effects can be accounted with the hardening potentials for the plastic behaviour $\Xi^p(\kappa_p)$ and damage behaviour $\Xi^d(\kappa_d)$, which are functions of hardening variables κ_p and κ_d for plasticity and damage, respectively. $\Psi^e(\boldsymbol{\varepsilon}_e)$ is the elastic strain energy and $\Psi^d(\boldsymbol{\varepsilon}_d, \phi)$ is the damage strain energy. The damage parameter ϕ can be written in terms of the reduction factor as $\phi = \varphi/(1-\varphi)$, where $\varphi \in [0, 1]$ is a measure of reduction in the load carrying area.
- The elastic domain can be specified as the domain in stress space where no change of internal variables, i.e. $\boldsymbol{\varepsilon}_p, \kappa_p, \phi, \boldsymbol{\varepsilon}_d, \kappa_d$, takes place. The boundaries of the domain is determined by the plastic failure criterion and the damage failure criterion with

$$f^p\left(\sigma, \kappa_p\right) \leq 0 \text{ and } f^d\left(\sigma, \kappa_p\right) \leq 0$$

The plastic and damage failure criteria are generally independent from each other. However, an a-priori assumed partitioning of the strain tensor in the form of $\mathrm{d}\boldsymbol{\varepsilon}_d = \varphi \mathrm{d}\boldsymbol{\varepsilon}$. simplifies the selection of the failure surfaces as it permits the use of single failure criterion, i.e., $f^p\left(\boldsymbol{\sigma}, \kappa_p\right) = f^d(\boldsymbol{\sigma}, \kappa_d)$ and $\mathrm{d}\kappa_d = \phi \mathrm{d}\kappa_p$ Therefore, the coupled elastoplastic-damage model can be easily calibrated to fit to the observed behaviour. The proposed approach also simplifies the numerical procedure, details of which can be found in Sarikaya and Erkmen [11].

2.1 Concrete Material Model

For materials that behave significantly different in tension and compression, it is a convenient approach to utilise a set of yield surfaces in order to characterise the stress–strain evolution for each regime. In this paper, we introduce a three-surface multi-surface plasticity framework in order to cover both compression and tension characteristics of concrete. Figure 1 below shows the three-surface plasticity model for combined tension and compression.

2.1.1 Zone I–Compression Zone Yield Surface

The plastic model that determines the envelope curve for stress–strain relationship consists of a potential surface, hardening law, which describes the deformation capacity in multiaxial compression, and a yield surface. For the compression zone

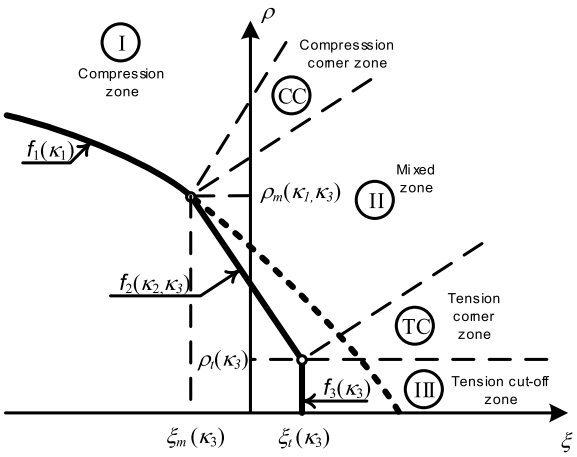

Fig. 1 Three-surface plasticity model for combined tension and compression

we employ the yield surface proposed by Menetrey and Willam [7] which is given as:

$$f_1(\xi, \rho, \theta, \kappa_1) = \left(\sqrt{1.5}\frac{\rho}{f_c}\right)^2 + q_h m_0\left(\frac{\rho}{f_c\sqrt{6}}r + \frac{\xi}{f_c\sqrt{3}}\right) - q_h q_s \leq 0 \quad (1)$$

where q_h and q_s controls the shape and location of the loading surface and m can be written as:

$$m = 3\frac{{f_c}^2 - {f_t}^2}{f_c f_t}\frac{e}{e+1} \quad (2)$$

in which f_c is the uniaxial compressive strength, f_t is the uniaxial tensile strength taken herein as $0.09 f_c$. Both the plastic potential and the yield surface are constituted by using the unified co-ordinates in the Haigh–Westergaard stress space, which are based on the stress invariants. The three co-ordinates ξ, ρ and θ can be expressed as:

$$\xi = \frac{I_1}{\sqrt{3} f c}, \quad (3)$$

$$\rho = \frac{\sqrt{2J_2}}{f c}, \quad (4)$$

$$\cos 3\theta = \frac{3\sqrt{3}}{2}\frac{J_3}{J_2^{3/2}} \quad (5)$$

where:

$$I_1 = \sigma_{11} + \sigma_{22} + \sigma_{33} \tag{6}$$

$$J_2 = \frac{1}{6}\left[(\sigma_{11} - \sigma_{22})^2 + (\sigma_{22} - \sigma_{33})^2 + (\sigma_{33} - \sigma_{11})^2\right] + {\tau_{12}}^2 + {\tau_{23}}^2 + {\tau_{31}}^2 \tag{7}$$

$$\begin{aligned} J_3 = &-\left(\frac{I_1}{3}\right)^3 + \left(\frac{I_1}{3}\right)^2 (\sigma_{11} + \sigma_{22} + \sigma_{33}) \\ &+ \left(\frac{I_1}{3}\right)(\tau_{12}\tau_{12} + \tau_{13}\tau_{13} + \tau_{23}\tau_{23} - \sigma_{11}\sigma_{22} - \sigma_{11}\sigma_{33} - \sigma_{22}\sigma_{33}) \\ &- \tau_{13}\tau_{13}\sigma_{22} - \tau_{23}\tau_{23}\sigma_{11} - \tau_{12}\tau_{12}\sigma_{33} + 2\tau_{12}\tau_{13}\tau_{23} + \sigma_{11}\sigma_{22}\sigma_{33} \end{aligned} \tag{8}$$

The eccentricity e defined in the Menetrey and Willam [7] model can be written as:

$$e = \frac{1 + \epsilon}{2 - \epsilon} \tag{9}$$

in which

$$\epsilon = \frac{f_t}{f_b}\frac{f_b^2 - f_c^2}{f_c^2 - f_t^2} \tag{10}$$

where f_b is the equibiaxial compressive strength taken herein as ${1.5 f_c}^{0.925}$. In Eq. 1, $r(\theta)$ is the polar radius as:

$$r(\theta) = \frac{v(\theta)}{s(\theta) + t(\theta)} \tag{11}$$

in which:

$$v(\theta) = 4\left(1 - e^2\right)\cos^2\theta + (2e - 1)^2 \tag{12}$$

$$s(\theta) = 2\left(1 - e^2\right)\cos\theta \tag{13}$$

$$t(\theta) = (2e - 1)\left[4\left(1 - e^2\right)\cos^2\theta + 5e^2 - 4e\right]^{1/2} \tag{14}$$

2.1.2 Zone I—Hardening/Softening Law

Hardening and softening of concrete can be simulated by varying the shape and location of the loading surface during plastic flow. The variation is controlled by

the hardening/softening parameter κ_p. During the hardening range q_h in Eq. 1 for concrete can be selected as Papanikolaou and Kappos [8].

$$q_h(\kappa_p) = k_o + (1 - k_o)\sqrt{1 - \left(\frac{\varepsilon_{vo}^p - \kappa_p}{\varepsilon_{vo}^p}\right)^2} \tag{15}$$

where:

$$k_o = \sigma_{co}/f_c \tag{16}$$

in which σ_{co} is the uniaxial concrete stress at the onset of plastic flow. In Eq. 15, ε_{vo}^p is the threshold value for the volumetric plastic strain at uniaxial concrete strength defined as:

$$\varepsilon_{vo}^p = \frac{f_c}{E_c}(1 - 2\upsilon) \tag{17}$$

where E_c and υ are the Young's modulus and Poisson ratio for concrete, respectively. During softening range q_s in Eq. 1 for concrete can be selected as Papanikolaou and Kappos [8]:

$$q_s(\kappa_p) = \left(\frac{1}{1 + \left(\frac{n_1 - 1}{n_2 - 1}\right)^2}\right)^2 \tag{18}$$

where $n_1 = \frac{\kappa_p}{\varepsilon_{vo}^p}$, $n_2 = \frac{\varepsilon_{vo}^p + t}{\varepsilon_{vo}^p}$ and $t = \frac{f_c}{15000}$. Note that f_c is considered in MPa.

2.1.3 Zone I—Potential Function

If we do not consider hardening/softening effects in the potential function, we get

$$g_1(\xi, \rho) = \frac{1}{f_c}(\xi - B\rho) = 0 \tag{19}$$

in which:

$$B = \rho_1 \frac{\psi_1 - \psi_2}{(\rho_1 - \rho_2)} - \psi_1 \tag{20}$$

In Eq. 20 ρ_1 is the normalized deviatoric stress indicators at uniaxial compressive strength as:

$$\rho_1 = \sqrt{\frac{2}{3}} \tag{21}$$

On the other hand, ψ_1 is the inclinations of the plastic strain vector under uniaxial strength given as:

$$\psi_1 = \sqrt{2}\frac{\left|\varepsilon_{3pu} - \varepsilon_{1pu}\right|}{\varepsilon_{vo}^{p}} \tag{22}$$

In the above equation ε_{3pu} is the axial plastic strain component at uniaxial compressive strength, which can be calculated as:

$$\varepsilon_{3pu} = \varepsilon_c - \frac{f_c}{E_c} \tag{23}$$

and ε_{1pu} is the lateral plastic strain component at uniaxial compressive strength, which is calculated as:

$$\varepsilon_{1pu} = \varepsilon_{2pu} = \frac{\varepsilon_{vo}^{p} - \varepsilon_{3pu}}{2} \tag{24}$$

In the equation above, ε_c is the total strain in the axial direction at uniaxial compressive strength and ε_{3pc} is the axial plastic strain component at triaxial compressive strength, which is defined as:

$$\varepsilon_{3pc} = \varepsilon_{cc} - \frac{1}{E_c}(f_{cc} - 2\upsilon\sigma_{pc}) \tag{25}$$

and ε_{1pc} is the lateral plastic strain component at triaxial compressive strength, that is obtained from:

$$\varepsilon_{1pc} = \varepsilon_{2pc} = \frac{\varepsilon_{vo}^{p} - \varepsilon_{3pc}}{2} \tag{26}$$

For concrete it can be assumed that $\varepsilon_{cc} = \varepsilon_c\left(1 + 17\frac{\sigma_{pc}}{f_c}\right)$, e.g., Papanikolaou and Kappos [8] and generally σ_{pc} is taken as $\sigma_{pc} = f_c$, and thus $\varepsilon_{cc} = 18\varepsilon_c$.

2.1.4 Zone III—Tension Cut-Off Zone Yield Surface

For the tension cut-off zone, a volumetric cut-off yield function is utilised.

$$f_3\left(\xi, \kappa^t\right) = \frac{\xi - T(\kappa_3)}{f_c} \leq 0 \tag{27}$$

where:

$$T(\kappa_3) = q_s^t T_0 \tag{28}$$

in which $q_s^t(\kappa_3)$ is the softening function for the tension cut-off zone and T_0 is the volumetric tensile cut-off limit. We control the cut-off limit in the form of

$$T_0 = h f_t \tag{29}$$

where h is a scalar obtained via calibration. The cut-off zone is constrained by a maximum deviatoric stress R^t, such that $\rho \leq R^t$.

2.1.5 Zone III—Softening Law

The softening law for the tension cut-off zone is

$$q_s^t = \exp\left(-\frac{\kappa_3}{n_3}\right) \tag{30}$$

in which n_3 is a scalar obtained via calibration. As f_3 move towards the origin due to the softening effect, intersection of f_2 and f_3 changes. This movement is constrained by the line given by $\rho = R^t$.

2.1.6 Zone III—Potential Function

Associated flow rule is utilised for the tension cut-off zone, i.e.

$$g_3 = f_3 \tag{31}$$

2.1.7 Zone II—Transition Zone Yield Surface

Transition zone yield surface is a linear function defined in the Rendulic plane of the stress. In the Rendulic plane, the yield line of the transition zone f_2 can be obtained using the end points, i.e. the corner stresses. While the end point of the tensile corner is constrained by imposing a deviatoric stress limit R^t, the compressive corner can be selected as an arbitrary point at which the two surfaces intersect. We impose the volumetric coordinate of that point as M so that the deviatoric component R^m can be determined from the condition $f_1 = 0$.Using the two definite end points, the linear yield function for the transition zone can be constructed as

$$f_2 = \frac{1}{f_c}\left(\rho - \frac{R^t(\xi - M) + R^m(T - \xi)}{T - M}\right) \leq 0 \tag{32}$$

The end points can change according to independent hardening/softening laws of compressive and tensile cut-off yield functions, i.e., $T = T(\kappa_3)$ and $R^m = R^m(\kappa_1)$.No hardening/softening effect shall be considered when the transition zone yield surface is active.

2.1.8 Zone II—Potential Function

Associated flow rule is utilised for the transition zone, i.e.

$$g_2 = f_2 \tag{33}$$

2.1.9 Damage Function

To update the damage parameter ϕ according to the evolution of plastic deformations we have adopted the relationship given in Grassl and Jirasek [3] defined as:

$$\varphi = \left(1 - e^{-C\frac{\kappa_p}{\varepsilon_{vo}^p}}\right) \tag{34}$$

in which C is a parameter that is calibrated based on stiffness degradation. We allow the possibility of two different values for compression and tension and a combination of the two at the other zones.

2.2 Steel Material Model

For the steel reinforcement the model is based on von Misses associated plasticity without strain hardening which is a simpler elastic-perfectly plastic model. The only two calibration parameters for uniaxial stress–strain relations are the elasticity modulus and the yield stress limit.

3 Numerical Element Modelling

3.1 Implementation of Multi-surface Plasticity

In order to obtain a unique solution in multi-surface plasticity, the linear complementarity problem (LCP) can be utilised. For instance, when two surfaces are active simultaneously, the LCP for the two-surface plasticity can be written following the procedure given in Jirasek and Bazant [4], i.e.

$$A\dot{\lambda} - b \geq 0 \tag{35}$$

$$\dot{\lambda} \geq 0 \tag{36}$$

$$\dot{\lambda}^T \left(A\dot{\lambda} - b\right) = 0 \tag{37}$$

in which

$$\mathbf{A} = \begin{bmatrix} \boldsymbol{f}_{1,\sigma} : \mathbf{E} : \boldsymbol{g}_{1,\sigma} + H_1 & \boldsymbol{f}_{1,\sigma} : \mathbf{E} : \boldsymbol{g}_{2,\sigma} \\ \boldsymbol{f}_{2,\sigma} : \mathbf{E} : \boldsymbol{g}_{1,\sigma} & \boldsymbol{f}_{2,\sigma} : \mathbf{E} : \boldsymbol{g}_{2,\sigma} + H_2 \end{bmatrix} \tag{38}$$

$$\mathbf{b} = \begin{Bmatrix} \boldsymbol{f}_{1,\sigma} : \mathbf{E} : \dot{\boldsymbol{\varepsilon}} \\ \boldsymbol{f}_{2,\sigma} : \mathbf{E} : \dot{\boldsymbol{\varepsilon}} \end{Bmatrix} \tag{39}$$

$$\dot{\boldsymbol{\lambda}} = \begin{Bmatrix} \dot{\lambda}_1 \\ \dot{\lambda}_2 \end{Bmatrix} \tag{40}$$

in which f_i and g_i stands for yield and potential functions, $\mathbf{E}$ is the elastic material tensor, H_i are the plastic moduli and $\dot{\lambda}_i$ are the plastic multiplier rates. Note that, for simplicity, $\mathbf{A}$, $\mathbf{b}$ and $\dot{\boldsymbol{\lambda}}$ are expressed considering when only two-surfaces are active, i.e., $(i = 1, 2)$. The LCP can be solved for $\dot{\boldsymbol{\lambda}}$ using $\mathbf{A}$ and $\mathbf{b}$. For $\dot{\boldsymbol{\lambda}}$ to be unique, the principal minors of the matrix $\mathbf{A}$ must be positive, i.e.

$$\boldsymbol{f}_{1,\sigma} : \mathbf{E} : \boldsymbol{g}_{1,\sigma} + H_1 > 0 \tag{41}$$

$$\boldsymbol{f}_{2,\sigma} : \mathbf{E} : \boldsymbol{g}_{2,\sigma} + H_2 > 0 \tag{42}$$

$$\det(\mathbf{A}) > 0 \tag{43}$$

Above equations are solved numerically at each integration point along the beam as well as within the cross-section according to the cutting-plane stress return algorithm.

3.2 *Beam-Type 1D Finite Element Formulation*

The above material model is implemented in a shear deformable beam-type finite element formulation. Using Timoshenko beam theory, it is possible to represent the state of deformation by three quantities u, v and θ representing the axial, translation deflections of the beam axis and in-plane rotation of the cross-section, respectively. Accordingly, a beam-type finite element formulation can be developed by interpolating these three generalized displacement functions. Standard linear interpolation of the axial displacement component u was used considering that the axial displacement is not coupled with the bending and shear deformations. The interpolation of the functions v and θ follows [10] in which the element was called interdependent interpolation element. The selected interdependent interpolation functions prevent the numerical locking behaviour. Based on selected interpolation functions, the virtual work can be written in algebraic form and the obtained equilibrium equations can be solved iteratively. We use a displacement control algorithm to follow the post peak behaviour, the details of which can be found in Jirasek and Bazant [4]. It should be noted that only the axial stress σ_{11} that is normal to the cross-section and the shear stress τ_{12} acting within the cross-section are assumed non-zero in Eqs. 6, 7 and 8.

4 Case Study

For the validation of the proposed method, three rectangular shear walls were modeled from the study of Qian and Chen [9]. All selected walls are fixed at bottom and free at the top. The specimens have a height of 1900 mm and length of 1000 mm. Reinforcement details of shear walls from top view are given below, all units are in millimetres in the figures (Figs. 2, 3 and 4).

Mechanical properties of concrete, parameters of shear wall specimens and properties of steel bars are given in the tables for each wall. In the case of reinforcements, same bars were used in all four specimens (Tables 1 and 2).

Mechanical properties of concrete, parameters of shear wall specimens and properties of steel bars are given in the following tables for each wall. In the case of reinforcements, same bars were used in all four specimens. The walls were subjected to a gradually increasing lateral load while under the effect of a constant axial load.

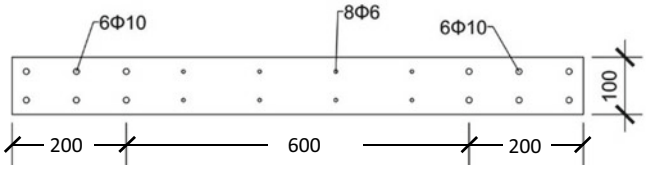

Fig. 2 Reinforcement details of SW-1

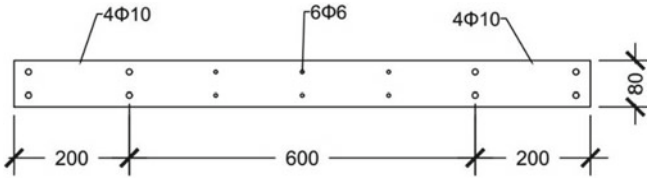

Fig. 3 Reinforcement details of CW-1

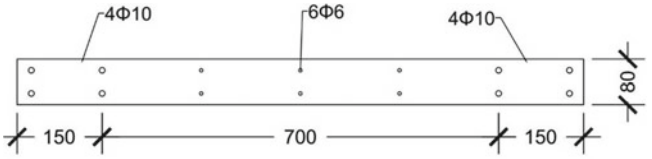

Fig. 4 Reinforcement details of CW-3

Table 1 Mechanical properties of concrete and parameters of shear wall specimens

Specimen	f_c (MPa)	f_c^t (MPa)	E_c (GPa)	N^t (kN)
SW-1	25.2	19.15	22.59	774
CW-1	24.4	18.55	22.23	384
CW-3	21.9	16.64	21.06	536

Table 2 Mechanical properties of steel bars

Grade of bar	d (mm)	f_y (MPa)	f_u (MPa)	E_s (GPa)
HBR 335	10	395	595	194
HBR 400	6	451.7	631.7	200

The axial load is calculated from the formula $N^t = (0.18–0.4)\ *A*f_c^t$, in which, A is the cross-sectional area of the shear wall and f_c^t is the axial compressive strength of the concrete which is given as $0.76*f_c$ in Qian and Chen [7]. They have also used modelling and compared with experimental results. In Figs 5, 6, and 7, Lateral Force-Lateral Deflection relations obtained by Qian and Chen [9] at the top of the cantilever shear wall are compared with those based on the modelling approach proposed herein. The results show very good agreement all the way up to failure especially when shear deformability of the beam element and shear stresses in the constitutive behaviour are considered. In modelling the shear walls, four elements were used over the height. Trapezoidal rule with 10 equally distributed integration points was used in each element.

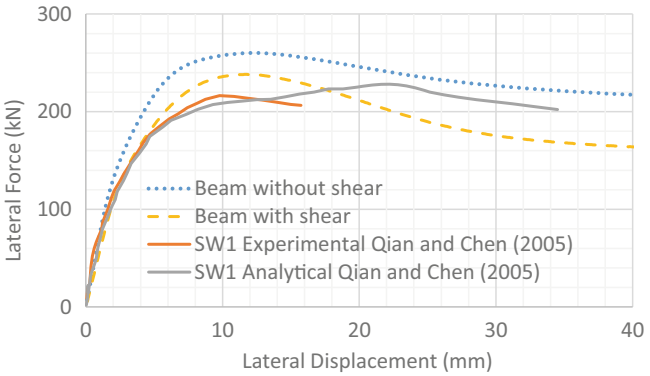

Fig. 5 Load—deflection curve for SW1

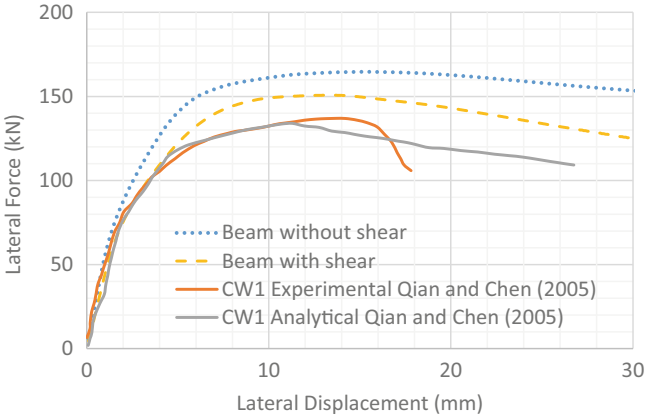

Fig. 6 Load—deflection curve for CW1

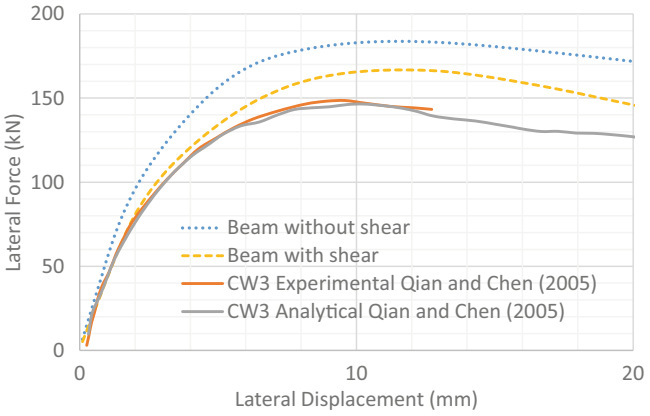

Fig. 7 Load—deflection curve for CW3

5 Conclusion

Details of a proposed multi-axial elasto-plastic damage-based model that can be used for the simulation of the concrete material under both tension and compression was described. The formulation for the material is implemented in the context of a 1D beam-type shear deformable finite element formulation. The modelling approach was used for simulating the behaviour of shear walls under lateral loading. The model predictions were compared with three experimental results from literature and good agreement was obtained up to failure. Similar to the fibre element formulations, cross-sectional properties and stress resultants depend on the reinforcements locations as well as the material properties of both concrete and steel. By removing and including the effect of shear deformations and the shear stress in the material model it was shown that considering shear effects results with a softer behaviour. It was also shown that the peak load carrying capacity is affected by the inclusion of shear stresses in the material model which is generally ignored in fibre element formulations that employ uniaxial constitutive relations. It is of interest to note that when the shear wall height to width ratio reduces plane section assumption of the Timoshenko beam might become less accurate. It would be interesting to implement the constitutive model for higher order shear deformable beam theories for comparison purposes and identify the effect of aspect ratio on the kinematic behaviour. It should also be noted that the failure mechanisms for shear walls may involve many other modes of behaviour such as base shear sliding, debonding of the reinforcement etc. which have not been considered in the proposed beam analysis.

References

1. Armero F, Oller S (2000) A general framework for continuum damage models. I. Infinitesimal plastic damage models in stress space. Int J Solids Struct 37(48–50):7409–7436
2. Erkmen RE, Attard M (2011) Displacement based finite element formulations for material nonlinear analysis of composite beams and treatment of locking behaviour. Finite Elem Anal Des 47:1293–1305
3. Grassl P, Jirasek M (2006) Damage plastic model for concrete failure. Int J Solids Struct 43:7166–7196
4. Jirásek M, Bazant Z (2002) Inelastic analysis of structures. Wiley, Chichester, West Sussex, England
5. Lee J, Fenves GL (1998) Plastic-damage model for cyclic loading of concrete. Journal of Engineering Mechanics, ASCE 124:892–900
6. Lemaitre J (1985) A continuous damage mechanics model for ductile fracture, pp 83–89
7. Menetrey P, Willam KJ (1995) Triaxial failure criterion for concrete and its generalization. Struct J 92(3):311–318
8. Papanikolaou VK, Kappos AJ (2007) Confinement-sensitive plasticity constitutive model for concrete in triaxial compression. Int J Solids Struct 44:7021–7048
9. Qian J, Chen Q (2005) A macro-model of shear walls for pushover analysis. Struct Build 158:119–132
10. Reddy JN (1997) On Locking-free shear deformable beam elements. Comput Methods Appl Mech Eng 149:113–132

11. Sarikaya A, Erkmen RE (2019) A plastic-damage model for concrete under compression. Int J Mech Sci 150:584–593
12. Simo JC, Ju JW (1987) Strain-and stress-based continuum damage models—I. Formulation. Int J Solids Struct 23(7):821–840
13. Spacone E, Filippo CF, Taucer FF (1996) A fibre beam-column model for nonlinear analysis of R/C frames: Part I formulation. Earthquake Eng Struct Dynam 25:711–725

Determination of Chloride Ion Penetration Depth of Blended Mortar Using Electrochemical Impedance Spectroscopy

S. Hassi, B. Menu, and M. Ebn Touhami

1 Introduction

Prestressed concrete cylinder pipe (PCCP) has been extensively used to convey water and wastewater to many cities around the world [1, 9, 11]. There are two types of PCCP: the lined cylinder pipe (LCP) and the embedded cylinder pipe (ECP) [1, 9]. Each consists of four main components: a core concrete, a steel cylinder, a prestressing wire, and a mortar coating as shown in Fig. 1. PCCPs have the lowest water main break rate per 100 km compared with any other pipe materials [16]. One of the significant imperfections of PCCPs which often leads to catastrophic failure is corrosion of the reinforcing spiral rebars [10]. In practice, most PCCPs are exposed to highly aggressive penetrating chemical agents such as chloride ions that attack the mortar coating and cause corrosion of the prestressing wires.

Since the mortar coating sprayed around the pipe protects the prestressing wires against corrosion, the ability to improve or accurately determine the resistance of a mortar coating to a potentially aggressive chemical environment in the right-of-way of PCCP pipelines is particularly important for water utilities. Many studies indicate that mineral additives such as silica fume and fly ash can be used to prevent the deterioration of reinforced concrete structures exposed to extreme aggressive chemical because they produce structures with finer pore structures and lower chloride diffusion coefficients than plain cement mixtures [2, 5, 7, 18]. Experiments have also shown that the incorporation of these mineral additives into mortar and concrete can improve their resistance to chloride ion penetration as well as enhance their strength and durability [3, 18].

S. Hassi (✉) · M. E. Touhami
Laboratoire Des Matériaux Avancés Et Génie Des Procédés, Ibn Tofail University, Kenitra, Morocco

B. Menu
Construction Daniel Dargis Inc, 5600 Hochelaga Est, # 140, Montreal, Qc 1N 3L7, Canada

S. Walbridge et al. (eds.), *Proceedings of the Canadian Society of Civil Engineering Annual Conference 2021*, Lecture Notes in Civil Engineering 240,
https://doi.org/10.1007/978-981-19-0507-0_50

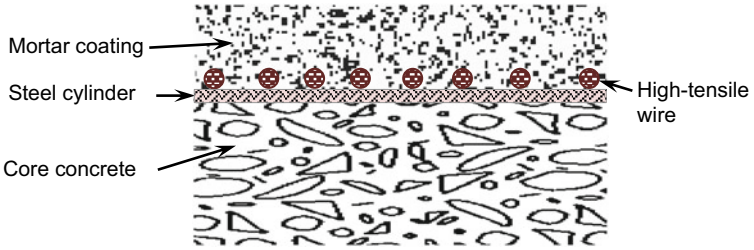

Fig. 1 The cross-section of the multilayer structure of PCCP-LCP

The most commonly used technique to assess chloride ion migration in cement-based materials is the silver nitrate ($AgNO_3$) colorimetric method [14]. One main disadvantage of this method is that the reliability, validity, and accuracy of the measurement rely on the skill and experience of the person who performs the test and the test duration [7]. For this reason, the electrochemical impedance spectroscopy (EIS) technique is increasingly been used to measure chloride ion migration in cement-based materials [4, 5, 7, 8, 15].

This work aims to use the *EIS technique* to study the corrosion behavior of reinforced PCCP mortar coatings blended with silica fume or fly ash and illustrate the fact that the EIS technique can be applied to predict the chloride ion migration depth of mortar blended with silica fume and fly ash under chloride penetration conditions. The reinforced mortar specimens were immersed in a 9.5 wt.% NaCl solution for up to 210 days. The overall study is expected to contribute towards the development of better chloride resisting PCCP mortar coatings that can improve the service life of PCCPs.

2 Experimental Program

2.1 Materials and Mixture Proportions

Three mortar coating mixtures were investigated in this study. The mortars were made with two types of cement: *portland composite cement* (PCC) and *sulfate resisting portland cement* (SRPC). *Silica fume* and *fly ash* were used to partially replace 10% of the cements. The chemical composition of the two types of cement (PCC and SRPC), the silica fume (SF), and fly ash (FA) are presented in Table 1. The mixture proportions are also shown in Table 2. The control mortar and the mortar containing fly ash were made with PCC cement while the mortar containing silica fume was made with SRPC cement. It is worth noting that SRPC cement was used for the silica fume blended mortar because it is recommended by the European standard EN 206–1 for manufacturing PCCP mortar coating that may be subjected to highly aggressive environments. The fine aggregate used in the present study was dune while the coarse

Table 1 Chemical composition of cements and mineral additives (%)

Chemical analysis %	PCC cement	SRPC cement	Silica fume (SF)	Fly ash (FA)
Calcium oxide (CaO)	54.6	46.8	0.3	4.4
Silica (SiO_2)	20.7	28.8	89.0	39.6
Alumina (Al_2O_3)	4.4	10.6	0.3	33.4
Iron oxide (Fe_2O_3)	2.6	3.4	0.9	3.4
Magnesium oxide (MgO)	2.9	2.2	1.5	2.1
Sodium oxide (Na_2O)	0.1	0.4	0.3	0.4
Potassium oxide (K_2O)	0.7	1.0	1.7	0.8
Sulfur trioxide (SO_3)	2.3	2.5	0.3	0.4

Table 2 Proportioning of mortar coating mixtures

Materials	Control	10% FA	10% SF
Cement, kg/m^3	450*	450*	442**
Water, l/m^3	172	172	162
w/cm†	0.38	0.34	0.33
Sand dune, kg/m^3	536	536	672
Aggregate, kg/m^3	1284	1284	1307.8
Fly Ash (FA), %	–	10%	–
Silica Fume (SF), %	–	–	10%

* PCC; ** SRPC; w/cm: † water-to-cementitious materials ratio

aggregate was crushed gravel with a maximum aggregate size of 8 mm. The coarse aggregate used had a bulk density of 2720 kg/m^3, an absolute density of 2740 ^{kg}/m^3, and absorption of 5.29%. The sand used also had a relative density of 2698 ^{kg}/m^3, an absorption of 2.01%, and a fineness modulus of 2.8.

The mixing was carried out in a 160-l mixer. The water was added in two steps to assure dispersion of the silica fume and fly ash. The mixtures were then cast into the 65 × 150 mm cylindrical mold for the EIS tests. After casting and consolidation, the specimens were covered and left in their mold in the lab for 24 h and demoulded. Then they were labeled and placed in a moist room (at 95 ± 5% relative humidity and 20 ± 2 °C) until the test. Three specimens were cast for each mortar investigated.

2.2 EIS Test Procedure

The EIS measurements were performed using a three-electrode setup comprising of an Ag/AgCl as a reference electrode, platinum as a counter electrode, and rebar as the working electrode. In this test, a reinforced steel bar electrodes of 5 mm diameter were cast into the 65 × 150 mm cylinder specimens as shown in Fig. 2a.

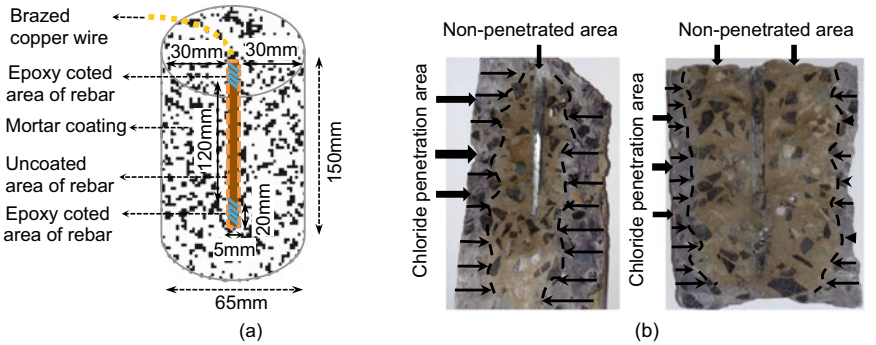

Fig. 2 Specimens used for the EIS test (**a**), and measurement of the chloride ion penetration depth (**b**)

Thus, the mortar coating thickness around the reinforced steel bar is about 30 mm. The rebar was soldered to a brazed copper wire to be connected to a potentiostat as a working electrode and covered with epoxy paint for protection against the aggressive solutions. After 28 days of moist curing, the specimens were fully immersed in a 9.5 wt.% NaCl solution to simulate the potential aggressive environment in the right of way of PCCP pipelines. The impedance spectra of the samples were measured at different exposure times of 1, 3, 8, 30, 90, and 210 days using EIS machine. The test was carried out in the room at 20 ± 2 °C.

For each specimen prepared for the EIS test, a corresponding specimen was prepared and fully immersed in a 9.5 wt.% NaCl solution to measure the chloride ion penetration depth using the $AgNO_3$ colorimetric method. The measurement period of the specimens corresponded to the EIS measurements. The mortar samples were axially split in order to clean up powder remnants in the section and sprayed with 0.1 mol/L $AgNO_3$ solution to determine the chloride ion penetration depth. The chloride penetration depth measurements were made every 2 cm after 30 s and the measurements were taken on both sides of each section (see Fig. 2b) using a calibrated ruler.

2.3 Equivalent Circuit (EC) Modeling

To analyze the electrochemical impedance spectrum data of the mortar coatings investigated in the present study, the Dong's EC model, $R_s(Q_1(R_{ct1}W_1))(Q_2(R_{ct2}W_2))$ [6, 8] was used to fit the measured results to acquire transport properties such as the resistance to charge transfer of the electrochemical system during the chloride ion migration process. A schematic representation of the equivalent circuit is depicted in Fig. 3. In this model, R_s is the electrolyte solution resistance; Q_1 is the double-layer capacitance between the solid/liquid phases; R_{ct1} is the ion transfer resistance in cement; W_1 is the Warburg resistance induced by the diffusion of ions in cement;

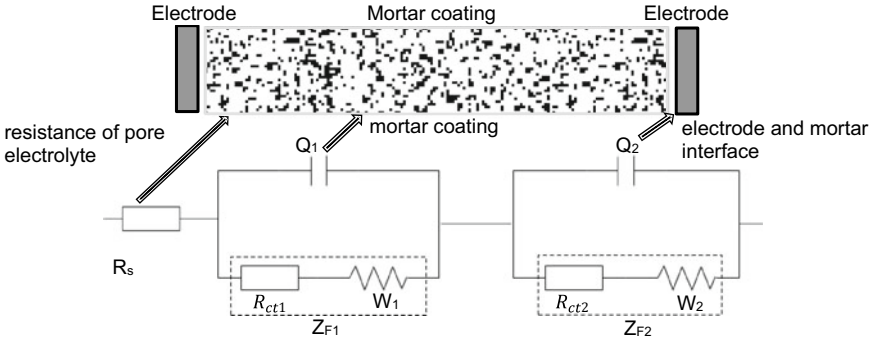

Fig. 3 The novel Equivalent Circuit Dong model $R_s(Q_1(R_{ct1}W_1))(Q_2(R_{ct2}W_2))$

R_{ct2} is the charge transfer resistance on the surface of electrodes; Q_2 is the double-layer capacitance between cement and electrodes; W_2 is the Warburg resistance induced by the diffusion of ions on the surface of the electrodes; $R_{ct1} + W_1 = Z_{F1}$ refers to the impedance caused by the Faraday's procedure inside the mortar; and $R_{ct2} + W_2 = Z_{F2}$, stands for the impedance caused by the Faraday's procedure between the mortar and electrodes.

For the above EC model, the total impedance of the circuit can be expressed as follows:

$$Z = R_s + \frac{Z_{F1}}{1 + j\omega Z_{F1} Q_1} + \frac{Z_{F2}}{1 + j\omega Z_{F2} Q_2} \tag{1}$$

where σ_1 is the conductivity of the cement-based material; σ_2 is the conductivity of the electrode plate; $Z_{F1} = R_{ct1} + \sigma_1 \omega^{-\frac{1}{2}}(1 - j)$ is the impedance of the Faraday process in the specimen; $Z_{F2} = R_{ct2} + \sigma_2 \omega^{-\frac{1}{2}}(1 - j)$ is the impedance of the Faraday process between the specimen and the electrode plate; $\omega = 2\pi f$; and $j = \sqrt{-1}$. The equation can then be rewritten as:

$$\begin{aligned} Z = R_s &+ \frac{R_{ct1} + \sigma_1 \omega^{-\frac{1}{2}}(1 - j)}{1 + j\omega R_{ct1} Q_1 + j\omega Q_1(\sigma_1 \omega^{-\frac{1}{2}} - j\sigma_1 \omega^{-\frac{1}{2}})} \\ &+ \frac{R_{ct2} + \sigma_2 \omega^{-\frac{1}{2}}(1 - j)}{1 + j\omega R_{ct2} Q_2 + j\omega Q_2\left(\sigma_2 \omega^{-\frac{1}{2}} - j\sigma_2 \omega^{-\frac{1}{2}}\right)} \end{aligned} \tag{2}$$

If $\omega \to \infty$ (i.e., very high frequency), then $\omega \gg (\frac{\sigma}{R_{ct}})^2, Q_1 = \frac{1}{W_c R_{ct1}}$, and $Q_2 = \frac{1}{W_c R_{ct2}}$. Thus, Eq. (2) becomes:

$$\left[Z' - R_s - \frac{1}{2}(R_{ct1} + R_{ct2})\right]^2 + Z''^2 = \left(\frac{R_{ct1} + R_{ct2}}{2}\right)^2 \tag{3}$$

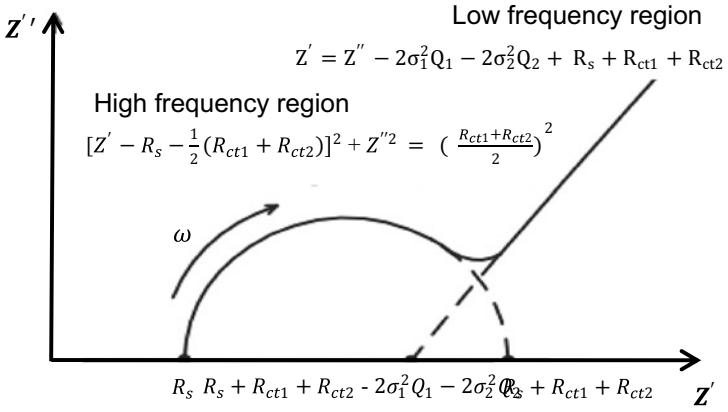

Fig. 4 Theoretical Nyquist diagram corresponding to the $R_s(Q_1(R_{ct1}W_1))(Q_2(R_{ct2}W_2))$ EC model

Equation (3) is the equation of the semi-circle of the Nyquist curve in the first quadrant. If $\omega \to 0$(very low frequency), then we can get:

$$Z' = Z'' - 2\sigma_1^2 Q_1 - 2\sigma_2^2 Q_2 + R_s + R_{ct1} + R_{ct2} \tag{4}$$

Equation (4) is the linear equation of the Nyquist plot. Combining Eqs. (3) and (4), a Nyquist plot can be obtained as shown in Fig. 4. The Nyquist curve in Fig. 4 is an impedance curve plotted on different frequencies in a complex plane: Z' as its real axis (horizontal axis) and Z'' as its imaginary axis (vertical axis).

It is necessary to mention that the fitting results obtained in the present study using the Dong's model $R_s(Q_1(R_{ct1}W_1))(Q_2(R_{ct2}W_2))$ were compared to the Shi's Randles model $(R_s(Q(R_{ct}W))R_s(Q(R_{ct}W))$ and the Gu's model $R_s(Q_1R_{ct1})(Q_2R_{ct2})$. The reader may refer to [6–8] for a full description of the Shi's model $(R_s(Q(R_{ct}W))R_s(Q(R_{ct}W))$ and the Gu's model $R_s(Q_1R_{ct1})(Q_2R_{ct2})$ because this level of detail is not the scope of the present paper.

3 Results and Discussion

3.1 Fitting Comparison Between the Models

As mentioned above, the impedance spectra data were fitted to the Shi's model $(R_s(Q(R_{ct}W))R_s(Q(R_{ct}W))$, the Gu's model $R_s(Q_1R_{ct1})(Q_2R_{ct2})$, and the Dong's model $R_s(Q_1(R_{ct1}W_1))(Q_2(R_{ct2}W_2))$ and the results were compared. Selected data for the impedance spectra fittings, at 30 days chloride penetration time, are presented

in Figs. 5, 6, and 7, respectively for the control mortar, the fly ash mortar, and the silica fume mortar. It can be observed in Fig. 5 that there is a good agreement between the three EC models and the experimental results of the control mortar. However, it is clear in Figs. 6 and 7 that the Shi's model $(R_s(Q(R_{ct}W))R_s(Q(R_{ct}W))$ and the Gu's model $R_s(Q_1R_{ct1})(Q_2R_{ct2})$ show a poor fit with the experiment results for the fly ash and the silica fume blended mortars when compared to the Dong's model $R_s(Q_1(R_{ct1}W_1))(Q_2(R_{ct2}W_2)))$ which showed a better fit. The lack of agreement between the models $(R_s(Q(R_{ct}W))R_s(Q(R_{ct}W))$ and $R_s(Q_1R_{ct1})(Q_2R_{ct2})$ and the experimental data is explained by the fact that these models do not accurately account for charge transfer and diffusion impedance of the ion diffusion in the mortar during the corrosion process [5, 7]. The reader can refer to several interesting publications to find more information [5, 6, 8].

Globally the results show that the Dong's model $R_s(Q_1(R_{ct1}W_1))(Q_2(R_{ct2}W_2))$ is more suitable for analyzing the corrosion process of blended mortars. The overall results are in agreement and supported by other studies [5, 7]. In this study, the

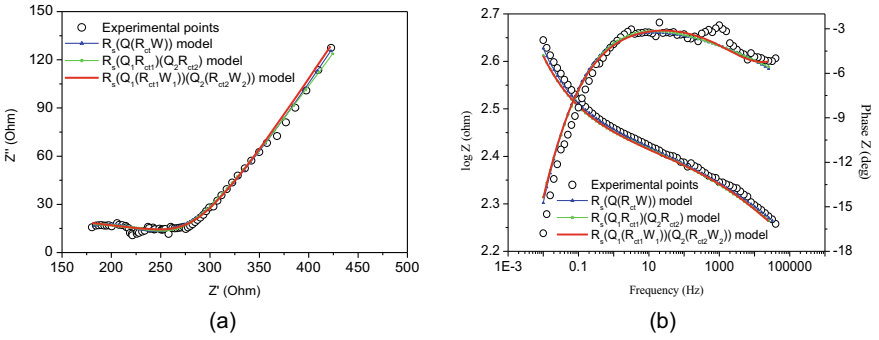

Fig. 5 Comparison of the impedance spectra fittings obtained for the control mortar at 30 days chloride penetration time: **a** Nyquist curves, and **b** Bode and phase curves

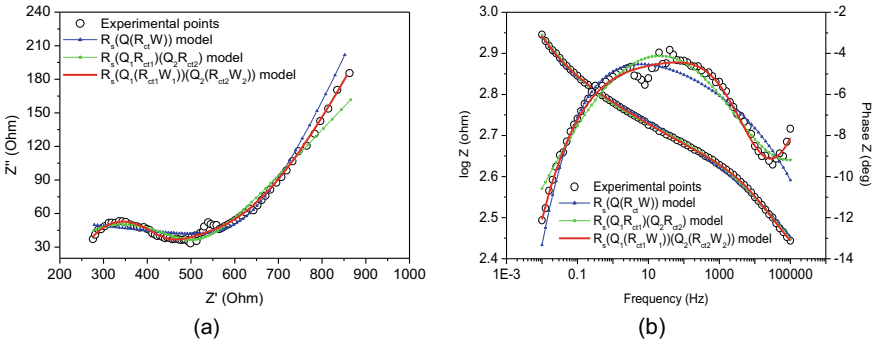

Fig. 6 Comparison of the impedance spectra fittings obtained for the fly ash blended mortar at 30 days chloride penetration time: **a** Nyquist curves, and **b** Bode and phase curves

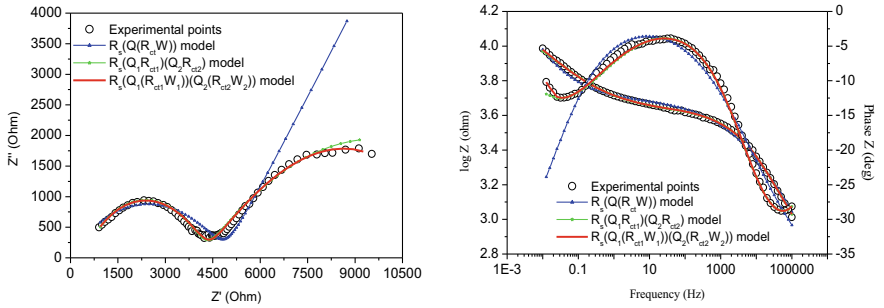

Fig. 7 Comparison of the impedance spectra fittings obtained for the silica fume blended mortar at 30 days chloride penetration time: **a** Nyquist curves, and **b** Bode and phase curves

model parameter R_{ct1} (i.e., resistance to ion transfer process) obtained from the data fitting with the Dong's model $R_s(Q_1(R_{ct1}W_1))(Q_2(R_{ct2}W_2))$ is used to analyze and predict the variation of the chloride depth penetration of the blended mortar coatings at different chloride penetration times.

3.2 *Prediction of Chloride Penetration Depth from EIS Measurements*

The resistance to ion transfer (R_{ct1}) values obtained from the data fittings with the Dong's model $R_s(Q_1(R_{ct1}W_1))(Q_2(R_{ct2}W_2))$ at different chloride penetration times are summarized in Table 3. The overall results indicate that the fly ash and silica fume blended mortars exhibited superior resistance to chloride ion transfer than the control mortar. The silica fume blended mortar showed the highest resistance to chloride ion transfer. The increased in the resistance to ion transfer inside the mortar when silica

Table 3 $R_{ct1}R_{ct1}$ values obtained from the curve fitting with model the Dong model $R_s(Q_1(R_{ct1}W_1))(Q_2(R_{ct2}W_2))$

Penetration time (days)	R_{ct1}(ohm)		
	Control	10% FA	10% SF
0	135.0	144.2	1192.0
1	112.3	118.4	1165.3
3	106.5	156.0	1641.0
8	93.5	204.5	2097.0
30	98.3	312.8	4187.0
90	151.9	336.4	4673.4
210	294.1	496.4	5479.0

fume and fly ash are added is due to the improvement in chloride binding capacity, which reduces the risk of corrosion [4, 20, 21]. Chloride ions are generally bound in Friedel's salt which reduces the porous structure of the concrete, thereby slowing the transport of chloride ions [4, 22]. The addition of silica fume and fly ash also reduce the amount of calcium hydroxide ($Ca(OH)_2$) crystals in the mortar, resulting in a dense and uniform texture of C-S–H gel [17, 19] and, consequently, higher resistance to conductive ion migration through the mortar. The overall corrosive aggressiveness of the 9.5% NaCl medium for the control mortar is somewhat confirmed by the high rate of chloride-induced corrosion of the prestressing wires encountered with the PCCPs coated using the control mortar in the Tafilalet and Greater Agadir regions of Morocco [11, 12].

The data further indicate that the R_{ct1} values of the silica fume and fly ash blended mortars exhibits a somewhat linear growth relationship with the chloride ion penetration time. Thus, $\Delta R_{ct1} = R_{ct1}(0) - R_{ct1}(t) \sim t$, where $R_{ct1}(0)$ is the R_{ct1} value at the beginning of chloride ion penetration ($t = 0$ days), and R_{ct1}(t) is the R_{ct1} value after t days of chloride ion penetration).

As mentioned earlier, the chloride ion penetration depths (d) of the mixtures were also measured during the chloride exposure cycles in an attempt to explore the link between the resistance to ion transfer, R_{ct1} and chloride ion penetration, d. The average values obtained are presented in Table 4. As expected, higher values are achieved at longer ages. It is also clear that the addition of silica fume and fly ash in mortar significantly reduced the chloride ion penetration depths due to the pozzolanic effect of these mineral additives [15, 20]. Further analysis of the results revealed that the chloride ion penetration depths are proportional to the square root of penetration time. Thus, $d \sim \sqrt{t}$ as shown in Fig. 8.

Given that both the chloride ion penetration depth (d) and the resistance to ion transfer (R_{ct1}) are linearly related to chloride penetration time (t) (i.e., $d \sim \sqrt{t}$ and $\Delta R_{ct1} \sim t$); the chloride ion penetration depth can be expressed in terms of R_{ct1} as follows [5, 7]:

$$d \sim \sqrt{\Delta R_{ct1}} \tag{5}$$

Table 4 Measured chloride penetration depths at different chloride penetration time

Penetration time (days)	Control (mm)	10% FA (mm)	10% SF (mm)
0	0.0	0.0	0.0
1	2.5	1.9	0.8
3	8.4	4.5	1.2
8	16.5	8.5	2.5
30	27.0	12.3	3.2
90	30.0	14.1	3.7
210	30.0	18.2	4.4

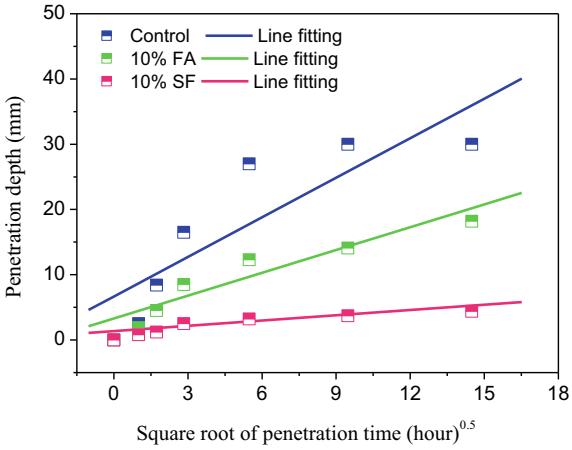

Fig. 8 Chloride penetration depth versus square root of migration time

Equation 5 was used to predict the depth of the chloride ion migration under the chloride attack of the three mortars and the results are compared in Fig. 9. The chloride ion penetration depths predicted at 210-day migration time along with the percentage errors are also shown in Table 5.

As can be observed in Fig. 9, there is a good agreement between the measured and predicted depth of chloride ion migration for the silica fume and fly ash blended mortars. The deviation between the predicted and measured values after 210 days of exposure to 9.5% NaCl solution is about 4.99% and 0.65%, respectively. By contrast, the deviation at the same migration time is about 24.39% for the control mortar (see Table 5). It can therefore be argued that the EIS fitting parameter R_{ct1} can be used to predict the chloride ion migration depth of mortar blended with silica fume or fly ash under chloride penetration in an acceptable manner. It is believed that this method can be used in practice to predict the early age and long-term potential for resistance to chloride penetration of blended PCCP mortar coatings in chloride-beading environments. It should be mentioned that a similar approach has been previously adopted by other researchers [5, 7] to predict the chloride ion penetration depth of fly ash and slag blended mortars.

4 Conclusions

In this study, the electrochemical impedance spectroscopy (EIS) method was used to investigate the effect of silica fume and fly ash incorporation on chloride ion penetration of PCCP mortar coating during chloride ion attacks. Based on the results and discussion presented, the following conclusions could be drawn:

- EIS measurement can be used to characterize the resistance to chloride ion penetration of PCCP mortar coatings incorporating silica fume and fly ash.

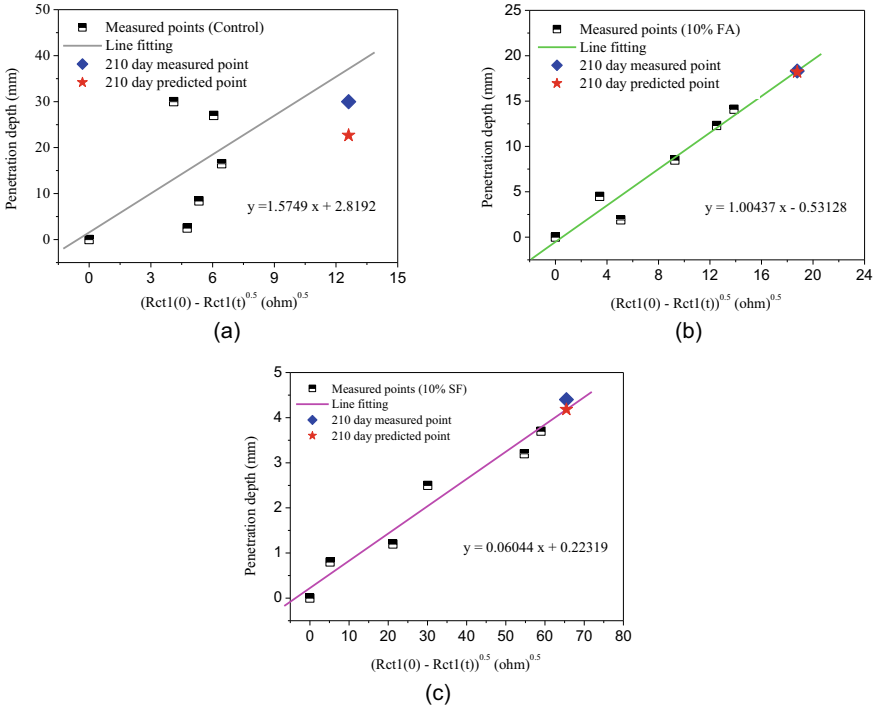

Fig. 9 Comparison of the predicted and measured chloride ion penetration depth at different chloride penetration times: **a** Control, **b** 10% FA, and **c** 10% SF

Table 5 Prediction results of chloride penetration depth of the three mortars

210 days	Control	10% FA	10% SF
Penetration depth (mm)	30.00	18.20	4.40
Prediction depth (mm)	22.684	18.318	4.181
Error (%)	24.386	0.647	4.988

- The EIS fitting parameter R_{ct1} can be used to predict the chloride ion migration depth of mortar blended with either silica fume or fly ash in an acceptable manner under chloride conditions.
- The chloride penetration depth of the silica fume and fly ash blended mortars are considerably smaller than the control mortar. Thus, the incorporation of silica fume and fly ash in a PCCP mortar coating can effectively increase the durability of PCCPs against aggressive penetrating chloride agents in the right-of-way of the pipelines.
- The incorporation of silica fume produced the highest reduction in chloride penetration resistance under the chloride attack.

Acknowledgements The authors would like to thank the National Office of Electricity and Drinking Water (O.N.E.E) committee of Morocco for their financial support. The authors also greatly appreciate the support received through the collaborative work undertaken with field managers and other representatives.

References

1. Al Wardany R (2008) Condition assessment of prestressed concrete cylindrical water pipes. In: 60th Annual WCWWA conference and trade show. Western Canada Water and Wastewater Association (WCWWA), Regina, S.K., Canada
2. Baltazar-Zamora MA, Bastidas MD, Santiago-Hurtado G, Mendoza-Rangel JM, Gaona-Tiburcio C, Bastidas JM, Almeraya-Calderón F (2019) Effect of silica fume and fly ash admixtures on the corrosion behavior of AISI 304 embedded in concrete exposed in 3.5% NaCl solution. Materials 12(23):4007
3. Bentur A (2007) Impact of additions: indicators for durability and strength performance. In: International RILEM workshop on performance based evaluation and indicators for concrete durability. RILEM Publications, Cachan, France, PRO-47, pp 297–310
4. Díaz B, Nóvoa X, Pérez M (2006) Study of the chloride diffusion in mortar: a new method of determining diffusion coefficients based on impedance measurements. Cement Concr Compos 28(3):237–245
5. Dong B, Gu Z, Qiu Q, Liu Y, Ding W, Xing F, Hong S (2018) Electrochemical feature for chloride ion transportation in fly ash blended cementitious materials. Constr Build Mater 161:577–586
6. Dong B, Li G, Zhang J, Liu Y, Xing F, Hong S (2017) Non-destructive tracing on hydration feature of slag blended cement with electrochemical method. Constr Build Mater 149:467–473
7. Dong B, Wu Y, Teng X, Zhuang Z, Gu Z, Zhang J, Xing F, Hong S (2019) Investigation of the Cl−migration behavior of cement materials blended with fly ash or/and slag via the electrochemical impedance spectroscopy method. Constr Build Mater 211:261–270
8. Dong B-Q, Qiu Q-W, Xiang J-Q, Huang C-J, Xing F, Han N-X, Lu Y-Y (2014) Electrochemical impedance measurement and modeling analysis of the carbonation behavior for cementititous materials. Constr Build Mater 54:558–565
9. Ge S, Sinha S (2014) Failure analysis, condition assessment technologies, and performance prediction of prestressed-concrete cylinder pipe: state-of-the-art literature review. J Perform Constr Facil 28(3):618–628
10. Goldaran R, Turer A, Kouhdaragh M, Ozlutas K (2020) Identification of corrosion in a prestressed concrete pipe utilizing acoustic emission technique. Construct Build Mater 242:118053
11. Hall SC (1998) Cathodic protection criteria for prestressed concrete pipe—an update. In: Corrosion 98, NACE International. San Diego, California, United States
12. Hassi S, Ejbouh A, Touhami ME, Berrami K, Ech-chebab A, Boujad A (2021a) Performance of prestressed concrete cylinder pipe in North Africa: case study of the water transmission systems in the tafilalet region of Morocco. J Pipeline Syst Eng Practice 12(2)
13. Hassi S, Touhami ME, Ejbouh A, Berrami K, Boujad A, Ech-chebab A (2021) Case study of the performance of prestressed concrete cylinder pipes in the greater Agadir of Morocco. J Pipeline Syst Eng Practice 12(2):05021001
14. Meck E, Sirivivatnanon V (2003) Field indicator of chloride penetration depth. Cem Concr Res 33(8):1113–1117
15. Neithalath N, Jain J (2010) Relating rapid chloride transport parameters of concretes to microstructural features extracted from electrical impedance. Cem Concr Res 40(7):1041–1051

16. Prosser DP (1996) Research, product improvement, new awwa standards, compliance certification and performance—contribute to the increased usage of prestressed concrete cylinder pipe. In: 1996 American water works association annual convention and exhibition. Toronto, Ontario, Canada
17. Sadrmomtazi A, Tahmouresi B, Kohani Khoshkbijari R (2018) Effect of fly ash and silica fume on transition zone, pore structure and permeability of concrete. Mag Concr Res 70(10):519–532
18. Smith BG (2001) Durability of silica fume concrete exposed to chloride in hot climates. J Mater Civ Eng 13(1):41–48
19. Torii K, Kawamura M (1994) Pore structure and chloride ion permeability of mortars containing silica fume. Cement Concr Compos 16(4):279–286
20. Uysal M, Yilmaz K, Ipek M (2012) The effect of mineral admixtures on mechanical properties, chloride ion permeability and impermeability of self-compacting concrete. Constr Build Mater 27(1):263–270
21. Yazıcı H (2008) The effect of silica fume and high-volume class C fly ash on mechanical properties, chloride penetration and freeze-thaw resistance of self-compacting concrete. Constr Build Mater 22(4):456–462
22. Yuan Q, Shi C, De Schutter G, Audenaert K, Deng D (2009) Chloride binding of cement-based materials subjected to external chloride environment—a review. Constr Build Mater 23(1):1–13

Numerical Investigation of the Structural Performance of Post-Tensioned Friction-Based Slab Column Connections in Two-Way Modular Precast Concrete Systems

M. Zhou, T. Hrynyk, S. Walbridge, D. Dikic, G. Rutledge, and M. Arsenault

1 Introduction

PACE building technology is an accelerated structural construction system involving prefabricated modular reinforced concrete (RC) infrastructure elements (e.g., slab panels and column elements) of regular size, shape, and geometry, which are adjoined during erection using post-tensioned (PT) tendons that double as dual-banded reinforcement along slab system column lines. Originally developed in the 1950s [1], these types of post-tensioned building systems have been used in buildings constructed throughout many regions of the world with the aim of reducing building construction costs and construction periods, optimizing the use of steel and concrete materials, and increasing the durability of precast building systems under extreme loading scenarios [2]. In comparison to conventional cast in place two-way RC slab systems (e.g., flat plate buildings), the tailored geometries of the PACE precast slab modules require less concrete per unit of floor area and are more conducive to permitting slab openings for through-floor mechanical access. Field experiences involving similar modular systems have demonstrated good performances under both service and extreme loading scenarios (e.g., earthquakes), making them a feasible and cost-effective alternative to more conventional two-way cast-in-place and one-way precast building systems employed in Canada. However, the detailing of these modular connections is atypical to North American precast construction in that they rely on friction as a primary mechanism for transferring gravity loads at precast connections.

M. Zhou (✉) · T. Hrynyk · S. Walbridge
Department of Civil and Environmental Engineering, University of Waterloo, Waterloo, Canada
e-mail: m269zhou@uwaterloo.ca

D. Dikic · G. Rutledge · M. Arsenault
PACE, Oshawa, Canada

S. Walbridge et al. (eds.), *Proceedings of the Canadian Society of Civil Engineering Annual Conference 2021*, Lecture Notes in Civil Engineering 240,
https://doi.org/10.1007/978-981-19-0507-0_51

The specific system considered herein consists of precast slab modules with integral ribs, precast columns, and precast beam elements that run along exterior column lines, and employs grouted post-tensioned connections. While the performance of this closely related systems, have been analytically and experimentally examined over the course of their development [1, 2], openly available experimental data and related numerical research aimed at quantifying the performance of this modular building system are generally limited. Publicly available literature focused on investigating the performance of post-tensioned modular two-way slab system is scarce; however, there have been several reported studies focused on evaluating the performance of precast post-tensioned RC beam-column connections that rely on beam-column friction for transferring load. For example, William et al. [3] developed a hybrid precast RC beam-column connection and tested ten prototype connections under cyclic loading. The hybrid connections consisted of mild reinforcement used to dissipate energy and straight post-tensioning tendons to provide shear resistance. A comparison between this connection and more traditional cast-in-place connections was presented, and the results generally showed that the hybrid precast connection could be designed in a manner similar to that used for conventional RC beam-connections. However, as a result of the post-tensioning, which remained elastic under all stages of simulated lateral loading, the hybrid connections led to smaller residual drifts when compared to the drift developed in the conventional RC connections. Similarly, an experimental research program conducted by Cheok and Lew [4] demonstrated that post-tensioned beam-column connections can indeed be constructed to achieve similar connection strengths and increased ductility compared to more conventional monolithic beam-column connections.

There have been only few reported investigations on the experimental performance of two-way post-tensioned slab systems employing friction-based connections [5] and related numerical studies [6]. These studies are perhaps the most closely related to the structural detailing of the post-tensioned connections employed in the PACE building system. In these prior research efforts, experimental work was done to study influences associated with material strength, post-tensioning forces, and grout properties on the performance of slab-column joints. Six modular joints were tested in an experimental program that was used to examine the influences of several key variables: initial post-tensioning force, concrete strength, and the presence of grout between slab and column joints. The experiment results illustrated that (1) increasing the post-tensioning force in the tendons led to increases in the capacities of the friction-based joints, (2) the grout forming slab-column connections was a key influencer of the friction performance of the connections, and (3) the coefficients of friction of the grouted concrete connections were generally larger than that typically recommended in modern design and modelling provisions [7]. Related numerical findings presented in [6] showed that the friction coefficient simulating the contact between the slab and column, and the post-tensioning forces in the strands, were directly related to the ultimate bearing capacity and ductility of the friction-based connections. The research also found that the stiffness degradation of the joints was slower than that of cast-in-place connections due to the post-tensioned

grouted connections, which reduced distributed joint cracking and bond-slip between reinforcement and concrete.

The above-noted studies provide context and guidance for the examination of the PACE building system connections presented in this paper, and also highlight the limited volume of directly comparable data that are available for appraising the structural performance of post-tensioned two-way modular slab systems.

2 Modular Slab-Column Connection Modelling

The connection details considered in the modelling presented in this paper are based on those used in the design of a specific PACE building system. In this case, the precast slab modules are considered to have an overall height of 250 mm, are 60 mm thick in the flange regions, and have 190 mm depth ribs spanning in each planar direction. The positive and negative reinforcement ratios in the slab modules are on the order of 0.40% and are provided in the form of deformed mild steel bars in the ribs. Post-tensioning tendons comprised of seven-wire strands run along the column lines in both directions of the slab, and are deviated such that they contribute to the negative bending resistance at the column locations and positive bending resistance between columns. Regularly spaced stirrups are provided within the ribs, and steel welded wire mesh is provided in the slab flange. The columns can be highly variable in terms of size and reinforcement; however, in this case, they were modelled with roughly 2.2% longitudinal reinforcement. Grout pockets are provided between the slab modules and columns, as well as between adjoining slab modules to permit tendon placement and to ensure well-distributed bearing conditions are provided between the slab modules and the columns, prior to performing column line tendon post-tensioning operations.

An idealized one-half slab-column connection was modelled to simulate the isolated connection region presented in Fig. 1. The finite element model included a full-height supporting column (i.e., one-half column height provided above and below the slab) and four unbonded post-tensioned tendons, which formed the basis of the slab-column connections. Figure 2 presents the ABAQUS model employed for both the gravity and lateral load connection analyses. Three-dimensional eight-node linear brick elements (C3D8) were used to represent all concrete and grout regions comprising the finite element model. To increase the computational efficiency, reduced integration solid elements (C3D8R) were used to model the concrete columns. Two-node truss bar finite elements (T3D2) were used to represent the post-tensioning tendons and were linked to the surrounding grout/concrete as well as the mild steel reinforcing bars present in the slab panels and columns. The post-tensioning tendons were coupled to the surrounding concrete/grout, via nodal coupling, in a manner that enforced the two-point tendon harping configuration employed in the system design. Perfect bond was assumed between the concrete

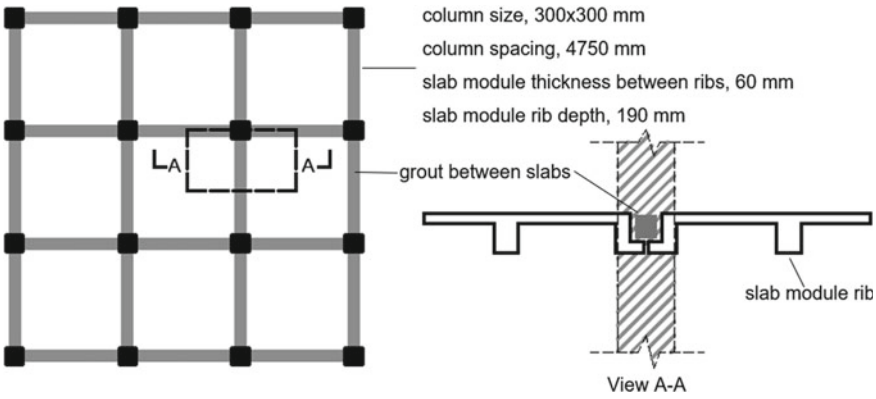

Fig. 1 Plan view of multi-bay PACE structure

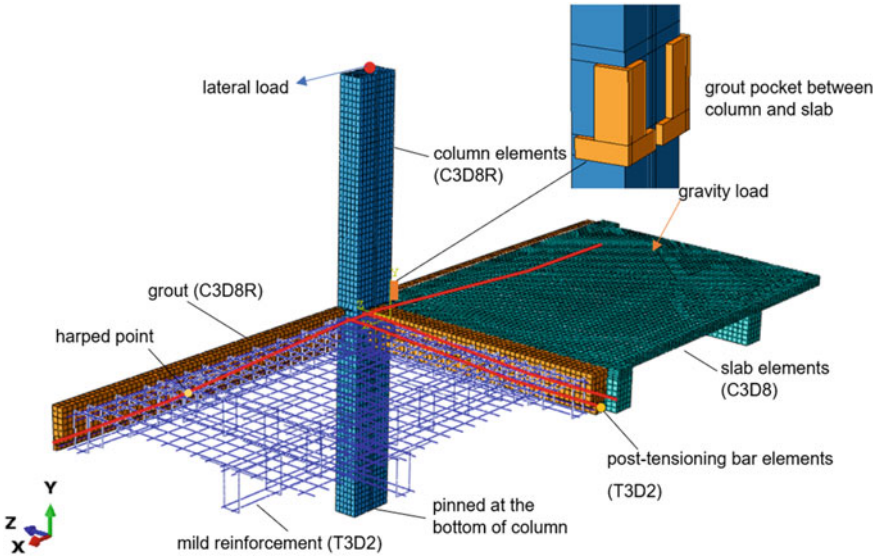

Fig. 2 Finite element model of slab-column connection

and reinforcement for all mild bars. On the basis of findings obtained from preliminary mesh sensitive studies, an approximate solid finite element size of 35 mm was determined to provide adequate resolution and convergence of results, and was generally employed for all concrete and grout regions.

2.1 Boundary Conditions and Contact Surfaces

The PACE modular slab building system relies heavily on friction development at the post-tensioned slab-column connections as a means of transferring vertical shear forces. As such, it is critical that the surface contact conditions between the precast modular elements (i.e., the columns and the surrounding slab modules) be explicitly considered in the numerical model. The contact pairs considered in the modelling included grout surfaces and slab surfaces. The default contact pressure-overclosure relationship in ABAQUS is referred to as a hard contact model. Hard contact implies that the surface transmits no contact pressure unless the nodes of the slave surface contact the master surface. The contact between the infill grout and the slab modules transmits both shear forces as well as normal force across their interface, and a friction parameter is used to define the shear transfer relationship between the contacting bodies. In this study, a friction coefficient of 0.60 was employed and was selected on the basis of recommendations provided in the *fib* Model [7] for grouted concrete-smooth surface contact conditions. It can also be noted that this friction coefficient is likely conservative, as it is less than that estimated on the basis of prior experimental [6] and analytical investigations [5]. Tendon post-tensioning was modelled by way of an initial temperature load and a reduced strand stiffness was employed in the isolated slab-column connection model to approximately account for the increased lengths (i.e., the reduced axial stiffnesses) of the post-tensioning tendons that would be employed in continuous multi-bay slab system that the idealized model is intended to represent.

Different boundary conditions were employed for the gravity and lateral load analyses. Figure 3 presents an overview of the boundary conditions and load conditions employed in the cyclic lateral and monotonic gravity analyses. In the case of lateral loading conditions (refer to Fig. 3a), the column was pin supported at its base and lateral displacements were imposed in the X-direction at the top of the column. In addition to the lateral displacements, surface pressure in the amount of the estimated service load was also applied to the slab in the lateral loading scenario. A fully reversed cyclic loading protocol with two displacement cycles at each amplitude was considered (refer to Fig. 4). The displacement amplitude was increased by

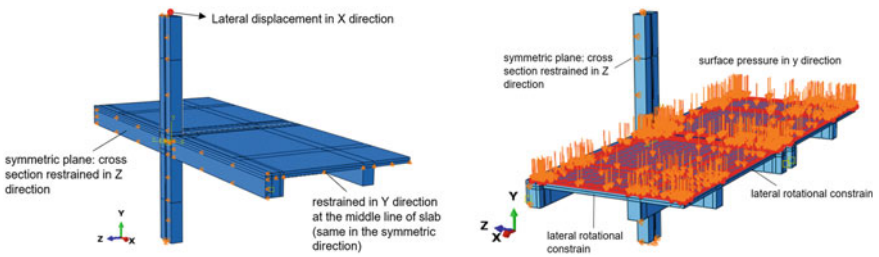

a. under cyclic lateral loading (+ service gravity) b. under gravity loading

Fig. 3 Applied loading and boundary conditions considered

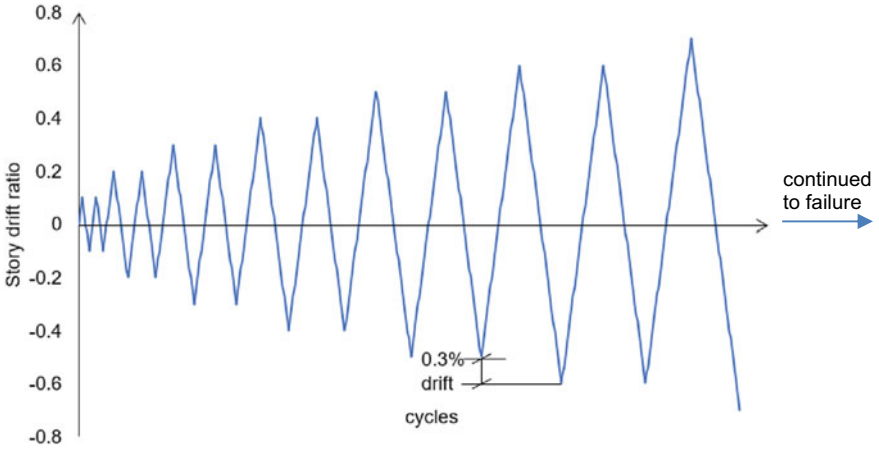

Fig. 4 Reversed cyclic lateral loading protocol

7.5 mm after the completion of each two-cycle set, which corresponded to a lateral drift increase of approximately 0.3%. A vertical compressive force was also applied to the top of the column in the amount of approximately $0.10 \cdot f'_c \cdot A_g$, representing and a column axial load ratio of 10%. In the case of gravity loading conditions (refer to Fig. 3b), a monotonically increasing uniform surface pressure was applied to the top surface of the precast slab modules. The 'free' edges of the slab modules were rotationally constrained in a manner that permitted the edges of the slab model to dilate and translate vertically, while still enforcing zero slab rotation along the centrelines of the slab modules. Note that this method of simulating slab continuity within idealized isolated slab column connection analyses has been shown to correspond well with full slab system analyses (i.e., with models that incorporate multiple slab bays in the model) under uniform gravity loading conditions [9].

2.2 Material Modelling

Concrete damaged plasticity (CDP), a continuum, plasticity-based, damage attenuation model was used to simulate the nonlinear response of the concrete elements under general loading conditions. Among the available models in ABAQUS that may be used for simulating the nonlinear response of concrete under variable stress states, the CDP model has been shown capable for simulating the response of structures subjected to monotonic as well as cyclic loading conditions, provide that suitable CDP material modelling parameters are employed. The modelling parameters used in the application of the CDP material modelling are presented in Table 1 and were principally based on those used by others in the modelling IMS friction-based connections [8] and the recommendations provided in the ABAQUS Analysis User's Guide

Table 1 Concrete plastic properties parameters

Dilation angle	Eccentricity	σ_{b0}/σ_{c0}	K_c	Viscosity parameter
40°	0.10	1.16	0.667	0.002

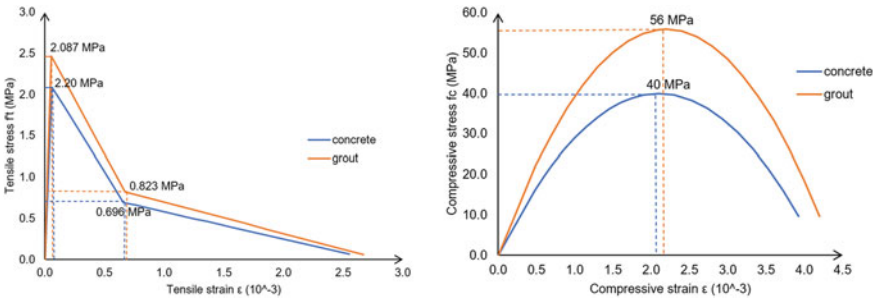

(a) under uniaxial tension (b) under uniaxial compression

Fig. 5 Assumed uniaxial stress–strain response for grout and concrete

[8]. Two primary failure mechanisms are considered in the CDP material modelling: (i) concrete cracking and (ii) concrete crushing. Key concrete material parameters employed in applying CDP yield criteria include the Poisson's ratio, υ, which was taken as 0.20, the dilation angle, ψ, the shape factor, K_c, the biaxial stress ratio, σ_{b0}/σ_{c0}, and the flow potential eccentricity, ε.

The uniaxial stress–strain response of concrete in tension is assumed to be linear elastic up to its tensile strength, f'_t. The characteristics of the post-cracking strain softening were determined from uniaxial tensile stress-crack width relationship for concrete as presented in [7]. A relationship closely-resembling Hognestad's parabola was used as the basis of the user-specified uniaxial stress–strain response of concrete and grout in compression. The concrete and grout tensile stress and strain curves obtained using uniaxial tensile stress-crack width relationship are shown in Fig. 5. Finally, all reinforcement, mild and high strength, was modelled as bilinear with an elastic-perfectly plastic relationship. Mild steel reinforcement was assumed to have a yield strength of 400 MPa and the 1860 MPa post-tensioning tendons were assumed to yield at a stress level of 1600 MPa.

3 Finite Element Analysis Results

Table 2 presents the matrix defining the different analyses that are presented in this paper. Models with different tendon stresses were considered in the gravity load analyses to investigate the effect of tendon stress levels on the flexural capacity of this system. With respect to the lateral load analyses, two cyclic analyses with

Table 2 Slab-column connection analysis matrix

Model No	Analysis case	Tendon stress (MPa)	Friction coeff
M1	gravity loading	1075 (long term)	0.60
M2	gravity loading	1340 (short term)	0.60
M3	lateral reversed cyclic	1075 (long term)	0.60
M4	lateral reversed cyclic	1075 (long term)	1.00

different connection friction coefficients were performed in an effort to investigate the significance of connection slip on the computed response.

Load-controlled analyses involving monotonically increasing surface pressures were used to estimate the gravity load resisting performance of the modular system under two different prestress loss scenarios: analysis M1 was done considering a long-term loss prestress scenario and analysis M2 represents an immediate/short-term tendon prestress loss scenario. Figure 6 shows the displaced shape of the isolated connection and the mild reinforcing bar stresses of the slab module for M1, immediately prior to failure. From the figure, it is apparent that yielding of the longitudinal steel was estimated to occur in all of the module ribs prior to failure. Figure 7 presents the M1 principal plastic strain vectors developed throughout the region of the slab column connection prior to failure. Note that in the case of cementitious materials such as grout and concrete, the tensile plastic strains are reflective of cracking. It can be seen that the most extensive cracking is estimated to occur within the grout pockets located between the column and slab modules; however, cracking also extends within the modular slabs and columns. Figure 8a, b present gravity load-response results for M1 and M2. Figure 8a shows load-connection slip response data and Fig. 8b presents load-slab displacement response data. On the basis of the results obtained for M1 and M2, it can be seen that the initial tendon force is

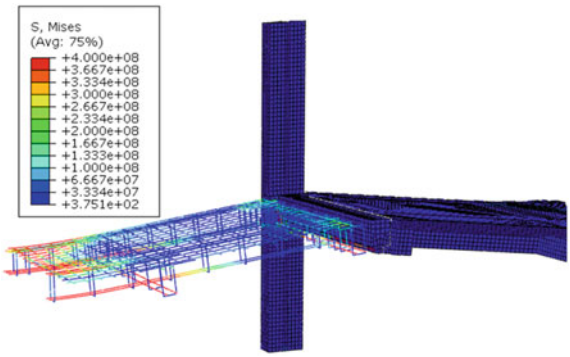

Fig. 6 Displaced shape and mild reinforcing bar stresses at ultimate (M1)

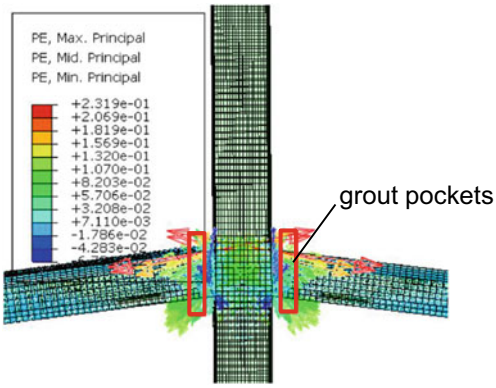

Fig. 7 Plastic deformation vector (M1)

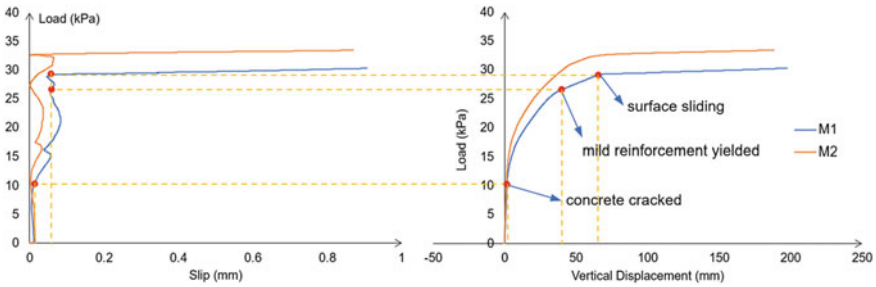

Fig. 8 **a** Computed gravity load-slip responses (analyses M1 and M2) **b** Computed gravity load–displacement responses (analyses M1 and M2)

estimated to little impact on the pre-cracking stiffness of the system; however, in the simulation accounting for increased tendon force losses stemming from anticipated long-term effects (e.g., creep, shrinkage, and relaxation), the post-cracking stiffness of the system was more significantly impacted as a result of the post-tensioning stress level decrease. In Fig. 8a, the relative vertical slip at the mid-depth location of the slab module is presented and as a representative measure of overall connection surface slip. For both tendon stress levels considered, it can be seen that connection slip propagates after extensive yielding of the slab module's mild reinforcement and concrete/grout crushing are estimated to occur. It can also be seen that the tendon stress level did impact the ultimate gravity load carrying capacity of the connection; however, this impact seems to be more directly related to the influence of axial compression on the slab module's flexural resistance as opposed to the influence of axial compression on the slip resistance of the connection. The maximum gravity load that the system was estimated to resist was estimated to be approximately 30 kPa when the effective long-term force-in-tendon was assumed, and the numerical results show that slab module mild steel yielding would occur prior to system failure. It is

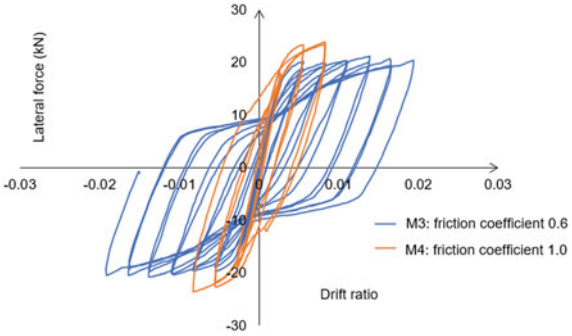

Fig. 9 Computed cyclic load–displacement responses (analyses M3 and M4)

interesting to note that in the absence of system post-tensioning, a yield line analysis [10] considering an isolated corner-supported slab module suggests that the flexural resistance of the lightly-reinforced slab module is approximately 10 kPa. However, the addition of axial compression within the slab leading to increased flexural resistance, the vertical shear carried directly by the inclined tendons, and the corner rotational restraints stemming from system continuity and from contact between the slab modules and the columns, collectively permit these lightly reinforced slab modules to carry significantly increased gravity loads as a result of the post-tensioning employed in the modular system. Ultimately, the capacity and performance of the modular system was controlled by flexural failure mechanisms under gravity loading and the friction-based connection was estimated to have little impact on the capacity of the connection or on connection performance prior to the onset of flexural failure.

Reversed cyclic analyses were used to estimate the suitability of the friction-based connections under lateral loading conditions. The hysteretic lateral load versus lateral displacement (and drift) curves of M3 and M4 are shown in Fig. 9. Recall that M3 and M4 were identical in all respects with the exception of connection friction. Analysis M3 employed a friction coefficient of 0.60, which was selected on the basis of established recommendations [7] and was aimed at capturing the likely slip-friction response of the joint, and M4 employed a friction coefficient of 1.0 in an effort to further mitigate connection slip from the simulation, while still permitting crack opening and closing within the grout pocket comprising the slab-column connection region, without modifying the finite element model connectivity or meshing. From the results presented, it can be seen that the load-deformation responses of the connection are near-symmetric for both cases of connection friction considered and show little impact of damage propagation or deformation offset stemming from initial loading direction. Apparent from a comparison of the two sets of results obtained from the cyclic analyses, connection slip was estimated to reduce the lateral load resistance of the connection by approximately 16% and also led to a marginal reduction of lateral stiffness (reduction of about 10%). Further, the general shape of the two-hysteresis differed, with the slip-permitted analysis exhibiting increased pinching. However, arguably the most noteworthy aspect of the response is the approximate

doubling of the connection ductility as a result of the presence of slip-friction, which was estimated to reduce the stress levels developed in the critical grout and concrete regions comprising the connection region. In both analysis cases (M3 and M4), failure was ultimately controlled by flexural failure mechanisms in the form of concrete and grout crushing at the connection region, near the top and bottom surfaces of the slab module.

For assessing the estimated drift levels obtained from analysis M3, which achieved a maximum drift ratio of approximately 1.9% under the prescribed cyclic lateral loading protocol, [11] drift-based shear strength reduction factors for RC flat plates subjected to seismic deformations can be used a reference. According to the Canadian design provisions, RC flat plate connections that are required to undergo such levels of drift, are subject to appreciable strength reduction factors, effectively limiting the shear strength of the connection to approximately 30% of their concentric shear resisting capacity. That stated, it should again be noted that the results shown for analysis case M3 were obtained considering the combined application of the entire gravity service load (i.e., full dead + full live) along with the prescribed lateral displacement protocol. Thus, on the basis of these results, it can be stated that the computed results obtained for the PACE modular system well-exceed the drift requirements associated with conventional RC flat plates and, based on those results, would be a suitable alternative for RC slab systems that are likely to experience lateral deformations. The displaced shape and damage development, by way of concrete/grout plastic strain contours, are shown for peak amplitude positive and negative drifts prior to failure (refer to Fig. 10). In the lateral load analyses, damage was estimated to first occur within the grout pockets and then propagate to the adjacent slab modules. Finally, it should also be noted that while not shown in Fig. 9, a lateral pushover analysis was conducted to estimate the influence of the cyclic loading on the modular friction-based connection. Under lateral pushover, the system was estimated to be governed by the flexural resistance of the column as opposed to the post-tensioned connection.

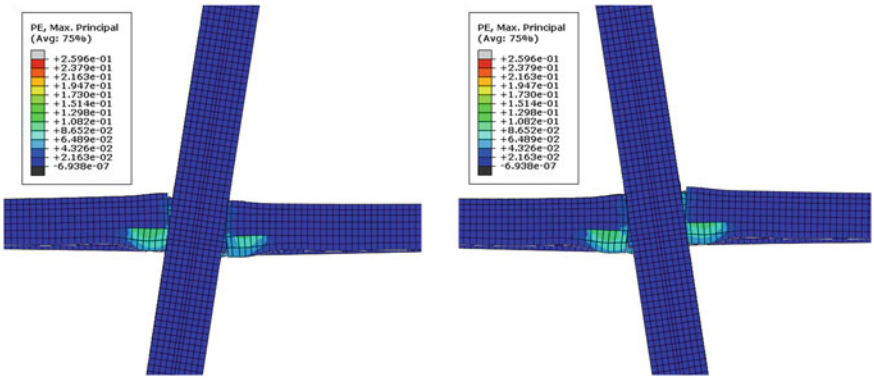

(a) peak amplitude positive displacement (b) peak amplitude negative displacement

Fig. 10 Displaced shape and plastic strain development (× 8 displacement magnification)

Thus, the reversed cyclic lateral loading protocol considered in analyses M3 and M4 is indeed a demanding loading scenario for the modular connection and was shown to induce material damages not captured in a pushover analysis.

4 Conclusion and Discussion

This paper presents results obtained from a series of NLFEA aimed at gaining insight on the structural response of post-tensioned friction-based slab-column connections under different loading conditions. On the basis of the results presented, the following key findings were obtained:

- Under gravity and lateral loading conditions, flexural failure mechanisms involving mild steel yielding and longitudinal concrete crushing were estimated to govern the response of the post-tensioned slab column connections. While the presence of the friction-based connections impacted connection response, it was not estimated to propagate premature slip-related failure mechanisms. Further, the post-tensioning tendons employed in the system were estimated to remain elastic over all phases of applied loading and response.
- Under anticipated service level gravity loading, negligible levels of concrete cracking, connection region opening (i.e., crack opening within the grout pockets), and connection slip at the friction connected joints were estimated to occur. Load levels far-exceeding the factored gravity load were required to develop damages in the form of cracking, crushing, or connection slip. For the specific PACE connection considered in these analyses, the structure had a reserve gravity load carrying capacity of approximately 3 times the factored gravity load. Finally, it should also be noted that extensive concrete cracking and mild steel yielding was estimated to occur within the slab modules, prior to developing damage in the immediate slab-column connection region.
- Under reversed cyclic lateral loading conditions, the influence of connection slip was estimated to marginally reduce system lateral load resistance and connection stiffness; however, was also estimated to enhance the ductility of the friction-based connection/modular system. The results from the analyses carried-out suggest that the presence of even small levels of connection slip dissipated the load demands on the critical concrete and grout regions comprising the slab-column connection and, as such, delayed the onset of concrete/grout crushing, which was ultimately found to be the controlling damage mechanism in all cases considered.
- The estimated drift capacity of the post-tensioned modular system employing friction-based shear connections at the slab-column regions was estimated to exceed minimum North American requirements specified for conventional RC flat plate connections. While PACE slab-column connections are admittedly not directly comparable to RC flat plates, satisfying the drift-based shear strength criteria provided in Canadian design provisions for flat plates, in part, demonstrates their suitability for applications in similar building structures.

The nonlinear finite element analyses presented in this paper confirm the feasibility of employing PACE friction-based slab-column connection systems in lieu of more conventional slab systems commonly used in predominantly-gravity load controlled systems. The results presented also shed light on the potential benefits of using modular systems with friction-based connections as a means of enhancing lateral deformability and resilience under a broad range of loading scenarios, including extreme lateral loading scenarios. Further, it should be noted that the deformation capabilities of flexure-governed RC components can be challenging to capture with high accuracy using numerical procedures. In this regard several arguably-conservative assumptions were employed in the analyses; however, it is recommended that experimental activities involving closely-related friction-based post-tensioned connections be performed to validate the promising ductility estimates developed through this work.

References

1. Petrovic B (1978) Prefabricated prestressed concrete skeleton system IMS. Int J Hous Sci Appl 2(4):369–375
2. Dimitrijevic R, Gavrilovic B (2000) Precast prestressed concrete skeleton in contemporary building–IMS System
3. Stone WC, Cheok GS, Stanton JF (1995) Performance of hybrid moment-resisting precast beam-column concrete connections subjected to cyclic loading. Struct J 92(2):229–249
4. Cheok GS, Lew HS (1993) Model precast concrete beam-to-column connections subject to cyclic loading. PCI J 38(4):80–92
5. Chen HY, Zhu HG, Ma HQ, Fan JC, Ni YD, Huo QJ (2020) Numerical analysis about the influence of column lateral friction torque on seismic performance of IMS system joints. Alex Eng J 59(1):165–176
6. Wu LL, Rui Wang LH, Xie LH, Jia L (2017) Experimental study on friction performance of integral prefabricated prestressed slab-column joints. J Hunan Univ Nat Sci 44(11)
7. Code M (2010) fib model Code for concrete structures. Berlin, Germany, Wilhelm Ernst & Sohn
8. Manual AU (2010) Dassault systèmes simulia corporation. Providence USA
9. Goh CYM, Hrynyk TD (2018) Numerical investigation of the punching resistance of reinforced concrete flat plates. J Struct Eng 144(10):04018166
10. Johansen KW (1962) Yield-line theory. Cement and Concrete Association
11. CSA A23.3:19 (2019) Design of concrete structures. Canadian Standards Association, Mississauga, ON, Canada

An Integrated Framework for the Design of Climate-Resilient Buildings in Canada

J. Kim, E. Kim, K. Kapsis, and D. Lacroix

1 Introduction

With a rapidly changing climate, the concept of resilience is emerging as an important consideration for Canada's building industry. Recent weather events such as floods (e.g., 2018 New Brunswick flood), wildfires (e.g., 2016 Fort McMurray fire), droughts, and heatwaves have shown devastating impacts of climate change on the environment, economy, and public health and safety, especially among vulnerable populations (e.g., seniors, low-income families, indigenous communities). Between 2003 and 2012, flooding alone has cost Canadian taxpayers $20 billion (CAD) in damages [12] and according to national-scale projections, extreme weather events are expected to increase in both frequency and intensity. The vast majority of existing buildings are vulnerable to the projected climate changes because they are not designed to deal with extreme weather events. There is an urgency to integrate resilience in building design and operation to ensure the safety and prosperity of our communities. This goes beyond the safety of structures during extreme events (e.g., earthquakes, hurricanes) and includes the resilience of interdependent building components such as systems and occupants under a changing climate. Existing literature often deals with these components in isolation and their interdependency is mostly missing in resilience considerations despite the fact that failing one could compromise the others.

This paper seeks to establish an integrated framework to designing for resilience in buildings by evaluating the role of the structure, building systems, and occupants and their interdependency in climate impacts. The paper consists of two major parts: (1) review of the current state of resilience considerations for structure, systems, and occupants in the context of Canada's climate risks and regional priorities, and (2)

J. Kim · E. Kim · K. Kapsis · D. Lacroix (✉)
University of Waterloo, Waterloo, Canada
e-mail: daniel.lacroix@uwaterloo.ca

S. Walbridge et al. (eds.), *Proceedings of the Canadian Society of Civil Engineering Annual Conference 2021*, Lecture Notes in Civil Engineering 240,
https://doi.org/10.1007/978-981-19-0507-0_52

discussion of their relationship and interdependency in improving climate resilience in building design and operation.

2 Climate Change in Canada

Canada has been warming up over the latter half of the twentieth century with an increase of 1.5 °C in average air temperature [5], which is particularly concerning given the rate of warming in Canada is double the global average over the same period. Rising temperatures has caused declines in snow and ice cover and warmer winter seasons across the country especially in northern regions. Warming of the climate has also altered precipitation and wind patterns with increases in rainfalls and storm events in many parts of the country [7]. The changing climate has serious implications for future vulnerability of the built environment as they can negatively affect structural integrity, essential services (i.e., water, energy), and occupant health and safety. In 2019, Natural Resources Canada (NRCan) published a detailed report [5] describing the impact of projected climate change in major regions of Canada (Fig. 1).

Based on this report, the regional characteristics of the projected climate changes are summarized in Table 1 and subsequent associated climate risks that are relevant to the built environment for each major region are identified in Table 2.

From a built environment perspective, the projected climate changes pose the following risks:

- Flooding: more frequent and intense rainfalls will increase urban and coastal flood risks. Combined with extreme water levels and high winds, floods can cause serious damages to coastal communities and buildings.

Fig. 1 Six regions of Canada [24]

Table 1 Projected regional climate change trends*

	Temperature			Precipitation	Snow, ice				Costal effects	
	Average extreme	CDD	HDD	Avg/extreme	Snow cover	Water availability	Sea/lake/river ice	Permafrost temp	Sea level rise	Wave height/duration
British Columbia	↑	↑	↓	↑	↓	↓			↑	
Prairies	↑	↑	↓	↑	↓	↓				
Ontario	↑	↑	↓	↑	↓		↑		↓	
Quebec	↑	↑	↓	↑	↓		↑	↑	↑	↑
Atlantic	↑	↑	↓	↑	↓		↑		↑	↑
Northern Canada	↑	↑	↓	↑	↓		↑	↑	↑	↑

*The climate change trends summarized in this table are based on findings in the NRCan report [5]

Table 2 Projected regional climate change trends

	Regional priorities*		
British Columbia	Drought	Flood	Water
Prairies	Flood	Drought	Wildfire
Ontario	Flood	Storm	Drought
Quebec	Flood	Storm	
Atlantic	Flood	Storm	
Northern Canada	Storm	Flood	

*The climate change trends summarized in this table are based on findings in the NRCan report [5]

- Extreme heat: more intense and frequent extreme hot temperatures will increase the severity of heatwaves, potential power outages, and heat-related health concerns especially among vulnerable populations (e.g., seniors).
- Drought: warmer winters and earlier snowmelt will cause higher winter stream flows while lowering summer stream flows. Such trends will lead to an increased risk of fresh water shortages during summer seasons in many parts of the country.
- Wildfires: higher temperatures and prolonged drought can increase wildfire risks particularly in prairie regions that can cause severe damages to building structure and health risks with poor air quality.

As shown in Table 2, each region faces different climate risks; hence, resilience solutions for buildings will need to be based on specific climate challenges of the region guided by scientific information and methods.

The next section provides a review of the current state of resilience considerations for major components of the built environment—structure, systems, and occupants in the context of Canada's climate risks and regional priorities.

3 Resilience Considerations for the Built Environment

Climate resilience refers to various concepts such as risk management, mitigation, adaptation, and sustainability. Even within the context of the built environment, resilience has different meanings and implications depending on the specific component being investigated. In this paper, the focus is on three major components of buildings—the structure, building systems, and occupants—in order to understand how resilience is defined and evaluated in building design and operation.

3.1 Structure

Resilience has become the new "buzzword" not only in engineering but also in various social and political contexts. Although there are many variations in the definition of resilience, a common overarching theme in the context of structural engineering is the ability for buildings and other infrastructure to absorb and recover from the impact of hazards with minimal damage to public safety, health and the economy. Design standards and guidelines have evolved over the years to adapt to changing needs and reflect advances in science but planning and engineering practices are still driven by risk management. There are no specific requirements for the building to be serviceable after a hazard event and no criteria for functional recovery or life-cycle considerations. These are key to achieving resilience in structures.

To date, much of the resilience discussion and research in structural engineering has centered around the performance of structures under extreme natural hazards such as earthquakes and hurricanes. However, an additional hazard that is often overlooked in structural resilience discussions is the impact of aging and deteriorating infrastructure. In addition to increasing the frequency and intensity of weather-related disasters, climate change is also expected to increase the likelihood and rate of deterioration of the built environment through corrosion, oxidation, and even decay in some materials [18, 26].

In order to meet structural resilience goals under natural hazards, it is not only necessary to reduce failure probabilities and mitigate the immediate impact of the hazards but also to minimize continuing effects through recovery. In this regard, the quantification of resilience and development of recovery models have been critical for identifying and understanding resilience needs. The resilience of a structure can be mathematically expressed as the integration of its functionality over time as [9] as shown in Eq. (1).

$$R = \frac{1}{t_r} \int_{t_0}^{t_0+t_r} Q(t)dt \tag{1}$$

where t_0 is the time at which the disaster event occurs, t_r is the time interval over which resilience is being evaluated, and Q(t) represents the functionality or serviceability level of the structure. This definition of resilience is graphically represented in Fig. 2 where resilience is simply the area under the functionality curve Q(t) whose analytical form depends on loss and recovery functions.

Accurate recovery functions are difficult to obtain due to the uncertainties involved in the recovery process but empirically derived and simplified models are available in the literature [9, 15].

Further interpreting resilience as illustrated in Fig. 2, it can be understood that the resilience of a structure can be enhanced by minimizing the initial impact on functionality at t_0 and reducing continued disruptions to functionality by reducing the recovery time. One way this can be achieved is through redundancy and improved robustness.

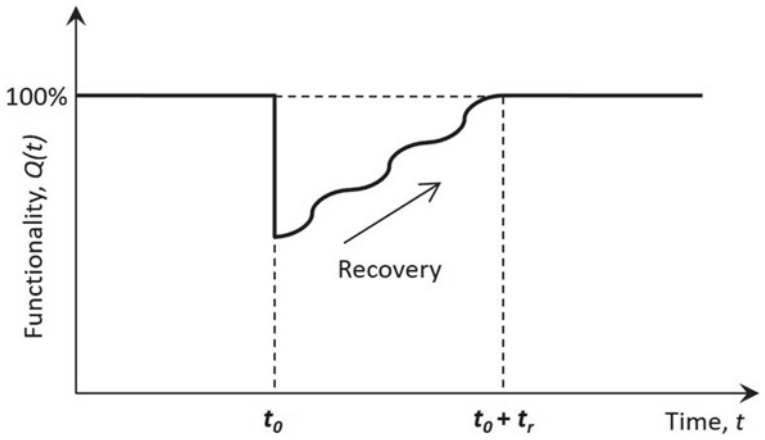

Fig. 2 Graphical representation of resilience

Recent extreme disasters such as the Tohoku earthquake (2011) and Hurricane Sandy (2012) generated an urgency to develop design guidelines and mitigation measures for hazard types and levels that were previously not considered. These range from general site characterization and design choices like requiring elevated building foundations or prohibiting reverse sloping driveways [11, 25] to component isolation or strengthening measures like self-centering or energy dissipation mechanisms [8].

There already exists methodology for assessing the resilience of structures under natural hazards as well as tools for improving resilience. However, it is important to highlight that structural safety and recoverability alone do not define resilience. For a building to be functional and habitable during and after a disaster event, the resilience of building systems and occupant health must also be ensured. Linking structural resilience to building systems and occupant well-being is a significant challenge that has not yet been addressed in the literature.

3.2 Building Systems

While it is essential for building structures to remain intact and quickly recover from climate change hazards ("have a roof over your head"), a climate-resilient building also needs to bounce back or (ideally) maintain operations ("snug as a bug in a rug") during and post-hazards, with minimal financial and environmental impact. This section briefly discusses building resilience from the point of view of energy and space conditioning systems in buildings. While water and wastewater systems are equally critical for building functions, they can be described as socio technical systems since their undisruptive operation relies not only on building resilience but extends to public works and public infrastructure resilience [14].

The frequency, duration and geographic distribution of weather-induced power outages is increasing overall, necessitating individual buildings to go into islanded mode, and clusters of buildings to become independent microgrids [3]. The rising number of power outage events is driven by aging power infrastructure, increased demand, and climate change [1]. Distributed energy resources (DER) can be implemented in new or existing buildings, to relieve the grid by providing ancillary services during normal operation (thus, mitigating rolling blackouts), and operate critical loads during power outages until grid recovery. DER are active building systems that can be categorized as (1) on-site electricity generation, (2) controllable loads (e.g., space and water conditioning systems such as heat pumps, electric lighting and hot water tanks) or (3) energy (thermal and electrical) storage.

Active systems can be easily implemented in new construction and existing buildings. Special care should be taken for their design and installation as to account for climate-induced risks specific to the region. For example, for a building located in an area prone to flooding, the solar inverters and mechanical equipment should be installed on the top floor to ensure operation during critical times.

On-site electricity generation can be implemented in the form of rooftop photovoltaic systems or building-integrated ones. The adoption of grid-forming inverters and electric (distributed or district) storage is also necessary to allow buildings to function in an isolated mode when the grid is down [4]. When possible, several DER should be considered such as thermal storage, smart heat pumps and electric vehicles (in the form of electric storage) to increase the overall building reliance [27]. Coupled with energy efficiency measures, DER are critical to maintaining grid stability and reducing greenhouse gas emissions (GHGs).

On-site generation may fail or not meet all energy demands during and post-hazards, thus it is important to incorporate passive measures/systems to enhance the thermal resilience of the building, reduce critical failures (e.g., indoor bursting pipes during an extreme cold event) and allow habitable indoor conditions (e.g., during a heat wave). The implementation of passive measures/systems in existing buildings can be challenging because they are often incorporated in the buildings permanent structures; therefore, it is important to consider incorporating them at the design phase. Examples of passive systems include [16, 17]:

- Well insulated airtight envelope to increase building thermal autonomy.
- Window-to-wall ratio and exterior solar shading to regulate solar gains and daylight.
- Thermal mass to reduce indoor temperature fluctuations.
- Operable windows to allow natural ventilation.
- Fire resistance measures to minimize risk of damage from wildfires (when applicable).

3.3 Occupants

The effects of climate change on buildings can have adverse effects on occupant comfort, health, and quality of life. Overheating in the building due to extreme summer temperatures and frequent heatwaves is a growing concern with increasing heat-related illness and mortality in southern regions of Canada (e.g., 90 + deaths from the 2018 heatwave in Quebec). Providing appropriate cooling solutions for the building occupants during extreme hot temperatures is increasingly important, especially amongst the elderly population who is vulnerable to heat-related health risks [20]. However, related efforts often lead to increased consumption of air conditioning that can exacerbate urban heat island effects and worsen carbon emission rates [6]. Hence, building designers need to consider alternate or complementary strategies that can achieve the same cooling effects as air conditioning for sustainable management of overheating issues [13]. The international comfort standards offer guidance on the use of adaptive comfort in naturally-ventilated space, cooling effects of elevated air speed, and thermal environmental control classifications that can lead to reduced cooling energy use and increased adaptive opportunities for the occupants [2]. As the current warming trends will likely continue over the lifespan of buildings, further work is needed to understand the effects of various cooling strategies—active and passive—and their combinational effects on thermal comfort and energy use under extreme heat. Furthermore, in a cold climate like Canada, the adverse effects on occupant comfort, health, and quality of life should not be overlooked. For example, in January 1998, the Great Ice Storm led to 34 fatalities and left millions without power for days to several weeks.

Air pollution from wildfires can also present significant health threats to the residents in the impacted area (e.g., Prairies) as well as surrounding regions. Depending on the extent and duration of the wildfire, outdoor pollutants such as smoke, debris, and ashes can remain in the air for days or weeks, and they can enter buildings via mechanical ventilation systems, natural ventilation, and infiltration (e.g., small cracks, air gaps) [23]. Hence, future building design needs to consider the effects of wildfire on indoor air quality in wildfire-prone areas to ensure safe and healthy living conditions. Standards development have begun to integrate fire resilience into building design (e.g., CSA S504 Fire resilient community planning, building design and materials for northern regions). Since each region may have unique wildfire challenges and air pollution issues, it is important to use standards in conjunction with local guidelines/requirements and develop regional expertise in wildfire resilience.

Some extreme weather events such as floods and wildfires may require emergency evacuations and temporary or permanent population displacement. Such events can be devastating to residents emotionally and financially and they can take significant time to recover and restore. In the case of floods, buildings may not be safe for people to return even after the flood subsides as wet envelope, interior finishing, and furniture can cause health risks [10]. With rising sea levels, some coastal communities can be subject to repeated flood events that can severely compromise livelihoods of the local people. In many cases, the effects of climate change do not affect all

people and communities equally. Certain segments of the population can be more vulnerable to these extreme weather events due to their health, social, and economic status. Therefore, resilience solutions must integrate equitable approach to provide sustainable living conditions to vulnerable populations in the built environment.

4 Discussion

4.1 Integrated Framework to Resilient Buildings

The preceding section highlights the three main components of the building environment and what resilience means in terms of each component. However, it is important to note that the three components are interrelated and all three are integral to a resilient design. Even a single component compromised in a disaster event would mean the building is not serviceable, and if a large portion of the built environment suffers non-recoverable failures, the entire community may be incapacitated for a prolonged period of time. The importance of the structural system, building systems, and occupant health in the resilience paradigm is portrayed in Fig. 3.

Resilience-based design is not a new idea and efforts have already been made to identify community-level resilience objectives and to disaggregate these objectives into performance targets for individual buildings [19, 21, 22], but there is a lack of guidance for meeting these targets and little progress has been made toward adapting resilience-based performance targets to building codes. This remains a significant challenge from both an engineering and cost perspective. In conventional design,

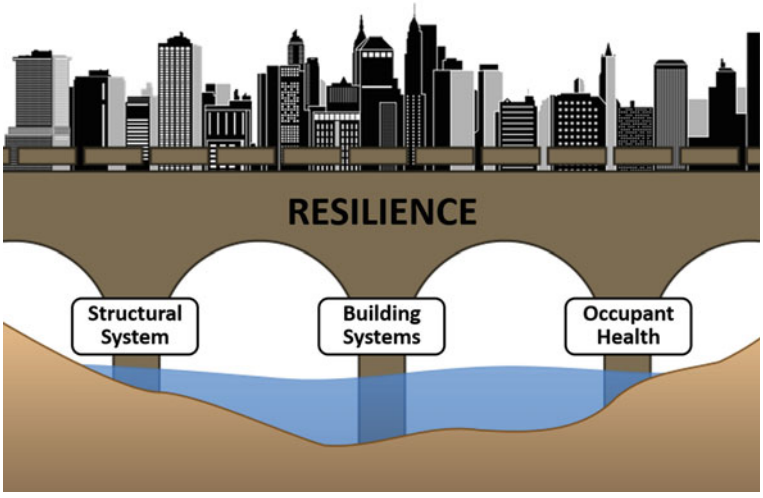

Fig. 3 The road to climate-resilient buildings

the structure, the building systems, and occupant health are all treated as independent problems with prescriptive standards and regulations for each component that will yield reliable performance but not one that is adequate with respect to a resilience framework. Given that the performance and recoverability of all three critical components are key to an overall resilient response to disasters, an integrated design approach needs to be developed in which the component designs complement each other to maximize the individual resilience of each component. For example, designing building systems and occupant health controls with redundancy and functionality goals, and complementing this with a structural system that can minimize the damage to building systems and occupant health controls. Developing complementary design requirements and choices that will maximize both the safety and functionality of each building components are crucial to building resilience.

4.2 Design and Regulatory Implications

When it comes to cities, buildings can be seen as the smallest physical unit involved in the urban infrastructure and use of resources. Currently, there are several initiatives and actions looking into climate change resilience and mitigation at an urban scale: from global networks such as the C40 Cities and the UN Urban Resilience Hub, to Canada's Excellence Research Chair (CERC) in Smart, Sustainable and Resilient Communities and Cities. While the performance objectives of these greater actions might be well defined, interpret them to design and performance requirements for new and retrofit buildings has been proven challenging.

When it comes to new buildings, design decisions and climate change mitigation strategies are going to affect building performance and their ability to withstand short- and long-term climate events for the next 50 to 120 years, being the typical service life of a building. Performance-based building codes and regulations can effectively guide climate resilient design, construction and operation, that enable future building or system alternations for climate change adaptation. In addition, the development of new standards is necessary to accommodate for various disruptive technologies introduced into buildings.

Current codes largely overlook the existing building stock. Policies coordinated at national or international level e.g. building energy labelling, flood plain evaluation and subsidies for disaster fortitude retrofits can reduce dependence on complex building controls, systems and off-site energy thus, enable resilience at the building scale for the ones who needs it the most.

5 Conclusions and Recommendations

In this paper, we propose an integrated framework to resilient buildings that complements and maximizes the performance major components of the building in a changing climate. Specifically, the role of three building components—structure, building systems, and occupants is discussed in the context of Canada's climate risks. Key findings and recommendations include:

- Functionality and habitability are important criteria in resilient structures and should be considered as part of resilience requirements along with safety and recovery during extreme weather events.
- Building systems should be designed and installed to account for specific climate risks to the region and integration of DER and passive systems is recommended to prevent critical failures and improve the overall building resilience (e.g., indoor comfort, energy diversity).
- Equitable resilience solutions along with increased adaptive opportunities for rising temperatures and extreme weather events will be critical to ensure safe and healthy living conditions for building occupants, especially among vulnerable populations.
- To maximize the resilience of buildings under climate driven disasters, an integrated framework is needed to develop complementary and synergistic designs of the structure, building systems and occupant controls.

Based on this proposed framework, future work will investigate specific relationship between building components and develop integrated design and engineering solutions that can inform building standards and regulations.

References

1. ASCE (2021) 2021 Infrastructure report card. Reston, VA: American Society of Civil Engineers.
2. ASHRAE Standard 55–2020 (2021) Thermal environmental conditions for human occupancy. Atlanta, GA: American Society of Heating Refrigerating and Air-Conditioning Engineers
3. ASHRAE (2019) Smart grid application guide: integrating facilities with the electric grid. American Society of Heating, Refrigerating and Air-Conditioning Engineers, Atlanta GA
4. Bacha S, Picault D, Burger B, Etxeberria-Otadui I, Martins J (2015) Photovoltaics in microgrids: an overview of grid integration and energy management aspects. IEEE Ind Electron Mag 9(1):33–46
5. Bush E, Lemmen DS (eds) (2019) Canada's changing climate report. Government of Canada, Ottawa, ON
6. Cândido C, De Dear R, Lamberts R, Bittencourt L (2010) Cooling exposure in hot humid climates: are occupants 'addicted'? Archit Sci Rev 53(1):59–64
7. Cannon AJ, Jeong DI, Zhang X, Zwiers FW (2020) Climate-resilient buildings and core public infrastructure: an assessment of the impact of climate change on climatic design data in Canada. Government of Canada, Ottawa, ON, p106
8. Chancellor NB, Eatherton MR, Roke DA, Akbaş T (2014) Self-centering seismic lateral force resisting systems: high performance structures for the city of tomorrow. Buildings 4(3):520–548

9. Cimellaro GP, Reinhorn AM, Bruneau M (2010) Framework for analytical quantification of disaster resilience. Eng Struct 32(11):3639–3649
10. Crook B, Burton NC (2010) Indoor moulds, sick building syndrome and building related illness. Fungal Biol Rev 24(3–4):106–113
11. FEMA (Federal Emergency Management Agency) (2011) Coastal construction manual. 4th edn. FEMA P-55, Washington, D.C
12. Gaur A, Gaur A, Simonovic S (2018) Future changes in flood hazards across Canada under a changing climate. Water 10(1441):1–21
13. Holmes MJ, Hacker JN (2007) Climate change, thermal comfort and energy: meeting the design challenges of the 21st century. Energy Buildings 39(7):802–814
14. Hosseini S, Barker K, Ramirez-Marquez JE (2016) A review of definitions and measures of system resilience. Reliab Eng Syst Saf 145(1):47–61
15. Karamlou A, Bocchini P (2017) From component damage to system-level probabilistic restoration functions for a damaged bridge. J Infrastruct Syst 23(3):04016042
16. Kesik T (2017) Resilience planning guide. University of Toronto
17. Kesik T, O'Brien L (2019) Thermal resilience design guide. University of Toronto
18. Kumar P, Imam B (2013) Footprints of air pollution and changing environment on the sustainability of built infrastructure. Sci Total Environ 444(2):85–101
19. Lin P, Wang N, Ellingwood BR (2016) A risk de-aggregation framework that relates community resilience goals to building performance objectives. Sustain Resilient Infrastruct 1(1–2):1–13
20. Lomas KJ, Porritt SM (2017) Overheating in buildings: lessons from research. Build Res Inf 45(1–2):1–18
21. Masoomi H, van de Lindt JW (2019) Community-resilience-based design of the built environment. ASCE-ASME J Risk Uncertainty Eng Syst Part A: Civ Eng 5(1):04018044
22. Mieler M, Stojadinovic B, Budnitz R, Comerio M, Mahin S (2015) A framework for linking community-resilience goals to specific performance targets for the built environment. Earthq Spectra 31(3):1267–1283
23. Nazaroff WW (2013) Exploring the consequences of climate change for indoor air quality. Environ Res Lett 8(1):015022
24. NRCan (2018) Facilitating regional adaptation planning, decision-making and action [Image]. Natural Resources Canada
25. Public Safety Canada (2019) Emergency management strategy for Canada: toward a resilient 2030. Retrieved: March 2, 2021
26. Stewart MG, Wang X, Nguyen MN (2011) Climate change impact and risks of concrete infrastructure deterioration. Eng Struct 33(4):1326–1337
27. Wadhera A, Ayoub J, Roy M (2019) Smart grid in Canada 2018. 2019–066 RP-FIN DER-SGNETS, Natural Resources Canada

Geogrid Reinforcement in the Treated Base Layer of Flexible Pavements

Susanna Mattar, Moustafa Tammam, Jolavian Mekhail, Omar Mahran, Nadine Soliman, Yara Badawy, Safwan Khedr, Omar El-Kadi, and Zahra Zayed

1 Introduction

Flexible pavements are the most widely used type of pavements since they are relatively inexpensive, and easily repaired, strengthened, and maintained. However, flexible pavements are susceptible to various damages. These damages may be aggravated when using low quality bitumen; like the case in Egypt where low quality bitumen constitutes a major concern in the road construction industry. Using such low-quality bitumen in pavement mix increases the pavement's susceptibility to failure; be it rutting, shoving, raveling, fatigue, or slippage cracking. This will result in a reduction in the pavement's lifespan. Innovative ways to strengthen flexible pavements, making them more resistant to high loads, have been significant in the field. Most of the mentioned problems in flexible pavements are associated with the presence of excessive stresses. Under the wheel load, excessive horizontal stresses develop; meaning that tensile radial stress is a main contributor to the modes of failure previously mentioned. Furthermore, load distribution is spread radially in flexible pavements at all levels and geogrids could help distribute and resist these stresses effectively.

Geogrids are geosynthetic material made up of connected parallel tensile ribs with openings large enough to allow strike-through of the surrounding material. In this study, the biaxial geogrid is used as the stresses induced by the wheel into the pavement are generated in all directions. Using geogrids as reinforcement is expected to improve the load distribution transfer across the pavement layers until it reaches the subgrade soil. Therefore, the use of geogrids in flexible pavements is anticipated to significantly contribute to solving the problem of pavement deterioration not only

S. Mattar (✉) · M. Tammam · J. Mekhail · O. Mahran · N. Soliman · Y. Badawy · S. Khedr · O. El-Kadi · Z. Zayed
The Department of Construction Engineering, The American University in Cairo, Cairo, Egypt
e-mail: Susannamattar@aucegypt.edu

S. Walbridge et al. (eds.), *Proceedings of the Canadian Society of Civil Engineering Annual Conference 2021*, Lecture Notes in Civil Engineering 240,
https://doi.org/10.1007/978-981-19-0507-0_53

in terms of the aforementioned distresses, but also by reducing the maintenance costs and extending the lifespan of the pavements.

It has become vital, especially in Egypt, to assimilate the use of geogrids into the construction methods of roads since it will greatly enhance its quality. The available literature about geogrids has exhibited the extent to which it can increase the serviceability of the road both in terms of increased stress resistance [1] and reduced rate of crack propagation. Several studies have also discussed how the different functions in which geogrids can reduce the induced stresses in pavements. Moreover, several papers were dedicated to investigating the optimum location of the geogrids in the pavement [2–4].

Fan et al. [4] investigated the effect of geogrid reinforcement on flexible pavement using both a numerical model analysis and a large-scale tank (LST) testing program. Through both analyses, it was concluded that placing the geogrid in the middle of the base layer has reduced the surface deflection in the asphalt concrete layer as well as being effective in reducing the rutting damage in the base and subbase layers. Another study conducted by Al-Qadi et al. [5] realised that if the base layer was thin (203 to 457 mm) then geogrid placement is optimal at the base-subbase interface, and if the base layer is thicker, then the geogrids should be placed at the upper third of the layer. Research also shows that the incorporation of geogrids allowed the flexible pavement to withstand a higher number of loading cycles, and, in turn, increase the service life of the road [6].

Abu-Farsakh et al. [7] also conducted a study which ascertained the aforementioned results. It was concluded that placing the geogrid at the base-subbase interface resulted in a reduction of the lateral strains both in the base and subbase layer, as well as reducing the vertical and shear strain at the top of the subbase layer. Moreover, they observed that geogrid reinforcement had notably reduced permanent surface deformation along with an increase in the pavement service life.

Siriwardane et al. [8] studied the effect of geogrid placement in the Hot Mix Asphalt (HMA) layer in a pavement section which was composed of the HMA layer, a gravel base, and a subbase layer (geotextiles were added between the base and subbase layer). They found out that stresses were better dissipated in the pavement layers and displacement was significantly reduced.

Imaji et al. [9] conducted full-scale testing trials which showed that the incorporation of geosynthetics (geogrids and geotextiles) significantly decreased both dynamic and static stresses in the base layer. The study also concluded that the addition of geosynthetics was able to curb lateral strain spreading, as well as increase rutting resistance.

Geogrids have also shown substantial performance in areas such as: airport pavements and machine foundations. In the former situation, geogrids were able to reduce stresses and strains in the pavement as well as reduce crack propagation [10], while in the latter situation, the usage of geogrids increased vibration absorption and reduced displacement [11].

The presented research addresses the enquiry about the optimum location of the geogrid in the binder layer of the flexible pavement.

2 Experimental Work

2.1 Lab Material Testing

Lab material testing was conducted to characterize the different materials used in the various layers of the flexible pavement; namely, asphalt concrete, be it surface or binder course layers, untreated base, geogrids, and the subgrade soil. These materials' physical and mechanical properties are needed as input to the finite element model assembled such that the numerical model represents the actual full-scale model. The lab tests conducted on the different materials were according to the ASTM. Results of the tests are shown in Tables 1, 2, 3 and 4.

Table 1 Test results for subgrade layer

Property	Test name	ASTM	Result
Gradation	Sieve analysis	C136-01	Silty sand
Specific gravity	Specific gravity	D854-14	2.8
γ dry max (KN/m^3)	Compaction	D698-12E2	20.0
Optimum Water Content (%)	Compaction	D698-12E2	9.6
Cohesion (KPa)	Direct shear	D3080	7.75
Angle of internal friction (ϕ^o)	Direct shear	D3080	45
Modulus of Elasticity (E) (MPa)	Consolidation	D2435	42
Poisson's ratio	(μ) (assumed)		0.3

Table 2 Test results for base layer

Property	Test name	ASTM	Result
γ dry max (KN/m^3)	Modified proctor compaction	D1557-12	20.6
Optimum Water Content (%)	Modified proctor compaction	D1557-12	6.5
CBR (%)	CBR	D1883-16	100
Modulus of Elasticity (E) (MPa)	Plate loading	D1195-09	80
Poisson's Ratio (μ) (assumed)			0.25

Table 3 Test results for geogrid properties

Property	Result
Tensile Strength (MPa)	40
Modulus of Elasticity (E) (MPa)	280
Unit Weight (KN/m^3)	1.1
Poisson's Ratio (μ) (assumed)	0.15

Table 4 Test results for asphalt concrete layers

Layer	Property	Test name	ASTM	Result
Binder	Flow (2.5 mm)	Flow & Stability	D6927-15	21.2
	Stability (KN)	Flow & Stability	D6927-15	8.2
	Dynamic Modulus of Elasticity (E*) (MPa)	Dynamic modulus	D3497	638
	Poisson's Ratio (μ) (assumed)	–	–	0.2
Surface	Flow (2.5 mm)	Flow & Stability	D6927-15	15.75
	Stability (KN)	Flow & Stability	D6927-15	10.7
	Dynamic Modulus of Elasticity (E*) (MPa)	Dynamic modulus	D3497	706
	Poisson's Ratio (μ) (assumed)	–	–	0.2

2.2 Full-Scale Testing

2.2.1 Test Design

Three full-scale pavement models were tested: a control with no geogrid and two reinforced geogrid samples; particularly, one had geogrid at the mid-binder layer, and one with geogrid at the surface-binder layers' interface. The tank had dimensions of 2 × 2 × 1 m. The layers' thicknesses were selected according to a typical section in the Egyptian code of practice, which suggested 20 cm of base layer, 10 cm of AC binder course layer, and 5 cm of AC surface layer. The subgrade soil was well-compacted to thickness 65 cm of,

The materials; namely, the subgrade, base, and asphalt concrete were mixed, placed sequentially in layers and compacted using a small plate compactor. The base layer was placed and compacted on two layers, sand cone tests were conducted to assure that the materials were well-compacted to their required degree of compaction. The asphalt concrete layers were placed and compacted on layers of 5 cm thick each.

2.2.2 Measurement Devices

The measurement devices in the test setup consisted of pressure gauges located at selected depths across the pavement layers, external LVDTs placed at the surface to measure the deformation, and the actuator through which the load is applied.

Six KDE-PA soil pressure gauges were distributed across the pavement layers to measure the induced stresses. The pressure gauges (P1 to P6) were placed at the locations most relevant to the objectives of the experiment and most likely to be affected by the tensile stresses as shown in Fig. 1. Figure 2 shows the complete setup.

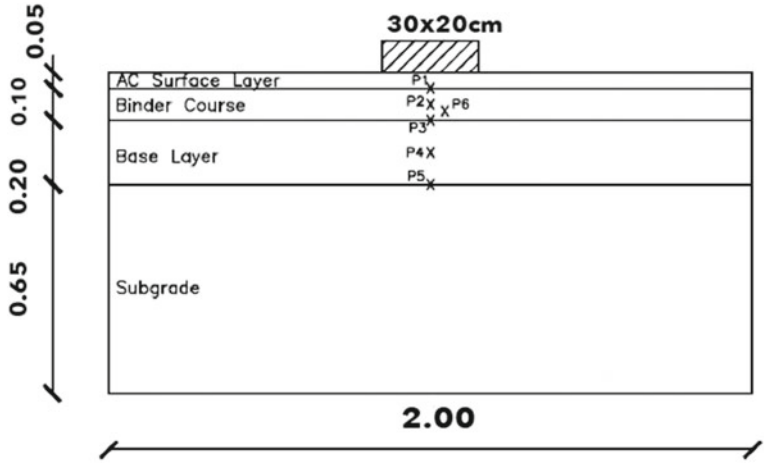

Fig. 1 Pressure gauges location (Elevation)

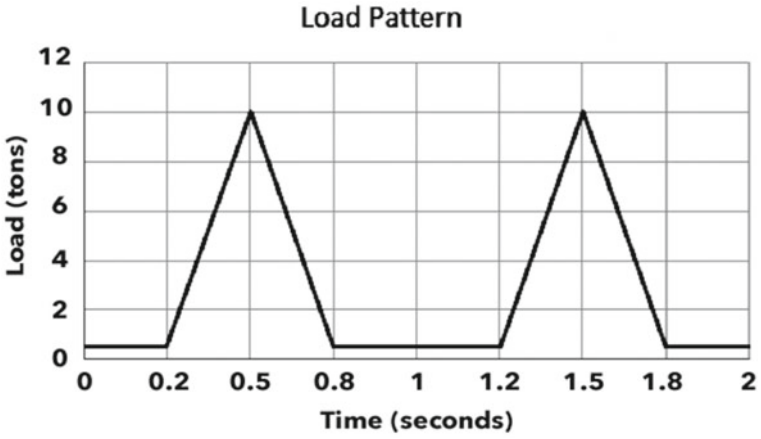

Fig. 2 Load pattern

2.2.3 Dynamic Loading Protocol

Pavements in the models were subjected to repetitive or dynamic loading to simulate the traffic loads. The load was applied on a rubber plate with an area of 30 × 20 cm that represents the contact area of a tire. The chosen load pattern is shown in Fig. 2. It simulates the traffic loads in a low-speed, every 1 s represents a cycle in which:

The static 0.5 tons, which is the minimum load applied, was applied in order to avoid impact during load application. Also, the ESAL equivalency table in the ECP and the ASHTO 1995 were used to calculate the load factor, hence, it is determined that each loading cycle is equivalent to 39 ESALs.

The aforementioned load pattern was assigned through the control system of the actuator. The load was applied in batches of cycles where one batch is 5,000 cycles, then the actuator is left to cool, then the next 5,000 cycles is applied and so on until failure.

Based on research and previous literature, the widely recognized failure criterion was selected to be defined as 1 inch (2.5 cm) of permanent deformation of the pavement structure. Other researchers have used this criterion; e.g. National Airport Pavement Test Facility [12].

3 Numerical Modeling

Three numerical models were developed, two of them with geogrids and one model, which is the control case, without geogrids. The model was based on an equivalent analysis of the static load, where the dynamic modulus of asphalt was used.

4 Analysis of Results

4.1 Full-Scale Model

4.1.1 Total Deformation Versus Time

Figure 3 shows the total deformation (mm) versus time (seconds) of the three models. When plotting the charts, it became apparent that there was a seating problem in the data collected. Seating problem caused by applying the load cycles in 5000 batches introduced some discontinuities. The data was adjusted to avoid this problem and assure all curves are continuous until the end of test as presented in Fig. 4.

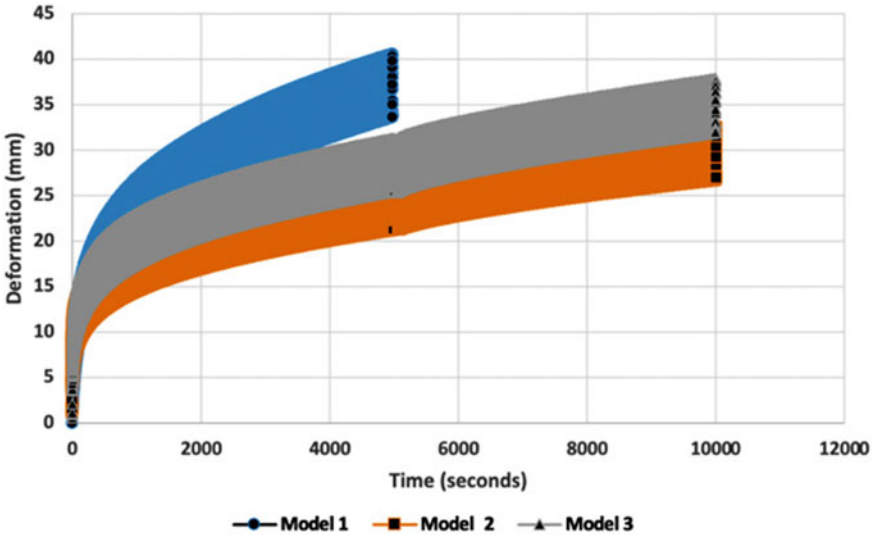

Fig. 3 Deformation versus time

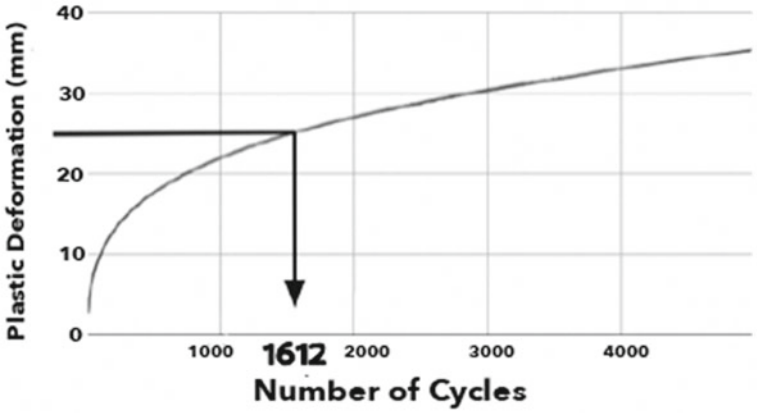

Fig. 4 Deformation versus cycles, model 1

4.1.2 Plastic Deformation Versus Number of Cycles

Given that the selected failure criteria for the pavement performance in this study is defined as 1 inch or 25.4 mm of total plastic deformation, the plastic deformation versus the number of cycles were plotted for each of the three models. When plotting the Plastic deformation versus the number of cycles charts, the minimum deformation during a cycle was used, assuming that the plastic deformation occurs when the load on the pavement is minimum in each cycle.

Figures 4, 5 and 6 illustrate and determine the number of cycles required for each sample to reach 25.4 mm deformation, which means failure according to the selected criterion.

The damage factor calculated earlier (equivalent to 39 ESALs) was used to calculate the equivalent ESALs for the failure of each model. Table 5 shows that model

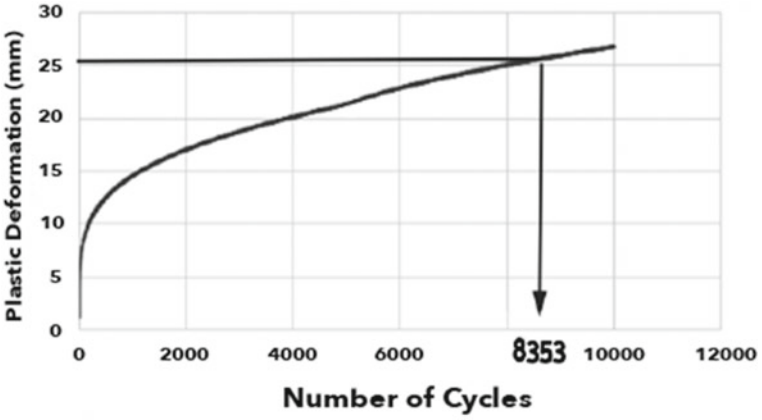

Fig. 5 Deformation versus cycles, model 2

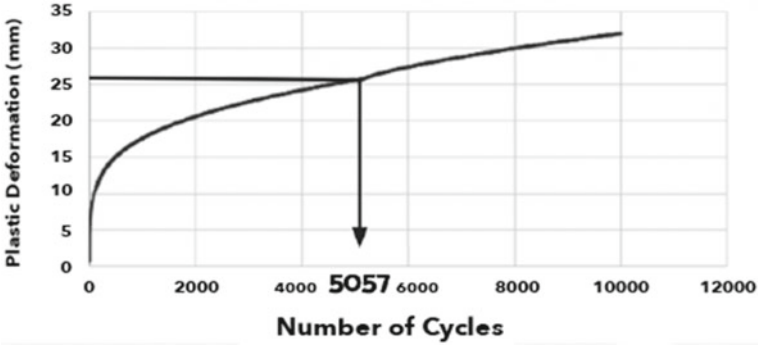

Fig. 6 Deformation versus cycles, model 3

Table 5 Enhanced performance percentages

Model number	Location of the geogrid (If any)	Cycles to failure	Equivalent ESALs	Enhanced performance %
1	None	1612	62,868	–
2	Mid-binder layer	8353	325,767	412.8%
3	Surface-binder layer interface	5057	197,223	213.7%

2 showed an enhanced performance of 418.2%, while model 3 showed an enhancement of about 213.7%. The full-scale testing, therefore, shows that between the two locations tested, the location of the geogrid that yielded the highest enhancement in the performance of the pavement system, is in the mid-binder layer.

4.1.3 Pressure Gauges Results

To further examine the behavior of the pavements with geogrids, the extent to which geogrids aided in dissipating the induced stresses was analyzed. Two of the pressure gauges installed within each model during loading at two different locations within the pavement were analyzed. The first is P4, which is placed in the middle of the base layer and the second is P5, which is placed at the interface between the base layer and the subgrade. The results of the three models were drawn on different datum to represent the difference in the height of the amplitude of the wavelength of each model. Trend analysis of the induced stresses at the aforementioned locations showed that the induced stress decreases with depth. Moreover, it was found that model 1 had the highest stress induced at both locations, as shown in Fig. 8. Model 2 yielded the highest enhancement of the performance with the lowest induced stress in both locations of the pressure gauges, followed by model 3. Figures 7 and 8 show that the presence of the geogrid within the pavement at both locations allowed the stress to be better dissipated, causing the lower layers of the pavement, the base, and subgrade layers, to experience less induced stress when compared to the control.

Therefore, the mechanism of stress dissipation of the geogrid enhanced the performance of the pavement system.

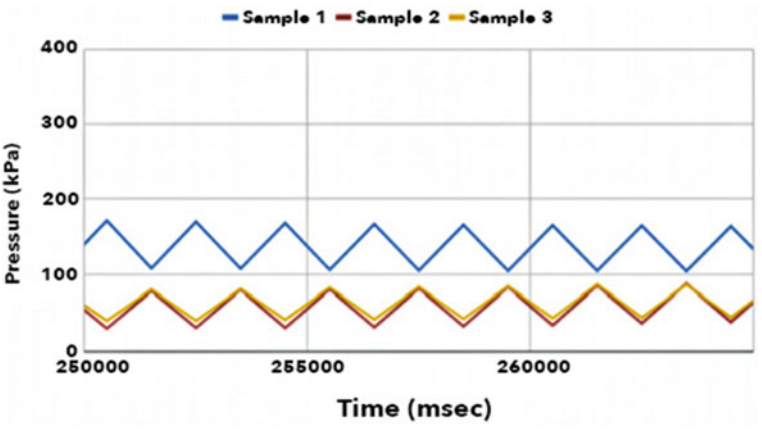

Fig. 7 Pressure gauge P5

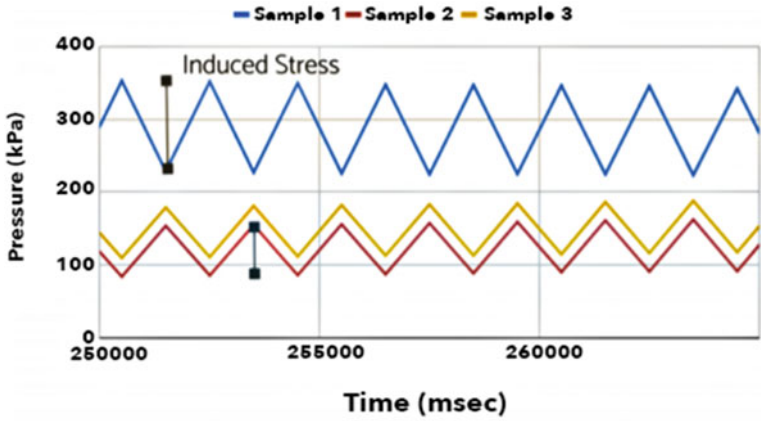

Fig. 8 Pressure gauge P4

4.2 Finite Element Model

Numerical analysis, if validated, gives a be vision for the stress distributions in various elements of the system. Moreover, it can facilitate the study of different parameters affecting the performance of the system by performing parametric analysis.

In this research, a nonlinear three-dimensional finite element model has been used, implementing an elastic-prefect plastic Mohr-Column constative model to simulate untreated base and subgrade layers elements. Von Mises constative model has been used to simulate asphalt concrete and binder layers, and elastic elements have been used to simulate the geogrid. The model dimensions simulated the large-scale experimental model with boundary conditions simulating the experimental container. The mechanical properties for model elements were obtained by standard laboratory tests for different materials used, as presented in Tables 1, 2, 3 and 4.

The primary purpose of implementing numerical analysis in this research is to assure that the boundary conditions are sufficient at the large-scale experimental model and will not affect the system's performance. Moreover, the nonlinear model allows performing parametric analysis to study various parameters affecting the system.

4.2.1 Model Verification

The finite element model has been validated by comparing numerical outputs to measured experimental results. Stress distribution within the layers in the actual tank for each model, measured by the pressure gauges placed at different locations in the layers, were compared with the finite element model's corresponding values. The results obtained from the FEA closely depicted the real model results. The pressure gauges used to verify the results were P5 and P4, and the difference in

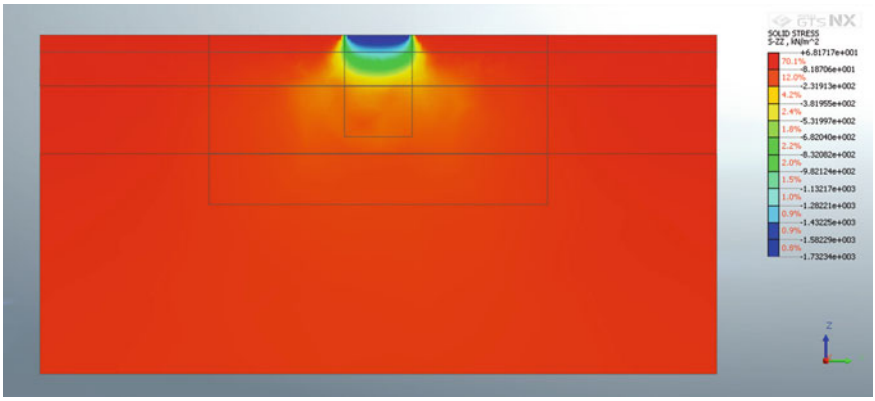

Fig. 9 Solid stresses; No geogrids

ratios between the average stress obtained by them in the control sample and their corresponding values was less than 20%. Accordingly, this means that the model is able to reasonably represent the tank's actual results.

4.2.2 Control Model Without Geogrids

The model's outcomes as shown in Fig. 9. The stress distribution showed the expected pattern of highest induced stresses that at the center of loading and decreases in the stresses towards the sides.

4.2.3 Model with Geogrids Between Surface and Binder Layers

The geogrid model showed a slight improvement in the distribution of stress than the model with no geogrids. The model's outcomes as shown in Fig. 10.

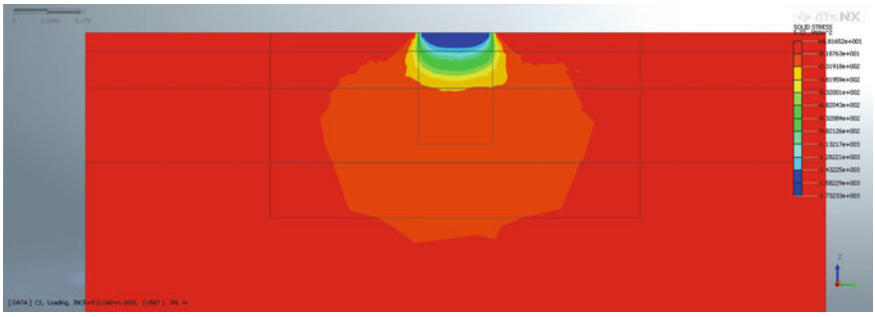

Fig. 10 Solid stresses; Geogrids between surface and binder

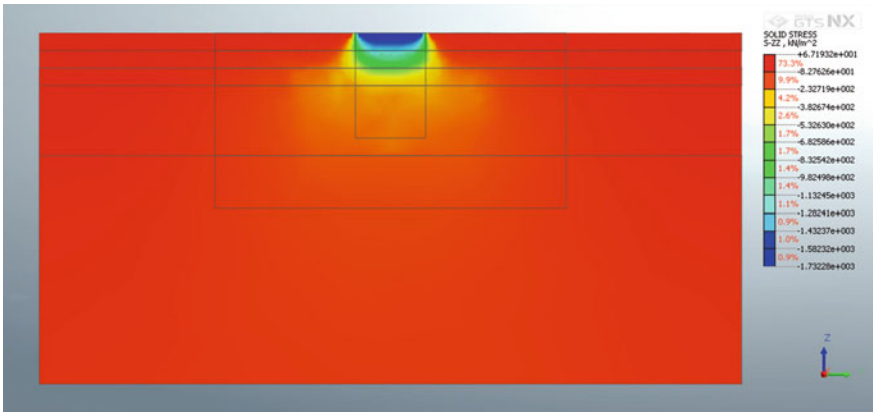

Fig. 11 Solid stresses; Geogrids mid-binder

4.2.4 Model with Geogrids at Mid Binder Layer

The geogrid model showed a better distribution of stress than the model with no geogrids, the geogrids helped to allocate forces by tensioning the geogrids, which often allowed particles to interlock in the asphalt layer, resulting in a better distribution of stresses in the below layers. The model's outcomes as shown in Fig. 11.

5 Conclusions

Upon analyzing the outcomes of both the full-scale model and the finite element model, it was concluded that the use of geogrid reinforcement in the treated base (binder course) layer has significantly enhanced the pavement's performance, in terms of reduced permanent deformation in the AC surface layer as well as better dissipation of induced stresses in the flexible pavement. Moreover, between the two tested geogrid locations, it was concluded that the better location for the geogrid is at the middle of the binder course layer. Upon comparing the obtained enhanced performance ratio to that of a previous study conducted in the American University in Cairo on the use of geogrids in the untreated base layer, it was concluded that geogrids provide better-enhanced performance in treated base layers than in untreated, such that it resulted in around 400% enhanced performance when placed in the treated base versus only 30% in the untreated base.

References

1. Widodo S, Subagio BS, Setiadji BH (2013) Geogrid as asphalt pavement reinforcement. https://www.researchgate.net/publication/235988364_Geogrid_as_Asphalt_Pavement_Reinforcement
2. Moghadas Nejad F et al (2015) Effect of using geosynthetics on reflective crack prevention. Int J Pavement Eng 16(6):477–487. *EBSCOhost*. https://doi.org/10.1080/10298436.2014.943128
3. Moussa G (2003) The optimum location of geotextile reinforcement in asphalt layers. 42. https://www.researchgate.net/publication/237276621_The_optimum_location_of_geotextile_reinforcement_in_asphalt_layers
4. Gu F, Luo X, Luo R, Lytton RL, Hajj EY, Siddharthan RV (2016) Numerical modeling of geogrid-reinforced flexible pavement and corresponding validation using large-scale tank test. Constr Build Mater 122:214–230. ISSN 0950–0618. https://doi.org/10.1016/j.conbuildmat.2016.06.081
5. Al-Qadi IL et al (2008) Geogrid in flexible pavements: validated mechanism. Transp Res Rec 2045(1):102–109. https://doi.org/10.3141/2045-12
6. Ferrotti G, Canestrari F, Virgili A, Grilli A (2011) A strategic laboratory approach for the performance investigation of geogrids in flexible pavements. Constr Build Mater 25(5):2343–2348. ISSN 0950–0618. https://doi.org/10.1016/j.conbuildmat.2010.11.032
7. Abu-Farsakh MY et al (2014) Mechanistic–empirical analysis of the results of finite element analysis on flexible pavement with geogrid base reinforcement. Int J Pavement Eng 15(9):786–798. *EBSCOhost*. https://doi.org/10.1080/10298436.2014.893315
8. Siriwardane H, Gondle R, Kutuk B (2010) Analysis of flexible pavements reinforced with geogrids. Geotech Geol Eng 28:287–297. https://doi.org.libproxy.aucegypt.edu/10.1007/s10706-008-9241-0
9. Imjai T, Pilakoutas K, Guadagnini M (2019) Performance of geosynthetic-reinforced flexible pavements in full-scale field trials. Geotext Geomembr 47(2):217–229. ISSN 0266–1144. https://doi.org/10.1016/j.geotexmem.2018.12.012
10. Abdesssemed M, Kenai S, Bali A (2015) Experimental and numerical analysis of the behavior of an airport pavement reinforced by geogrids. Constr Build Mater 94:547–554. ISSN 0950–0618. https://doi.org/10.1016/j.conbuildmat.2015.07.037
11. Venkateswarlu H, Ujjawal KN, Hegde A (2018) Laboratory and numerical investigation of machine foundations reinforced with geogrids and geocells. Geotext Geomembr 46(6):882–896. ISSN 0266–1144. https://doi.org/10.1016/j.geotexmem.2018.08.006
12. Illukpitiya P, Gopalakrishnan C (2004, March 5) Decision-making in soil conservation: Application of a behavioral model to potato farmers in Sri Lanka. Land Use Policy. https://www.sciencedirect.com/science/article/abs/pii/S026483770400002X

Defect Based Condition Assessment of Steel Bridges

A. Elbeheri, A. Bagchi, and T. Zayed

1 Introduction

After a comprehensive review for steel bridge NDT, it was found that each technology has more capabilities for one or more type of defects but not valid for all types of defects which necessitate that two or more technology to be combined to have the most reliable Bridge evaluation. In researcher's other publication a proposed NDE combine two method, Image Processing, and IR thermography to detect both surface (Corrosion) and subsurface defects (Cracks). As a result of using more than one measure for inspection it was a must to develop a model which combine defects different measures and come with a unified condition index.

2 Steel Bridges

At the time the first iron and steel bridges were being built there was little knowledge about the special advantages and disadvantages of these new materials. Research on steel bridges often was initiated by dramatic bridge failures or a series of smaller defects. From an engineer's point of view, it is easy to reduce bridge collapses to

A. Elbeheri (✉) · A. Bagchi
Concordia University, Montreal, Canada
e-mail: a_elbeh@live.concordia.ca

A. Bagchi
e-mail: ashutosh.bagchi@concordia.ca

T. Zayed
Hong Kong Polytechnic University, Hong Kong, China
e-mail: tarek.zayed@polyu.edu.hk

S. Walbridge et al. (eds.), *Proceedings of the Canadian Society of Civil Engineering Annual Conference 2021*, Lecture Notes in Civil Engineering 240,
https://doi.org/10.1007/978-981-19-0507-0_54

errors in design or to material flaws. However, human, and economic losses should be reminders of the importance to study the causes carefully in order to avoid repetition.

2.1 Steel Bridges Main Defects

2.1.1 Cracks

Ductile failure, brittle fracture, and buckling/instability usually occur under static loading conditions wherein the applied load exceeds a critical load. In contrast, most structures are subjected to repeating loads of varying magnitude, which are most often below yield strength and design stress levels. Fatigue failure is characterized by the initiation and growth of a cracks due to the repeated loading of the structure, which generates microscopic inelastic damage at regions of local stress concentration [24].

2.1.2 Corrosion

Corrosion is one of the most important causes of deterioration in steel bridges. In the United States 40% of the bridges are built of steel 00oo-0. In some states, such as Michigan, the number exceeds 60% [15]. There is a need for rational criteria which can be used to determine the actual strength and remaining life of existing structures. The primary cause of corrosion is the accumulation of water and salt (marine environment or deicing media) on bridge steel. The source of water and salt is either from deck leakage or from the accumulation of road spray and condensation. The source of the moisture often determines the pattern of corrosion on a bridge. The rate of corrosion will depend upon the contaminants in the moisture and the ambient temperature.

According to [15] there are five main forms of corrosion which can affect a steel girder bridge. The most prevalent form is a general loss of surface material, this condition will lead to the gradual thinning of members.

To evaluate the effects of corrosion on structural performance, the various regions where corrosion will occur must be evaluated in terms of net remaining area, structural behavior, and structural loading. The loss of section in a component will cause a reduction in the carrying capacity of that component. The amount of capacity reduction will depend on whether the component is in tension or compression. Tension capacity is computed as the net remaining area times the tensile strength. Compressive capacity depends upon the net area, geometry, and boundary conditions of the element. In a steel girder, corrosion may affect the capacity in bending, shear, and bearing. Bending will be considered mainly at the mid-span of a girder or above an intermediate support.

2.1.3 Creep

Vecchio and LPI [24] Described Creep as the damage accumulated from inelastic deformation of plain carbon and alloy steel under constant load even if the service stress is substantially below the yield strength as a result of thermal activation at elevated temperatures.

3 Defects Assessment Aggregation

A composite indicator (CI) refers to an index derived from some specific individual indicators for measuring the aggregated performance of a multi-dimensional issue. Technically, it is a mathematical aggregation of a set of individual indicators that measure multi-dimensional concepts but usually have no common units of measurement [22]. To a large extent, the usefulness of a CI depends heavily on the underlying construction scheme. According to [22], its construction involves the definition of study scope, selection of underlying variables, data collection and pre-processing, data weighting and aggregation, and post analysis of the CI derived, among which data weighting and aggregation has been an interesting but controversial topic [8].

Multi-criteria decision making (MCDM) is a well-established methodology that could guide/help decision makers to evaluate existing or potential alternatives where multiple conflict criteria exist [9]. It has been widely applied in many areas, including the construction of composite indicators (CIS). A problem in applying MCDM to construct a CI is the determination of an appropriate MCDM method. While there are many alternative MCDM methods, none could the most suitable Solution.

Multi-criteria decision techniques are used for problems that involve various alternatives which need to be compared against a set of criteria that are conflicting in preferences (increasing or decreasing) or are measured in differing units. The steps of formulating such problems are shown as well as the guidelines for selecting the suitable technique for the problem at hand.

3.1 Previous MCDM Applications

MCDM have been widely applied in many different fields. For instance, it was used in facility layout selection [16], laser cutting applications [18], and facility layout selection (Chakraborty, Ray, and Dan 2013). Further, it was employed in the selection and ranking of qualified personnel [1] and maintenance contractors [5].

Madic et al. [18] used a new MCDM method called Weighted aggregated sum product assessment (WASPAS) to determine the optimum combination of various parameters in laser cutting. This method combined two well-known MCDM methods namely: the weighted sum method (WSM) and the weighted product method (WPM). The weights of the criteria were determined by using the analytical hierarchy process

(AHP) method since not all of them have the same level of importance. Complete ranking of the nine alternatives was carried out using the WASPAS method. To validate and check the stability of this ranking, the same problem was solved using the operational competitiveness ratings analysis method (OCRA) and the results revealed the perfect correlation between the rankings obtained using the two methods with a Spearman's correlation coefficient value of 0.95.

Kuo et al. [16] used data envelopment analysis (DEA) to solve the problem of facility layout selection for a company in Taiwan. DEA is a linear programming technique that can assess the efficiency of production units characterized by multiple outputs and inputs. The efficiency is calculated as a weighted sum of its outputs divided by the weighted sum of its inputs and is constrained to the interval (0,1).

Howard [12]highlighted that the weighted sum method (WSM) is the simplest and most widely applied MCA technique. It has been used many times such as evaluating ground water extraction options in Northern Adelaide Plains of South Australia by [13]. WSM is also used in various environmental management and water resource planning applications.

The simple additive weighting (SAW) method has been widely applied in a variety of critical MCDM problems. A study conducted in [25] indicated the superiority of this technique over others including the Weighted Product Method (WPM). Further, it was used by [1]to facilitate the selection of qualified personnel in an organization in the Telecommunication sector in Iran, owing to the great effect this selection process has on the quality of the workmanship in public and private entities. Therefore, a framework was developed using the SAW method to aid in the analytical decision-making process involved rather than relying on intuitive decisions.

The framework proposed by Chou et al. [7]integrates simple additive weighting with fuzzy set theory and the factor rating system to evaluate facility location alternatives. This is one of the most critical decisions in supply chain management and design as the strategic location of the various facilities such as: warehouses and distribution centres maximizes performance and profitability. The SAW method proved to be less exhaustive and time consuming compared to other complex methods such as the AHP, especially with numerous criteria. The proposed approach was applied to a previous problem and the results were the same which proves that the method is reliable and efficient.

Grey system theory is based on the ability to predict future events by making use of limited older data that is inadequate to build a reliable model. Omoniwa [23] used grey relational analysis (GRA) to solve Multi Criteria Robot Selection Problems in a fast and accurate manner, It was capable of differentiating between alternatives, a property that is lacking in many MCDM methods and thus may present multiple choices [23]. The results indicated how simple this technique is to implement and provide satisfactory results to aid the decision maker [23].

The effectiveness of construction and maintenance activities depends on many conflicting and interconnected factors regarding the owner and the contractor. The owner aspires to minimizing the cost, having a certain time schedule for completion and having an acceptable level of service and quality of work. At the same time,

the contractor aims to satisfy the client/owner and minimize the cost and disturbances. The traditional selection method is to award the contract to the lowest bidder. However, as important as this factor is, it is obviously not sufficient as a selection criterion. The MOORA method was applied for the selection and ranking of the 15 largest maintenance contractors of dwellings in Vilnius, Lithuania in a non-subjective way. This method was employed to ensure the selection of the suitable contractor in order to give the stakeholders the confidence that this contractor is able to achieve the project goals [5].

The success and competitiveness of a manufacturing organization is highly dependent on the proper selection of materials. An incorrect selection may have catastrophic effects of premature failure of the final product. Since each available material has its own advantages, disadvantages, functional characteristics and limitations, the designer should have a clear understanding of the criteria and objectives involved in the selection process [14]. Therefore, MOORA method was applied in this study as it provides a logical, systematic and non-subjective approach to make a decision. The ranking obtained by this approach was highly accurate compared to the earlier studies conducted on the same decision-making problem, which proves its effectiveness. Another manufacturing application was discussed by Chakraborty [6] which involved the selection of automated inspection systems, flexible manufacturing systems, and industrial robots. The top ranked alternatives corroborate the results obtained by previous studies for these problems. This provides solid evidence for the flexibility and reliability of this adopted approach.

3.2 Ranking Systems for Assigning Weights

Several research efforts have utilized MCDM in the area of construction management such as green construction rating systems [20], feasibility studies ([19], 59–68) and others. It is important to decide on assigning the correct weights for the criteria included in the multi-criteria decision-making problem [17]. Literature contains numerous methods that are used to calculate the weights of criteria such as: the Analytical Hierarchy Process (AHP) [17], Fuzzy Logic [21], preference ranking organization method for enrichment evaluations (PROMETHEE) [4] and Simos' ranking method [20].

Simos' ranking method is considered one of the simple approaches that has the ability to convert the numerical values assigned by decision makers to weights. This procedure is widely accepted as it has proven its success when applied in many real-life applications giving realistic results [10]. According to this method, each criterion is written on a card and all the cards are given to the user to rank them from the least important to the most important. If the user wishes to give two or several criteria the same rank, s/he is asked to hold these cards together as a subset. Afterwards, the user is asked to illustrate the importance between the ranked criteria by placing white cards between successive cards (criteria). As per the ranking given to the cards, a numerical value is given to each criterion representing the degree of its importance

and these values are used to find the non-normalized and normalized weights of the criteria [10].

The AHP technique allows the hierarchical formulation of a complex problem where criteria are clustered and grouped [17]. Decision makers are required to make consistent pair-wise comparison between the criteria using the nine-scale of measurement with the aim of calculating the global priorities for them. This process has its drawbacks because as the problem complexity increases (many criteria involved), the consistency in expressing the knowledge is likely to decrease as the process tends to be very confusing. There is a measure to monitor the inconsistency called the "Consistency Ratio" that shouldn't exceed 0.1 to guarantee consistent results. In case of inconsistency, the re-assessment process will be tedious and very time consuming which tends to be very impractical especially in situations where time is crucial and a quick solution for the problem is needed [17].

As a result, Simos' ranking method is preferred in cases that involve a large number of criteria to avoid the inconsistency issues. Another reason is that the large number of matrices involved will be incredibly time consuming and confusing for the experts filling them.

4 Development of Defects-Based Aggregation Model

Aggregation process consist of two main steps, 1—calculation the weights for each defect, 2—calculation the overall index according to these weights.

4.1 Calculating Attributes Weights

Calculating attributes weights is a very crucial in decision making process. The weights of criteria affect the decision taken by experts and decision makers in substantial manner. This section discusses Shannon entropy to calculate the weights of different defect. Two defects where considered in this study Corrosion and cracks as most of municipalities consider only these two.

Shannon Entropy

The concept of Shannon entropy is introduced in order to calculate the weights of attributes. Shannon introduced the concept of information entropy in 1948 [11]. Entropy can be defined as average amount of information [2] The criteria weights in the entropy method are calculated according to the degree of index dispersion [2]. Shannon entropy calculation methodology is divided into four steps [2]:

The first step is to calculate the Weight (P_{ij}) which is calculated using Eq. 1.

$$P_{ij} = \frac{x_{ij}}{\sum_{i=1}^{m} x_{ij}} (1 \leq i \leq m, 1 \leq j \leq n) \tag{1}$$

where; P_{ij} represents the weight of the i-th alternative with respect to j-th attribute. x_{ij} represents.

measure of performance of the i-th alternative with respect to j-th attribute. Entropy value of j-th attribute is calculated using equation. The alternative here means the bridge and the attribute means the defect.

The second step is to calculate the Entropy value and it is calculated using Eq. 2:

$$e_j = -k * \sum_{j=1}^{n} P_{ij} * ln P_{ij} (1 \leq i \leq m, 1 \leq j \leq n) \tag{2}$$

where;

$k = \frac{1}{\ln(m)}$ ej refers to the Entropy value of j-th attribute.

The third step is to calculate variation coefficient for different attributes, and it is calculated using Eq. 3.

$$d_j = 1 - e_j \tag{3}$$

where;

d_j represents variation coefficient of j-th attribute.

The fourth step is to weight for each attribute and it is calculated using Eq. 4.

$$w_j = \frac{d_j}{\sum_{j=1}^{n} d_j} \tag{4}$$

where; w_j represents weight of each attribute.

Depending on the process of weights obtained, a suitable MCDM method will be identified.

4.2 Calculation the Overall Index According to These Weights

4.2.1 Weighted Summation Method (WSM)

In this technique, all the criteria are transformed into a scale (from 0 to 1, where 1 represents the best performance) which are multiplied by the weights and then added to calculate a utility score for each alternative. The most preferred alternative is the one that corresponds to the highest and lowest utility score in the case of maximization and minimization, respectively. Equation 5 shows the calculation of the utility score per alternative [19]

$$\mathbf{P_i} = \sum_{\mathbf{j}=1}^{\mathbf{n}} \mathbf{f_{ij}} \times \mathbf{w_j} (1 \leq \mathbf{i} \leq \mathbf{m}, 1 \leq \mathbf{j} \leq \mathbf{n}) \tag{5}$$

where; P_i represents the WSM score of each alternative, f_{ij} represents measure of performance of the ith alternative in terms of the j-th criterion, w_j represents the weight of importance of the jth criterion and m, n represents number of alternatives and criteria, respectively.

4.2.2 Simple Additive Weighting (SAW)

The Simple Additive Weighting method (SAW) is among the most widely used multi-criteria decision-making problem. This method is relatively simple and easy to use compared to other MCDM techniques, which makes it easily adopted by any interested parties. It can provide a complete ranking of the proposed alternatives. It can account for both increasing (maximizing) and decreasing (minimizing) criteria in the same assessment in a simple way. The most important advantage of this method is the way it deals with the raw data (the performance measure of each alternative against each criteria/attribute) using a proportional linear transformation keeping the relative order of the magnitude of these measures equal [25].

This method is based on the concept of the weighted average [25] and consists of two main steps namely: 1—enabling the comparison of the decision criteria by scaling them and then, 2—adding the scaled values of all criteria to calculate a score for each alternative and rank the proposed alternatives [1].

The first step is normalizing the score of each alternative in each criterion as per Eq. 6 for the maximizing criteria and Eq. 7 for the minimizing criteria.

$$r_{ij} = x_{ij} \Big/ \left(\max_i x_{ij} \right). \tag{6}$$

$$1/x_{ij} \Big/ \left(\max_i x_{ij} \right). \tag{7}$$

Then, the preference of an alternative is computed as per Eq. 8 ([20], 176–182):

$$S_i = \sum_{j=1}^{M} w_j \times r_{ij} \tag{8}$$

where; S_i is the preference of the ith alternative, r_{ij} is the normalised score of the ith alternative for the jth criterion, x_{ij} is an element represents the original value of the jth criterion of the ith alternative, w_j is the importance (weight) of the jth criterion, n is the number of alternatives, m is the number of criteria.

4.2.3 Group Decision Making

Group decision making is very important to aggregate results obtained from the two multi-criteria decision-making techniques which will provide consensus decision making. This section introduces the group decision making technique adopted in this research which is called Additive Group Ranking Technique [3]. This method calculates the final index of each bridge as per Eq. 9 using the index obtained for that bridge from the several decision-making techniques used.

$$r^G = 1 - \frac{\sum_{DM=1}^{G} w_{DM} \times r_{DM}}{G} \tag{9}$$

where, r^G represents rank obtained for each alternative by group decision-making method, r_{DM} represents rank obtained for each alternative from decision-making method, w_{DM} represents relative influence of each decision-making method and G represents number of decision-making techniques.

5 Data Analysis and Collection

The main key data for the proposed model is the data needed for Shannon entropy model as it will define the weights of each defect. For these data we rely on inspection report from deferent municipalities in Canada. the main available municipal reports was from MTQ (Quebec, Canada), MTO (Ontario, Canada) and Alberta, Canada. Each group of reports will be processed Separately as each municipality has its own system and preferences. From then the weights of each defects will be calculated and the rest of condition rating process will be proceeded.

6 Conclusions

This research targeted the development of a comprehensive bridge condition assessment tool that can translate Different detected defect measurements into detailed and informative bridge condition rating. It is believed that the proposed approach will assist in reducing sources of data uncertainty in the bridge inspection process, whether originating from the subjectivity involved in visual inspection or from the imprecision of non-destructive evaluation techniques. Overall, the presented model aims at making condition assessment reliably express the detected bridge defects.

References

1. Afshari A, Mojahed M, Yusuff RM (2010) Simple additive weighting approach to personnel selection problem. Int J Innov Manage Technol 1(5):511
2. Akyene T (2012) Cell phone evaluation base on entropy and TOPSIS. Interdisc J Res Bus 1(12):9–15
3. Banerjee R, Ghosh DN (2013) Faculty recruitment in engineering organization through fuzzy multi-criteria group decision making methods. Int J u-and e-Serv Sci Technol 6(4):139–154
4. Brans J-P, Vincke Ph, Mareschal B (1986) How to select and how to rank projects: the PROMETHEE method. Eur J Oper Res 24(2):228–238
5. Brauers WKM, Zavadskas EK, Turskis Z, Vilutiene T (2008) Multi-objective contractor's ranking by applying the Moora method. J Bus Econ Manag 9(4):245–255
6. Chakraborty S (2011) Applications of the MOORA method for decision making in manufacturing environment. Int J Adv Manuf Technol 54(9–12):1155–1166
7. Chou S-Y, Chang Y-H, Shen C-Y (2008) A fuzzy simple additive weighting system under group decision-making for facility location selection with objective/subjective attributes. Eur J Oper Res 189(1):132–145
8. Esty DC, Levy M, Srebotnjak T, De Sherbinin A (2005) Environmental sustainability index: benchmarking national environmental stewardship. New Haven: Yale Cent Environ Law Policy 47–60
9. Figueira J, Mousseau V, Roy B (2005) ELECTRE methods. In: Multiple criteria decision analysis: State of the art surveys, Springer
10. Figueira J, Roy B (2002) Determining the weights of criteria in the ELECTRE type methods with a revised Simos' procedure. Eur J Oper Res 139(2):317–326
11. Ghorbani M, Arabzad SM, Bahrami M (2012) Implementing Shannon entropy, SWOT and mathematical programming for supplier selection and order allocation. Int J Supply Chain Manage 1(1):43–47
12. Howard AF (1991) A critical look at multiple criteria decision making techniques with reference to forestry applications. Can J For Res 21(11):1649–1659
13. Hyde KM, Maier HR, Colby CB (2004) Reliability-based approach to multicriteria decision analysis for water resources. J Water Resour Plan Manag 130(6):429–438
14. Karande P, Chakraborty S (2012) Application of multi-objective optimization on the basis of ratio analysis (MOORA) method for materials selection. Mater Des 37:317–324
15. Kayser JR, Nowak AS (1989) Capacity loss due to corrosion in steel-girder bridges. J Struct Eng 115(6):1525–1537
16. Kuo Y, Yang T, Huang G-W (2008) The use of grey relational analysis in solving multiple attribute decision-making problems. Comput Ind Eng 55(1):80–93
17. Lin C-C, Wang W-C, Yu, Wen-Der (2008) Improving AHP for construction with an adaptive AHP approach (A3). Autom Constr 17(2):180–187
18. Madic M, Antucheviciene J, Radovanovic M, Petkovic D (2016) Determination of manufacturing process conditions by using MCDM methods: application in laser cutting. Eng Econ 27(2):144–150
19. Marzouk M, Amer O, El-Said M (2013) Feasibility study of industrial projects using Simos' procedure. J Civ Eng Manag 19(1):59–68
20. Marzouk M, Nouh A, El-Said M (2014) Developing green bridge rating system using Simos' procedure. HBRC J 10(2):176–182
21. Moufti SA, Zayed T, Dabous SA (2014) Defect-based condition assessment of concrete bridges: fuzzy hierarchical evidential reasoning approach. Transp Res Rec 2431(1):88–96
22. Nardo M et al (2005) Handbook on constructing composite indicators
23. Omoniwa B (2014) A solution to multi criteria robot selection problems using grey relational analysis. Int J Comput Inform Technol 3(2):329–332
24. Vecchio RS, LPI, Inc. (2006) Condition assessment of steel structures. ASCE
25. Zanakis SH, Solomon A, Wishart N, Dublish S (1998) Multi-attribute decision making: a simulation comparison of select methods. Eur J Oper Res 107(3):507–529

Use of Equivalent Standard Fire Duration to Evaluate the Internal Temperatures in Rc Walls Exposed to Fire

M. Lazhari, M. A. Youssef, and S. F. EL-Fitiany

1 Introduction

Standard fire curves are not suitable for performance-based design because they cannot be correlated to natural fire incidents. They fail to consider compartment-specific parameters. Several temperature–time curves, which have major differences, in implementation and complexity were proposed in the literature to model natural fires [5]. The nature fire severity can be modeled using a standard fire with an equivalent duration [1]. Such an approach has several benefits including the utilization of existing data, testing, and computer programs [1]. Previous methods for estimating the equivalent duration t_e focused on steel members, which highly differ from reinforced concrete (RC) sections in their internal thermal gradients and fire-related properties. The existing time equivalent methods can be divided into thermal and mechanical methods. The mechanical methods are based on structural behaviour while the thermal methods focus on the temperature or thermal energy of an element subjected to fire.

The most common thermal methods are the equal area method, maximum temperature method, and energy method. The equal area method, developed by Ingeborg (1928), is the first widely recognized time equivalent theory. The general idea of this method is finding the t_e at which the area under a chosen design fire curve is equal to the area under the standard fire curve. However, this method ignores the heating rate, maximum temperature, and cooling rate. Therefore, the evaluated t_e can be the same for short hot fires and long cold fires, which have the same area

M. Lazhari (✉) · M. A. Youssef · S. F. EL-Fitiany
Department of Civil and Environmental Engineering, Western University, London, Canada
e-mail: mlazhari@uwo.ca

M. A. Youssef
e-mail: youssef@uwo.ca

S. Walbridge et al. (eds.), *Proceedings of the Canadian Society of Civil Engineering Annual Conference 2021*, Lecture Notes in Civil Engineering 240,
https://doi.org/10.1007/978-981-19-0507-0_55

despite having extremely different heat distribution profiles. The maximum temperature method was [17, 19] defines t_e as the time needed for a standard fire to generate the same maximum temperature as the design fire. The maximum temperature method provides great correlation to natural events because it accounts for compartment area, fuel load, and ventilation. However, it was found to consistently produce unreliable results for concrete members [16, 20]. The thermal energy methods [13] match the cumulative thermal energy from a selected design fire to that from the standard fire. Energy methods are not easy to apply and do not consider the specific energy input needed to develop the internal gradients for RC sections.

The mechanical methods include the load capacity and maximum deflection methods. The Load capacity method focuses on the mechanical response of an isolated element exposed to fire [16]. This method supplies a greater level of accuracy in evaluating the fire severity on load capacity. However, section capacity is highly influenced by the cross-section details. Therefore, the method requires significant computational and/or experiments. Also, it leaves potentially wide deviations in other load responses, deflections, and interactions at the system level.

The maximum deflection method calculates the t_e based on the maximum deflection of an isolated element [1]. This method provides greatly accurate deflection predictions; however, it focuses on a single mode of failure (deflection) similar to the load capacity method.

This paper highlights the importance of internal thermal gradients in RC walls. It proposes simple equations to determine the t_e for RC walls exposed to natural fire incidents from one side. A similar approach was utilized by Kuehnen and Youssef [14] for RC beams.

2 Thermal Gradient in RC Wall Section

For RC walls exposed to fire, the temperature level slowly transfers from the surface to the inner layers, which leads to the development of large thermal gradients. Figure 1 shows a qualitative representation of the average internal temperature profile for RC walls subjected to fire on one side. The RC section is first divided into a two-way mesh to conduct heat transfer analysis as presented in Fig. 1a. The maximum temperature is recorded at the mesh points for the duration of the fire exposure. Then, as shown in Fig. 1b, the meshed units are grouped into horizontal layers and the average temperature is calculated for each layer to allow conducting sectional analysis considering bending about the weak axis of the wall. Figure 1c represents the maximum average temperature for each layer throughout the fire period.

The maximum temperature of each layer occurs at the end of the fire duration for a standard fire. However, for natural fires, thermal inertia at the start of the Cooling phase results in a temperature Lag, with some inner layers reaching their maximum temperature shortly after the fire begins to decay [8]. Therefore, the average internal temperature profile is not representing case-specific but rather represents the most severe fire effect on the section. [2, 6–8, 23] demonstrated the suitability of

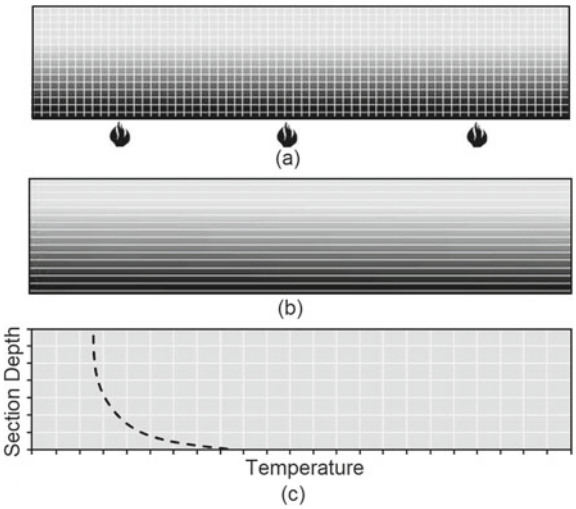

Fig. 1 Heat transfer modelling: **a** Heat transfer mesh, **b** Average temperature layers, and **c** average temperature profile

average internal temperature profiles to conduct performance-based design considering fire events. The importance of assessing internal thermal gradients during the performance-based design of fire-exposed RC members was also highlighted by [21] and Guo and Shi [10].

3 Time Equivalent Parametric Study

A parametric study was conducted to evaluate the equivalent t_e. There are two widely used standard fire curves, which are ASTM and ISO standard fires [3] and [12]. In this study, the ISO standard fire was proposed to identify t_e. The three main parameters to characterize the general shape of a natural fire are the maximum temperature (T_{max}), time of maximum temperature (t_{max}), and total duration (t_{total}). The valid range for the three-main parameters has been determined based on the natural fires mentioned in the literature [4, 11]. Values for t_{max} were chosen at 5 min intervals resulting in values ranging from 15 to 120 min; values of t_{total} were chosen at 10 min intervals resulting in fire durations ranging from 20 to 240 min, and T_{max} values were chosen to start at 350 °C, then increase at 50 °C intervals until reaching 700 °C, then at 25 °C intervals until reaching 1200 °C. In this study, a total of 10,781 design fires were considered.

Using the three parameters mentioned above, the full design fire curve can be developed. The heating branch is defined using equation A.1 of the Eurocode code [9], then a linear profile is assumed for the cooling branch. The cross-section of the theoretical concrete wall was selected as 3000 by 300 mm. The thermal conductivity, density, and specific heat of siliceous aggregates were determined using the relationships provided by [15].

Table 1 Coefficients for Eq. (1) for t_{max} from 15 to 120 min and t_{final} from 20 to 240 min

	Mean criterion	Conservative criterion			
T_{max} (°C)	350–1200	350–750	751–950	951–1100	1101–1200
Coefficient					
X_1	−39.43000	−21.0100	−5.540000	592.0000	−999.6000
X_2	−0.132940	−0.06524	−0.109840	−0.790000	−11.60800
X_3	0.683100	0.67558	0.813800	2.207000	6.211000
X_4	0.084150	0.07901	0.010900	−1.366000	0.932200
X_5	−0.000624	−0.00015	0.000000	−0.001000	−0.003421
X_6	−0.000306	−0.000799	−0.000317	0.001518	0.003353
X_7	−0.000039	−0.000077	0.000000	0.000799	0.000000
X_8	0.000618	0.000406	0.000309	−0.001482	−0.009232
X_9	0.000093	−0.000070	0.000000	0.001122	0.012169
X_{10}	0.000319	0.000607	0.000243	−0.001628	−0.005455

3.1 Methodology and Results

The finite difference method (FDM) is utilized to conduct the heat transfer analysis. Details of the proposed method can be found in [15]. For each natural fire, the average internal temperature profile (AITP-D) is first evaluated. Then, the average internal temperature profile for a standard fire (AITP-S) with duration t is evaluated. To define the mean t_e, the duration t is incrementally increased until the mean difference between AITP-D and AITP-S for the section layers reaches a minimum value. A conservative t_e was also defined, where the duration t is incrementally increased until the AITP-S provides higher temperatures than AITP-S for all section layers.

The obtained t_e values were then examined, which led to the development of Eq. (1) for walls exposed to fire from one side. The equation and coefficients (X_1 to X_{10}), shown in Table 1, were calculated using least-squares regression analysis, with probability (p) < 0.001 and correlation (R^2_{adj}) > 95%. The obtained t_e values using the equation have a maximum error of 15%. This error is unavoidable due to the extreme in temperature between the surface and inner layers.

$$t_{eq} = X_1 + X_2 t_{max} + X_3 t_{total} + X_4 T_{max} + X_5 t_{max}^2 + X_6 t_{total}^2 + X_7 T_{max}^2 + X_8 t_{max} t_{total} + X_9 t_{max} T_{max} + X_{10} t_{total} T_{max} \frac{T_{max}}{t_{total}} > 60\text{Cperminute} \quad (1)$$

To further show the validity of Eq. 1, results for a RC wall with a cross section of 3000 by 300 mm are presented. Figure 2 presents the average internal temperature profile considering selected design fire (AITP-D) with maximum temperature 550 °C at 15 min and total duration of 20 min. It is clear that the AITP-S mean provides closer predictions than the AITP-S conservative, which had relatively high error

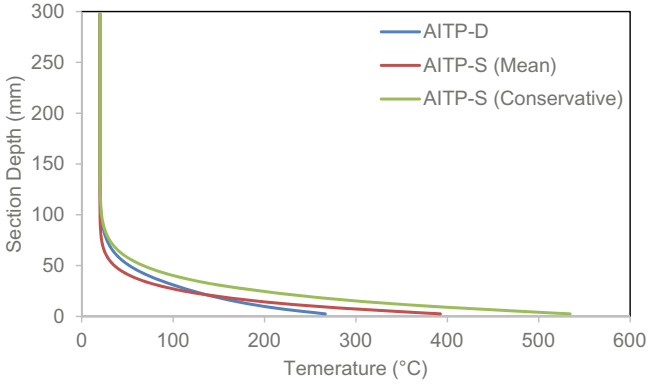

Fig. 2 Average internal temperature profile of AIPT-D, AITP-S (mean), and AITP-S (conservative) at a maximum temperature of 550 °C

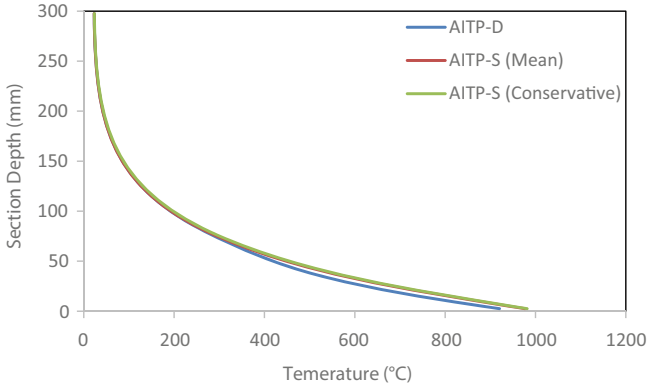

Fig. 3 Average internal temperature profile of AIPT-D, AITP-S (mean), and AITP-S (conservative) at a maximum temperature of 1000 °C

at the section surface to ensure that the average layer temperature for all sections is higher than the AITP-D. Figure 3 represents average internal temperature profiles for the RC wall considering design fire (AITP-D) with maximum temperature 1000 °C at 95 min and total duration of 120 min. For this fire incident, it can be seen that both the AITP-S mean and conservative estimates are having better fit with the AITP-D.

4 Conclusions

RC walls are essential structural components for any building. Therefore, it is important to study their performance under fire loads. Majority of the published methods

for structural fire engineering are based on standard fire curves. This paper provides a simple approach to convert a natural fire curve to an equivalent standard fire, and thus allow the use of data available in the literature. Two equivalent durations are proposed in this research. One provides more accurate results but can be unconservative, while the second is conservative but can produce higher errors. The errors resulting from both methods was found to reduce for long duration fires.

Acknowledgements The authors are grateful for the financial support provided by the Libyan Ministry of Education, the National Science and Engineering Research Council of Canada (NSERC), and Western University.

References

1. Buchanan AH (2001) Structural design for fire safety, 2nd edn. Wiley
2. Alhadid M (2017) Behavior of fire-exposed RC frames before and after jacketing. Department of Civil and Environmental Engineering, Western University, Diss
3. ASTM E-119 (2018) Standard test methods for fire tests of building construction and materials. American Society for Testing and Materials, West Conshohocken, PA, USA
4. Byström A, Xudong C, Wickström U, Milan V (2012) Measurement and calculation of adiabatic surface temperature in a full-scale compartment fire experiment. J Fire Sci 31(1):35–50
5. Cooper LY, Steckler KD (1996) Methodology for developing and implementing alternative temperature-time curves for testing the fire resistance of barriers for nuclear power plant applications
6. El-Fitiany SF, Youssef MA (2014) Simplified method to analyze continuous reinforced concrete beams during fire exposure. ACI Struct J 111(1)
7. El-Fitiany SF, Youssef MA (2009) Assessing the flexural and axial behaviour of reinforced concrete members at elevated temperatures using sectional analysis. Fire Saf J 44(5):691–703
8. El-Fitiany SF, Youssef MA (2017) Fire performance of reinforced concrete frames using sectional analysis. Eng Struct 142:165–181
9. EN 1991–1–2 (2002) Eurocode 1: actions on structures—Part 1–2: actions on structures exposed to fire, European Committee for Standardization, Brussels, Belgium
10. Guo Z, Shi X (2011) Strength of concrete at elevated temperatures. Exp Calculation Reinf Concr Elevated Temp 2–16
11. Implementation of Eurocodes (2005) Handbook 5—Design of buildings for the fire situation. Leonardo Da Vinci Joint Research Project
12. ISO 834 (2014) Fire resistance tests—Elements of building construction. International Organization for Standards, Geneva, Switzerland.
13. Kodur VKR, Pakala P, Dwaikat MB (2010) Energy based time equivalent approach for evaluating fire resistance of reinforced concrete beams. Fire Saf J 45(4):211–220
14. Kuehnen RT, Youssef MA (2019) Equivalent standard fire duration to evaluate internal temperatures in natural fire exposed RC beams. Fire Saf J 108:102831
15. Lie TT (1992) Structural fire protection: manual of practice. American Society of Civil Engineers, New York, NY
16. Xie P, Abu A, Spearpoint M (2015) Comparison of existing time-equivalent methods and the minimum load capacity method. In: Harada K et al (eds) 10th Asia-Oceania Symposium on Fire Science and Technology, Fire Science and Technology, Tsukuba, Japan, pp 263–271
17. Pettersson O. (1975) The connection between a real fire exposure and the heating conditions according to standard fire resistance tests: with special application to steel structures. Lund, Sweden: Lund Institute of Technology, Division of Structural Mechanics and Concrete Construction

18. Purkiss JA, Li LY (2017) Fire safety engineering design of structures. CRC Press, Boca Raton, FL
19. Schneider U, Kersken-Bradley M, Max U (1990) Neuberechnung der Wärmeabzugsfaktoren w für die DINV 18230: Teil 1 - Baulicher Brandschutz Industribau. Fraunhofer IRB Verlag, Stuttgart, Germany (In German)
20. Thomas G, Buchanan A, Fleischmann C (1997) Structural fire design: the role of time equivalence. Fire Saf Sci 5:607–618
21. Wang Y, Burgess I, Wald F, Gillie M (2012) Performance-based fire engineering of structures
22. Xie P, Abu A, Spearpoint M (2015) Comparison of existing time-equivalence methods and the minimum load capacity method. Fire Sci Technol 2016:263–271
23. Youssef MA, Diab MA, El-Fitiany SF (2015) Shear capacity of RC beams at elevated temperatures. Mag Concr Res 67(22):1190–1203

Feasibility of Using Fiber-Reinforced Polymer Bars as Internal Reinforcement in Concrete Arch Slab Bridges

S. El-Gamal, H. Al-Shukeili, and A. Al-Nuaimi

1 Introduction

Bridges have a very important role in the transportation system because they connect places and ease movement with less time. There are different types of bridges such as arch bridges, beam bridges, truss bridges, and suspension bridges. Arch bridges are very ancient structures, which were usually built of stone and masonry blocks. Since the second half of the nineteenth century, most bridges have been constructed of reinforced concrete (RC). Similar to several RC structures especially those in harsh environments, RC arch bridges are facing some problems such as steel corrosion. Engineers and researchers found that Fiber Reinforced Polymer (FRP) is a good alternative of steel because of its excellent corrosion-resistant, lightweight and high tensile strength. Its stiffness is also good although it is less than the stiffness of steel. Several research and field studies investigated using of FRP bars as steel alternative in new structures including bridges [1, 3, 8–10], parking garage slabs [5–7], and concrete pavement [2, 4, 11]. Most of these research studies and field applications investigated the use of FRP bars in straight structural elements such as slabs.

Some research studies investigated the use of FRP sheets for the rehabilitation of existing RC arch slabs. Zanardo et al. [14] evaluated the performance of some short span RC arch bridges in Italy. Because the bridges were not safe according to the new design codes, they were retrofitted with FRP sheets. They concluded that the ultimate bending moments have been improved after strengthening. Zhang et al. [15] strengthened five small-scale RC arches using CFRP sheets and strips. They

S. El-Gamal (✉)
Department of Civil and Architectural Engineering, Sultan Qaboos University, (On Leave From Menoufia University, Egypt), Muscat, Oman
e-mail: sherif@squ.edu.om

H. Al-Shukeili · A. Al-Nuaimi
Department of Civil and Architectural Engineering, Sultan Qaboos University, Muscat, Oman

S. Walbridge et al. (eds.), *Proceedings of the Canadian Society of Civil Engineering Annual Conference 2021*, Lecture Notes in Civil Engineering 240,
https://doi.org/10.1007/978-981-19-0507-0_56

concluded that strengthening enhanced their capacity and improved their rigidity. Xie et al. [13] investigated the behavior of CFRP-strengthened buried RC arches subjected to subsurface localized impulsive loads. They concluded that using CFRP strips as a strengthening material in buried arches restricted the structural failure and enhanced the rigidity and the capacity. Wang et al. [12] studied the behavior of strengthened RC arches (which are exposed to blast loading) with CFRP sheets using different configurations. They concluded that fully strengthened arches had the highest blast resistance.

To the knowledge of the authors, no studies have investigated the use of FRP bars as internal reinforcement in new arch slabs. The behavior of arch slabs reinforced with FRP bars is still not explored. Therefore, it is important to investigate the behavior of concrete arch slab bridges reinforced with FRP bars and to compare their performance with those reinforced with conventional steel. This research study investigates the feasibility of using glass and carbon FRP bars in reinforcing concrete arch slab bridges instead of conventional steel reinforcement.

2 Experimental Program

2.1 Description of Test Specimens

In this project, four arch slabs with similar dimensions were constructed. The arches were a half-scale of an existing RC bridge called Valli-di-Pol Bridge in Italy. Figure 1 shows the dimensions of the arch slabs constructed in this study. All specimens have an outside span of 392.2 cm. The width of the arches is 50 cm and the thickness varies from 10 cm at the middle to 17.5 cm at the ends. Two wooden molds were constructed for the concrete casting of the arch specimens.

Two parameters related to the longitudinal reinforcement of the arches were investigated. This included the type of reinforcement and the reinforcement ratio. The

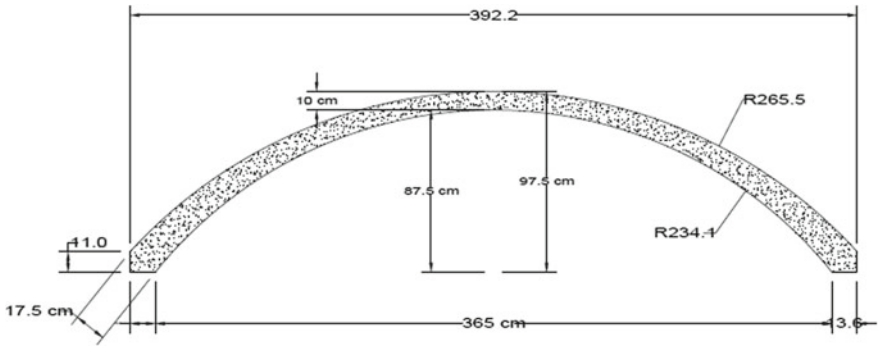

Fig. 1 Dimensions of the constructed arches (all dimensions are in cm)

Table 1 The parameters used in this research

Parameter	Specimen code	Type of reinforcement	Reinforcement in each layer	Total reinforcement ratio (%)
Reinforcement type	S3	Steel (reference)	3ϕ10 T&B (Steel)	0.95
	G3	Glass FRP	3ϕ10 T&B (GFRP)	0.95
Reinforcement ratio	G2	Glass FRP	2ϕ10 T&B (GFRP)	0.63
	G3	Glass FRP	3ϕ10 T&B (GFRP)	0.95
	G4	Glass FRP	4ϕ10 T&B (GFRP)	1.27

where T: top longitudinal reinforcement; B: bottom longitudinal reinforcement

specimens were divided into two groups. Each group contained two or more specimens as shown in Table 1. In the first group, two different reinforcing materials were used for the longitudinal reinforcement: steel (S3) and GFRP (G3). S3 was the reference specimen, which was reinforced with three top and bottom deformed steel bars of 10 mm diameter. G3 had the same amount of reinforcement as S3 but with GFRP bars. The second group included two more specimens (G2 and G4) in addition to the G3 specimen. The FRP reinforcement ratio was increased from 0.95% in G3 to 1.27% in G4 and was decreased to 0.63% in G2. All specimens were reinforced with 8 mm diameter steel links spaced at 300 mm along the arch.

2.2 Properties of Materials

Ready-mix concrete was used to cast the specimens. The average concrete compressive strength was 55.3 MPa with a standard deviation of 3.96, while the average tensile strength from the Brazilian and the flexural tests were 3.1 ± 0.33 MPa and 3.34 ± 0.29 MPa, respectively. Steel and GFRP bars of 10 mm diameter were used as top and bottom longitudinal reinforcement. Steel bars of 8 mm diameter were used as stirrups in all test specimens. The GFRP bars used in this research were manufactured by Pultron Composites, UAE. The mechanical properties of the steel and the GFRP bars are listed in Table 2.

Table 2 Properties of steel and FRP bars

Type	Nominal diameter (mm)	Cross-sectional area (mm^2)	Tensile strength (MPa)	Elastic modulus (GPa)	Ultimate strain (%)
GFRP	10	71.3	1150	60.5	1.90
Steel	10	78.5	446*	210	2.12^{+}
Steel links	8	50.2	255*	205	1.24^{+}

*Yield strength, $^{+}$Yield strain

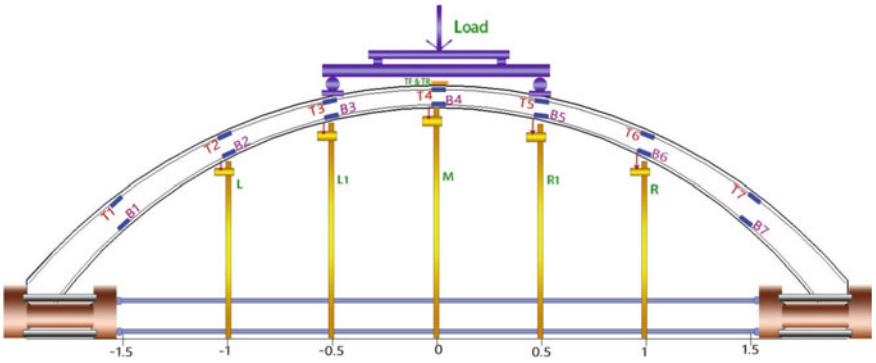

Fig. 2 Schematic view of locations and names of strain gauges and LVDTs

2.3 Construction of Test Specimens

Two wooden forms were constructed and used for concrete casting. To ease fixing the longitudinal bars with the required curvature; tiny holes were drilled on the forms at the ends and at the middle. Concrete cookies were placed on the three locations and tied by steel wires from the backside of the forms. The steel links were then laid and three of them were tied to the concrete cookies. Then, the bottom and the top longitudinal bars were inserted and tied to the links. Before concrete casting, seven strain gauges spaced at 50 cm were installed on the bottom bars as well as on the top bars. In addition, two strain gauges were glued on the top surface of the arches at the mid-span for concrete strains measurements. Furthermore, five LVDTs were used to measure the vertical deflection along the span of the arches. Figure 2 shows the positions and names of the strain gauges and LVDTs.

2.4 Testing Setup

Two steel supports were used to fix the ends of the arches. High strength threaded steel bars (38 mm diameter) were used to connect the two steel supports to prevent any horizontal displacement between them. After adjusting the proper distance between the supports, the arch was mounted on the supports. All arches were loaded using two loads spaced at 1 m using a 250 kN actuator and a spreader beam at a loading rate of 1 mm/min. All readings were automatically recorded using a data actuation system connected to a computer. Figure 3 shows a photo of one arch during testing.

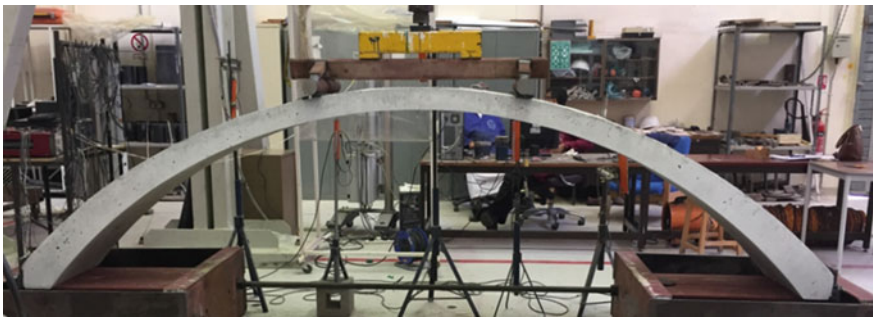

Fig. 3 One arch specimen during testing

3 Test Results and Discussions

3.1 Summary of Test Results

Table 3 summarizes the main test results of this study. The cracking load of all specimens ranged between 32 and 71kN and the number of cracks at failure varied between 25 and 40 cracks as shown in Fig. 4. The minimum ultimate load was 154 kN and the maximum ultimate load was 248.3 kN. Compared to the reference arch (S3), G4 showed higher capacities while G3 and G2 showed lower capacities. The control arch failed by top steel yielding at the quarter span (the position of the maximum negative moment) followed by concrete crushing at the bottom surface of the arch at the same location. The FRP-RC arches failed by concrete crushing at the quarter span followed by FRP crushing or concrete shear failure. All FRP-RC arches showed

Table 3 Summary of test results

Specimen	P_{cr} (kN)	No. of cracks at failure	P_{yield} (kN)	P_{max} (kN)	Δ_{Pmax} (mm)	Capacity increase (%)*	Failure Mode
S3	61	25	187.6	231.4	23.95	–	SY + CC
G2	32	28	–	154.0	34.80	−33.4	CC
G3	46	35	–	194.0	47.32	−16	CC + FC
G4	60	36	–	248.3	32.85	7.4	CC + SF

P_{cr}: cracking load
P_{yield}: yielding load
P_{max}: maximum load
Δ_{Pmax}: Mid-span deflection at maximum load
*Compared to the P_{max} of S3
CC: concrete crushing
SF: shear failure
SY: steel yielding
FC: FRP crushing

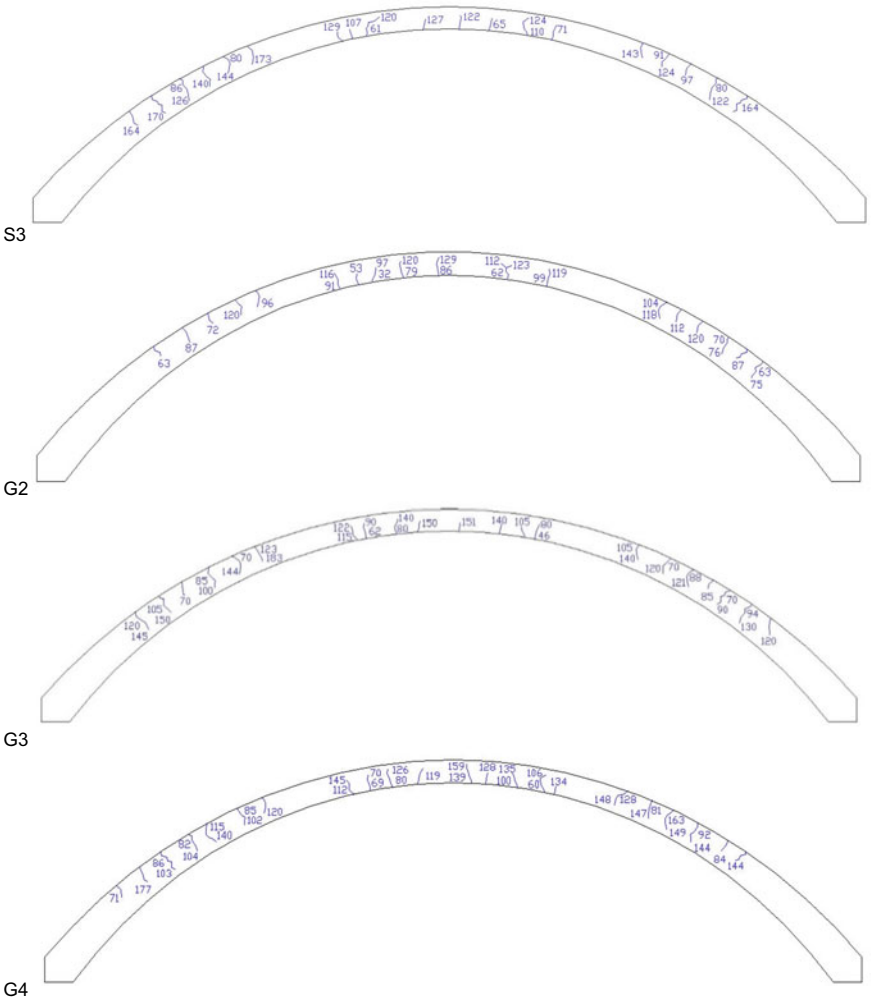

Fig. 4 Crack patterns of all test specimens

higher mid-span deflection at maximum load compared to the reference arch (S3) as shown in Table 3.

3.2 Effect of Reinforcement Type

The two arches with similar reinforcement ratio (S3 and G3) showed a comparable cracking performance; however, S3 showed higher cracking load (61 kN) compared to G3 (46 kN). The number of cracks at failure was higher in G3, which had (35)

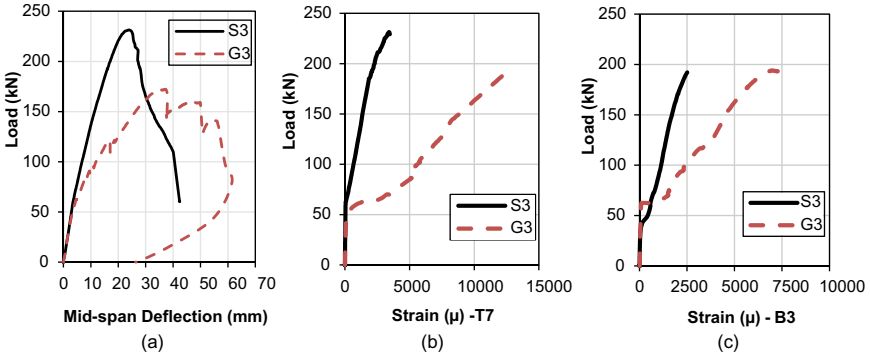

Fig. 5 Effect of reinforcement type (S3 and G3): **a** mid-span deflection; **b** maximum strains in top reinforcement; **c** maximum strains in top reinforcement

cracks compared to 25 cracks in S3 (Table 3). This indicates that using the GFRP bars as reinforcing material resulted in more number of cracks compared to the reference arch reinforced with steel. The top steel at the quarter span of the S3 arch started to yield at a load of 187.6 kN, however, the arch continued to support load until it failed by concrete crushing at a maximum load of 231.4 kN. G3 specimen failed by concrete crushing accompanied with GFRP bars crushing at a maximum load of 194 kN, which was higher than the yield load of S3 but it was lower than its maximum load by 16%.

The load versus mid-span deflections of the two arches is shown in Fig. 5a. Before cracking, the two arches showed similar deflection behavior. After cracking, the S3 arch slab showed lower deflection than the G3 arch slab. It can be seen that, at a load level of about 100 kN, the measured deflection at mid-span in G3 was about 10.3 mm. This value was about 35% higher than the measured deflection in S3. This could be related to the larger stiffness of steel bars compared to the GFRP bars. Figures 5b and 4c show the maximum recorded tensile strains in the top and bottom reinforcement of S3 and G3 arches. These curves show that minor strains were recorded in all specimens at lower load levels then the strains increased rabidly after cracking. Higher strains were recorded in G3 compared to lower strains in S3. For example, at a load level of 150 kN, the maximum strains in the bottom reinforcement of specimen G3 were higher than the measured strain in S3 by 163%. These higher strains in G3 compared to S3 could be also related to the difference in the stiffness between the steel and the GFRP bars. It should be mentioned that the maximum measured tensile strains in the top GFRP bars reached 65% of the GFRP ultimate tensile strains (Table 2). It can be concluded that the G3 arch showed good capacity and comparable behavior to the reference arch (S3). This demonstrates that GFRP bars can be used to replace steel reinforcement in arch slab bridges to enhance their durability and increase their lifetime.

3.3 *Effect of Reinforcement Ratio*

Table 3 shows that the cracking load was 60 kN in G4 ($\rho = 1.27\%$) followed by 53kN in G3 ($\rho = 0.95\%$) and the minimum cracking load was 31kN in G2 ($\rho = 0.63\%$). The cracking load of specimen G3 was only 6% lower than that of G4 but it was 33% higher than that of G2. In addition, at failure, specimen G4 showed a higher number of cracks (36 cracks) than specimens G3 (35 cracks) and G2 (28 cracks). This indicates that the cracking load and number of cracks decreased as the reinforcement ratio decreased. Table 3 also shows that G3 specimen ($\rho = 0.95\%$) had a maximum load of 194kN. When the ratio of the GFRP reinforcement was decreased to 0.63%, the capacity of G2 decreased by 20.6%. On the other hand, when the GFRP reinforcement ratio was increased to 1.27%, the capacity of the G4 arch was increased by about 28%. This indicates that the ultimate capacity increased as the amount of reinforcement increased, which is expected due to the increase in the section capacity. G2 and G3 specimens failed by concrete crushing in the bottom surface of the arches at the quarter span. In the G3 specimen, the concrete crushing was accompanied by the crushing of the bottom GFRP bars. In the G4 specimen, a compression failure occurred at the quarter spans as in G2 and G3, but the arch finally failed by a compression shear failure under one of the loading points as shown in Fig. 6c.

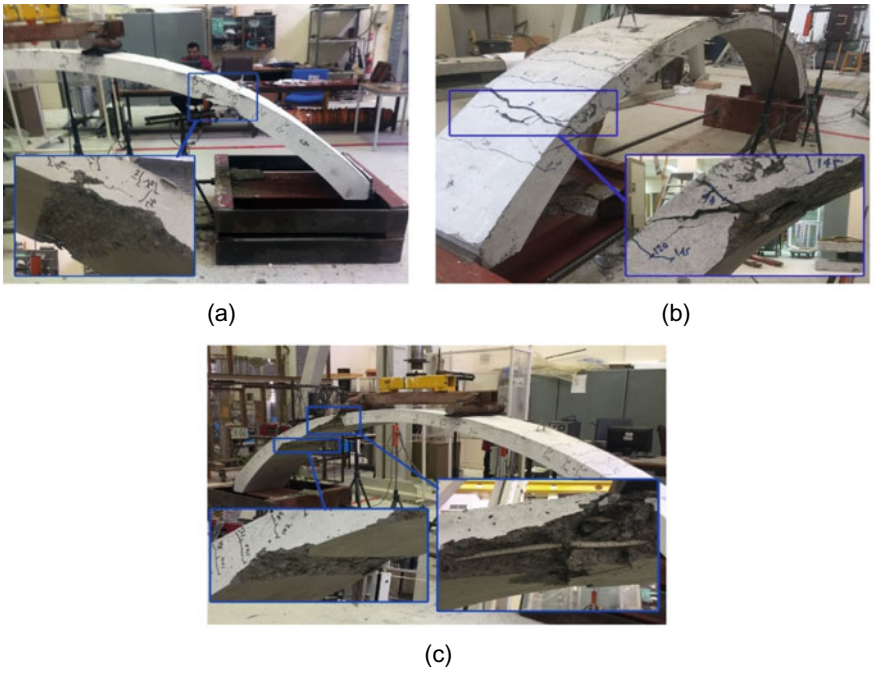

Fig. 6 Failure of test specimens: **a** G2; **b** G3; and (G4)

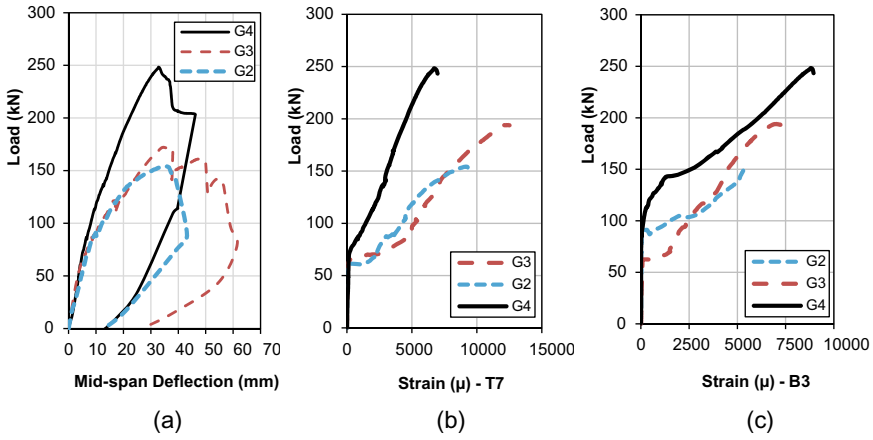

Fig. 7 Effect of reinforcement ratio (G2, G3 and G4): **a** mid-span deflection; **b** maximum strains in top reinforcement; **c** maximum strains in top reinforcement

Figure 7a shows the load versus mid-span deflection curves of the three archs. Before concrete cracking, the behavior was almost similar where small deflections were recorded in the three specimens. After cracking, higher deflections were recorded in G2 followed by G3 and fewer deflection values were recorded in G4. These results imply that the GFRP reinforcement ratio had almost no effect on the deflections at the lower load levels but it shows an effect on the deflections at higher load levels where the mid-span deflections decreased as the reinforcement ratio increased. Figures 7b and 5c show load versus maximum strains in the top and the bottom GFRP reinforcement, respectively. Similar to Group 1 specimens, up to cracking loads, minor strains were recorded. After cracking, higher strains were recorded in the three specimens. The specimens G2 and G3 show close strains until failure. The G4 specimen, however, showed lower strains compared to G3 and G2. It is worth mentioning that, at failure, the maximum tensile strains in the top GFRP reinforcement of specimens G2, G3 and G4 were about 56%, 64% and 36% of the ultimate strain of GFRP bars, respectively. The test results of this group reveal that as the reinforcement ratio increased, the capacity of the arches increased but the measured deflections and strains decreased. It is worth noting that the G4 ($\rho = 1.27\%$) showed higher capacity than the S3 ($\rho = 0.93\%$). This indicates that the capacity of the reference arch can be reached by using a slightly higher reinforcement ratio of GFRP bars.

4 Conclusions

Based on the test result of this research study, the following conclusions can be derived:

- GFRP-RC arches showed good and comparable behavior to the steel-RC arch. This demonstrates that the GFRP bars can be used to replace steel reinforcement in arch slab bridges.
- The ultimate capacity of the reference arch reinforced with steel was slightly higher (16%) than that of G3 arch reinforced with similar GFRP reinforcement ratio. However, the steel in the reference arch (S3) started yielding at a lower load level than the ultimate capacity of the G3 arch.
- Increasing the amount of GFRP reinforcement enhanced the capacity of the arches. Increasing the GFRP reinforcement ratio from 0.95% in G3 to 1.27% in G4 increased the capacity by 28%.
- Using a higher GFRP reinforcement ratio ($\rho = 1.27\%$) in G4 gave a 7% higher capacity than the reference arch (S3) reinforced with less amount of steel ($\rho = 0.95\%$). Therefore, to replace steel bars with GFRP bars in RC-arch slabs without affecting their performance, it is recommended to replace the steel bars with a slightly larger amount of GFRP bars.

Acknowledgements The authors would like to acknowledge Sultan Qaboos University, Civil and Architectural Engineering Department, and all the technicians at the structural laboratory for their help and support.

References

1. Benmokrane B, El-Salakawy E, El-Gamal SE, Sylvain G (2007) Construction and testing of an innovative concrete bridge deck totally reinforced with glass FRP bars: Val-Alain bridge on highway 20 East. J Bridge Eng ASCE 12(5):632–645
2. Benmokrane B, Eisa M, El-Gamal SE, Thébeau D, El-Salakawy E (2008) Pavement system suiting local conditions. ACI Concr Int Mag 2008:34–39
3. Bouguerra K, Ahmed E, El-Gamal SE, Benmokrane B (2011) Testing of full-scale concrete bridge deck slabs reinforced with Fiber Reinforced Polymer (FRP) Bars. Constr Build Mater 25(10):3956–3965
4. Eisa M, El-Gamal SE, El-Salakawy E, Benmokrane B (2008) Design and construction of first continuous reinforced concrete pavement using GFRP reinforcing bars. In: Proceedings of the 5th Middle East Symposium on Structural Composites for Infrastructure Applications (MESC-5), Hurghada, Egypt
5. El-Gamal SE, Benmokrane B, El-Salakawy E, Cousin P, Wiseman A (2007) Durability and structural performance of CFRP-RC parking garage's slabs after eight years in service conditions. In: Proceedings of the 3rd International Conference on Durability and field applications of reinforced polymers (FRP) composites for construction (CDCC 2007), Quebec City, Quebec, Canada, 49–58
6. El-Gamal SE, Benmokrane B, El-Salakawy E (2009a) Cracking and deflection behavior of one-way parking garage slabs reinforced with CFRP bars. ACI Spec Publ SP-264–3:33–52

7. El-Gamal SE, Benmokrane B, El-Salakawy E, Cousin P, Wiseman A (2009b) Durability and structural performance of CFRP-RC parking garage's slabs after being in service for eight years. Canadian J Civ Eng 36(4):617–627
8. El-Gamal SE, El-Salakawy EF, Benmokrane B (2007a) Influence of reinforcement on the behavior of concrete bridge deck slabs reinforced with FRP bars. J Compos Constructions ASCE 11(5):449–458
9. El-Gamal SE, El-Salakawy E, Benmokrane B (2005) Behavior of concrete bridge deck slabs reinforced with FRP bars under concentrated loads. ACI Struct J 102(5):727–735
10. El-Ragaby A, El-Gamal SE, El-Salakawy E, Benmokrane B (2006) Static and fatigue performance of concrete bridge deck slabs reinforced with glass FRP bars. In: 7th International Conference in Short and Medium Bridges, Montreal, Quebec, Canada, p 10
11. Thébeau D, Benmokrane B, El-Gamal SE (2010) Three-year performance of continuously reinforced concrete pavement with GFRP bars. In: Proceedings of the 11th International Symposium on Concrete Roads, Seville, Spain, p 11
12. Wang P, Jiang M, Zhou J, Wang B, Feng J, Chen H, Jin F (2018) Spalling in concrete arches subjected to shock wave and CFRP strengthening effect. Tunn Undergr Space Technol 74:10–19
13. Xie W, Jiang M, Chen H, Zhou J, Xu Y, Wang P, Jin F (2014) Experimental behaviors of CFRP cloth strengthened buried arch structure subjected to subsurface localized explosion. Compos Struct 116:562–570
14. Zanardo G, Pellegrino C, Bobisut C, Modena C (2004) Performance evaluation of short span reinforced concrete arch bridges. J Bridge Eng ASCE 9(5):424–434
15. Zhang X, Wang P, Jiang M, Fan H, Zho J, Li W, Jin F (2015) CFRP strengthening reinforced concrete arches: strengthening methods and experimental studies. Compos Struct 131:852–867

Developing and Investigating the Performance of Thermal Insulation Lightweight Sandwich Wall Panels

S. El-Gamal, A. Al-Kalbani, and O. Al-Hatmi

1 Introduction

In the Arabian Gulf region, the outdoor temperature can reach up to 60 °C in summer. This high temperature requires enormous electric power for the cooling of buildings as the external walls in most buildings are made of single skin walls using solid or hollow concrete blocks. Using of cavity walls or insulating materials is limited to some governmental and commercials buildings due to their high cost [1]. Several research studies have investigated the mechanical and thermal properties of different concrete blocks and tried to develop blocks with low thermal conductivity. Pierzchlewicz [21] developed several concrete hollow blocks with different thickness and holes configurations (staggered and aligned holes). Their thermal conductivity ranged from 0.57 to 0.68 W/mK and from 0.87 to 0.92 W/mK for the blocks with staggered and aligned holes, respectively. Hamid [12] developed interlocking blocks made with lightweight leeka aggregates and silt. The blocks showed very low thermal conductivity (0.375 W/mK) due to their low density and high air voids. They concluded that this low thermal conductivity satisfies the target thermal design requirements for a comfortable interior temperature without the need of mechanical air-conditioning. [1] using vermiculite and expanded polystyrene (EPS) beads to develop two types of hollow blocks with densities of 798 and 1168 kg/m^3 and compressive strengths of 2.2 and 3.3 MPa, respectively. They concluded that the developed blocks satisfy the Omani standard (OS 1, 1998) compressive strength requirements for non-load bearing masonry. The thermal conductivity of the blocks was about 0.62 W/mK.

S. El-Gamal (✉)
Department of Civil and Architectural Engineering, Sultan Qaboos University (on Leave from Menoufia University, Egypt), Muscat, Oman
e-mail: sherif@squ.edu.om

A. Al-Kalbani · O. Al-Hatmi
Department of Civil and Architectural Engineering, Sultan Qaboos University, Muscat, Oman

S. Walbridge et al. (eds.), *Proceedings of the Canadian Society of Civil Engineering Annual Conference 2021*, Lecture Notes in Civil Engineering 240,
https://doi.org/10.1007/978-981-19-0507-0_57

However, the recorded temperatures inside rooms build from these blocks reached 38ºC after only about 100 h. This might be related to the mortar layers used to connect the blocks, which worked as thermal bridges in the walls and reduced the insulation efficiency.

On the other hand, sandwich wall panels are also being used to construct walls. They usually consist of two outer thin concrete layers (wythes) and inner lightweight core. Sandwich walls have fewer thermal bridges than blocks and are expected to have better thermal resistance compared to regular concrete blocks [18]. The thermal transmittance of thin lightweight precast sandwich cladding panels was investigated by O'Hegarty et al. [19]. The tested sandwich panels achieved an average thermal transmittance of 0.324 Wm^{-2} K^{-1}. They concluded that the major source of heat loss in thin wall design is the thermal bridging, which account for up to 71% of the total thermal transmittance of the tested thin sandwich panel. Several research studies investigated the structural performance of sandwich panels. [11] investigated the structural feasibility of an EPS based lightweight concrete full scale sandwich wall panel. The panel achieved a failure stress of 3.89 N/mm^2. [22] studied the compressive and flexural behavior of composite panels made of lightly profiles steel skins and lightweight concrete, which showed good ductility in flexure. [13] studied the flexural behavior of four sandwich panels with RC concrete wythes and inner flat or ribbed EPS layer. Diagonal steel bars were used to connect the outer layers. All panels showed bi-linear load deflection response, which revealed that the flat or ribbed EPS did not affect the behavior of the sandwich wall panels. O'Hegarty et al. [17] also studied the flexural behavior of four precast concrete sandwich panels made of high-performance fiber reinforced concrete outer layers and foam insulations. Carbon fiber reinforced polymer (CFRP) bars were used as shear ties. All panels showed a ductile failure and the capacity of the panel increased as the outer layer thickness increased. [5] tested four precast insulated concrete sandwich panels with truss shaped continuous shear connectors in flexure. No separation of layers was observed in all tested panels, which proved the efficiency of the used shear connectors.

Shear ties or connectors are essential to connect the outer layers of the panels to increase their capacity. Steel shear ties can form thermal bridges that allows the temperature to move from one side of the wall to the other side. Glass fiber reinforced polymer (GFRP) bars are known with their high tensile strength, corrosion resistance, and low thermal conductivity. They have been used in several concrete applications including the rehabilitation of existing structures [6, 7, 9] and as internal reinforcement in new structures [4, 8, 10, 23]. Due to their low thermal conductivity, several research studies have investigated their use as shear ties in sandwich panels. [16] tested fourteen different types of shear ties. They concluded that determining the most suitable shear ties type depends on their shear strength, tension strength, stiffness, thermal conductivity, installation effort required, and cost. [24] investigated different types, sizes, and cross-sectional dimensions of GFRP connectors. They concluded that the end treatment of the connectors can lead to a better shear strength of the GFRP connectors. However, cross sections shape, sizes, and spacing had insignificant effects on the shear strength. [15] investigated the performance of two cross-shaped GFRP connectors. The GFRP connectors provided a good anchorage

pull-out force of 14.7 and 11.4 kN. [14] studied the performance of four different types of GFRP shear connectors in sandwich panels. Test results shows that all the GFRP connectors approximately similar response. However, GFRP shear connector with solid webs was found to increase the ultimate resistance of the panel slightly more than the other types of connectors.

2 Objectives

The main objective of this research study was to develop and investigate the mechanical and thermal properties sandwich wall panels with two outer lightweight concrete layers and inner EPS sheet. Vermiculite aggregates and EPS beads were used as partially replacement of the natural coarse aggregates in the outer concrete layers of the panels. The effect of using GFRP ties to connect the two outer layers of the panels was also investigated.

3 Materials Used and Test Specimens

3.1 Concrete (Outer Layers)

Normal weight and lightweight concrete mixes were used in the outer concrete layers of the sandwich panels. The normal weight concrete had a target compressive strength of 50 MPa. The maximum size of the coarse aggregate in the mix was 10 mm and the concrete mix proportions are listed in Table 1. Different lightweight concrete mixes were produced by partially replacing the natural coarse aggregate in the normal weight concrete mix with EPS beads and vermiculite. Figure 1 shows photos of the polystyrene beads and the vermiculite aggregates used in this study.

Table 1 Mix proportions for normal weight concrete

Materials	Content (kg/m^3)
Cement	430
Coarse aggregate (10 mm)	990
Sand	660
Water	215

Fig. 1 Polystyrene beads and vermiculite

Fig. 2 Expanded polystyrene (EPS) foam

3.2 Expanded Polystyrene Plates (Inner Layer)

EPS sheets were used as the inner layer in the sandwich panels. The dimensions of the EPS sheets were 500 mm length × 500 mm width × 140 mm thickness. The density of the EPS sheets was 10.5 kg/m^3. Figure 2 shows a photo of the EPS sheets used in this study.

3.3 GFRP Shear Ties

GFRP bars were used as shear ties in the developed sandwich panels. For each panel, four ribbed GFRP bars of 6 mm diameter were used to connect the two outer concrete layers of the panels. The GFRP bars were 200 mm length and were machined at both end as shown in Fig. 3 to connect the outer concrete layers of the sandwich panels.

Fig. 3 Photo of the GFRP shear ties

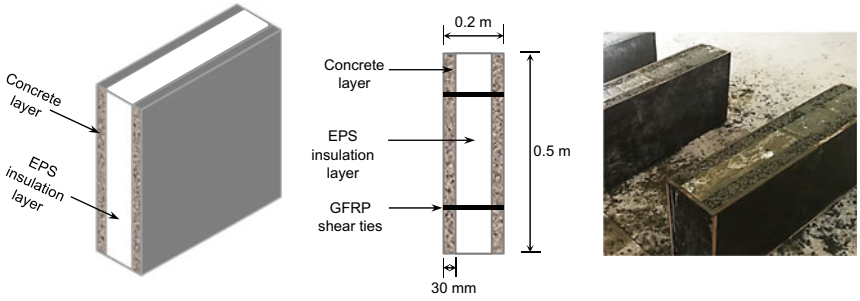

Fig. 4 Dimensions of the panels and the panels after casting

3.4 Sandwich Panels

Several panels of 500 × 500 × 200 mm each, composed of an inner ESP layer and two outer concrete layers were constructed. The thickness of the inner EPS layer was 140 mm while the thickness of each outer concrete layer was 30 mm. Four GFRP bars spaced at 40 cm were used as shear ties to connect the outer concrete layers. The cross section of the panel is shown in Fig. 4.

3.5 Test Parameters

Two parameters were investigated in this study. The first parameter was the effect of using GFRP shear ties to connect the outer concrete layers of the panels. This parameter was investigated in eight panels with normal concrete mixes (Ref. panels). Four panels were prepared with grooves in the polystyrene inner layer (Ref-Grooves) and other four panels were prepared with GFRP shear ties (Ref-Ties). The second parameter was the effect of using polystyrene beads and vermiculite in the outer concrete layers of the panels as partially replacement of the natural coarse aggregates. To investigate this parameter, 20 sandwich panels were constructed (4 for each set). The

Table 2 Test matrix of sandwich panels

Name	Lightweight aggregate	Coarse aggregate replacement ratio (%)	No. of panels	Notes
Ref-Grooves	–	–	4	Without shear ties
Ref-Ties	–	–	4	
Poly-53%	Polystyrene	53	4	
Poly-68%	Polystyrene	68	4	With GFRP shear ties
Poly-84%	Polystyrene	84	4	
Ver-53%	Vermiculite	53	4	
Ver-84%	Vermiculite	84	4	

replacement ratios were 53, 68 and 84% by volume of the natural coarse aggregates. A summary of the experimental program is listed in Table 2.

3.6 Testing and Instruments

From each set of sandwich panels, three panels were tested in compression after curing for 28 days and the fourth panel was used for thermal conductivity measurements. A 4000 kN capacity hydraulic testing machine was used to test the sandwich panels under compression at a loading rate of 1 mm/min. Figure 5 shows one panel during testing in the hydraulic testing machine. Hot Disk M1 Machine was used to measure the thermal conductivity for each layer of the sandwich panel. Equation (1) was used to calculate the effective thermal conductivity of the multi-layer sandwich panel. Figure 6 shows Hot Disk M1 Machine.

$$k = \frac{k_1 A_1 + k_2 A_2 + k_3 A_3}{A_{total}} \tag{1}$$

Fig. 5 Hydraulic testing machine

Fig. 6 Hot disk M1 machine

where: k_1, k_2, k_3 is the thermal conductivity of each layer, A_1, A_2, A_3 is the cross-sectional area of each layer.

4 Results and Discussions

4.1 Summary of Test Results

Table 3 summarizes the main results of the tested panels. It can be noticed that the average weight of the panels ranged between 37.9 kg in the Ref-Grooves panels to 24.3 kg in the Poly-84% panels. This resulted in average densities of 758 and 486 kg/m^3, respectively. The average capacities ranged between 1289 kN in the Ref-Ties panels to 196 kN in the Ver-84% panels, which resulted in compressive strengths of 12.8 and 1.96 MPa, respectively. Regarding the thermal conductivity of the panels, the maximum thermal conductivity were measured in the two reference panels (Ref-Grooves and Ref-Ties) with a thermal conductivity of 0.69 and 0.68 W/m.K, respectively. The minimum thermal conductivity (0.25 W/m.K) was recorded in the Poly-84% panels (with 84% replacement ratio of polystyrene beads).

4.2 Effect of Using GFRP Shear Ties

Figure 7 shows a comparison between the density, compressive strength, and thermal conductivity of the two reference specimens with grooves and with shear ties. It can be noticed that both sets of panels have similar average density and thermal conductivity as they are made from the same concrete mix. However, the Ref-Ties specimens (with GFRP ties) show higher compressive strength (13% more) compared to the specimens with grooves. In addition, the Ref-Ties panels show higher axial displacement at maximum load than the panels with grooves. This indicates that the presence of the GFRP shear ties delayed the failure and enhanced the axial capacity

Table 3 Summary of test results of the tested panels

Panel	Weight (kg)	Density (kg/m^3)	Maximum load (kN)	Compressive Strength (MPa)	Displacement at maximum load (mm)	Thermal conductivity (W/m.K)		
						Concrete layer	Insulation layer	Panel
Ref-Grooves	37.9	758	1131	11.3	2.28	2.22	0.03	0.69
Ref-Ties	37.1	741	1280	12.8	2.83	2.21		0.68
Poly-53%	29.81	596	420.96	4.21	2.19	1.28		0.41
Poly-68%	27.53	551	325.23	3.25	3.39	0.93		0.30
Poly-84%	24.31	486	202.11	2.02	3.73	0.76		0.25
Ver-53%	32.31	646	313.9	3.14	2.78	1.47		0.46
Ver-84%	31.30	626	196.35	1.96	3.28	1.06		0.34

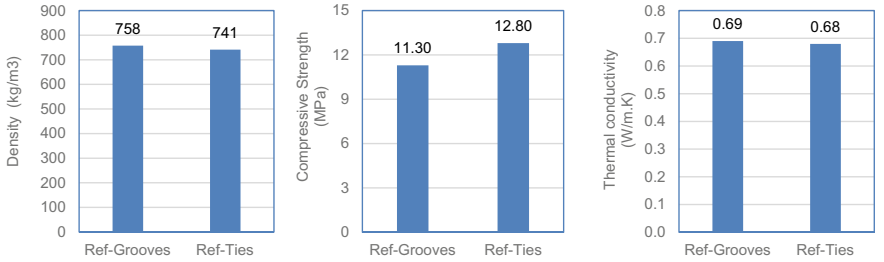

Fig. 7 Comparison between Ref-Grooves and Ref-Ties panels

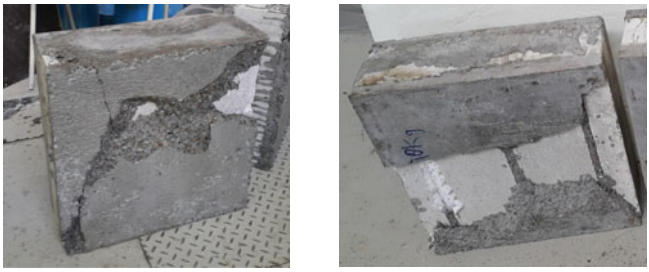

(a) Ref-Ties panel (b) Ref-Groove panel

Fig. 8 Typical failure mode of the reference panels

and the corresponding axial displacement. The GFRP shear ties connected the two outer concrete layers together as seen in Fig. 8a, which enhanced the capacity of the panels. However, in the Ref-Groove panels, Fig. 8b shows that the outer concrete layers were separated from the inners polystyrene insulation layer, which resulted in a lower axial capacity at a lower axial displacement compared to the REF-Ties panels. Therefore, in all panels with lightweight aggregates, it was decided to use GFRP shear ties in all panels. It is worth mentioning that the compressive strength of both types of panels are higher than the concrete compressive strength of the commercially available concrete hollow blocks (5 to 10 MPa) but they show much lower thermal conductivities (0.68 W/m.K compared to 1.6 W/m.K).

4.3 Effect of Lightweight Aggregates Replacement Ratio

Figures 9 and 10 show the relation between the polystyrene and vermiculite replacement ratios and the density, the compressive strength, and the thermal conductivity of the panels. Figures 9a and 10a show that as the polystyrene and vermiculite replacement ratios increase, the density of the panels decrease. The densities of the panels with polystyrene beads were 596, 551, and 486 kg/m^3 for the replacement ratios of 53,

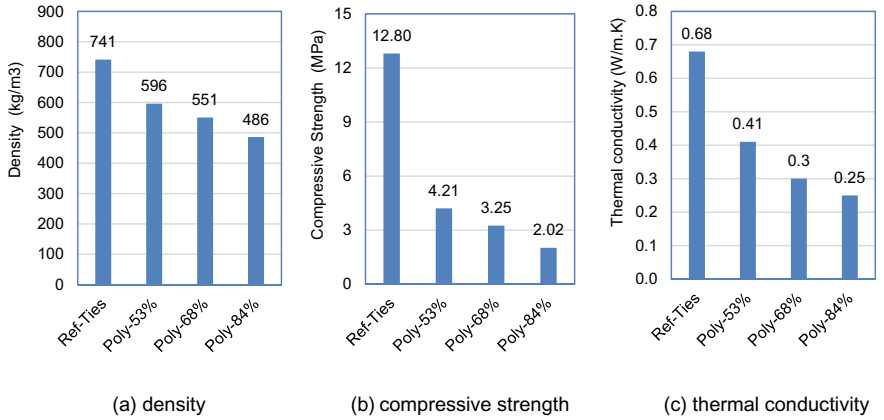

Fig. 9 Effect of polystyrene replacement ratio

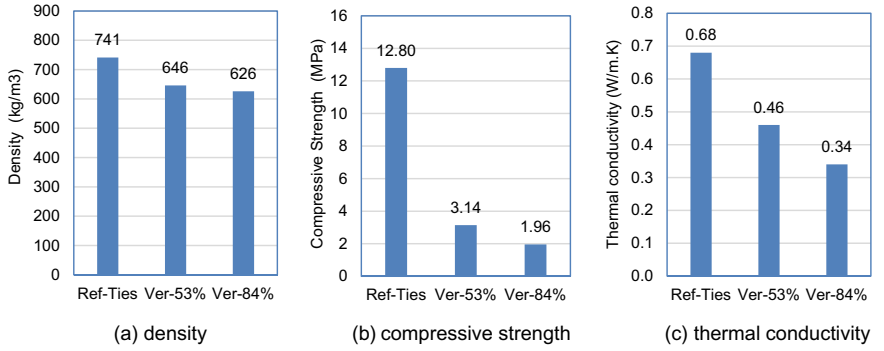

Fig. 10 Effect of vermiculite replacement ratio

68, and 84%, respectively. These densities were less than the density of the Ref-Ties panels by about 19.6, 24.6, and 34.4%, respectively. For the panels with vermiculite aggregates, the densities were 646 and 626 kg/m^3 for the 53 and 84% replacement ratios, respectively, which were less than the density of the Ref-Ties panels by about 12.8 and 15.5%. It is worth mentioning that the densities of the developed panels are much lower than the density of commercially available concrete hollow blocks (1193 kg/m^3). In addition, they are less than the densities of lightweight concrete blocks developed by [1] (798 and 1168 kg/m^3). Furthermore, they are much lower than the density of the commercially available blocks with thermal insulation layer (1418 kg/m^3). The lower weight and densities of the panels developed in this study is expected to reduce the self-weigh of the walls in buildings. This will result in smaller structural elements.

Figures 9b and 10b show that as the polystyrene and vermiculite replacement ratios increase, the compressive strengths decrease. The compressive strengths of the

panels with 53, 68, and 84% replacement ratios of polystyrene beads were 4.21, 3.25, and 2.02 kg/m^3, respectively. These values were less than the compressive strength of the Ref-Ties panels by about 67.1, 74.6, and 78.6%, respectively. The compressive strengths of the panels with 53 and 84% replacement ratios of vermiculite aggregates were 3.14 and 1.96 kg/m^3, respectively. These values were less than the compressive strength of the Ref-Ties specimen by about 75.5 and 84.7%, respectively. It is worth mentioning that the compressive strength of the panels with different polystyrene beads replacement ratios are comparable to the results of [1] (2.2 and 3.3 MPa). In addition, the panels with 53 and 68% replacement ratios are satisfying the Omani standards (OS 1) requirements for non-load bearing walls.

Figures 9c and 10c show that as the polystyrene and vermiculite replacement ratios increase, the thermal conductivity of the panels decrease. Figure 9c shows that the thermal conductivities of the panels with polystyrene beads were 0.41, 0.30, and 0.25 W/m.K for the replacement ratios of 53, 68, and 84%, respectively. These values were less than the thermal conductivity of the Ref-Ties panels by about 39.7, 55.9, and 63.2%, respectively. The thermal conductivities in the panels with vermiculite aggregates were 0.46 and 0.34 W/m.K for the 53 and 84% replacement ratios, respectively (Fig. 10c), which were less than the thermal conductivity of the Ref-Ties specimen by about 32.4 and 50%, respectively. Compared to commercially available concrete hollow blocks, the thermal conductivities of all panels with lightweight aggregates are much lower than their thermal conductivity (1.6 W/m.K). They were also lower than the results obtained by [1] and [21] and were comparable with the results of [12]. These lower thermal conductivity values obtained in this research study will result in better thermal insulation in buildings and is expected to reduce the electric power consumption required for cooling of buildings.

4.4 Effect of Lightweight Aggregate Replacement Material

Figure 11 shows a comparison between the densities, compressive strengths, and thermal conductivities of panels with polystyrene bead and vermiculite aggregates. It can be noticed that the panels with vermiculite aggregates have higher densities and thermal conductivities than similar panels with polystyrene beads. The increase in the density of the panels with vermiculite aggregates was about 18% on average compared to the panels with polystyrene beads. The average increase in the thermal conductivity values of the panels with vermiculite aggregates was about 24.1% compared to the panels with polystyrene beads. This indicates that the panels with polystyrene bead have better thermal insulation properties that those with vermiculite aggregates.

On the other hand, the panels with vermiculite aggregates have lower compressive strength than similar panels with polystyrene beads. The compressive strengths of the panels with polystyrene beads were about 35.5 and 55% greater that the compressive strengths of the panels with vermiculite aggregates at replacement ratios of 53 and 84%, respectively. The results show that panels with polystyrene beads are better

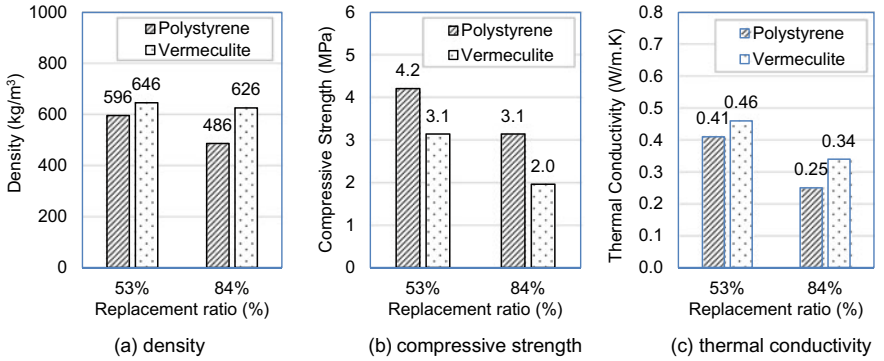

Fig. 11 Effect of the type of the lightweight material

than the panels with vermiculite as they gave lower densities, better compressive strengths, and better thermal insulation properties.

5 Conclusions

Based on the test result of this research study, the following conclusions can be derived:

- The developed sandwich panels with natural aggregates (reference panels) showed lower densities and higher compressive strengths than the commercially concrete hollow blocks and thermal insulation blocks available in Oman.
- The average thermal conductivity of the developed reference panels was about 42% of the thermal conductivity of the commercially available concrete hollow blocks and it was comparable to the thermal conductivity of the local available thermal insulation blocks.
- Using GFRP shear ties was more effective than using grooves. The GFRP ties delayed the failure and enhanced the capacity of the panels by about 13% compared to the panels with grooves.
- As the polystyrene and vermiculite replacement ratios increased, the density, compressive strength, and thermal conductivity of the sandwich panels decreased.
- The densities of the panels with lightweight aggregates ranged between 486 and 646 kg/m^3. These densities were less than the density of the reference panels by about 12.8 to 34.4%. There were also much lower than the densities of the commercially available concrete hollow blocks and concrete thermal insulation blocks.
- The compressive strengths of the panels with polystyrene beads ranged between 4.21 and 2.02 kg/m^3 and ranged between 3.14 and 1.96 kg/m^3 for the panels with

vermiculite. The developed panels with 53 and 68% lightweight aggregates can be used for non-load bearing walls.

- The thermal conductivities of the panels with polystyrene beads and vermiculite aggregates ranged from 0.41 to 0.25 W/m.K and from 0.46 to 0.34 W/m.K, respectively. These values were lower than the thermal conductivities of all commercially concrete blocks available in Oman. The lower thermal conductivity values of the developed lightweight panels is expected to result in a better thermal insulation in buildings and is expected to reduce the electric power consumption.
- The results show that the panels with polystyrene beads are better than the panels with vermiculite as they gave lower densities, higher compressive strengths, and lower thermal conductivities.

Acknowledgements The authors would like to acknowledge Sultan Qaboos University, Civil and Architectural Engineering Department, and all the technicians at the structural laboratory for their help and support.

References

1. Al-Jabri KS, Hago AW, Al-Nuaimi AS, Al-Saidy AH (2005) Concrete blocks for thermal insulation in hot climate. Cem Concr Res 35:1472–1479
2. Al-Jabri KS, Hisada M, Al-Oraimi SK, Al-Saidi AH (2009) Copper slag as sand replacement for high performance concrete. Cement Concr Compos 31(7):483–488
3. ASTM E72. Standard Test Methods of Conducting Strength Tests of Panels for Building Construction. ASTM International, West Conshohocken
4. Benmokrane B, Eisa M, El-Gamal SE, Thébeau D, El-Salakawy E (2008) Pavement system suiting local conditions. ACI Concr Int Mag 34–39
5. Daniel RJ, Prabakar J, Alagusundaramoorthy P (2019) Experimental study on the flexural behavior of insulated concrete sandwich panels with wires as shear connectors. Alex Eng J 58(3):901–908
6. El-Gamal SE, Al-Nuaimi A, Al-Saidy A, Al-Lawati A (2014) Flexural strengthening of RC beams using near surface mounted fibre reinforced polymers. In: Proceedings of the Brunei International Conference on Engineering and Technology, Institut Teknologi Brunei, Brunei Darussalam, p 10
7. El-Gamal SE, Al-Nuaimi AS, Al-Saidy AH, Al-Shanfari K (2019) Flexural behavior of RC beams strengthened with CFRP sheets using different strengthening techniques. J Eng Res 16(1):35–43
8. El-Gamal SE, AbdulRahman B, Benmokrane B (2010) Deflection behaviour of concrete beams reinforced with different types of GFRP bars. In: Proceedings of the 5th International Conference on FRP Composites in Civil Engineering, Beijing, China, p 4
9. El-Gamal SE, Al-Salloum Y, Alsayed S, Aqel M (2012) Performance of near surface mounted GFRP bars in concrete. J Reinf Plast Compos 31(22):1501–1515
10. El-Gamal SE, El-Salakawy EF, Benmokrane B (2007) Influence of reinforcement on the behavior of concrete bridge deck slabs reinforced with FRP bars. J Compos Constr 11(5):449–458
11. Fernando P, Jayasinghe M, Jayasinghe C (2017) Structural feasibility of Expanded Polystyrene (EPS) based lightweight concrete sandwich wall panels. Constr Build Mater 139:45–51

12. Hamid A (2003) Development of a New Load-Bearing Masonry Wall System for Building Construction in Hot Climate. In: Proceedings of the 9th Arab Structural Engineering Conference, Emerging Technologies in Structural Engineering, vol 1, Abu Dhabi, United Arab Emirates. pp 27–37
13. Hou H, Ji K, Wang W, Qu B, Fang M, Qiu C (2019) Flexural behavior of precast insulated sandwich wall panels: full-scale tests and design implications. Eng Struct 180:750–761
14. Hou H, Wang W, Qu B, Dai C (2020) Testing of insulated sandwich panels with GFRP shear connectors. Eng Struct 209:109954
15. Huang J, Jiang Q, Chong X, Ye X, Wang D (2020) Experimental study on precast concrete sandwich panel with cross-shaped GFRP connectors. Mag Concr Res 72(3):149–162
16. Naito C, Hoemann J, Beacraft M, Bewick B (2012) Performance and characterization of shear ties for use in insulated precast concrete sandwich wall panels. J Struct Eng 138(1):52–61
17. O′Hegarty, R., West, R., Reilly, A., Kinnane, O. 2019. Composite Behaviour of Fibre-Reinforced Concrete Sandwich Panels with FRP Shear Connectors. *Engineering Structures*, 198, 109475.
18. O'Hegarty R, Kinnane O (2020) Review of precast concrete sandwich panels and their innovations. Constr Build Mater 233:117145
19. O'Hegarty R, Reilly A, West R, Kinnane O (2020) Thermal investigation of thin precast concrete sandwich panels. J Build Eng 27:100937
20. OS 1 - Omani Standard No. 1 (1998) Precast concrete blocks. Ministry of commerce and industry, directorate general for specifications and measurements, p 10
21. Pierzchlewicz J (1996) Modern concrete wall-units with improved thermal resistance for housing in hot climate. Sci Technol 1:69–80
22. Ridha M, Li D, Clifton G, Ma X (2019) Structural behavior of composite panels made of lightly profiled steel skins and lightweight concrete under concentric and eccentric loads. J Struct Eng 145(10):04019093
23. Thébeau D, Benmokrane B, El-Gamal SE (2010) Three-Year performance of continuously reinforced concrete pavement with GFRP bars. In: Proceedings of the 11th International Symposium on Concrete Roads, Seville, Spain. p 11
24. Woltman G, Tomlinson D, Fam A (2013) Investigation of various GFRP shear connectors for insulated precast concrete sandwich wall panels. J Compos Constr 17(5):711–721

Consequences on Residential Buildings in Greater Montreal for a Repeat of the 1732 M5.8 Montreal Earthquake

P. Rosset, L. Chouinard, and M.-J. Nollet

1 Introduction

On September 16, 1732, an earthquake struck the region of Montreal at 11a.m. The written reports of this event, mainly from the Religious Hopistallers of the Hôtel-Dieu Hospital, indicate that the ground shaking did significant damage to 300 houses, destroyed chimneys, cracked walls, and induced fire in 185 buildings [10]. According to some accounts, the ground motion did not cause much damage to the masonry of the fortifications surrounding the city. At this time, the city, founded 90 years earlier, comprised approximately 3000 inhabitants and fewer than 400 buildings clustered along the southern edge of the Island of Montreal. [10] estimated the intensity of the event to VIII on the Modified Mercalli scale (MMI) and the magnitude around 5.8. In 2020, the urbanized area extended tens of kilometres beyond the original settlement and the surrounding population is estimated around 3.8 million. The current level of urban development coupled to the level of the seismic hazard for the region results in Montreal being the second-ranking city at risk in Canada [2].

In order to provide the Ministère de la sécurité publique of Quebec with an estimate of damage and losses in case of a large credible earthquake close to the Montreal Metropolitan Community (MMC), the effects of the repetition of the 1732 earthquake are investigated. The analysis is carried out using HazCan, the Canadian version of Hazus software for risk assessment, which has been widely used in the USA. This release of Hazus permits users to create study regions in Canada based on Statistics

P. Rosset (✉) · L. Chouinard
Department of Civil Engineering and Applied Mechanics, McGill University, Montreal, QC, Canada
e-mail: philippe.rosset@affiliate.mcgill.ca

M.-J. Nollet
Department of Construction Engineering, École de Technologie Supérieure, Montreal, QC, Canada

S. Walbridge et al. (eds.), *Proceedings of the Canadian Society of Civil Engineering Annual Conference 2021*, Lecture Notes in Civil Engineering 240,
https://doi.org/10.1007/978-981-19-0507-0_58

Canada 2006 census boundaries and data [22]. In Canada, [14] used it for downtown Ottawa, [11] for Vancouver, and [23] for the island of Montreal. Rosset et al. [21] investigated the effects of this scenario for Montreal, which is presently extended to the MMC with updated data.

A detailed zonation map in terms of V_{s30} [18, 20] is used to classify sites following the National Building Code of Canada [13] in order to include the potential effects on ground motion amplification due to the presence of soft and recent soil deposits in several areas of the MMC. Demographic and building data were compiled from census and property assessment rolls, respectively, according to classifications specified in HazCan at the spatial scale of census dissemination areas.

The effects of ground motion on buildings are divided into four levels, from slight to complete damage. Direct economic losses are then derived from the distribution of damage by construction types and estimated values of buildings and content. Finally, the estimate of shelter needs and the quantity of debris from structural and non-structural damage are discussed from a perspective of crisis management.

2 Data Collection

The analysis is conducted at the scale of dissemination areas (DA), which are the smallest standard geographic area for which all census is disseminated by Statistics Canada. The MMC includes 82 municipalities, 16 on the island of Montreal, grouped into 14 regional county municipalities (RCM). The MMC is divided into 6116 DA as shown in Fig. 1.

2.1 Soil Data

The influence of soft soils on the distribution of the ground shaking after an earthquake has been extensively studied during the last decades. For the MMC, the clay deposited by the late Pleistocene Champlain Sea, which covered most of southern Quebec and Ontario [8] has been shown to be very sensitive when disturbed by construction, earthquakes, or stream erosion. An illustration of amplification effect was provided by the damage on the external masonry wall of the Montreal-East City Hall during the 1988 M5.9 Saguenay earthquake, whose epicentre was more than 300 km from Montreal [12]. An analysis of site conditions showed a 17 m thick layer of marine clay, which induced average amplifications of 5 for frequencies between 2–3 Hz, and which corresponded to the resonance frequency of the then-existing building [5].

Rosset et al. [20] have proposed a microzonation of the island of Montreal in terms of V_{s30} (the average shear wave velocity of the first 30 m of soil) converted to site classes (NBCC, 2015) by combining information from seismic measurements,

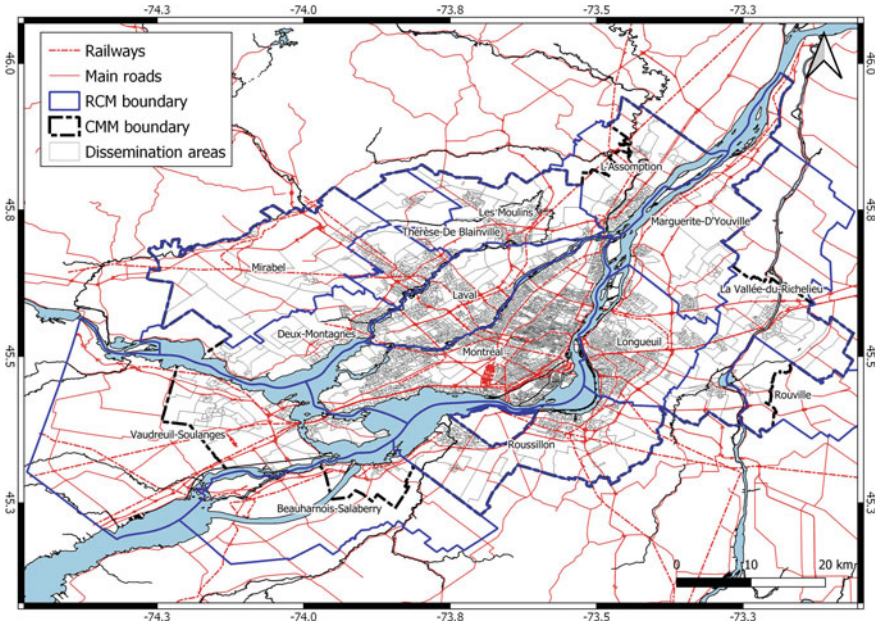

Fig. 1 Division of the MMC into dissemination areas and municipalities (RCM)

borehole data and geological data. An analysis of felt reports from recent earthquakes, provided by the Did You Feel It system of Natural Resources Canada, has shown a strong correlation between the intensity derived from these reports and soil classification [19].

The mapping was extended to the MMC by performing additional seismic measurements and by correlating the dominant resonance frequency of soil deposits to V_{s30} for the city of Longueuil and Laval ([16, 17] respectively). A simplified 3D regional geological model [15] was also used in combination with previously derived shear wave velocity-depth relations for each soil types of the 3D geological model (Chouinard and Rosset, 2021 in preparation). Figure 2 shows the interpolated site classes (following the NBCC-2015 classification) derived from seismic measurements (black dots), V_s seismic measurements (orange square) and the 3D geological model on a regular grid. The information of the map is used to define the average soil class of each DA and the corresponding amplification factors to be applied on calculated ground motions.

2.2 Population and Building Data

The total population is about 3.8 million, which are distributed into DA using the 2016 census of Statistic Canada. This dataset provides night-time population, which

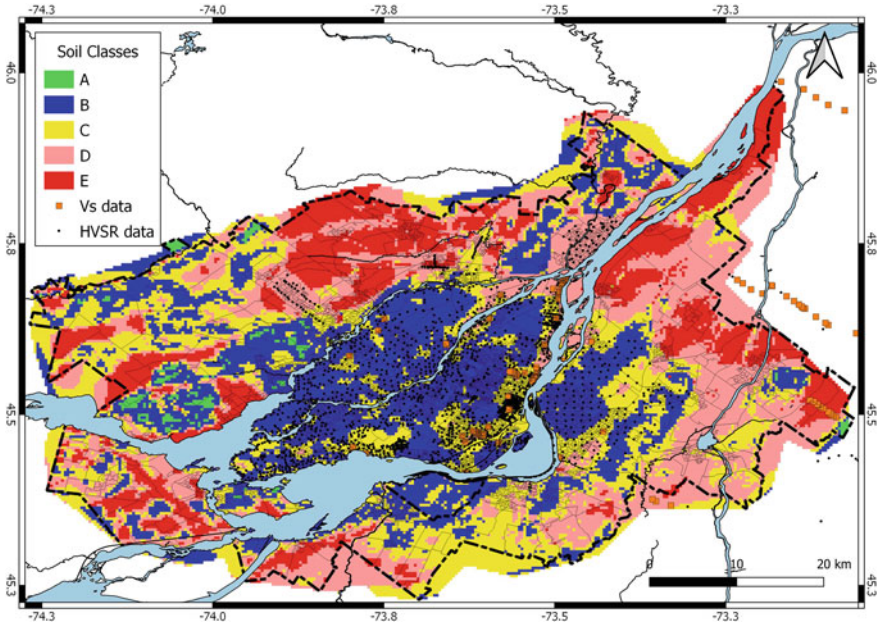

Fig. 2 Microzonation of the MMC in terms of site classes following the NBCC-2015

is converted to daytime population using home-to-work commuting studies [3, 4]. Several other socioeconomic parameters such as age distribution, incomes, ethnic origin were compiled to complete the analysis in HazCan.

In Hazus, the distribution of residential buildings for each DA is defined by the distribution of occupancy types, the percentage of construction types and design levels. The occupancy types consider the number of apartments from single-family houses to multiplexes (see [7] for details). Four main construction types describe the built environment of the MMC,wood frame structures (W1), unreinforced masonry wall structures (URM), concrete frame wall structures (C) and in a lesser proportion, steel frame structures (S). The C and S types are divided into sub-categories depending on the construction frame and infill walls. The mobile houses are separated from the other buildings.

Other structural parameters affecting structural capacity and response such as the building height (low-rise, mid-rise, high-rise) and seismic design criteria (pre-code, low-code and moderate-code) are also considered [7]. These parameters have been derived from the 2018 property assessment roll available at the level of individual buildings. About 872 000 buildings were grouped by occupancy types within each DA. The Table 1 shows this distribution for the island of Montreal and for the other municipalities of the MMC. Single family houses are predominant outside of Montreal (86.4%) while this value is 56% in Montreal, the duplex and triplex accounting for 34% of the total.

Table 1 Distribution of buildings by occupancy types for Montreal and the neighboring municipalities

Occupancy types	Numbers of dwellings	Off Montreal number	Off Montreal %*	Montreal number	Montreal %*
RES1	1	451,901	86.38	196,640	56.25
RES2		4,879	0.93	3	–
RES3A	2	30,969	5.92	82,792	23.68
RES3B	3–4	20,338	3.89	37,615	10.76
RES3C	5–9	9,615	1.84	25,991	7.44
RES3D	10–19	2,874	0.55	4,988	1.43
RES3E	20–49	1,254	0.24	1,520	0.43
RES3F	>49	479	0.09		
Total		522,309	99.84	349,549	99.99

*The total for the percentage is not 100% since a few buildings are a typical

A district by district review of the data provided by the assessment roll was performed to distribute the buildings by construction type considering the historical evolution of major architectural trends, the evolution of building standards and of the urbanization of the territory. The construction material and lateral resistance system were assigned by considering the year of construction, the number of floors, and the location of the buildings within the city [21]. Similar rules were also extended for neighboring municipalities to assign occupancy and construction types [6]. Table 2 shows the distribution of buildings by main structural types for Montreal and neighbouring municipalities. The majority of the residential houses are wood light frame structures. In Montreal, unreinforced masonry houses and steel frame buildings represent 14.3% and 2.1% of the total stock, respectively and these numbers are reduced to 0.4% and less outside of the city.

Table 2 Distribution of buildings by construction types for Montreal and the neighboring municipalities

Building types	Structural frame	Off Montreal number	Off Montreal %	Montreal number	Montreal %*
W	Wood	501,363	96.0	295,602	84.6
C	Concrete	14,051	2.7	448	0.1
URM	Unreinforced masonry	2,023	0.4	47,562	13.6
MH	Mobile home	4,879	0.9	3	–
S	Steel			5,743	1.6
Total		522,316		34,9358	

*The total for the percentage is not 100% since few buildings were not included in a type

Table 3 Distribution of design code levels by construction types for Montreal

Code design	Year built	Design code by building types* (in %)							
		W1	URM L, M	C1L	C1M	C1H	C2 L, M	C2H	S1 L,M
Pre-code	Before 1970	59	100	7	37	41	–	2	100
Low code	1970–1990	26	–	88	37	41	3	9	–
Moderate code	After 1990	15	–	5	26	18	97	89	–
Total number of buildings		229,607	51,502	773	357	482	563	259	5 354

*W1 = Light wood frame; URM = Unreinforced masonry; MH = mobile home; C1 = Concrete Moment Frame; C2 = Concrete Shear Walls; S1 = Steel Moment Frame; L = 1–2 floors; M = 4–7 floors; H = 8 + floors

Table 4 Distribution of design code levels by construction types for the municipalities outside Montreal

Code design	Year built	Design code by building types* (in %)							
		W1	URM L, M	MH	C1 L	C1 M	C1 H	C2 L, M, H	S1 L,M
Pre-code	Before 1970	26	100	11	27	17	9	–	
Low code	1970–1990	37	–	69	63	78	83	–	
Moderate code	After 1990	37	–	19	10	5	9	100	
Total number of buildings		496,981	2,020	4,651	8,871	106	23	4,015	

*Same legend than Table 3

In Hazus, the fragility curve defined for each structural type varies as a function of the design level, which is highly dependent on the year of constriction. For Quebec, 1970 is a pivotal year for seismic design since it is the date when capacity-based design and structural ductility considerations were first introduced. Structures built before 1970 are considered as *pre-code* and the ones built after this date *low-code.* The year 1990 marks a new transition with the introduction of new seismic requirements in several design standards. The highest level of seismic design considered for residential buildings constructed after 1990 is moderate (*moderate code* in Hazus). Table 3 gives the percentages of buildings for a given code level by building types for Montreal and Table 4 for the municipalities outside Montreal.

2.3 Exposure of the Residential Buildings

Two approaches were used to estimate the value of buildings by DA; one consisted in summing the assessment roll value of individual buildings within an DA, another by multiplying the total surface of the buildings by the median value per square metre for

each occupancy type in a given DA, using the assessment roll data. Both approaches give similar results with the dataset outside Montreal but the second method was found to be better suited to the inhomogeneous dataset for Montreal. Figure 3 shows the distribution of the total value by occupancy type in and outside Montreal. The

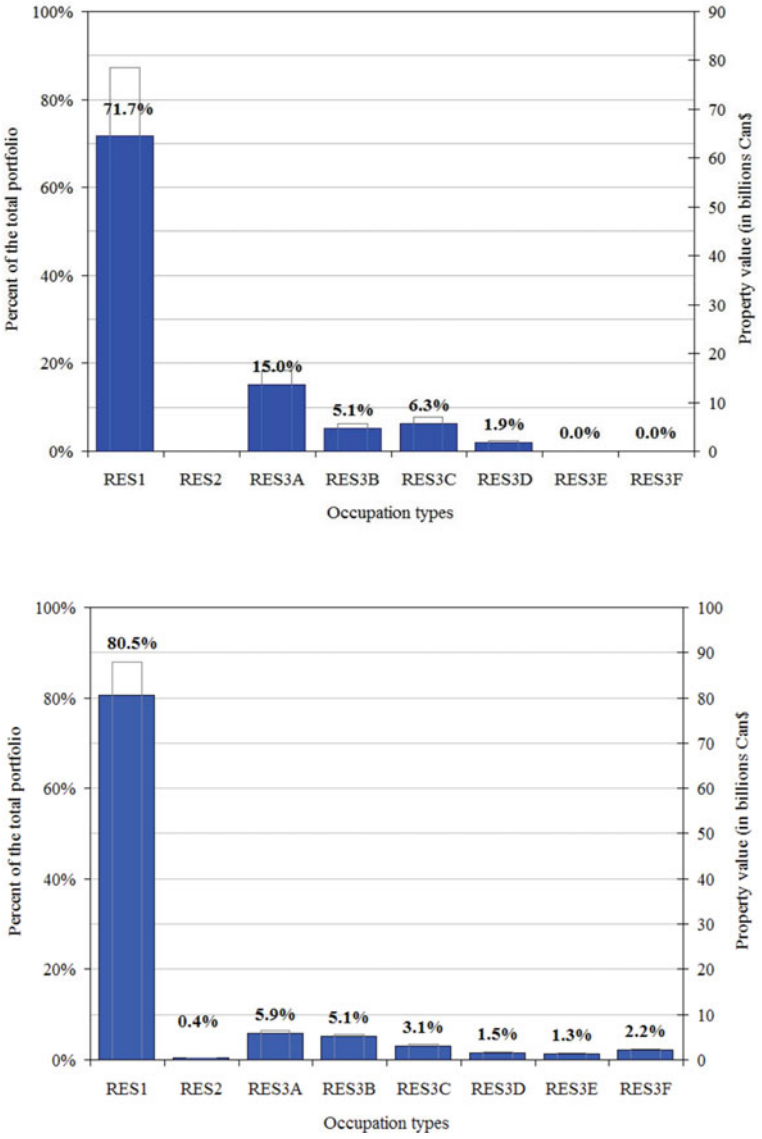

Fig. 3 Distribution of total property value by occupancy types (in billions of Can$) for Montreal (top) and the surrounding municipalities (bottom)

total building exposure is estimated around 189 billion of Can$ (2018 value), the single-family houses counting for 64% of the total.

The content exposure is estimated by using the ratio between the content value and the property value provided by CatIQ (Catastrophe Indices and Quantification Inc., Toronto) at the level of the Forward Sortation Area as provided by postal codes. The distribution of this ratio varies within the MMC and is around 51% ± 9% for 2018. The corresponding ratio is combined to the building exposure for each DA of the study region to estimate the content exposure. In total the exposure of buildings and content is about 285 billion Can$.

3 Damage and Loss Estimate

The calculated risk scenario is for a replication of the M5.8 1732 Montreal earthquake. The magnitude is estimated around 5.8 and the epicentre located at 45.5 N and 73.6 W as provided by the Geological Survey of Canada. The depth is set at 10 km, which is the default depth for such an event in this region. A ground motion relation combining six attenuation relations developed for the Central and Eastern US (CEUS2008) is used and described in the Hazus manual (Sect. 4.2, Table 4.5, [7]). The influence of site conditions is added to the ground motions using the information of the microzonation map provided in Fig. 2 for each DA. The map of the Fig. 4 shows the resulting PGA distribution at the scale of the dissemination areas.

3.1 Building Damage

The effect of the earthquake on buildings are divided in four levels from slight to complete damage as shown in Table 5 for Montreal and the municipalities outside Montreal. Buildings with complete and important damage represent 2.4% and 14.6% of the total for single-family houses and other residential types, respectively. These values are reduced outside of Montreal and increased in Montreal where the percentage of masonry buildings with low resistance is the highest.

The plot in the Fig. 5 shows the percentage of damage by level for the main types of construction. The light wood frame buildings, which are predominant in the MMC, is the construction type which suffers the least damage with a proportion of around 3% of the stock having important and complete damage. Houses with unreinforced masonry walls are the most affected with 37% having important and complete damage. The location of these buildings is mainly in the region of the old town close to the selected epicentre. Steel frame building are similarly affected.

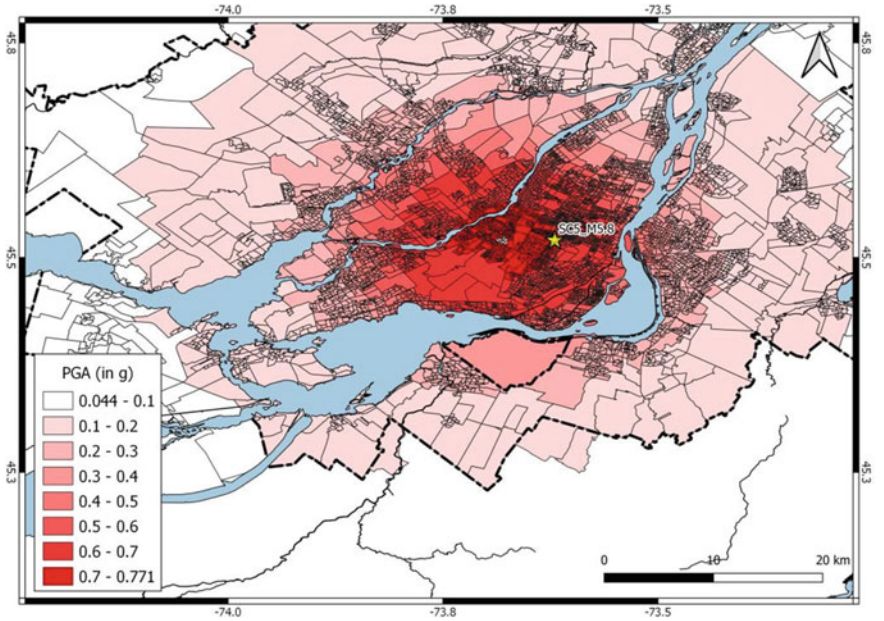

Fig. 4 PGA distribution for the earthquake scenario (in g). The star locates the point source rupture

Table 5 Building damage by levels of damage and main occupancy types

Region	Occupancy types	Number of buildings and percentage (in brackets) by level of damage				
		No	Slight	Moderate	Important	Complete
Montreal	Single family houses	94,328 (48.0)	55,909 (28.4)	35,138 (17.9)	8,784 (4.5)	2,481 (1.3)
	Other residential	36,148 (23.5)	42,723 (27.8)	44,084 (28.7)	20,112 (13.1)	10,609 (6.9)
Outside Montreal	Single family houses	332,613 (73.6)	86,066 (19.0)	29,177 (6.5)	3,778 (0.8)	554 (0.1)
	Other residential	46,586 (66.2)	14,356 (20.4)	7,680 (10.9)	1,524 (2.2)	275 (0.4)
MMC	Single family houses	426,941 (65.8)	141,975 (21.9)	64,315 (9.9)	12,562 (1.9)	3,035 (0.5)
	Other residential	82,734 (36.9)	57,079 (25.5)	51,764 (23.1)	21,636 (9.7)	10,884 (4.9)

3.2 Economic Loss Estimate

There are an estimated 872 000 buildings in the region with a total building replacement value (excluding contents) of 189 billion of Can$. The value of content, as

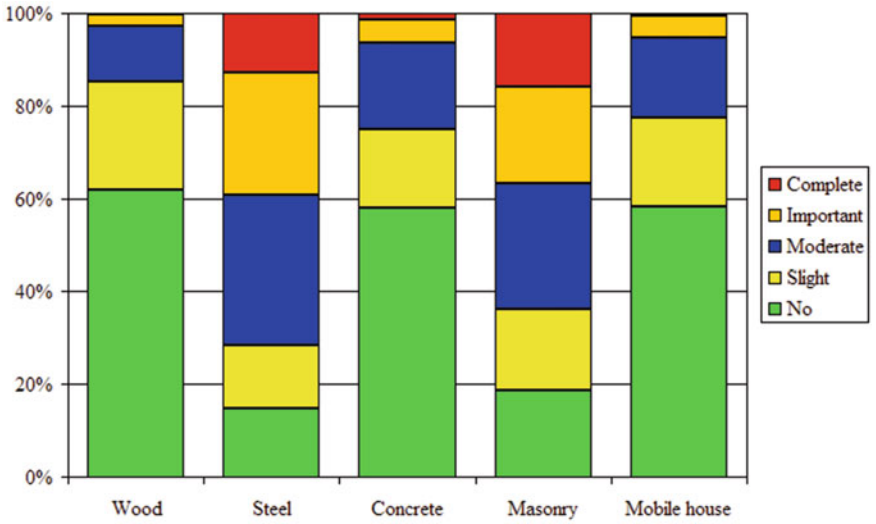

Fig. 5 Distribution of damage by levels for the main types of construction

given by insurance, add around 96 billion to this value. Direct losses due to structural damage and non-structural damage as well as their content are separated in the calculation of the economic impacts. The Table 6 shows the percentages of losses by construction type relative to the total building value for structural and non-structural damage and to the total content value for content damage.

Table 6 Percentage of losses and exposures by construction types

Building type*	Structural (a) (%)	Non-structural (b) (%)	Total (a + b) (%)	Content (%)	Building exposure (in millions Can$)	Content exposure (in millions Can$)
W	0.6	3.7	4.3	3.0	164,533	85,304
S	1.4	6.8	8.2	8.0	933	395
C	1.0	5.4	6.4	2.8	10,004	5,024
URM	3.1	13.6	16.6	9.5	13,041	5,299
MH	1.2	3.5	4.7	1.2	427	241
Total	0.8	4.4	5.2	3.4	**188,938**	**96,263**

*The abbreviations are given in Table 2

3.3 Indirect Effects

Two indirect effects of interest for crisis management are provided, debris management and shelters needs, which are derived from building damage assessments. Hazus estimates the amount of debris that will be generated by the earthquake into two categories: (a) Brick/Wood and (b) Reinforced Concrete/Steel. This distinction is made because of the different types of material handling equipment required to remove the debris. The model estimates that a total of 6.7 million tons of debris will be generated, brick and wood comprise 52% of the total, with the remainder being reinforced concrete and steel. It corresponds to 260,000 truckloads (at 25 tons/truck) to remove the debris generated by the earthquake.

Hazus estimates the number of households that are expected to be displaced from their homes due to the earthquake and the number of displaced people that will require accommodations in temporary public shelters. The model estimates 120,000 households to be displaced due to the earthquake. Of these, 60,000 people (out of a total population of 3.9 million) would seek temporary housing in public shelters.

4 Discussion

The present paper provides a first estimate of the effects on residential buildings of a repeat of the 1732 M5.8 shallow earthquake located in the centre of Montreal. The distribution of ground motions is calculated using a composite attenuation relations taking into account the site conditions for a rupture source point. At this stage, it is a first approximation, which will be refined in future studies by accounting for the uncertainties on source rupture and attenuation relations.

The slight and moderate damage category accounts for more than 85% of the total damage to residential buildings. The most affected buildings are the ones made of unreinforced masonry walls with 37% important and complete damage and to a lesser extent the older steel frame multi-floor building. The resistance of the latter need to be further analyzed but they represent less than 1% of the building stock. The masonry buildings are located mainly in the historical part of Montreal and surrounding municipalities.

In terms of economic losses, the repetition of the 1732 earthquake will cost around 10 billion Can$, non-structural damage accounting for 85% in average of the costs. This value represents around 5.2% of the total property value. The content exposure is estimated using insurance industry data on the ratio of building to content exposure at a different scale than the dissemination areas (203 regions for the MMC). The total content value is estimated around 96 billion and the cost of the content replacement could be higher than 3.4% of the total (3.2 billion Can$). The total loss is then estimated around 13.2 billion including the contents (5% of the total exposure).

This a first attempt to provide with a risk analysis at the scale of the dissemination area for the metropolitan area of Montreal using up-to-date data from national and

local statistical services. The collected data are stored in a GIS in order to produce thematic maps useful for mitigation. The next steps are to use the collected population data at the dissemination area scale to calculate average annualized losses and to compare results using different approaches and softwares [1, 9] to improve data sets and the performance of these tools.

Acknowledgements This project was funded by the Ministère de la sécurité publique of Quebec as one of the activities to develop a framework for the reduction and prevention of major disasters in Quebec (2013–2022). The authors acknowledge the reviewer for his constructive comments.

References

1. Abo El Ezz A, Smirnoff A, Nastev M, Nollet MJ, McGrath H (2019) ER2-Earthquake: interactive web-application for urban seismic risk assessment. Int J Disaster Risk Reduction 34:326–336
2. Adams J (1989) Seismicity and seismotectonics of southeastern Canada. In: Earthquake Hazards and the Design of Constructed Facilities in the Eastern United States, Annals of the New York Academy of Sciences, 558
3. ARTM (2005) Enquête Origine-Destination 2003—La mobilité des personnes dans la région de Montréal, Autorité régionale de transport métropolitain, 176
4. ARTM (2010) Enquête Origine-Destination 2008—La mobilité des personnes dans la région de Montréal, Autorité régionale de transport métropolitain, 210
5. Chouinard L, Rosset P (2012) On the use of single station ambient noise techniques for microzonation purposes: the case of montreal. In: Shear Wave Velocity Measurement Guidelines for Canadian Seismic Site Characterization in Soil and Rock, JA Hunter, HL Crow (eds.) Geological Survey of Canada, Open File 7078, 85–93.
6. Chouinard L, Rosset P, Nollet M-J (2020) Le risque sismique résidentiel dans le Grand Montréal, Évaluation des dommages et des conséquences. Internal report, McGill University, p 68
7. FEMA (2003) Multi-hazard loss estimation methodology earthquake model HAZUS®MH MR4 technical manual. Department of Homeland Security, Federal Emergency Management Agency, Mitigation Division, Washington, D.C.
8. Gadd, N.R. 1988. Lithofacies relationships in a freshwater–marine transition of the Champlain Sea. In Gadd, N.R. (ed.), The Late Quaternary Development of the Champlain Sea Basin. *Geological Association of Canada*, Special Paper 35, p. 83-–90.
9. Journeay JM, Chow W, Wagner C, Yip J (2021) Physical exposure and patterns of human settlement in Canada. Geological Survey of Canada Open Data Publication (in preparation)
10. Leblanc G (1981) A closer look at the September 1732, Montreal earthquake. Can J Earth Sci 18(3):539–550
11. Mahsuli M, Haukaaas T (2013) Seismic risk analysis with reliability methods, Part II: analysis. Struct Saf 42:63–74
12. Mitchell D, Tinawi R, Law T (1990) Damage caused by the November 25, 1988 Saguenay earthquake. Can J Civ Eng 17(3):338–365
13. National Building Code of Canada (2015) National research council of Canada. Can Comm Build Fire Codes 1:708; 2:696
14. Ploeger SK, Atkinson GM, Samson C (2010) Applying the HAZUS-MH software tool to assess seismic risk in downtown Ottawa, Canada. Nat Hazards 53:1–20
15. Ross M, Parent M, Lefebvre R (2005) 3D geologic framework models for regional hydrogeological and land-use management: a case study from Quaternary basin of south-western Quebec, Canada. Hydrogeol J 13:690–707

16. Rosset Ph, Chouinard L (2011) Microzonage de la ville de Laval, Phase I. Internal Report, McGill University, p 51
17. Rosset Ph, Chouinard L (2010) Microzonage de la ville de Longueuil, phase I. Internal report, McGill University, p 6
18. Rosset Ph, Chouinard LE (2009) Characterization of site effects in Montreal, Canada. Nat Hazards 48:295–308
19. Rosset Ph, Bent A, Chouinard L (2020) Correlating DYFI data with seismic microzonation in the region of montreal. Earth Science Research (ESR) 9(2):85–92. https://doi.org/10.5539/esr.v9n2p85
20. Rosset Ph, Bour-Belvaux M, Chouinard LE (2015) Estimation and comparison of Vs30; microzonation maps for montreal using multiple sources of information. Bull Earthq Eng 13(8):2225-2239
21. Rosset Ph, Kert M, Youance S, Nollet M-J, Chouinard L (2019) Could montreal residential buildings suffer important losses in case of major earthquakes?. In: Extended abstract of the 12th Canadian Conference on Earthquake Engineering, Quebec, Canada, p 7
22. Ulmi M, Wagner CL, Wojtarowicz M, Bancroft JL, Hastings NL, Chow W, Rivard JR, Prieto J, Journeay JM, Struik LC, Nastev M (2014) Hazus-MH 2.1 Canada user and technical manual: earthquake module. Geological Survey of Canada, Open File 7474, p 245
23. Yu K, Rosset Ph, Chouinard LE (2016) Seismic vulnerability assessment for montreal. Georisk 10(2):164–178